AMES GRANT

FINAL REPORT

NAG2-146 IN-91-CR

~~NAS2-6658~~

183412

PIONEER F/G DATA ANALYSIS OF THE ULTRAVIOLET EXPERIMENT

342 P.

(1971 - 1981)

Submitted by

Darrell L. Judge - Principal Investigator
Space Sciences Center and Department of Physics
University Park
Los Angeles, California 90089-1341

VOLUME II

FINAL REPORT

NAS2-6658

PIONEER F/G DATA ANALYSIS OF THE ULTRAVIOLET EXPERIMENT

(1971 - 1981)

Submitted by

Darrell L. Judge - Principal Investigator
Space Sciences Center and Department of Physics
University of Southern California
University Park
Los Angeles, California 90089-1341

Robert W. Carlson - Co-Principal Investigator
Earth and Space Science Division
Jet Propulsion Laboratory
California Institute of Technology
4800 Oak Grove Drive
Pasadena, California 91109

Current Co-Investigators:

Joseph A. Kunc
Fun-Min Wu*
Space Sciences Center
University of Southern California
University Park
Los Angeles, California 90089-1341

Sponsoring Agency Official:

Beverly Robertson
Administrator
Department of Contracts and Grants
Stonier Hall, Room 325
University of Southern California
University Park
Los Angeles, California 90089-1141

* Also at
TECOS Computing, Inc.
1800 Broadview Drive
Glendale, California 91208

VOLUME II

SCIENTIFIC RESULTS

The following reports have been prepared describing our Pioneer 10/11 observations and our theoretical results related to the analysis and interpretation of the Pioneer data. These include our work on the interplanetary physics as well as our study of the atmospheres and environments of Jupiter, Saturn, and their satellites.

Page No.

1. "Pioneer 10 Observation of the Ultraviolet Glow in the Vicinity of Jupiter", Science 183, 317 (1974), D. L. Judge and R. W. Carlson. 12

This report describes the preliminary Pioneer 10 encounter results, particularly the first observation of helium in the atmosphere of Jupiter and the discovery of a hydrogen cloud orbiting Jupiter.

2. "Initial Pioneer 10 Results on the Interplanetary and Interstellar Hydrogen and Helium Glow", Winter Meeting, A.P.S., Los Angeles, 1972, D. L. Judge, R. W. Carlson, K. Suzuki and A. L. Morse. 16

The report deals with the interplanetary glow and the first positive evidence for interplanetary He emissions. The flow direction (α = 240°) was discussed.

3. "Pioneer 10 Ultraviolet Photometer Measurements of Interplanetary Hydrogen and Helium" Winter Meeting, AGU, San Francisco, 1973, D. L. Judge, R. W. Carlson, K. Suzuki and A. L. Morse. 17

Additional parameters of the interplanetary gas were discussed, and the influence of self-reversed lines.

4. "Pioneer 10 Ultraviolet Photometer Observations at Jupiter", presented at the 55th Annual Spring Meeting of the AGU, Washington, D. C., April, 1974, R. W. Carlson, and D. L. Judge. (Invited paper). 18

The Jupiter H_2/He ratio was presented along with the

Page No.

the cloud results and a theory of the source and loss mechanisms involving the plasmasphere.

5. "Possibility of O III λ 304 Å Emissions in the Extreme Ultraviolet Airglow", Letter, J. Geophys. Res. 77, 6282 (1972), R. W. Carlson. 19

Based on terrestiral measurements, one of the possible components of the interplanetary glow observed by Pioneer 10 was thought to be due to He^+. This problem was examined and it was found that the interpretation of the terrestrial measurements can be confused by O^{++}.

6. "Pioneer 10 Ultraviolet Photometer Observations at Jupiter Encounter", J. Geophys. Res. 79, 3623 (1974), D. L. Judge and R. W. Carlson. 21

The initial results from the Jupiter Encounter are analyzed in rather complete fashion.

7. "Atmospheres of Outer Planet Satellites", Exploration of the Outer Solar System", MIT Press, 1975, R. W. Carlson. 32

8. "Pioneer 10 Ultraviolet Photometer Observations of the Jovian Hydrogen Torus", Icarus, 24, 395 (1975), R. W. Carlson and D. L. Judge. 60

9. "Pioneer 10 Observations of the Interplanetary Ultraviolet Glow", presented at Fall Meeting, Amer. Geophys. Union, San Francisco, 1975, K. Suzuki, R. W. Carlson, D. L. Judge and A. L. Morse. 65

10. "On the Invertibility of Mutual Occultation Light Curves", presented at 1975 D.P.S. Meeting, Columbia, Md., February 1975, R. T. Brinkmann. 66

11. "On the Invertibility of Mutual Occultation Light Curves", Icarus 27, 69 (1976). 67

12. "Electron Impact Ionization of Io's Sodium Emission Cloud", Geophys. Res. Lett. 2, 469 (1975), R. W. Carlson D. L. Matson, and T. V. Johnson. 88

Page No.

13. "The Problem of Hydrogen at Io", presented at the Division for Planetary Sciences (AAS) meeting, Austin, Texas, April, 1976, R. W. Carlson and D. L. Judge — 92

14. "Pioneer 10 Ultraviolet Photometer Observations of Jupiter: the Jovian Helium to Hydrogen Ratio", Jupiter, University of Arizona Press, 1976, R. W. Carlson and D. L. Judge. — 93

15. "Sodium D-Line Emission from Io: Line Profiles and and Synoptic Observations", presented at the Division for Planetary Sciences (AAS) Meeting, Austin, Texas, April 1976, D. L. Matson, R. W. Carlson, J. T. Bergstralh, J. W. Young, and T. V. Johnson. — 116

16. "Pioneer Ultraviolet Photometer Measurements of the Jovian Satellites", Jupiter, University of Arizona Press, 1976, D. L. Judge, R. W. Carlson, F. M. Wu and U. G. Hartmann. — 117

17. "Io's Atmosphere and Ionosphere: New Limits on Surface Pressure from Plasma Models", presented at the Division for Planetary Sciences (AAS) Meeting, Austin, Texas, April 1976, T. V. Johnson, D. L. Matson, and R. W. Carlson. — 151

18. "Io's Atmosphere and Ionosphere: New Limits on Surface Pressure from Plasma Models", Geophys. Res. Lett., 3, 293 (1976), T. V. Johnson, D. L. Matson and R. W. Carlson. — 152

19. "Europa: Ultraviolet Emissions and the Possibility of Atomic Oxygen and Hydrogen Clouds", Astrophy. J., 225, 325 (1978), F. M. Wu, D. L. Judge and R. W. Carlson. — 156

20. "Electron Heating of Interplanetary Medium", Astrophy. J., 225, 1045 (1978), F. M. Wu and D. L. Judge. — 166

21. "Europa: Ultraviolet Emissions and the possibility of Atomic Oxygen and Hydrogen Clouds", presented at the Fall Meeting, American Geophys. Union, San Francisco, 1977, F. M. Wu and D. L. Judge. — 171

22. "Electron Heating of Interplanetary Medium" presented at the Fall Meeting, Amer. Geophys. Union, San Francisco, 1977, F. M. Wu and D. L. Judge. — 172

23. "Temperature and Flow Velocity of the Interplanetary Gases Along Solar Radii", 1979, Ap. J. 231, 574 (1979), F. M. Wu and D. L. Judge. — 173

Page No.

24. "Modification of Solar Lines Propagating Through the Interplanetary Medium", J. Geophys. Res., 84, 1979, F. M. Wu and D. L. Judge. 185

25. "Temperature and Flow Velocity of Interplanetary Gas along Solar Radii and the Resulting Modification of Solar Lines Propagating through the Interplanetary Medium", presented at the Fall Meeting, American Geophys. Union, San Francisco, 1978, F. M. Wu and D. L. Judge. 189

26. "Pioneer 10 UV Photometer Observations of the Interlanetary Glow at Heliocentric Distances from 2 to 17 AU" presented at the Spring Meeting, American Geophys. Union, Washington, 1979, F. M. Wu and D. L. Judge. 190

27. "Extreme Ultraviolet Observations of Astrophysical Plamsa" presented at U.S.-Japan Seminar of Plasma Spectroscopy, Kyoto, Japan, May 7 - 11, 1979, D. L. Judge; also published in the proceedings. 191

28. "A Re-Analysis of the Observed Interplanetary Hydrogen Hy- Emission Profiles and the Drived Local "Interstellar" Gas Temperature and Velocity", Astrophys. J., 239, 389 (1980), F. M. Wu and D. L. Judge. 195

29. "Pioneer 11 Ultraviolet Photometer Measurements of the Saturn System" presented at Fall Meeting of the AGU, San Francisco, December 3 to 7, 1979, D. L. Judge, F. M. Wu and R. W. Carlson. (Invited Paper). 201

30. "Ultraviolet Photometer Observations of the Saturnian System", Science 207, 431 (1980), D. L. Judge, F. M. Wu, and R. W. Carlson. 202

31. "Observations of Extreme Ultraviolet Emissions from the Saturnian Plasmasphere", J. Geophys. Res., 85, 5853 (1980, F. M. Wu, D. L. Judge and R. W. Carlson. 206

32. "Survival Probabilities for Interstellar Hydrogen Flowing into the Interplanetary System from Far Regions of the Heliosphere", Planet. Space Sci. Vol. 28, pp. 815 - 821, Pergamon Press Ltd., 1980, J. A. Kunc. 210

33. "H_2^+ Ultraviolet Emissions from Jupiter", presented at the Spring Meeting of the AGU, Baltimore, 1981, F. M. Wu and D. L. Judge. 217

34. "Electron-Capture Cross Sections for Some Astrophysical Proce-ses", Geophysical Research Letters, 8, 177 (1981), J. A. Kunc and D. L. Judge. 218

Page No.

35. "Photochemistry of SO_2 in the Atmosphere of Io and Implication on Atmospheric Escape", submitted for publication to JGR, June 1981, S. Kumar. 220

36. "Pioneer 10 Ultraviolet Photometer Observations of the Interplanetary Glow at Heliocentric Distances from 2 to 14 A.U., Astrophysical Journal 245: 1145 - 1158, May 1981, F. M. Wu, K. Suzuki, R. W. Carlson, and D. L. Judge. 248

37. "Heating of the Interstellar Medium by the Solar Wind", Astrophysical Journal, 1981, J. A. Kunc, F. M. Wu and D. L. Judge. (In press). 262

38. "Radial Energy Distribution of the Low Energy Protons in Io's Atmosphere", D. L. Judge and J. A. Kunc. (Manuscript in preparation). 292

39. "Some Remarks of the Use of Spacecraft-Based Measurement to Describe the Dynamics of Planetary Magnetospheres", 1981, J. A. Kunc and D. L. Judge. (Manuscript in preparation). 332

Pioneer 10 Observations of the Ultraviolet Glow in the Vicinity of Jupiter

D. L. Judge, R. W. Carlson

Abstract. *A two-channel ultraviolet photometer aboard Pioneer 10 has made several observations of the ultraviolet glow in the wavelength range from 170 to 1400 angstroms in the vicinity of Jupiter. Preliminary results indicate a Jovian hydrogen (1216 angstrom) glow with a brightness of about 1000 rayleighs and a helium (584 angstrom) glow with a brightness of about 10 to 20 rayleighs. In addition, Jupiter appears to have an extensive hydrogen torus surrounding it in the orbital plane of Io. The mean diameter of the torus is about equal to the diameter of the orbit of Io. Several observations of the Galilean satellites have also occurred but only a rather striking Io observation has been analyzed to date. If the observed Io glow is predominantly that of Lyman-α, the surface brightness is about 10,000 rayleighs.*

The ultraviolet instrument (1) on Pioneer 10 is a two-channel photometer designed to observe the resonance emissions from atomic hydrogen and helium at 1216 Å (the H Lyman-α line) and 584 Å respectively. The instrument uses a filter and photocathodes to isolate these two emission features.

Detailed calculations (2) show that the hydrogen and helium resonance lines are the strongest features to be expected from the outer atmosphere of Jupiter, and arise from resonance scattering of the incident solar hydrogen and helium lines; thus, only broadband isolation of these lines is required. The He channel uses a thin aluminum film as a filter and LiF as a photocathode, resulting in a spectral band pass of approximately 200 to 800 Å. The hydrogen channel uses the fron surface of the Al film

as a photocathode for which the photoelectric response extends up to about 1400 Å. This channel is sensitive to both hydrogen and helium emissions, but the former is more intense by more than an order of magnitude, so the recorded signals accurately represent the Lyman-α intensity.

The optical axis of the photometer is oriented at 20° to the spacecraft spin axis while the instantaneous field of view is approximately 1° by 20° with the longer dimension tangential to the 20° are swept out by the spacecraft rotation.

This orientation was chosen to give two views of Jupiter, the first occurring at approximately 50 Jovian radii (R_j), and outside the predicted radiation belts, while the second observation period occurred at about 10 R_j. In addition, several observations of the Galilean satellites were possible during the 5 days before closest approach.

During the first Jupiter viewing period emissions from the planet were observed in both the hydrogen and helium channels but the data obtained during the second viewing period suffered degradation due to the energetic radiation belt particles. The preliminary estimate of the hydrogen Lyman-α intensity is somewhat less than 1000 rayleighs (3) while that of the He emission is approximately 10 to 20 rayleighs. Helium emissions have not previously been observed from Jupiter although the presence of He has been speculated on for many years.

The present Lyman-α measurements are lower than the sounding rocket observations of Rottman et al. (4). This discrepancy may be partially due to variations in the solar Lyman-α flux, differences in atmospheric properties which depend on solar activity, and calibration uncertainties.

Ultraviolet emissions were also observed in the hydrogen channel from the innermost Galilean satellite Io (JI). It is reasonable to assume

that these emissions correspond to Lyman-α since the surface of Io is thought to consist of hydrogen-bearing ices of NH_3 and H_2O (5). The atomic hydrogen could result from photolysis and particle bombardment of the atmosphere and surface. If H Lyman-α is the main contributor, the source brightness is approximately 10,000 rayleighs. Such an intensity would seem to require an excitation mechanism in additon to resonance scattering. Aurora-like activity, as produced by energetic electrons accelerated toward Io by its motional electromotive force (6), seems an attractive possibility.

Finally, hydrogen channel signals were observed from the equatorial plane of Jupiter during periods when neither the planet nor its satellites were in the field of view. These emissions of several hundred rayleighs in intensity are tentatively interpreted as due to a toroidal cloud of neutral hydrogen in orbit around Jupiter, similar to the hydrogen torus proposed by McDonough and Brice (7) for Saturn and Jupiter (8). Preliminary analysis indicates that this gas cloud occurs at approximately the orbit of Io, suggesting that this satellite is the source.

References and Notes

1. The instrument was built at the Analog Technology Corp., Pasadena, California, under the supervision of D. Willingham. The liaison with Ames Research Center and the spacecraft interface were handled by T. Wond and R. Tworowski.
2. R. W. Carlson and D. L. Judge, Planet. Space Sci. 19, 327 (1971).
3. One rayleigh corresponds to a column excitation rate of 10 photons cm^{-2} sec^{-1}.
4. G. J. Rotiman, H. W. Moos, C. S. Freer, Astrophys. J. 184, L89 (1973).
5. T. V. Johnson and T. B. McCord, Icarus 13, 37 (1972).
6. P. Goldreich and D. Lynden-Bell, Astrophys. J. 156, 59 (1969).
7. T. R. McDonough and N. M. Brice, Icarus 20, 136 (1973).
8. _____, private communication, July 1973.

Initial Pioneer 10 Results on the Interplanetary and Interstellar Hydrogen and Helium Glow*.

D. L. Judge, R. W. Carlson, K. Susuki, A. L. Morse

Abstract presented at the Winter meeting of the APS, Los Angeles, 1972.

Recent measurements of the hydrogen Ly-α and helium 584 Å resonance scattering as observed from the Pioneer 10 spacecraft will be presented. The spatial distribution of both hydrogen and helium can be inferred from these data and indicate that the maximum densities occur near the plane of the ecliptic. The result on the hydrogen distribution is in agreement with previous earth orbiting spacecraft investigations. The helium glow has not been previously measured. The present data represent the first such measurements obtained over a large radial distance from the sun and thus provide unique data on the density and velocity of the two gases in the "local" interstellar medium. Implications of a model consistent with the experimental observations will be presented.

* Work supported by the National Aeronautics Space Administration.

Pioneer 10 Ultraviolet Photometer Observations of the Interplanetary Glow*.

D. L. Judge, R. W. Carlson, K. Suzuki, A. L. Morse

Abstract presented at the Winter Meeting of the AGU, San Francisco, 1973.

The ultraviolet experiment on Pioneer 10 is a two channel photometer designed to measure the interplanetary/interstellar, and Jovian hydrogen and helium glow at λ1216 Å and λ584 Å, respectively. A description of the instrument will be given along with a discussion of the observations obtained during the interplanetary cruise. The observed emissions from the interplanetary gas are interpreted as arising from resonance scattering of the solar H and He lines. Since the lifetime of neutral atoms in the interplanetary region is short, owing to solar ultraviolet photo-ionization and charge exchange with the solar wind, various models have been proposed as sources for the interplanetary glow. The Pioneer 10 data are compared with these theoretical models and are found to be consistent with an interstellar wind model in which relative motion between the solar system and the local interstellar gas results in a flux of neutral atoms penetrating into the solar system. The density distribution, speed and flow direction of the inflowing gas are model parameters determined from the flight data. Present results on both the hydrogen and helium parameters will be presented.

* This work is based upon research reports prepared for the Ames Research Center, NASA, under Contract Mod 7 NAS2-6558.

Pioneer 10 Ultraviolet Photometer Observations at Jupiter*.

R. W. Carlson, D. L. Judge

Abstract presented at the 55th Annual Spring Meeting of the AGU, Washington, D. C. April 1974

A two channel ultraviolet photometer on Pioneer 10 observed ultraviolet emission in the vicinity of Jupiter during the Pioneer 10-Jupiter encounter. The results show a Jovian atomic hydrogen Lyman-α (1216 Å) glow of approximately 500 Rayleighs and a helium (584 Å) glow of $\sim$20 Rayleighs. These data are interpreted using a model atmosphere and radiative transfer calculations to give the effective atmospheric eddy diffusion coefficient and the lower atmosphere He/H_2 ratio. In addition to the Jovian observations, ultraviolet emissions from the Galilean satellites were investigated. Io was found to possess a bright ultraviolet glow wth a brightness of several thousand Rayleighs and is suggested to be due to hydrogen Lyman-α. Ultraviolet emissions were also observed from the equatorial plane of Jupiter when neither the planet nor the satellites were in the field of view. These observations are interpreted as a hydrogen cloud in orbit around Jupiter and occurring at approximately the orbit of Io. The data are used to determine the dimensions and densities of the cloud.

* This work is based upon research supported by NASA Ames Research Center under Contract No. NAS2-6558.

VOL. 77, NO. 31 JOURNAL OF GEOPHYSICAL RESEARCH NOVEMBER 1, 1972

Possibility of O III λ304-A Emissions in the Extreme Ultraviolet Airglow

R. W. CARLSON

Department of Physics, University of Southern California
Los Angeles, California 90007

Recent measurements of extreme ultraviolet airglow emissions in the 200- to 400-A region [*Ogawa and Tohmatsu*, 1971; *Young et al.*, 1971] have been interpreted as emissions arising from resonance scattering of solar extreme ultraviolet radiation by He^+ ions. This letter points out that these measurements and future airglow observations at this wavelength may contain a significant contribution from doubly ionized atomic oxygen ions, a species that has been found in the ionosphere and has a resonance line nearly coincident with the He^+ line.

The He II resonance line occurs at λ303.782 A, whereas the $2p^2\ ^3P_2$–$2p3d\ ^3P_2^\circ$ transition of O^{++} occurs at λ303.799 A. When it is assumed that the solar He II line is broadened over the wavelength difference of 17 mA (caused, for example, by chromospheric turbulence velocity fields), O^{++} ions can absorb and re-emit the solar He^+ line. Indeed, such a process is well known in gaseous nebulae. The importance of O^{++} emissions in relation to He^+ in the terrestrial atmosphere can be assessed by a comparison of the respective column densities appropriate for the observational conditions and the oscillator strengths of the two transitions.

The observation of an ion with a mass-to-charge ratio of 8 (assumed to be O^{++}) has been reported by *Hoffman* [1967, 1969] and *Hoffman et al.* [1969]. The rocket results of Hoffman et al. covering the altitude range 400–700 km show O^{++} densities greater than He^+ densities by an average factor of 1.3. Two sets of satellite data, for which the ratio of the integrated ion densities is approximately equal, are also given for the altitude range 700–1000 km. On the other hand, *Hoffman* [1969] gives O^{++} densities less than He^+ densities by >1 order of magnitude. The occurrence of the O^{++} ion has been investigated theoretically by *Walker* [1970]. He suggests that the drift velocity of O^{++} in the region 300–550 km is determined by the motion of the dominant O^+ ion and calculates the O^{++} density from the rate of photoionization and the ambipolar diffusion velocity of O^+ ions. The resulting densities are greater than those observed in the rocket measurements of Hoffman et al. by approximately 1 order of magnitude. Although the O^{++} ion is not widely observed (possibly owing to instrumental differences or large temporal or spatial variations) and the available results show large variations, we contend that the O^{++} density may be comparable to the He^+ density.

The oscillator strength of the O III $^3P_2$–$^3P_2^\circ$ transition is given by *Weise et al.* [1966] as f(O III) = 0.11, the atomic scattering albedo being $\bar{\omega} \simeq 0.98$, in comparison with f(He II) = 0.4162. It is assumed that the J levels of the O III ground state are populated according to their statistical weight and that the two lines are scattered isotropically. When it is assumed that the solar line is flat over the 17-mA wavelength interval and the lower-altitude abundances of Hoffman et al. for a hypothetical dayglow observation are used, the relative intensities of the two lines are

$$\frac{4\pi I(\text{O III})}{4\pi I(\text{He II})} = \frac{2J+1}{\sum(2J+1)} \cdot \frac{\bar{\omega} f(\text{O III})}{f(\text{He II})} \frac{N(\text{O III})}{N(\text{He II})}$$

$$\simeq \frac{5}{9} \cdot \frac{(0.98)(0.11)}{(0.4162)} \cdot 1.3$$

$$\simeq 0.2$$

A self-reversed solar He II line would increase this ratio. Comparison with the existing evening measurements is somewhat more difficult, owing

Copyright © 1972 by the American Geophysical Union.

to uncertainties in the variation of the two ion densities, both latitudinally and diurnally. Although the 304-A observations of *Young et al.* [1971] appear to be satisfactorily explained by *Meier and Weller* [1972] as scattering by He^+ in the plasmasphere, an O^{++} contribution does not seem entirely impossible.

It is concluded that the O III line may be of some consequence in the extreme ultraviolet airglow, particularly for a self-reversed solar line, and therefore some caution in the interpretation of 304-A airglow purely in terms of He^+ densities is suggested.

Acknowledgments. Parts of this work were supported by NASA contract NAS 2-6558.

• • •

The Editor thanks R. R. Meier and A. F. Nagy for evaluating this letter.

REFERENCES

Hoffman, J. H., Composition measurements of the topside ionosphere. *Science*, *155*, 322, 1967.

Hoffman, J. H., Ion mass spectrometer on the Explorer 31 satellite, *Proc. IEEE*, *57*, 1063, 1969.

Hoffman, J. H., C. Y. Johnson, J. C. Holmes, and J. M. Young, Daytime midlatitude ion composition measurements, *J. Geophys. Res.*, *74*, 6281, 1969.

Meier, R. R., and C. S. Weller, EUV resonance radiation from helium atoms and ions in the geocorona, *J. Geophys. Res.*, *77*, 1190, 1972.

Ogawa, T., and T. Tohmatsu, Sounding rocket observation of helium 304- and 584-A glow, *J. Geophys. Res.*, *76*, 6136, 1971.

Walker, J. C. G., The density of O^{++} ions in the topside ionosphere, *Planet. Space Sci.*, *18*, 559, 1970.

Weise, W. L., M. W. Smith, and B. M. Glennon, *Atomic transition probabilities*, vol. I, *Hydrogen through Neon*, *Nat. Stand. Ref. Data Ser. 4*, p. 97, U.S. Government Printing Office, Washington, D.C., 1966.

Young, J. M., C. S. Weller, C. Y. Johnson, and J. C. Holmes, Rocket observations of the far UV nightglow at Lyman alpha and shorter wavelengths, *J. Geophys. Res.*, *76*, 3710, 1971.

(Received May 26, 1972;
accepted June 30, 1972.)

Pioneer 10 Ultraviolet Photometer Observations at Jupiter Encounter

R. W. CARLSON AND D. L. JUDGE

Department of Physics, University of Southern California, Los Angeles, California 90007

A two-channel extreme ultraviolet photometer on Pioneer 10 was used to investigate hydrogen and helium emissions from the atmosphere of Jupiter and emissions associated with the Galilean satellites. The hydrogen Lyman α signal observed from Jupiter corresponded to 400 R in brightness. By using the results of Wallace and Hunten, the eddy diffusion coefficient is found to be $K = 3 \times 10^{8\pm1}$. The He I λ584-Å emission rate was found to be 5.1 R. The radiative transfer problem for the resonantly scattered He I emissions was investigated in the coherent approximation. With these results, the observed brightness, and the derived eddy diffusion coefficient the He/H_2 ratio in the mixing region of the atmosphere was found to be $[He]/[H_2] = 0.18_{-0.10}^{+0.40}$. Emissions attributed to H I Lyman α were found at the orbital radius of Io and appear to be due to resonance scattering by a toroidal cloud of H in orbit around Jupiter. The torus is not complete, however, but extends over ~120° of the orbit, approximately centered at Io. The cloud is less than the size of Jupiter in the vertical extent, and the observed brightness indicates a total of ~2×10^{29} H atoms in the cloud.

The Pioneer 10 mission was designed to investigate the interplanetary region and the planet Jupiter and its environment at encounter in December 1973. This mission has provided a unique opportunity to investigate through optical measurements the interplanetary gas and the atmospheres of Jupiter and its satellites. Of particular interest are the two most abundant elements in the cosmos, hydrogen and helium. The strongest optical transitions in these elements, the resonance lines, occur in the vacuum region of the ultraviolet, and thus their ground-based detection is impossible. A two-channel extreme ultraviolet photometer for investigation of these emissions was included in the scientific payload of the Pioneer 10 spacecraft and has obtained successful measurements of the interplanetary gas and at Jupiter encounter. The interplanetary results have been presented [*Judge et al.*, 1972, 1973] and will be discussed in more detail in subsequent papers. This work is concerned with the encounter results that have been presented in preliminary form [*Carlson and Judge*, 1974; *Judge and Carlson*, 1974]. A brief description of the instrument and the trajectory is given below, followed by results and their analysis.

INSTRUMENTATION

The weight, power, and reliability constraints necessitated the choice of a simple photometric system for the ultraviolet measurements. The Pioneer 10 ultraviolet experiment is a two-channel photometer that uses the transmission properties and photoelectric response of materials to measure intensities in two spectral regions. A schematic diagram of the instrument is shown in Figure 1. The field of view is defined by a mechanical collimator. Radiation transmitted through the collimator is incident upon a thin film filter through which short-wavelength photons are transmitted. These photons strike a photocathode, thereupon producing photoelectrons that are accelerated through a 180-V potential into the input cone of a channel electron multiplier. The front surface of the filter is used as a photocathode with a second electron multiplier to detect the longer-wavelength Lyman α photons. The pulses of charge appearing at the anodes are amplified with charge sensitive amplifiers and passed to a discriminator. An electronic switch commutates between the two channels every two rolls of the spacecraft, i.e., approximately every 25 s. The pulses are accumulated over the frame period of the spacecraft telemetry system (⅓ s at Jupiter encounter). The accumulated counts are logarithmically compressed to 9 bits and sampled by the telemetry system for transmission.

A cover was placed over the entrance aperture to prevent dust particles from entering the instrument and to protect the thin film filter from escaping air currents during launch. The cover was deployed 6 days after launch.

The instrument weighs 680 gm (1.5 lb) and consumes 0.67 W. The angular response characteristics, the spectral response, and aspects of the electron multipliers are discussed below.

Angular response. The field of view of the photometer is determined by a mechanical collimator of the McGrath type. The optical axis of the collimator is oriented at an angle θ_0 to the spacecraft spin axis (Figure 2), a scanning motion resulting as the spacecraft rotates. The design value of θ_0 is 20°, whereas from stellar observations the actual value was found to be $\theta_0 = 20.25° \pm 0.10°$.

The collimator consists of a series of seven plates arranged in the spacing suggested by *McGrath* [1968] with an overall length of 10.16 cm. Each plate contains five rectangular apertures with widths of 0.203 cm; the lengths (and the corresponding number of baffles) are 1.92 (1 baffle), 1.76 (2 baffles), and 1.36 (2 baffles) cm. The long dimension of the baffles is oriented tangentially to the cone swept out by the spacecraft revolution. The entrance area of the collimator is $A = 0.66$ cm², and the effective solid angle of acceptance $\Omega = 3.28 \times 10^{-3}$ sr, resulting in a geometric factor of 433 photons/s R for a uniform diffuse source. The angular response for a point source at angles (θ, $\Delta\psi$) as defined in Figure 2 is shown in Figure 3. The angular resolution is $\Delta\theta \approx 1°$.

The response of the instrument to a finite extended source such as Jupiter is obtained by integrating over the field of the object. In addition, one must include the finite integration time and the angular velocity of the spacecraft rotation.

The plates of the collimator were coated with platinum black to reduce internal reflections. Measurements of the off-axis response in the near ultraviolet showed rejections of approximately 10^4 for $|\Delta\theta| = 5°$ and approximately 10^6 for $|\Delta\theta| > 10°$. It is expected that the off-axis rejection is even greater in the extreme ultraviolet.

Spectral response. Since the hydrogen and helium

Copyright © 1974 by the American Geophysical Union.

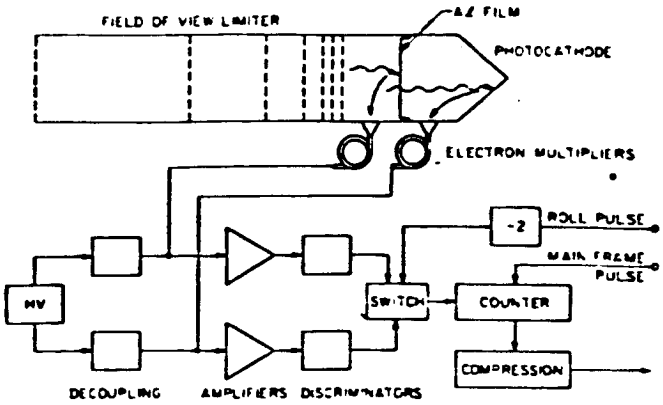

Fig. 1. Schematic diagram of the ultraviolet photometer instrument. Short-wavelength photons passing through the field of view limiter and Al filter strike a LiF photocathode to produce photoelectrons. These events are then amplified and counted. The front of the Al film is used for detection of longer-wavelength photons.

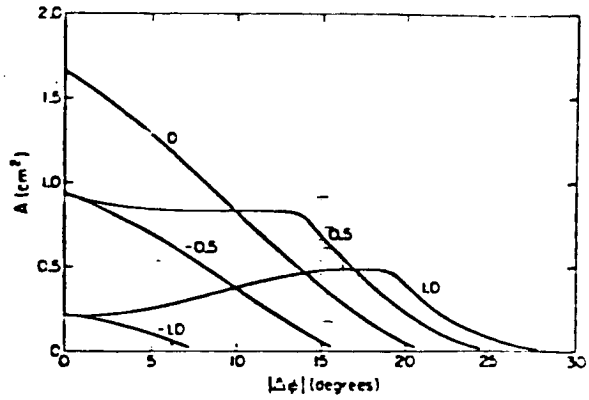

Fig. 3. Angular response of the collimator. The effective area is shown as a function of displacement in clock angle for various differences in cone angle $\theta - \theta_0$.

resonance lines, at λ1216 Å and λ584 Å, respectively, are expected to be the dominant features in the interplanetary and Jovian emission spectrum, only broad band isolation of these features is required. Because the hydrogen intensity is much greater than the helium line, it is necessary to discriminate effectively against it in the He channel. To accomplish this function, the present photometer uses an Al thin film filter approximately 1500 Å thick coated on both sides with 100 Å of SiO and a LiF-coated photocathode. The transmission properties of aluminum have been studied by *Hunter et al.* [1965] and others. Laboratory experience has shown it to be one of the most stable and shock resistant of the metallic filters used in the extreme ultraviolet. The photocathode material was chosen because of its large photoelectric yield at 584 Å and the relative insensitivity to H Lyman α radiation [*Samson*, 1967; *Byram et al.*, 1961].

The spectral response of the instrument was measured in relation to the response of sodium salicylate, for which the yield has been found to be constant in the spectral region of interest [*Samson*, 1967]. The measurements were placed on an absolute scale, using a rare gas double ionization chamber. The resulting efficiency as a function of wavelength is shown in Figure 4. For a uniform diffuse source that fills the field of view the sensitivity of the instrument at λ584 Å is 7.3 counts/s R and 4.9 counts/s R at 1216 Å. This latter channel is sensitive also to shorter-wavelength radiation, but these emissions are much weaker than the H Lyman α signal, and their contribution to the long-wavelength channel can be ignored. The sensitivity of the helium channel to Lyman α was found to be a factor of 1000 less than that of the hydrogen channel. This residual sensitivity is greater than would be expected on the basis of film transmissions and photoelectric response measurements and is due to photoelectrons liberated from the back surface of the filter.

Particular care was taken to extend the calibration to long wavelengths in order to evaluate the contribution from Rayleigh scattered radiation from the atmosphere of Jupiter. By using the albedo of *Anderson et al.* [1969], this contribution is found to be small, of the order of 10 counts/s.

Electron multipliers and associated circuitry. The electron

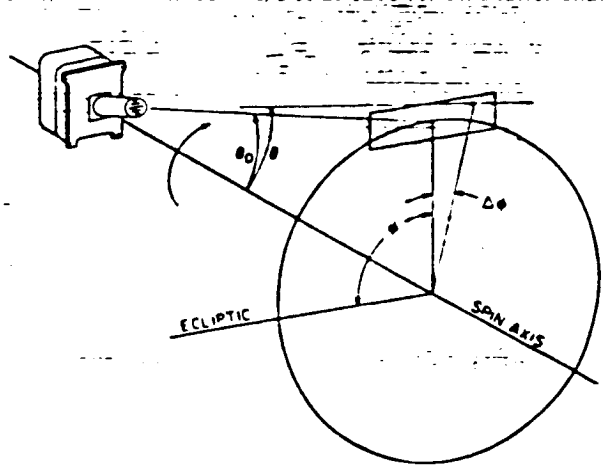

Fig. 2. Viewing geometry of the photometer. The optical axis is at an angle $\theta_0 \approx 20°$ to the spin axis. The angle ϕ is the clock angle relative to the ecliptic.

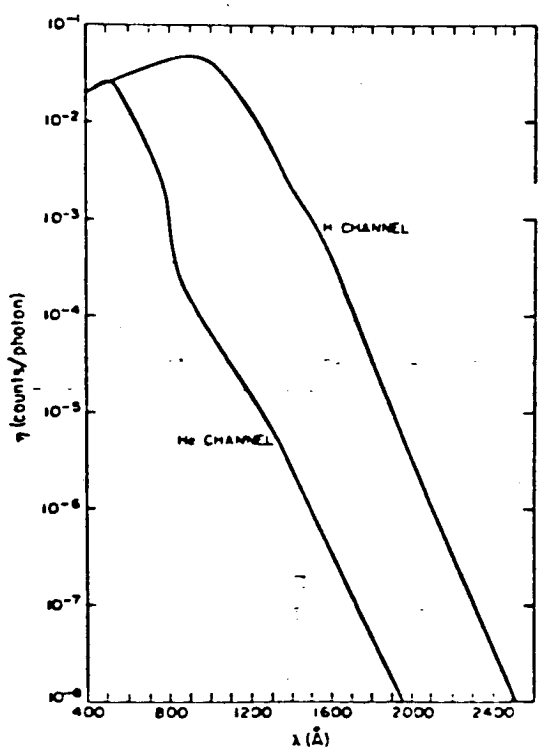

Fig. 4. Spectral response of the photometer. The quantum efficiency in photoelectrons per photon is shown for the two channels as a function of wavelength and includes photoelectric response, filter transmission, and collection efficiency.

multipliers used in the experiment are Bendix model 4028 continuous channel multipliers and are operated with an anode to cathode voltage of 3500 V. This results in gains of approximately 5×10^7 and places the multipliers in the gain saturation mode. The pulses appearing at the anode are amplified with charge sensitive amplifiers, followed by fixed dead time (3 μs) discriminators. The dynamic range of the amplifier-discriminator combination is 1000:1. The upper level is set at 10 times the nominal multiplier output to allow for any individual gain variations, and the lower limit, a factor of 100 less than the nominal output, is designed to allow for any gain degradation of the multipliers during the mission.

This degradation of channel multipliers with use has been of some concern. Studies in this laboratory and elsewhere have shown that if the units are properly screened before selection, the channel multipliers can be operated to at least 2×10^{12} total accumulated counts with no serious indication of fatigue. The accumulated counts in the present instrument are 1.5×10^{11} for the hydrogen channel and much less for the other channel.

The dark counting rate for the two channels is approximately 3 counts/s and is due to radiation from the radio isotope thermoelectric generators on the spacecraft.

TRAJECTORY, VIEWING OPPORTUNITIES, AND BACKGROUND RATES

The Pioneer spacecraft is spin-stabilized with the spin axis fixed in inertial space and adjusted to be earth pointing, and thus maximum data transmission is provided by the high-gain antenna, which is coaxial with the spin axis. The photometer optical axis is positioned at an angle of $\theta_0 \simeq 20°$ with respect to the spin axis; consequently, the field of view swept out by the spin motion is an annular ring 40° in diameter that is fixed in the celestial sphere. The period between spin axis reorientations is determined by the relative earth-Pioneer trajectory and is typically 10–20 days.

The spacecraft as seen from the earth moves west with respect to Jupiter and from south to north. Conversely, an observer moving with the spacecraft would see the Jovian system moving west to east. The minimum cone angle θ attained by Jupiter is $\simeq 10°$. The apparent motion and the angular size of Jupiter, as well as the instrumental field of view, are shown in Figure 5. It is evident from the figure that two viewing periods of Jupiter occur, the first being centered on day 335 at 1600 with a duration of approximately 20 hours and the second occurring on day 337 at 2100 and lasting approximately 3 hours. (All times employed here are earth received times expressed in UT. Periapsis passage occurred on day 338 at 0310.) The planetocentric distance at these times was 46 R_J (Jovian radii) and 9 R_J, respectively. The design value of the cone angle θ_0 was chosen with the predicted Jovian radiation belts in mind. The first low-resolution view of the planet was intended to provide intensity measurements from outside the radiation zones, and the second period was intended to provide higher-resolution scans in a region where the energetic charged particle background was not too intense. In reality, the radiation belts were quite different than was expected, and their influence will be discussed in a following paragraph.

The phase angle of Jupiter at the time of the first viewing period was 30°, decreasing to 15° at the second opportunity.

The orbital motion of the Galilean satellites and the west to east motion of the Jovian system across the field of view

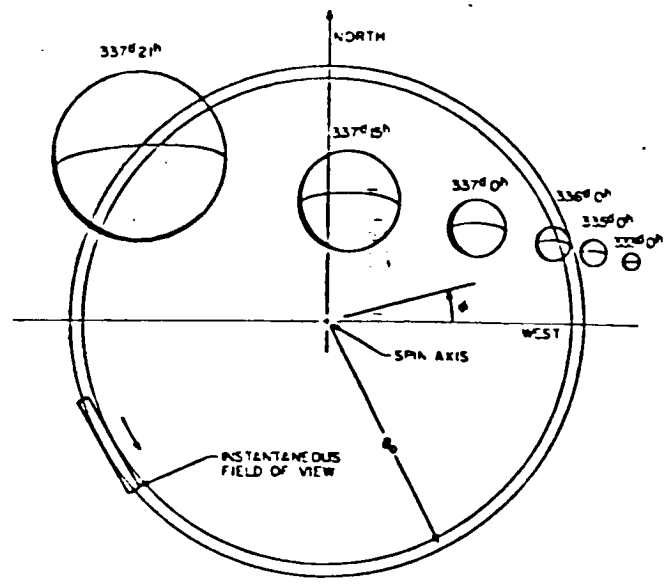

Fig. 5. Jupiter viewing opportunities. The apparent motion of Jupiter across the field of view results in two viewing periods.

provided several opportunities to observe these planets and their environment. Figure 6 shows the cone angles of the Galilean satellites. The specific observations are discussed in a following section.

The only stars in the field at encounter were of spectral class A or later and too cold to emit radiation detectable with the photometer.

The spacecraft crossed the bow shock and entered the magnetosheath of Jupiter on day 330, several days earlier than was expected. Prior to that time the photometer readings corresponded to the interplanetary glow, approximately 150 R of H I Lyman α (750 counts/s) and approximately 0.7 R for the He I λ584 Å (5 counts/s). Occasional bursts of noise due to upstream high-energy particles were observed and correlated with similar observations by the high-energy charged particle experiments on the spacecraft. When the spacecraft crossed the bow shock, the counting rate increased for both channels, the hydrogen channel showing an increase by a factor of 5 and the helium channel showing an increase by an approximate factor of 10. On the approach to Jupiter the average counting rate increased in both channels, with fluctuations corresponding to the rotation period of Jupiter. The observed intensities and temporal fluctuations, particularly for the helium channel, correlated very well with the high-energy particle measure-

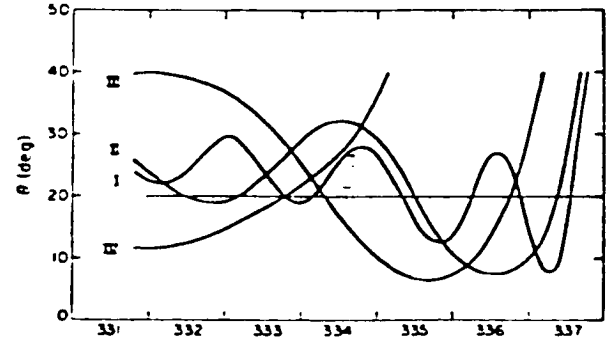

Fig. 6. Satellite viewing opportunities. The cone angle of the Galilean satellites (I–IV) is shown as a function of day. The 20° field is shown; each crossing of this line corresponds to an observing opportunity.

ments as obtained by the University of Iowa experiment and others, this correlation suggesting that the background counts were due to the secondary electrons and γ rays produced by these energetic particles. Occasional anticorrelation with the helium channel and high-energy data was observed in the hydrogen channel, implying an additional source of background counts for this channel during those periods. A possible candidate might be a high-temperature plasma that could enter the open field of view limiter.

Even though the background counting rate was relatively high, successful ultraviolet observations could be obtained, owing to the spin scanning of the spacecraft. The background was observed to be generally isotropic, whereas the optical signals were highly directional. Therefore the ultraviolet signals could be identified as features of small angular width superimposed on a slowly varying background.

In addition to producing the background noise counting rate, the radiation belts of Jupiter influenced the experiment in another fashion. On December 3, 1973 (day 337), the flux of energetic electrons and protons showed a rapid increase. A corresponding rise in the background was observed in the present instrument, the relative increase being greatest for the helium channel. On day 337 at 1500 a maximum was attained, followed by a decrease in the background rate, even though the proton and electron fluxes continued to increase. This decrease was due to a temporary loss of sensitivity; indeed by the end of day 337 the count rate for both channels had been reduced to a few counts per second, well below even the interplanetary value. Consequently, no ultraviolet data were obtained during the second viewing period of Jupiter. This unfortunate degradation of the instrument sensitivity was only temporary, however. After the spacecraft left the vicinity of Jupiter, the counting rate gradually returned to the interplanetary value within a time scale of several days. This behavior leads one to suspect that the loss in sensitivity was due to damage to circuit components and subsequent annealing.

OBSERVATIONS OF JUPITER

Experimental measurements. Successful measurements were obtained in both channels during the first observation period. The long-wavelength channel results are shown in Figure 7, and Figure 8 shows measurements obtained in the short-wavelength channel. The clock angle ϕ of Jupiter during this period was $\phi = 20°$ and is indicated in the figures. A feature at this angle is evident in both channels. For both channels a constant background level has been subtracted, the

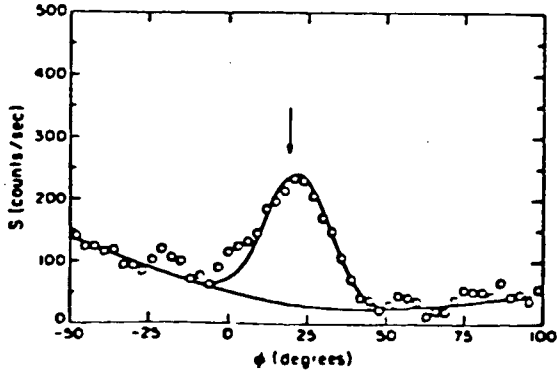

Fig. 7. Hydrogen Lyman α observations of Jupiter. The predicted clock angle of Jupiter is indicated with the arrow. The observed count rate corresponds to 400 R.

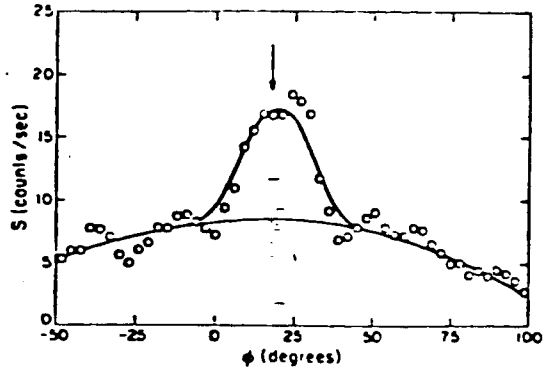

Fig. 8. He I λ584-Å observations of Jupiter. The predicted clock angle of Jupiter is indicated with the arrow. The observed count rate corresponds to 5.1 R.

amount resulting being ~3500 counts/s for the first channel and ~300 counts/s for the second. A small periodic noise component can be seen in the data. This is due to a stroboscopic effect in the integration period when the background level is varying with time. The emission rates corresponding to these measurements for a uniform diffuse disc can be obtained after consideration of the spectral response, integration, and averaging times and the geometry of the observations. The interplanetary background also must be included. If it is assumed that the observed emissions correspond to the H I λ1216-Å and He I λ584-Å lines, then the emission rates correspond to 400 R and 5.1 R, respectively. This assumption is quite reasonable and is discussed in the appendix.

Interpretation of the hydrogen Lyman α glow. Molecular hydrogen in the upper atmosphere of Jupiter is dissociated by the incident solar extreme ultraviolet radiation, principally through the following ionospheric reactions: $H_2 + h\nu \rightarrow H_2^+ + e$, $H_2^+ + H_2 \rightarrow H_3^+ + H$, and $H_3^+ + e \rightarrow H_2 + H$, with minor contributions from photodissociation of H_2 and other reactions. The subsequent chemical association of hydrogen atoms is through three-body recombination reactions, i.e., $H + H + M \rightarrow H_2 + M$ in lower regions of the atmosphere. These reactions are relatively slow, and a significant concentration of hydrogen atoms can result. The resonance line of atomic hydrogen, H I Lyman α, is a strong feature in the solar spectrum and can be scattered by the ambient hydrogen atoms, this scattering producing an ultraviolet emission feature. Other mechanisms that can contribute to this glow include radiative recombination of ionospheric protons, photoelectron excitation, and photodissociative excitation. However, as is discussed in the appendix, their contribution is relatively small, and resonance scattering can be considered the major excitation mechanism.

The concentration of atomic hydrogen was first considered by *Zabriskie* [1960], *Shimizu* [1966], and *Gross and Rasool* [1964]. Subsequently, *Hunten* [1969] showed that inclusion of eddy diffusion would increase the downward transport and the H recombination rate and thus reduce the calculated densities. He further pointed out that a measurement of the Lyman α glow could be used to determine the eddy diffusion coefficient, since the intensity of the hydrogen glow depends upon the total H column density. *Shimizu* [1971] has computed the hydrogen atom distribution for various values of the eddy diffusion coefficient and levels of solar activity along with the thermospheric temperature profile and its variation with solar activity.

The predicted Jovian atomic hydrogen column density may be optically thick at the center of the resonance line, and one must resort to radiative transfer calculations to relate the column density of H and the resulting Lyman α day glow intensity. The curve of growth of the predicted Lyman α intensity as a function of the H column abundance was calculated by *Carlson and Judge* [1971]. This problem has been considered more recently by *Wallace and Hunten* [1973], who included the effect of absorption by a nonuniform distribution of CH_4. The results of the two sets of calculations are in quite good agreement.

In the present work we use the results of Wallace and Hunten to determine the effective eddy diffusion coefficient K for the upper atmosphere of Jupiter. It must be recognized that the Lyman α glow depends not only upon the eddy diffusion coefficient but also on the intensity of the solar Lyman α line, the rate of production of atomic hydrogen by the solar extreme ultraviolet, and the temperature of the Jovian upper atmosphere. These three quantities vary with solar activity and must be considered in interpreting the intensity data and comparing with other observations. The solar Lyman α intensity was adopted from the measurements of *Vidal-Madjar et al.* [1973] and their observed variations of the line center intensity with the Zurich sunspot number Rz. The solar ultraviolet flux was obtained from the values of *Hinteregger* [1970], and the variation with solar activity was related to the 10.7-cm radio flux, the measurements of *Hall and Hinteregger* [1970] being used. Wallace and Hunten presented theoretical Lyman α reflectivities for temperatures of 150°K and 250°K. The temperature calculations of *Shimizu* [1971] suggest an exospheric temperature between 130°K and 176°K at solar minimum (which is appropriate for the present observations); consequently, the reflectivities at 150°K were considered appropriate for interpretation of the present observations.

The reflectivity obtained from Pioneer 10 and referred to zero-phase angle was $4\pi I/\pi F = 0.052$ and is indicated in Figure 9 as measurement C. The resulting value for the eddy diffusion coefficient is $K \simeq 3 \times 10^9$ cm²/s, although the uncertainty in the experimental measurements allows a possible variation of 3×10^7 to 3×10^9 cm² cm⁻¹.

Two other measurements of the Jovian Lyman α glow are indicated in Figure 9. The sounding rocket measurement of *Rottman et al.* [1973] corresponding to 4.4 kR is shown as measurement A and was obtained on January 25, 1971. Further measurements were obtained by E. B. Jenkins, L. Wallace, and J. F. Drake (private communication, 1973) with the Copernicus Orbiting Astronomical Observatory on June 21, 1973. A simple averaging analysis of their data indicates a brightness of 1 kR, whereas a more accurate least squares fit yields 660 R ± 350 R at the 70% confidence level. The latter result is shown in Figure 9 as measurement B and is in substantial agreement with the present measurements. The discrepancy in reflectivity between the Rottman et al. results and the Pioneer and Copernicus measurements is roughly a factor of 4 when variations in the solar Lyman α line and the production rate of atomic hydrogen are taken into account. Variations in the exospheric temperature also must be included. Wallace and Hunten find an increase of approximately 50% for a temperature increase of 150°K–250°K. On the basis of the temperature calculations of Shimizu and the solar conditions at the time of the rocket measurements, the higher temperature is probably more appropriate for the rocket observations, and the discrepancy is reduced to somewhat less than a factor of 3.

It is possible that the rocket measurements and the Copernicus measurements included contributions from the hydrogen cloud. The Pioneer 10 measurement of Jupiter reported here was obtained when Io (and the H cloud) was at greatest elongation as seen from the spacecraft; thus Io contributed little to the Jovian signal.

A lower limit of 7×10^8 cm² s⁻¹ for K has been suggested by *Veverka et al.* [1974] on the basis of the observation of structure in the refractivity profile observed in the β Scorpii occultation. M. Shimizu (private communication, 1974) has estimated theoretically the eddy diffusion coefficient for the Jovian atmosphere by investigating the dispersion relation for internal gravity waves. He finds $K \simeq 10^7$–10^9 cm² s⁻¹, in reasonable agreement with the present lower estimates.

Interpretation of the helium glow. Consideration of the various mechanisms for producing the Jovian extreme ultraviolet glow leads one to the conclusion that resonance scattering of the solar He line is the major excitation process (see the appendix). The atmosphere is expected to be optically thick, and the process that limits the intensity of the diffusely reflected He line is absorption by H_2. The situation can be described with the aid of Figure 10, which shows the profile of the He resonance scattering cross section (the Voigt profile) and the H_2 absorption cross section. At the line center the resonance cross section is much greater than the absorption cross section, and a He/H_2 gas would predominantly scatter at that wavelength. If He and H_2 were mixed equally, the gas would behave roughly as a scattering medium out to ~15 Doppler units from line center and as an absorber outside this interval. If the relative amount of H_2 were increased, the frequency interval over which scattering would occur would be decreased, the result being a more narrow and less intense day glow emission feature.

An additional complication to the resonance scattering

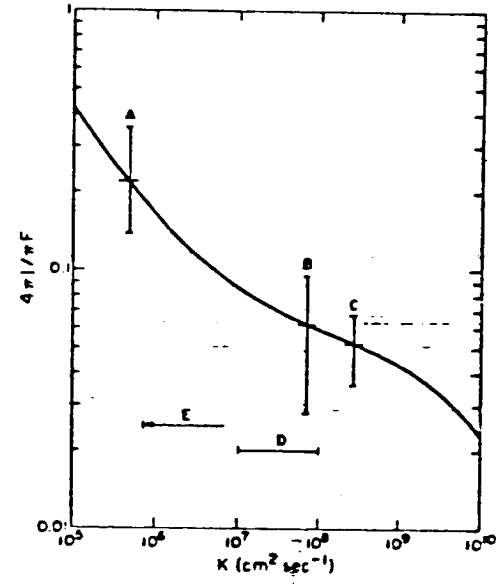

Fig. 9. Lyman α reflectivity of Jupiter. The theoretical curve is from *Wallace and Hunten* [1973] for 150°K, renormalized to the solar flux value at encounter. The reflectivity is a function of the ratio of the eddy diffusion coefficient to the H atom production rate. We have used 4×10^8 cm⁻² s⁻¹ for the latter quantity. Experimental measurement A is from *Rottman et al.* [1973]; measurement B, E. B. Jenkins, L. Wallace, and J. F. Drake (private communication, 1973); and measurement C, Pioneer 10. The theoretical estimate of M. Shimizu (private communication, 1974) is shown as measurement D, and measurement E is the lower limit from *Veverka et al.* [1974].

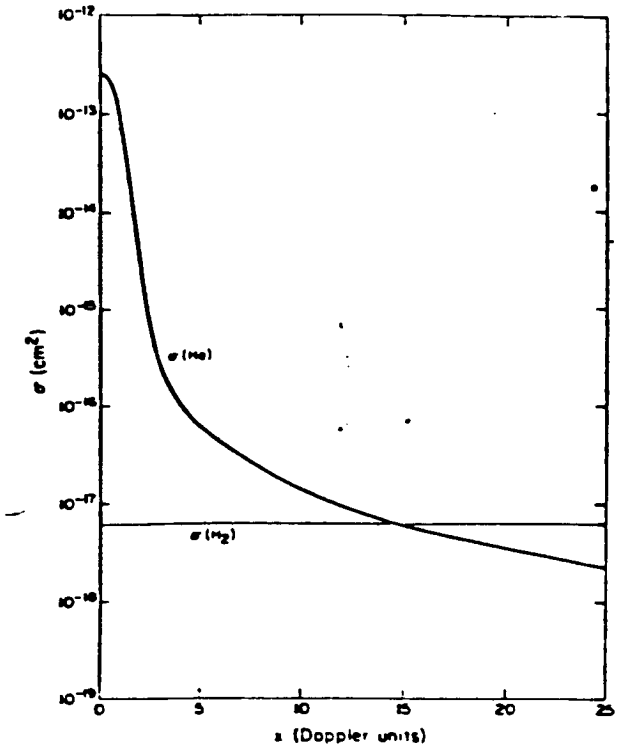

Fig. 10. Scattering cross section for He and absorption cross section of H_2. These values are shown as a function of the separation from line center in units of the Doppler width.

problem is the nonuniform mixing ratio of He and H_2 in the Jovian upper atmosphere due to the gravitational separation of these gases. It has been found that planetary upper atmospheres can be described with two regions, separated at a transition level termed the turbopause. Below this level, mechanical (eddy) mixing dominates, and the gas is uniformly mixed, whereas above the turbopause, molecular diffusion is dominant, and diffusive or gravitational separation occurs. The turbopause is located at the density level where the molecular and eddy diffusion coefficients are equal and for the present results occurs at approximately the 10^{10}-cm^{-3} density level.

The two other parameters that describe the upper atmosphere are the temperature profile and the ratios of the various constituents in the lower mixed region, in this case the ratio of He to H_2. As is discussed above, a temperature of 150°K appears to be a reasonable estimate for the present case. The remaining parameter, to be determined from the helium measurements, is the mixing ratio r (by number) of He and H_2: $r = [He]/[H_2]$.

The radiation transport aspects of the Jovian helium glow was discussed by *Carlson and Judge* [1971]. It was noted there that the frequency redistribution in the Doppler core could be described with the complete frequency redistribution approximation, whereas scattering in the radiation damping wings could be treated as being coherent. Since the Doppler core is probably saturated, owing to the large optical depths at the line center, it might be expected that the coherent approximation can be used for the entire line. *Wallace* [1971] has examined the frequency redistribution problem for terrestrial O I λ1300 Å and found that the coherent approximation over the entire distribution is indeed quite suitable when one is calculating the planetary albedo. Consequently, completely coherent scattering is assumed in the present work. We neglect polarization and assume isotropic scattering. The latter assumption is perhaps a poor one for helium, which scatters according to the Rayleigh phase function; however, the effect of multiple scattering should reduce this influence.

At each level in the atmosphere and at each frequency x (in Doppler units) from the line center an optical depth can be defined as

$$\tau(x, z) = \sigma_{He}(x)N(He|z) + \sigma_{H_2}N(H_2|z) \qquad (1)$$

where zero optical depth occurs outside the atmosphere and N represents column densities at the altitude z. The resonance cross section of He is $\sigma_{He}(x)$, and σ_{H_2} is the H_2 photoabsorption cross section. At the same altitude we define a single scattering albedo $\tilde{\omega}(x, z)$ as

$$\tilde{\omega}(x, z) = \frac{\sigma_{He}(x)n(He|z)}{\sigma_{He}(x)n(He|z) + \sigma_{H_2}n(H_2|z)} \qquad (2)$$

where n represents the corresponding number density at altitude z. If the altitude z is referenced to the turbopause, the number densities are [*Wallace and Hunten*, 1973]

$$n(H_2|z) = n_0e^{-z/H} \qquad (3a)$$

$$n(He|z) = rn_0(e^{-z/H}/1 + e^{z/H}) \qquad (3b)$$

whereas the column densities are found to be

$$N(H_2|z) = n_0He^{-z/H} \qquad (4a)$$

$$N(He|z) = rn_0H[e^{-z/H} - \ln(1 + e^{-z/H})] \qquad (4b)$$

Here n_0 is the H_2 density at the helium turbopause and is determined from

$$n_0 = b/K \qquad (5)$$

where $b = 1.81 \times 10^{19}$ cm^{-1} s^{-1} [*Wallace and Hunten*, 1973]. The scale height for molecular hydrogen is denoted by H. By using (1)–(4), the effective single scattering albedo can be found and is shown in Figure 11 for various frequencies x as a function of the optical depth at that same frequency. The optical depths at which the turbopause is located also are shown in the figure.

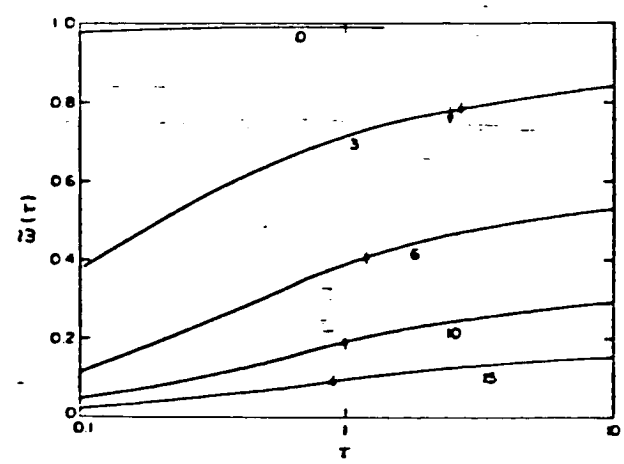

Fig. 11. Effective single scattering albedo. The value of $\tilde{\omega}$ is shown for various values of x in the line profile as a function of the optical depth in the atmosphere at the same x. The location of the turbopause is indicated for the various curves.

The radiative transfer equation in integral form is written

$$S(\tau) = S_0(\tau) + \bar{\omega}(\tau) \int S(\tau')E_1(|\tau - \tau'|)\, d\tau' \qquad (6)$$

where $S(\tau)$ is the source function and is the emission rate per unit area per unit optical depth per Doppler width. The driving term $S_0(\tau)$ represents the absorption and reemission of the solar line,

$$S_0(\tau) = \pi F \frac{\Delta\lambda_D}{\Delta\lambda_s} \bar{\omega}(\tau) \exp(-\tau/\mu_0) \qquad (7)$$

where πF is the total incident line flux, $\Delta\lambda_D$ is the Doppler width, and $\Delta\lambda_s$ is the effective width of the solar line. The solar zenith angle is $\cos^{-1} \mu_0$.

The equations were solved by iteration for various values of K, r, and μ_0 at several values of x in the line. From the resulting source function the apparent emission rate $4\pi I(\mu)$ when one is viewing the atmosphere from outside at an angle $\cos^{-1} \mu$ was found as a function of x from

$$4\pi I(\mu) = \int S(\tau')e^{-\tau'/\mu}\, d\tau'/\mu \qquad (8)$$

The resulting line profile is shown in Figure 12 for $K = 3 \times 10^8$ cm^2 s^{-1} and $\mu = \mu_0 = 1$. The total intensities were found by integrating over the line profile. The results of the calculations are given in Figure 13.

The experimental observations were normalized to the line profile measurements of the solar He I resonance line obtained recently by G. Cushman and W. A. Rense (private communication, 1973). They observed an effective width of $\Delta\lambda_s \simeq$ 120 mA, which combined with the observed value of 5.1 R and the total intensity of the solar line scaled from Hinteregger's measurements gives the value indicated in Figure 13. The resulting helium to molecular hydrogen ratio (by number) appropriate for the mixing region of the atmosphere is $r = 0.18$. The uncertainty in determining K by the present method leads

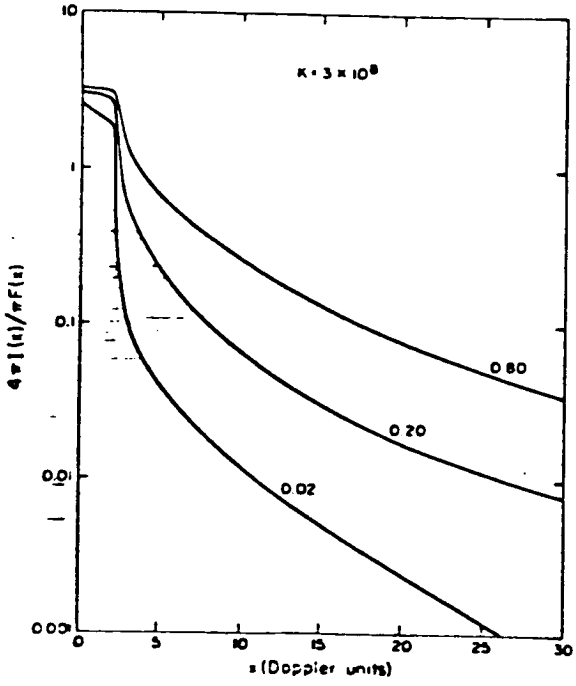

Fig. 12. Theoretical line profiles for the He line. An eddy diffusion coefficient of 3×10^8 cm^2 s^{-1} was used. Results for three different [He]/[H_2] ratios are shown.

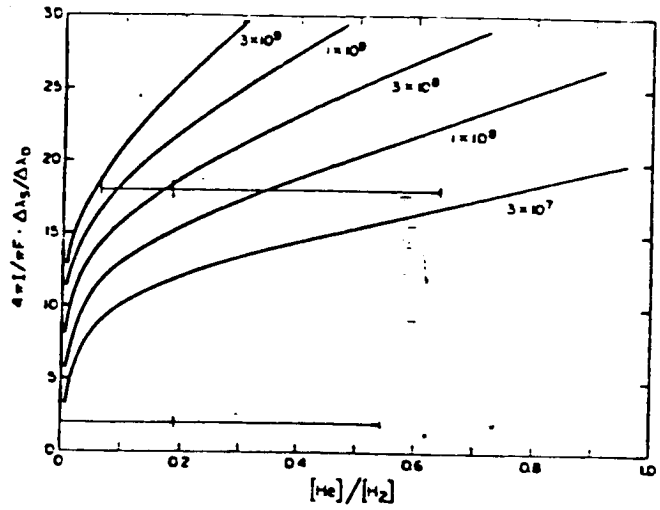

Fig. 13. Curve of growth of the He I λ584-Å line from Jupiter. The intensity of the line, relative to the width and flux of the solar line, is shown as a function of the [He]/[H_2] mixing ratio for various values of K. The upper bar corresponds to the Pioneer 10 measurements, and the lower is from the β Scorpii occultation. Both measurements give [He]/[H_2] ≈ 1/5 but with rather large error limits.

to a corresponding uncertainty in r, admitting values ranging from 0.06 to 0.60. Somewhat similar results were inferred from the β Scorpii occultation measurements by *Elliot et al.* [1974]; they found a value of $r = 0.19$ with error limits similar to the present results. Their results also are indicated in the figure. Consideration of both experiments suggests that the atmosphere of Jupiter is relatively hydrogen rich with a probable He/H_2 mixing ratio of approximately ⅕. These results are consistent with solar abundances ([He]/[H_2] = 0.11) [*Hunten and Münch*, 1973], although even these parameters are not accurately known [*Hirshberg*, 1973]. The present helium data can be used to determine a more precise helium to hydrogen mixing ratio if the eddy diffusion coefficient can be determined with more precision.

SATELLITE-RELATED OBSERVATIONS

Experimental measurements. As is shown in Figure 7, the Galilean satellites crossed the field of view several times, owing to the orbital motion of the satellites and the relative easterly motion of the Jovian system. However, no obvious signals were observed in either channel until the field of view came within ~6 R_J from Jupiter, the orbital position of Io (JI). The possibility of weak emissions associated with the outer three Galilean satellites is not ruled out but will require further analysis. In the present work we report only on those hydrogen channel emissions associated with Io. The present stage of analysis is necessarily incomplete and should be viewed as a preliminary report.

The cone angle of Io is shown in Figure 14 as a function of time, along with sample measurements, plotted versus clock angle, obtained at the indicated times. Approximately prior to day 333 at 1200 no features were observed (part A in Figure 14). Signals were observed, beginning at approximately day 333 at 1500, when the field of view crossed into the orbit of Io but before Io itself entered the field of view. The signals continued as Io crossed the field of view (part B in Figure 14). Following this crossing the feature was absent for several hours (part C in Figure 14). The emission signal returned approximately on day 334 at 0000, before Io entered the field of view (part D in Figure 14) and continued for approximately 12 hours. Io and

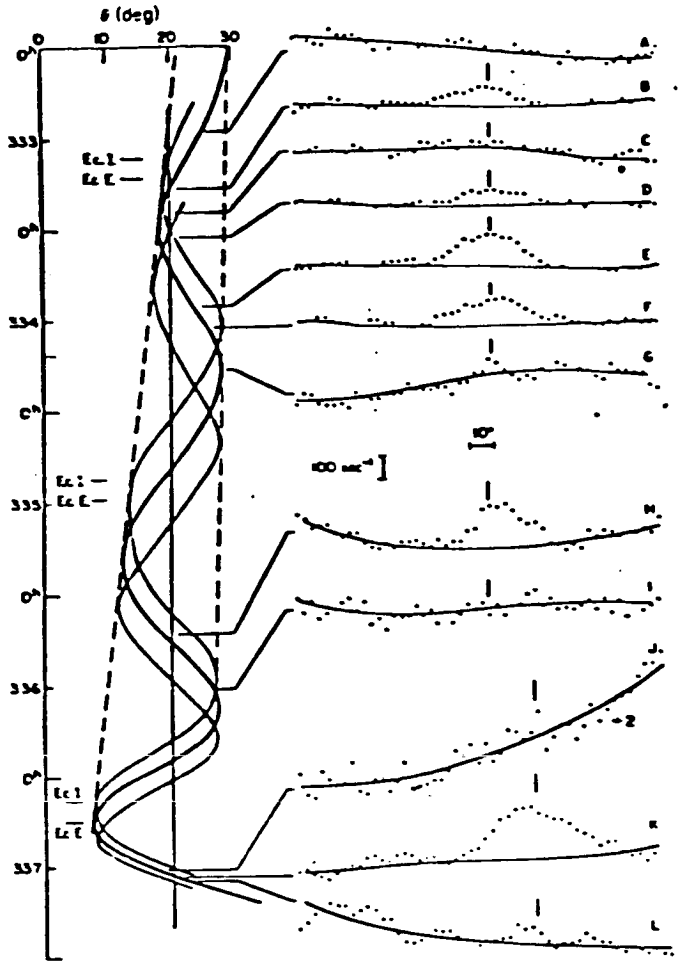

Fig. 14. Observations related to Io and the hydrogen cloud. The cone angle of Io is shown as the middle heavier curve as a function of time. The instrumental cone angle of 20° is shown as the vertical line. Samples of H channel data are shown for the indicated times. The clock angle of Io is shown as the short vertical bar. The leading and trailing edges of the H cloud are sketched in and indicate an angular extent of ~120°. The times of Io eclipse ingress (Ec. I.) and eclipse egress (Ec. E.) also are indicated.

Ganymede were in the field of view only a small fraction of this time, and these satellites could not contribute directly to the observed signal during the remaining observations, owing to the off-axis rejection properties of the instrument. During day 335 Jupiter was in the field of view; however, the planet had left the field of view early on day 336. Signals not attributable to Jupiter were observed for approximately 8 hours, during which time Io passed through the field of view (parts H and I in Figure 14). Finally, Io was in the field of view for a very short time on day 337 at 1300, and emissions were measured at approximately the same time (parts J, K, and L in Figure 14). However, the time duration of the observed signals was longer than that required for Io to pass through the 1° field of view.

Interpretation. Since the emission features under discussion were observed in the long-wavelength (hydrogen) channel only and since hydrogen is so abundant and the Lyman α line is readily produced by resonance scattering, it is a reasonable assumption that the observed emissions correspond to the H I Lyman α line. There are many other possibilities that can be considered, for example, the photodissociative excitation of H_2, but resonantly scattered Lyman α seems an attractive initial assumption. The measurements indicate that the source of these emissions is associated with Io, since their occurrence is correlated with crossings of this satellite through the field of view. The volume producing these emissions must be much larger than JI itself, since signals were observed when Io was well outside the field of view.

These facts can be interpreted as a hydrogen cloud in orbit around Jupiter at the orbital position of Io, similar to the hydrogen cloud suggested by *McDonough and Brice* [1973] for Titan (S-VI) and possibly the satellites of Jupiter. They point out that atoms that can escape from these satellites probably do not possess sufficient energy to escape from the vicinity of the planet and are bound in closed orbits until they are lost by ionization or recapture. These orbiting atoms would tend to produce a toroidal-shaped cloud, the density (and its distribution) being determined by ionization losses.

The cloud observed in the present measurements is not a complete torus, since signals were observed only during certain portions of the Ionian orbit. The leading and trailing boundaries of the observed cloud are indicated in Figure 14 and correspond to the times when the signals appeared or disappeared. From these measurements it is estimated that the orbital extent of the cloud is approximately 120°, i.e., one third of a torus, and is approximately centered around Io.

Although the angular resolution normal to the equatorial plane of the Galilean satellites is too coarse to allow a determination of the vertical extent of the cloud, an upper limit to this dimension can be obtained with the following considerations. At the end of day 333 the emissions were absent for a short period, even though the cloud was in the field of view. However, the viewing geometry and the orientation of the orbital plane at that time were such that the instrumental field of view intersected the shadow of Jupiter at the orbit of Io. Since no emissions were observed from the shadowed cloud, the observed emissions are due to solar excitation, e.g., resonance scattering, and the vertical cloud dimensions must be less than the diameter of Jupiter. McDonough and Brice argue that the vertical dimension Δz should be related to the orbital radius R, the orbital velocity V, and the mean atom velocity (after escape) $\langle v \rangle$ as $\Delta z = 2R\langle v \rangle/V$. These results imply that $\langle v \rangle < 3$ km/s.

If one assumes that the vertical dimension of the cloud is 1 R_J, then the observed counting rate leads to a surface brightness of ~300 R and a radial column density of ~3 × 10^{12} cm^{-2}. The corresponding radial optical thickness is then of the order of unity, and the optically thin single scattering assumption used to derive these densities may not be totally accurate. The total number N of atomic hydrogen atoms in the cloud can be obtained from the angular size with the result $N \simeq 2 \times 10^{32}$ and is independent of the assumed vertical thickness if single scattering is appropriate.

It is quite reasonable to associate the source of these atoms with processes occurring at Io, particularly since this satellite appears also to be the source of a sodium cloud [*Brown and Chaffee*, 1974; *Trafton et al.*, 1974]. *McElroy et al.* [1974] have suggested that photodissociation of a postulated SO_2 atmosphere [cf. *Sinton*, 1973] would produce abundant quantities of hydrogen that can readily escape from the planet. The relative amount of atomic and molecular hydrogen is not easily estimated, however, and would require detailed photochemical calculations. *Matson et al.* [1974] have suggested that the source of the observed Na is sputtering from the surface of Io by magnetospheric particles. This mechanism would also be a source of neutral hydrogen from the sputtering

of ices, which may occur in shadowed regions [*Watson et al.*, 1961], and previously absorbed protons [*Gott and Potter*, 1970]. An additional mechanism for producing neutral hydrogen would be neutralization of magnetospheric and plasmaspheric protons in the atmosphere of Io.

The lifetime of the atoms in the cloud can be estimated in order of magnitude from the following. For atoms that escape from Io with mean velocity $\langle v \rangle$ tangent to the orbit the relative change in orbital period t is $\delta t/t \simeq 3(\langle v \rangle/V)$, where V is the orbital velocity of Io ($V = 17$ km/s). If the mean lifetime before loss by ionization or charge exchange is τ, then the angular separation between Io and the point of loss is $\Delta\Theta \sim 2\pi\tau\delta t/t^2$, or $\tau = t\Delta\Theta/6\pi\langle v \rangle = 1/3R\Delta\Theta/\langle v \rangle$.

The mean expansion velocity $\langle v \rangle$ for atoms escaping from an exosphere at temperature T is [*Chamberlain*, 1963] $\langle v \rangle \simeq [1/(3)^{1/2}]U$, where $U = (2kT/M)^{1/2}$. If 150°K is assumed, $U \simeq 1.6$ km/s, and $\langle v \rangle \simeq 0.9$ km/s, resulting in the lifetime $\tau \simeq 2 \times 10^6$ s. This estimate is rather rough; a more accurate treatment would include investigation of the three-body problem in addition to further analysis of the observations.

The lifetime against photo-ionization is much greater than the present estimate (3×10^6 s), this fact suggesting that charge exchange with magnetospheric and plasmaspheric protons is the dominant loss mechanism, producing slow ions and fast neutrals that can escape from the planet. If the protons involved in the charge exchange are associated with a low-energy thermal plasma, for which the charge exchange cross section is $\sigma \simeq 4 \times 10^{-16}$ cm^2 [*Fite et al.*, 1960], then the flux of protons ϕ required to produce the observed lifetime is $\phi \simeq 1/\tau\sigma \simeq 10^6$ cm^{-2} s^{-1}. For a corotating plasma the velocity relative to Io and the cloud is ~60 km/s, and densities of ~200 cm^{-3} would be required if interaction with such a plasma were the only loss mechanism. This density is somewhat higher than that calculated by *Ioannidis and Brice* [1971], its higher value suggesting that the higher-energy plasma also may be effective.

In the very early analysis of the encounter data [*Judge and Carlson*, 1974] it was noted that perhaps Io itself was a source of ultraviolet emissions. Further analysis of these data indicates that most of the observed emissions, if not all, can originate from the cloud.

SUMMARY

The Pioneer 10 ultraviolet photometer experiment observed hydrogen and helium emissions from the atmosphere of Jupiter. The H I Lyman α results were used for determining the eddy-mixing coefficient in the upper atmosphere, yielding $K \simeq 3 \times 10^6$ cm^2 s^{-1}. By using this value and the He I λ584-Å observations, along with radiative transfer calculations, the lower atmosphere mixing ratio of He and H_2 was found to be $[He]/[H_2] \simeq 0.18$. Neither value is very precise, but they do indicate a H_2 rich atmosphere with rather more eddy mixing than had previously been estimated.

Observations of an extended atomic hydrogen cloud in orbit around Jupiter were obtained. The cloud occurs at the orbit of Io and is less than 2 R_J in vertical thickness. It extends ~120° around the orbit and is approximately centered at Io. The preliminary estimate of the cloud content is ~2×10^{38} atoms with a mean lifetime of ~2×10^6 s.

APPENDIX: EXCITATION OF ULTRAVIOLET EMISSIONS AT JUPITER

Two hypotheses used in the present work are: (1) the major features in the extreme ultraviolet spectrum of Jupiter are the H I λ1216-Å Lyman α and He I λ584-Å lines and (2) the dominant excitation mechanism is resonance scattering of the incident solar lines. Such assumptions are usually made in interpretation of terrestrial and planetary spectrophotometric measurements, and although experience has shown that they are generally valid, they are of sufficient importance that justification is required. The purpose of this appendix is to evaluate the importance of other excitation processes and emissions, including those due to photodissociative and photoionization excitation, photoelectron excitation, and ion recombination reactions.

The formation of the Jovian ultraviolet day glow by photon excitation has been considered by *Carlson and Judge* [1971], and *Olivero et al.* [1973] have calculated the contribution from photoelectron excitation. Although these studies indicate that the major components of the spectrum will be the Lyman α and λ584-Å lines produced by resonance scattering of the incident solar resonance lines, the numerical values must be reexamined in light of more recent solar flux measurements. Additionally, one must consider the solar cycle variation of the solar ultraviolet, since the time of the Pioneer 10 encounter corresponded to a very low level of solar activity (the appropriate 10.7-cm flux was $F_{10.7} \simeq 72 \times 10^{-22}$ W m^{-2} Hz^{-1}, and the Zurich sunspot number was $Rz \simeq 5$). In this work we have used the solar flux values recommended by *Hinteregger* [1970], scaled to the low solar activity at encounter.

The Lyman α line can be produced in H_2 gas through photodissociation in the 800- to 850-Å region via the $B^1\Sigma_u^+$ continuum. Nearly every photon absorbed in this region will produce Lyman α emissions; using the scaled solar fluxes and averaging over the planetary disc, we find ≃30 R due to this process.

This line can be produced also via the dissociative excitation of H_2 by photoelectrons. Olivero et al. have calculated for conditions of medium solar activity that 180 R of Lyman α will arise from this process. Not only must this value be scaled for solar activity, but the solar flux model [*Nisbet*, 1970] employed in their calculations appears to overestimate seriously the short-wavelength flux, i.e., the flux in the region that produces the exciting photoelectrons. For example, in the 100- to 200-Å region the model appears to be a factor of 8 higher than the corresponding Hinteregger values. This mechanism is evaluated here by using the appropriate solar flux, the excitation efficiency of *Miles et al.* [1972], and simple energy arguments, yielding 5–10 R of λ1216 Å for this process.

Hydrogen resonance radiation can be produced also in the radiative recombination of ionospheric protons. The ion density profile has been computed by various investigators, most recently by *Capone and Prasad* [1973] and *Atreya et al.* [1974]. With a peak electron and proton density of 10^6 cm^{-3}, an ion scale height of 100 km, and a recombination rate coefficient of 6×10^{-10} cm^3 s^{-1}, approximately 1 R of Lyman α will be produced. Since the major electron-ion recombination mechanism in the Jovian ionosphere is probably dissociative recombination of H_2^+, the possibility of producing excited hydrogen atoms in this process should be evaluated. The potential surface of H_2^+, with dissociation products H + H + H^+, has been calculated by *Csizmadia et al.* [1970], who find a dissociation energy of approximately 9.5 eV, which is ~1.5 eV below the energy required to produce H(n = 2) + $H_2(X^1\Sigma_g^+, v'' = 0)$ through dissociative recombination. Therefore if H_2^+ is produced in the ground state or with little vibrational energy, it is energetically impossible to produce the Lyman α

line through this process. Similarly, if there is vibrational deactivation of H_3^+ or if the H_2 is produced in vibrationally excited or triplet states, no radiation would be expected.

The He I λ584-Å line can be produced by photoelectron excitation in addition to resonance scattering. The calculations of *Olivero et al.* [1973] indicate that only 0.03 R of λ584-Å radiation will be produced in this process, and this would be reduced when solar flux considerations are taken into account. Ionospheric He^+ is a very minor component, and neutral He emissions arising from radiative recombination will be negligible. The high excitation potential of the He line would seem to preclude any chemical excitation of the line.

Other features that might be considered to be present in the ultraviolet spectrum of Jupiter are Lyman β, the Lyman and Werner bands of H_2, and the He II λ304-Å line. The He_2 continuum requires such specialized excitation conditions that it will surely be inconsequential. If the H atoms are optically thick for both Lyman α and Lyman β, the relative intensities will be proportional to the solar flux available for scattering, and therefore the Lyman β intensity would be only a few percent of Lyman α. This ratio would become smaller for thin atmospheres. The Lyman bands of H_2 generally occur outside the region of sensitivity; however, the Werner bands could be detected by the photometer. The photoelectron contribution was estimated similarly to the way in which the electron dissociation excitation case was estimated, a crude estimate of ~40 R resulting.

The He^+ line at λ304 Å could arise from resonance scattering by ionospheric or plasmaspheric helium ions. However, He^+ is an extremely minor component in the Jovian ionosphere. *Atreya et al.* [1974] find a peak density of 0.13 cm^{-3}, at which point the total ion density is $\sim 3 \times 10^3$, a factor of 2×10^4 greater. Consequently, one would expect little λ304-Å radiation from ionospheric scattering, nor would one expect a significant He^+ concentration in the plasmasphere and consequently no corresponding airglow emissions. In fact, plasmaspheric emissions would have been seen before Jupiter was in the field of view, but no indications of such signals have been found. The He II resonance line can be produced also through the simultaneous photo-ionization and excitation of neutral He and was previously estimated by *Carlson and Judge* [1971] for rather high solar flux values and little H_2 absorption. By using more realistic atmospheric and solar models and averaging over the disc, it is estimated that the contribution amounts to ~0.5 R.

We finally note that we have assumed that auroral excitation processes do not contribute significantly to the observed emissions and that quantitative estimates of this process are hindered by lack of any knowledge of Jovian particle precipitation or the basic auroral acceleration mechanisms.

Acknowledgments. It is a pleasure to acknowledge the Pioneer project office, particularly C. F. Hall, J. E. Lepetich, T. Wong, and R. Twarowski, and the various offices of the University of Southern California for their continued support. The instrument was constructed by the Analog Technology Corporation, excellent project management being provided by D. Willingham. This work was supported by NASA contract NAS2-6558 with the Ames Research Center.

REFERENCES

Anderson, R. C., J. G. Pipes, A. L. Broadfoot, and L. Wallace, Spectra of Venus and Jupiter from 1800 Å to 3200 Å, *J. Atmos. Sci.*, *26*, 874, 1969.

Atreya, S. K., T. M. Donahue, and M. B. McElroy, Jupiter ionosphere: Prospects for Pioneer 10, *Science*, *184*, 154, 1974.

Brown, R. A., and F. H. Chaffee, Jr., High resolution spectra of sodium emission from Io, *Astrophys. J.*, *187*, L125, 1974.

Byram, E. T., T. A. Chubb, and H. Friedman, Attempt to measure night helium glow—Evidence for metastable molecules in the night ionosphere, *J. Geophys. Res.*, *66*, 2095, 1961.

Capone, L. A., and S. S. Prasad, Jovian ionospheric models, *Icarus*, *20*, 200, 1973.

Carlson, R. W., and D. L. Judge, The extreme ultraviolet dayglow of Jupiter, *Planet. Space Sci.*, *19*, 327, 1971.

Carlson, R. W., and D. L. Judge, Pioneer 10 ultraviolet photometer observations at Jupiter (abstract), *Eos Trans. AGU*, *55*, 339, 1974.

Chamberlain, J. W., Planetary coronae and atmospheric evaporation, *Planet. Space Sci.*, *11*, 901, 1963.

Csizmadia, I. G., R. E. Kari, J. C. Polanyi, A. C. Roach, and M. A. Robb, Ab initio SCF-MO-CI calculations for H^-, H_2, and H_3^+ using Gaussian basis sets, *J. Chem. Phys.*, *52*, 6205, 1970.

Elliot, J. L., L. H. Wasserman, J. Veverka, C. Sagan, and W. Liller, The occultation of Beta Scorpii by Jupiter, 2, The hydrogen-helium abundance in the Jovian atmosphere, *Astrophys. J.*, *190*, 719, 1974.

Fite, W. L., R. F. Stebbings, D. G. Hummer, and R. T. Brackmann, Ionization and charge transfer in proton-hydrogen atom collisions, *Phys. Rev.*, *119*, 663, 1960.

Gott, J. R., III, and A. E. Potter, Lunar atomic hydrogen and its possible detection by scattered Lyman-α radiation, *Icarus*, *13*, 202, 1970.

Gross, S. H., and S. I. Rasool, The upper atmosphere of Jupiter, *Icarus*, *3*, 311, 1964. (Reproduced in *Erratum*, *4*, 110, 1965.)

Hall, L. A., and H. E. Hinteregger, Solar radiation in the extreme ultraviolet and its variation with solar rotation, *J. Geophys. Res.*, *75*, 6969, 1970.

Hinteregger, H. E., The extreme ultraviolet solar spectrum and its variation during the solar cycle, *Ann. Geophys.*, *26*, 547, 1970.

Hirshberg, J., Helium abundance of the sun, *Rev. Geophys. Space Phys.*, *11*, 115, 1973.

Hunten, D. M., The upper atmosphere of Jupiter, *J. Atmos. Sci.*, *26*, 826, 1969.

Hunten, D. M., and G. Münch, The helium abundance on Jupiter, *Space Sci. Rev.*, *14*, 433, 1973.

Hunter, W. R., D. W. Angel, and R. Tousey, Thin films and their uses for the extreme ultraviolet, *Appl. Opt.*, *4*, 891, 1965.

Ioannidis, G., and N. M. Brice, Plasma densities in the Jovian magnetosphere: Plasma slingshot or Maxwell demon?, *Icarus*, *14*, 360, 1971.

Judge, D. L., and R. W. Carlson, Pioneer 10 observations of the ultraviolet glow in the vicinity of Jupiter, *Science*, *183*, 317, 1974.

Judge, D. L., R. W. Carlson, K. Suzuki, and A. L. Morse, Initial Pioneer 10 results on the interplanetary and interstellar hydrogen and helium glow, *Bull. Amer. Phys. Soc.*, *17*, 1184, 1972.

Judge, D. L., R. W. Carlson, K. Suzuki, and A. L. Morse, Pioneer 10 ultraviolet photometer observations of the interplanetary glow (abstract), *Eos Trans. AGU*, *54*, 1194, 1973.

Matson, D. L., T. V. Johnson, and F. P. Fanale, Sodium D-line emission from Io: Sputtering and resonant scattering hypothesis, *Astrophys. J.*, *192*, 1974.

McDonough, T. R., and N. M. Brice, A Saturnian gas ring and the recycling of Titan's atmosphere, *Icarus*, *20*, 136, 1973.

McElroy, M. B., Y. L. Yung, and R. A. Brown, Sodium emission from Io: Implications, *Astrophys. J.*, *187*, L127, 1974.

McGrath, J. F., Jr., New technique for the design of an extreme ultraviolet collimator, *Rev. Sci. Instrum.*, *39*, 1036, 1968.

Miles, W. T., R. Thompson, and A. E. S. Green, Electron-impact cross sections and energy deposition in molecular hydrogen, *J. Appl. Phys.*, *43*, 678, 1972.

Nisbet, J. S., On the construction and use of the Penn State Mk I ionospheric model, *NASA Contract. Rep. 115894*, 1970.

Olivero, J. J., J. N. Bass, and A. E. S. Green, Photoelectron excitation of the Jupiter dayglow, *J. Geophys. Res.*, *78*, 2812, 1973.

Rottman, G. J., H. W. Moos, and C. S. Freer, The far-ultraviolet spectrum of Jupiter, *Astrophys. J.*, *184*, L89, 1973.

Samson, J. A. R., *Techniques of Vacuum Ultraviolet Spectroscopy*, pp. 222–227, John Wiley, New York, 1967.

Shimizu, M., Atomic and molecular processes in the upper atmospheres of planets, *Rep. Ionos. Res. Space Res. Jap.*, *20*, 271, 1966.

Shimizu, M., The upper atmosphere of Jupiter, *Icarus*, *14*, 273, 1971.

Sinton, W. M., Does Io have an ammonia atmosphere?, *Icarus*, *20*, 284, 1973.

Trafton, L., T. Parkinson, and W. Macy, Jr., The spatial extent of sodium emission around Io, *Astrophys. J.*, *190*, L85, 1974.
Veverka, J., J. Elliot, L. Wasserman, and C. Sagan, The upper atmosphere of Jupiter, *Astron. J.*, *179*, 73, 1974.
Vidal-Madjar, A., J. E. Blamont, and B. Phissamay, Solar Lyman alpha changes and related hydrogen density distribution at the earth's exobase (1969-1970), *J. Geophys. Res.*, *78*, 1115, 1973.
Wallace, L., The effect of non-coherency on the intensity of resonantly scattered sunlight in a planetary atmosphere, *Planet. Space Sci.*, *19*, 377, 1971.
Wallace, L., and D. M. Hunten, The Lyman-α albedo of Jupiter, *Astrophys. J.*, *182*, 1013, 1973.
Watson, K., B. C. Murray, and H. Brown, The behavior of volatiles on the lunar surface, *J. Geophys. Res.*, *66*, 3033, 1961.
Zabriskie, F. R., Studies on the atmosphere of Jupiter, Ph.D. dissertation, Princeton Univ., Princeton, N. J., 1960.

(Received May 28, 1974;
accepted June 17, 1974.)

ATMOSPHERES OF OUTER PLANET SATELLITES

R. W. Carlson
University of Southern California, Los Angeles, Calif.

Abstract

Only three of the many satellites in the outer solar system are now known or thought to possess atmospheres: Io, Ganymede, and Titan, and the physical properties of these atmospheres are briefly reviewed here. Evidence for an atmosphere around Io (Jupiter-I) is found in recent optical observations of sodium and hydrogen atomic resonance emissions associated with the satellite. These emissions are found to originate from a volume which is much greater than Io itself, forming a partial toroid around Jupiter. Suggestive evidence for an atmosphere on Ganymede (Jupiter-III) is found in stellar occultation measurements. In light of spectroscopic limits on CH_4 and NH_3, other possible atmospheric constituents are considered along with their production and loss mechanisms. These brief considerations suggest that A, O_2, N_2, and Ne are possible candidates for an atmosphere on Ganymede. Titan (Saturn-VI) has been long known to possess a CH_4 atmosphere, but recent work indicates that the amount present is greater than had originally been estimated. In addition, evidence for molecular hydrogen has also been found. The high thermal-infrared brightness temperatures of this satellite have also received much attention,

It is a pleasure to acknowledge many interesting discussions with T. V. Johnson, D. L. Judge, D. L. Matson, and T. R. McDonough. Portions of this work were supported under NASA Grant NAS-2-6558 with the Ames Research Center.

*Research Staff Physicist, Department of Physics.

and have been interpreted as a high altitude inversion layer or a greenhouse effect.

Introduction

As early as 1921, in discussing the escape of gases from planetary atmospheres, Sir James Jeans[1] wrote that "an atmosphere has been observed on Titan" and then goes on to mention "the suspected atmospheres on two of Jupiter's satellites." These would seem very prescient remarks indeed, since the only outer planet satellites which are presently thought to possess atmospheres are Titan and two of the Galilean satellites of Jupiter, and the evidence for these was not found for twenty years or more after Jeans wrote those thoughts. It should not be surprising, however, that some of the satellites possess atmospheres. They (and other outer solar system satellites) are comparable to, or exceed, the planet Mercury in size and although less massive they are of sufficiently low temperature that thermal evaporation (Jeans' escape) is greatly reduced. What is surprising are the details of actual atmospheres, which represent extremes as great as can be found among the planets. On the one hand, Titan exhibits a very thick and relatively permanent molecular atmosphere, while in contrast Io is seen to possess a tenuous and short-lived atmosphere composed of atomic hydrogen and metal atoms. The major portion of our body of knowledge concerning these atmospheres has been established in only the past few years, and the field is rapidly developing. Many of the present activities are directed toward specific atmospheric questions, e.g., composition, temperature photochemistry, and escape processes, but it is also recognized that these studies have even greater implication since the atmospheres are related to surface and interior compositions and the environment provided by the central planet. Their continued study will aid in understanding these environments and the physical-chemical history of the satellites and will surely be among the major scientific objectives in future missions to the giant planets.

The purpose of this work is to condense and summarize for the non-specialist, recent developments in studies of these atmospheres and to offer some speculation on what fu-

ture developments may offer. The Galilean satellites have been discussed by Cruikshank[2] while Titan's atmosphere has received enough attention to warrant a volume of its own.[3] The general properties of the physical satellites has been reviewed by Morrison and Cruikshank.[4] An extensive summary of the outer solar system by Newburn and Gulkis[5] is also of interest. A summary of some of the pertinent data concerning these objects is given in Table I.

Io

Post-Eclipse Brightening

The first evidence, still controversial, for a rarefied atmosphere on Io is found in its apparent anomalous photometric behavior following passage through the shadow of Jupiter - post eclipse brightening. This phenomena, first observed by Binder and Cruikshank[7], shows an excess brightness for the satellite of ~ 0.1 mag (~ 10%) immediately following eclipse which decays during the succeeding 10-20 minutes. The phenomena is not seen for the other satellites nor is it observed before eclipse.

Binder and Cruikshank[7] suggested that a condensable atmosphere produced this differential brightness by forming a surface layer or haze of brighter material (frost or snow) by condensation during eclipse cooling. It then sublimes back into the atmosphere in a short period following eclipse. Lewis[8] presented physical-chemical models of the larger outer satellites and discussed the atmospheric implications of these models. For Io, he preferred NH_3 or an inert gas,

Table I Physical Properties

	Mass (10^{26}gm)	Radius (km)	Density (gm/cc)	Escape Velocity (km/sec)
Io (J-I)	0.910	1820	3.50	2.58
Ganymede (J-III)	1.490	2635	1.95	2.75
Titan (S-VI)*	1.401	2500	2.14	2.73
		(2900)	(1.37)	(2.53)

*Values in parentheses are based on recent lunar occultation measurements.[6]

rather than CH_4, as the suspected condensate and estimated the atmospheric abundance by two methods. He first noted that it would require of order 1 mg/cm^2(or~ 1 cm-atm) to produce the differential reflectivity. Secondly, the amount of ice that can be sublimed by absorption of the available solar energy in the 15 min post-eclipse period (assuming an albedo of 0.8) is roughly the same (~ 0.8 cm-atm). At the temperature of Io, ~ 140°K, this abundance would produce a surface pressure of ~ 1 x 10^{-7} bar, comfortably below the upper limit of 3 x 10^{-5} bar set by the NH_3 vapor pressure. The agreement between these estimates supports Binder and Cruikshank's original suggestion as a viable hypothesis.

A problem posed by the post-eclipse brightness phenomena is its sporadic nature. Many eclipse reappearances have been investigated by different observers using a variety of techniques, yielding both positive and negative results, the latter casting some doubt as to the reality of the effect. Unfortunately, very few events have been observed simultaneously by several observers and it is therefore difficult to differentiate between mere instrumental effects caused by scattered light from Jupiter and a truly satellite-related phenomena which is intermittent in occurrence.

The erratic nature of the effect prompted Fallon and Murphy[9] to suggest the possibility of transient atmospheres, perhaps due to irregular outgassing. An alternative idea was advanced by Cruikshank and Murphy[10], who argued that a strong temperature variation in vapor pressures, and the temperature differences between perhelion and aphelion, could produce an effect varying with the Jovian anomalistic year since considerably more gas (of unspecified composition) would be available at perhelion where the mean temperature is higher. A seasonal effect was proposed by Sinton[11], arguing that during the solistices non-illuminated polar regions would act as a cold trap, freezing out much of the postulated NH_3 atmosphere, but sufficient atmosphere is present at the equinoxes to produce the post eclipse brightening anomaly. He presented a rather detailed model of the Ionian atmosphere, consistent with then existing measurements and containing ~ 0.5 cm-atm of NH_3, heated to ~ 245°K and perhaps including as much as 4 cm-atm of molecular nitrogen.

ATMOSPHERES OF OUTER PLANET SATELLITES

Recent observations[12] using instruments which are less sensitive to scattered light have given negative results. These data are of particular interest since they were obtained during a period when both Sinton's and Cruikshank and Murphy's hypotheses predicted positive results.

Spectroscopic and Occultation Limits

Various spectroscopic studies have been performed on Io and the remaining Galilean satellites, resulting in upper limits for the presence of certain gases. Kuiper[13] placed limits of 200 cm-atm and 40 cm-atm respectively for CH_3 and NH_3. Owen[14] extended these measurements by photographing the infrared spectrum; based on the absence of the strong 8873 A band he placed a limit of 100 cm-atm of methane. Recently, Fink et al.[15] using a Michelson interferometer, looked for features of CH_4 and NH_3 in the 2.3 μ region. Finding none, they were able to place limits of 0.5 cm-atm for both NH_3 and CH_4 which corresponds to 6×10^{-8} bar partial pressures.

Another technique - stellar occultations - can be used to discern the presence of an atmosphere (or the lack thereof). If an object with sufficient atmospheric density passes in front of a star, refraction will bend the light grazing the atmosphere toward the center of the shadow (if the atmosphere is normally dispersive). This bending produces a gradual shadow boundary whereas an abrupt boundary would be found in the absence of an atmosphere. The first photoelectric observations of an occultation were performed by Baum and Code[16] who observed an occultation by Jupiter. In May 1971, Io occulted the C component of β Scorpii and the event was observed by several groups[17-19]. All of the observations showed a sharp light curve, within limits set by instrumental time response, diffraction, and the finite stellar diameter. Smith and Smith[18] placed limits on the refractivity of the gas at the surface and therefore the corresponding number density. For N_2, CH_4, and H_2 these limits are 6×10^{12}, 9×10^{12} and 3×10^{15} molecules/cm^3 respectively. Assuming a temperature of 100°K, the surface pressure limits are 9×10^{-8} and 1.3×10^{-7} bar for N_2 and CH_4, corresponding to column abundance limits of 0.4 and 1.3 cm-atm. Limiting NH_3 abundance would be of the same order, and may be consistent

with the atmospheric abundances suggested by Lewis[8] and Sinton[11] particularly since the occultation pressure and abundance limits vary as $T^{5/2}$.

Sodium Emissions

The above discussion indicates that evidence for an atmosphere on Io is largely negative: rather severe upper limits are placed by the occultation and spectroscopic measurements and the post eclipse brightening anomaly remains unconfirmed. Definite and conclusive proof of atmospheric phenomena surrounding Io, far different than ever would have been expected, was recently discovered by Brown[20,21]. In his first planetary observational work, he obtained spectra of the Galilean satellites which showed sodium D line emission features from Io. These results were first reported in 1973 and quickly confirmed by other observers.[22-24] A spectrum obtained with a Wampler type coude scanner of the JPL Table Mountain Observatory is shown in Fig. 1. The spectral shift of the line due to the Doppler effect and Io's orbital velocity is clearly evident. The intensities observed by the various groups is variable (discussed below) with average intensity being many tens of thousands of Rayleighs.[25]

Trafton et al.[22] and Macy and Trafton[23] investigated the distribution of these emission features around Io, finding that the source is an extended region around the satellite extending as great as 50 Io radii from the satellite (in the orbital plane) and roughly 5 radii above the plane. The most intense region appears to be an area around Io whose radius is approximately twice the radius of Io.

The D lines, the resonance lines of neutral sodium, are well known features in the terrestial airglow, occurring in the day, twilight, and nightglow, and in aurora, the source of the sodium atoms being meteoritic with perhaps some contribution from oceanic salt. The excitation mechanisms for the earth's sodium emissions are resonance scattering (day and twilight), chemical excitation, and energy transfer from vibrationally excited N_2 (aurora). Reviews and discussions o of the terrestial Na problem are described by Hunten[26], Chamberlain[27] and Bates[28].

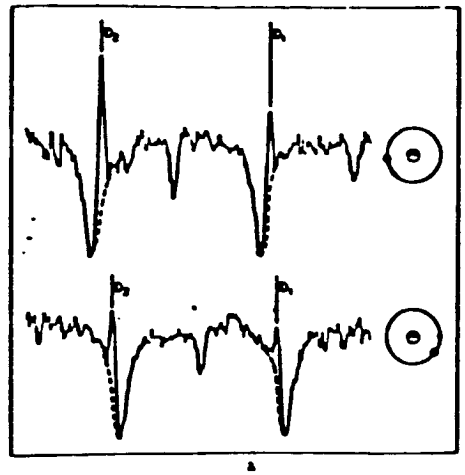

Fig. 1. Coudé spectra of sodium emissions from Io obtained at the Table Mountain Observatory by J. T. Bergstrahl, D. L. Matson and T. V. Johnson (Reference 24). The orbital position of the satellite is indicated on the right. The sun is to the bottom of the page.

The problems posed by the existence of metal emission features from Io can be classified as (1) the source of the Na and the mechanism by which it introduced into the extended atmosphere, (2) the excitation mechanism for the observed emission, (3) the eventual fate of the atoms after they escape the influence of the satellite, and (4) what kinetic, ionospheric, and photochemical interactions occur during the interval between production and loss?

An answer to the first question is provided by the studies of the Jet Propulsion Laboratory group, Fanale et al.[29], who suggest that the surface composition of Io involves salt deposits enhanced in sodium, while Matson et al.[30] argue that sodium atoms are liberated from the surface and injected into the atmosphere by sputtering processes.

In the model of Fanale et al.[29], Io and the remaining Galilean satellites were formed from chondritic material and H_2O with the relative proportions differing due to the influence of Jupiter acting as a significant source of heat in the early stages of formation. Subsequent radioactive heating in the interior melted the ice and bound water which then percolated to the surface and evaporated. As this water passed through the interior it became saturated with salts, carrying them to the surface and depositing them upon evaporation. The hypothesis is supported by several experimental studies

including the spectral reflectivity of Io and laboratory experiments with carbonaceous chondritic material.

Matson et al.[30] argue that the sodium is removed from the surface by particle impact - sputtering. One source of the impacting particles could be the energetic magnetospheric ions, another source may involve the plasma sheaths thought to exist around Io[31]. The induced EMF across Io in the moving Jovian magnetic field may produce plasma sheaths around the satellite which in turn can develop large electrical potentials between the plasma and areas on the surface of Io. If ions are produced in these regions, they may be accelerated into the surface with energies of perhaps several hundred Kev. The source of these ions could be previously sputtered atoms which are photoionized or directly ionized in the sputtering process.

Two other suggestions have been advanced to explain the presence of Na. McElroy et al.[32] suggest that Na and other metal atoms are present in solution in ammonia ice on the surface but they do not offer a mechanism for transfer to the atmosphere. It should be noted that the reflection spectrum of Io does not show any ice absorption bands in contrast to the remaining Galilean satellites. Sill[33] suggested that the sodium cloud originates from meteoritic material swept up by Jupiter, followed by decomposition by the energetic trapped radiation belt particles. This model does not explain the unique association of the sodium cloud with Io, however.

A mechanism for producing the observed Na-D emissions was suggested by McElroy et al.[32] as energy transfer from vibrationally excited N_2, a process that is thought to occur in terrestial aurorae. The initial vibrational excitation was thought to be produced by aurorae - like phenomena at Io, the N_2 being present as a photolysis product of their assumed NH_3 atmosphere. Two factors guided this choice of excitation mechanism. First, the observational data available at that time seemed to show that the emission was sporadic (as are aurorae) and second, the emitting region was thought to be highly localized which implied higher surface brightnesses than could be supplied by resonance scattering of sunlight.

Further observational data by Trafton et al.[22] showed that the emission arose from a more extended region than originally was supposed meaning a lower surface brightness and suggesting to Matson et al.[30] and Trafton et al.[22] that resonance scattering was the dominant excitation process.

Synoptic measurements by Bergstrahl et al.[24] at the Table Mountain Observatory showed that the emission was not sporadic, but varied smoothly with Io's rotational phase as seen from the sun and that intensities at the same orbital phase were quite repeatable over time scales covering many revolutions. The rotational or orbital variation is due to the Doppler shift of the atoms relative to the sun which modulates the emission intensity because of variations in intensity of the solar emission over the Fraunhofer line profile, the Swings effect, so well known in comets. The Table Mountain data agree well with theoretical predictions of the orbital phase variation when the solar profiles are taken into account and prove that resonance scattering is the dominant source. The long term observations demonstrate that the densities of Na are roughly constant, arguing against sporadic auroral phenomena.

Observations by Trafton et al.[22] and Macy and Trafton[23] show that sodium is not confined to the immediate vicinity of Io, but forms an extended cloud far outside the gravitational influence of Io. The atoms must therefore escape from Io, whose escape velocity is 2.5 km/sec, and the subsequent dynamics are determined largely by the gravitational potential of Jupiter. After escape, the atoms will orbit Jupiter in Keplerian trajectories as they do not in general possess enough energy to escape the vicinity of the planet, and the resulting density distribution would tend to form a cylindrically symmetric toroidal distribution unless the lifetime is limited. McDonough and Brice[34,35] were the first to point out the possible existence of gaseous toroids around the major planets. One process which will limit the lifetime is photoionization. However, the lifetime of Na atoms against photoionization at the orbit of Jupiter is $\sim 1.5 \times 10^6$ sec, much greater than Io's orbital period (1.5×10^5 sec) and the torus would be expected to be more complete than is observed.[22-23] In addition to photoionization, Macy and Trafton[23] investiga-

ted ionization by ions in the plasmasphere of Jupiter, finding this mechanism an inadequate explanation owing to the low charge exchange cross section for non-resonant systems. It is suggested here that electron impact ionization by thermal electrons in the Jovian plasmasphere is the dominant loss mechanisms. Using the ionization rate coefficients of Lotz,[36] a plasma energy of 4 ev (see Intriligator and Wolfe[37]), and plasma densities of 200/cm^3 obtained by Carlson and Judge[38] and McDonough[39], the lifetime of Na atoms is found to be $\sim 1.1 \times 10^5$ sec, in reasonable agreement with the lifetime estimated by Macy and Trafton[23] based on their observations of the cloud geometry.

Interactions with other possible atmospheric constituents by the sodium atoms during the interval between production and loss is unknown at present. Part of this uncertainty is due to lack of knowledge of other components in the atmosphere, and further uncertainty lies in the poor state of knowledge concerning the gas phase chemistry of Na. It seems possible that some other component is present but the total amount of atmosphere must be small, or the exospheric temperature must be very high, else the sodium atoms would lose sufficient energy in collisions that escape would be impeded too greatly. Further observational work, coupled with investigations of Na gaseous chemistry should delineate some of the possibilities. Certain of the possible candidates as atmospheric components (e.g. N_2, H_2, O, A, Mg, N, C, Si) are most readily observed in the extreme ultraviolet and may not be properly investigated until suitable instrumentation is available for long term study on a Jupiter orbiting mission.

Hydrogen Emissions

A second component, atomic hydrogen, was detected in an extended cloud around Io through ultraviolet photometric measurements of the HI Lyman - α line reported by Judge and Carlson[40] and Carlson and Judge[38,41]. The excitation mechanism is similar to the sodium case: resonance scattering of the incident solar flux, and the distribution of atoms is also qualitatively similar, forming an incomplete torus

around Jupiter approximately centered at Io. While it is apparent that Io is responsible for the observed distribution, it is less clear what the actual mechanism is that produces the atomic hydrogen. McElroy et al.[32] suggests that copious amounts of hydrogen will be produced in the photolysis of the hypothetical NH_3 atmosphere and will readily escape the planet. An alternative hypothesis[38, 39] suggests that magnetospheric and plasmaspheric protons are neutralized in the atmosphere and surface of Io, followed by escape into the torus.

In addition to being a possible source mechanism, the Jovian plasma protons are very likely involved in the H atom destruction processes. The charge exchange cross section between protons and neutral hydrogen atoms is very large,[42] being an exact energy resonance condition. If the slowly moving H atoms charge exchange with protons co-rotating with the Jovian magnetic field, the resultant will be slow ions and energetic neutrals which possess enough velocity to escape Jupiter, thereby depleting the torus. Estimates of the lifetime of H atoms in the torus, based on the cloud geometry, yield values of $\sim 2 \times 10^5$ sec, which imply plasma densities of 200 cm^{-3} or somewhat greater (Carlson and Judge[38, 40]) and are in reasonable agreement with the theoretical discussion of McDonough[39].

Ionosphere

Radio occultation measurements have been very valuable in studying the ionospheres and atmospheres of the terrestial planets, and the same technique was recently applied to the atmosphere of Io. Kliore et al.[43] detected an ionosphere on this satellite with a measured peak electron density of $\sim 6 \times 10^4$ cm^{-3} on the day side and $\simeq 10^4$ cm^{-3} on the night side. The day side plasma scale height was found to be 220 km. They note that if the Mars atmosphere is a close analogy, then atmospheric densities of 10^{10}-10^{12} cm^{-3} would be found at the surface where the pressure would be 10^{-8}-10^{-10} bar. This corresponds to column abundances of 0.003 -0.3 cm-atm and below the aforementioned stellar occultation limits. These investigators point out that one is probably seeing a rather different type of ionosphere, since it is more fully ionized than one would expect at this solar

distance, and since the ionosphere probably extends down to the surface.

McElroy and Yung[44] investigated the ionospheric properties of several model atmospheres, including both purely molecular atmospheres and those containing sodium. They found that ionization rates were too slow, and recombination too fast for a molecular atmosphere to exhibit the observed ionosphere. Inclusion of atomic sodium which is ionized much more rapidly and recombines more slowly brings the calculated densities closer to reality although complications such as diurnal atmospheric abundances, vertical motions, plasma interactions, and corpuscular ionization may enter into the problem and are difficult to distinguish with our present limited state of knowledge.

Further observations are clearly desirable in order to fully describe the spatial and temporal ionospheric variations and allow a more complete theoretical description. Since occultation measurements in the outer solar system are limited to measurements near the terminator, a complete description may not be forthcoming until plasma probes (and hopefully mass spectrometers) investigate the ionosphere close to the satellite on an orbiter mission.

Ganymede

The present state of knowledge concerning an atmosphere is suggestive but not conclusive, similar to the case of Io prior to the discovery of sodium and hydrogen emissions and the Ionian ionosphere. Whereas a stellar occultation provided an upper limit to the atmosphere of Io, a similar event with Ganymede did show evidence of an atmosphere. In the following section we discuss these results, followed by speculation on the possible atmospheric constituents.

Occultation Results

On 7 June 1972, Ganymede occulted the 8th magnitude star SAO 186800 and observations were made in three locations: Kodaikanal, India; Lembang (Java), Indonesia; and Darwin, Australia and reported by Carlson et al.[45]. Unfortunately, the occultation path occurred more northerly than had been

predicted and the Australian site was ~50 km too far south to observe the event. The measurement was a difficult one as the difference in magnitudes resulted in an intensity drop of only~ 5%. Nevertheless, the data were of sufficient quality to determine the radius and suggest, on the lack of abrupt intensity changes in the signal, the presence of an atmosphere. An approximate lower limit to the surface pressure was placed at 10^{-3}mb, which would correspond to ~ 5 cm-atm for a constituent with a mean molecular mass of~ 30. The major component cannot be methane or ammonia, since Fink et al.[15] placed upper limits on these molecules in order of magnitude less than densities suggested by the occultation.

Discussion of Possible Atmospheric Constituents

The possible presence of an atmosphere other than the two attractive candidates, NH_3 and CH_4, poses an interesting problem, particularly since the Jovian environment offers unique processes for both producing and depleting an atmosphere. We begin by discussing possible sources for an atmosphere, followed by remarks on loss processes.

The first source one might consider is outgassing from the interior of the satellite. As is well known, the rare gases He and Ar present in the terrestial atmosphere arise as radioactive decay products from uranium, thorium, and potassium (K^{40}, which produces A^{40} through K capture decay). Helium will escape so readily from Ganymede that it cannot be the specie observed in the occultation. An approximate upper limit to the argon content in the atmosphere is readily estimated assuming solar composition for elements other than hydrogen and helium and assuming the mass contribution by H is as H_2O ice. Using the isotopic abundance of K^{40}, the half life of 1.3×10^9 years, and the K capture branching ratio of 11%, one finds a present day production rate of $\sim 10^5$ A^{40} atoms/cm^2 sec and a total of $\sim 6 \times 10^{22}$ (20m-atm) produced over geologic time. It is unlikely that all of this gas has reached the surface and even more unlikely, as discussed below, that all of it would be permanently retained in the atmosphere.

In analogy with the terrestial atmosphere, N_2 might be considered as a possible contribution from outgassing, but

it is impossible to make any quantitative estimates. Presumably, most of the nitrogen in the solar nebula that formed the outer solar system was in the form of NH_3, and the ammonia present at Ganymede is to be found in solution in a liquid water mantle[8]. However, N_2 could be formed as a photolysis product of any small amount of NH_3 which finds its way to the surface and into the atmosphere.

The surface itself, composed of H_2O ice, could be a source of atmospheric molecules through the process of sputtering, as is found for Io. In the case of Ganymede, sputtering would probably produce, in addition to H_2O molecules, H, OH, and O, the latter atoms possibly recombining to produce an atmosphere of O_2. The production would be self-limiting, however, since a modest atmosphere would shield the surface from the particles responsible for the sputtering. (The range of a 1 MeV proton is ~2 cm-atm).

The magnetospheric particles themselves could be a source for the atmosphere, whether or not they impact the surface. Incident particles will be stopped at the surface or in the atmosphere, recombine, and thereby contribute to the atmosphere. The major component of the magnetospheric plasma, protons, will immediately escape as hydrogen atoms, but ions with greater mass may also be present in the plasma. If one assumes that the source of the Jovian magnetosphere is the solar wind, and that solar abundances are maintained, then elements worthy of consideration are O, C, N, and Ne. These atoms are both massive enough to not be readily lost through thermal evaporation and sufficiently abundant that they may significantly contribute to the atmosphere. Assuming a total plasma flux of 10^6 cm^{-2} sec^{-1}, with solar abundances, one might expect ~10^3, 5×10^2, 10^2 and 10^2 cm^{-2} sec^{-1} for O, C, N, and Ne respectively. Atomic oxygen and nitrogen can associate to form relatively inert atmospheric molecules by surface catalysis or by atmospheric three body reactions.

The above source mechanisms must be weighed against possible loss processes in order to evaluate their possible contribution. One obvious escape mechanism is Jeans' escape or thermal evaporation; this mechanism is inefficient

for the heavier atoms and molecules such as Ne, N_2, O_2 and A. If Jeans' escape is the only mechanism by which particles escape (an unlikely situation) then one can estimate the effectiveness of the sources discussed above in terms of a critical temperature for the outer atmosphere. This critical temperature is defined for each molecule such that the escape rate just equals the influx rate. If the temperature is below the critical temperature, then the net accumulation rate (influx less loss) can result in the accumulation of an atmosphere over geologic time. In Table 2 we summarize the possible influx rates and corresponding critical temperatures. If the exospheric temperature is comparable to the surface temperature (~ 140°K) and Jeans escape were the only loss mechanism, then it is possible that significant amounts of A, O_2, N_2, and Ne could accumulate to form a modest atmosphere on Ganymede.

Jeans' escape represents only a lower limit to the total escape rate; there are other mechanisms which are potentially much more rapid. One other means of escape is through molecular dissociation processes such as photodissociation and dissociative recombination, where the fragments are produced with sufficient kinetic energy to escape gravitational attraction as suggested by Brinkmann[46] for the atmosphere of Mars.

Table 2 Critical Temperature for Accumulation of an Atmosphere

Specie	Assumed Flux ($cm^{-2}sec^{-1}$)	Critical Temperature (°K)
A	10^5	500
O_2	10^3	200
N_2	10^2	300
Ne	10^2	200

A third class of escape mechanisms is brought about through ionization and the magnetic environment of Jupiter. Since Jupiter and its magnetic field rotate much faster than the orbital period of Ganymede, a V x B field will be produced which is several orders of magnitude greater than the gravitational force and can accelerate atmospheric ions away from the planet into the magnetosphere. This is thought to be the means by which the lunar atmosphere is depleted[47], in the lunar case the velocity and magnetic field being properties of the solar wind rather than a planetary field. In the absence of natural magnetic shielding (or diamagnetic behavior as discussed below), potentially every ion created by solar ultraviolet photoionization could be lost by this process. Since the total solar ultraviolet which can ionize an N_2 atmosphere (for example) at the orbit of Jupiter is $\sim 10^9$ photons cm^{-2} sec^{-1}, and ionizations yields are close to unity, the V x B acceleration could play a dominant role in the loss of a gaseous atmosphere.

One can examine the efficiency with which the induced electric field removes ions by finding the time it takes an ion moving under the induced V x B field to leave the atmosphere and comparing it to the recombination time. If the recombination time is large compared to the time necessary to remove the ion, then escape could be very efficient; if the lifetime of an ion and the time interval during which the V x B potential can act is shorter then this loss mechanism could be impeded.

The recombination time can be evaluated as $\tau_r = 1/\alpha n(e)$ where α is the recombination rate coefficient and n(e) the electron density. This density is estimated here by assuming local equilibrium: $\alpha \cdot n^2(e) = n_o/\tau_p$ where n_o is the neutral density and τ_p the neutral lifetime against photoionization. The recombination lifetime is thus $\tau_r = \sqrt{\tau_p/\alpha n_o}$. The time necessary to remove an ion τ_{loss} may be approximated by the time required to move a plasma scale height (twice the neutral scale height, H), with an average drift velocity v_d, the latter quantity being related to the induced electric field through the ionic mobility K: $v_d = KE$, resulting in $\tau_{loss} = 2H/KE$.

The induced electric field at Ganymede is $\sim 10^{-4}$ v/cm, and ionic mobilities (at STP) are $K \sim 1.5\text{-}2\ cm^2/volt\text{-}sec$, resulting in $\tau_{loss} \sim 10$ sec for an assumed scale height of 25 km.

For the atoms of interest, the peak ionization rate will occur at densities $n_o \sim 2 \times 10^{10}\ cm^{-3}$ with ionization lifetimes of 5×10^7 sec. For atoms as Ne and A, recombination occurs radiatively with $\alpha \approx 10^{-11}\ cm^3/sec$ giving a recombination lifetime of $\tau_r \approx 10^4$ sec. Consequently, an atmosphere of Ne or A could be readily diminished by the magnetic field of Jupiter. Molecular recombination processes (dissociative recombination) are much faster than radiative processes so the situation for a molecular atmosphere is more favorable. For $N_2, \alpha \approx 3 \times 10^{-7}\ cm^3\ sec^{-1}$ resulting in a recombination lifetime of 100 sec. We therefore conclude that a molecular atmosphere is less likely to be swept away by magnetic fields, but nevertheless high loss rates may be suffered from this process unless some sort of shielding is available.

A permanent magnetic field could provide such a shielding mechanism, as the earth's atmosphere is shielded from the solar wind (except during geomagnetic reversals). While the possibility of a satellite magnetic field is not ruled out by observations, it seems somewhat unlikely since Ganymede rotates so slowly it would be difficult to generate an internal dynamo.

Another, more likely, possibility is an ionospheric interaction generated by the Lorentz force. One can discuss such an interaction from several points of view. One description is in terms of a polarization field which opposes the V x B force. Since electrons and ions would be accelerated toward, and removed from, opposite faces, one can imagine excess "surface" charges (residing in the outer ionosphere) which produces an opposing electric field and retards ion and electron loss from the atmosphere. Another process is described in terms of the magnetic field produced by ionospheric currents as was considered by Dessler[48] for the interaction of Mars with the solar wind plasma and magnetic field. He argues that if the conductivity of a body is high enough so

that the time required for magnetic diffusion is longer than the time required for the solar wind to sweep past the body, then the interaction will produce currents and a magnetic field which decreases the V x B field in the body. If the Jovian magnetic field and the co-rotating thermal plasma can be treated analogously, and Ganymede possesses an ionosphere of sufficient conductivity, then it is possible that such an interaction might occur, reducing the loss rate and producing a very interesting magnetic and plasma structure in the vicinity of Ganymede which would be observable by appropriate magnetometers and plasma probes.

The above comments are necessarily incomplete, but they indicate that if Ganymede does in fact possess an atmosphere, then it could be the product of some very interesting physical processes, both with regards to its production and loss mechanisms. Clearly, further observations are desirable.

Titan

Titan was the first satellite to be found to possess an atmosphere when, in 1944, Kuiper[49] found CH_4 absorption bands at 6190 Å and 7260 Å. He noted that the amount of methane was comparable to, but somewhat less than, that observed on Jupiter and Saturn. A later estimate was given as 200 m-atm[13]. Until recently, this value was accepted, and Titan was thought to have a rather tenuous atmosphere with a surface pressure of ~ 2mb. This picture has changed drastically in the past few years, primarily due to spectroscopic observations and investigations in the thermal infrared. This work, supported by photometric and polarization measurements, indicates that Titan has a very thick atmosphere of surprising composition and with a most interesting thermal profile. Sufficient interest has been generated that a Titan workshop was held at the NASA Ames Research Center in 1973 under the chairmanship of D. M. Hunten[3].

Spectroscopic Studies

The spectroscopic work on Titan is primarily due to Trafton, who investigated the methane bands and found a factor of ten more methane[50] than did Kuiper, assuming CH_4 to be the mzjor specie present. Since the spectral profile is deter-

mined by pressure broadening, the observations are compatible with less methane only with the addition of some other gas, and then only in much greater proportions, consequently the minimum total atmosphere present corresponds to a pure CH_4 atmosphere.

Trafton[51] also found evidence for a second component in the atmosphere - molecular hydrogen. This was a very unexpected result since the lighter gases would be expected to escape this satellite with such ease. Despite this potentially rapid loss mechanism, the spectral observations indicate the possibility of a large H_2 abundance, of order 5 km-atm, which implies that the loss must be inhibited by some mechanism and/or a large source of H_2 must be operating. McDonough and Brice[34, 35] attempted to resolve the H_2 loss problem by recycling thd gas in a torus around Saturn. They pointed out that atoms which escape from Titan do not possess sufficient energy to escape from the central planet, but orbit Saturn until lost by ionization or recaptured by a satellite. They estimated that the effective loss rate could be reduced by as much as two orders of magnitude by this recapture process. The effectiveness of this process has been questioned by Hunten[52] who argues that recapture will increase the coronal densities and the escape rate until the next escape flux is the same as would be found in the absence of recycling. Hunten[53] pointed out that the escape of H_2 could be inhibited by diffusion in the atmosphere, and suggested an atmosphere containing something like 50 km-atm of N_2 would reduce the escape rate by roughly an order of magnitude. The N_2 could be formed through photolysis of NH_3 which may be present in the atmosphere in small quantities.

Trafton [54] also has presented intriguing evidence for an additional component in the form of unidentified features in the 1.06 and 1.1μ regions. Such features are found in the spectrum of Uranus, but not Saturn, and could be due to methane photolysis products or to isotopic methane. Too little is known about the spectroscopic properties of these molecules and it is hoped that laboratory experiments will be pursued, along with the observational aspects, in order to further our understanding of Titan and the outer planets.

Thermal Structure

The second area which has prompted much of the interest in Titan is the high brightness temperatures found in the thermal infrared. For a body with the albedo of Titan at the orbit of Saturn, the sunlit disc-averaged brightness temperature would be expected to be ~ 110°K in the absence of an atmosphere. A thick atmosphere as Titan possesses would moderate the diurnal temperature variation, and the observed temperature would be expected to approach ~ 84°K. However, the observed temperatures over much of the spectrum are much higher than this. For example, the recent measurements of Gillett et al[55]. show temperatures of 158°K at 8μ, decreasing to 128°K at 13μ. It was suggested earlier by Allen and Murdock[56], who found a temperature of 125°K in the 10-14 μ region, that a greenhouse effect was occurring. This hypothesis was developed by Sagan[57] and Pollack[58] and it appeared that such was the case for Titan.

An alternate explanation was proposed by Danielson et al.[59] which was developed as a consequence of explaining the observed low albedo in the ultraviolet. They noted that this low albedo implied absorption by high altitude aerosol particles. The absorbed energy, in being transferred to the gas, would increase its temperature, and be re-emitted in molecular transitions. Two likely transitions, which may be present in the measurements of Gillett et al.[55] are CH_4 at 7.7μ and C_2H_6 at 12.2μ. The photochemical calculations of Strobel[58] show that C_2H_6 is present in sufficient quantities to produce the 12 μ feature. The high altitude absorbing aerosols could be solid methane or particles composed of the photolysis products of methane-i.e.-photochemical smog. The latter process seems certain to happen (particularly to a resident of Los Angeles), and has been quantitatively estimated by Strobel[60], who finds that approximately 20% of the methane dissociation irreversibly produces higher hydrocarbons.

The choice between the two models (or a combination of both) should be forthcoming as infrared and microwave observations are extended. Recent observations by Briggs[61] at 8085 MHz (3.7 cm), have been reported as a radio brightness temperature of 115° ± 40°. Since all of the proposed

atmospheric constituents are transparent at this frequency, these microwave results probably refer to the surface temperature. Using the emissivity of ice, Briggs[60] finds a surface temperature of 135° ± 40°K which tends to support the existence of a greenhouse effect, although he cautions that the results could also be consistent with temperatures as low as 80°K as would occur in the absence of a greenhouse effect. The measurements of Low and Rieke[62] do not show structure in the 17 and 28u region which would be expected from the H_2 pressure induced transitions; this seems to rule out a massive H_2 greenhouse effect. Low and Rieke suggest a weak greenhouse effect with surface temperatures of 80-90°K.

It is important to note that many of the above measurements were interpreted using then existing radius estimates for Titan, ~ 2500 km. However, a recent lunar occultation observed by Veverka[6] gives a much larger radius (2900±200 km), which would significantly reduce the numerical values of brightness temperature, bringing them down to values which could be expected without a large greenhouse effect.

Future Possibilities

A stellar occultation would be of great value in determining the thermal profile of the atmosphere, although the resulting interpretations is composition dependent. The ingenuous suggestion of Brinkmann[63] has transformed the annoying "spikes" observed in stellar occultations, which result from atmospheric inhomogenities, into a powerful method for determining relative compositions. By observing an occultation in several wavelength bands, the wavelength dependence of the refractivity can be determined, allowing one to discern relative compositions. The slow wavelength variation of indices of refraction limits the method to relatively simple compositions of two (or perhaps three) components. Predictions of stellar occultations have been carried out by G. Taylor for the past twenty years. He is now using the SAO catalog for the brighter planets and satellites and has initiated a search for occultations by Titan of stars fainter than those listed in the SAO catalog. Unfortunately, no occultations appear in the offing for the very near future. On statistical grounds, one would expect ~ 2 useful occultations per year and an excellent event once every 5 years[64].

R. W. CARLSON

A spacecraft radio occultation would be extremely useful in determining the thermal picture of Titan, although the analysis is again composition dependent. A radio occultation, which obtains both the ionospheric profile and the lower atmosphere refractivity profile will also allow a choice between different model compositions, since the ionospheric profile would be quite different for a predominantly H_2 atmosphere than an N_2 atmosphere for example.

A radio occultation which probes the lower atmosphere and places a level for the solid surface would be of value in choosing between surface and interior models, since the methane atmosphere could arise from a CH_4 hydrate, solid or perhaps liquid CH_4, or even an H_2O-NH_3-CH_4 fluid with no real boundary, and the surface pressure (or absence of a surface) is different for these cases.

The composition of the atmosphere can be studied by suitable optical measurements on a fly by (or better an orbiting) spacecraft. Since the ratio of atmospheric scale height to planetary radius is comparable to the terrestial planets, a relatively closer approach is possible than for the major planets, allowing one to observe the atmosphere at the limb of the satellite without the overwhelming background from the bright disc. Some emissions of interest would be those of N_2, N_2+, NH, CH, and CN, the latter radials being possible photochemical products of a CH_4-H_2-N_2 atmosphere. The background problem is not so serious in the ultraviolet where one can attempt to observe atomic resonance transitions (H, C, N), the Lyman and Werner bands of H_2, and the Birge-Hopfield bands of N_2.

Observations of the toroid would also be useful to study the escape problem of H_2, and to determine the relative amounts of H and H_2 escaping from Titan and the exospheric temperature. Taberie[65] has calculated the atmospheric density profile of atomic hydrogen and then computes the flux of atomic and molecular hydrogen into the torus. She finds that the flux ratio of H and H_2 varies from 10^{-6} for an atmosphere containing equal H_2 and CH_4 to 1.6×10^{-1} for a predominantly N_2 atmosphere. Consequently, measurement of the H_2 Lyman and Werner band emissions, in comparison to the HI Lyman-α line, will allow a determination of the rela-

tive torus abundances and provide useful information on the atmosphere and its composition.

Concluding Remarks

The satellites of the major planets are a diverse collection of objects and currently of great interest. It is seen that several of these bodies possess atmospheres which can be related to surface or interior properties. Since atmospheres can be studied by remote optical sensing, without the necessity of direct probes, much of the first information about the history, interiors, and surfaces of the satellites will be obtained through atmospheric studies. In the future we can expect stellar and radio occultation measurements, further optical observations, both ground based and in wavelength regions inaccessible from the ground, ionospheric plasma probe experiments, outer atmosphere and toroid mass spectra, and eventually probe missions directly into the atmospheres.

These notes have been directed toward the atmospheres of Io, Ganymede, and Titan. With regards to the remaining satellites for which atmospheres have not been observed, we close by recalling Kuiper's remark that the matter should not be regarded as closed.

References

[1]Jeans, J.H., The Dynamical Theory of Gases, 3rd Ed. Cambridge University Press, 1921, p.348.

[2]Cruikshank, D.P., "Atmospheres of Galilean Satellites", presented at IAU Coll. No. 28, Planetary Satellites, Ithaca, N.Y., to be published in the proceedings, Cornell Univ. Press.

[3]Hunten, D.M., (Ed.), The Atmosphere of Titan, NASA SP-340, Scientific and Technical Information Office, Washington, D.C., 1974.

[4]Morrison, D. and Cruikshank, D.P., "Physical Properties of the Natural Satellites", Space Science Reviews, Vol. 15, 1974, p.641

[5]Newburn, R.L. and Gulkis, S., "A Survey of the Outer Planets, Jupiter, Saturn, Uranus, Neptune, and Pluto, and their Satellites", Space Science Reviews, Vol. 3, 1973, p. 179.

[6]Elliot, J. L., Veverka, J., and Goguen, J., paper presented at IAU Coll. No. 28, Planetary Satellites, Ithaca, N.Y., 1974.

[7]Binder, A.B. and Cruikshank, D.P., "Evidence for an Atmosphere on Io", Icarus Vol. 3, 1964, p. 299.

[8]Lewis, J.S., "Satellites of the Outer Planets: Their Physical and Chemical Structure", Icarus, Vol. 15, 1971, p. 174.

[9]Fallon, F.W. and Murphy, R.E., "Absence of Post-Eclipse Brightening of Io and Europa in 1970", Icarus, Vol. 15, 1971, p. 492.

[10]Cruikshank, D.P. and Murphy, D.P., "The Post-Eclipse Brightening of Io", Icarus, Vol. 20, 1973, p. 7.

[11]Sinton, W.M., "Does Io Have An Ammonia Atmosphere?", Icarus, Vol. 20, 1973, p. 284.

[12]Franz, O.G. and Millis, R.L., "A Search for Post-Eclipse Brightening of Io in 1973, II.", Icarus, Vol. 23, 1974, p. 23.

[13]Kuiper, G.P., in The Atmospheres of the Earth and Planets, ed. by. G.P. Kuiper, University of Chicago Press, 1952.

[14]Owen, T., "Saturn's Rings and the Satellites of Jupiter: Interpretation of Infrared Spectra", Science, Vol. 149, 1965, p. 974.

[15]Fink, U., Dekkers, N.H., and Larson, H.P., "Infrared Spectra of the Galilean Satellites of Jupiter", Astrophys. J. (Lett.), Vol. 179, 1973, p. L155.

[16]Baum, W.A. and Code, A.D., "A Photometric Observation of the Occultation of σ Arietis by Jupiter", Astron. J., Vol. 58, 1953, p. 108.

[17]Fallon, F.W. and Devinney, E.J.Jr., "Observation of the Occultation of β-Sco C by Io", Icarus, Vol. 17, 1972, p. 216.

[18]Smith, B.A. and Smith, S.A., "Upper Limits for an Atmosphere on Io", Icarus, Vol. 17, 1973, p. 218.

[19]Bartholdi, P. and Owen, F., "The Occultation of Beta Scorpii by Jupiter and Io, II, Io.", Astron. J., Vol. 77, 1972, p. 60.

[20]Brown, R.A., in Exploration of the Planetary System, Proceedings of IAU Copernicus Symposium (IAU Symposium No. 65), ed. by A. Woszczyk and C. Iwaniszwiska, (in press).

[21]Brown, R.A. and Chaffee, "High Resolution Spectra of Sodium Emission from Io", Astrophys. J. (Lett.), Vol. 187, 1974, p. L125.

[22]Trafton, L., Parkinson, T., and Macy, W.M.Jr., "The Spatial Extent of Sodium Emission Around Io", Astrophys. J. (Lett.), Vol. 190, 1974, p. L85.

[23]Macy, W.M.Jr. and Trafton, L., "Io's Sodium Emission Cloud", To be published in Icarus, 1975.

[24]Bergstrahl, J.T., Matson, D.L., and Johnson, T.V., "Sodium D-Line Emission From Io: Synoptic Observations from the Table Mountain Observatory", Astrophys. J. (Lett.) Vol. 195, 1975, p. L1.

[25]The Rayleigh is a measure of surface brightness corresponding to $10^6/4\pi$ photons/sec-cm^2(column)-sterad. See Reference 27, p. 569.

[26]Hunten, D.M., "Spectroscopic Studies of the Twilight Airglow", Space Science Reviews, Vol. 6, 1967, p. 493.

[27]Chamberlain, J.W., Physics of the Aurora and Airglow, Academic Press, New York, 1961.

[28]Bates, D.R., in Physics of the Upper Atmosphere, ed. by J. A. Ratcliffe, Academic Press, New York, 1960.

[29]Fanale, F.P., Johnson, T.V., and Matson, D.L., "Io: A Surface Evaporite Deposit?", Science, Vol. 186, 1974, p. 922.

[30]Matson, D.L., Johnson, T.V., and Fanale, F.P., "Sodium D-Line Emission From Io: Sputtering and Resonant

Scattering Hypothesis", Astrophys. J. (Lett.), Vol. 192, 1974, p. L43.

[31]Gurnett, D. A., "Sheath Effects and Related Charged-Particle Acceleration by Jupiter's Satellite Io", Astrophys. J., Vol. 175, 1972, p. 525.

[32]McElroy, M.B., Y. L. Yung, and R. A. Brown, "Sodium Emission from Io: Implications", Astrophys. J. (Lett.), Vol. 187, 1974, p. L127.

[33]Sill, G. T., "Sources of Sodium in the Atmosphere of Io", presented at the 5th Annual Meeting of the Division of Planetary Sciences, AAS, Palo Alto, California, 1975.

[34]McDonough, T.R., and Brice, N.M., "New Kind of Ring Around Saturn", Nature, Vol. 212, 1973, p. 513.

[35]McDonough, T.R. and Brice, N.M., "A Saturnian Gas Ring and the Recycling of Titan's Atmosphere", Icarus, Vol. 20, 1973, p. 136.

[36]Lotz, W., "Electron-Impact Cross-Sections and Ionization Rate Coefficients for Atoms and Ions", Astrophys. J. (Suppl.) Vol. 14, 1967, p. 207.

[37]Intriligator, D.S. and Wolfe, J.H., "Initial Observations of Plasma Electrons from the Pioneer 10 Fly By of Jupiter", Geophys. Res. Lett., Vol. 1, 1974, p. 281.

[38]Carlson, R.W. and Judge, D.L., "Pioneer 10 Ultraviolet Photometer Observations at Jupiter Encounter", J. Geophys. Res., Vol. 79, 1974, p. 3623.

[39]McDonough, T.R., "A Theory of the Jovian Hydrogen Torus", to be published in Icarus, 1975.

[40]Judge, D.L. and Carlson, R.W., "Pioneer 10 Observations of the Ultraviolet Glow in the Vicinity of Jupiter", Science, Vol. 183, 1974, p. 317.

[41]Carlson, R.W. and Judge, D.L., "Pioneer 10 Ultraviolet Photometer Observations of the Jovian Hydrogen Torus: The Angular Distribution", to be published in Icarus, 1975.

[42]Fite, W.L., Stebbings, R.F., Hummer, D.G., and Brackmann, R.T., "Ionization and Charge Transfer in Proton-Hydrogen Atom Collisions", Phys. Rev., Vol. 119, 1960, p. 663.

[43]Kliore, A., Cain, D.L., Fjeldbo, G., Seidel, B.L., and Rasool, S.I., "Preliminary Results on the Atmospheres of Io and Jupiter from the Pioneer 10 S-Band Occultation Experiment", Science, Vol. 183, 1974, p. 323.

[44]McElroy, M.B. and Yung, Y.L., "The Atmosphere and Ionosphere of Io", Astrophys. J., Vol. 196, 1975, p. 227.

[45]Carlson, R.W., Bhattacharyya, J.C., Smith, B.A., Johnson, T.V., Hidayat, B., Smith, S.A., Taylor, G.E. O'Leary, B.T., and Brinkmann, R.T., "An Atmosphere on Ganymede from It's Occultation of SAO 186800 on 7 June 1972", Science, Vol. 182, 1973, p. 53.

[46]Brinkmann, R.T., "Mars: Has Nitrogen Escaped?", Science, Vol. 174, 1971, p. 944.

[47]Hodges, R.R.Jr., Hoffman, J.H., and Johnson, F.S., "The Lunar Atmosphere", Icarus, Vol. 21, 1974, p. 415.

[48]Dessler, A.J., in The Atmospheres of Mars and Venus, ed. by. J. C. Brandt and M. B. McElroy, Gordon and Breach, New York, 1968.

[49]Kuiper, G.P., "Titan: A Satellite with an Atmosphere", Astrophys. J., Vol. 100, 1944, p. 378.

[50]Trafton, L., "The Bulk Composition of Titan's Atmosphere", Astrophys. J., Vol. 175, 1972, p. 295.

[51]Trafton, L., "On the Possible Detection of H_2 in Titan's Atmosphere", Astrophys. J., Vol. 175, 1972, p. 285.

[52]Hunten, D.M., in The Atmosphere of Titan, ed. by D.M. Hunten, NASA SP-340, Scientific and Technical Information Service, Washington, D.C., 1974.

[53]Hunten, D.M., "The Atmosphere of Titan", Comments on Astrophys. Space Science, Vol. 4, 1972, p. 149.

[54]Trafton, L., "Titan: Unidentified Strong Absorptions in the Photometric Infrared", Icarus, Vol. 21, 1974, p. 175.

[55]Gillett, F.C., Forrest, W.J., and Merrill, K., "8-13 Micron Observations of Titan", Astrophys. J. (Lett.), Vol. 184, 19 , p. L93.

[56]Allen, D.A., and Murdock, T.L., "Infrared Photometry of Saturn, Titan, and the Rings", Icarus, Vol. 14, 1971, p. 1.

[57]Sagan, C., "The Greenhouse of Titan", Icarus, Vol. 18, 1973, p. 649.

[58]Pollack, J.B., "Greenhouse Models of the Atmosphere of Titan", Icarus, Vol. 19, 1973, p. 43.

[59]Danielson, R.E., Caldwell, J.J., and Larach, D.R., "An Inversion in the Atmosphere of Titan", Icarus, Vol. 20, 1973 p. 437.

[60]Strobel, D.F., "The Photochemistry of Hydrocarbons in the Atmosphere of Titan", Icarus, Vol. 21, 1974, p. 466.

[61]Briggs, F.H., "The Radio Brightness of Titan", Icarus, Vol. 22, 1974, p. 48.

[62]Low, F.J. and Ricke, G.H., "Infrared Photometry of Titan", Astrophys. J. (Lett.), Vol. 190, 1974, p. L143.

[63]Brinkmann, R.T., "Occultation by Jupiter", Nature, Vol. 230, 1971, p. 515.

[64]O'Leary, B.T., "Frequency of Occultation of Stars by Planets, Satellites, and Asteroids", Science, Vol. 175, 1972, p. 1108.

[65]Taberie, N., "Distribution of Hydrogen and it's Lyman-Alpha Intensity in the Atmosphere of Titan", Icarus, Vol. 23, 1974, p. 365.

Pioneer 10 Ultraviolet Photometer Observations of the Jovian Hydrogen Torus: The Angular Distribution

R. W. CARLSON AND D. L. JUDGE

Department of Physics, University of Southern California, Los Angeles, California 90007

Received August 12, 1974; revised September 20, 1974

The Pioneer 10 ultraviolet photometer observations of the Jovian hydrogen torus are analyzed to obtain the angular distribution. The cloud is asymmetric about Io, where the atoms presumably originate, with the greater density occurring in the trailing portion. A simple model which assumes Jeans escape from the atmosphere of Io is developed and compared to the observations. The results suggest that the exospheric temperature is high (~3000 K) and that the ionization lifetime of the cloud atoms is $\sim 1 \times 10^5$ sec.

Introduction

The presence of a cloud of hydrogen atoms in orbit around Jupiter at the orbital radius of Io and approximately centered about that satellite was found experimentally by Pioneer 10 ultraviolet photometer observations of the resonantly scattered Lyman-α line and announced by Judge and Carlson (1974). The origin of the cloud is presumably due to atoms escaping from Io. Such a cloud of orbiting hydrogen was predicted earlier by McDonough and Brice (1973) for Saturn and was also suggested by them for the Jovian system. Their model is based on the fact that atoms which escape from the atmospheres of the satellite generally do not possess sufficient energy to escape the central planet; the atoms move in bound orbits until lost by ionization. For ionization lifetimes which are long compared to the orbital period, the atoms will undergo many revolutions before loss and the resulting density distribution will approximate a cylindrically symmetric torus.

The Pioneer observations indicate, however, that the Jovian torus is not complete but occurs over approximately one third of the total circumference (Carlson and Judge, 1974).

In this work, the predicted angular distribution is evaluated with a simple physical model and is then compared to the Pioneer 10 observations. While the temporal variations of the H cloud are not well established, recent observations of the sodium emission cloud (Bergstrahl *et al.*, 1974) show that the source of these atoms is constant in time. It therefore seems reasonable to assume steady state thermal evaporation (Jeans escape) from the atmosphere of Io as the source of the cloud. With this assumption, the steady-state angular density is obtained assuming a constant loss rate. This latter quantity and estimates of the exospheric temperature of Io are deduced by comparing the observations with the model.

Experimental Observations

The hydrogen torus was observed during several of its orbits in the Pioneer 10 encounter phase at Jupiter, the most complete set of measurements being obtained on 30 November 1973 (334^d). At that time the spacecraft was approximately 60 Jovian radii (R_J) from the planet. The cloud was observed at an orbital phase angle of approximately 150° measured with respect to superior conjunction as seen from the spacecraft. During most of this period the far side of the orbit was in the shadow of Jupiter,

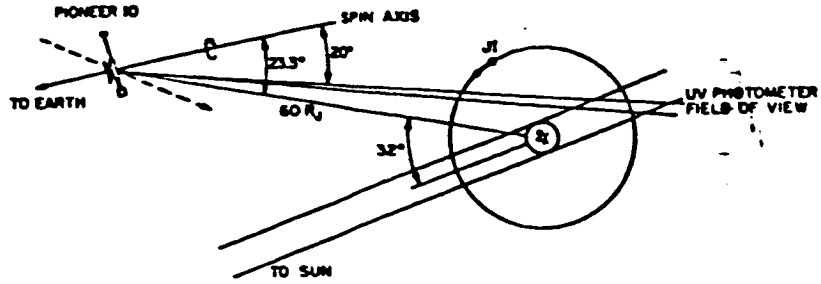

FIG. 1. The approximate geometry of the Pioneer 10 spacecraft on 30 November 1973. The figure is not drawn to scale.

consequently not contributing to the resonantly scattered emissions. The geometric aspects of the observations reported here are indicated in Fig. 1.

Details of the instrumentation and analysis are presented elsewhere (Carlson and Judge, 1974); it is sufficient to note here that the Pioneer spacecraft is spin stabilized with the photometer field of view (1° × 10° FWHM) oriented 20° to the spin axis. This spin scanning allows one to discern weak optical features even in the presence of the high background induced by magnetospheric particles. Examples of these spin scans of the hydrogen torus are shown in Fig. 2 and further peak intensity data are presented later.

Io was in the field of view during a large portion of the time corresponding to the second scan (3^h38^m–5^h52^m) in Fig. 2. It is clear that there is no enhancement at that time and further, that the maximum intensity actually occurs several hours later, after Io has left the field of view. Consequently, the angular distribution of atoms in the cloud must be asymmetric about Io.

The surface brightness of the torus is uncertain due to uncertainties in the vertical extent of the cloud. From the lack of observed emissions when the cloud was on the far side of the orbit and in the shadow of Jupiter, it was concluded that the vertical extent must be less than the diameter of the planet (Carlson and Judge, 1974). If the vertical extent of the cloud is 1 Jovian radii, then the observed maximum signal (~125 counts sec^{-1}) corresponds to approximately 300 Rayleighs. With an excitation rate of $g \simeq 10^{-4} sec^{-1}$ $atom^{-1}$ at Jupiter, then the column density in the direction of observation is approximately $3 \times 10^{12} cm^{-2}$. From the observed angular width of ~120° (see Fig. 4) and the assumed vertical extent of $1 R_J$, then the total number of H atoms in the cloud is $\sim 2 \times 10^{33}$.

PREDICTED ANGULAR DISTRIBUTION

The origin of these hydrogen atoms and their destruction mechanisms are not established, and it is instructive to compare the observations with a model in

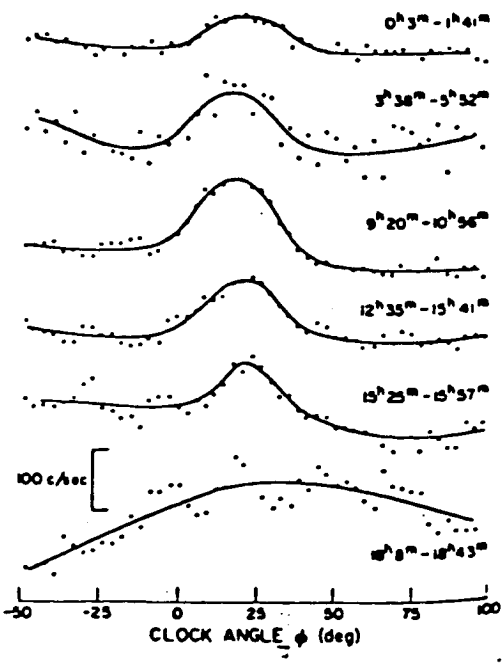

FIG. 2. Samples of Pioneer 10 H channel spin scans of the hydrogen torus on 30 November 1973.

an attempt to gain information relative to these mechanisms. In this work we assume that the orbits for atoms escaping with a certain velocity and direction can be described with an average angular velocity relative to Io. The continuity equation is written for an assumed constant loss rate, and integrated using the assumption of Jeans escape from the atmosphere of Io.

Orbits for atoms escaping from Io are shown in Fig. 3. Those atoms escaping in the direction of orbital motion populate the trailing portion of the cloud while escape in the opposite direction increases the angular velocity and populates the forward or leading part. Atoms escaping from both the inner and outer points possess orbital periods which are greater than that for Io, and populate the trailing portion. It can be seen from these trajectories that the relative angular velocities are not constant, but oscillate about the mean value. Recognizing that the oscillations will smooth the distribution, one can proceed to calculate the densities in the constant angular velocity approximation.

Consider a group of atoms which are escaping Io with velocity v (after escape)

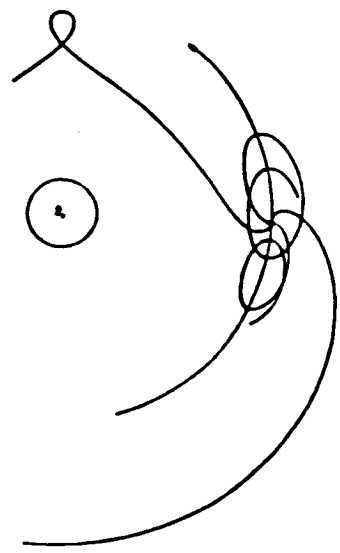

FIG. 3. Trajectories for hydrogen atoms leaving Io with excess velocity of 2 kmsec^{-1} in the coordinate system revolving with Io about Jupiter.

and at an angle $\cos^{-1}\mu$ with respect to velocity vector of Io. These atoms then produce an angular density $n\ (v,\mu,\theta)$ (e.g., in atoms rad^{-1}) where θ is the orbital angle measured with respect Io. If the life time of the atoms is τ, then the continuity equation is

$$\frac{\partial}{\partial\theta}[\Delta\omega(v,\mu)\,n(v,\mu,\theta)] = -n(v,\mu,\theta)/\tau, \quad (1)$$

where $\Delta\omega$ is average difference between the angular velocities of Io and the atoms about Jupiter. From elementary mechanics,

$$\Delta\omega = \omega_0[1 - 2\mu v/V - (v/V)^2]^{3/2} - \omega_0, \quad (2)$$

where ω_0 and V are the angular and orbital velocities of Io, respectively. For $v \ll V$, then

$$\Delta\omega/\omega_0 \simeq -3\frac{v}{V}\mu - \frac{3}{2}\left(\frac{v}{V}\right)^2. \quad (3)$$

Solving Eq. (1) gives

$$n(v,\mu) \propto \exp\left[-\frac{|\theta|}{3\tau\omega_0(\mu v/V \pm v^2/2V^2)}\right], \quad (4)$$

where the positive sign corresponds to the trailing portion of the cloud and $\mp(1/2)(v/V) < \mu < 1$. Both the forward hemisphere and a portion of the back hemisphere populate the trailing portion of the cloud, the relative amounts depending on the velocity. Assuming that the atoms escape from Io isotropically, then

$$n(v,\theta) = n_0\int_{\mp 1/2(v/V)}^{1} d\mu \times \exp\left[-\frac{|\theta|}{3\tau\omega_0(\mu v/V \pm v^2/2V^2)}\right], \quad (5)$$

where $n_0(v)$ is a normalization constant.

The atoms escaping from a planetary atmosphere are not monenergetic, but possess a distribution of velocities. We assume here that the escape can be represented by thermal evaporation characterized by a temperature T_c. It is convenient to express velocities in terms of the thermal velocity U, where

$$U = (2kT_c/m)^{1/2}. \quad (6)$$

Referring to Chamberlain (1963), the

distribution of velocities at large distances from Io ($\lambda = mMG/KT_c r = V_{esc}^2/U^2 \to 0$) is found from the kernel of his Eq. (35) after integrating over angular momentum coordinates. The total number of atoms escaping with velocities $\xi < v/U < \xi + d\xi$ is

$$4\pi^{1/2} N_c e^{-\lambda_c} r_c^2 e^{-\xi^2}(\lambda_c + \xi^2)\xi d\xi, \quad (7)$$

where r_c is the radius of the critical level and N_c is the number density at that altitude. This escape rate must be balanced by the integrated loss rate

$$2d\xi \int_0^\infty d\theta n(v,\theta)/\tau \simeq \frac{6\pi\tau n_0(r)\, d\xi}{TV}. \quad (8)$$

The last result is obtained assuming $v/V \ll 1$. Equating the production and loss rates determines $n_0(r)$, with the result that the total density is

$$n(\theta) = \frac{2TVN_c e^{-\lambda_c} r_c^2}{3\sqrt{\pi}} \times [\lambda_c F_0^{\pm}(\theta/\theta_0) + F_2^{\pm}(\theta/\theta_0)], \quad (9)$$

where

$$\theta_0 = 6\pi U\tau/TV, \quad (10)$$

$$F_m^{\pm}(x) = \int_0^\infty \xi^m e^{-\xi^2} \int_{2\rho\xi/2}^1 d\mu \times \exp\left[-\frac{x}{\mu\xi \pm 1/2\rho\xi^2}\right] \quad (11)$$

and $\rho = U/V$.

The total number of atoms in the cloud is easily obtained, assuming $v/V \ll 1$ as

$$N = 2\pi^{1/2} N_c e^{-\lambda_c} r_c^2 U\tau(1 + \lambda_c). \quad (12)$$

Discussion

The observational data are shown in Fig. 4 along with angular distributions calculated from Eqs. (9)–(11) for temperatures of 100 K and 3000 K. At low temperatures, the predicted distribution is nearly symmetric, contrary to the observations. To produce the amount of asymmetry observed, high velocities, and thus high temperatures are required. The Pioneer 10 results indicate that temperatures of order 3000 K ($U \simeq 7\,\mathrm{km\,sec^{-1}}$) are appropriate although neither the theory nor the experimental data allow a very precise determination.

The effective angular width of the cloud is ~120°, and exhibits a decrease which can be fit with the parameter $\theta_0 = 4$, implying $U\tau \simeq 6 \times 10^5$ km. If the temperature of the Ionian atmosphere is 3000 K, then $\tau \simeq 1 \times 10^5$ sec. The lifetime against photoionization is $\sim 3 \times 10^6$ sec, consequently an additional mechanism must be responsible for the high loss rate. Charge exchange with the magnetospheric plasma is an obvious candidate. For a corotating thermal plasma densities of order 500 cm^{-3} are suggested.

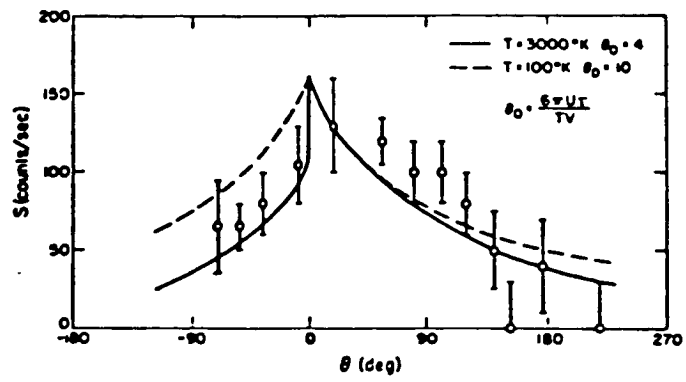

Fig. 4. The observed H Lyman-α intensity as a function of the orbital angle with respect to Io. Positive values of θ are for the tailing portion of the cloud. The solid curve is a fit of (9) with $\theta_0 = 4$ and $T = 3000$ K while the dashed curve is for $\theta_0 = 10$ and $T = 100$ K. The discontinuity in the curves at $\theta = 0$ is due to the simplified theory and will be smoothed by oscillations of the atoms about their mean angular velocity.

It was previously estimated that the total number of hydrogen atoms in the cloud was $N \sim 2 \times 10^{33}$. The corresponding escape rate from Io must be $\sim 5 \times 10^{10}\,cm^{-2}\,sec^{-1}$. If the escape process is indeed thermal, and represented by an exospheric temperature of ~3000K, then the H atom density at the critical level is $\sim 2 \times 10^{5}\,cm^{-3}$ and the hydrogen column density in the exosphere is $6 \times 10^{13}\,cm^{-2}$.

It is important to note that the escape process may be nonthermal, in which case the concept of an exosphere and the corresponding kinetic temperature would be less meaningful. Nevertheless, for isotropic escape, the observed asymmetry implies escape with relatively high velocities. Corresponding high velocities (and perhaps high temperatures) are suggested by the sodium emission linewidth obtained by Macy and Trafton (1975). They found a width of 70mÅ (FWHM) which would correspond to a velocity of $\sim 1.8\,km\,sec^{-1}$ and temperatures of perhaps several thousand degrees.

Acknowledgment

This work was supported by The National Aeronautics and Space Administration under Contract No. NAS 2-6558 with the Ames Research Center.

References

Bergstrahl, J. T., Matson, D. L., and Johnson, T. V. (1974). Sodium *D* line emissions from Io: Synoptic observations from Table Mountain Observatory. Paper presented at IAU Symposium No. 28, Planetary Satellites, August 1974, Ithaca, N.Y. *Astrophys. J.*, in press.

Carlson, R. W., and Judge, D. L. (1974). Pioneer 10 ultraviolet photometer observations at Jupiter encounter. *J. Geophys. Res.* **79**, 3623–3633.

Chamberlain, J. W. (1963). Planetary coronae and atmospheric evaporation. *Planet. Space Sci.* **11**, 901.

Judge, D. L., and Carlson, R. W. (1974). Pioneer 10 observations of the ultraviolet glow in the vicinity of Jupiter. *Science* **183**, 317–319.

Kliore, A. J., Fjeldbo, G., Seidel, B. L., Sweetnam, D. N., Sesplaukis, T. T., Woiceshyn, P. M., and Rasool, S. I. (1975). The atmosphere of Io from Pioneer 10 radio occultation measurements. *Icarus* **24**, 407–410.

Macy, W., and Trafton, L. (1975). Io's sodium emission cloud. *Icarus* **25**, in press.

Discussion

Yung: For a good fit to the spatial distribution of Lyman-α, Carlson and Judge require the hydrogen atoms emitted by Io to have a high temperature ~3000K. However, the electron profile deduced by Kliore *et al.* (1975) shows that the upper atmosphere is probably not hotter than 500K. A possible solution to explain the two temperatures would be: the atmosphere of Io is in a quiescent state during occultation while the toroid hydrogen comes from Io at times when the satellite is aurorally active.

Pioneer 10 and 11 Ultraviolet Photometer Observations of the Interplanetary Hydrogen and Helium Glow: The Radial Dependence

K. Suzuki, R. W. Carlson, D. L. Judge

Abstract presented at the Fall Meeting of the AGU, San Francisco, 1975

The Pioneer 10 and 11 missions to Jupiter and the outer solar system include photometric instrumentation for observation of the ultraviolet resonance lines of atomic hydrogen and helium. During cruise phase, continuing measurements are being performed of the interplanetary H and He glow, which is produced through resonance scattering by interstellar gas flowing into and through the solar system. The density and emission profile of this gas depends upon the density, velocity, direction, and temperature of the inflowing gas and ionization loss rates. The large radial extent sampled by the Pioneer spacecraft can be used to determine these parameters. The radial and angular variations indicate an inflowing velocity of approximately 20 km/sec., flowing parallel to the ecliptic plane from 240° - 260° right ascension. An interstellar He to H number density ratio of $\sim$15% is found.

On the Invertibility of Mutual Occultation Light Curves

R. T. Brinkmann

Abstract presented at the Division for Planetary Sciences (AAS) Meeting, Columbia, Md, February 1975

It has been suggested that a series of mutual eclipse/occultation light curves involving the Galilean satellites can be inverted to produce albedo maps of the satellites' surfaces. A modelling study has been conducted to determine whether the inversion can be accomplished in the presence of realistic amounts of noise and systematic error. Synthetic light curves of our own moon occulted by another moon just like it were generated, noise superimposed and the inversion attempted. It is found that the process works pretty well in the presence of amount of noise representative of routine high-quality photometry. Light curves of Galilean satellite events obtained during late 1973 should be capable of yielding maps with a resolution exceeding 20 km in the case of Europa.

ICARUS 27, 69–89 (1976)

On the Inversion of Mutual Occultation Light Curves

R. T. BRINKMANN[1]

Physics Department, University of Southern California, Los Angeles, California 90007

Received March 14, 1975; revised April 18, 1975

The extent to which mutual occultation light curves, of the type that occur among the Galilean satellites of Jupiter, can be inverted to produce albedo maps of the surfaces has been investigated. Model calculations have been done utilizing the Earth's own moon as the object of study. It is found that the inversion process can be successfully accomplished even in the presence of amounts of random noise typical of routine high-quality photometry of the Galilean satellites. The inversion process is also reasonably tolerant of systematic errors in the light curves, such as those due to photometric nonlinearity. Unless the limb-darkening distribution is pathological or the geometric elements adopted are seriously in error it should be possible to produce fairly high resolution maps of at least some of the Galilean satellites.

Introduction

In late 1973 and early 1974 a series of several hundred mutual eclipses and occultations of Jupiter's Galilean satellites occurred, as seen from the Earth (Brinkmann, 1973; Brinkmann and Millis, 1973; Milbourne and Carey, 1973; Aksnes, 1974). A large number of these events were observed photometrically from various stations around the world. In principle, the resulting light curves can be "inverted" to produce albedo maps of the satellites' surfaces (Brinkmann, 1973) and, in fact, some early attempts in this direction have been made (Murphy and Aksnes, 1973; Vermilion *et al.*, 1974; Herzog and Beebe, 1975). These attempts have used only a few light curves and the procedures used leave doubts as to the uniqueness of the inferences drawn. The present author has for some time been investigating the possibility of analyzing all the data available from the Lowell Observatory data bank (Brinkmann and Millis, 1973) in a more rigorous fashion. Since the actual data contain not only noise but also possible small systematic errors—and since a rigorous a posteriori error analysis may be prohibitively difficult and lesser attempts possibly misleading—it was decided to conduct modeling studies to determine the extent to which albedo maps derived from occultation and eclipse light curves do in fact correspond to the actual albedo of the satellites involved. In this paper only occultations are considered, owing to limitations on computer availability.

The object chosen for study was the near side of our own Moon. Albedo differences on the Galilean satellites are expected to be at least as large as on our own Moon so this should be a sufficiently conservative case. Several simplifying assumptions were made in these calculations, many of which will not be permissible in analyzing the actual Galilean satellite data. Some of these assumptions are as follows. (1) The moon always presents the same face to the observer. (2) It is occulted by another moon just like it, of equal apparent size. (3) The sun, a point source, is infinitely far away. (4) The entire observable hemisphere of the moon is illuminated: there is no terminator visible. (5) Relative satellite motion for the various events is at a constant, uniform rate along straight, parallel lines at known locations. (6) There is no limb darkening.

These assumptions simplify the analysis. The results of the analysis are applicable

[1] Now retired

Copyright © 1976 by Academic Press, Inc.
All rights of reproduction in any form reserved.
Printed in Great Britain

to the actual situation of the Galilean satellites with the sole proviso that if strong limb darkening is present and if, for some reason, it cannot be determined and included in the analysis (if, for instance, it varies wildly over the surface), then trouble may result. The picture of Ganymede obtained by Pioneer 11 (Anonymous, 1975), however, shows no such limb darkening.

The starting point is the high resolution, photographic-photometric albedo map of our own moon of Pohn and Wildey (1970). This map was overlain with a 70 by 70 square grid (corresponding, in normal projection, to 50 km on a side) and the albedo within each square carefully eye-ball-integrated to produce a mean value for each square. Some of the squares contained no moon and were given a value of zero. Albedos for squares containing some lunar limb apply only to the portion of the square containing moon. This 70 by 70 array constitutes the basic data of this study.[1] The array is designated D and the elements D_{ij}, where i designates the row and j the column.

Occultation Light Curves

In this study we consider only occultations. Eclipses are slightly more difficult to deal with, as a shadow function must be convolved into the analysis. They also require considerably more (a factor of 5 or 10) computer time and storage space. (These remarks apply to actual Galilean satellite eclipses: With a point-source, infinitely distant sun, eclipses and occultations would be virtually equivalent.) Most of the computations in this study were run on a PDP 11/45 minicomputer.

In a straightforward computer-generated plot of the 70 by 70 albedo array the grid structure would be objectionably apparent. This is an artifact of the digitizing process and must be done away with if we are to have confidence in our results (and to avoid the objection that we are biasing our results by using the same grid or coaligned commensurate grids for

[1] As a matter of interest, the mean normal albedo determined in this way was 0.1186.

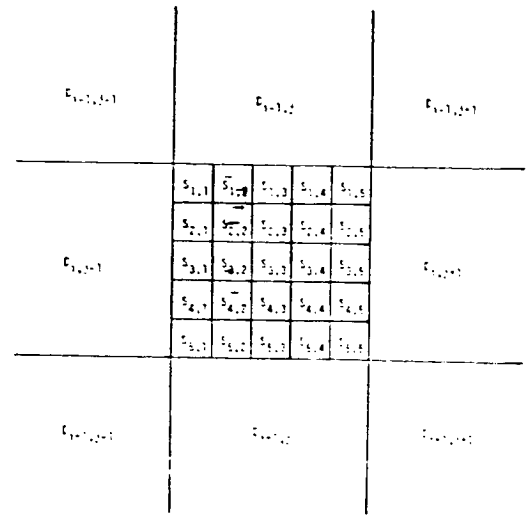

FIG. 1. The division of an element of the albedo array, $D_{i,j}$, into subelements, $S_{k,l}$, $k = 1, 5$; $l = 1, 5$.

digitizing and for analysis). This is done in the following way. We divide each of the 4900 elements into 25 square subelements, $S_{k,l}$, $k = 1, 5$; $l = 1, 5$. Using the nomenclature of Fig. 1 we first set

$$S_{3,3} = D_{i,j}.$$

If any of the surrounding D values ($D_{i-1,j-1}$, $D_{i-1,j}$, etc.) is undefined (because one or both of its subscripts is either 0 or 71) it is assigned the value of the defined D value with 0 subscripts increased to 1 and 71 subscripts decreased to 70. If any of the surrounding D values is zero (that is, if that area element contains no moon) it is assigned the value $D_{i,j}$. We set

$$S_{1,1} = (D_{i,j} + D_{i,j-1} + D_{i-1,j-1} + D_{i-1,j})/4,$$

$$S_{1,5} = (D_{i,j} + D_{i-1,j} + D_{i-1,j-1} + D_{i,j-1})/4,$$

$$S_{5,5} = (D_{i,j} + D_{i,j+1} + D_{i+1,j-1} + D_{i+1,j})/4,$$

$$S_{5,1} = (D_{i,j} + D_{i-1,j} + D_{i-1,j-1} + D_{i,j-1})/4,$$

and

$$S_{1,3} = (D_{i,j} + D_{i-1,j})/2,$$

$$S_{3,5} = (D_{i,j} + D_{i,j-1})/2,$$

$$S_{5,3} = (D_{i,j} + D_{i+1,j})/2,$$

$$S_{3,1} = (D_{i,j} + D_{i,j-1})/2.$$

We interpolate linearly among the 9 S values so calculated to obtain the other 16 S values. Then we sum all 25 S values and renormalize them so that they average to $D_{i,j}$. (In practice, the normalization is done before the other 16 S values are computed by interpolation.) This procedure "smooths the edges" of the 70 by 70 elements and eliminates the visible traces of the digitization process. This is the lunar albedo map adopted for this work. It is still only necessary to store 4900 numbers in the computer and the resolution is still of the order of 50 km.

The albedo "maps" presented in this paper were generated on a "Cal-Comp" type of plotter. Ten different shades of gray are available for each subelement, $S_{k,l}$. However, since extreme values at either end of the scale are seldom used, the effective number of shades of gray is nearer five or six. The "photometric density" of the various shades is not strictly linear with albedo: dot patterns were selected to give what seemed a reasonable monotonic progression of densities. Furthermore, to accentuate albedo differences, or contrast, the shades of gray were assigned values from "nearly white" to "nearly black." Actual albedo variations are smaller than this. Consequently, differences between shades of gray appear larger than they really are. This aids intercomparison of maps but tends to make the agreement, or correlation, between maps appear less than it really is. Some of the contrast disappeared in the photographic reproduction. Additionally, limitations on plotting width available, plotting time required (about 0.1 sec per dot) and minimum dot size for available pens resulted in a coarser grid of dots than would otherwise be desired. A further problem is that the characteristics of the pen frequently changed considerably from plot to plot and from the beginning to the end of a single plot. Thus, the plots in this paper are rather crude representations of the results achieved, though they should be adequate for the present purpose. It is hoped that if and when actual Galilean satellite data are inverted a better means of pictorial representation will be available.

We subdivide each area subelement, $S_{k,l}$, into an 8 by 8 array of sub-subelements. Each sub-subelement is represented by a pair of X–Y coordinates specifying its position (the position of its center). Whether a dot appears at a given sub-subelement in a computer plot depends on the dot pattern associated with the albedo of its parent subelement and the sub-subelement's location in the subelement, S. However, in computing the synthetic light curves and inverting, the albedo of a subelement was uniformly "partitioned" among its sub-subelements. Thus, in place of the two-dimensional lunar disk we have an array of $70 \times 70 \times 5 \times 5 \times 8 \times 8 = 7\,840\,000$ points. Of these about

$$[(70^2 - \pi \times 34.758^2)/70^2] \times 7\,840\,000 = 1\,767\,334$$

lie outside the lunar radius and are associated with an albedo value of zero. The remaining approximately 6 000 000 points are associated with one of the 4900×25 subelement albedos determined by the 4900 measured albedos. This grid size corresponds to 1.25 km in the lunar normal plane and is sufficiently fine to assure that digitization noise will not affect the results of this study.

Synthetic occultation light curves used in this study were computed with the full 1.25 km resolution. The various inversion programs, however, utilize a user-specified resolution. In this paper a resolution of 1/18th diameter (about 200 km), rather than 1/70th, was used. This was done because of limitations on computer time (and storage space) available. A wide range of model computations was to be done and it was felt that the overall behavior of the inversion process could be adequately studied with this lower resolution. Furthermore, the impact parameters of the occultation events synthesized in this study were uniformly spaced at about 1/18th lunar diameter, so it is not expected that much additional detail could have been recovered by increasing the computational resolution.

Occultation light curves are generated as follows. An impact-parameter, or miss

distance, a time step, a starting time, and a stopping time are selected. The impact parameter must be between −3475.8 and +3475.8km. The computer programs are flexible enough to allow the time step to vary (or, for that matter, to allow the occulting moon to be of a different apparent size than the occulted), but for this analysis a constant time step was felt to be adequate. Typically a time step of 5sec is used. The relative speed of the two moons was fixed at 10km/sec.

An initial calculation is done with the two moons completely separated. A summation is made of the albedos associated with each of the 6-million-plus "dots" comprising the moon to be occulted. This is the preevent intensity; its units are not important. This intensity is doubled to allow for the fact that the occulting moon will also be "in the aperture" during the event.

The time is now set equal to the starting time, which is normally chosen to be just after the time at which the two disks begin overlapping. Conceptually, the occulting moon is now repositioned in such a way that it partially overlies the occulted moon (see Fig. 2). The albedos associated with the dots that have been covered up are now subtracted from the initial sum. This revised albedo sum, expressed as a fraction of the initial albedo sum, is the relative intensity at this time. The time is then sequentially incremented by the time step. Albedos associated with dots newly covered are subtracted from the albedo sum of the previous step. Eventually, dots will begin to be uncovered as well. Accordingly, the albedos associated with these dots are added to the albedo sum from the previous step. The new albedo sum, at each new time, is divided by the initial albedo sum to produce the relative intensity at that time. The stopping time is normally chosen just before the time when the event is over. The light curve for the given impact parameter is the set of time-relative intensity pairs.

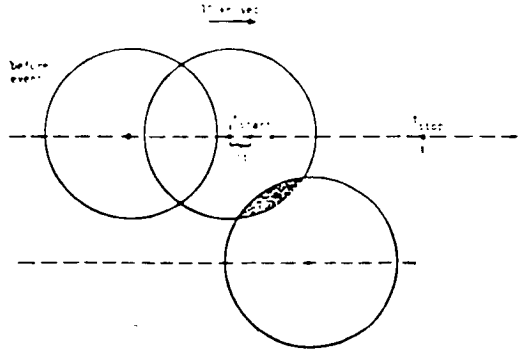

FIG. 2. Occultation geometry. As the occultation gets under way, points on the lunar surface are covered from view. As the event proceeds, points will begin to be uncovered as well.

Light curves calculated in this manner for our moon at impact parameters uniformly spaced between −3400 and +3400km at 200km intervals are shown in Fig. 3 (with artificial noise superimposed). Also shown in this figure are curves computed for a uniformly bright lunar disk given by a simple geometric expression. Differences between the two sets of curves (or the lack of differences) contain the information about the albedo of the real moon. Differences, it can be seen, are typically about 2%. For the Galilean satellites they may be somewhat greater, but it is still clear that accurate relative photometry will be needed to produce good results. Fortunately, the least-squares approach to be adopted in this work may be able to extract albedo information even if the noise in the data is comparable to the differences in Fig. 3. That is one of the things we wish to ascertain. The cusp in the "head-on" occultation (Fig. 3) appears because the two bodies have the same apparent size. If they were of different sizes there would be a "plateau" region for total and annular occultations.

The light curves calculated by this process are ready to have noise and/or systematic error incorporated and then to serve as "observed data" in the subsequent attempts to infer the original albedo array. We postpone to a later section the details of the types of noise and error used.

THE INVERSION PROCESS

The computed light curves, modified so as to simulate noise and instrumental-atmospheric peculiarities, are now assumed

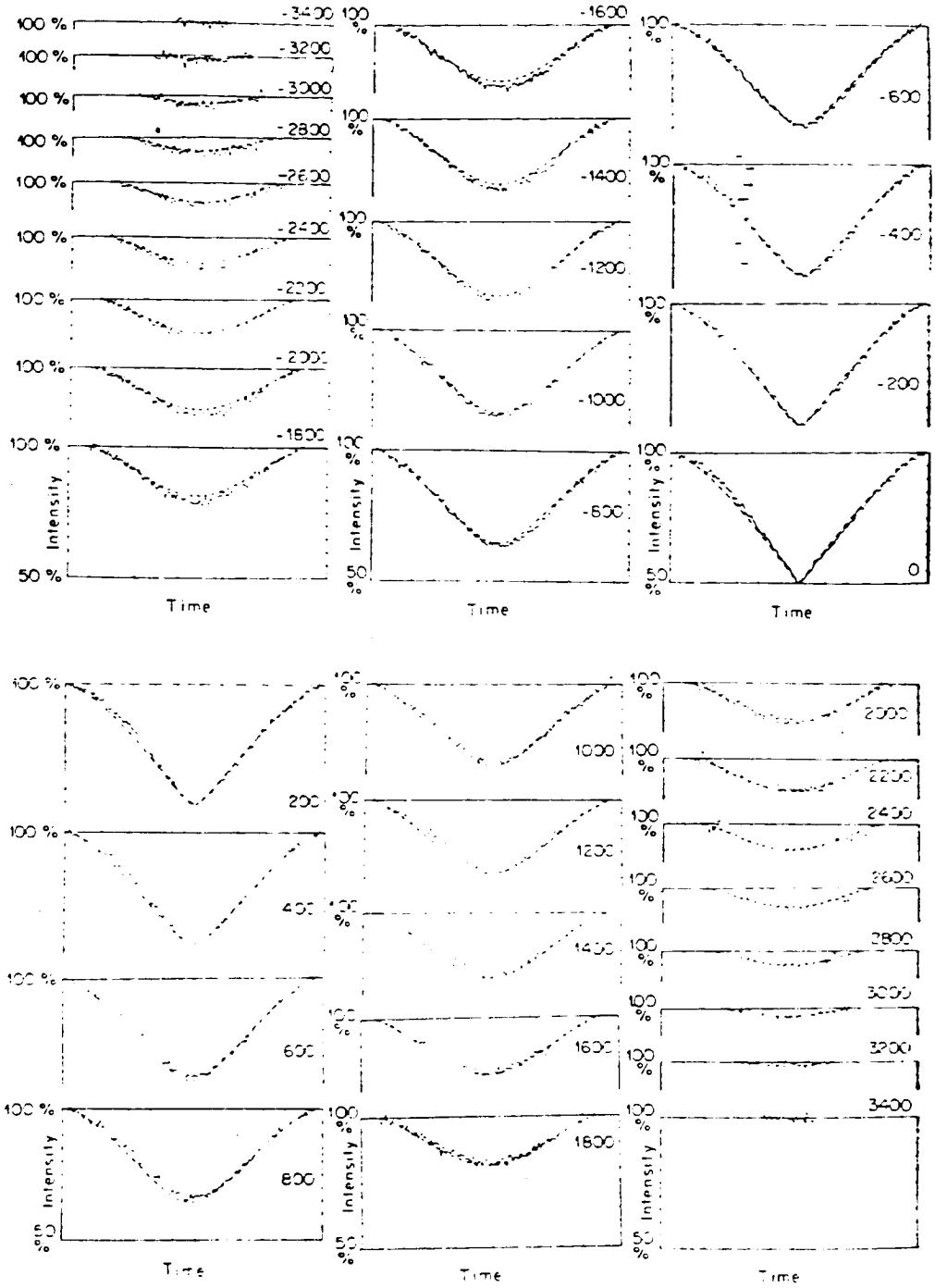

FIG. 3. Synthetic light curves for our moon computed as described in the text (solid curves) and with noise superimposed. The noise is nearly Gaussian with variance ±1% at 100% intensity varying linearly to ±½% at 50% intensity (bottom of figure). Impact parameters range from +3400 to −3400 km in steps of 200 km. Dashed curves show results for a uniformly bright moon, with no noise. Differences between the two types of curves are diagnostic of the albedo markings. Time is shown in intervals of 1 minute.

to be "data," i.e., the results of measurement. The 70 by 70 grid of albedo values used to compute these light curves will not be used again until it is time to compare our inferred albedos with the known albedos, except as specifically mentioned.

Initially, a "differential" mode of computation was adopted. Rather than consider the value of a light curve at various times, we consider instead the *change* in the value of the light curve between two successive times. If a light curve contains n points (times) it will contain $n-1$ time steps. We denote the change in a light curve during a given time step by δI_t. During this time step the number of sub-subelements, or dots, in each of the $n \times n$ (where $n \leqslant 70$ is the number of resolution elements per diameter) albedo elements may change (except those containing no moon). We designate the change in the number of dots contributing from albedo element $D_{i,j}$ during time step t by $\delta c^t_{i,j}$. We call this, for want of a better terminology, the "change factor." It may be positive, negative, or (usually) zero. It is a simple geometric quantity and does not depend on any known or assumed albedos in any way.

Since we know nothing, as yet, about the albedo distribution on the surface, we cannot enforce the "gradation" procedure as we did in the preceding section. We assume that the albedo in each of the sub-subelements is the same as the albedo of its associated element of the 70 by 70 array. A more sophisticated approach could enforce the gradation. Alternatively, it is possible in principle to iterate the gradations into the solution after the initial solution has been obtained, but we do not consider these possibilities in this paper. (The computer plots of the results, however, will have the gradation enforced for appearance's sake.)

To determine approximately the unknown albedos, $D_{i,j}$, $i = 1, n$; $j = 1, n$ ($n \leqslant 70$), we minimize the least-squares expression

$$\sum_t w_t \left(\delta I_t - \sum_{i=1}^{n} \sum_{j=1}^{n} \delta c^t_{i,j} D_{i,j}\right)^2 \qquad (1)$$

with respect to the albedos, $D_{i,j}$. Here the sum over t is over all the time steps for all the occultations and w_t is a weighting factor associated with the "observed data" at this time step, δI_t is the observed data change at this time step (the difference between sequential light curve intensities, as computed in the preceding section), the $\delta c^t_{i,j}$ are the change factors as already defined, and the $D_{i,j}$ are the unknown albedos. The weighting factor allows one to weight light curves differently (e.g., light curves obtained on large, accurately guided telescopes with stable, efficient detector-recorders on clear, atmospherically stable nights would receive high weighting). One can weight different parts of the same light curve differently (e.g., if observing conditions changed during the event). In this analysis we take all the weighting factors equal to 1. The "change factors" are computed in the same computer program that computed the light curves (they do not utilize the known, starting albedos) and are stored, after data compression, on a large random-access disk file.

Differentiating expression (1) with respect to one of the unknown albedos, $D_{k,l}$, and setting the result equal to zero produces an equation linear in the unknowns:

$$\sum_t w_t \left(\delta I_t - \sum_{i=1}^{n} \sum_{j=1}^{n} \delta c^t_{i,j} D_{i,j}\right) \delta c^t_{k,l} = 0. \qquad (2)$$

In all, there are as many such equations, as there are unknowns, namely, $n \times n$ minus those elements that geometrically lie entirely outside the lunar disk and hence can make no contribution to the light curves. Utilizing the change factors stored in the disk file, we can then compute the coefficients of the unknowns in the linear equations and, using the "observed data" values, solve for the unknown albedos.

There are two problems, however, or perhaps two aspects of the same problem. It is possible that some of the unknowns will be poorly defined by the data, depending on the distribution of impact parameters and consistency of the data. Perhaps the goodness of fit of the synthetic

to the "observed" light curves is insensitive to a given albedo element or to all such elements in a given area. Or perhaps, though the average albedo in a given area, large or small, may be well determined, the fit is just about as good if all the elements in this area have the same value or if they have appreciably different values. Clearly some sort of "smoothing," when permitted by the data, would be desirable, not only to improve the appearance of the resulting map but also to avoid the computational difficulties associated with floating point overflows underflows and divisions by zero.

Let us add to the expression in (1) a smoothing term:

$$\sum_t w_t \left(\delta I_t - \sum_{i=1}^{n} \sum_{j=1}^{n} \delta c^t_{i,j} D_{i,j}\right)^2 - K \sum_{i=1}^{n} \sum_{j=1}^{n} \left(D_{i,j} - \sum_{k=-\infty}^{\infty} \sum_{l=-\infty}^{\infty} v_{i-k,\,j-l} D_{k,l}\right)^2. \quad (3)$$

Here K is a parameter that can be changed to vary the overall degree of smoothing. The coefficients $v_{m,n}$ are weighting factors sum-normalized to 1. For large m, n the value of $v_{m,n}$ is zero so that the number of terms actually included in the inner summation need not be excessive. If we wished, for example, to use only nearest neighbors in the smoothing process we would have

$$v_{0,1} = v_{1,0} = \tfrac{1}{4}, \qquad \text{all other } v_{i,j} = 0.$$

If the element under consideration lies near the edge of the moon some of its neighbors may have the value zero or may be undefined (one or both subscripts may be zero or negative). In these cases we redefine the albedo for those elements to be the same as the albedo of the element in question. Suppose we wished to use nearest neighbors and next-nearest neighbors. Then we would have to specify the relative weighting to be accorded these two types of neighbors.

A computation was done to determine the extent of albedo correlations with distance on our Moon. The 70 by 70 albedo array was used. Figure 4 shows the results of the computation. An average was made of the absolute value of the albedo difference between all possible pairs of albedo values (excluding zero values) whose elements have a given center-to-center separation distance. Such an average was obtained for all possible separation distances. The horizontal axis in Fig. 4 is separation distance in kilometers and the vertical axis is average albedo difference. As the separation approaches the lunar diameter, 3475.8 km, the statistics become poor, explaining the erratic behavior in this region. From Fig. 4 we see that area elements separated by more than about 600–800 km on our Moon are not much more highly correlated in albedo than any two lunar elements picked at random. Elements closer than several hundred kilometers are fairly highly correlated, however. We choose to use for smoothing purposes neighbors no further apart than $50\,\text{km} \times 17^{1/2} \times (70/n) = 206.2\,\text{km} \times (70/n)$. The weighting factors $v_{m,n}$ are given in Table I. They are obtained by dividing the "number density factor" by the average correlation squared and normalizing to 1. The "number density factor" is a somewhat artificial term obtained by "eyeball smoothing" a plot of "change of separation distance" versus "separation distance" as one scans through Table I. The number of $m - n$ combinations that produce a separation distance within a given range increases as the separation distance increases. Thus, the number density factor prevents undue weight from being given to large $m - n$ combinations. Division by the square of the "average correlation" is the appropriate statistical procedure in an instance such as this in which we have several estimates of a quantity with varying uncertainties. This is the method used to derive the quantities $v_{m,n}$. Other methods could have been used. The results should not be sensitive to the details used.

The weighting factors $v_{m,n}$ are valid as defined only for $n = 70$. For $n = 18$, as is the case for the present study, the "separation distances" (Table I) should have been larger by a factor of $70/n$ and the "average correlations" appropriately corrected. Because of an oversight, and the inability to rerun the programs when this point was

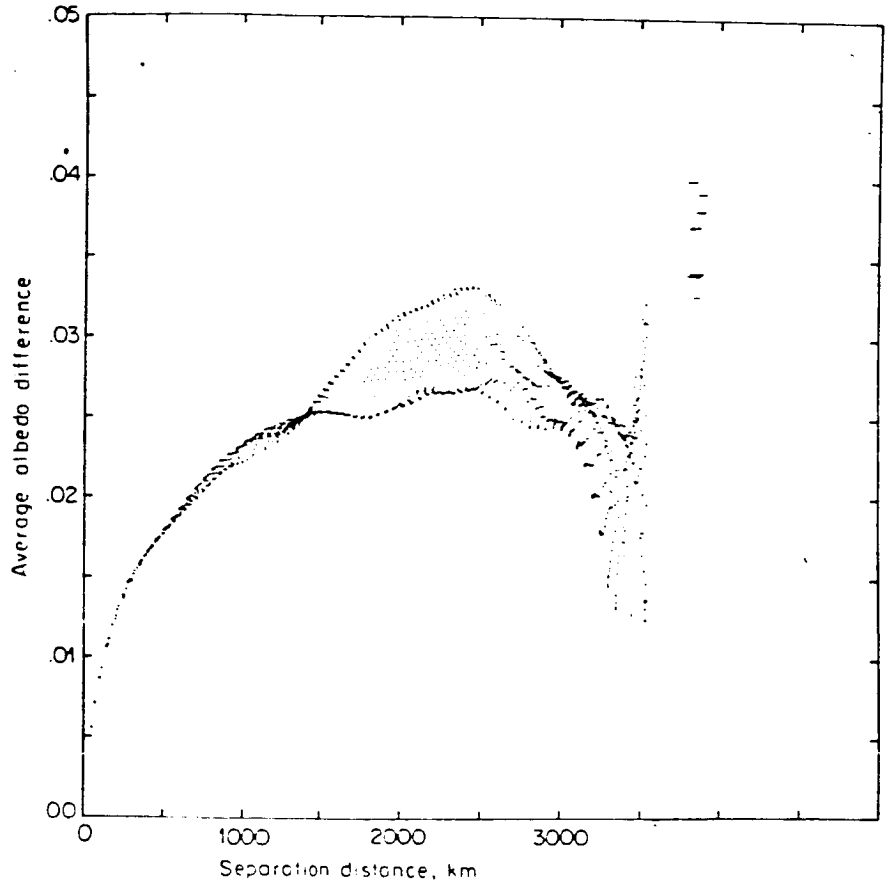

FIG. 4. Albedo correlation versus separation distance on our moon. The 70 by 70 albedo grid was used. Horizontal coordinate is the separation distance in kilometers. Vertical axis is the average albedo difference (always positive) for all pairs of nonzero albedo elements with a given separation distance.

TABLE I

WEIGHTING FACTORS $v_{m,n}$

m[a]	n[a]	Separation distance[b]	Average correlation[c]	Number density factor	$v_{m,n}$
1	0	1.00000	5.56166	1.00	0.44642
1	1	1.41421	7.10825	0.75	0.20497
2	0	2.00000	8.63945	0.55	0.10175
2	1	2.23607	9.27300	0.45	0.07227
2	2	2.82843	10.5946	0.38	0.04675
3	0	3.00000	10.7577	0.32	0.03818
3	1	3.16228	11.0920	0.28	0.03143
3	2	3.60555	11.9428	0.24	0.02324
4	0	4.00000	12.3053	0.21	0.01915
4	1	4.12311	12.5254	0.18	0.01584

[a] $v_{m,n} = v_{n,m}$; $v_{0,0} = 0$.
[b] Unit is 50 km.
[c] From Fig. 4, in albedo units of 0.001.

appreciated, the weighting factors are not rigorously valid. However, this is not expected to be too important, since the solution of the linear equations is not expected to be very sensitive to the details of the smoothing process, but only to the overall degree of smoothing. Furthermore, there is no guarantee that albedo correlation with separation distance for the Galilean satellites will be similar to that for our Moon.

If we differentiate expression (3) by one of the unknown albedos, $D_{m,n}$, and set the result equal to zero, we obtain an equation linear in the unknowns:

$$\sum_t w_t \left(\delta I_t - \sum_{i=1}^{N} \sum_{j=1}^{N} \delta c^t_{i,j} D_{i,j}\right) \delta c^t_{m,n} + K \left(D_{m,n} - \sum_{i=-\infty}^{\infty} \sum_{j=-\infty}^{\infty} v_{(i-m),(j-n)} D_{i,j}\right) - K \sum_{\substack{i=1 \\ \neq m}}^{N} \sum_{\substack{j=1 \\ \neq n}}^{N} \left(D_{i,j} - \sum_{k=-\infty}^{\infty} \sum_{l=-\infty}^{\infty} v_{(i-k),(j-l)} D_{k,l}\right) v_{(i-m),(j-n)} = 0. \quad (4)$$

Here w_t, δI_t, $\delta c^t_{i,j}$ and $D_{i,j}$ have already been defined; K is the "smoothing parameter," and the $v_{i,j}$ are the weighting factors for smoothing purposes (from Table I). Although there are summations from $-\infty$ to $+\infty$, since $v_{i,j} = 0$ for $i^2 + j^2 > 17$, in practice only a rather modest number of terms need to be retained, even for large N. Here, we have let N replace the former n to avoid confusion with the subscript n. The double summation over the v's appearing in the last term need only be performed once and thereafter can reside as a table in the computer memory. As before, any D having a value of zero is redefined to be $D_{m,n}$, as is any D value having a zero or negative subscript. We can obtain an equation such as (4) for every unknown. Solving these linear equations gives the albedos sought.

This procedure fits, not to the data themselves, but rather to changes in the data. If we wish to fit to the data themselves instead, all that is necessary in the foregoing equations is to replace δI_t by I_t and $\delta c^t_{i,j}$ by $c^t_{i,j}$; I_t is the intensity at time t and $c^t_{i,j}$ is the contribution (i.e., number of "dots" contributing) of the i, jth element at time t. The parameter K will take on larger values, in general, if the fit is made to the data rather than to the time derivatives of the data. Both procedures should give equivalent results when the amount of noise is very small. As the amount of noise becomes more appreciable the differential approach may not work as well as fitting to the data proper. Indeed this was found to be the case.

Noise and Error

Figure 3 shows the computed synthetic light curves with noise superimposed. The noise, generated by a pseudorandom number generator, approximates Gaussian noise with variance 1%. This is the rms difference between the smooth (not depicted) and noisy curves. The rms fluctuations within the "data" of Fig. 3 would be 1.414% and the "noise bandwidth" would be 2%. Computations were also done with variances of 0.5 and 2%. Careful but routine relative photometry can approach the least noisy of these cases. The data points are at 5sec intervals; if the initial measurement frequency had been 1sec, as is often the case, then the noise in the raw data would have had variances larger by a factor of $\sqrt{5}$ (if random noise predominated).

For wide-band photometry of the Galilean satellites with a small (~24") telescope and a 5sec integration period one would expect from theoretical considerations roughly 0.2% noise due to photon statistics and perhaps 0.3% noise due to atmospheric scintillation. There are other, one hopes less important, sources of noise. Our $\pm\frac{1}{2}$% and $\pm$1% rms cases are expected to bracket much of the available data adequately, though confirmation of this must await a further study. About half the more than 200 light curves available for the Galilean satellites have noise levels not appreciably worse than our 1% case (R. Millis, private communication). An example of an actual light curve, one of a half-dozen obtained by the author, is shown in Fig. 16.

We distinguish systematic error from noise in that the former has a time constant appreciably larger than the integration

period. Principal sources are often changes in atmospheric transmission and instrumental drift or nonlinearity. Computations were also done with data simulating a "random systematic error." A random number R from a uniform distribution (between 0 and either ½ or 1%) was generated for each of the light curves. Each intensity I (between 0 and 1) was then replaced by $I + (1 - I)*R$. This is equivalent to locating the "zero levels" of the light curves incorrectly.

Results

The first results presented were obtained in the differential mode, in which the fits were not to the light curves themselves, but rather to changes in the light curves, or to the slope of the light curves. That the two procedures are not the same is illustrated schematically in Fig. 5. The points in the upper part of the figure have been least-squares fit by a straight line. The line, dashed in the figure, has a positive slope. In the bottom part of the figure the slopes are shown as open circles. Fitting a straight line to these slopes would result in a second-degree polynomial on the data scale. Fitting a constant to the slopes results in a family of straight lines (on the data scale) with zero slope. Adjusting the constant of integration (via another round of least-squares fitting) produces a fit to the data, but it is clearly a different fit than was obtained by fitting directly to the data. The differential mode computations were performed because this approach, it was hoped, might be less sensitive to small discontinuities in the data. It was found, though, that when realistic amounts of noise were superimposed on the data the results were overly sensitive to the details of the superimposed noise.

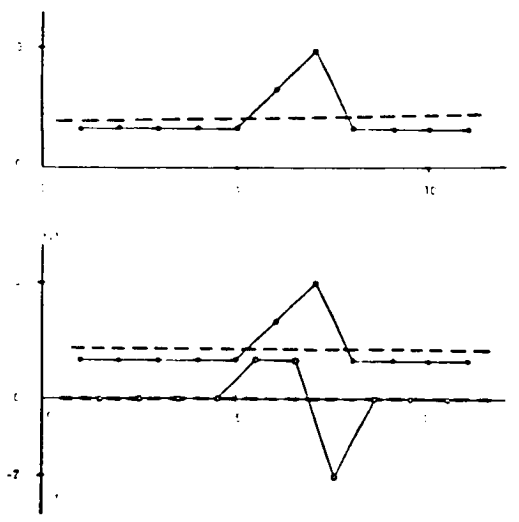

Fig. 5. Differences between fitting to data (top) and fitting to slope (bottom). Open circles are slopes, closed dots data. Straight-line fit to data (top) has positive slope. Constant fits to slope (bottom) is zero so straight-line fit to data has zero slope.

Figure 6 shows results of the inversion process in the differential mode with no superimposed noise. The nine moons illustrated represent different degrees of imposed smoothing: the smoothing parameter increases by a factor of 10 from moon to moon. The upper left moon has too little smoothing: the lower right has too much. Intermediate values give a very nice picture of the moon as we know it. A photograph of the Moon (Fig. 7) can be used for comparison, although the resolution in the photograph is better than the 200km set in the computer program. Clearly, a great deal could be learned from similar pictures of the Galilean satellites. These results confirm that the computer programs contain no major errors and lay to rest any arguments that the faint-in-heart might advance regarding the theoretical noninvertibility of mutual event light curves.

In the upper half of Fig. 8 we present results still in the differential mode, but this time with ±1% rms noise superimposed on the light curves. The two cases are for increased degrees of smoothing. The moon on the left does not have enough smoothing: the one on the right has too much. Directly below these moons are moons obtained the same way but with no noise superimposed on the light curves (from Fig. 6). Here the method appears not to be so successful. There is a great deal of information in the upper left moon but it is not as obvious as we would like,

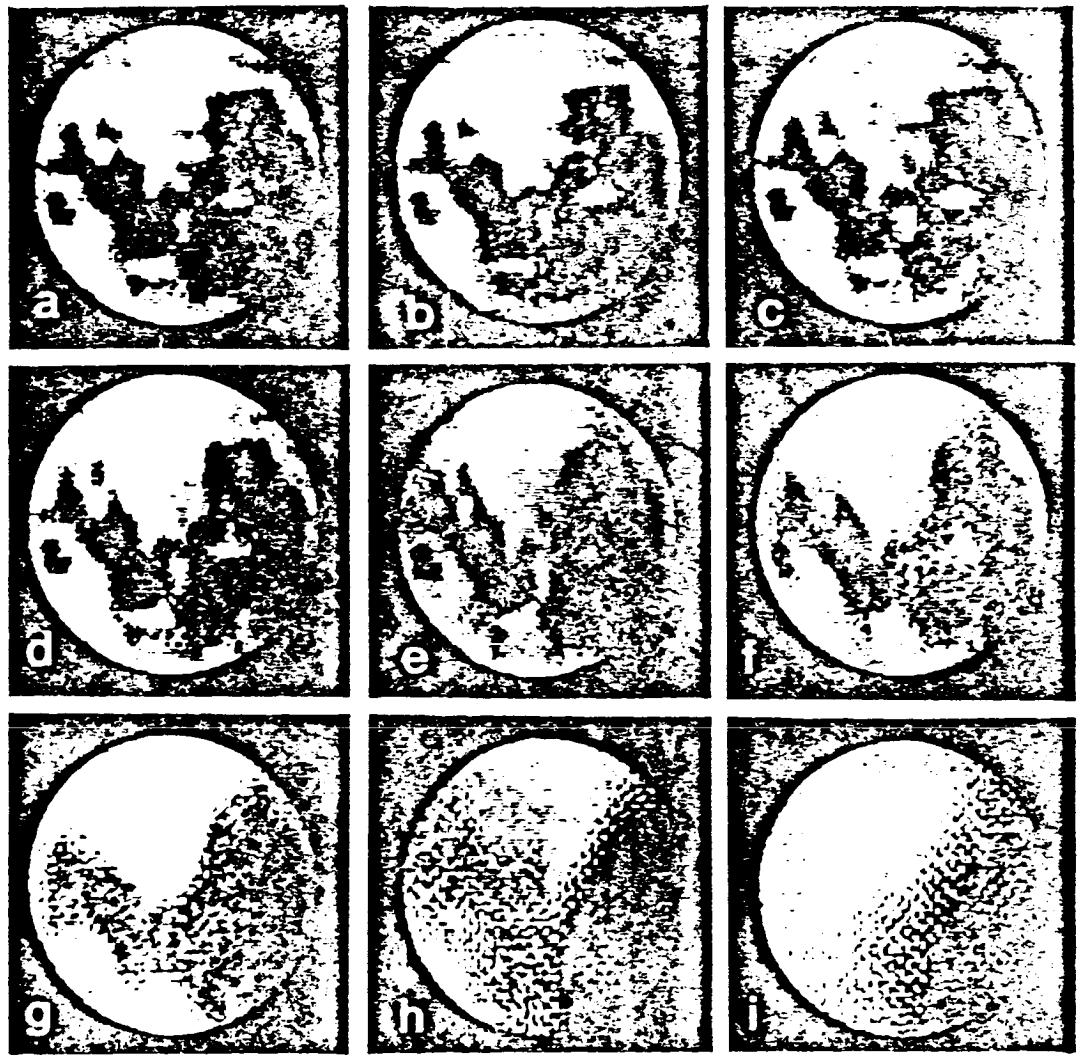

FIG. 6. Moons inverted in the differential fitting mode from noiseless light curves. Smoothing parameter increases by a factor of 10 from step to step.

nor as reliable. Perhaps a moon with slightly more smoothing than the one in the upper left would have been a little more satisfactory, but it would probably still have fallen short of the goal.

Consequently, the remaining computations were done in the direct-data-fit mode, as described previously. A series of moons generated in this mode with different degrees of smoothing and no noise is shown in Fig. 9. This series is to be compared with the series in Fig. 6, which was for the differential mode (fitting to light curve slopes rather than the light curves themselves). Again, the smoothing parameter increases by a factor of 10 from moon to moon. Even when there is very little smoothing the solution remains precise: There is none of the grid structure apparent as there was in the first few moons of Fig. 6.

Next, computations were done, again in direct-data-fit mode, with $\pm\frac{1}{2}\%$ random noise and various values for the smoothing parameter. The results are shown in Fig. 10. The smoothing parameter, as before, changes by a factor of 10 between moons.

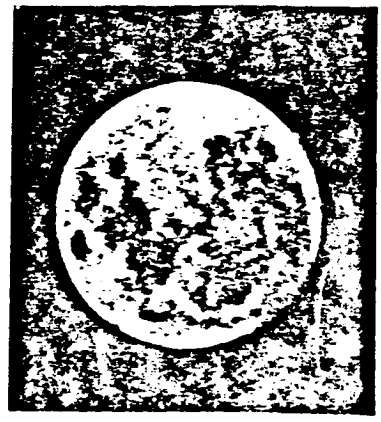

FIG. 7. Photograph of the Moon at a somewhat better resolution than that utilized in the computer-generated plots.

The first moon in Fig. 10 displays the characteristic "checkerboard" pattern that results when too little smoothing is used on noisy data. As the smoothing parameter is increased the patchy structure disappears and the real features remain. As the smoothing is increased further, even the real features are forced to disappear. If there is too much noise the middle stage will be missing.

Figure 11 contains moons generated in the same manner as those in Fig. 10 but with the smoothing parameters intermediate between those of the second and third moons of Fig. 10. Thus, it is an "expansion" of part of the range between these two cases. The smoothing parameter changes here by $10^{0.1} = 1.26$ from moon to moon. We see that it is important to determine the optimum smoothing parameter fairly accurately.

In Fig. 12 we show results similar to those of Fig. 10, except with $\pm 1\%$ rms noise instead of $\pm \frac{1}{2}\%$. The third of the six moons has the correct order-of-magnitude smoothing parameter. Even at this noise level the gross features of the moon are discernible. In Fig. 13 results are presented for $\pm 2\%$ rms noise. It appears that the

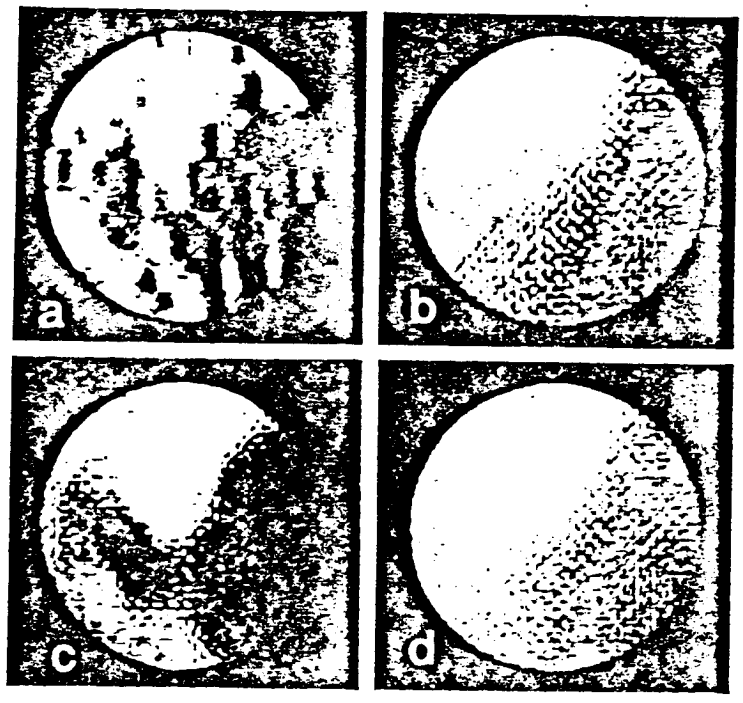

FIG. 8. Top: Moons inverted in differential mode from light curves with $\pm 1\%$ rms noise. Bottom: Corresponding curves with no noise.

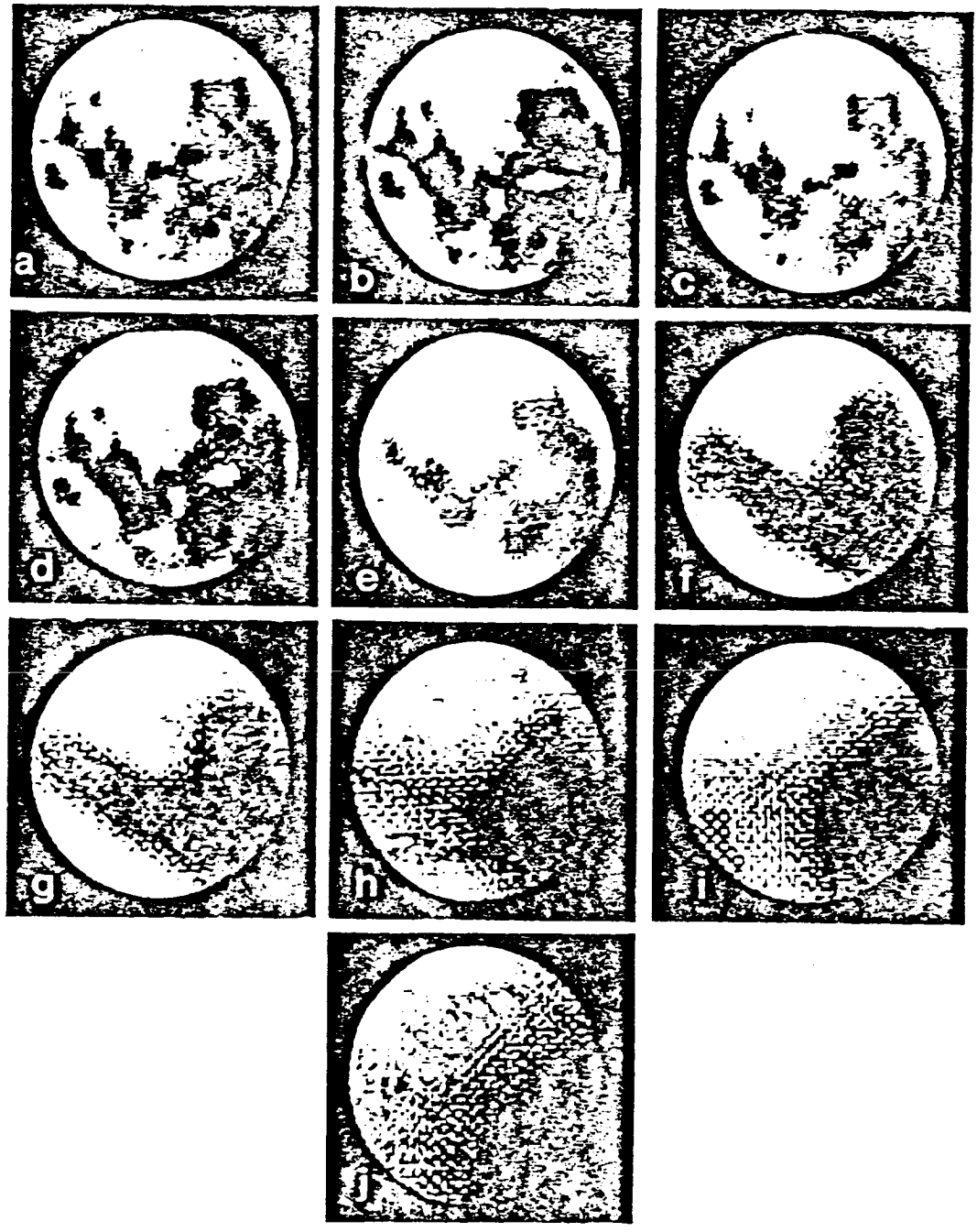

FIG. 9. Moons inverted in the direct-data-fitting mode from noiseless light curves. Smoothing parameter increases by a factor of 10 from step to step.

method has begun to fail at this point (this is pretty noisy data, however). The three moons were all computed for the same smoothing parameter in this case, but with different sets of random numbers used to generate the noise in the light curves. The smoothing parameter was simply estimated on the basis of the previous calculations.

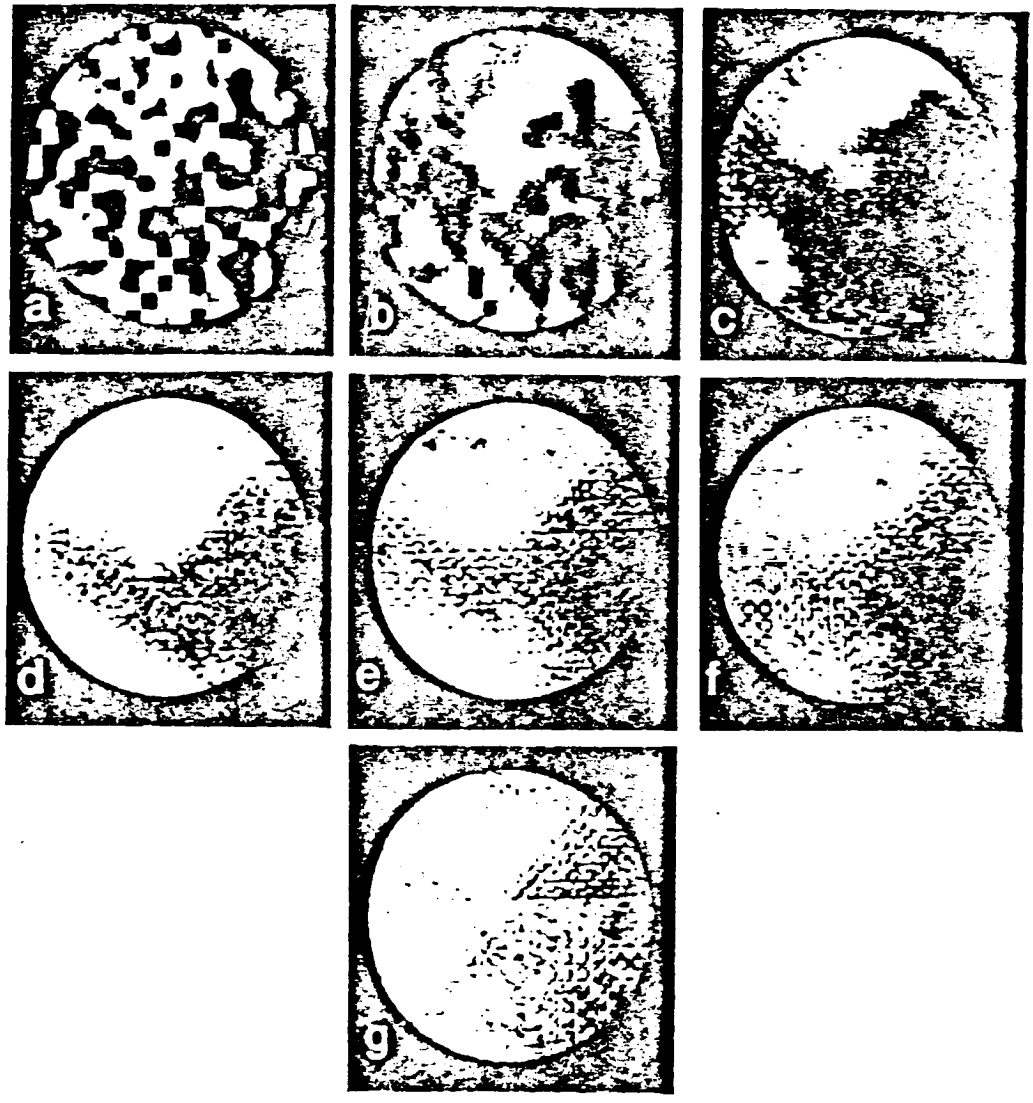

FIG. 10. Like Fig. 9, but with $\pm\frac{1}{2}\%$ noise superimposed on the light curves.

Additional computation with different smoothing parameters would probably have improved the accuracy somewhat.

In Fig. 14 we show results with no random noise, but $\pm\frac{1}{2}\%$ "random–systematic" error, as discussed previously. By comparing with the series in Fig. 9 it can be seen that this amount of systematic error does not unduly hamper the inversion process.

Several other computations were done with combinations of random noise and systematic error. However, in these cases systematic surveys over the smoothing parameter could not be conducted so it is more difficult to interpret the results. It appears, however, that realistic amounts of noise and error can be tolerated without catastrophic degradation of the inversion process. Figure 15, for example, shows a moon resulting from inverting light curves having $\pm\frac{1}{2}\%$ rms random noise and $\pm\frac{1}{2}\%$ systematic error.

THE GALILEAN SATELLITES

In applying the method to the existing actual data for the Galilean satellites it will be necessary to make provision for a

FIG. 11. Like Fig. 10, but with smoothing parameter covering only a portion of the range between the second and third moons in Fig. 10. Smoothing parameter changes by $10^{0.1}$ between steps.

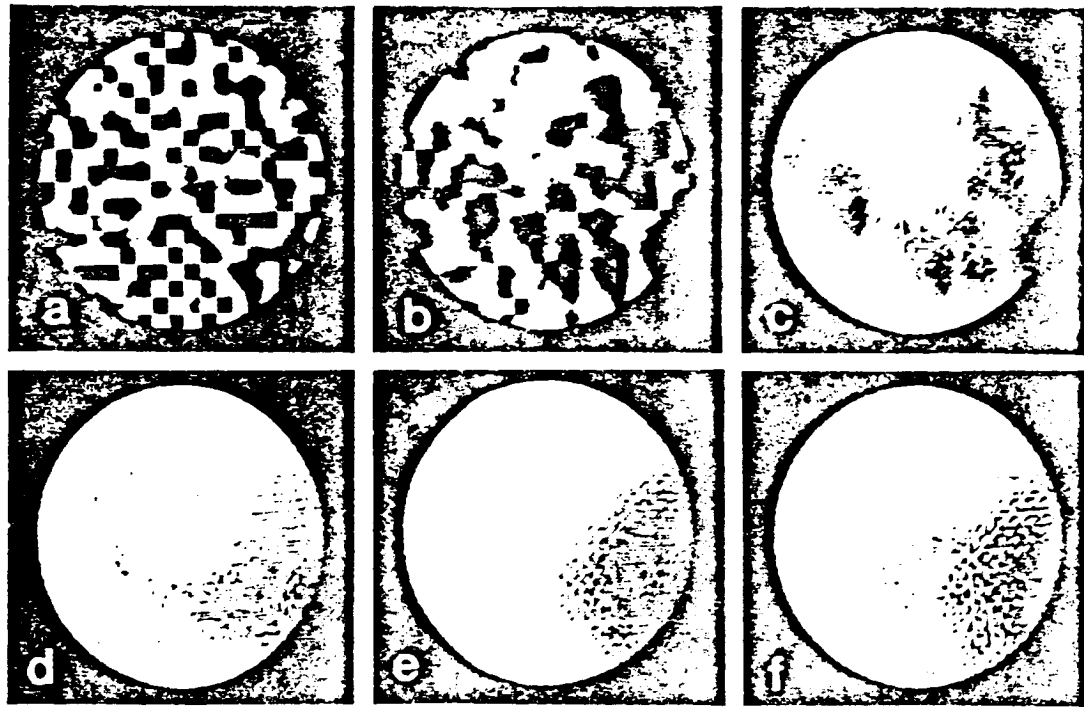

FIG. 12. Like Fig. 10, but with twice as much noise, ±1% rms, superimposed on the light curves.

FIG. 13. Like Fig. 10, but with four times as much noise, ±2% rms, superimposed on the light curves.

number of effects not considered in this study: rotation of the satellites, presence of a shadow terminator in the field of view, illumination by Jupiter, eclipses as well as occultations, and possibly the effects of limb darkening. None of these, except possibly the last if it is severe and variable, should pose insurmountable practical difficulties.

Mention should also be made of the effects of uncertainties in the orbital elements and radii. As with limb darkening, the problems largely disappear if the target satellite does not rotate, provided the grid structure adopted is sufficiently flexible to allow the satellite to "show up" in a slightly different location or of a slightly different size than expected (these effects and limb-darkening effects may be intermixed). Uncertainties in the occulting satellite's radius are equivalent to changing the radius of the *target* satellite and changing the overall brightness of both satellites by a constant factor. Preliminary analysis of these events, and of recent stellar occultations, has produced and is producing much-improved values for these elements. Determining the best approach to take to these problems in analyzing the actual data is part of the actual analysis and, as such, is not within the scope of this paper.

CONCLUSION

The computational apparatus has been set up to invert mutual occultation light curves to produce satellite albedo maps. Results of modeling studies using our own Moon confirm the original expectations that the light curves can be successfully inverted in the presence of realistic amounts of noise and error.

APPENDIX I

Computations: Practical Considerations

The computations consist of three main steps and several subsidiary ones. In the first main step the light curves and change factors are calculated and stored in disk files. In the second step the change factors and a smoothing parameter are used to calculate the coefficients of the albedos in the linear equations (4). In the third step the equations are solved for the unknown albedos. Subsidiary steps include (1) superimposing noise and systematic error on the light curves and storing these in another file, (2) producing computer halftone plots of the results for visual analysis, and (3) conducting comparisons between the known and computed albedo distributions. The subject of error analysis is considered in a later section.

For purposes of illustration we adopt the following numbers: We assume there will be 35 light curves having an average of about 100 time steps each. Of the $N \times N$ elements in the albedo array only about $N \times N \times (\pi/4)$ contain some moon and thus need to be considered. On any one step approximately $1/N$ of the $\pi N^2/4$ elements have nonzero change factors (for eclipses the fraction would be larger by a factor of perhaps 5 or 10 because of the

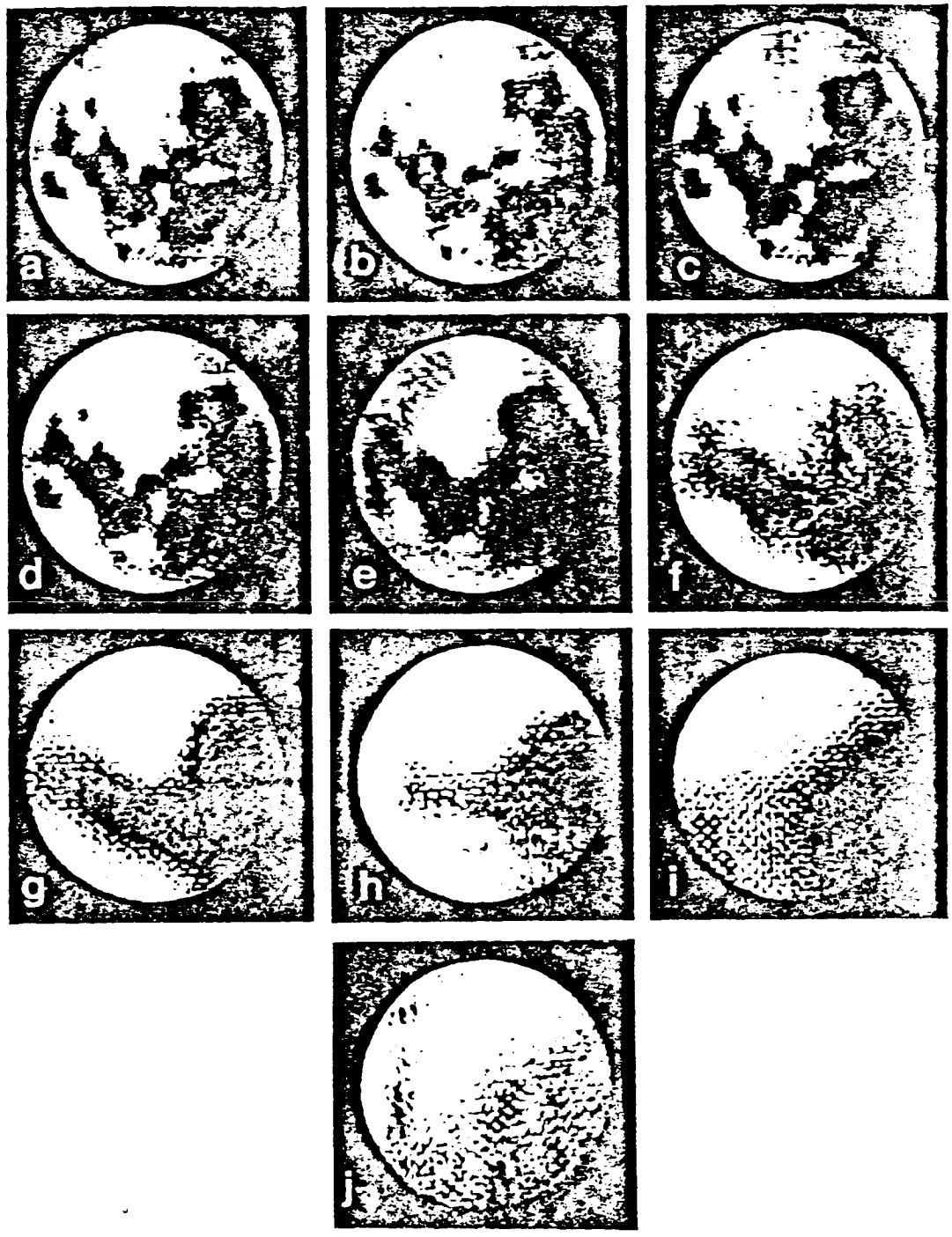

FIG. 14. Moons inverted in the direct-data-fitting mode from light curves with no noise but with $\pm\frac{1}{2}\%$ systematic error. Smoothing parameter increases by a factor of 10 from step to step.

FIG. 15. Moon inverted in the direct-data-fitting mode from light curves with $\pm\frac{1}{2}\%$ rms noise and $\pm\frac{1}{2}\%$ systematic error. Single smoothing parameter was estimated from previous runs.

large width of the shadow edge). A slight assumption is made that if, during a time step, all four corners of an albedo element remain either entirely inside or entirely outside the advancing perimeter of the occulting body, then the change factor for that square for that time step is zero. If this condition is not satisfied, then all of the $(5 \times 5) \times (8 \times 8)$ coordinate pairs comprising the element are tested against the perimeters of both the occulting body at the end of the time step and the occulted body. This testing requires the equivalent in computer time of about 10 multiplications for each coordinate pair. From the number of these points that contribute to the light curve at the end of the time step we subtract the corresponding number stored from the previous time step to produce the change factor for this albedo element for this time step. For computation of the light curves the additional procedure of weighting each contributing point with its associated subelement albedo is followed (Fig. 1). Most of the computing time is spent testing the sub-subelements of the relatively few albedo elements which do change during a given time step. The equivalent number of multiplications involved in this step is then about $35 \times 100 \times (\pi N^2/4) \times (1/N) \times 5 \times 5 \times 8 \times 8 \times 10$ (about $4.4N \times 10^7$). This is a large number of multiplications, but not a prohibitively large number. Computations were run on the Lunar Science Institute's PDP 11/45 minicomputer. It was well suited to this job because (1) it could be dedicated to the job for many hours in a row without antagonizing others (utilization by others was less than 1 hr per day), (2) relatively few time-consuming disk read write operations were required, and (3) the small portion of the program containing the inner DO-loops over the 1600 sub-subelements was written in assembly language, rather than Fortran, allowing full utilization of the floating point processor's speed.

The second main step in the computations consists of computing the coefficients of the unknown albedos in Eq. (4). There are two parts to this step, the first involving the change factors from the preceding step, the second involving the smoothing parameter and interneighbor weighting factors. Most of the computer time in this step is spent on the first part. The equivalent number of multiplications is about $35 \times 100 \times (\pi N^2/4) \times (\pi N^2/4) \times (1/N) \times 2$

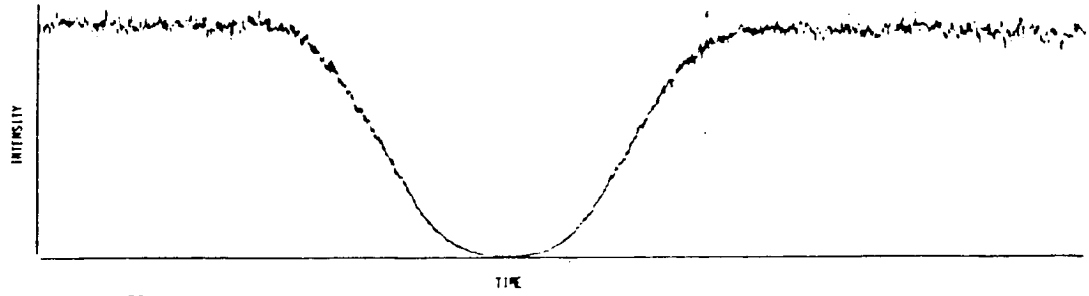

FIG. 16. Example (replotted raw data) of a light curve, not atypical of the better data available, obtained by the author on October 22, 1973, from the Canary Islands. Ganymede eclipses Europa. Time and intensity are linear and the duration of the trace is about 25 min. Time constant is 1 sec.

(about $4.7N^3 \times 10^3$). This is smaller than the number in the first step for the appropriate range of N, but the number of disk operations is much larger (a disk operation on the PDP 11/45 takes about 0.1 sec). The number of disk operations can be reduced if more core storage is available: It is not then necessary to scan through the entire file of change factors for each of the $\pi N^2/4$ unknowns. If enough core is available to store 10 rows of coefficients, for example (40 000 words in this case), the number of disk operations can be reduced by about the same factor. It is not necessary to reduce the number of disk operations to some predetermined value but it is important that the computer spend a substantial fraction of its time computing and not just waiting for disk file reads and writes. Enough core was available that this phase of the computations could also be run on the PDP machine. Note that the output file of coefficients is, in our case, $(\pi N^2/4)^2$ double-precision floating point words. The array is symmetric so this number can in principle be reduced by a factor of 2, but it is still a large number.

The third main step is the solution of the linear equations. There are three principle means of solving a system of linear equations: iteration, straightforward elimination, and Monte Carlo techniques. Goldstein and Von Neumann (1947, 1951) have demonstrated that if certain precautions are taken (notably, positioning for size after each step and symmetrizing the matrix of coefficients if necessary) one can expect to lose 3 bits in the accuracy of the solution by the elimination method for each factor of 2 increase in the number of equations (and, of course, unknowns). The present author has determined that, if the dynamic range of the coefficients is fairly modest (which should be guaranteed by our inclusion of the smoothing term), the results on matrices of size up to at least 320 accord well with the results of Goldstein and Von Neumann and are not dependent on the inclusion of positioning for size. Since 4000 (the largest system of equations considered in this study and about the largest size practicable) is 2^{12} we see that about $3 \times 12 = 36$ bits of precision will be lost in the solution process. Consequently, on a 32-bit floating point word machine double precision will be required. The CDC 6400, also considered for some of the computations, has a 60-bit word (a 48-bit characteristic) so that single precision may suffice. For these reasons, and since the coefficient array is not diagonal dominant, it was decided to solve the linear equations by the elimination method. The equivalent number of floating point arithmetic operations is about $(\pi N^2/4)^3 \times \frac{2}{3}$ (about $0.39 \times N^6$). The number of disk operations, as in the preceding step, is large but can be kept to an acceptable level by multiple row core-storage techniques. Clearly, except on the very fastest machines (like the CDC 7600 or the Illiac), solution of a system as large as $N = 70$ is going to take some hours. However, for $N = 18$ the requirements are much more modest.

As mentioned previously, an 18 by 18 grid was employed in this study. Decreasing the grid size by a factor of f only decreases the amount of work in step 1 by about a factor of f because, although there are fewer albedo elements, a greater fraction of them are actively involved in the occultation during any one time step (because they are bigger). The effective number of multiplications in step 2 decreases by f^3. In step 3, however, the improvement is by a full factor of f^6. The number of disk operations is less sensitive to f.

The effect of increasing the amount of "observed data" to be analyzed (either by decreasing the time step size or increasing the number of light curves) is as follows. The effective number of multiplications in steps 1 and 2 increases linearly with the amount of "data," whereas the corresponding number for step 3 does not change. Thus, since step 3 is expected to be the most time consuming, the penalty for increasing the data base is rather mild.

For our present modeling purposes we wish to employ different sets of "observed data" (corresponding to different kinds or amounts of noise and/or systematic error superimposed on the same "exact" data). In this instance only step 3 must be rerun. [In fact, if one chose to obtain the inverse

of the matrix of coefficients rather than simply to diagonalize it (a several-fold more time-consuming task), one could handle additional sets of "data" with only the order of $(\pi N^2/4)^2$ additional multiplications.] We also wish to change the smoothing parameter, K. In this case we can either rerun steps 2 and 3 or, more efficiently, set K equal to the *change* of the new K over the old K and only rerun that portion of step 2 that involves the smoothing terms and all of step 3. Thus, most of the computing time in this study was spent in solving large systems of linear equations.

For eclipses we can expect steps 1 and 2 to run about a factor of 10 longer, and step 3 to remain as is.

Appendix II

Error Analysis

Error analysis of a "picture" is difficult. Error analysis of a "picture" in which the resolution varies erratically from point to point is even more difficult. The question that will arise is: Is a given feature "real"? If a given feature appears on our resultant albedo map, is it likely that there is a corresponding feature on the satellite? Or does the range of "satisfactory fits" to the data include a number of maps in which the feature is absent? Or, if the data do indeed require the feature to be present, is this likely to be the result of noise and or systematic error in the data? The "feature" in question may be a single albedo element or, more often, a number of such elements.

One of the purposes of this study is to experiment with different kinds and amounts of noise and systematic error to determine the extent to which spurious "features" can appear. However, at this point a few words on the subject may be appropriate. One simple test that can be made with actual data, if enough are available, is to divide the data into two or more "piles" and process each pile separately. If the feature appears in each of the resulting maps then it is likely to be real. If it does not, it does not necessarily follow that it is not real, for the region containing the feature may simply be poorly defined by one or more of the separate piles of data. A good approach to take with the Galilean satellite data, since many of the events will have been observed by more than one station, might be to put different observations of the same event into different piles. Since the geometry of observation is nearly identical, the "resolution" in the vicinity of the feature will be more nearly the same for maps produced from the individual piles. It may also be wise to intercompare different observations of the same event carefully to ascertain the nature and extent of noise and error.

Another approach is to vary the smoothing parameter, K. As it is increased, features will begin to disappear, first those poorly defined by the data and last, those the data most insistently require.

Suppose we are interested in determining the extent to which a single albedo element can vary and remain "consistent" with the data. We can obtain an estimate of this as follows. For convenience let us designate by $a_{i,j}^{k,l}$ the coefficient of albedo value $D_{i,j}$ in the k, lth equation (4), by $b_{k,l}$ the constant vector, and by $D'_{i,j}$ the solution vector:

$$\sum_{i=1}^{N} \sum_{j=1}^{N} a_{i,j}^{k,l} D'_{i,j} = b_{k,l}; \quad k = 1, N; l = 1, N. \tag{5}$$

Now, we insist that the albedo of a given element, the m, nth element, be not $D'_{m,n}$ but rather $D'_{m,n} - \Delta$. If all the other $D'_{i,j}$ are to remain the same, the constant vector must be replaced by a vector with elements

$$b_{k,l} + a_{m,n}^{k,l} \Delta, \qquad k = 1, N; l = 1, N. \tag{6}$$

We must determine the maximum (or minimum) value of Δ for which the probability that the vectors (6) and $b_{k,l}$ are two random samples of the same quantity (where the probability distribution of the elements is known: a Gaussian distribution, for example, with specified variance) is greater than some specified value (e.g., e^{-1}). This is a time-consuming chore for $\pi N^2/4$ elements, and when that was done it would then be necessary to consider all possible pairs, triplets, etc., of

elements varying in unison for a complete error analysis. A rigorous error analysis, therefore, will be prohibitively difficult.

Acknowledgments

This work has dragged on for several years because I have not applied myself to it as I should have. During that time it was supported by the University of Southern California, the R. T. Brinkmann Galilean Satellite Research Fund, and the Lunar Science Institute. Lowell Observatory and Kitt Peak National Observatory have made facilities available.

References

Aksnes, K. (1974). Mutual phenomena of Jupiter's Galilean satellites, 1973–74. *Icarus* **21**, 100–111.

Anonymous (1975). Ganymede from Pioneer 10. *Sky & Tel.* **49**, 8

Brinkmann, R. T. (1973). Jovian satellite-satellite eclipses and occultations. *Icarus* **19**, 15–29.

Brinkmann, R. T., and Millis, R. L. (1973). Mutual phenomena of Jupiter's satellites in 1973–74. *Sky & Tel.* **45**, 93–95.

Goldstein, H. H., and von Neumann, J. (1947). Numerical inverting of matrices of high order. *Bull. Amer. Math. Soc.* **53**, 1021–1099.

Goldstein, H. H., and von Neumann, J. (1951). Numerical inverting of matrices of high order. II. *Proc. Amer. Math. Soc.* **2**, 188–202.

Herzog, A. D., and Beebe, R. F. (1975). Interpretation of surface features of Europa obtained from occultations by Io. *Icarus* **26**, 30–36.

Milbourne, S. W., and Carey, J. V. (1973). Mutual phenomena of Jupiter's satellites. *Handbook Brit. Astron. Assoc.*, 36–37.

Murphey, R. E., and Aksnes, K. (1973). A polar cap on Europa. *Nature* **244**, 559–560.

Pohn, H. A. and Wildey, R. L. (1970). A photoelectric photographic study of the normal albedo of the Moon. In *Contributions to Astrogeology*. Geological Survey Professional Paper 599-E.

Vermilion, J. R., Clark, R. N., Greene, T. F., Seamans, J. F., and Yantis, W. F. (1974). A low resolution map of Europa from four occultations by Io. *Icarus* **23**, 89–96.

ELECTRON IMPACT IONIZATION OF IO'S SODIUM EMISSION CLOUD

R. W. Carlson

Department of Physics, University of Southern California, Los Angeles, California

D. L. Matson and T. V. Johnson

Jet Propulsion Laboratory, California Institute of Technology
Pasadena, California

Abstract

The geometry of the sodium cloud associated with Io (Jupiter I) indicates that the lifetime of the neutral sodium atoms is an order of magnitude less than the photoionization lifetime. We suggest that ionization by thermal plasma electrons in the Jovian magnetosphere is the dominant Na loss process. Using plasma densities deduced from Pioneer 10 measurements, the lifetime and density distributions are calculated for Na and other species which may be present in the cloud around Io. Electron ionization of Na is found to be an order of magnitude faster than photoionization, in agreement with the lifetime deduced from Na cloud observations.

Introduction

Intense sodium D-line emission features have been observed in the vicinity of Io (J-1), the innermost Galilean satellite of Jupiter (Brown, 1973; Brown and Chaffee, 1974). Resonance scattering of the incident solar flux was suggested by Matson *et al.* (1974) and Trafton *et al.* (1974) as the excitation mechanism for these lines. This suggestion was verified by the synoptic observations of Bergstralh *et al.* (1975) which showed that the orbital variation of the emission is as predicted by resonance scattering. The source of the sodium atoms is thought to be the surface of Io, the atoms being sputtered off the surface by incident magnetospheric particles (Matson *et al.*, 1974). Sodium-rich surface compositions such as evaporite salts (Fanale *et al.*, 1974, 1975) are favored but not required by current models. While Io appears to be the initial source of the atoms, they possess sufficient kinetic energy to escape the satellite, yet have insufficient velocity (for the majority of atoms) to escape from the Jovian system. The distribution of atoms therefore tends to form a toroid around Jupiter, in the manner suggested by McDonough and Brice (1973) for hydrogen escaping from Titan.

The spatial extent of the sodium cloud was discovered by Trafton *et al* (1974), and has been investigated by Meckler and Eviatar (1974), Macy and Trafton (1975), Wehinger *et al.* (1975), and Münch and Bergstralh (1975). Macy and Trafton found that the cloud extends one-fifth of the circumference or greater along the orbit of Io, but does not form a complete torus at their detection limit. Photographic spectra (Meckler and Eviatar, 1974; Wehinger *et al.*, 1975) show that very faint emission does occur completely around Io's orbit, concentrated toward the orbital plane, but the brightness distribution is not yet accurately determined.

Based on their observations, Macy and Trafton estimated that the lifetime of these sodium atoms is approximately one Io orbital period ($\sim 1.5 \times 10^5$ sec) which is an order of magnitude shorter than the lifetime against photoionization. Evidently some additional loss process must be occurring. Macy and Trafton noted the possibility of charge exchange with protons in the Jovian magnetosphere which is the loss process thought to occur for the hydrogen torus (Carlson and Judge, 1974), but they point out that the cross section for charge exchange, $H^+ + Na \rightarrow H + Na^+$, appears too small (at energies of the thermal plasma) to account for the short lifetime. Similarly, the cross section for proton impact ionization, $H^+ + Na \rightarrow H^+ + Na^+ + e^-$ (Peach, 1966a), is also too small at thermal plasma energies to account for the Na loss rate. At higher energies the particle fluxes are thought to be too small for a significant loss rate.

In this work we suggest that the dominant loss mechanism for the Na atoms is electron impact ionization by thermal plasma electrons. The plasma densities and temperatures are discussed below and the ionization rate calculated for sodium, hydrogen, and other atoms of interest which are likely components of the surface of Io (Fanale *et al.* 1974, 1975). Density distributions resulting from the postulated loss process are also presented for certain cases. Eviatar *et al.* (1975) have independently noted the ionization of Na by electron impact and have examined the consequences of the resulting Na^+ ions.

Jovian Plasma Densities

The thermal plasma in the magnetosphere of Jupiter was investigated by the Pioneer 10 Plasma Analyzer Experiment which observed plasma electrons in the outer magnetosphere (Intriligator and Wolfe, 1974) and protons in the inner regions (Frank *et al.*, 1975). The temperatures observed in the two sets of measurements were not the same ($\sim$4 ev for the electrons and $\sim$100 ev for the protons) and probably indicate different conditions in the two regions. However, without direct observations of the plasma electrons in the inner region, specification of the electron temperature is uncertain and one must consider two cases.

In Case A, the electron temperature is assumed to be 4 ev corresponding to that observed by Intriligator and Wolfe (1974). The electron density in the vicinity of Io can be estimated by assuming charge neutrality and that the proton density is that required to explain the H atom loss rate ($\sim 10^{-5}$ sec^{-1} corresponding to $\sim$200 electron-ion pairs/cm^3) obtained from the Pioneer 10 observations of the hydrogen torus (Carlson and Judge, 1974, 1975). The second model (Case B) is based on the analysis by Frank *et al.* (1975) of the proton component and assumes that the electron and ion temperatures (and densities) are equal. They found that densities in the 108 ev–4.8 kev region at the orbital position of Io were $\sim$15-20 protons/cm^3 with temperatures of $\sim$100 ev. Assuming a Maxwellian distribution which appears justified by their measurements, the contribution for energies <108 ev can be calculated, resulting in densities of $\sim$30 electron-ion pairs/cm^3. The charge exchange lifetime of atomic hydrogen at these densities and velocities are also in good agreement with that inferred from the Pioneer 10 ultraviolet measurements. The parameters of these plasma models are summarized in Table 1.

Electron Ionization Rates

The ionization rate coefficients α, is defined by

Copyright 1975 by the American Geophysical Union

Table 1

Parameters of Assumed Plasma Models

	Case A	Case B
Temperature (ev)	4	100
(°K)	4.6×10^4	1.2×10^6
Most Probable Electron Velocity (cm sec^{-1})	1.2×10^8	5.9×10^8
Plasma Density (cm^{-3})	200[a]	30[b]
Electron Flux (cm^{-2} sec^{-1})	2.4×10^{10}	1.8×10^{10}

[a]Assumed constant
[b]Varies with distance from Jupiter

$$a = \frac{\int v\sigma(v)\Phi(v)\,d^3v}{\int \Phi(v)\,d^3v} \qquad (1)$$

Where v is the electron velocity, $\sigma(v)$ is the ionization cross section, $\Phi(v)$ the Maxwellian velocity distribution function, and $d^3v = v^2dv$. The rate coefficient was obtained for temperatures of 4 and 100 ev for Na, H, Si, Mg, K, and Ca and presented in Table 2. For Na and H, the rate coefficient has been calculated by Lotz (1967), while the remaining were calculated here using Eq. 1 and appropriate cross section data listed in Table 2. The electron ionization rate ν_e for an electron density n_e is

$$\nu_e = an_e \qquad (2)$$

and is given in Table 2 along with computed photoionization rates. In Case B, the electron density varies with distance from Jupiter; the value given is for the orbital position of Io.

It can be seen from Table 2 that the major loss process for Na is electron ionization, being an order of magnitude faster than photoionization, and that in both Cases A and B the resulting lifetime is in good agreement with the lifetime estimate of Macy and Trafton (1974). For all of the atoms considered here, the e^- ionization process is much faster than photoionization. Electron ionization of atomic hydrogen is only about 10% of the $H+H^+$ charge exchange rate or less, and thus is not the dominant process for hydrogen loss.

Density Distributions

With a model for the atomic loss processes, it is possible to calculate the resulting density distributions, subject to certain assumptions regarding the initial source conditions of the atoms. In these initial calculations we have computed relative column densities for columns normal to the orbital plane. These densities, if further integrated along a line of sight in the orbital plane, would be appropriate (in the optically thin case) for integrated surface brightness measurements using a long slit oriented normal to the plane of the orbit (i.e. no resolution along the slit). The Doppler shift in the Fraunhofer line and multiple scattering effects would also have to be included in any more detailed studies and comparisons with observations.

Table 2

Electron and Photo-Ionization Rates in the Jovian Environment

		Neutral Species					
		H	Na	Mg	Si	K	Ca
Ionization Potential (ev)		13.6	5.14	7.65	8.15	4.34	6.11
Photoionization Rate ν_{ph} (10^{-6} sec^{-1})[a]		0.0033	0.68	0.016	0.70	1.00	1.5
Case A	Rate Coefficient a (10^{-8} cm^3 sec^{-1})	0.043	4.3	0.97	2.3	5.80	3.3
	Electron Ionization Rate ν_e (10^{-6} sec^{-1})	0.086	8.6	1.9	4.9	12.	6.6
	Lifetime $\tau = (\nu_{ph}+\nu_e)^{-1}$ (10^5 sec)	b	1.1	5.2	1.9	0.77	1.2
Case B	Rate Coefficient a (10^{-8} cm^3 sec^{-1})	3.1	17.0	11.0	39.	32.0	21.
	Electron Ionization Rate ν_e (10^{-6} sec^{-1})	0.93	5.1	3.3	12.	9.6	6.3
	Lifetime $\tau = (\nu_{ph}+\nu_e)^{-1}$ (10^5 sec)	b	1.7	3.0	0.79	0.94	1.3
References		c	c	d	e	f	g

a Calculated using cross sections compiled by Hudson and Kieffer (1971)
b The hydrogen lifetime is determined largely by charge exchange with protons, $\tau \approx 2\times10^5$ sec (Carlson and Judge, 1974)
c Lotz (1967)
d The relative cross sections of Kaneko (1961) were normalized to Peach's (1966) theoretical values
e Peach (1968) – theoretical cross section
f Tripathi et al. (1969) – theoretical cross section
g McFarland (1967) – Experimentally determined cross sections

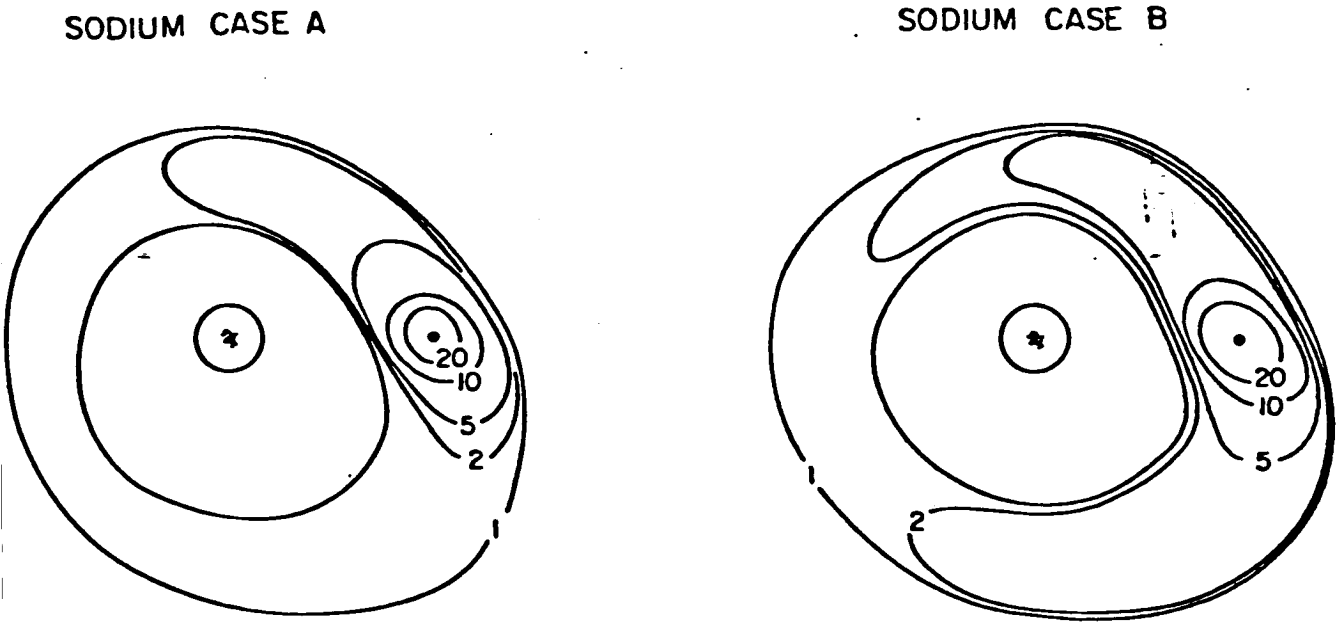

Fig. 1. Calculated relative column densities for sodium atoms which have escaped from Io with 1 km/sec excess velocity. The two different cases correspond to different plasma densities, temperatures, and the resulting loss rates (see Text). Within approximately 1/2 Jovian radius (~20 Io radi) the column density is found to be cylindrically symmetric and varies inversely with distance from Io. At large distances from Io a toroidal geometry is found with differences in the leading and trailing portions which may produce the orbital phase intensity asymmetry observed by Bergstralh *et al.* (1975).

It is assumed that atoms are produced uniformly over the surface of Io by sputtering and ejected normal to the surface. The assumption of uniform sputtering is probably incorrect but a more realistic model is not presently available. Variation to some level is indicated both by color differences across Io's surface (Johnson, 1971) which may be due to varying chemical composition, and by variations in the charged particle impact rate due to a plasma sheath (Shawhan *et al.* 1975). An initial velocity of 3.5 km/sec was chosen, based on the sputtering measurements of Politiek and Kistemaker (1969), which corre-

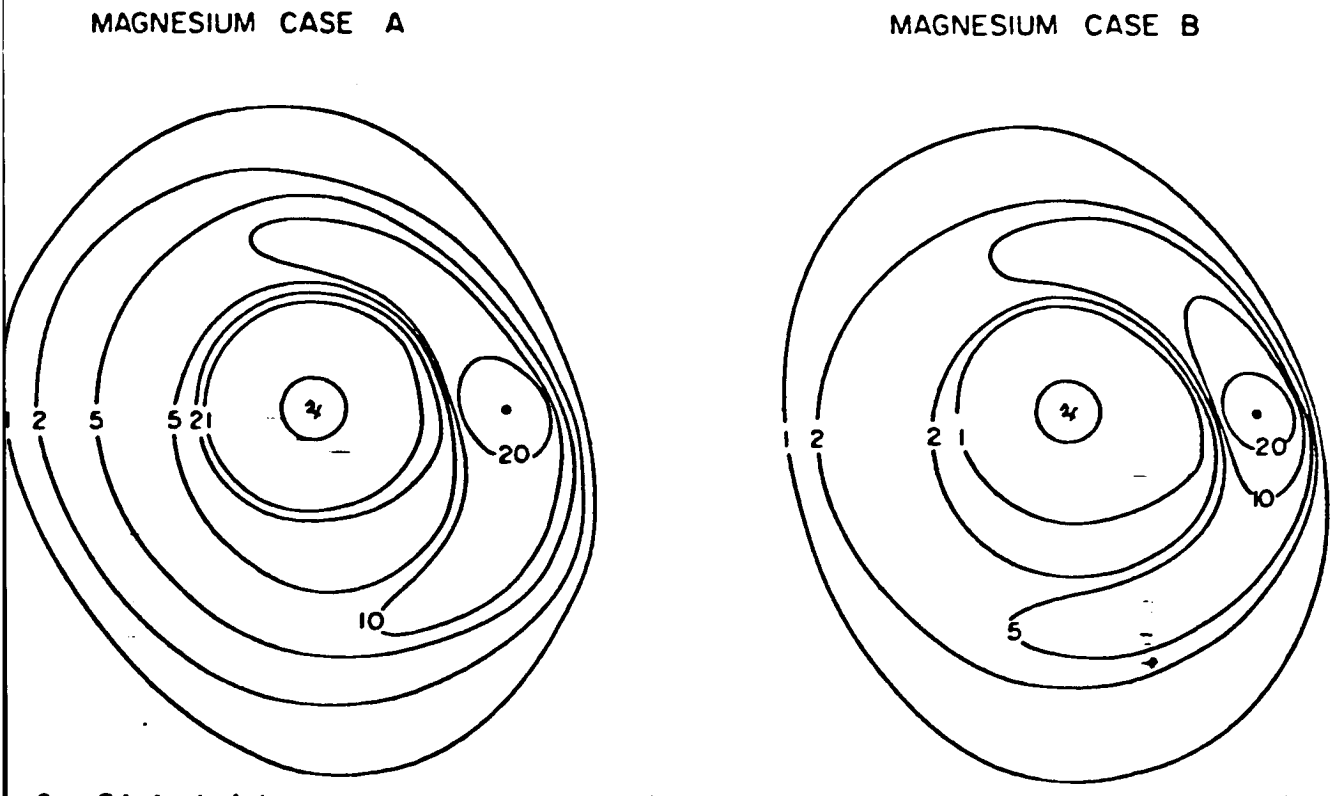

Fig. 2 Calculated relative column densities for magnesium for ionization rates given by the two different plasma models. This view, as in Fig. 1, is from the north pole and the rotation of Io is counterclockwise. The velocity and flux of escaping atoms are identical to Fig. 1. Note the greater densities and more fully developed torus than those for sodium, a consequence of the smaller electron ionization rate. The actual density values will depend upon the surface compositional abundances.

sponds to a velocity of 1 km/sec (relative to Io) after escape. Higher velocities for some of the atoms have been reported (Trafton, 1975) but the bulk of the distribution appears to occur at low velocities. The trajectories of the atoms, moving under the influence of the gravitational fields of Jupiter and Io, were computed numerically and during successive time increments the flux was reduced by a value corresponding to the model loss rate.

The results for Na and Mg, which are predicted to have quite different lifetimes, are shown in Figures 1 and 2. It can be seen that the effect of the lifetime is quite significant in that the predicted magnesium torus is larger and much more fully developed than the Na torus. The profile of the sodium torus appears to be in qualitative agreement with the observations, but a detailed comparison is not possible. Future observational work on the distribution of emissions in the cloud can be used to verify and refine the atomic lifetime values. A suggested observation, which is sensitive to the lifetime, is the ratio of the intensity seen viewing Io at greatest elongation to that obtained from the opposite side of the orbit. The geometry of this suggested observation reduces the effect of Doppler shift in the Fraunhofer line. In the present numerical experiments, the integrated column density ratio was found to be relatively insensitive to the injection velocity (increasing the velocity after escape by a factor of two changed the ratio by 10-15%) whereas the variation of the ratio with lifetime was found to be more significant and could be described by $(0.45\pm0.05)e^{-(1.4\pm0.1)T/\tau}$ where T is the orbital period of Io and τ the lifetime at the radial position of Io. It was assumed that single scattering was appropriate and that the observations are performed with a long slit normal to the orbital plane and ~3 arc sec in width. If photoionization were the only loss process for Na, the intensity ratio would be ~40%, and would have been readily observed in the measurements of Meckler and Eviatar (1974) and Macy and Trafton (1975).

The density profiles computed here assume electron ionization loss rates which are constant in time. Since the plasma densities may exhibit a dependence on the orientation of the magnetic field and other parameters, the loss rates and resulting densities could show some time variability. Continued optical observations could prove a useful monitor of the Jovian plasma.

Acknowledgement

Portions of this work were supported under NASA Contract NAS 2-6558. This paper presents the results of one phase of research carried out at the Jet Propulsion Laboratory, California Institute of Technology, under Contract No. NAS 7-100.

References

Bergstralh, J. T., D. L. Matson, and T. V. Johnson, "Sodium D-line emission from Io: synoptic observations from Table Mountain Observatory," Astrophys. J. (Letters), 195, L131, 1975.

Brown, R. A., "Optical line emission from Io," in Exploration of the Planetary System, Proceedings IAU Copernicus Symposium 4 (IAU Symposium 65), ed. A. Woszczyk and C. Iwaniszewska. Reidel, Dordrecht (1975)

Brown, R. A., and F. H. Chaffee, Jr., "High resolution spectra of sodium emission from Io," Astrophys. J. (Letters), 187, L125, 1974.

Carlson, R. W. and D. L. Judge, "Pioneer 10 ultraviolet photometer observations at Jupiter encounter," J. Geophys. Res., 79, 3623, 1974.

Carlson, R. W. and D. L. Judge, "Pioneer 10 ultraviolet photometer observations of the Jovian hydrogen torus: the angular distribution," Icarus, 24, 395, 1975.

Eviatar, A., Y. Meckler, and F. V. Coriniti, "Jovian sodium plasma," submitted to Astrophys. J., 1975.

Fanale, F. P., T. V. Johnson, and D. L. Matson, "Io: a surface evaporite deposit?," Science, 186, 922, 1974.

Fanale, F. P., T. V. Johnson, and D. L. Matson, "Io's surface and the histories of the Galilean satellites," in Planetary Satellites (Proc. IAU Coll. 28), ed. J. Burns, University of Arizona Press, Tucson, in press (1975).

Frank, L. A., K. L. Ackerson, J. H. Wolve, and J. D. Mihalov, "Observation of plasmas in the Jovian magnetosphere," J. Geophys. Res., 80, 1975 (in press).

Hudson, R. D., and L. J. Kieffer, "Compilation of atomic ultraviolet photoabsorption cross sections for wavelengths between 3000 and 10 Å, Atomic Data, 2, 205, 1971.

Intriligator, D. S., and J. H. Wolfe, "Initial observations of plasma electrons from the Pioneer 10 flyby of Jupiter," Geophys. Res. Lett., 1, 281, 1974.

Johnson, T. V., "Galilean satellites: narrow band photometry 0.30-1.10 microns," Icarus, 14, 94, 1971.

Kaneko, Y., "Single and double ionization of Na, K, and Mg by electron impact," J. Phys. Soc. Japan, 16, 2288, 1961.

Lotz, W., "Electron impact cross-sections and ionization rate coefficients by atoms and ions," Astrophys. J. (Suppl.), 14, 207, 1967.

Macy, W. W., Jr., and L. M. Trafton, "Io's sodium emission cloud," Icarus, 24, 1975.

Matson, D. L., T. V. Johnson, and F. P. Fanale, "Sodium D-line emission from Io: sputtering and resonant scattering hypothesis," Astrophys. J. (Letters), 192, L43, 1974.

McDonough, T. R., and N. M. Brice, "A Saturnian gas ring and the recycling of Titan's atmosphere," Icarus, 20, 136, 1973.

McFarland, R. H., "Electron-impact ionization measurements of surface ionizable atoms," Phys. Rev., 159, 20, 1967.

Meckler, Y. and A. Eviatar, "Spectroscopic observations on Io," Astrophys. J. (Letters), 193, L151, 1974.

Münch, G. and J. T. Bergstralh, "Sodium D-line emission from Io: Spatial brightness distribution from multislit spectra," 6th Annual Meeting, Division for Planetary Sciences, American Astronomical Society, Columbia, Maryland, Feb. 1975.

Peach, G., "Ionization of sodium and magnesium by electron and proton impact," Proc. Phys. Soc., 87, 375, 1966a.

Peach, G., "Electron exchange in the collisional ionization of atoms with outer s electrons," Proc. Phys. Soc., 87, 381, 1966b.

Peach, G., "Ionization of neutral atoms with outer 2p and 3p electrons by electron and proton impact," J. Phys. B (Proc. Phys. Soc.), 1, 1088, 1968.

Politiek, J. and J. Kistemaker, "The flux distribution of sputtered potassium atoms," Rad. Effects, 2, 129, 1969.

Shawhan, S. D., C. K. Goertz, R. F. Hubbard, D. A. Gurnett and G. Joyce, "Io accelerated electrons and ions," presented at the Magnetospheres of the Earth and Jupiter, Frascati, May, 1974. To be published in the Proceedings.

Trafton, L., T. Parkinson, and W. Macy, Jr., "The spatial extent of sodium emission around Io," Astrophys. J. (Letters), 190, L85, 1974.

Trafton, L., "High resolution spectra of Io's sodium emission," submitted to Astrophys. J. (Letters), 1975.

Tripathi, A. N., K. C. Mathur, and S. K. Joshi, "Electron-impact ionization and excitation cross sections of atoms with two outer-shell electrons," J. Phys. B (Proc. Phys. Soc.), 2, 878, 1969.

Wehinger, P. A., S. Wyckoff, and A. Frohlich, "Mapping of sodium emission associated with Io and Jupiter," IAU Coll. No. 30, Jupiter, Tucson, May, 1975.

(Received July 28, 1975;
accepted August 7, 1975.)

The Problem of Hydrogen at Io.

R. W. Carlson, D. L. Judge

Abstract presented at the Division for Planetary Sciences (AAS) Meeting, Austin, Texas, April 1976

Ultraviolet emissions associated with Io observed by Pioneer 10 have been suggested to be the atomic hydrogen Lyman-alpha line excited by resonance scattering. A fundamental question is related to the source of the atoms - is Io the initial source or does the satellite merely act as a catalyst to recombine magnetospheric protons and electrons. With regard to this question, the identification and characteristics of the emission cloud will be discussed and the observations compared to numerical calculations of the cloud geometry.

The plasma source is perhaps plausible since an adequate supply of protons and electrons can be found in photoelectron-ion escape from Jupiter, however the sweeping rate of the satellite may not be great enough to supply the cloud. In addition, protons driven into the surface could recombine and associate to form molecular hydrogen as suggested for the moon. Finally, if the plasma sheath interaction is correct, the resulting cloud geometry would appear different than that observed.

A more likely source of hydrogen is Io itself, since sublimation rates can provide adequate hydrogen compounds and H atoms can be produced by electron impact dissociation and ionospheric dissociative recombination, as suggested by Johnson et al. Furthermore, the observed cloud geometry is more compatible with such a source process.

PIONEER 10 ULTRAVIOLET PHOTOMETER OBSERVATIONS OF JUPITER: THE HELIUM TO HYDROGEN RATIO

R. W. CARLSON

and

D. L. JUDGE
University of Southern California

Pioneer 10 ultraviolet photometer observation of 5.1 Rayleighs (R) of HeI 584 Å emissions from the disc of Jupiter verifies the presence of Jovian atmospheric helium. The excitation process is resonance scattering of incident solar helium radiation. Quantitative estimates of the He-to-H_2 mixing ratio in the lower atmosphere of Jupiter can be obtained by using Jovian atmospheric models, radiative transfer calculations, and the strength of the solar line; an initial determination has been obtained by Carlson and Judge (1974). We have recently measured the profile and intensity of the solar line and found, as have other experimenters, that it is more intense than was originally supposed, implying a lower albedo and less helium. The various measurements of the solar line are reviewed along with the two parameters – the eddy mixing rate and thermospheric temperature – which appear in the model atmosphere. In addition, the radiative transfer calculations are refined to include the anisotropic phase function for helium resonance scattering, and the accuracy of the coherent-scattering assumption is verified. Using the Pioneer 10 helium emission rate and eddy diffusion coefficient, the range of helium-to-hydrogen ratios by volume is found in the present analysis to be $0 < [He]/[H_2] \leq 0.28$ for an atmospheric temperature of 150°K. If the high electron temperatures observed by the Pioneer radio occultation experiment reflect equally high neutral temperatures, then more helium is indicated but in this case the Lyman-α albedo and eddy diffusion coefficient must be re-evaluated. For the present, however, we consider the cooler thermosphere to be most realistic since ample terrestrial evidence exists for electron temperatures much greater than the corresponding neutral temperature.

Comparison of the present and other helium-to-hydrogen mixing ratio measurements suggests that the best current estimate is the solar abundance, ($[He]/[H_2] = 0.11$), in which case the eddy diffusion coefficient for the Jovian atmosphere is $K = 3 \times 10^7$ cm^2 sec^{-1}.

The Jovian helium abundance and its possible variations in the atmosphere, envelope, and deep interior are of considerable cosmogonic interest. Unfortunately, the high excitation potential of helium precludes its direct

observation using groundbased instrumentation. One method to discern the presence of helium is through spacecraft observation of the He resonance line, which occurs at 584 Å in the vacuum ultraviolet region. This line will appear in emission from Jupiter, being formed by resonance scattering of the solar HeI 584 Å radiation incident on the upper atmosphere. The detection of this line and characterization of the Jovian He-H_2 abundance ratio was one of the major objectives of the ultraviolet photometer experiment on Pioneer 10.

A description of the experiment and planetary results have been presented by Carlson and Judge (1974, 1975) and Judge and Carlson (1974). The instrument is a two channel photometer with one channel employing an Al thin film filter and LiF photocathode to isolate a spectral band containing the helium resonance line. The second channel is for observation of the atomic hydrogen Lyman-α resonance line (1216 Å). Mechanical collimation defines the field of view and the entrance aperture. The axis of the collimator is oriented 20° to the spacecraft spin axis, consequently an annular field 40° in diameter is swept out during each spacecraft spin period. Each 12-sec spin produces ~ 32 samples, each with a tangential and sagittal angular width of ~ 1° by 10°.

Jupiter was in the field of view during two periods of the Pioneer 10 encounter, although the influence of high-energy magnetospheric particles allowed useful data to be obtained only during the first viewing opportunity. Positive identification of signals in the short wavelength channel, identified as HeI 548 Å radiation, verify the existence of helium in the atmosphere of Jupiter. The average emission rate over the disc observed at 30° phase angle was found to be 5.1 R. Using this emission rate a quantitative estimate of the atmospheric He-H_2 abundance ratio can be determined by comparison with theoretical resonance scattering models. These models require (1) knowledge of the source of radiation being scattered by the helium atoms—that is, the intensity and profile of the solar HeI line; (2) a model of the atmosphere which describes the mixed and gravitationally separated regions and the atmospheric temperature; and (3) radiative transfer calculations which include multiple scattering by He and absorption by H_2.

A previous estimate of the number-density ratio in the mixed region of the atmosphere $[He]/[H_2] \sim 1/5$ was obtained by Carlson and Judge (1974) using the Pioneer 10 observations, the solar flux values available at the time, an assumed 150°K atmosphere, and multiple scattering calculations which assumed coherent isotropic scattering and neglected polarization effects.

We have recently remeasured the intensity and profile of the solar He line (Maloy *et al.* 1976) and found, along with other experimenters, that it is more intense than originally had been supposed, implying a lower value for the diffuse 584 Å reflectivity of Jupiter and therefore less He than previously estimated. The improved solar flux value and the substantial reduction in helium abundance inferred from these measurements suggest that the ac-

curacy of the assumptions employed in the model calculations should be verified. In addition, the Pioneer 10 occultation experiment indicates high plasma temperatures for the outer ionosphere which may imply a higher neutral temperature. In this chapter we discuss measurements of the solar line and improve the radiative transfer calculations by including the anisotropic scattering phase function for helium and the frequency redistribution (i.e., non-coherence) which occurs in resonance scattering. Higher temperatures and their impact on the resulting He-H_2 abundance are also discussed.

I. RESONANCE SCATTERING BY HELIUM

The resonance transition of He($1s2p\ ^1P_1^0$–$1s^2\ ^1S_0$) occurs at $\lambda_0 = 584.334$ Å (21.21 eV). For a gas kinetic temperature T, the Doppler width of the gas is

$$\frac{\Delta\lambda_D}{\lambda_0} = \frac{\Delta\nu_D}{\nu_0} = \frac{U}{c} \tag{1}$$

where U is the most probable speed,

$$U = \sqrt{\frac{2kT}{M}}. \tag{2}$$

At frequencies ν displaced $\xi = (\nu - \nu_0)/\Delta\nu_D$ Doppler units from line center, the atomic absorption cross section is

$$\sigma(\xi) = \sigma_0\phi(\alpha, \xi) \tag{3}$$

with α the ratio of the natural to Doppler width, $\phi(\alpha, \xi)$ the Voigt profile normalized to unity at line center for $\alpha = 0$, and

$$\sigma_0 = \frac{\pi e^2}{mc}\frac{f}{\sqrt{\pi}\Delta\nu_D}. \tag{4}$$

The oscillator strength for the helium transition is $f = 0.2762$ Wiese *et al.* 1966) and at 150°K, $\Delta\lambda_D = 1.55$ mÅ, $\alpha = 1.05 \times 10^{-2}$, and $\sigma_0 = 3.0 \times 10^{-13}$ cm^2. For moderate optical thicknesses, or if there is sufficient absorption by another species (as in the case here with H_2 photoionization) then one can, to good approximation, neglect the natural radiation damping wings of the line and use the Doppler profile,

$$\phi(\alpha, \xi) \simeq e^{-\xi^2}. \tag{5}$$

A small fraction of the photons absorbed produce the infrared 1s2p–1s2s line while the remainder re-emit the resonance line with probability

$$\tilde{\omega}_0 = \frac{A(1s2p\text{–}1s^2)}{A(1s2p\text{–}1s2s) + A(1s2p\text{–}1s^2)}. \tag{6}$$

The transition rates A are given by Wiese *et al.* (1966) from which $\tilde{\omega}_0 = 0.9989$.

The scattered photons are not distributed isotropically; rather, since $J = 0$ and $\Delta J = 1$, they are distributed according to the Rayleigh phase function (Hamilton 1947)

$$p(\Theta) = \frac{3}{4}(1 + \cos^2 \Theta) \tag{7}$$

where Θ is the angle between the incident and scattered photon. In resonance scattering this represents the maximum possible anisotropy.

After scattering, the photons do not in general possess the same frequency incident owing to the Doppler effect in scattering (Henyey 1940). This effect is simply demonstrated by the following. Consider an atom moving with velocity v. It will absorb a photon at frequency ν propagating in the same direction if the Doppler shifted frequency is at resonance $\nu(1 - v/c) = \nu_0$ (approximating the natural line shape with a delta function). Since the atom radiates coherently in its rest frame (neglecting recoil), the observed emission frequency will depend upon the angle of emission. In forward scattering, the frequency is unchanged whereas it will be oppositely situated from line center in backward scattering. For intermediate scattering angles the frequencies will be shifted closer to line center.

Hummer (1962) has evaluated the angle-integrated probability that a photon of relative frequency ξ' is absorbed and re-emits at ξ, $R(\xi' \to \xi)$. In the case of the phase function for Rayleigh scattering and neglecting the natural wings, the probability distribution function in frequency is

$$P(\xi' \to \xi) = \frac{R(\xi' \to \xi)}{e^{-\xi'^2}} \tag{8}$$

$$= \frac{3}{8} e^{\xi'^2} \left\{ \frac{\sqrt{\pi}}{2} \, erfc(|\bar{\xi}|)[3 + 2(\xi^2 + \xi'^2) + 4\xi^2\xi'^2] - e^{-|\bar{\xi}|^2} |\bar{\xi}|(2|\underline{\xi}|^2 + 1) \right\}$$

where $|\bar{\xi}|(|\underline{\xi}|)$ is the greater (lesser) of $|\xi|$ and $|\xi'|$. This distribution is illustrated in Fig. 1. Later considerations [Eq. (28)] make use of the relations (Hummer 1962)

$$R(\xi' \to \xi) = R(\xi \to \xi') \tag{9}$$

and

$$\int_{-\infty}^{\infty} R(\xi' \to \xi) d\xi' = e^{-\xi^2} \tag{10}$$

where $R(\xi' \to \xi)$ here differs from Hummer's value by a normalization constant.

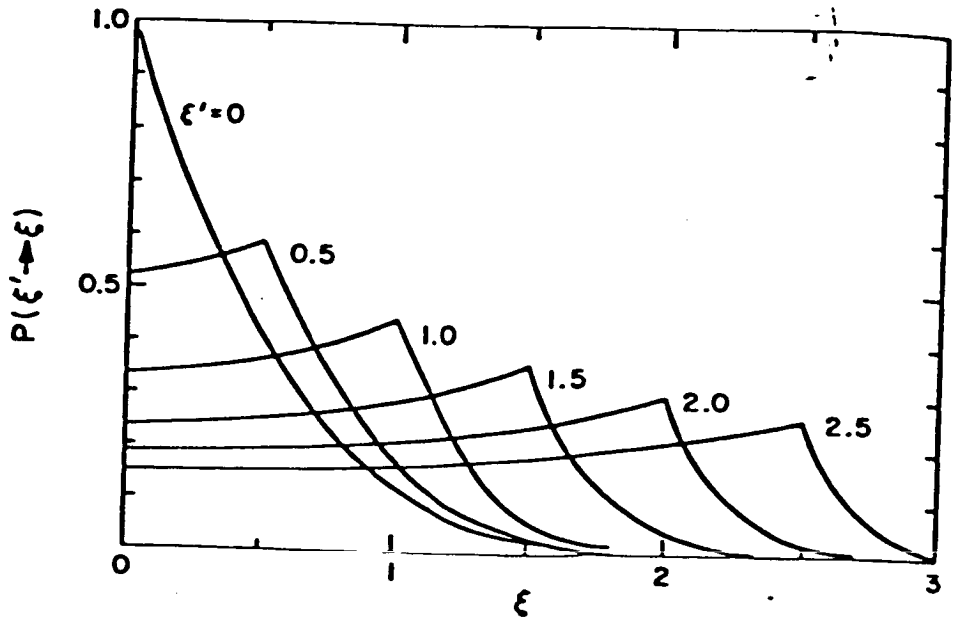

Fig. 1. The probability density function for frequency redistribution in resonance scattering by He. It is assumed that the damping wings of the line are important. The incident and scattered frequencies are measured in Doppler widths displaced from the center of the line. The distributions are symmetric about line center.

II. THE SOLAR HELIUM LINE

The strength of an airglow feature produced by resonance scattering depends upon the spectral intensity of the solar line over the interval of the planetary absorption profile. The width of the planetary absorption feature is generally small compared to the width of the solar line (a few mÅ compared to a solar He line width of roughly one hundred mÅ), and therefore direct measurement of the solar line in the appropriate wavelength interval requires very high resolution measurements. However, the required high resolving powers are difficult to attain in rocket and satellite spectrometers, particularly in the extreme ultraviolet where losses in the optical elements are considerable, so at present one must resort to a less direct determination of the spectral intensity.

Two methods are available. The first is determination of the total solar line intensity and use of a measured or inferred line profile, while the second method uses a known quantity of helium gas (e.g., terrestrial thermospheric He) to absorb and re-radiate the solar line. Measurement of the intensity (i.e., of the He airglow) allows one to infer the solar spectral intensity at the center of the line.

Measurements of the total intensity of the solar line have been performed by several experimenters, perhaps the most widely used being those of the Air Force Cambridge Research Laboratory (AFCRL) group (e.g., Hinteregger 1970). These data, which show an intensity variation with solar activity and the solar 10.7 cm radio flux, were used in our previous analysis of the Jovian He abundance with extrapolation to the low level of solar activity at the time of Pioneer 10 encounter. Recently Hinteregger's values have been questioned since those fluxes may not be sufficient to produce the observed exospheric and ionospheric properties (Roble and Dickinson 1973; Swartz and Nisbet 1973). While the question is not yet resolved, the AFCRL group has remeasured the solar spectrum (Heroux *et al.* 1974) and found that certain lines, including the He line, are more intense than indicated previously. Our own measurements are in substantial agreement with both the latter and with observations of other experimenters. A summary of these and other 584 Å flux measurements, including our own, is presented in Fig. 2.

The profile and width of the solar helium line has received less experimental effort than the intensity. A curve-of-growth analysis of the solar line transmitted through varying amounts of terrestrial helium gave only an approximate lower limit to the width: ~ 140 mÅ field width at half maximum (*FWHM*) when a Gaussian line profile was assumed (Carlson 1973). The first direct measurements of the profile (Doschek *et al.* 1974) were obtained photographically at a resolution of 60 mÅ and indicated an approximate Gaussian line shape (but with a slightly flatter central region) with a width $FWHM = 140 \pm 15$ mÅ. Photographic spectra of a small region of the quiet solar disc by Cushman *et al.* (1975) show an *FWHM* of 80 mÅ and 100 mÅ for an active region.

Line shape measurements by our laboratory (Maloy *et al.* 1976) employed a helium filled spectrometer and the curve-of-growth technique. It was found that the line shape could be accurately represented by a Gaussian with $FWHM = 122 \pm 10$ mÅ. A similar experiment (Delaboudinière and Crifo 1975) provides a lower limit of 110 mÅ *FWHM* in their preliminary analysis. Theoretical calculations by Milkey *et al.* (1973) predict a flatter profile with $FWHM \approx 150$ mÅ. In this chapter we have used our measured line width, an assumed Gaussian profile, and various total intensity measurements to generate the line center spectral intensities shown in Fig. 2.

The second method of inferring the central intensity of the solar line, comparison of airglow intensities with that predicted by known He distributions and radiative transfer calculations, has been summarized by Meier and Weller (1972) for several rocket measurements of the terrestrial airglow and for their own satellite measurements (Meier and Weller 1974). The latter measurements are preferred, not only because they are free of atmospheric absorption effects, but they also allow an intercomparison with the present measurements of Jupiter and the sun through mutual observations of the interplanetary helium glow, as discussed in Sec. IV.

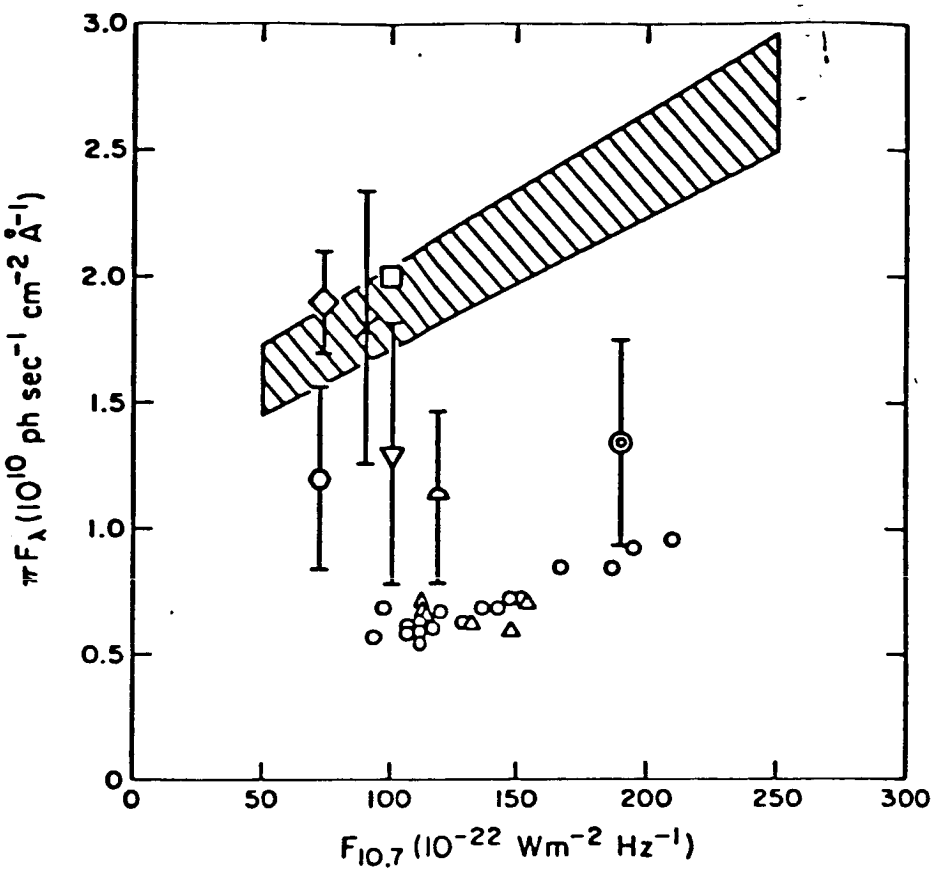

Fig. 2. The solar He I 584 Å spectral flux at line center as a function of the solar 10.7 cm (2800 MHz) radio flux. The values displayed are based upon direct measurements, integrated intensity measurements normalized with our observed line shape (Maloy *et al.* 1976), and values inferred from airglow data. The normalized integral values are represented by the circles (Hinteregger 1970; Hall and Hinteregger 1970), the double circle (Timothy *et al.* 1972), hexagon (Hinteregger *et al.* 1965), half circle (Heroux *et al.* 1974), cross (Maloy *et al.* 1976), and triangles (apex up) (Reeves and Parkinson 1970; Dupree *et al.* 1973; Dupree and Reeves 1971). In addition, the shaded area is from the regression analyses of total intensity data from Orbiting Solar Observatory, OSO-6, by Woodgate *et al.* (1973). The direct photographic measurements of Cushman *et al.* (1975) are indicated with the triangle (apex down) while the terrestrial (Meier and Weller 1974) and Venus Mariner 10 (Kumar and Broadfoot 1975) values obtained from airglow measurements are represented by the square and diamond respectively.

Mariner 10 data on the Cytheran helium glow (Kumar and Broadfoot 1975) can also be used for determination of the solar intensity, even though the helium content of the Venus atmosphere is unknown, because the reflected intensity of a resonantly-scattering atmosphere that is moderately

optically thick is almost independent of the total column abundance in the absence of dissipative absorption (*not* the case for Jupiter where H_2 absorption is present at all altitudes). These two inferred values are also indicated in Fig. 2.

In our original analysis of the Jovian He glow (Carlson and Judge 1974), a line center flux of 0.5×10^{10} photons sec^{-1} cm^{-2} $Å^{-1}$ (at 1 A.U.) was used, which was based on Hinteregger's total flux and a provisional value for the effective line width. It can be seen from Fig. 2 that even at the low level of solar activity at Pioneer 10 encounter ($F_{10.7} = 72 \times 10^{-22}$ Wm^{-2} Hz^{-1}) the line center flux is probably greater than that which was used. It is difficult to obtain an accurate value from the rather scattered experimental values displayed in Fig. 2, but we suggest (biased somewhat toward our own measurement, the airglow values and the recent AFCRL results) that choosing $\pi F_\lambda = 1.45 \pm 0.4 \times 10^{10}$ photons sec^{-1} cm^{-2} $Å^{-1}$ (at 1 A.U.) offers a reasonable representation of the HeI 584 Å solar flux at the time of the Pioneer 10 encounter.

Since the solar hydrogen ultraviolet lines exhibit self-reversal, it might be imagined that the same may be true for the helium lines. Three lines of evidence argue against significant self-reversal, however. First are the line-center flux values inferred from airglow measurements. If there were strong reversal, these values would be lower than the normalized integral flux values; in fact, they are among the highest values shown in Fig. 2. Secondly, any reversal effects from the outer chromosphere would be expected to display absorption widths that are characteristic of relatively high temperatures and velocities and could have been seen at the resolving power employed by Cushman *et al.* (1975). No such absorption is evident in their spectra. Finally, the theoretical model of Milkey *et al.* (1973) shows that the line can be formed with little self-reversal although other models (Zirin 1975) do produce strong self-reversal (Milkey 1975).

III. JOVIAN ATMOSPHERIC MODELS

In addition to helium atoms which scatter the resonance line, the atmosphere of Jupiter contains molecular hydrogen which will absorb this radiation through photoionization. Other components such as methane will also absorb, but the effect of these minor constituents is small relative to H_2 absorption. It is the simultaneous absorption by H_2 which determines the strength of the airglow signal, and allows a determination of the relative He-H_2 composition through a measurement of the intensity of the glow.

The scattering and absorptive properties are not constant throughout the atmosphere, but vary with altitude due to the gravitational separation of the molecular constituents. In contrast to atmospheres of the terrestrial planets, where the absorbing component is generally heavier and produces an absorbing lower boundary because of its smaller scale height, the atmospheres of

the major planets become relatively more absorbing with increasing altitude since the scale height of the absorbing H_2 is larger than that for He. In the lower regions, mechanical mixing by large scale turbulent motion produces uniform mixing and height-independent scattering and absorbing properties. Calculations of the diffusely reflected helium glow must include the altitude-dependent absorption and the transition from the mixed and gravitationally separated regions using a suitable model of the atmosphere.

The transition level between the mixed region, where eddy diffusion dominates, and the region where molecular diffusion produces gravitational (diffusive) separation is termed the turbopause. At that level, the eddy and molecular diffusion coefficients are equal. The latter varies inversely with number density, so if the eddy coefficient is K, in cm^2 sec^{-1}, the number density of H_2 at the turbopause is

$$n_0 = b/K \tag{11}$$

where $b = 1.81 \times 10^{19}$ cm^{-1} sec^{-1} at 150°K (Wallace and Hunten 1973) and varies as the square root of the temperature. Referring the altitude z to the turbopause and with H denoting the scale height for H_2 ($H = kT/m_{H_2}g =$ 26.3 km at 150°K), then treating He as a minor constituent, the H_2 and He number densities are (Wallace and Hunten 1973)

$$n(H_2|z) = n_0 e^{-z/H} \tag{12a}$$

$$n(He|z) = r n_0 e^{-z/H}/(1 + e^{z/H}) \tag{12b}$$

The vertical column densities are

$$N(H_2|z) = n_0 H e^{-z/H} \tag{13a}$$

$$N(He|z) = r n_0 H[e^{-z/H} - \ln(1 + e^{-z/H})]\,. \tag{13b}$$

Here, r denotes the volume ratio of He to H_2 in the mixing region far below the turbopause. Estimation of the mixing ratio r from airglow measurements requires knowledge of the remaining two parameters of the model, the eddy diffusion coefficient and temperature, which are discussed below.

Few methods are presently available to determine the eddy diffusion coefficient. One means is measurement of the Lyman-α airglow, since the abundance of atomic hydrogen depends upon the rate of downward flow by eddy diffusion to regions of higher density where recombination occurs (Hunten 1969; Wallace and Hunten 1973). Ultraviolet photometer measurements of this glow from Pioneer 10 gave values of $K \approx 3 \times 10^{8\pm1}$ cm^2 sec^{-1} for temperatures of 150°K (Carlson and Judge 1974), and are reasonably well supported by the Copernicus Lyman-α measurements of Wallace, Jenkins and Drake (personal communication) which imply a value of $K \approx 10^{8\pm\frac{1}{2}}$ cm^2 sec^{-1}. Rocket measurements of the Lyman-α glow from Jupiter (Rottman *et al.* 1973) have indicated a higher albedo and lower eddy diffusion coefficient, $K \approx 10^6$ cm^2 sec^{-1}.

The abundance of other aeronomic species can be used to infer the magnitude of the eddy coefficient. Photochemical calculations by Strobel (1973) based on the lower values for K ($= 5 \times 10^5$ cm^2 sec^{-1}) predicted C_2H_2 and C_2H_6 abundances some two orders of magnitude less than the experimentally observed values of Ridgway (1974). Subsequent calculations by Strobel (1974) employed an altitude dependent K, consistent with the Pioneer 10 and Copernicus values, with results compatible with the observational estimates so long as Ridgway's observations probe down to the 10^{-1} atm level.

A lower limit to K is provided by a stellar occultation measurement of density inhomogeneities in the atmosphere, which are presumably due to atmospheric turbulence (Veverka *et al.* 1974).[1] These fluctuations were seen to persist up to at least the 3×10^{13} cm^{-3} density level which corresponds to $K > 7 \times 10^5$ cm^2 sec^{-1}.

Theoretical discussions of the sources of atmospheric turbulence and their diffusivities are presented by French and Gierasch (1974) and Shimizu (1974). Inertia gravity waves are considered in both analyses, and the diffusion coefficient is calculated as a function of the horizontal wavelength. French and Gierasch (1974) have assumed a vertical wavelength of 13 km, based on prominent occultation features, and find values of K up to 7×10^6 cm^2 sec^{-1} for horizontal wavelengths of 10 km. They suggest that $K = 3 \times 10^6$ cm^2 sec^{-1} and that the horizontal wavelength is ~ 50 km. Shimizu (1974) has performed essentially the same calculation but chooses different characteristic wavelengths based on terrestrial analogy, suggesting that $K = 10^7 - 10^8$ cm^2 sec^{-1}. French and Gierasch also considered acoustic waves and found for the corresponding diffusivity $K = 7 \times 10^7$, but they point out that the energy carried in such waves seems prohibitive and that continuous wave motion of this type seems improbable.

The above estimates of the eddy diffusion coefficient are summarized in Table I. For the present we leave K as a free parameter but note that the majority of the evidence favors relatively high values, $K \gtrsim 10^7$ cm^2 sec^{-1}.

The choice of the thermospheric temperature and temperature profile is presently rather uncertain. The earliest works on this subject were theoretical calculations by Gross and Rasool (1964), McGovern (1968), Shimizu (1971), McGovern and Burke (1972), Gross (1972), and Strobel and Smith (1973). All of these models assumed solar ultraviolet heating only, but they treated the cooling mechanisms and heat conduction processes somewhat differently. The Pioneer 10 encounter occurred near solar minimum for which an isothermal atmosphere at 150°K was considered representative (Carlson and Judge 1974) based on the computations of Shimizu (1971).

Attempts have been made to determine the temperature of the upper atmosphere based on inversion of occultation light curves (Hubbard *et al.*

[1]See also pp. 269 and 273.

TABLE 1

Estimates of the Eddy Diffusion Coefficient K *for the Upper Atmosphere of Jupiter*

Method	K (cm^2 sec^{-1})	Reference
Pioneer 10 Lyman-α	$3 \times 10^{8 \pm 1}$	*a*
Copernicus Lyman-α	$10^{8 \pm 1}$	*a, b*
Sounding Rocket Lyman-α	10^6	*c*
Stellar Occultation	$>7 \times 10^5$	*d*
Theory: Inertia Gravity Waves	10^7–10^8	*e*
Theory: Inertia Gravity Waves	3–7×10^6	*f*
Theory: Acoustic Waves	7×10^7	*f*

a. Carlson and Judge (1974).
b. Wallace, Jenkins, and Drake (personal communication).
c. Rottman *et al.* (1973).
d. Veverka *et al.* (1974).
e. Shimizu (1974).
f. French and Gierasch (1974).

1972; Vapillon *et al.* 1973; Veverka *et al.* 1974), but the results for the same event are not mutually consistent and it appears that only a temperature characteristic of the upper stratosphere can be derived. The combination of the various β-Sco occultation data suggests that the temperature is ~ 170°K at the 0.01 mb level (p. 23). It seems quite impossible to make any inferences about the thermosphere directly from stellar optical occultation data.

The only other experimental temperature datum pertains to the opposite extreme of the atmosphere (relative to the He and H line formation region). The ionospheric profiles observed by the Pioneer occultation experiments (Fjeldbo *et al.* 1975)[2] found topside-ionosphere electron temperatures of 900 ± 500°K. In the lower regions, substantial layering was found which does not lend itself to ionospheric modeling based on terrestrial analogy. The question of concern here is, what implications does this observed electron temperature hold for the neutral temperature in the lower thermosphere? Certainly there is no compelling reason to assume equal neutral, ion, and electron temperatures since ample terrestrial evidence exists for electron temperatures larger by a factor of two or more than the corresponding neutral temperature. In fact, Goertz (1973) has calculated electron, ion, and neutral temperatures for the upper atmosphere of Jupiter and found electron temperatures of a factor of three greater than the neutral gas temperature.

The high plasma temperatures observed by Pioneer radio occultations refer to a region far above the altitudes where resonance scattering by H and

[2]See p. 240.

He occur. The altitudes where the Pioneer plasma temperature determinations were obtained were some 2000 km above the cloud tops, whereas the region of airglow line formation is roughly 500–800 km above the clouds depending upon the specific atmospheric model. Temperatures between these two regions can be quite different. In calculations by Goertz, peak plasma temperatures are attained at altitudes above 1000 km and the largest temperature gradients occur in the 700–1000 km interval. Jovian ionospheric electron temperatures have also been calculated by Henry and McElroy (1969), who find that the onset for temperature gradients occurs in the region where H_2 densities are $\sim 10^7$ cm^{-3}, an altitude significantly above the density levels where line formation takes place. At lower altitudes and higher densities, where significant resonance scattering occurs, Henry and McElroy's model is isothermal with a temperature of 150°K, identical to that used in the previous analysis of the Lyman-α glow. Goertz' model exhibits neutral temperatures of ~ 275°K in the line formation region. If this temperature were appropriate at the time of Pioneer 10 encounter, then the observed Lyman-α glow would mean $K \gtrsim 3 \times 10^8$.

If one does assume that the neutral thermospheric temperature is elevated up to the plasma temperature observed by the Pioneer radio occultation, then one is faced with the problem of identifying the heating mechanism, since the solar ultraviolet would seem insufficient. Particle precipitation is a possible mechanism, but such a process must also meet the low flux requirement for any Lyman-α glow produced by particle excitation. A viscous interaction between the ionosphere (which tends to rotate with the magnetic field at System III velocity) and the neutral atmosphere rotating at a different velocity could be a possible heat source. Terrestrial analogies of ionospheric winds are known and are thought to be responsible for the sporadic-E layer. While it is possible that some of the layering observed in the Jovian ionosphere could be a manifestation of this effect, we have made crude estimates of the magnitude of the heat source and found it insufficient. Hunten (p. 26) has independently suggested this process as a candidate energy source. The dissipation of wave energy associated with eddy diffusion has been suggested by Prasad (1975) and Atreya and Donahue (p. 313). The calculations performed so far indicate that this mechanical heating could be a significant process, but the numerical values are still very uncertain.

A problem introduced by neutral temperatures elevated to the observed plasma temperature is in the interpretation of the low Lyman-α albedo observed by Pioneer 10 and Copernicus. At higher temperatures the albedo will increase (for a fixed-eddy diffusion coefficient) due to increased H-atom column densities and to variation of the Doppler width. The low albedo, if reinterpreted for higher temperatures, implies much greater (and perhaps unrealistic) values for K. The previous analysis may become inapplicable, however, due to other processes becoming important at high temperatures (e.g., increased H-atom recombination rates and diurnal variations in the H-atom

abundance owing to the diffusion time constant becoming comparable to the rotation period). In the present work we have assumed two temperatures, 150°K and 450°K, but prefer the lower value as being more appropriate for the neutral temperature in the region of line formation.

IV. RADIATIVE TRANSFER OF THE JOVIAN HELIUM AIRGLOW LINE

We have discussed the physics of scattering by He, the incident solar line, and a model of the atmosphere of Jupiter. Combining these with multiple-scattering calculations will give the predicted airglow intensity which is to be compared to observation. The previous analysis (Carlson and Judge 1974) assumed coherent scattering as a reasonable approximation since numerical calculations by Wallace (1971) of the diffusely reflected airglow of terrestrial atomic oxygen showed little difference between coherent scattering and scattering with frequency redistribution. This assumption may be unwarranted for the present case due to the different altitude distribution of absorbing species and radiation imprisonment effects. To examine this possibility, we derive the radiative transfer equation for isotropic scattering which includes frequency redistribution, and then develop approximate solutions. A first-order correction for the phase function of anisotropic scattering is then applied and the disc-averaged albedo is calculated for coherent and incoherent scattering.

In the description of atmospheric densities, Eqs. (12) and (13), we define x to be proportional to the H_2 density,

$$x = e^{-z/H} \tag{14}$$

and denote the H_2 absorption cross sections at 584 Å as σ_d (6.2×10^{-18} cm^2). Then at a frequency that is ξ Doppler widths from line center, the vertical optical depth is

$$\tau(x, \xi) = \tau_0\{x + \eta(\xi)\,[x - \ln(1 + x)]\} \tag{15}$$

where

$$\tau_0 = n_0 H \sigma_d \tag{16a}$$

and

$$\eta(\xi) = r\frac{\sigma_0}{\sigma_d}\,\phi(\alpha, \xi)\,. \tag{16b}$$

The fraction of all photons absorbed in unit volume at x, that are re-emitted as a resonance line photon, is

$$\tilde{\omega}(x, \xi) = \frac{\tilde{\omega}_0\sigma(\xi)n(\mathrm{He}|z)}{\sigma(\xi)n(\mathrm{He}|z) + \sigma_d n(\mathrm{H_2}|z)} \tag{17}$$

or

$$\tilde{\omega}(x, \xi) = \frac{\tilde{\omega}_0 \eta(\xi) x}{1 + x + x\eta(\xi)}. \tag{18}$$

Assume a plane parallel atmosphere and let $S(x', \xi')$ be the emission rate per unit x per cm^2 per Doppler width. $S(x)$ is related to the volume emission rate $Q(z)$ [cm^{-3} sec^{-1} Doppler width^{-1}] through $xS(x) = HQ(z)$. The number of photons passing through a plane at x is

$$\frac{1}{4\pi}\int_0^{2\pi} d\phi \int_0^1 d\mu\, e^{-\frac{|\tau(x,\xi') - \tau(x',\xi')|}{\mu}} S(x', \xi'). \tag{19}$$

The number absorbed per unit x, at x is

$$-\frac{1}{2}\frac{\partial}{\partial x}\int_0^1 d\mu\, e^{-\frac{|\tau(x,\xi') - \tau(x',\xi')|}{\mu}} S(x', \xi') \tag{20}$$

or

$$\frac{1}{2}\frac{\partial \tau(x, \xi')}{\partial x}\int_0^1 \frac{d\mu}{\mu} e^{-\frac{|\tau(x,\xi') - \tau(x',\xi')|}{\mu}} S(x', \xi'). \tag{21}$$

Of these absorbed photons, the fraction $\tilde{\omega}(x, \xi')$ reappear as photons at frequency ξ with probability distribution $P(\xi' \to \xi)$. Integrating over μ, we find the contribution at ξ is

$$\frac{1}{2}\tilde{\omega}(x, \xi')\, P(\xi' \to \xi)\, \frac{\partial \tau(x, \xi')}{\partial x}\, E_1[|\tau(x, \xi') - \tau(x', \xi')|]\, S(x', \xi') \tag{22}$$

where $E_1(|\tau - \tau'|)$ is the first exponential integral. Integration of the above over altitude x' and frequency ξ' gives the net contribution to the source function at x due to photons previously scattered. The total source function includes those and also the incident solar photons initially scattered at x, $S_0(x, \xi)$. The resulting source function is

$$S(x, \xi) = S_0(x, \xi) + \frac{1}{2}\int_{-\infty}^{\infty} d\xi'\, \tilde{\omega}(x, \xi')\, P(\xi' \to \xi)\, \frac{\partial \tau(x, \xi')}{\partial x}\int_0^{\infty} dx'\, S(x', \xi')\, E_1[|\tau(x', \xi') - \tau(x, \xi')|] \tag{23}$$

with

$$S_0(x, \xi) = \Delta\lambda_D \, \pi F_\lambda \int_{-\infty}^{\infty} d\xi' \, \tilde{\omega}(x, \xi') \, P(\xi' \to \xi) \, e^{-\pi x \cdot \xi / \mu_0} \left(\frac{\partial \tau(x, \xi')}{\partial x} \right) \tag{24}$$

where solar radiation is incident at $\cos^{-1}\mu_0$ and πF_λ is the spectral flux at line center in photons $\sec^{-1}$ cm^{-2} $Å^{-1}$. While machine calculations can be used to solve Eq. (23) to any required degree of accuracy, the added frequency dimension necessitates lengthy computations and it is desirable to develop an approximate solution. We first note that in the coherent case, $P(\xi' \to \xi) = \delta(\xi - \xi')$ and so

$$S(x, \xi) = S_0(x, \xi) + \frac{1}{2}\tilde{\omega}(x, \xi) \frac{\partial \tau}{\partial x} \int_0^{\infty} dx' \, E_1[\,|\tau(x, \xi) - \tau(x', \xi)|\,] \, S(x', \xi) \tag{25a}$$

where,

$$S_0(x, \xi) = \Delta\lambda_D \, \pi F_\lambda \, \tilde{\omega}(x, \xi) \, \frac{\partial \tau(x, \xi)}{\partial x} \, e^{-\pi x \cdot \xi / \mu_0} \tag{25b}$$

can be accurately described by the following approximation due to Biberman [see Van Blerkom and Hummer (1969)]. Since $s(\tau, \xi)\, d\tau = S(x, \xi)\, dx$ where $s(\tau, \xi)$ is the number of emissions per unit optical depth at ξ (i.e., photons $\sec^{-1}$ cm^{-2} per optical depth per Doppler width), then if $s(\tau, \xi)$ varies over τ much more slowly than the first exponential integral, it can be taken outside the integral [i.e., $s(\tau, \xi) \simeq s(\tau', \xi)$] resulting in

$$S(x, \xi) = \frac{S_0(x, \xi)}{\epsilon(x, \xi) + L(x, \xi)} \tag{26}$$

where

$$\epsilon(x, \xi) = 1 - \tilde{\omega}(x, \xi) \tag{27a}$$

$$L(x, \xi) = \frac{1}{2}\tilde{\omega}(x, \xi) \, E_2[\tau(x, \xi)] \tag{27b}$$

and E_2 is the second exponential integral.

The same reasoning can be applied to the incoherent case and simplified further by assuming that the frequency dependence of the source function is proportional to the absorption cross section. From Eqs. (9), (10), and (23) we then find

$$S(x, \xi) = \frac{S_0(x, \xi)}{\langle \epsilon(x, \xi) \rangle + \langle L(x, \xi) \rangle} \tag{28}$$

in which

$$<\epsilon(x, \xi)> = \int_{-\infty}^{\infty} P(\xi \to \xi') \, [1 - \tilde{\omega}(x, \xi')] \, d\xi' \tag{29a}$$

and

$$<L(x, \xi)> = \frac{1}{2} \int_{-\infty}^{\infty} P(\xi \to \xi') \, \tilde{\omega}(x, \xi') \, E_2[\tau(x, \xi')] \, d\xi' \, . \tag{29b}$$

These functions physically represent the loss rate of photons of frequency ξ, scattered to ξ'. The first term represents subsequent local reabsorption and dissipative loss while the second gives the rate of loss by escape from the medium without scattering.

The correction for Rayleigh scattering can be made by noting that repeated scattering of a photon produces near-isotropy, i.e., the photon loses memory of the initial direction. In fact, most of the anisotropy in the source function is due to the initial scattering of the solar photon, i.e., $S_0(x, \xi)$ (Chandrasekhar 1960). If observed at an angle Θ to the incident radiation, the first scattering contributes $p(\Theta)S_0$ to the emerging radiation. Higher order scattering, which can be assumed isotropic, contributes $S(x, \xi) - S_0(x, \xi)$. Therefore the emerging flux at $\mu = \cos\Theta$ is approximately

$$4\pi I(\mu) = \int_{-\infty}^{\infty} d\xi \int_{0}^{\infty} \frac{dx}{\mu} \, e^{-\tau(x, \xi)/\mu} \{S(x, \xi) + [p(\Theta) - 1] \, S_0(x, \xi)\} \, . \tag{30}$$

This method of approximation was checked by comparing it and Chandrasekhar's exact H function solutions for the Rayleigh case and conservative, coherent scattering. The agreement between the two was found to be excellent, with errors of only a few percent.

The disc averaged emission rate is given by

$$<4\pi I> = 2 \int_{0}^{1} \mu \, d\mu \, 4\pi I(\mu, \mu_0) \, . \tag{31}$$

We have used $\mu = \mu_0$ (but $\Theta = 30°$) and a single term Gaussian quadrature to evaluate the average brightness, i.e.,

$$<4\pi I> \approx 4\pi I\left(\mu = \mu_0 = \frac{2}{3}\right) . \tag{32}$$

These seem justifiable assumptions since the variation of $4\pi I$ with μ was found to be quite slow.

With the above formulae one can evaluate the importance of frequency redistribution in formation of the Jovian He airglow line and the adequacy

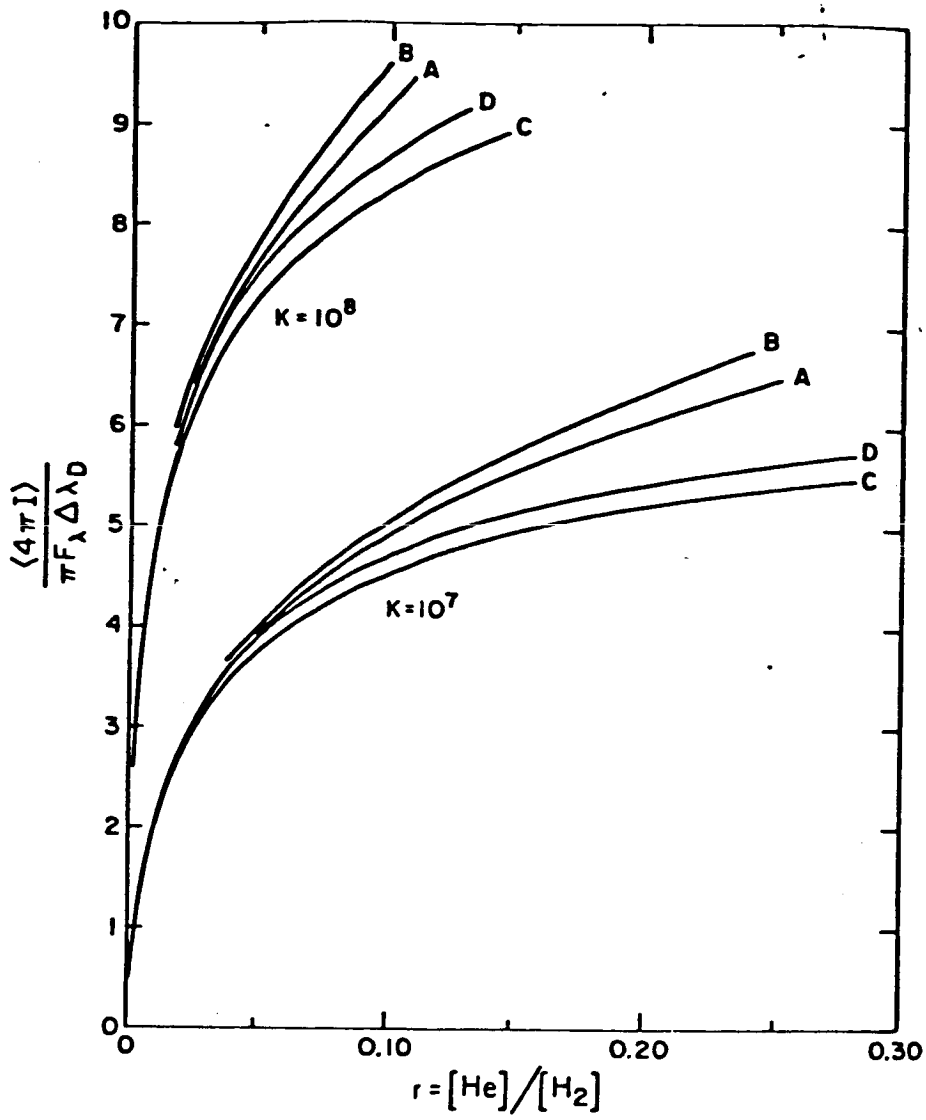

Fig. 3. The average emission rate from Jupiter as a function of the $[He]/[H_2]$ ratio for a 150°K atmosphere computed with various assumptions. Curve *A* is an exact iterative solution to Eq. (25) assuming coherent scattering and the Voigt profile. Curve *B* is the Biberman approximation [Eq. (26), (27)] with the above assumptions. Curve *C* includes frequency redistribution with the Doppler profile [Eq. (5)] while Curve *D* uses the same formulation as *C* but for coherent scattering. It is concluded that the influence of frequency redistribution is negligible for interpretation of the present observations, and the solutions corresponding to Curve *A* provide sufficient accuracy.

of the coherent approximation. We have calculated solutions for an isothermal 150°K atmosphere with $K = 10^7$ and 10^8 cm^2 sec^{-1} and the following cases: A – an exact numerical solution (by iteration) of Eq. (25) for coherent scattering using the Voigt profile; B – the Biberman approximation [Eqs. (26) and (27)] for coherent scattering with the Voigt profile; C – the approximate solution [Eqs. (28) and (29)] to non-coherent scattering using the Doppler profile and the redistribution function given by Eq. (8); D – the same as the preceding case except substituting $P(\xi' \rightarrow \xi) = \delta(\xi - \xi')$ in the numerical code, i.e. coherent scattering. Results for these cases are shown in Fig. 3. The scant difference between solutions A and B shown in the figure demonstrates that Biberman's approximation is excellent, while the dissimilarities of B and D indicate the minor (but not insignificant) importance of including the Lorentzian wings of the line. Note the small difference between the solutions for cases C and D, indicating that the coherent approximation overestimates the albedo by only ~ 3%. Even though we have neglected the wings in this comparison, the conclusion that the coherent approximation is quite adequate still holds since scattering in the wings is itself very nearly coherent (Carlson and Judge 1971). For comparison with the observations then, we have assumed coherent scattering with the Voigt absorption profile, and solved Eq. (25) by iteration. The results are presented in the following section.

V. RESULTS AND DISCUSSION

The disc-averaged 584 Å apparent emission rate was calculated for various values of K and two different temperatures, 150°K and 450°K. For a given He-H_2 abundance and K the albedo is generally less at higher temperatures since the increased scale height places more H_2 in and above the region of He resonance scattering. The albedos are placed on an absolute scale, expressed in Rayleighs (R), using the central flux (at 1 A.U.) of $\pi F_\lambda = 1.45 \times 10^{10}$ photons sec^{-1} cm^{-2} Å^{-1} as previously discussed. These results are shown in Fig. 4 along with the observed datum of 5.1 R. The combination of the absolute calibration errors, measurement uncertainties, and uncertainties in the solar flux, combine to give an estimated error limit of ±50%.

A literal interpretation of the Pioneer values ($\langle 4\pi I \rangle = 5.1$ R, $K = 3 \times 10^8$, assuming 150°K) implies a low helium-to-hydrogen ratio, on the order of one percent, which might indicate depletion of helium in the Jovian atmosphere (Stevenson and Salpeter p. 97). But the case for such depletion is weak since the range of uncertainties in both the albedo and K admit $0 < [He]/[H_2] \leq 28\%$. This range of values is consistent with other determinations of the $[He]/[H_2]$ ratio obtained by a variety of methods: the β-Sco stellar occultation, and infrared measurements from aircraft and Pioneer. Values obtained by those methods are summarized in Fig. 5 along with the solar value (Hunten and Münch 1973) of $[He]/[H_2] = 0.11$, although even

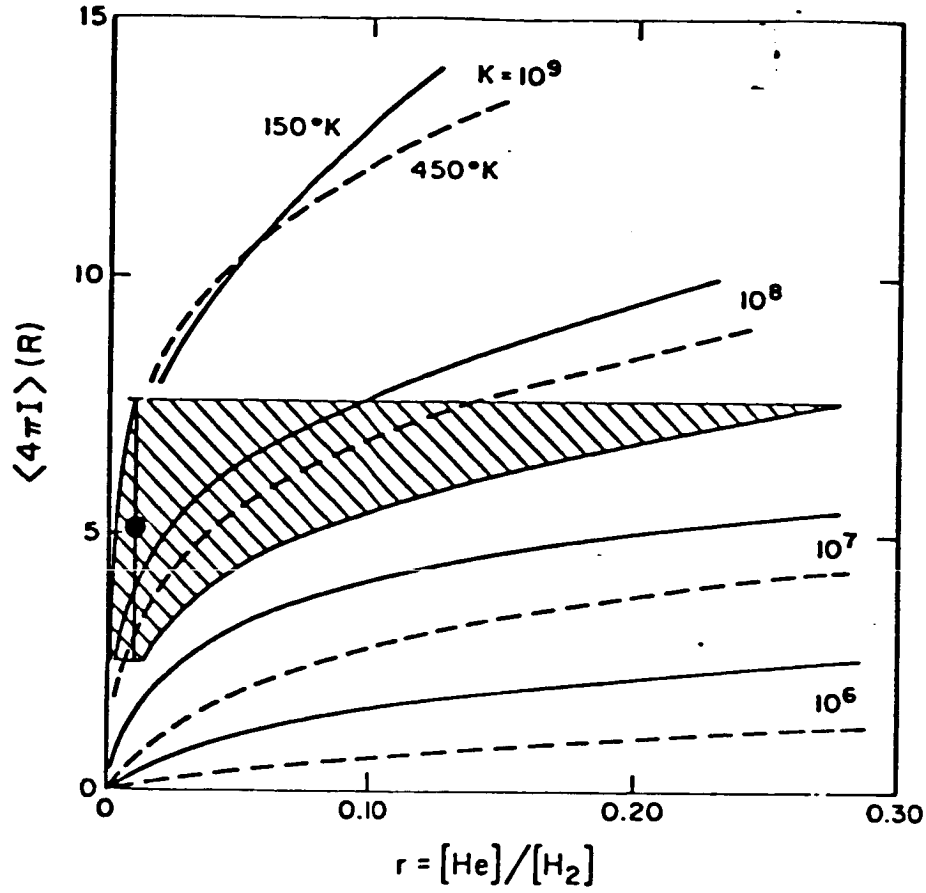

Fig. 4. The experimental and theoretical average He I 584 Å emission rates from Jupiter. The model calculations were performed for coherent scattering and the Voigt profile by exact iterative solution of Eq. (25), and normalized using $\pi F_\lambda = 1.45 \times 10^{10}$ photons sec^{-1} cm^{-2} $Å^{-1}$ (at 1 A.U.). The Pioneer 10 datum (5.1 R) is shown and the combined range of uncertainties is indicated. Using the eddy diffusion coefficient determined from the Pioneer-10 Lyman-α albedo ($K = 3 \times 10^{7}$ cm^2 sec^{-1}), indicated by the shaded area, the [He]/[H_2] volume abundance ratio is found to be less than 28% but greater than zero.

the solar value is quite uncertain (Hirschberg 1973). Consideration of these available measurements suggests that presently the most reasonable number to adopt corresponds to the solar value. If one does indeed assume solar composition, the inferred value of K is quite reasonable: $K = 3 \times 10^7$ cm^2 sec^{-1}, and consistent with both the Pioneer and Copernicus values. The relatively low $K = 10^6$ cm^2 sec^{-1} from sounding rocket Lyman-α observations seems difficult to reconcile with the various estimates of the He abundance and the Pioneer helium albedo.

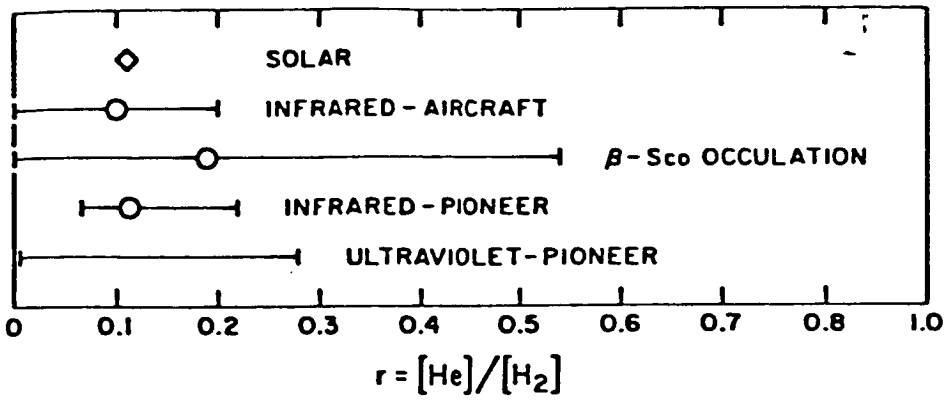

Fig. 5. Summary of various determinations of the Jovian atmospheric $[He]/[H_2]$ abundance ratio. Shown is the solar value from Hunten and Münch (1973), the aircraft data from Pollack (1976), a stellar occultation determination (Elliot *et al.* 1974), the Pioneer infrared data (Orton p. 206) and the present range for the ratio. The combination of these data suggest solar composition.

Since the ultraviolet determination of the helium abundance depends upon relative measurements of two quite different radiation sources—the sun and Jupiter—with two quite different instruments, it is important to be able to assess their relative consistency. In fact, this can be done by intercomparison with a third set of measurements for which mutual observations of the interplanetary helium glow have been made. Weller and Meier (1974) observed the interplanetary He 584 Å glow as have the Pioneer photometers. Their measurements, obtained from Earth orbit at $\alpha = 18^h$ show emission rates of 1.5 ± 0.5 R while our own Pioneer 10 values for the same geometry give ~ 1.8 R. Meier and Weller (1974) also measured terrestrial He airglow with the same instrument and were able to deduce the solar flux value $\pi F\lambda = 2 \times 10^{10}$ photons sec^{-1} cm^{-2} $Å^{-1}$ since the thermospheric helium content is rather well known. When variations with solar activity are taken into account, their solar flux and that used in this work agree to within 25%. Not only do these values of brightness and solar flux agree well in the relative sense, which is the only necessary requirement, but they also agree well in absolute magnitude. This adds confidence to the Lyman-α observations on Pioneer 10 since the relative calibration between the two channels is more accurate than the absolute calibration.

The He-H_2 ratio found above holds only if the Jovian thermospheric temperature is not significantly higher than the assumed 150°K. At 450°K, the calculations indicate increased He abundances (for the same K). However, if these higher neutral temperatures are found, the Lyman-α albedo and eddy diffusion coefficient will have to be reconsidered.

VI. SUMMARY

Observations of 5.1 R diffusely reflected HeI 584 Å emissions from the atmosphere of Jupiter by the ultraviolet photometer on Pioneer 10 establish the expected presence of He in the giant planet. In order to make a quantitative estimate of the relative abundance, we have measured the width and intensity of the solar line and compared these measurements with other data in order to estimate a line-center flux (at the time of Jupiter encounter) of $1.45 \pm 0.4 \times 10^{10}$ photons sec^{-1} cm^{-2} $Å^{-1}$ at 1 A.U. The assumption of coherent scattering in formation of the Jovian airglow line was investigated and found to be an accurate approximation. The anisotropic angular scattering function for He was included in model calculations of the average disc brightness. The present status of knowledge of the atmospheric temperature and eddy diffusion coefficient, which are required in the resonance scattering model calculations, have been briefly reviewed. Assuming an isothermal 150°K atmosphere and the range of eddy diffusion values from the Lyman-α observations of Pioneer 10, the atmospheric helium-to-hydrogen abundance ratio is found to be greater than zero but less than approximately 28%. Calculations performed for a 450°K atmosphere indicate higher He abundances if such a high neutral temperature is truly characteristic. However, this case would require a reassessment of the eddy diffusion coefficient and Lyman-α albedo.

Acknowledgement. This work was supported by Contract NAS2-6558 with the NASA Ames Research Center.

REFERENCES

Carlson, R. W. 1973. Resonance absorption of the solar HeI 584 Å line by telluric helium. Unpublished analysis of OSO-6 observations.

Carlson, R. W., and Judge, D. L. 1971. The extreme ultraviolet dayglow of Jupiter. *Planet. Space Sci.* 19:327–343.

———. 1974. Pioneer 10 ultraviolet photometer observations at Jupiter encounter. *J. Geophys. Res.* 79:3623–3633.

———. 1975. Pioneer 10 ultraviolet photometer observations of the Jovian hydrogen torus: the angular distribution. *Icarus* 24:395–399.

Chandrasekhar, S. 1960. *Radiative transfer.* pp. 145–149. New York: Dover.

Cushman, G. W.; Farwell, L.; Godden, G.; and Rense, W. A. 1975. Solar line profiles of HeI 584 Å and HeII 304 Å. *J. Geophys. Res.* 80:482–486.

Delaboudinière, J. D., and Crifo, J. F. 1975. The profile of the Helium I 584 Å line from the sun. XVIII COSPAR meeting, Varna, Bulgaria.

Doschek, G. A.; Behring, W. E.; and Feldman, V. 1974. The widths of the solar HeI and HeII lines at 584, 537, and 304 Å. *Astrophys. J.* 190:L141–L142.

Dupree, A. K.; Huber, M. C. E.; Noyes, R. W.; Parkinson, W. H.; Reeves, E. M.; and Withbroe, G. L. 1973. The extreme ultraviolet spectrum of a solar active region. *Astrophys. J.* 182:321–333.

Dupree, A. K., and Reeves, E. M. 1971. The extreme ultraviolet spectrum of the quiet sun. *Astrophys. J.* 165:599–613.

Elliot, J. L.; Wasserman, L. H.; Veverka, J.; Sagan, C.; and Liller, W. 1974. The occultation of Beta-Scorpii by Jupiter. II. The hydrogen helium abundance in the Jovian atmosphere. *Astrophys. J.* 190:719–729.

Fjeldbo, G.; Kliore, A.; Seidel, B.; Sweetnam, D.; and Cain, D. 1975. The Pioneer 10 radio occultation measurements of the ionosphere of Jupiter. *Astron. Astrophys.* 39:91–96.

French, R. G., and Gierasch, P. J. 1974. Waves in the Jovian upper atmosphere. *J. Atmos. Sci.* 31:1707–1712.

Goertz, C. K. 1973. Jupiter's ionosphere and magnetosphere. *Planet. Space Sci.* 21:1389–1398.

Gross, S. H. 1972. On the exospheric temperature of hydrogen-dominated planetary atmospheres. *J. Atmos. Sci.* 29:214–218.

Gross, S. H., and Rasool, S. I. 1964. The upper atmosphere of Jupiter. *Icarus* 3:311–322.

Hall, L. A., and Hinteregger, H. E. 1970. Solar radiation in the extreme ultraviolet and its variation with solar rotation. *J. Geophys. Res.* 75:6959–6965.

Hamilton, D. R. 1947. The resonance radiation induced by elliptically polarized light. *Astrophys. J.* 106:457–465.

Henry, R. J. S., and McElroy, M. B. 1969. The absorption of extreme ultraviolet radiation by Jupiter's upper atmosphere. *J. Atmos. Sci.* 26:912–917.

Henyey, L. G. 1940. The Doppler effect in resonance lines. *Proc. Natl. Acad. Sci. U.S.* 26: 50–54.

Heroux, L.; Cohen, M.; and Higgins, J. E. 1974. Electron densities between 110 and 300 km derived from solar EUV fluxes of August 23, 1972. *J. Geophys. Res.* 79:5237–5244.

Hinteregger, H. E. 1970. The extreme ultraviolet solar spectrum and its variation during a solar cycle. *Ann. Geophys.* 26:547–554.

Hinteregger, H. E.; Hall, L. A.; and Schmidtke, G. 1965. Solar XUV radiation and neutral particle distribution in the July 1963 thermosphere. *Space Research V* (D. G. King-Hele, P. Muller, and G. Righini, eds.), pp. 1175–1190. Amsterdam: North Holland.

Hirschberg, J. 1973. Helium abundance of the sun. *Rev. Geophys. Space Phys.* 11:115–131.

Hubbard, W. B.; Nather, R. E.; Evans, D. S.; Tull, R. G.; Wells, D. C.; van Citters, G. W.; Warner, B.; and Vanden Bout, P. 1972. The occultation of Beta Scorpii by Jupiter and Io. I. Jupiter. *Astron. J.* 77:41–59.

Hummer, D. G. 1962. Non-coherent scattering. I. The redistribution functions with Doppler broadening. *Mon. Not. Roy. Astron. Soc.* 125:21–37.

Hunten, D. M. 1969. The upper atmosphere of Jupiter. *J. Atmos. Sci.* 26:826–834.

Hunten, D. M., and Münch, G. 1973. The helium abundance on Jupiter. *Space Sci. Rev.* 14: 433–443.

Judge, D. L., and Carlson, R. W. 1974. Pioneer 10 ultraviolet photometer observations in the vicinity of Jupiter. *Science* 183:317–318.

Kumar, S., and Broadfoot, A. L. 1975. He 584 Å airglow emission from Venus. Mariner 10 observations. *Geophys. Res. Lett.* 2:357–360.

Maloy, J. O.; Carlson, R. W.; Hartmann, U.; and Judge, D. L. 1976. Observations of the profile and intensity of the solar helium λ 584 Å resonance line. In draft.

McGovern, W. E. 1968. Exospheric temperatures of Jupiter and Saturn. *J. Geophys. Res.* 73:6361–6363.

McGovern, W. E., and Burke, S. D. 1972. Upper atmosphere thermal structure of Jupiter with convective heat transfer. *J. Atmos. Sci.* 29:179–189.

Meier, R. R., and Weller, C. S. 1972. EUV resonance radiation from helium atoms and ions in the geocorona. *J. Geophys. Res.* 77:1190–1204.

———. 1974. EUV observations of the latitudinal variation of He. *J. Geophys. Res.* 79: 1575–1578.

Milkey, R. W. 1975. Comments concerning the photoionization model for excitation of resonance lines of HeI and HeII in the solar chromosphere. *Astrophys. J.* 199:L131–132.

Milkey, R. W.; Heasley, J. N.; and Beebe, H. A. 1973. Helium excitation in the solar chromosphere: HeI in a homogeneous chromosphere. *Astrophys. J.* 186:1043–1052.

Pollack, J. B. 1976. Estimates of Jupiter's helium to hydrogen ratio and vertical temperature structure from aircraft observations in the 16–40 micron region. In draft.

Prasad, S. S. 1975. Possible new Jovian thermospheric models. *Astrophys. J.* 200:L171–L174.

Reeves, E. M., and Parkinson, W. H. 1970. An atlas of extreme ultraviolet spectro heliograms from OSO-IV. *Astrophys. J. Suppl.* vol. 21.

Ridgway, S. T. 1974. Jupiter: identification of ethane and acetylene. *Astrophys. J.* 187:L41–L43. (Erratum 192:L51).

Roble, R. G., and Dickinson, R. E. 1973. Is there enough solar extreme ultraviolet radiation to maintain the global mean thermospheric temperature? *J. Geophys. Res.* 78:249–257.

Rottman, G. J.; Moos, H. W.; and Freer, C. S. 1973. The far ultraviolet spectrum of Jupiter. *Astrophys. J.* 184:L89–L92.

Shimizu, M. 1971. The upper atmosphere of Jupiter. *Icarus* 14:273–281.

———. 1974. Atmospheric mixing in the upper atmospheres of Jupiter and Venus. *J. Geophys. Res.* 79:5311–5313.

Strobel, D. S. 1973. The photochemistry of hydrocarbons in the Jovian atmosphere. *J. Atmos. Sci.* 30:489–498.

———. 1974. Hydrocarbon abundances in the Jovian atmosphere. *Astrophys. J.* 192:L47–L49.

Strobel, D. F., and Smith, G. F. 1973. On the temperature of the Jovian thermosphere. *J. Atmos. Sci.* 30:718–725.

Swartz, W. E., and Nisbet, J. S. 1973. Incompatibility of solar EUV fluxes and incoherent scatter measurements at Arecibo. *J. Geophys. Res.* 78:5640–5657.

Timothy, A. F.; Timothy, J. G.; and Willmore, A. P. 1972. The ion chemistry and thermal balance of the E- and lower F-regions of the daytime ionosphere: an experimental study. *J. Atm. Terr. Phys.* 34:969–1035.

Van Blerkom, D., and Hummer, D. G. 1969. The normalized on-the-spot approximation for line transfer problems. *J. Quant. Spectrosc. Radiat. Transfer* 9:1567–1571.

Vapillon, L.; Combes, M.; and Lecacheux, J. 1973. The β Scorpii occultation by Jupiter. II. The temperature and density profiles of the Jovian upper atmosphere. *Astron. Astrophys.* 24:135–149.

Veverka, J.; Wasserman, L. H.; Elliot, J.; and Sagan, C. 1974. The occultation of β Scorpii by Jupiter. I. The structure of the Jovian upper atmosphere. *Astron. J.* 79:73–84.

Wallace, L. 1971. The effect of non-coherency on the intensity of resonantly scattered sunlight in a planetary atmosphere. *Planet. Space Sci.* 19:377–389.

Wallace, L., and Hunten, D. M. 1973. The Lyman-alpha albedo of Jupiter. *Astrophys. J.* 182:1013–1031.

Weller, C. S., and Meier, R. R. 1974. Observation of helium in the interplanetary/interstellar wind—the solar wake effect. *Astrophys. J.* 193:471–476.

Wiese, W. L.; Smith, M. W.; and McGlennon, B. M. 1966. *Atomic transition probabilities vol. I. Hydrogen through neon.* NSRDS-NBS 4. Washington, D.C.: U.S. Government Printing Office.

Woodgate, B. E.; Knight, D. E.; Uribe, R.; Sheather, P.; Bowles, J.; and Nettleship, R. 1973. Extreme ultraviolet line intensities from the sun. *Proc. Roy. Soc. A.* 332:291–309.

Zirin, H. 1975. The helium chromosphere, coronal holes, and stellar X-rays. *Astrophys. J.* 199:L63–L66.

Sodium D-Line Emission from Io: Analysis of Line Profiles

R. W. Carlson, D. L. Matson, T. V. Johnson, J. T. Bergstralh

Abstract for Planetary Sciences (AAS) Meeting, Austin, Texas, April 1976.

High resolution sodium D-line emission profiles have been obtained of the Io sodium emission cloud. The line shapes are asymmetric due to anisotropic velocity distributions and the Doppler effect. These data are compared to theoretical line shapes for initial velocity distributions characteristic of sputtering by energetic particles. A variety of source distributions over the surface of Io were considered. It was found that the experimental profiles are compatible with those predicted by sputtering and that the ejection of sodium atoms seems to occur in the leading hemisphere of Io.

PIONEER 10 AND 11 ULTRAVIOLET PHOTOMETER OBSERVATIONS OF THE JOVIAN SATELLITES

D. L. JUDGE, R. W. CARLSON, F. M. WU and U. G. HARTMANN
University of Southern California

The Pioneer 10 and 11 Jupiter probes have provided several opportunities for observation of the Jovian satellites J I through J V. From these data a tenuous atmosphere of hydrogen for Io has been identified and, in the present work, an additional short-wavelength ($\lambda < 800$ Å) emission associated with an extended cloud centered on Io is reported and interpreted as arising from the radiative decay of excited atomic ions. Characteristic x-rays produced by electron bombardment of Io's surface may also contribute to the signal. Emission features associated with Amalthea (J V) and Europa (J II) are also observed. Signals apparently associated with J V occur in the long-wavelength channel while emissions were observed in the short-wavelength channel during J II observations. The data of the long-wavelength channel are interpreted as arising from atomic hydrogen Lyman-α emission in all cases. The source species for the short-wavelength emissions cannot at this time be unambiguously determined, but the wavelength range of the signals is well established.

The present observations of the Jovian satellites, J I through J V, have proved to be extremely interesting, providing a number of new and unexpected results. At the time the Pioneer 10 and 11 missions were planned, none of the satellites of Jupiter were known to have an atmosphere, either bound or unbound. The earth-based observation of a sodium cloud associated with Io, and that of a possible tenuous atmosphere at Ganymede have both occurred since the Pioneer 10 launch in 1972.[1] [For a review of earlier work the reader is referred to articles by Newburn and Gulkis (1973), Morrison and Cruikshank (1974), and Carlson (1975).] The sodium observation has been of particular interest and has given rise to intensive efforts to understand the complex interaction of this satellite with the Jovian magnetosphere. Io

[1]See pp. 1103 and 1004.

is relatively unique among the thirteen known Jovian satellites with several observations to set it apart from its companions: (a) the decametric radio modulation, (b) the now known Na and H clouds, (c) the strong variation in color from pole to equator, (d) Io's significant sweeping and injection of charged particles from and into Jupiter's magnetosphere, and finally, (e) the most recent observation reported here of extended, short-wavelength emission with $\lambda < 800$ Å. Some of the possible interpretations of this observation will be discussed in later sections.

In addition to the sodium and hydrogen observations at Io, and the extended cloud of these gases in orbit about Jupiter, there is further evidence that ultraviolet emissions are associated with another Galilean satellite, Europa (J II), and with the innermost satellite, Amalthea (J V). Prior to the groundbased observations of sodium at Io, the only suggested Jovian satellite atmospheres were those of Ganymede and Io, the former tentatively identified by stellar occultation measurements while post-eclipse brightening suggested an atmosphere on the latter. Since stellar occultations are rare and only give limited information about the actual atmospheric constituents, direct photometric observation can be highly rewarding.

The wavelength region investigated in the present study has been limited to observations shortward of ~ 1400 Å, a region for which the earth's atmosphere is opaque. The ultraviolet photometer which obtained the data to be discussed covered two broad spectral regions shown in Fig. 1. The short-wavelength band is sensitive only to emissions shortward of ~ 800 Å, and includes the 584 Å resonance line of helium. The region of sensitivity of the long-wavelength channel includes the hydrogen resonance line at 1216 Å. Although detection of emissions other than those from neutral hydrogen and helium are certainly possible, the instrument design was based on the expected dominance of these two gases in the Jovian and interplanetary glow. The broadband nature of the instrument response, however, requires careful interpretation of emissions from less well-characterized sources, such as the Jovian satellites. In fact, as discussed in subsequent sections, the demands of self-consistency require that signals observed in the "helium" or short-wavelength channel be ascribed to a source other than helium atoms for the present satellite observations.

Photometer data presented in the following sections are left in terms of count rates, unless a reasonable estimate of source geometry could be determined. Conversion to an equivalent apparent brightness requires detailed information about the spatial extent of the source being viewed, as well as convolution with the angular response of the instrument and the viewing geometry appropriate to the particular observation.

The next two sections present the details of the encounter viewing geometry for the photometer and the equations necessary to convert count rates to brightness. Subsequent and main sections will discuss the Io observations in each of the two channels, followed by their respective interpreta-

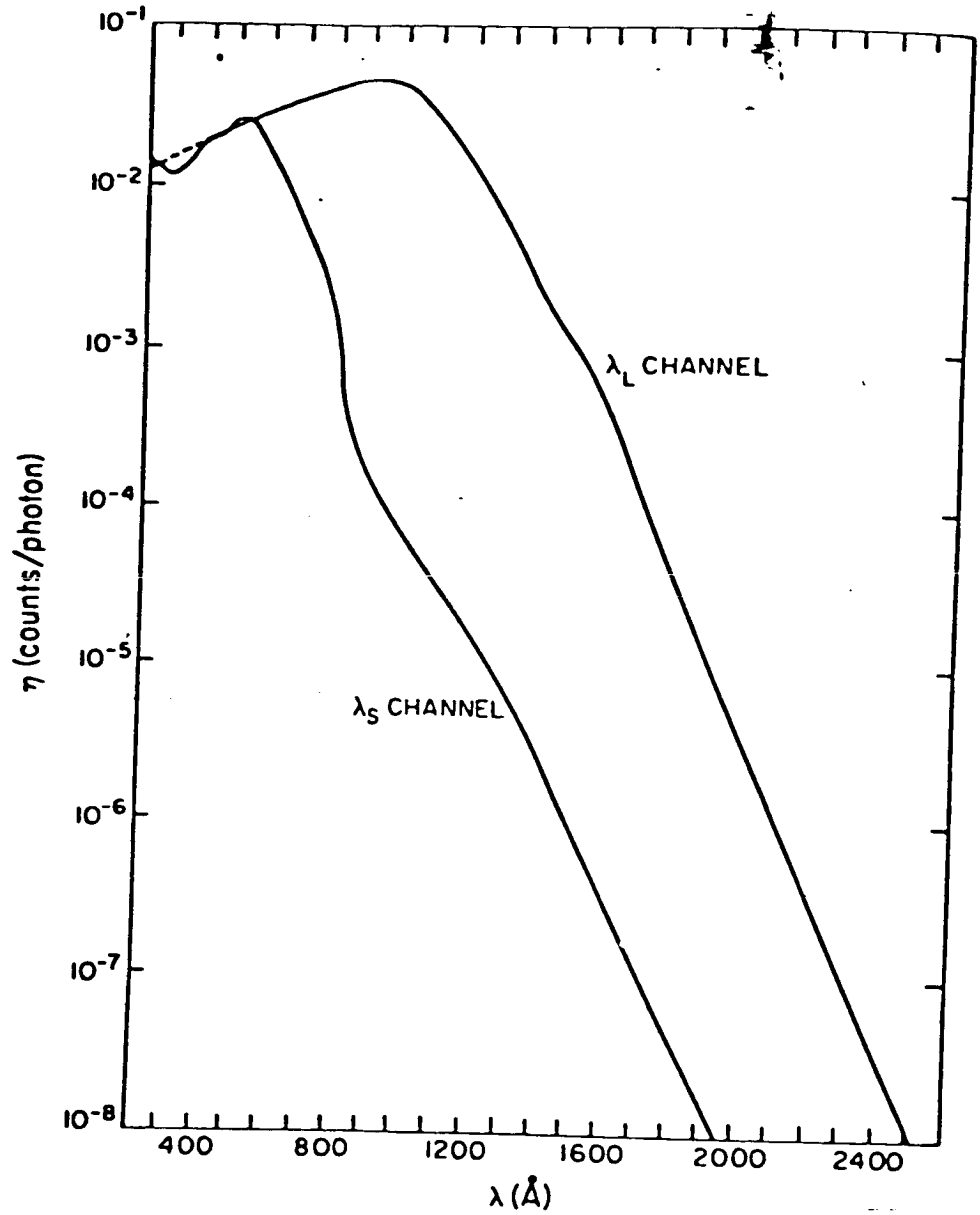

Fig. 1. Spectral sensitivity of the two-channel ultraviolet photometer of the University of Southern California on board both Pioneers 10 and 11.

tions. Next, the Amalthea and Europa observations will be presented with a discussion of plausible source mechanisms for these heretofore unreported emissions. Finally, two short sections on Ganymede and Callisto complete the satellite observational survey.

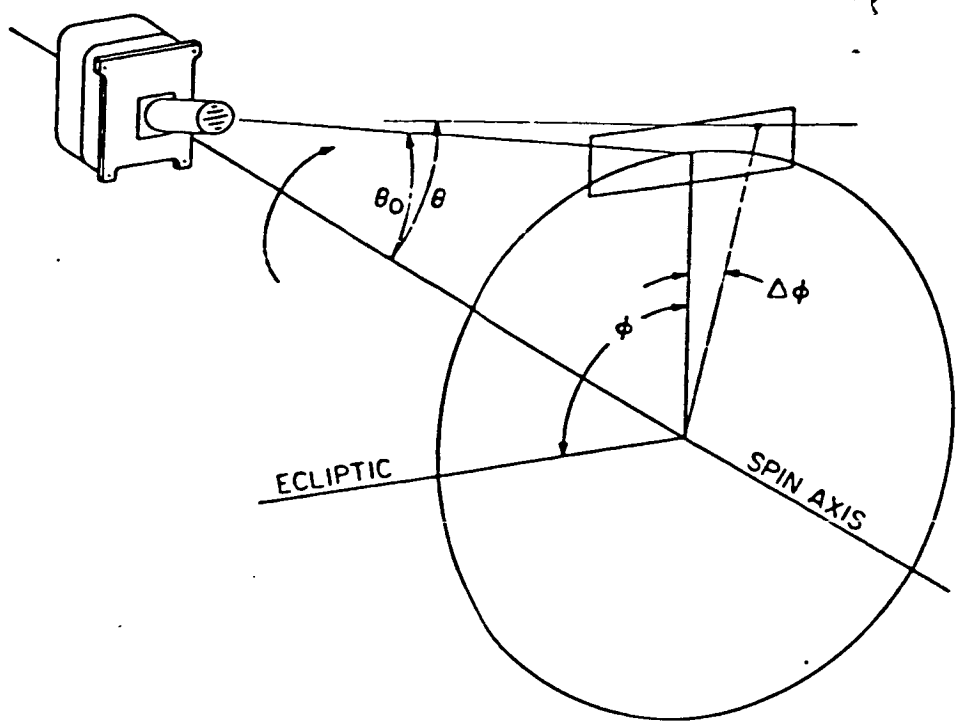

Fig. 2. The optical axis of the photometer is at an angle $\theta_0 \sim 20°$ to the spin axis of the spacecraft. The angle ϕ is the clock angle relative to the ecliptic. The instantaneous field of view is nominally $1° \times 10°$.

I. VIEWING GEOMETRY

The field of view of the photometer is limited by a mechanical collimator whose optical axis is oriented at an angle $\theta_0 = 20°$ to the spacecraft spin axis (Fig. 2). The scanning motion that results from spacecraft rotation sweeps the field of view over the surface of a 40° cone having its vertex at the spacecraft and oriented along the spin axis. During both Pioneer 10 and 11 encounters the spin axis was parallel to the spacecraft-Earth line and nearly in the plane of the Jovian satellite orbits; the curve traced by the intersection of the instrument's line-of-sight with the orbital plane of the satellites is a hyperbolic section as sketched in Fig. 3. As the photometer clock angle ϕ increases from zero through 90° to 180°, the projection of the field of view onto the plane of the satellite orbits follows the hyperbola from one asymptote through its vertex to the other asymptote. At the time of the observations, prior to periapsis, the spacecraft was below the orbital plane and all satellite emission features therefore occur with clock angles $0 < \phi < 180°$. Viewed from Jupiter's north pole, looking down onto the plane of the satellites, Figs.

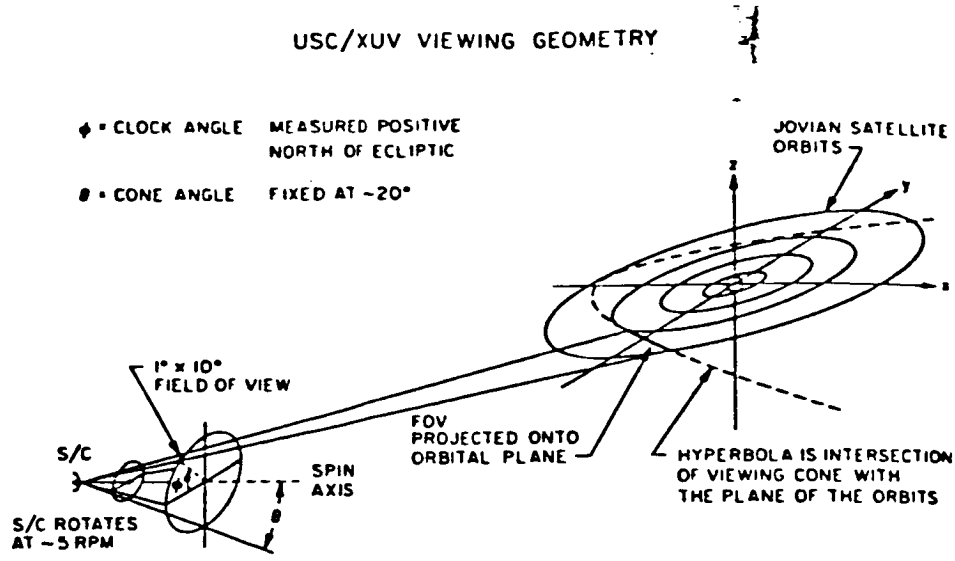

Fig. 3. The field of view projected onto the satellite orbital plane traces a hyperbola as the spacecraft rotates from $\phi = 0°$ to $\phi = 180°$.

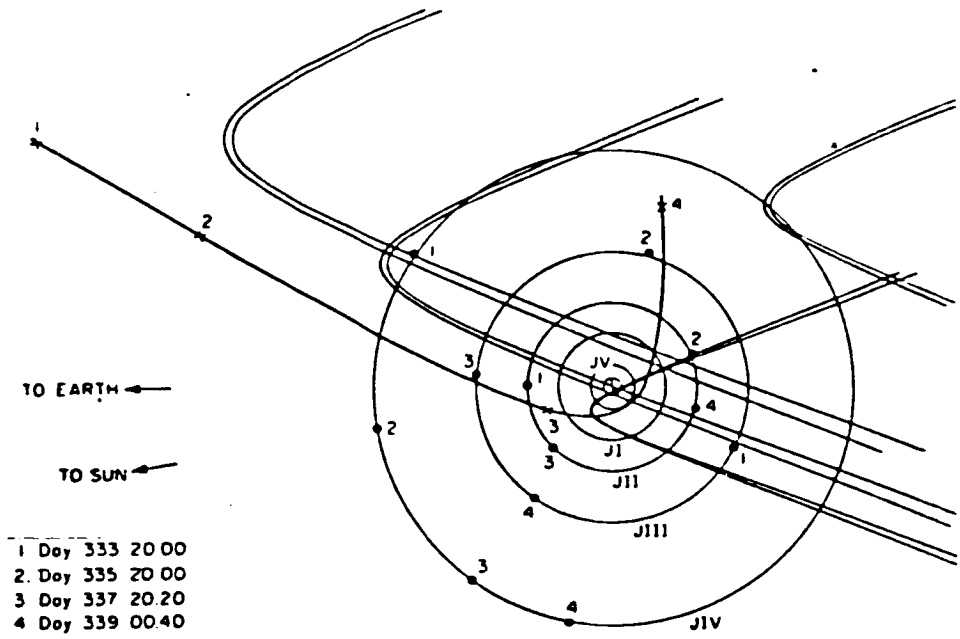

PIONEER 10 USC/UV PHOTOMETER
PROJECTION OF FIELD OF VIEW
(IN THE PLANE OF THE SATELLITE ORBITS)

Fig. 4*a*. Viewing hyperbolas in the satellite plane as seen from above Jupiter's north pole for Pioneer 10. The width of the hyperbolas represents the 1° cone angle width over which the photometer is sensitive. Four different spacecraft positions are shown and the satellite orbits are labeled by each satellite's position at that time.

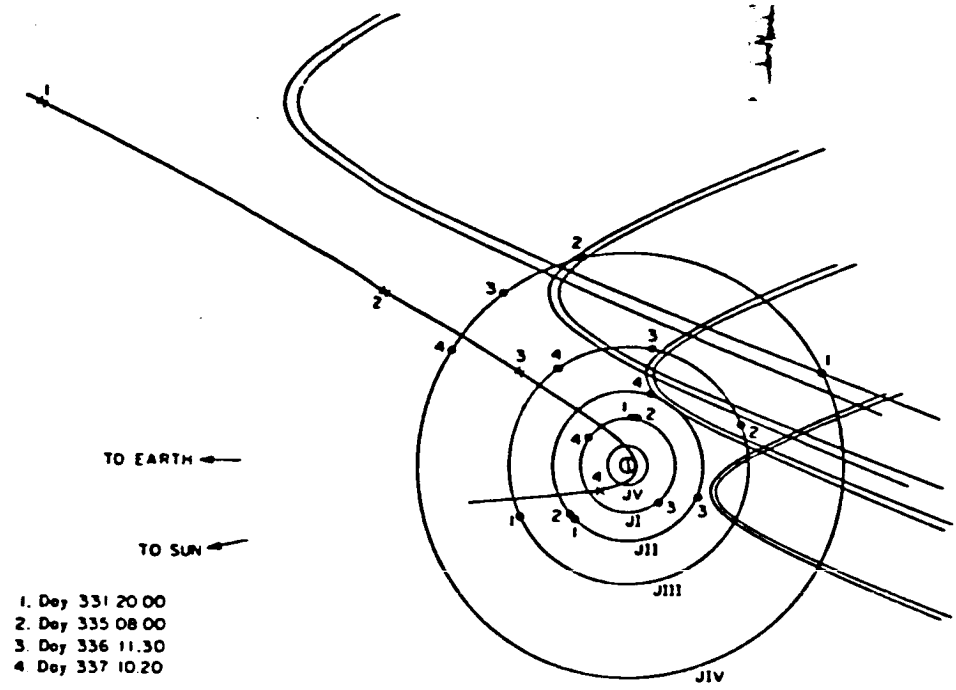

PIONEER 11 USC/UV PHOTOMETER
PROJECTION OF FIELD OF VIEW
(IN THE PLANE OF THE SATELLITE ORBITS)

Fig. 4*b*. The same sequence as for Fig. 4*a* but for Pioneer 11.

4*a* and 4*b* show a computer drawn progression of encounter viewing over several days for Pioneers 10 and 11, respectively. The width of the hyperbolas as shown reflects the 1° cone angle over which the photometer is sensitive.

Satellite viewing opportunities are indicated on the time axes of the data plots (Figs. 5, 6 and 7) and inset figures are included to show the orbits and positions of the satellites in relation to the field of view at that time, as well as the shadow of Jupiter. Fiducial marks along the orbits represent one-hour intervals, and the horizontal line points toward Earth. The section of the field of view shown in each case is centered near $\phi \sim 15°$ with $\Delta\phi \sim \pm 5°$.

II. RELATION OF COUNT RATE TO APPARENT SURFACE BRIGHTNESS

The rate at which photons are received by the photometer due to a small source element with apparent surface brightness $4\pi I$ photons sec^{-1} cm^{-2} and projected area Δa is

$$S = \frac{A}{4\pi r^2} \times 4\pi I \times \Delta a \text{ photons sec}^{-1} \qquad (1)$$

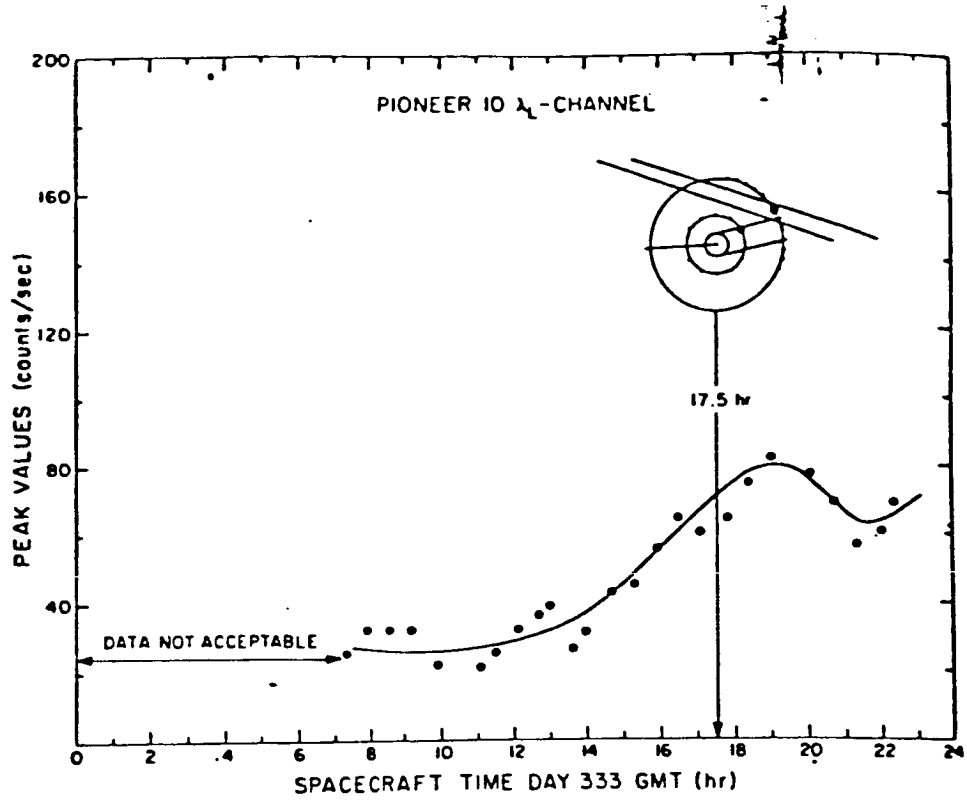

Fig. 5. Long-wavelength channel data for Day 333 was averaged over a period of 0.5 hr to obtain each point shown. The inset shows the positions of Amalthea and Io at $17^h\ 50^m$ when Io is centered in the field of view with clock angle $\phi \sim 10°$.

where r is the distance between the spacecraft and the source of emission: A is the effective area of the acceptance aperture, and is a function of source position (θ, ϕ) (Carlson and Judge 1974). For a source at the center of the field of view (θ_0, ϕ_0), A is just the geometrical area of the aperture which is 1.66 cm^2.

The response of the instrument to a finite extended source, such as the disc of Jupiter or an Io cloud is obtained by integrating $A(\theta, \phi)$ over the field of the object. For a source of strength $4\pi I(\theta, \phi)$ extending from θ_1 to θ_2 in cone angle and ϕ_1 to ϕ_2 in clock angle, the photon rate in photons per sec for the photometer at (θ_0, ϕ_0) is

$$S = \frac{\sin\theta_0}{4\pi} \int_{\theta_1}^{\theta_2} d\theta \int_{\phi_1}^{\phi_2} d\phi\ 4\pi I(\theta, \phi)\, A(\theta, \phi - \phi_0). \tag{2}$$

Here, we have used the fact that $da = r^2 \sin\theta_0\, d\theta\, d\phi$. The apparent surface brightness of a source with uniform emission, in photons sec^{-1} cm^{-2}, can then be written as

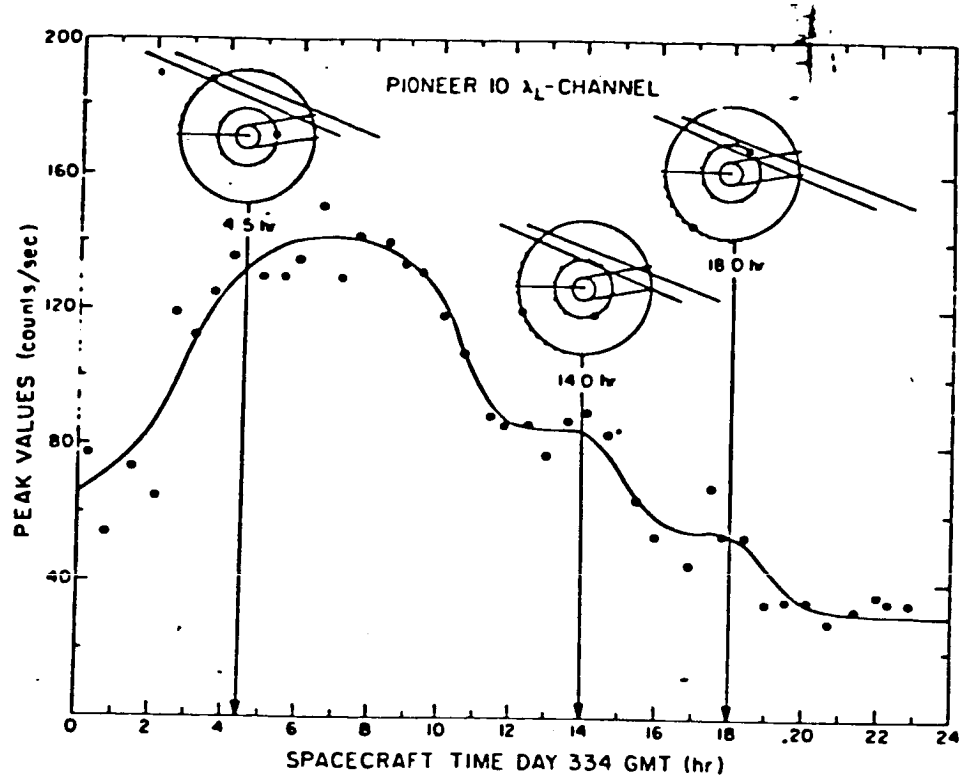

Fig. 6. Long-wavelength channel data for Day 334 was averaged over a period of 0.5 hr to obtain each point shown. The insets show the positions of Amalthea and Io for the times indicated. The structure at $14^h\ 00^m$ and $18^h\ 00^m$ is interpreted as emissions associated with Amalthea. The uncertainty in the data may be more than the point scatter would indicate.

$$4\pi I = S \Big/ \left[\frac{\sin\theta_0}{4\pi} \int_{\theta_1}^{\theta_2} A(\theta, 0) \times (\phi_2 - \phi_1)\, d\theta \right] \qquad (3)$$

Here we have neglected the variation of $A(\theta, \phi - \phi_0)$ in ϕ. This is justified since we know $\Delta\phi$ $(= \phi_2 - \phi_1)$ for the cases considered is always much smaller than the photometer resolution in clock angle ($\sim 25°$). For example, for a typical Pioneer 10 observation a source with a vertical dimension of 1 R_J (perpendicular to the orbital plane) will subtend only $\Delta\phi \sim 2°$ at Day 333 and $\Delta\phi \sim 2.5°$ at Day 334; thus, using $A(\theta, 0)$ rather than $A(\theta, \phi)$ will introduce little error for most sources. For an extended source centered in the field of view, with $\theta_2 - \theta_1$ larger than 1°, such as the Io cloud, the above formula can be further approximated by

$$4\pi I \approx 6.3 \times 10^4 \times S/\Delta\phi \text{ photons sec}^{-1}\text{ cm}^{-2}. \qquad (4)$$

Here, we have evaluated the integral in Eq. (3) and used $\theta_0 = 2\theta^p$; $\Delta\phi$ is ex-

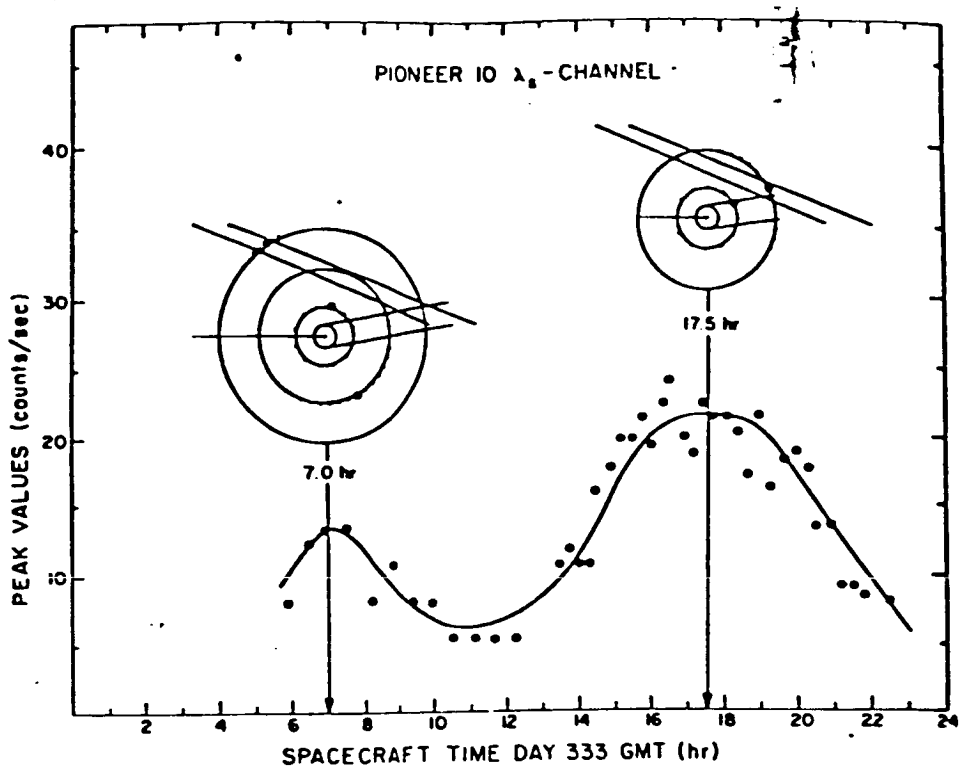

Fig. 7. Short-wavelength channel data for Day 333 was averaged over a period of 1 hr to obtain each point shown. The inset at $17^h\ 50^m$ shows the position of Amalthea and Io at that time. The inset at $7^h\ 00^m$ includes the position of Europa as well. The small peak at $7^h\ 00^m$ could be characteristic x-rays from Europa's disc, whereas the signal at $17^h\ 50^m$ is interpreted as due to radiative decay of excited atomic ions centered on Io.

pressed in degrees. (To obtain $4\pi I$ in Rayleighs, divide by 10^6.) For very small sources, such as the satellite discs, angular variations can be neglected altogether and the conversion of S to brightness becomes a function of area ratios:

$$4\pi I = \frac{4S}{1.66}\left(\frac{r}{R}\right)^2 \text{ photons sec}^{-1}\text{ cm}^{-2}. \tag{5}$$

Here R is the radius of the disc, and r is the distance from the spacecraft to the satellite.

Finally, we note that the photon flux S is related to the count rate C of the instrument by

$$S = C/\eta_\lambda \tag{6}$$

where η_λ is the spectral response of the photometer at wavelength λ. The

value of η_λ as a function of λ for both the long-wavelength and short-wavelength channels is shown in Fig. 1. In particular, the sensitivity of the short-wavelength channel at $\lambda = 584$ Å is 1/59 counts per photon and that of the long-wavelength channel at $\lambda = 1216$ Å is 1/88 counts per photon.

III. LONG-WAVELENGTH CHANNEL OBSERVATIONS OF IO

The long-wavelength channel data from Pioneer 10 (Fig. 6) have been discussed at length previously (Carlson and Judge 1974, 1975; Judge and Carlson 1974). These data have been interpreted as resonantly scattered Lyman-α from atomic hydrogen in orbit about Jupiter, Io being the "source" of the particles. The current extended analysis of the data confirms the earlier results and, in addition, suggests that temporal variations in the cloud density cannot be ruled out from the data. The viewing opportunities for Io and the measured peak count-rates are summarized in Table I.

The long-wavelength channel (λ_L) data as a function of time for Days 333 and 334, 1973, with the viewing geometry, are given in Figs. 5 and 6. The data were averaged for either 30 or 60 minutes, depending on data quality, throughout the observation period. Since the spacecraft was spinning with a period of about 12 seconds it was possible to extract signals buried in the high-energy particle background noise by utilizing *a priori* knowledge of the location of Io. For each spin, at the appropriate clock angle (rotation position), a feature is expected corresponding to emission from Io. Thus, by both temporal and spatial filtering, enhancement of the signal-to-noise ratio was achieved. Recognition of a true emission peak was based on both its width in clock angle (minimum FWHM of 25° for a point source), and its continued presence at the appropriate clock angle for a time at least as long as that during which the satellite itself occupied the field of view.

The data of Day 333 clearly show that emissions are detected at least 3 hours before Io enters the field of view, that the peak emission occurs at $19^h 00^m$, ~ 1.5 hr after Io is centered in the field of view, and that signals are present thereafter through the end of the day. The dip following the peak emission corresponds to a time when the trailing portion of the cloud being viewed is shadowed by Jupiter and from these data both the excitation mechanism (resonant scattering of solar Lyman-α) and the spatial extent of the cloud have been inferred (Carlson and Judge 1974). Because of the effect of Jupiter's shadow, neither the true peak counting rate nor the exact extent of the cloud asymmetry can be unequivocally determined from the data of Day 333. For the Day 334 viewing opportunity, however, the situation is not complicated by shadow effects and the peak counting rate of ~ 140 counts sec^{-1} occurs ~ 2.5 hr after Io is centered in the field of view and emissions attributable to Io continue for perhaps 12 hr thereafter. (The "lumps" at 14^h and 18^h are possibly due to Amalthea.) For an orbital rate of ~ 8°.5 per hour, the peak emission trails Io by ~ 20° and the total extent of the cloud is esti-

TABLE I

Viewing Opportunities of Io (J I) (Field of View Centered on J I)

GMT (Day/hr)	S/C-satellite distance (R_J)	Comments	λ_L-channel signal[a]		λ_S-channel signal[a]	
			Peak (counts/sec)	Comments[b]	Peak (counts/sec)	Comments[b]
Pioneer 10						
333/17.5	75	Part of Io cloud in Jupiter's shadow	65	–	20	–
334/4.5	61	–	130	–	< 20	limited by instrument resolution
335/7.0	56	Jupiter in the field of view; Io behind Jupiter	< 350	limited by instrument resolution	11	possible Jupiter emission
336/4.5	32	Jupiter starts to leave the field of view	172	part of the signal is due to Jupiter emission	< 70	limited by instrument resolution
336/21.0	28		No peak	extreme background variation	< 80	limited by instrument resolution
337/12.0	18		< 200	limited by instrument resolution	< 250	limited by instrument resolution

[a]The averaging time is 0.5 hr for the λ_L-channel and 1 hr for the λ_S-channel, except on Day 336, for which the λ_S-channel data were averaged for 0.5 hr.

[b]Resolution of the instrument = background/64.

mated to be ~ 120°. The peak counting rate of Day 333 is only about one half or less of that observed on Day 334 despite the fact that the distance from the spacecraft to Io changed only from ~ 75 to ~ 61 R_J. Even though the effect of the shadow cannot be accurately assessed without more information on cloud size and shape than can be inferred from present data, the relative counting rates for the two days cannot rule out changes in the cloud parameters of perhaps 20% over this time interval. These changes could be either true temporal variations, a coupling of the emissions to the orbital phase of Io, or coupling to the magnetic field of Jupiter.

IV. INTERPRETATION OF THE λ_L OBSERVATIONS OF IO

The emission data of the long-wavelength channel previously reported have been interpreted as coming from an atomic hydrogen cloud in orbit about Jupiter with the following characteristics (Carlson and Judge 1974, 1975):

column density	3×10^{12} cm^{-2}.
cloud angular extent	~ 1/3 of Io's orbit in the orbital plane.
cloud thickness	~ 1 R_J (assumed).
emission intensity	300 Rayleighs of Lyman-α.
total number of hydrogen atoms	~ 2×10^{33} atoms.
loss process	charge exchange with magnetospheric protons.
possible production processes	(1) proton flux neutralized at the surface or in a tenuous atmosphere (McDonough 1975). (2) photodissociation of atmospheric NH_3 (McElroy and Yung 1975). (3) sputtering of hydrogen-bearing compounds at the surface of Io. (4) electron impact dissociation of a hydrogen-bearing molecular atmosphere (Johnson, *et al.* 1976).
cloud temperature	~ 3000°K (may not be in thermal equilibrium).

The present improved data are in good agreement with the earlier results. However, the large signal, and the apparently increased asymmetry evident on Day 334 relative to Day 333 (possibly a shadow effect), suggest that the high temperature of the cloud, inferred from its asymmetry, may not be required in order to explain the data. If a sporadic source were invoked, a much lower average atmospheric temperature could be accommodated, in

agreement with the Pioneer 10 radio occultation data which suggest a temperature of 400°K (although one must hasten to note that the derived ionospheric temperatures are model dependent). Since it is known that the Jovian magnetosphere (at least the outer regions) is highly dynamic and that the magnetospheric particles interact strongly with Io, as well as with several other inner satellites, a time-dependent source, and hence atmosphere, would be consistent with other Pioneer observations. On the other hand, if the processes of the hydrogen and sodium atom source are related, the temporal constancy of the sodium cloud (Bergstralh *et al.* 1975) would suggest a constant hydrogen source.

The extent to which a current system of the type suggested by Shawhan *et al.* (1975) and Goldreich and Lynden-Bell (1969) connecting Jupiter and Io could account for either a variable or steady-state source of atmospheric particles is not yet clear. It should be noted, however, that the magnitude of any such current system is at least not always as great as suggested by the above authors. The Pioneer 11 spacecraft flew within 6000 km of the flux tube connecting Jupiter with Io. According to E. J. Smith (personal communication), the helium vector magnetometer did not observe a field change either in magnitude of direction during this time. Taking their quantization of 500 γ (high field value) as an upper limit to the field due to a current system of the Io flux tube, it is found that a current as low as 10^5 A would have produced a measurable perturbation. This maximum acceptable current is two orders of magnitude below the value of Shawhan *et al.*, and one order below that of Goldreich and Lynden-Bell.

V. SHORT-WAVELENGTH CHANNEL OBSERVATIONS OF IO

Obvious but unexpected signals were observed in the short-wavelength channel of the Pioneer 10 photometer on Day 333 beginning at $\sim 14^h\ 00^m$, when the field of view crossed into the orbit of Io but before Io itself entered the view. Prior to this time, the signal-to-noise ratio was less than one, the noise after filtering being about 10 counts sec^{-1} on Day 333. The signals reached a maximum of ~ 20 counts sec^{-1} as Io itself came into the field of view and continued, but with diminishing value, as Io left the field of view. At $\sim 23^h\ 00^m$ the signal count rate decreased to the noise level and no features were observed thereafter.

An example of the data as a function of clock angle is given in Fig. 8, and clearly indicates an emission feature at the 10° clock angle of Io. The extent of the emitting cloud is difficult to estimate. However, only ~ 2 hr are required for Io itself to cross the field of view while the emission feature persists for more than 6 hr (see Fig. 7). It is obvious that the short-wavelength channel emission signals extend beyond the solid surface of Io, and into a region at least 2 to 3 R_J distant from Io (approximately $\pm 20°$).

If one assumes that the vertical dimension of the cloud is 1 R_J, as was adopted for the hydrogen cloud, then the observed count rate of 20 counts

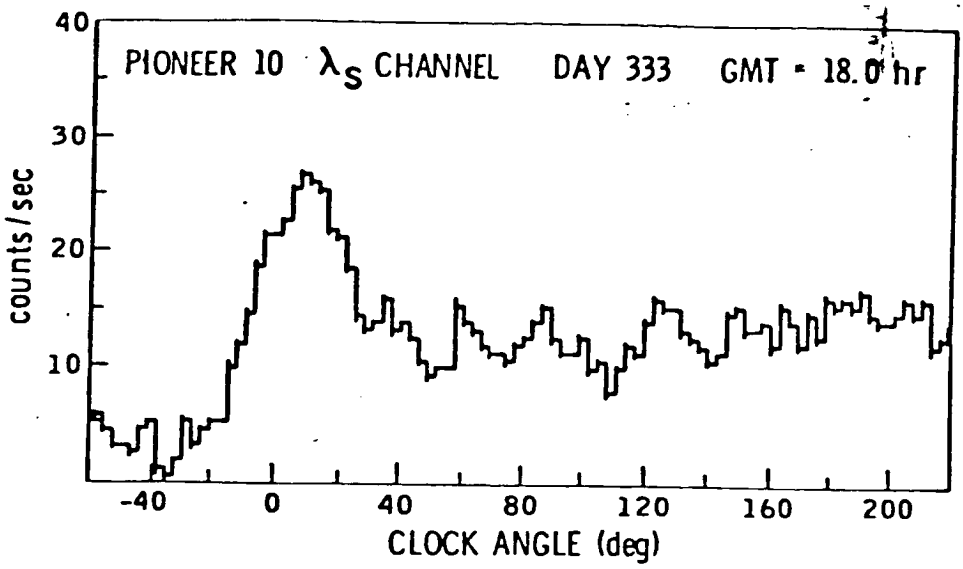

Fig. 8. The λ_S signal versus clock angle after averaging over a period of 1 hr. The feature at $\phi \sim 10°$ is interpreted as radiative decay of excited atomic ions in an extended region of space centered on Io.

sec^{-1} leads to a surface brightness of ~40 Rayleighs. On the other hand, if the emission feature comes mostly from a source the size of Io, a brightness of ~25 kiloRayleighs (kR) is required using the detection efficiency at 584Å.

In order to limit the possible sources of the emission we note that the short-wavelength channel is sensitive to radiation at wavelengths $\lesssim$ 800 Å. In the observation of Jupiter, there is no problem identifying the source of the emission feature in this channel since a consistent model of Jupiter's atmosphere would suggest only He as a significant scattering source in this wavelength range (Carlson and Judge 1974). However, both the constituents and excitation mechanisms appropriate to Io's atmosphere remain somewhat uncertain. Thus, positive identification of the short-wavelength emission is difficult to establish. In the following sections some possible sources for producing the emission features with $\lambda < 800$ Å at Io are discussed.

VI. INTERPRETATION OF THE λ_S OBSERVATIONS OF IO

A number of species are possible sources for the short-wavelength radiation. The most likely candidates are neutral helium, excited ions, bremsstrahlung and characteristic x-rays. Each is considered as a source of either extended emissions or restricted to the disc of Io, and is discussed below.

A. Extended Cloud Emission

Helium. The first extended short-wavelength emission to be considered is the possibility of helium resonance emission, since the He I resonance line (584 Å) is a prominent feature in the solar ultraviolet spectrum. This solar emission, incident on a helium atmosphere, will be resonantly scattered with an excitation rate (g-value)[2] at Io of 6×10^{-7} sec^{-1} atom^{-1}.

Helium atoms can of course also be excited by particle impact. The excitation rates for particle excitation, accurate to an order of magnitude, are summarized in Table II. The electron and proton fluxes and cross-section data from Carlson *et al.* (1975) are also listed in Table II. From this table we see that the particle impact excitation rates for producing excited helium are less than the excitation rate by resonance scattering. Thus, if it is assumed that resonance scattering dominates the observed emission at Io, the presently observed brightness of 40 R (assuming a source 1 R_J in vertical extent) requires a He column density of $4\pi I/g = 7 \times 10^{13}$ atoms/cm^{-2}. Since helium escapes so rapidly from Io, the production of a helium torus would be inevitable (if Io was a source of helium). We therefore rule out a localized atmosphere around Io (i.e., within a few scale heights) as the source of observed emissions. It would also be impossible for such an atmosphere to produce the observed intensity by resonance scattering, since even if the atmosphere were thick enough to scatter the entire solar line, an intensity of only ~ 250 R would be produced, which is to be compared with 25 kR if from the highly localized atmosphere.

Trafton (1976) has placed an upper limit to the density of metastable 2^3S helium atoms near Io of 4×10^8 cm^{-2}. The relative population of metastable and ground-state helium atoms can be related by examining the mechanisms for production and loss of triplet helium in the near Jupiter environment. The most efficient means of populating the triplet levels is electron excitation, and there does exist thermal plasma at the orbit of Io with sufficient energy (~ 100 eV) for excitation (Frank *et al.* 1976). In the absence of other destruction mechanisms, electron collisions would produce a population of excited He characteristic of the electron temperature. However, other processes can destroy metastable helium; these include photoionization, two-photon decay, and electron ionization. The destruction rates for these processes are respectively: $\sim 6 \times 10^{-5}$, $\sim 2 \times 10^{-5}$ (McElroy 1965), and $\sim 6 \times 10^{-6}$ sec^{-1} (estimated using Gryzinski's cross sections and the plasma measurements of Frank *et al.* 1976). The cross section for producing triplet helium atoms can be estimated from the experiments of St. John *et al.* (1964) and Jobe and St. John (1967). We find a total triplet excitation cross section at 100 eV of $\sim 1.5 \times 10^{-18}$ cm^2 which gives a production rate of 3×10^{-8} per second per He atom. The ratio of neutral to metastable atoms is then

[2] $g = F_\lambda \lambda^2 (\pi e^2/m_e c^2) f = (8.83 \times 10^{-13}$ cm$) \times (\pi F_\lambda) \lambda^2 f$. For He 584 Å, $\pi F_\lambda = 7.4 \times 10^8$ sec^{-1} cm^{-2} Å^{-1} at the orbit of Jupiter (Maloy *et al.* 1976) and $f = 0.28$.

TABLE II

The Helium Excitation Rate Produced by Particle Impact

Particle	Flux (sec^{-1} cm^{-2})	Cross Section (cm^2)	Excitation Rate ($atom^{-1}$ sec^{-1})	Reference for Cross Section
Electron	$\sim 10^{10}$	$\leq 10^{-16}$	$< 10^{-6}$	Altshular (1952)
Proton	$\sim 10^{9}$	$\leq 10^{-17}$	$< 10^{-8}$	Bell (1961)
H atom	$\sim 10^{7}$ [a]	$\leq 10^{-18}$	$< 10^{-11}$	Bates and Crothers (1967)

[a]High-energy H flux = column density of H/lifetime of low-energy H $\sim 10^{12}/10^{5} = 10^{7}$ sec^{-1} cm^{-2}.

$(6 \times 10^{-5} + 2 \times 10^{-5} + 6 \times 10^{-6})/3 \times 10^{-8} = 3 \times 10^{3}$. This results in an upper limit to helium atoms of $\sim 1.2 \times 10^{12}$ cm^{-2} based on Trafton's (1976) measurements, which argues that the emissions observed by Pioneer 10 are not due to helium.

Consideration of possible production and loss mechanisms for helium can also provide an estimate of the amount of helium in the Io cloud. For the earth, radioactive decay of uranium and thorium and their subsequent decay products provides the atmospheric helium. Such a source sufficient to supply the required column density at Io would be surprising indeed, unless Io is unusually enriched in radioactive elements, and is not considered here.

A second potential source of helium is the neutralization of magnetospheric alpha particles at Io. The total α-particle flux in the Jovian magnetosphere has not been determined to great precision, but order of magnitude limits on both the source flux and subsequent loss of helium atoms are discussed below.

Pioneer 10 data indicate that the ratio of the flux of α-particles to that of protons is a highly variable function of particle energy and distance from Jupiter. Trainor *et al.* (1974) find $6 \times 10^{-4} < J_\alpha/J_p < 6 \times 10^{-3}$ for 3–6 MeV per nucleon particles between 30 R_J and 90 R_J. Simpson *et al.* (1974) find values for the ratio at 1 MeV per nucleon as large as 2×10^{-2} for some distances in the 30–90 R_J range. Giving slightly more weight to the lower-energy data where fluxes are higher, a reasonable upper limit might be $J_\alpha/J_p \lesssim 10^{-3}$. With low-energy proton fluxes possibly as high as 10^{9} cm^{-2} sec^{-1} (Frank *et al.* 1976) at the orbit of Io, the estimated upper bound to the α-particle flux would be $J_\alpha \lesssim 10^{6}$ cm^{-2} sec^{-1}, although it must be recognized that the initial sources of the energetic magnetospheric particles and the thermal plasma could be quite different, exhibiting quite different particle abundances.

If the α-particles swept up by Io's disc are neutralized and leave the satellite as ground-state helium atoms via Jeans escape, their mean expansion

velocity $\langle v \rangle = \sqrt{2kT/3m_\alpha} \approx 0.46$ km sec^{-1}. To explain the observed orbital extent of $\pm\Delta\theta \lesssim 20°$ requires a lifetime $\tau_\alpha \lesssim 1/3R\Delta\theta \langle v \rangle_\alpha$ which is $\sim 1.1 \times 10^5$ sec (Carlson and Judge 1974) implying a total column density, in the extended cloud, of $n \sim (R_{Io}/R_J)^2 J_\alpha \tau_\alpha \sim 7.4 \times 10^7$ cm^{-2}. The observed signal, however, requires a column density of $n \sim 7 \times 10^{13}$ cm^{-2}, several orders of magnitude higher than that estimated from an optimistic interpretation of available particle flux data. In addition, to limit a possible helium cloud to within 20° of Io requires a highly efficient loss process. The most probable process is likely to be electron impact ionization which has a maximum cross section of $\sigma \lesssim 4 \times 10^{-17}$ cm^2 (Lotz 1967) peaked near 0.1 keV. This would require a low-energy electron flux $J_{el} \sim 1/\tau\sigma \gtrsim 2.3 \times 10^{11}$ cm^{-2} sec^{-1} at 0.1 keV, and is not consistent with the measured value which is estimated to be $< 10^{10}$ cm^{-2} sec^{-1}.

Therefore, in addition to Trafton's measurements, there are several theoretical reasons why atomic helium is probably not the source of the signal observed in the short-wavelength channel: (a) the most reasonable estimate of the integral alpha-particle flux at the orbit of Io is insufficient to explain the observed signal intensity, and (b) even if adequate amounts of helium were somehow produced by other mechanisms, there appears to be no loss process that is efficient enough to limit the extent of such a cloud to the observed 40°. Having shown that atomic helium is not a likely source of the observed emissions, we next consider atomic ions since substantial amounts of sodium are known to exist in the vicinity of Io (Trafton *et al.* 1974; Brown 1974).

Sodium and Other Atoms. Another potential source of the observed short-wavelength emission is the Na II resonance lines near 400 Å. These emissions can be produced by both particle ionization-excitation and resonant scattering of solar radiation by the ion. We consider first the loss mechanisms for Na atoms, which produce Na^+ ions in the extended atmosphere, in addition to the excitation processes leading to emission of the Na II resonance lines.

It has been estimated by Macy and Trafton (1975) that the sodium atoms are lost from the extended Io cloud at a rate of 6×10^{-6} sec^{-1}. It has been argued by Carlson *et al.* (1975) that the primary Na loss mechanism is through electron ionization with a rate of $\sim 5 \times 10^{-6}$ sec^{-1}, in good agreement with the observed sodium cloud geometry. However, the charge exchange of sodium with magnetospheric protons also contributes to the loss rate of sodium in the Io cloud. Charge transfer between H^+ and Na was not included by Macy and Trafton (1975) and Carlson *et al.* (1975) because of the large internal energy defect (8.5 eV) between the ground states of hydrogen and sodium, leading to a low cross section at energies of the thermal plasma. But, as pointed out by Grüebler *et al.* (1970), the energy defect between the first excited state ($n = 2$) of hydrogen and the ground state of Na is only about

1.7 eV, and the condition for near resonance is satisfied. Thus, the contribution of the $n = 2$ state of hydrogen may result in significant charge transfer between H^+ and Na. The cross section for this charge transfer is $\sim 10^{-14}$ cm^2 in the energy range from 1 to 10 keV (Grüebler *et al.* 1970). This is quite large compared to the cross section for electron ionization of sodium, $\sim 4 \times 10^{-16}$ cm^2, for energies from 10 to 100 eV.

To estimate the importance of this charge transfer process we note that the proton flux at Io's orbit in the 0.108–4.8 keV region can, according to Frank *et al.*, be represented by a thermal distribution with a temperature of ~ 100 eV, but with perhaps an additional high-energy tail, with a spectral index of ~ 1.3. The integral flux greater than 1 keV is then found to be $\sim 10^8$ cm^{-2} sec^{-1}, while the mean cross section for charge transfer in the 1–10 keV range is $\sim 7 \times 10^{-15}$ cm^2, and results in a sodium loss rate due to proton impact of $\sim 7 \times 10^{-7}$ sec^{-1}. The relative importance of this process clearly depends on the actual value of the proton flux adopted.

The Na loss process may occur through simultaneous ionization and excitation. The emission rate of Na II lines through such loss is considered below. The excited states of Na^+, such as $2p^5(^2P^0_{\frac{1}{2}})3s$ and $2p^5(^2P^0_{\frac{1}{2}})3d$ are about 30 to 40 eV above the $2p^6$ ground state. The wavelengths for the transitions from these excited states to the ground state are between 300 and 400 Å, and would thus be detected in the short-wavelength channel. For electrons, the cross section for the ionization excitation process is $\sim 2 \times 10^{-17}$ cm^2, with a maximum at $E = 200$ eV (Omidvar *et al.* 1972). For a flux density of 10^{10} electrons cm^{-2} sec^{-1}, the excitation rate is then 2×10^{-7} sec^{-1} per Na atom. Using an average Na column density of 10^{10}–10^{11} cm^{-2} in the vicinity of Io leads to an estimated emission rate of 0.002–0.02 R for the Na II lines. This intensity is over two orders of magnitude less than the observed emission. The cross section for ionization excitation of Na through H^+ impact has not been measured. However, this ionization excitation cross section can be estimated from the model of Gryzinski (1965) for charge transfer, giving a value $\sim 10^{-17}$ cm^2, with a maximum at 40 keV. Assuming the H^+ integral flux for energies greater than 10 keV to be 10^7 cm^{-2} sec^{-1}, an excitation rate of 10^{-10} sec^{-1} results, and is much smaller than that for electron ionization excitation.

Once created in an extended atmosphere, ground state Na II may be excited by electrons or protons, or may resonantly scatter incident solar radiation; these effects are shown below to be negligible.

The electron and proton excitation cross sections of Na^+ have not been measured. An upper limit to the electron excitation cross section is found by adopting the ionization cross section of Na II, $\sigma \sim 10^{-17}$ cm^2 at $E \sim 100$ eV (Lotz 1967). An electron flux on the order of 10^{10} cm^{-2} sec^{-1} then yields an excitation rate of $\sim 10^{-7}$ sec^{-1}, which is about the same order of magnitude as that for ionization excitation of sodium. Since the proton ionization cross section only becomes significant at about 1 MeV, the proton ionization exci-

tation rate will be on the order of 10^3 smaller than that for electron excitation ionization. The large difference in rates results from the fact that the proton and electron ionization cross section peaks occur at greatly different energies and hence fluxes. The ratio of electron to proton flux at their peak cross sections yields the factor of 10^3. If we assume proton ionization excitation to have the same efficiency as that for electrons, proton excitation will clearly be negligible.

Next we consider Na II resonance scattering at 372 Å and 300 Å. These lines have not been isolated in the solar spectrum; an upper limit to the flux might be placed at $\sim 10^7$ sec^{-1} cm^{-2} Å^{-1}. For $\lambda \sim 372$ Å, this implies a resonance scattering rate of $\sim 10^{-8}$ sec^{-1}, even smaller than that for electron excitation of Na^+. Unless the Na^+ density is significantly greater than neutral Na in the vicinity of Io, these relatively low excitation rates argue against particle and photon impact on Na^+ in producing the observed emissions. The limited spatial extent of the short-wavelength emissions strengthens this argument. Newly created ions will be swept up by the co-rotating Jovian magnetic field and form a cylindrically symmetric distribution since the rotation period is probably much less than the lifetime. Such a distribution was not observed in the emission profile.

The limited orbital extent of the emissions ($\pm 20°$) is consistent with the limited orbital extent of the observed neutral Na emissions (Brown and Yung;[3] Trafton *et al.* 1974), and the strongest emission mechanisms discussed above are associated with the observed neutral sodium cloud. However, it appears that radiation from sodium ions alone cannot account for Io's short-wavelength emission. There exists the possibility that other elements (e.g., K, Ne, N) are present with sodium in the Io cloud. These elements can also contribute to the observed short-wavelength emission through simultaneous ionization and excitation by energetic particles. For example, for atomic nitrogen the ionization cross section of the 2s shell ($\sim 10^{-16}$ cm^2 at $E \sim 100$ eV) by electron impact is comparable to the cross section for the 2p shell (Omidvar *et al.* 1972; Lotz 1967). Removal of the 2s electron leaves the ion in the excited 2s $2p^3$ $3S^0$ state, which then decays emitting 645 Å radiation. Using 10^{10} cm^{-2} sec^{-1} as the electron flux and 10^{-16} cm^2 as the cross section for excitation ionization leads to a reaction rate of 10^{-6} sec^{-1}. Thus a nitrogen abundance of 10^{13} atom cm^{-2} is required to account for the λ_S-channel intensity measurement of 10 Rayleighs.

B. Surface Emission

Although it is apparent that the λ_S-channel emissions appear to come from an extended region around Io, the total peak signal may contain a substantial contribution from the disc of Io itself. We consider below three

[3]See p. 1103.

processes: (a) emission from excited Na^+ produced at the surface of Io by sputtering, (b) characteristic x-rays produced by energetic particle bombardment of the elements in Io's surface layer, and (c) bremsstrahlung from high-energy particles impacting the surface. The third will be shown to be negligible, whereas the other two may contribute to the observed signal.

Surface Sputtering. The primary source of sodium atoms and ions in the cloud of Io is thought to be sodium-rich evaporite salts, such as sulfates (Fanale *et al.* 1974) on the surface of Io which release sodium through sputtering by magnetospheric particles (Matson *et al.* 1974).

Recently Nash *et al.* 1975 measured the sodium-D line emission produced by proton bombardment of silicate and halite rock samples. The sputtering yield (number of sputtered sodium atoms in the 3p state per proton) was found to be 10^{-3}. A total sputtering yield of 10^{-2} for proton bombardment (including all the ejected atoms and ions) has been reported by Carter and Colligon (1968). The ratio of neutral atoms (including all states of excitation) to ions in the sputtered ejecta is unknown. However, it has been observed that the majority of particles sputtered from alkali halides under ion bombardment are ions (Campbell and Cooper 1972; Batanou 1963), in contrast to metals where the sputtered particles are primarily neutral atoms. Thus, it seems reasonable to assume that the proton sputtering yield for ions might be as high as 10^{-2} and that some of the ions are in excited states.

Since the low-energy proton flux at Io is about 10^9 protons cm^{-2} sec^{-1}, under the assumptions discussed above, the production of excited sodium ions by proton sputtering will be less than but perhaps comparable to 10^7 ions cm^{-2} sec^{-1}. The flux of particles which produce sputtered atoms and ions could include heavier magnetospheric nuclei and re-impacting ions, in which case the emission rate could be greater. If the emission comes only from the decay of sputtered ions, the brightness of Io's disc would be 10 R. This estimate ignores secondary processes since it is noted that Na^+ ions which are sputtered from NaCl crystals have an energy of only 1–10 eV (Miyagawa 1973; Stuart *et al.* 1969). For the Na-D lines emission, however, Nash *et al.* (1975) observed that a 3.0 keV proton flux of density 1.7×10^{13} cm^{-2} sec^{-1} produced an intensity of 2.6×10^{10} photons cm^{-2} sec^{-1}, while a 5.0 keV flux of 2.8×10^{13} cm^{-2} sec^{-1} only increased the intensity to 3.5×10^{10} cm^{-2} sec^{-1}. If it is assumed that the emission efficiency (photons/proton) is dependent on the incident power density P according to a power law, $\epsilon \propto P^{\gamma}$ ($\gamma \sim 0.3$), then a 1 MeV proton flux of density 10^7 cm^{-2} sec^{-1} could produce a Na-D line emission of several kiloRayleights (Nash *et al.* 1975). If the same power law holds for the Na^+ emission lines, a brightness as large as 10 kR could result. Such an extrapolation to high energies and to Na^+ is a rather gross assumption, however, and the 10 kR value should be considered as an upper limit.

Characteristic X-Rays. A second possible source of short-wavelength radiation from the disc is the characteristic radiation. Here the energy loss by a bombarding particle is primarily through excitation of inner shell electrons of the surface atoms. The radiation which results when the atoms return to the unexcited state is the characteristic radiation or valence-band emission, depending upon the initial energy level of the electron involved in the radiation. The emission spectra of possible elements in Io's surface layer, such as Na, Mg and Al, are well known (Arakawa and Williams 1973; Rooke 1963; Hansen and Arakawa 1972). The wavelengths of the L-shell band emission are 200–400 Å, and are thus within the sensitivity range of our short-wavelength channel.

The cross section for inner shell ionization due to bombarding electrons has been derived by Gryzinski (1965) and is given by

$$\sigma_i = \frac{n\sigma_0}{U_i^2} g_i(E_e/U_i) . \tag{7}$$

Here $\sigma_0 = \pi e^4 = 6.56 \times 10^{-14}$ eV^2 cm^2, U_i is the ionization energy of inner shell electrons, n is the number of electrons in the shell, and E_e is the energy of the incident electron. The function $g_i(E_e/U_i)$ contains the energy dependence of the cross section and has a maximum value of about 0.2 for $E_e/U_i \sim 2$ to 10. For the 2p electrons of the sodium atom, $U_i = 50$ eV, and the L-shell ($n = 8$) ionization will be produced primarily by 0.1–1 keV electrons. The L-shell ionization cross section in this energy range is then 10^{-17} to 10^{-16} cm^2.

The relationship between the x-ray production cross section σ_x and the ionization cross section σ_i is $\sigma_x = \bar{\omega}\sigma_i$. Here $\bar{\omega}$ is the average radiation yield for the appropriate atomic shell (i.e., the fraction of the shell vacancies which are filled radiatively). For the L-shell of an atom with atomic number < 30, the value of $\bar{\omega}$ depends on the structure of the solid and is taken[4] to be between 10^{-2}–10^{-4}. Thus, the electron cross section for producing L-shell radiation is $\sigma_x \sim 10^{-21}$–10^{-18} cm^2.

The number of x-rays created by each incoming electron, per cubic centimeter, is

$$\begin{aligned} \phi &= \sigma_x(\text{cm}^2) \times \left(\frac{\text{number of atoms}}{\text{cm}^3}\right) \\ &= \sigma_x\left(\frac{N_0\rho}{A}\right) \end{aligned} \tag{8}$$

where N_0 is Avogadro's number, A is atomic mass and ρ is the density of the

[4] $\bar{\omega}$ for the L-shell of atoms with $Z < 26$ has not been measured or calculated. The quoted range of values adopted here was estimated from the existing values of $\bar{\omega}$ for other atoms. See, for example, Chen and Crasemann (1971).

material. Taking into account the self absorption of the x-rays as they escape from the material, the x-ray yield per electron is equal to

$$Y = \int_0^{R_0/\rho} \phi e^{-\mu\rho x} dx$$
$$= \frac{\phi}{\mu\rho}(1 - e^{-\mu R_0}) \tag{9}$$

where μ is the mass absorption coefficient for x-rays, and R_0 is the range of an incident electron in gm cm^{-2}. The photon absorption cross sections of simple molecules, in the 400 Å spectral region, are on the order of $\sigma \sim 10^{-17}$ cm^2 (see, for example, Lee *et al.* 1973). The mass absorption coefficient at these wavelengths for an atom with $A \sim 20$ gm/mole is then $\mu = (N_0/A)\sigma = 3 \times 10^5$ cm^2 gm^{-1}. For a range, R_0, on the order of 10^{-5} gm cm^{-2} (Katz and Penfold 1952) the term $\exp(-\mu R_0) \sim \exp(-3)$ is much less than 1. The yield of photons per electron can thus be simply written as

$$Y \sim \phi_x/\mu\rho$$
$$\sim \sigma_x/\sigma\,. \tag{10}$$

For σ_x between 10^{-21}–10^{-18} cm^2, the x-ray yield Y is 10^{-4} to 10^{-1} photons per electron.

Assuming a flux density of 10^{10} cm^{-2} sec^{-1} for low-energy electrons, the characteristic radiation intensity is 10^{-3}–10^0 kR, and thus would not contribute significantly to the signal of the λ_S channel. However, we note that the above estimate did not consider the presence of the "secondary" electrons inside the material, which can cause additional x-radiation. Lacking accurate cross section data, the possibility that characteristic emissions also contribute to the signals detected by the short-wavelength channel on Pioneer 10 cannot be ruled out.

No essential difference exists between the cross section for ionization by protons and by electrons, if they have the same velocity. Since the mass of a proton is a factor of 1836 that of an electron, L-shell ionization of sodium requires MeV protons. The available proton flux in this range is small, on the order of 10^7 cm^{-2} sec^{-1}, and the characteristic radiation due to proton excitation is thus expected to be much less significant than that due to electron excitation.

Bremsstrahlung. The third potential source of short-wavelength radiation from the disc, bremsstrahlung, is a continuous x-ray emission spectrum resulting from the inelastic collision of electrons with nuclei. The spectral distribution of bremsstrahlung for material with atomic number Z bombarded by an electron with energy E_i is

$$dI = 2KZ(E_i - E_\lambda)\, dE_\lambda \text{ for } 0 < E_\lambda < E_i \tag{11}$$

where I is the bremsstrahlung energy, E_λ is the photon energy and K is a constant. For $E_i < 2.5$ MeV, K is $(0.7 \pm 0.2) \times 10^{-3}$ MeV^{-1} (Evans 1955).

The bremsstrahlung spectrum extends over all energies from 0 to E_i. However, the detection range of the λ_S channel is limited, as we have noted, to radiation with $\lambda < 800$ Å ($E_\lambda \sim 1.5 \times 10^{-5}$ MeV). Moreover, for radiation with $\lambda < 1$ Å ($E_\lambda \sim 1.2 \times 10^{-3}$ MeV), there is no angular resolution in the ultraviolet photometer since the instrument collimator is transparent to such radiation; hence, no peak signal could be detected. Thus, the total detectable bremsstrahlung photon flux is

$$n = \phi(E_i) \int_{1.5 \times 10^{-5}}^{E_m} \frac{2KZ(E_i - E_\lambda)}{E_\lambda} \, dE_\lambda$$
$$= 2KZ\,\phi(E_i) \left[E_i \ln \frac{E_m}{1.5 \times 10^{-5}} + (E_m - 1.5 \times 10^{-5}) \right] \tag{12}$$

where $\phi(E_i)$ is the electron flux density at energy E_i and E_m is the smaller of E_i and 1.2×10^{-3} MeV; both E_i and E_m are expressed in MeV.

To estimate the bremsstrahlung contribution we calculate the signal to be expected from both keV and MeV electrons. We adopt an electron flux of 10^9 cm^{-2} sec^{-1} at 1 keV and 10^8 cm^{-2} sec^{-1} at 1 MeV. Using $Z \sim 10$ and $K = 0.7 \times 10^{-3}$ MeV^{-1}, the detectable bremsstrahlung flux from Io's disc is 4×10^4 photons cm^{-2} sec^{-1} for keV electrons and it is $\sim 9 \times 10^6$ photons cm^{-2} sec^{-1} for MeV electrons. These values are several orders of magnitude less than the intensity inferred from the λ_S-channel data. Thus, the bremsstrahlung radiation cannot contribute significantly to the signal observed in that channel. It should be noted that the above calculation does not include the effects of self-absorption; including this will further reduce the bremsstrahlung flux. While protons also give rise to bremsstrahlung, the production cross section is only $(1/1836)^2$ that of electrons and is accordingly insignificant.

Summarizing our interpretations of the Io short-wavelength emission, we note separate contributions from the area surrounding the satellite and from its surface. The most plausible interpretation of the data suggests that the observed emissions arise from (1) decay of excited Na^+ and other ions produced by particle impact ionization-excitation of the neutrals in the extended cloud, and (2) the decay of excited Na^+, produced by sputtering at the disc, as well as possible soft x-ray band emissions. The resolution of the photometer in both clock angle and wavelength does not allow a quantitative estimate of the various contributions to the total signal, but our data strongly suggest that the above mentioned mechanisms are those most likely to be consistent with the known properties of this most spectacular of the Galilean satellites.

VII. AMALTHEA

Little is known about Amalthea (J V), partially because of its small size, $R_{JV} \sim 120$ km (Rieke 1975), and because its low relative brightness (visual magnitude 13) and its closeness to Jupiter (2.2 R_J) make observation difficult. In the absence of accurate mass and radius data it is not possible to determine its density. However, the orbital characteristics would imply that J V belongs to the Galilean satellite group. Magnetospheric particle impact on Amalthea may be much more intense than that for the Galilean satellites, and one might expect to observe ultraviolet emissions due to such an interaction. The present ultraviolet observations of Amalthea represent the first such measurements and are therefore of considerable interest.

The viewing opportunity for Amalthea extended from approximately 12^h 00^m on Day 334 to 19^h 00^m of Day 336. During this period Amalthea entered the field of view 9 times. The observational results are summarized in Table III. Most of these data, however, are not useful either because the background count rate was too great or because Jupiter was also in the field of view. The experimental data are presented below followed by an interpretation of the measurements.

A. Long-Wavelength Channel Observations

The long-wavelength data shown in Fig. 6 indicate that a weak signal is present at the end of Day 334. The signal count rate is ~ 40 counts sec^{-1} and well above the noise level. The source of the signal has been assumed to be the cloud of hydrogen trailing Io (Carlson and Judge 1975). However, according to the viewing geometry, these signals could also be due to a hydrogen cloud of Amalthea. In support of this interpretation it may be noted in Fig. 6 that the signals are not monotonically decreasing with increasing orbital angle measured from Io, as expected if Io were the only source of the observed signal. An increasing signal is observed at 14^h 00^m of Day 334. This coincides with the fact that the extent of the field of view inside Amalthea's orbit increases significantly at this time. It is thus tentatively suggested that a portion of the apparent asymmetry of the observational data (with respect to Io's orbital position) is caused by emission from a hydrogen cloud at the orbit of Amalthea.

It should be noted, however, that at this time the spacecraft is less than 7 R_J below the orbital plane, while it is still far away from Jupiter (about 60 R_J). A sphere with a diameter of 1 R_J at Io's orbital position would subtend about 2°.5 in clock angle. On the other hand, two points in the orbital plane with a separation of Io's orbital radius (~ 6 R_J) also only subtend $\sim 2°$ in clock angle. Thus, for this geometry it is not possible to resolve (in clock angle) two sources with a separation of less than Io's orbital radius, and Amalthea's contribution to the total signal cannot be unambiguously isolated from that

TABLE III

Viewing Opportunities of Amalthea (J V) (Field of View Centered on J V)

GMT (Day/hr)	S/C-satellite distance (R_J)	Comments	λ_L-channel signal[a]		λ_S-channel signal[a]	
			Peak (counts/sec)	Comments[b]	Peak (counts/sec)	Comments[b]
Pioneer 10						
334/18.0	59	Amalthea only in view	50	possible emission from extended (100°) Io cloud	20	limited by background variation
334/19.0	57	Amalthea only in view	40	possible emission from extended (100°) Io cloud	< 20	limited by instrument resolution
335/4.5	54	Jupiter entering the field of view	< 250	limited by resolution of instrument	10	possible Jupiter emission
335/9.0	47	Jupiter in the field of view	< 250	limited by resolution of instrument	13	partly due to Jupiter emission
335/15.5	48	J V signal blocked by Jupiter	< 100	limited by background variation	< 20	limited by instrument resolution
335/22.0	39	Jupiter in the field of view	183	primarily Jupiter emission	< 60	limited by instrument resolution
336/2.5	41	Jupiter in the field of view	172	primarily Jupiter emission	< 100	limited by instrument resolution
336/11.0	31	possible contribution from trailing Io cloud	No peak	extreme background variation	< 90	limited by background variation
336/13.0	32	possible contribution from trailing Io cloud	No peak	extreme background variation	< 90	limited by background variation

[a]The averaging time is 0.5 hr for the λ_L-channel and 1 hr for the λ_S-channel, except on Day 336, for which the λ_S-channel data were averaged for 0.5 hr.

[b]Resolution of the instrument = background/64.

of the distant tail of Io's cloud. The viewing geometry in the orbital plane is given in Fig. 6.

It is difficult to establish the extent of an Amalthea cloud from the present data. However, it can be estimated from the expression (Carlson and Judge 1974)

$$\Delta\theta \simeq 3 \langle v \rangle \tau / R_A . \tag{13}$$

Here $\Delta\theta$ is the angular extent of the cloud measured with respect to Amalthea. $\langle v \rangle$ and τ are the mean velocity and mean life-time of the atoms, respectively. R_A is the orbital radius of Amalthea. With a 100 eV proton flux of 2×10^9 cm^{-2} sec^{-1} at Amalthea's orbit (Frank *et al.* 1976) and assuming that the H atoms are lost through proton charge exchange with a cross section of $\simeq 4 \times 10^{-15}$ cm^2, τ is $\simeq 1 \times 10^5$ sec. The temperature of Amalthea is 150°K (Rieke 1975) and the corresponding Jeans mean expansion velocity is $\langle v \rangle \sim 0.9$ km sec^{-1}. Hence, we get $\Delta\theta \sim 1.9$ radian.

The total angular extent of the cloud is thus $\simeq 3.8$ rad (218°). Accordingly, the Amalthea cloud is probably not a complete torus. Using 40 counts sec^{-1} as the optical emission from the Amalthea cloud and assuming the vertical dimension of the cloud to be 1 R_J (as for Io), the surface brightness would be about 100 Rayleighs, for a Lyman-α source.

During the viewing opportunity on Day 335, the background count rate was quite high, and no emission feature was evident. Later during the day and early the next day, signals were present, but these were mostly due to Jupiter. After $11^h\ 00^m$ of Day 336, because of background noise, no useful data were obtained.

B. *Short-Wavelength Channel Observations*

A signal with a count rate of about 20 counts sec^{-1} appeared on Day 334 at $18^h\ 00^m$ as Amalthea first entered the field of view. However, the signals were spread over a clock angle of 80° and only persisted for ~ 1 hr. Since the signal was present for such a short time and was spread over such a large angular extent, it is difficult to account for the observations in terms of optical emissions; most likely they must be attributed to interference from a unidirectional high-energy particle flux. For such a case, assuming a 25° optical emission[5] superimposed on the wide background signal, the optical emission is estimated to be less than ~ 10 counts sec^{-1}. For the viewing opportunities of Day 335 and later, the short-wavelength channel data are either very noisy or contaminated by emission contributions from Jupiter. Assuming 10 counts sec^{-1} to be the maximum optical emission from Amalthea's disc, its maximum brightness near 400 Å is estimated at 2500 kR.

[5]An optical emission from a point source will extend over ~ 25° in clock angle.

VIII. EUROPA

The density of Europa is nearly the same as that of Io (~ 3 gm cm^{-3}). Unlike Io, its spectral reflectance clearly indicates that H_2O covers most of the satellite's surface, which Fanale *et al.* (1974) suggest is composed mainly of hydrated salt and ice. The lack of evidence for sodium in the visual observational data may simply indicate that either there is less sodium available at the surface to be sputtered or that the presence of H_2O at the surface makes the sputtering process less efficient. The possibility of meteoritic material supplying the sodium seems unlikely, although it cannot be ruled out. Ganymede apparently has more meteoroid impacts than Europa, yet there is no direct observational evidence in either the ultraviolet or visible spectral region for sodium as a surface or atmospheric constituent on that satellite (Morrison and Cruikshank 1974).

Europa, like Io, apparently interacts strongly with the magnetospheric particles. This is evident from the sweeping of high-energy particles at Europa's orbit, as at the orbits of Amalthea and Io.

A. Short-Wavelength Channel Observations of Europa

Referring to Fig. 8, the data show a clear emission signal of ~ 13 counts sec^{-1} peaked at $7^h\ 00^m$ hours of Day 333. At this time Io is almost directly on the other side of Jupiter from Europa and is not likely to contribute to the observed signal. Emissions are present for about 2 hours, which is the time required for the satellite to pass through the field of view. Assuming a source of Europa's size ($R = 1550$ km), the apparent brightness is about 14 kilo-Rayleighs (at $\lambda \sim 400$ Å). Other Europa viewing opportunities are either contaminated by signals from other objects in the field of view or limited by noise, permitting only upper limits to be determined, as given in Table IV.

B. Interpretation of Europa's Short-Wavelength Channel Observations

The proton density in the vicinity of Europa is 10 cm^{-3} with energy 400 eV (Frank *et al.* 1976) and the proton flux is $\sim 3 \times 10^8$ cm^{-2} sec^{-1}.

Proton bombardment of Europa's surface would be expected to sputter surface atoms into the surrounding space and thereby create an atmosphere. Since there is no evidence for an atmosphere or ionosphere at Europa, the sputtering process at the surface may be insignificant, perhaps due to the water frost thought to be covering much of the surface.

Europa's surface is also bombarded by an intense electron flux. This bombardment will cause characteristic x-ray radiation from the surface elements. The possible elements in Europa's surface, such as Na, Mg, K, and Ca have valence band x-ray emissions with wavelengths between 200 and 700 Å, and within the sensitivity of the short-wavelength channel. Assuming a surface composition and electron flux similar to that at Io and using the same rather uncertain cross section data, a perhaps conservative estimate of

the x-ray contribution to the observed brightness of Europa is $\lesssim 1$ kR. Further consideration of this and other processes is required to establish the origin of the observed short-wavelength emissions.

IX. GANYMEDE

The mean density of Ganymede is about 2 gm cm^{-3} and it probably has a small rocky core and a liquid mantle covered with ices of water, ammonia and methane. The surface is apparently reasonably uniform as observed in eclipse radiometry, although large-scale variations in its albedo are evident. The infrared spectrum implies water ice at the surface, an observation consistent with the other available optical data.

It has also been suggested through stellar occultation measurements that Ganymede possesses a tenuous atmosphere (Carlson *et al.* 1973). The constituents have not been determined nor has the stability of such an atmosphere. An atmosphere with surface pressure greater than 10^{-3} mb was observed during the above stellar occultation. Since no infrared emission features associated with the atmosphere have been observed, it is perhaps composed of constituents such as N_2, O_2, Ne, or A, which have no dipole moment.

Particle impact at Ganymede is less significant than at the orbits of the inner satellites. This is perhaps important in explaining the Pioneer 10 and 11 data which indicate that no ultraviolet emissions are associated with Ganymede. Table V contains a summary of our findings and, using the Pioneer 11 data from Day 335, the upper limits of apparent brightness for the disc are estimated to be ~ 4 kR for $\lambda \sim 1200$ Å and ~ 2 kR for $\lambda \sim 400$ Å.

X. CALLISTO

The photometric observations of Callisto indicate that its surface may consist of high reflectance silicates. Callisto's low density of 1.4 gm cm^{-3} would be caused by a relatively minor amount of heavy elements, implying little radioactive heating; because Callisto was formed at a relatively large distance from Jupiter, tidal heating may also be small. Further, there is no strong evidence for water ice at the surface as inferred from infrared observations.

The charged particle flux at Callisto is greatly reduced from that at the inner satellites, and is probably not important in determining the production and/or loss of an atmosphere.

No ultraviolet emission signals were observed from Callisto. Using the Pioneer 11 data at Day 335 given in Table VI, the upper limit of apparent brightness for Callisto's disc is estimated to be 9 kR for $\lambda \sim 1200$ Å and 7 kR for $\lambda \sim 400$ Å.

TABLE IV

Viewing Opportunities of Europa (J II) (Field of View Centered on J II)

GMT (Day/hr)	S/C-satellite distance (R_J)	Comments	λ_L-channel signal[a]		λ_S-channel signal[a]	
			Peak (counts/sec)	Comments[b]	Peak (counts/sec)	Comments[b]
Pioneer 10						
332/9.5	85	–	< 230	limited by instrument resolution	< 11	limited by instrument resolution
333/7.0	70	angular separation between J II and J I is 130°	< 40	limited by instrument resolution	13	–
335/11.0	57	Jupiter in the field, Europa at the back of Jupiter	< 300	limited by instrument resolution	12	Jupiter emission contribution
337/8.0	9	–	< 150	limited by instrument resolution	< 250	limited by instrument resolution
Pioneer 11						
336/23.0	12	–		No data due to high charged particle and/or radiation background	< 150	limited by instrument resolution
337/1.0	10	–		No data due to high charged particle and/or radiation background	< 150	limited by instrument resolution

[a]The averaging time is 0.5 hr for the λ_L-channel and 1 hr for the λ_S-channel.

[b]Resolution of the instrument = background/64.

TABLE V

Viewing Opportunities of Ganymede (J III) (Field of View Centered on J III)

GMT (Day/hr)	S/C-satellite distance (R_J)	Comments	λ_L-channel signal[a]		λ_S-channel signal[a]	
			Peak (counts/sec)	Comments[b]	Peak (counts/sec)	Comments[b]
Pioneer 10					< 20	limited by instrument resolution
334/6.0	77	View is within 10° of Io	120	probably all due to Io cloud emission	< 30	limited by instrument resolution
336/17.0	22	–	No peak	extreme background variation		
Pioneer 11					< 10	limited by background variation
335/12.5	42	–	< 45	limited by instrument resolution	< 60	limited by instrument resolution
336/9.0	20	–	< 64	limited by instrument resolution		

[a]The averaging time is 0.5 hr for the λ_L-channel and 1 hr for the λ_S-channel, except on Pioneer 10 Day 336, for which the λ_S-channel data were averaged for 0.5 hr.

[b]Resolution of the instrument = background/64.

TABLE VI

Viewing Opportunities of Callisto (J IV) (Field of View Centered on J IV)

GMT (Day/hr)	S/C-satellite distance (R_J)	Comments	λ_L-channel signal[a]		λ_S-channel signal[a]	
			Peak (counts/sec)	Comments[b]	Peak (counts/sec)	Comments[b]
Pioneer 10						
333/21.0	44	Io cloud in the field of view	60	Io cloud emission contribution	10	Io cloud emission contribution
Pioneer 11						
331/19.0	107	–	< 90	limited by background variation	< 90	limited by background variation
335/6.0	28	–	< 60	limited by instrument resolution	< 80	limited by instrument resolution

[a]The averaging time is 0.5 hr for the λ_L-channel and 1 hr for the λ_S-channel.

[b]Resolution of the instrument = background/64.

XI. SUMMARY

The ultraviolet photometers on Pioneers 10 and 11 have established the three innermost of five Jovian satellites as sources of optical emissions with $\lambda < 1400$ Å. Amalthea's apparent hydrogen cloud and possible but uncertain short-wavelength emissions are the least well established of the present results, and further observations are highly desirable. Io is most certainly accompanied by a cloud of atomic hydrogen that resonantly scatters the solar Lyman-α at 1216 Å. It is also a source of shorter wavelength emissions, $\lambda < 800$ Å, that could result from the radiative decay of excited Na^+ and other atomic ions in its near environment. Soft x-ray band emissions of elements in Io's surface layer and radiative decay of sputtered ions from Io's surface also contribute to the detected short-wavelength signals. Additional laboratory data are required to establish whether or not these sources are significant, however. Signals in this lower wavelength range are detected from the surface of Europa as well. Although the origin of Europa's emissions remain somewhat uncertain, their existence underscores the common characteristic shared by all three of the inner satellites: the observed emissions and clouds are associated with a significant sweeping up of energetic particles in the Jovian magnetosphere.

Acknowledgement. This work was supported by Contract NAS2-6558 with the NASA Ames Research Center.

REFERENCES

Altshular, S. 1952. Excitation cross section for helium atoms. *Phys. Rev.* 87:992–994.

Arakawa, E. T., and Williams, M. W. 1973. Satellites in the x-ray emission spectra of Li, Be, and Na. *Phys. Rev.* 138:4075–4078.

Batanou, G. M. 1963. Emission of charged particles from alkali halide crystals bombarded with potassium ions. *Soviet Phys.-Solid State* 4:1306–1312.

Bates, D. R., and Crothers, D. S. F. 1967. Inelastic collisions between hydrogen and helium atoms. *Proc. Phys. Soc.* 90:73–80.

Bell, R. J. 1961. Excitation of helium to the $(1s, 2p)^1P$ and $(1s, 3p)^1P$ states by proton and alpha particle impact. *Proc. Phys. Soc.* (London) 78:903–911.

Bergstralh, J. T.; Matson, D. L.; and Johnson, T. V. 1975. Sodium D-line emission from Io: synoptic observations from Table Mountain Observatory. *Astrophys. J.* 195:L131–L135.

Brown, R. A. 1974. Optical line emission from Io. *Exploration of the planetary system.* (A. Woszczyk and C. Iwaniszewska, eds.) pp. 527–531. Dordrecht-Holland: D. Reidel Publ. Co.

Campbell, III, A. B., and Cooper, C. B. 1972. Mass spectrometric study of sputtering of KB by low-energy Ar^+ and Xe^+ ions. *J. Appl. Phys.* 43:863–866.

Carlson, R. W. 1975. Atmospheres of outer planet satellites. *A.I.A.A. Progress in astronautics and aeronautics.* (E. Greenstaed, D. Intriligator and M. Dryer, eds.) Cambridge, Mass.: Massachusetts Institute of Technology Press. In press.

Carlson, R. W.; Bhattacharyya, J. C.; Smith, B. A.; Johnson, T. V.; Hidayat, B.; Smith, S. A.; Taylor, G. E.; O'Leary, B. T.; and Brinkmann, R. T. 1973. An atmosphere on Ganymede from its occultation of SAO 186800 on 7 June 1972. *Science* 182:53–55.

Carlson, R. W., and Judge, D. L. 1974. Pioneer 10 ultraviolet photometer observations at Jupiter encounter. *J. Geophys. Res.* 79:3623–3633.

———. 1975. Pioneer 10 ultraviolet photometer observations of the Jovian hydrogen torus: the angular distribution. *Icarus* 24:395–399.

Carlson, R. W.; Matson, D. L.; and Johnson, T. V. 1975. Electron impact ionization of Io's sodium emission cloud. *J. Geophys. Res. Lett.* 2:469.

Carter, G., and Colligon, J. S. 1968. *Ion bombardment of solids.* New York: American Elsevier.

Chen, M. H., and Crasemann, B. 1971. Theoretical L_2- and L_3-subshell fluorescence yields and L_2-L_3 X Coster-Kronig transition probabilities. *Phys. Rev.* A4, 1–7.

Evans, R. D. 1955. *The atomic nucleus.* New York: McGraw-Hill.

Fanale, F. P.; Johnson, T. V.; and Matson, D. C. 1974. Io: a surface evaporite deposit? *Science* 186:922–924.

Frank, L. A.; Ackerson, K. L.; Wolfe, J. H.; and Mihalov, J. D. 1976. Observations of plasma in the Jovian magnetosphere. *J. Geophys. Res.* 81:457–468.

Goldreich, P., and Lynden-Bell, D. 1969. Io, a Jovian unipolar inductor. *Astrophys. J.* 156: 59–78.

Grüebler, W.; Schmelzbach, P. A.; König, V.; and Marmier, P. 1970. Charge exchange collisions between hydrogen ions and alkali vapour in the energy range of 1 to 20 keV. *Helv. Phys. Acta* 43:254–271.

Gryzinski, M. 1965. Classical theory of atomic collisions. I. Theory of inelastic collisions. *Phys. Rev.* 138:A336–358.

Hansen, W. F., and Arakawa, E. T. 1972. High energy x-ray satellites of $L_{2,3}$ emission bands of Na, Mg, Al, and Si. *Z. Physik* 251:271–288.

Jobe, J. D., and St. John, R. M. 1967. Absolute measurements of the 2^1P and 2^3P electron excitation cross sections of helium atoms. *Phys. Rev.* 164:117–121.

Johnson, T. V.; Matson, D. L.; and Carlson, R. W. 1976. The atmosphere of Io: new limits based on magnetospheric plasma models. *Geophys. Res. Lett.* In preparation.

Judge, D. L., and Carlson, R. W. 1974. Pioneer 10 observations of the ultraviolet glow in the vicinity of Jupiter. *Science* 183:317–318.

Katz, L., and Penfold, S. 1952. Range-energy relations of electrons and the determination of beta-ray end point energies by absorption. *Rev. Mod. Phys.* 24:28–44.

Lee, L. C.; Carlson, R. W.; Judge, D. L.; and Ogawa, M. 1973. The absorption cross sections of N_2, O_2, CO, NO, CO_2, N_2O, CH_4, C_2H_4, C_2H_6 and C_4H_{10} from 180–700 Å. *J. Quant. Spectrosc. Radiat. Transfer* 13:1023–1031.

Lotz, W. 1967. Electron-impact ionization cross sections and ionization rate coefficients for atoms and ions. *Astrophys. J. Suppl.* 14:207–268.

Macy, W., and Trafton, L. 1975. A model for Io's atmosphere and sodium cloud. *Astrophys. J.* 200:510–519.

Maloy, J. O.; Carlson, R. W.; Hartmann, U. G.; and Judge, D. L. 1976. Rocket measurements of the profile and intensity of the solar He I λ584 Å resonance line. *J. Geophys. Res.* In preparation.

Matson, D. L.; Johnson, T. V.; and Fanale, F. P. 1974. Sodium D-line emission from Io: sputtering and resonant scattering hypothesis. *Astrophys. J.* 192:L43–L46.

McDonough, T. R. 1975. A theory of the Jovian hydrogen torus. *Icarus* 24:400–406.

McElroy, M. B. 1965. Excitation of atmospheric helium. *Planet. Space Sci.* 13:403–433.

McElroy, M. B., and Yung, Y. L. 1975. The atmosphere and ionosphere of Io. *Astrophys. J.* 196:227–250.

Miyagawa, S. 1973. Energy spectrum of Na^+ ions sputtered from NaCl. *J. Appl. Phys.* 44: 5617–5618.

Morrison, D., and Cruikshank, D. P. 1974. Physical properties of the natural satellites. *Space Sci. Rev.* 15:641–739.

Nash, D. B.; Matson, D. L.; Johnson, T. V.; and Fanale, F. P. 1975. Production of Na-D line emission from rock specimens by proton bombardment: implications for Io emissions. *J. Geophys. Res.* 80:1875–1879.

Newburn, R. L., and Gulkis, S. 1973. A survey of the outer planets, Jupiter, Saturn, Uranus, Neptune, and Pluto, and their satellites. *Space Sci. Rev.* 14:179–271.

Omidvar, K.; Kyle, H. L.; and Sullivan, E. C. 1972. Ionization of multielectron atoms by fast charged particles. *Phys. Rev.* A5:1174–1187.

Rieke, G. H. 1975. The temperature of Amalthea. *Icarus* 25:333–334.

Rooke, G. A. 1963. Plasmon satellites of soft x-ray emission spectra. *Phys. Letters* 3:234–236.

Shawhan, S. D.; Goertz, C. K.; Hubbard, R. F.; Gurnett, D. A.; and Joyce, G. 1975. Io-accelerated electrons and ions. *The magnetospheres of Earth and Jupiter.* (V. Formisano, ed.) pp. 375–389. Dordrecht-Holland: D. Reidel Publ. Co.

Simpson, J. A.; Hamilton, D. C.; McKibben, R. B.; Mogro-Campero, A.; Pyle, K. R.; and Tuzzolino, A. J. 1974. The protons and electrons trapped in the Jovian dipole magnetic field region and their interaction with Io. *J. Geophys. Res.* 79:3522–3544.

St. John, R. M.; Frank, L. M.; and Lin, C. C. 1964. Absolute electron excitation cross section of helium. *Phys. Rev.* 134:A888–A897.

Stuart, R. V.; Wehner, G. K.; and Anderson, G. S. 1969. Energy distribution of atoms sputtered from polycrystalline metals. *J. Appl. Phys.* 40:803–812.

Trafton, L. 1976. A search for emission features in Io's extended cloud. *Icarus* (special Jupiter issue). In press.

Trafton, L.; Parkinson, T.; and Macy, W. 1974. The spatial extent of sodium emission around Io. *Astrophys. J.* 190:L85–L89.

Trainor, J. H.; McDonald, F. B.; Teegarden, B. J.; Webber, W. R.; and Roelof, E. C. 1974. Energetic particles in the Jovian magnetosphere. *J. Geophys. Res.* 79:3600–3613.

Io's Atmosphere and Ionosphere: New Limits on Surface Pressure from Plasma Models.

T. V. Johnson, D. L. Matson, R. W. Carlson

Abstract presented at the Division for Planetary Sciences (AAS) Meeting, Austin, Texas April, 1976

We have studied charge particle impact as a mechanism for the production of Io's ionosphere. Pioneer 10 thermal plasma measurements and magnetospheric plasma models which explain the observed spatial distribution of neutral hydrogen and sodium atoms in the vicinity of Jupiter's satellite Io imply electron fluxes of $\sim 10^{10}$ cm^{-2} sec^{-1}. The fluxes and the temperature ($\sim$100 eV) of this plasma suggest that electron impact ionization is the dominant process in forming the ionosphere of Io. It is found that the surface number density of the neutral species required to match the observed electron density profiles is $\sim 10^{9}$ cm^{-3} or less. This value is two orders of magnitude lower than previous estimates.

This paper presents the results of one phase of research carried out at the Jet Propulsion Laboratory, California Institute of Technology, under Contract Number NAS 7-100, sponsored by the National Aeronautics and Space Administration.

IO'S ATMOSPHERE AND IONOSPHERE: NEW LIMITS ON SURFACE PRESSURE FROM PLASMA MODELS

T. V. Johnson and D. L. Matson

Jet Propulsion Laboratory, California Institute of Technology, Pasadena, California 91103

R. W. Carlson

Department of Physics, University of Southern California, Los Angeles, California 90007

Abstract

We have studied charge particle impact as a mechanism for the production of Io's ionosphere. Pioneer 10 thermal plasma measurements and magnetospheric plasma models which explain the observed spatial distribution of neutral hydrogen and sodium atoms in the vicinity of Jupiter's satellite Io imply electron fluxes of $\sim 10^{10}$ cm^{-2} sec^{-1}. The fluxes and the temperature ($\sim$100 eV) of this plasma suggest that electron impact ionization is the dominant process in forming the ionosphere of Io. It is found that the surface number density of the neutral species required to match the observed electron density profiles is $\sim 10^9$ cm^{-3} or less. This value is two orders of magnitude lower than previous estimates.

Introduction

Recently, the satellite Io (J1) has been the object of intensive observational and theoretical studies. Large "clouds" of neutral atomic species have been observed, not only associated with Io but also extending to great distances and removed from the gravitational influence of the satellite. These include sodium (Brown, 1974; Trafton et al., 1974), hydrogen (Carlson and Judge, 1974) and potassium (Münch, 1975; and Trafton, 1975). An overview of this field is given by Brown and Yung (1976) who review recent Io observations and some current interpretations of the data.

The question of whether or not Io also possesses a significant, gravitationally bound atmosphere has been of great interest in studying Io-related phenomena. In addition to the intrinsic interest that such an atmosphere would have for theories of origin and evolution of volatiles, even a very tenuous atmosphere of $\sim 10^{-10}$ bars (or number density $\sim 10^{10}$ cm^{-3}) would be sufficient to thermalize material released from the surface by charged particle sputtering while an atmosphere of less than $\sim 10^{-11}$ bars (or $\sim 10^9$ cm^{-3}) would allow virtually free trajectories from the surface (Matson et al., 1974). In addition, an atmosphere can act both as a shield against low energy proton bombardment (e.g. McElroy and Yung, 1975) and as a source of ions (Matson et al., 1974).

The possibility of an atmosphere on Io was suggested over a decade ago by Binder and Cruikshank (1964) as a result of post-eclipse brightening observations. A stellar occultation by Io in 1971 established an upper limit to the atmosphere of approximately 10^{-7} bars (Smith and Smith, 1972). The radio occultation experiment using the Pioneer 10 spacecraft showed that Io had a well-developed ionosphere with peak electron densities of $\sim 6 \times 10^4$ cm^{-3}, similar to the ionospheres of Mars and Venus (Kliore et al., 1974, 1975).

Copyright 1976 by the American Geophysical Union.

Relating the observed electron density profiles to a neutral atmosphere has been the subject of recent work. McElroy and Yung (1975) have presented detailed analyses of various ionospheric models while other ionospheric models have been considered by Whitten et al. (1975). The purpose of this paper is to examine the consequences of applying recent information concerning the magnetospheric plasma fluxes to McElroy and Yung's model which involves charged particle ionization processes. The result is that a neutral number density of $\sim 10^9$ cm^{-3} at the surface is an upper limit for any molecular or atomic atmosphere under these conditions.

Plasma Models

Information concerning the characteristics of the thermal magnetospheric plasma in the vicinity of Io comes from three sources: 1) observations of the atomic hydrogen cloud, 2) in situ measurements made by Pioneer 10 instruments, and 3) observations of the sodium cloud. Briefly, the limited extent of the hydrogen cloud requires an ionization process much more efficient than photoionization, the most likely process being charge-exchange ionization by plasma protons. To achieve the required ionization rates, proton fluxes of $\sim 10^9$ cm^{-2} sec^{-1} are needed, which corresponds to densities of a few tens to hundreds of particles cm^{-3}, depending on the effective plasma temperature (Carlson and Judge, 1974; see also McDonough, 1975 and McElroy and Yung, 1975).

Pioneer 10 in situ measurements have also been used to determine the characteristics of the magnetospheric plasma. Frank et al. (1976) used the plasma analyzer data to infer the presence of a thermal plasma of about 100 eV temperature and about 30 cm^{-3} density. Sentman et al. (1976) find that similar plasma densities are required to explain electron pitch angle scattering by whistler mode instabilities suggested by data from the University of Iowa energetic particle detectors (Van Allen et al., 1975). The observations of very low sodium D-line emission intensities at positions near 180° from Io in its orbit (Macy and Trafton, 1975, Wehinger et al., 1976, Mekler and Eviatar, 1974) also require ionization processes at least one order of magnitude more efficient than photoionization (Trafton and Macy, 1975a). Carlson et al. (1975) have shown that electron impact ionization of sodium can produce the required ionization rates for plasma models which are consistent with both the hydrogen observations and the Pioneer 10 data. Trafton and Macy (1975b) suggest that similar particle fluxes are needed to account for yet another independent effect: a reported asymmetry in the sodium emission distribution near Io.

In addition to the above evidence, Brown (1976) has suggested the presence of a dense, cool plasma ($\rho \sim 10^3$ cm^{-3}, $T \sim 2$eV) to explain the observations of the forbidden lines of singly ionized sulphur reported by Kupo et al. (1976). This plasma is cooler and more dense than that inferred by Frank

et al. We choose for this paper to use the plasma characteristics appropriate to the plasma inferred by Frank et al. (see Table 1, drawn from Carlson et al., 1975) since these refer to measurements made in the vicinity of Io near the time of the radio occultation experiment and also are compatible with the other lines of evidence discussed above.

Ionospheric Models

McElroy and Yung (1975) have examined ionospheric models having a variety of ion sources and sinks. Their two preferred models are a mixture of ammonia and sodium, with photoionization of sodium the dominant ion source (their Model 4) and an ammonia atmosphere with charged particle ionization of NH_3 as the major ion source (their Model 6). The characteristics of their Model 6 are a scale height of 75 km, a surface number density of 3×10^{11} cm^{-3} (or a pressure of $\sim 10^{-8}$ bars), and a charged particle flux of 3×10^{7} cm^{-2} sec^{-1} of either 10 keV electrons or 10 MeV protons. McElroy and Yung discuss the scaling of their electron density calculations for different energies of incident particles. For the 100 eV plasma which is compatible with the observational data, their scaling relationships (their Eq. 36 and Fig. 18) indicate electron fluxes of $\cdot 10^{10}$ cm^{-2} sec^{-1}, which is an excellent agreement with the value in Table 1. The agreement between the two fluxes is important because the value computed from the atmospheric model is independent of the flux tabulated in Table 1. The former depends only upon atmospheric parameters and the ionization cross sections, while the latter was found from an independent set of observational constraints.

For this energy and flux the corresponding surface number density required to satisfy the overall characteristics of the electron profile is 10^{9} cm^{-3} or a surface pressure of 10^{-11} bars. This is two orders of magnitude lower than McElroy and Yung's nominal model. While in our model the energy per electron has decreased and the flux has increased by nearly the same amount, this low density results because the cross sections for ionization by 100 eV electrons are more than two orders of magnitude larger for most species (i.e. a few x 10^{-16} cm^{2}, compared to $\sim 10^{-18}$ cm^{2} for energies of 10 keV, see Kieffer and Dunn, 1966). It is noted that the low energy flux considered here yields a more severe constraint on neutral atmospheric density than those found using a lesser flux of higher energy particles. For the neutral densities involved, the atmosphere appears as a "thin" target to high energy particles and their ionization rate is correspondingly much less. This conclusion is not critically dependent upon the molecular species present since all of the relevant molecular ionization and recombination rates are similar in magnitude.

In order to calculate electron density profiles we use Eq. (33) from McElroy and Yung:

$$N_e(z) = \left[\frac{N(z)\,\sigma E F_e}{35\alpha}\right]^{1/2} \exp\left(-\frac{N(z)\,\sigma H}{2}\right)$$

where $N_e(z)$ = electron density (cm^{-3}) at altitude, z, $N(z)$ = neutral density (cm^{-3}) at altitude, z; $N(z) = N(O) \exp(-z/H)$; σ = ionization cross section (cm^{2}); E = energy of electrons (eV); F_e = unidirectional flux of electrons (cm^{-2} sec^{-1}) above the atmosphere; H = neutral scale height (km); α = recombination rate constant (cm^{3} sec^{-1}); and 35 = assumption that on the average 35 eV are required to produce an electron-ion pair. We take the electron parameters from Table 1, $F_e = 3 \times 10^{9}$ cm^{-2} sec^{-1} (unidirectional), E = 100 eV. For the Pioneer 10 entry occultation data we use H = 75 km. Values for the dissociative recombination rate coefficient for most molecular species are $\alpha \sim 10^{-7}$ cm^{3} sec^{-1}; a value of $\alpha = 1.17 \times 10^{-7}$ cm^{-3} sec^{-1} fits well for our model. Different values increase or decrease the electron profile slightly or require a small change in the estimate of the energy or flux. Figure 1 shows the electron density calculated using the above parameters. The model shown for the entry data has a value of $N(O)\,\sigma = 5 \times 10^{-7}$ cm^{-1}. Most species have a peak in their ionization cross section near 100 eV of a few times 10^{-16} cm^{2}; we use a range of $\sigma = 1\text{-}5 \times 10^{-16}$ cm^{2} as a reasonable estimate of the possible variation due to composition. Thus the neutral number density at the surface is found to be $N(O) = 1\text{-}5 \times 10^{9}$ cm^{-3}.

The assumed 75 km scale height corresponds to a temperature of 275 K if the neutral atmosphere is composed of NH_3. For O_2 it would be 515 K. A molecular oxygen atmosphere derived from the photolysis of H_2O has been suggested for Ganymede by Yung and McElroy (1975) and might also be considered for Io. As a consistency check, the temperature difference between the 150 K surface and the region of maximum heat deposition (assumed to be 0.48 erg/sec cm^{2} at 75 km in altitude, Table 1) can be used to calculate heating efficiencies. These are on the order of 20% for both molecular constituents, when thermal conductivities of 5000 and 2000 erg sec^{-1} sec^{-2} (K/cm)$^{-1}$ are used for NH_3 and O_2 respectively. Heating efficiencies of this magnitude are reasonable, lending support to the present ionospheric model. Representative values for the Earth's atmosphere are on the order of 30 to 50 percent (Amayenc et. al., 1975). Similar conclusions about charged particle heating were reached by McElroy and Yung (their Fig. 17).

An uncertainty existing in both entry and exit profiles is the exact altitude of the peak electron density. Since the diameter deduced for Io from the radio occultation is ~75 km larger than the stellar occultation value (Kliore et al. 1974, 1975; Taylor et al., 1971; O'Leary and Van Flandern, 1972; Taylor, 1972) there may be an error of this magnitude in the altitude

Table 1. Plasma Characteristics at the Orbit of Io

Parameter	Electrons	Protons
Plasma Temperature (kT/e)	100	100 eV
T	1.2×10^{6}	1.2×10^{6}K
Plasma Density (n)	30	30 cm^{-3}
Most Probable Speed (v)	5.9×10^{8}	1.4×10^{7} cm sec^{-1}
Omnidirectional Particle Flux (nv)	1.8×10^{10}	4.2×10^{8} cm^{-2} sec^{-1}
Unidirectional Particle Flux (1/6 nv)	3.0×10^{9}	6.9×10^{7} cm^{-2} sec^{-1}
Unidirectional Energy Flux (1/6 kT/e nv)	3.0×10^{11}	6.9×10^{9} eV cm^{-2} sec^{-1}
(1/6 kT nv)	0.48	1.1×10^{-2} erg cm^{-2} sec^{-1}

These values are appropriate for an observer co-rating with the Jovian magnetic field. The co-rotation velocity relative to Io (~56 km/sec) is small compared to the electron velocity but not the proton velocity. k=Boltzman constant, e=electron charge.

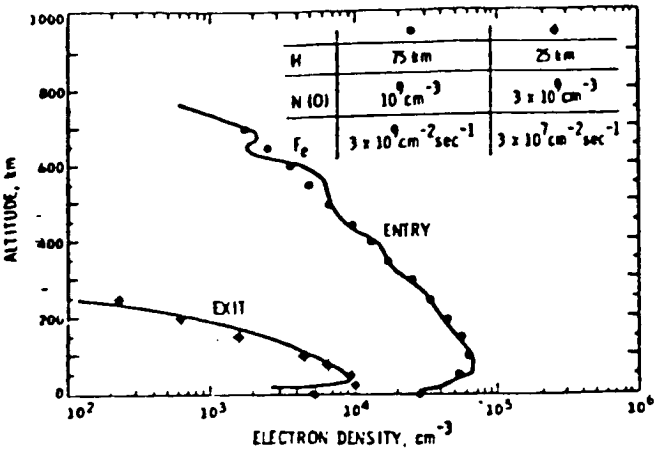

Fig. 1 Io's ionosphere and electron impact ionization models. Solid lines show the Pioneer 10 radio occultation data for both the entry and the exit electron density profiles (Kliore et al., 1975). The symbols plot individual computations made using the model discussed in the text.

scale for either or both profiles. The altitude of peak electron density is primarily affected by the density and cross section product; the range assumed for σ is sufficiently large to also include this possible error in peak altitude.

The large difference in the electron density profiles for the entry and exit occultations (see Fig. 1) has been source of interest in all models (see McElroy and Yung, 1975, Brown and Yung, 1976 and Whitten et. al., 1975 for previous discussions). For charged particle ionization the difference has been associated with differences in charged particle incident flux (McElroy and Yung, 1975) perhaps due to the existence of plasma sheath effects (see Shawhan, 1976 and Brown and Yung, 1976). Figure 1 shows a fit to the exit data for H = 25 km, $F_e = 3 \times 10^7$ cm^{-2} sec^{-1} and N(O) $\sigma = 1.5 \times 10^{-6}$ cm^{-1}. If we assume σ constant from entry to exit hemispheres (ie., a homogeneous atmosphere) then $N(O)_{exit} = 3 - 15 \times 10^9$ cm^{-3}. The greatly decreased heating from electrons on the exit side in this model implies that the atmospheric temperature should be near the nighttime average of ~100K instead of the several hundred degrees K calculated for the entry side (McElroy and Yung, 1975). This temperature difference is compatible with the exit scale height of 25 km versus 75 km for entry. Also, the differences in the surface number density and scale height combine to produce equal column densities at the surface (i.e. N(O)H) and therefore equal surface pressure. Of course, there would be pressure differences at altitude in this case. The dynamic behavior of such an atmosphere, heated by both sun (diurnal) and charged particle impact (with presently an unknown spatial and temporal variability) will provide an interesting challenge to investigators. Finally, we note that since the column density required for the exit profile is the same (to within observational uncertainties) as for the entry profile, an argument in this model can be made against any major atmospheric component being condensable at Io's nighttime temperatures.

The above fit for the exit data is not, of course, unique. In particular the peak electron density and the general slope of the distribution can be matched by keeping the electron flux relatively constant and reducing the atmospheric density (e.g. a condensable component model). The simple particle ionization model used here would not produce the observed low altitude maximum in the electron density since the reduced atmosphere is such a "thin" target. In a model incorporating diffusive loss of ions to the surface such a low altitude peak might be produced even in a thin atmosphere, however.

Discussion

The models discussed above show that for neutral, isothermal, molecular atmospheres the surface density must be less than a few times 10^9 cm^{-3} for the ionospheric electron density profile to be consistent with the Jovian magnetospheric plasma electron densities. What effects do these new plasma fluxes have for other possible atmospheres? First, pure atomic atmospheres require even lower neutral number densities. Although the ionization cross sections for most atomic species are the same order of magnitude as those of molecular species, the atomic recombination rates (radiative recombination) are several orders of magnitude slower than molecular dissociative recombination. This produces greater electron densities for the same number density of neutrals. Second, combined molecular-atomic models incorporating relatively large amount of sodium, such as McElroy and Yung's Model 4 also produce too large an electron density unless the surface pressure is $<10^{-11}$ bars since the electron ionization rate of sodium is greater than the photoionization rate assumed for Model 4, while sodium ion recombination still occurs through the relatively slow radiative recombination process.

We note that there are significant limitations to both the available data and the ionospheric models. First, we have only a "snap shot" of the ionosphere from the Pioneer 10 radio occultation data. Such major issues as whether the entry/exit difference is to be correlated with day/night changes or trailing side/leading side effects or position in the Jovian magnetosphere cannot be resolved using only these two profiles. Second, the models presented by McElroy and Yung and the one used in this paper do not treat the detailed interaction of Io with the thermal plasma. In more realistic models, plasma sheaths, currents in the ionosphere and/or the Io flux tube and the possibility of an intrinsic magnetic field for Io must be considered. Such plasma and magnetospheric effects are related not only to the production and dynamics of the ionosphere (as suggested here) but also perhaps to the sputtering of atoms from the surface and the Io modulation of the decametric radiation. Only further spacecraft occultation experiments can easily resolve some of the issues raised above and allow better models to be tested. It is important that serious consideration be given to these experiments in planning the upcoming Mariner Jupiter-Saturn flights. When these data are obtained they will be used to test advanced models and will further our understanding of this unique environment.

Finally, we consider the consequences of these models for possible sources for the neutral hydrogen flux. The flux required to maintain the hydrogen torus in steady state is 2-5 x 10^{10} cm^{-2} sec^{-1} (Carlson and Judge, 1974, 1975). This is approximately a factor of 20 to 50 above current estimates of proton influx (~10^9 cm^{-2} sec^{-1}) but it is possible that plasma protons could provide the necessary source of hydrogen in view of the uncertainties still surrounding the interaction of Io with Jupiter's magnetosphere (see McDonough, 1975; Brown and Yung, 1975). If a strong source of hydrogen at Io is required, however, McElroy et al. (1974) and McElroy and Yung (1975) have maintained that the most likely source is photo-dissociation of a hydrogen bearing molecule such as ammonia. Molecular densities of $<10^9$ cm^{-3} suggested here render this proposed photodissociative source of hydrogen much less potent. However, since the major electron-ion recombination process in a molecular atmosphere is dissociative recombination, there exists a possible source of atomic hydrogen in models involving a

hydrogen bearing molecule (e.g. H_2O, H_2S, NH_3) that is approximately equal to the electron flux ($\sim 10^{10}$ cm^{-2} sec^{-1}). This could provide the correct order of magnitude to supply the hydrogen cloud.

Conclusions

1. Current constraints on the Jovian magnetospheric plasma densities in the vicinity of Io require electron fluxes of $\sim 10^{10}$ cm^{-2} sec^{-1}, which suggests that electron impact ionization by 10-100 eV plasma electrons may be the dominant process for forming Io's ionosphere in any neutral atmosphere model. If plasma sheaths exist, they may alter the energy and flux of incoming particles from those considered here, however.

2. For these fluxes, surface molecular number densites of less than a few times 10^9 cm^{-3} are sufficient to match Io's observed electron density profiles. A pure atomic atmosphere would require even lower densities. Both of these density ranges allow most atoms (such as sodium and potassium) sputtered from the surface to reach the cloud about Io and yet do not rule out such an atmosphere as a possible source of the neutral hydrogen cloud.

3. Further radio occultations of Io are desperately needed because they supply the strongest constraints for models of its atmosphere and ionosphere.

Acknowledgments

We wish to thank D. M. Hunten, KPNO and W. Huntress, JPL, for useful discussions and comments. Portions of this work were supported by NASA Contract NAS 2-6558. This paper presents one phase of research carried out at the Jet Propulsion Laboratory, California Institute of Technology, under Contract Number NAS 7-100.

References

Amayenc, P., D. Alcayde, and G. Kockarts, Solar extreme UV heating and dynamical processes in the midlatitude thermosphere, JGR, 80, 2887, 1975.

Binder, A. B. and D. P. Cruikshank, Evidence for an atmosphere on Io, Icarus, 3, 299, 1964.

Brown, R. A., Optical line emission from Io, in Exploration of the Planetary System, Proceedings IAU Copernicus Symposium 4 (IAU Symposium 65), ed. A. Woszczyk and C. Iwaniszewska. Reidel, Dordrecht (1975).

Brown, R. A. and Y. L. Yung, Io, its atmosphere and optical emissions, in Jupiter the Giant Planet, ed. T. Gehrels, University of Arizona Press, Tucson (1976).

Brown, R. A., A model of Jupiter's sulphur Nebula, submitted to Astrophys J. (letters), 1976.

Carlson, R. W. and D. L. Judge, Pioneer 10 ultraviolet photometer observations at Jupiter encounter, J. Geophys. Res., 79, 3623, 1974.

Carlson, R. W. and D. L. Judge, Pioneer 10 ultraviolet photometer observations of the Jovian hydrogen torus: The angular distribution, Icarus, 24, 395, 1975.

Carlson, R. W., D. L. Matson, and T. V. Johnson, Electron impact ionization of Io's sodium cloud, Geophys. Res. Letters, 2, 469, 1975.

Frank, L. A., K. L. Ackerson, J. H. Wolfe, and J. D. Milhalov, Observations of plasma in the Jovian magnetosphere, J. Geophys. Res., 81, 000, 1976).

Intriligator, D. S. and J. H. Wolfe, Initial observations of plasma electrons from the Pioneer 10 flyby of Jupiter, Geophys. Res. Lett., 1, 281, 1974.

Kieffer, L. J. and G. H. Dunn, Electron impact ionization cross-section data for atoms, atomic ions, and diatomic molecules: I. Experimental data, Rev. Mod. Phys., 38, 1, 1966.

Kliore, A., D. L. Cain, G. Fjeldbo, and B. L. Seidel, Preliminary results on the atmosphere of Io and Jupiter from the Pioneer 10 S-band occultation experiment, Science, 183, 323, 1974.

Kliore, A. J., G. Fjeldbo, B. L. Seidel, D. N. Sweetnam, T. T. Sesplaukis, and P. M. Woiceshyn, The atmosphere of Io from Pioneer 10 radio occultation measurements, Icarus, 24, 407, 1975.

Kupo, I., Yu. Mekler, and A. Eviatar, Detection of ionized sulphur in the Jovian magnetosphere, Astrophys. J. (Letters), in press, 1976.

Macy, W. W., Jr. and L. M. Trafton, Io's sodium emission cloud, Icarus, 25, 432, 1975.

Matson, D. L., T. V. Johnson, and F. P. Fanale, Sodium D-Line emission from Io: Sputtering and resonant scattering hypothesis, Astrophys. J., 192, L43, 1974.

McDonough, T. R., A theory of the Jovian hydrogen torus, Icarus, 24, 400, 1975.

McElroy, M. B. and Y. L. Yung, The atmosphere and ionosphere of Io, Astrophys. J., 196, 227, 1975.

Mekler, Y. and A. Eviatar, Spectroscopic observations of Io, Astrophys. J. (Letters) 193, L151, 1974.

Münch, G., private communication, 1975.

O'Leary, B. and T. C. Van Flandern, Io's triaxial figure, Icarus, 17, 209, 1972.

Sentman, D. D., C. K. Goertz and J. A. Van Allen, Plasma densities in the inner Jovian magnetosphere, Abstract, EOS, 57, 316, 1976.

Shawhan, S. D., Io sheath-accelerated electrons and ions, in Jupiter the Giant Planet, ed. T. Gehrels, University of Arizona Press, Tucson, 1976.

Smith, B. A. and S. A. Smith, Upper limits for an atmosphere on Io, Icarus, 17, 218, 1972.

Taylor, G. E., The determination of the diameter of Io from its occultation of β Scorpii C on May 14, 1971, Icarus, 17, 202, 1972.

Taylor, G. E., B. O'Leary, T. C. Van Flandern, P. Bartholdi, F. Owen, W. B. Hubbard, B. A. Smith, S. A. Smith, F. W. Fallon, E. J. Devinney, and J. Oliver, Occultation of Beta Scorpii C by Io on May 14, 1971, Nature, 234, 405, 1971.

Trafton, L., Detection of a potassium cloud near Io, Nature, 258, 690, 1975.

Trafton, L. and W. Macy, Jr., An oscillating asymmetry to Io's sodium emission cloud, Astrophys. J. (Letters), 202, L155, 1975.

Trafton, L., T. Parkinson, and W. Macy, Jr., The spatial extent of sodium emission around Io, Astrophys. J. (Letters), 190, L85, 1974.

Van Allen, J. A., B. A. Randall, D. N. Baker, C. K. Goetz, D. D. Sentman, M. F. Thomsen, and H. R. Flindt, Pioneer 11 observations of energetic particles in the Jovian magnetosphere, Science, 188, 459, 1975.

Wehinger, P. A., S. Wyckoff, and A. Frohlich, Mapping of the sodium emission associated with Io and Jupiter, in Jupiter the Giant Planet (Proceedings of I.A.U. Colloquium No. 30), ed. T. Gehrels, University of Arizona Press, Tucson, 1976.

Whitten, R. C., R. T. Reynolds, and P. F. Michelson, The ionosphere and atmosphere of Io, Geophys. Res. Letters, 2, 49, 1975.

Yung, Y. L. and M. B. McElroy, Ganymede: Possibility of an oxygen atmosphere, BAAS, 7, 387, 1975.

(Received February 25, 1976;
accepted March 23, 1976.)

THE ASTROPHYSICAL JOURNAL, 225:325–334, 1978 October 1
© 1978. The American Astronomical Society. All rights reserved. Printed in U.S.A.

EUROPA: ULTRAVIOLET EMISSIONS AND THE POSSIBILITY OF ATOMIC OXYGEN AND HYDROGEN CLOUDS

F.-M. WU, D. L. JUDGE, AND R. W. CARLSON
Department of Physics, University of Southern California
Received 1977 August 19; accepted 1978 April 13

ABSTRACT

Emission signals from Europa with wavelength $\lambda < 800$ Å were detected by the *Pioneer 10* ultraviolet photometer. In the present paper, using improved procedures for data reduction, we determine the spatial region as well as the intensity of the suggested emission sources. The observations indicate a cloud with a radius of $\sim 1.5\ R_J$ (Jupiter's radius) and an apparent brightness $4\pi I$ of ~ 10 rayleighs, for a wavelength of 500 Å. It is argued that neutral oxygen atoms, along with neutral hydrogen, are produced through dissociation of water ice on the surface of Europa by particle impact. Electron impact ionization excitation of oxygen atoms in the resulting cloud then gives rise to the observed emission. Using the present source brightness and cloud radius results, we estimate an oxygen column density of $\sim 10^{13}$ cm^{-2}, while the density of atomic hydrogen is at most 10^{11} cm^{-2} and 10^{12} cm^{-2} for molecular hydrogen.

Subject headings: planets: Jupiter — planets: satellites — ultraviolet: general

I. INTRODUCTION

Clouds of orbiting atoms associated with the satellites in the Saturnian and Jovian systems were first suggested by McDonough and Brice (1973*a*, *b*). Their suggestion was based on the fact that atoms which escape from the atmospheres of the satellites generally do not possess sufficient energy to escape the gravitational attraction of the central planet. Since then, sodium and potassium clouds associated with Io have been found through Earth-based observations (Brown 1974; Trafton, Parkinson, and Macy 1974; Trafton 1975), and a hydrogen cloud has been discovered through *Pioneer 10* ultraviolet photometer observations (Judge and Carlson 1974).

While clouds at Europa have not been previously identified, the surface of Europa is largely covered by H_2O ice (Pilcher, Ridgway, and McCord 1972; Kieffer and Smythe 1974; Fink and Larson 1975) and, like that of Io, is immersed in and impacted by a high flux of particles (Frank *et al.* 1976). Since H_2O ice is dissociated by particle bombardment (Wickramasinghe and Williams 1968; Brown *et al.* 1977), atomic oxygen and hydrogen clouds originating from Europa's surface seem quite plausible. The production and ionization of such clouds are considered in this work. From the oxygen and hydrogen emissions, their abundance in Europa's cloud can be determined.

II. OBSERVATIONAL DATA

Details of the ultraviolet photometer instrument on the *Pioneer 10* and *11* spacecraft have been given by Carlson and Judge (1974) and Judge *et al.* (1976). The photometer has two channels, λ_s and λ_L, which are sensitive to emissions with $\lambda < 800$ Å and $\lambda < 1400$ Å, respectively. An electronic switch alternately selects one of the two channels every two rolls of the spacecraft. The field of view of the photometer is determined by a collimator whose optical axis is oriented at a half-cone angle of $\theta_0 = 20°.25$ with respect to the spacecraft spin axis. The spin scanning, which has a period of about 12.5 s, allows one to extract optical emission features in the presence of a high background signal.

To identify the weak Europa signals, averaging times of 1 to 2 hours were required. In addition, cycles with high background or background variation were excluded from the averaged data. (A cycle of data is defined as the data accumulated during one complete rotation of the spacecraft.) For an interval of 1.5 hours there are $N = 216$ cycles accumulated for each channel. An example of the improvement realized by the data selection procedure is shown in Figure 1. The upper curve results from averaging all the cycles of data accumulated during the interval 7.63–9.07 hours, while the lower curve is obtained by excluding 20 cycles of data with "high" background variation. The variation of the background with clock angle in the upper curve is significant, with differences of background count rates for different clock angles up to ~ 35 counts s^{-1}. In contrast, the emission signal is unambiguously present in the lower curve with a count rate of ~ 16 counts s^{-1}.

The λ_s and λ_L data for the morning of day 333 of 1973 (spacecraft time UT) resulting from the improved procedures are presented in §§ II*a* and II*b*. During these observations Europa was at a distance of $\sim 70\ R_J$ from the spacecraft and was in the photometer field of view at a clock angle of 20°. The clock angle of the field is measured clockwise from the ecliptic plane to the plane determined by the viewing direction and the spin axis (Fig. 2).

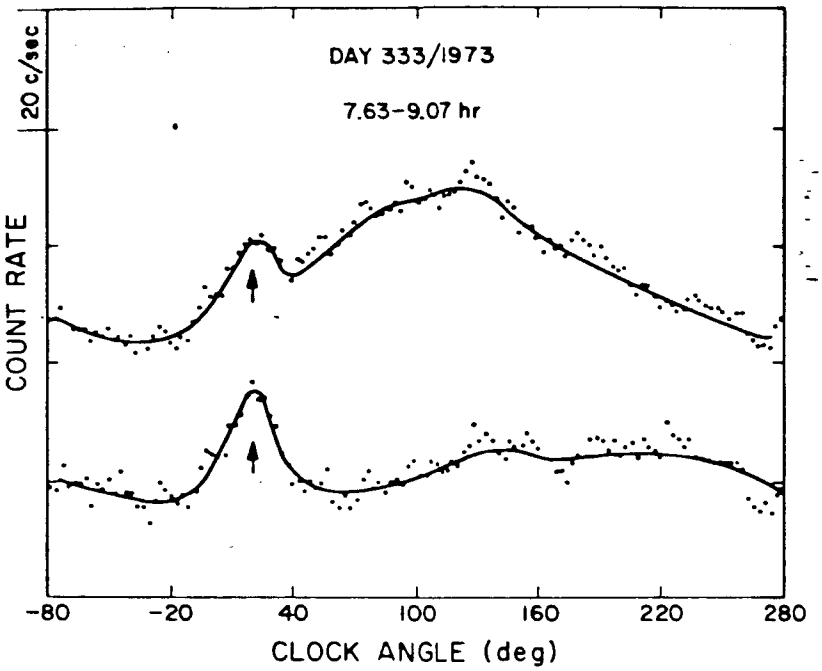

FIG. 1.—λ_s channel signals at 7.63–9.07 hours of 1973 day 333. The upper curve results from averaging all cycles of data accumulated in this period, while the lower curve excludes the cycles with rapid background variation.

a) λ_s Channel Observations

Figure 3 shows the λ_s channel data. The amplitudes in counts s^{-1} are plotted against the clock angle of the field of view. The optical signals at $\phi \sim 20°$ appear above the slowly varying background starting at 3.5 hours and last 7.5 hours. These signals may be readily identified both by the clock angle at which they appear and by the half-width of $\sim 30°$ which represents the combined instrument response and data integration time (Carlson and Judge 1975). It is noted, however, that some weak signals, such as those in the period from 4.63 to 5.90 hours, may have a half-width a little wider than expected, perhaps due to interference from the background noise.

With the long time average, the background noise in most cases is small. In general, the amplitude of the emission signals can be determined to an accuracy better than 5 counts s^{-1}. The time variation of the emission signals is shown in Figure 4, along with the viewing field of the photometer at 7 hours of day 333. It can be seen that the signal is maximum at 7–8 hours,

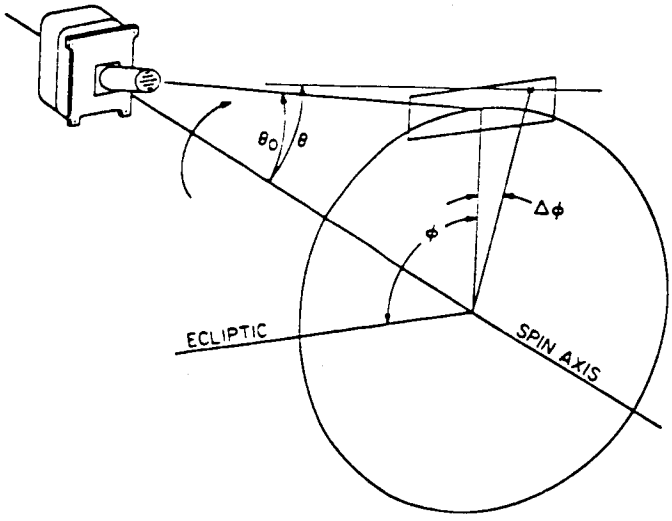

FIG. 2.—The optical axis of the photometer is at an angle $\theta_0 \sim 20°$ to the spin axis of the spacecraft. The angle ϕ is the clock angle relative to the ecliptic. The instantaneous field of view is nominally 1° × 10°.

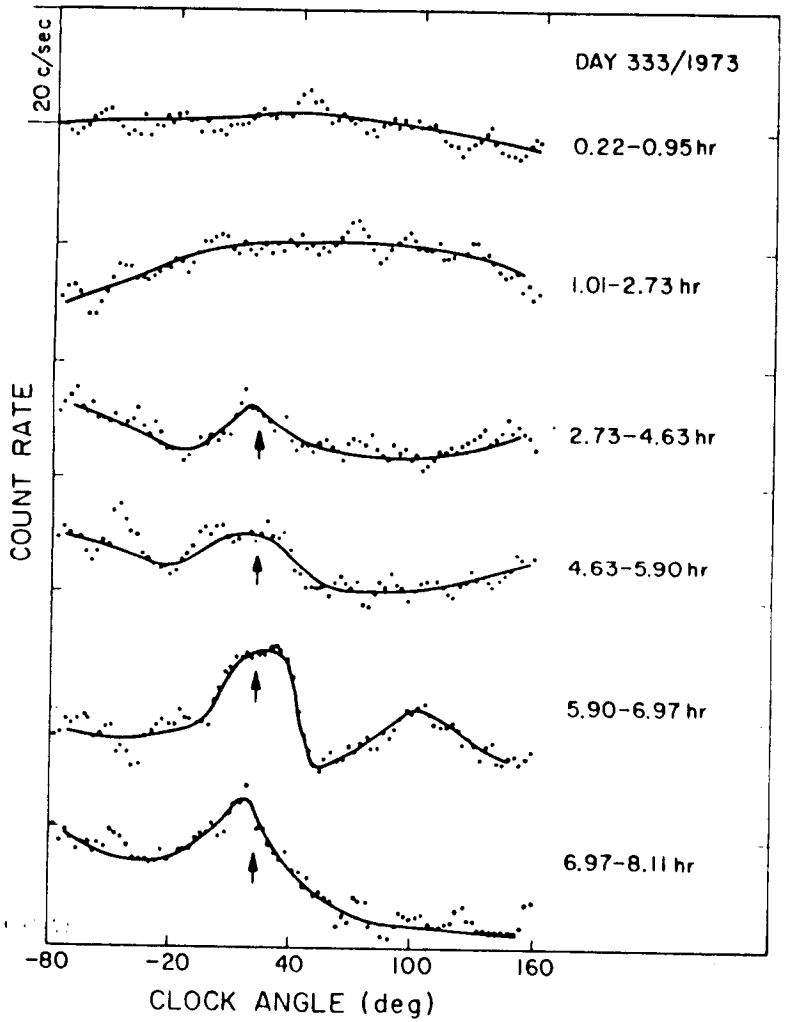

FIG. 3a

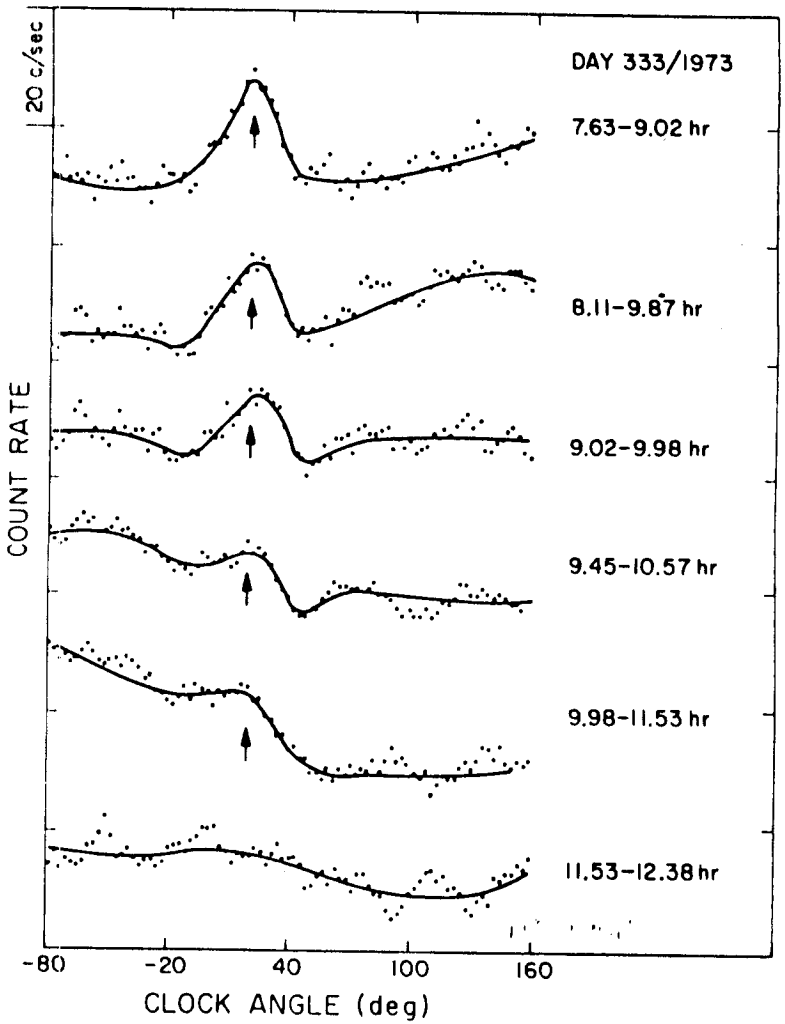

FIG. 3b

FIG. 3.—Emission signals from Europa for $\lambda < 800$ Å (λ_1 channel)

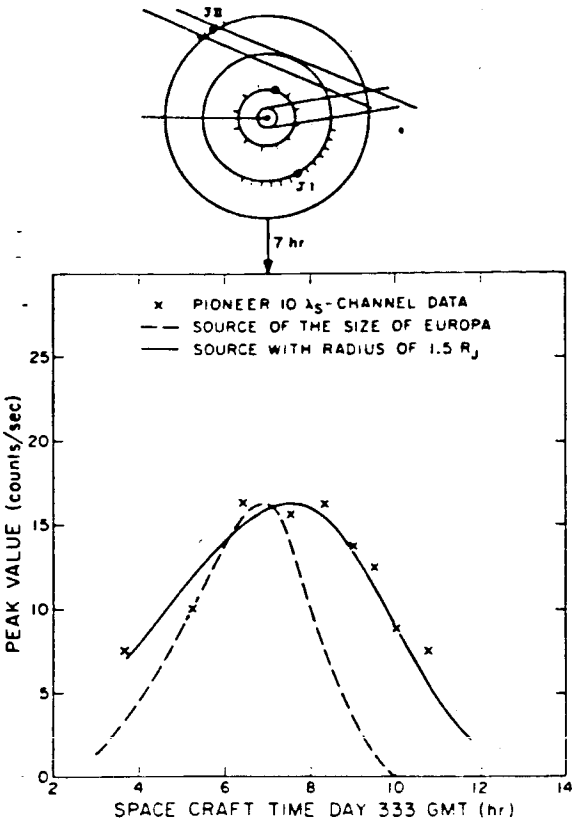

FIG. 4.—Peak values of the λ_s channel signals and the field of view of the photometer of day 333. The satellite orbits are labeled by each satellite's position at 7 hours. The observed data are compared with the calculated intensities for the emission from (1) Europa's own disk and (2) from a region with radius of 1.5 R_J.

corresponding to the time when Europa is near the center of the field of view. Moreover, as was noted above, the emission signal at $\phi \sim 20°$ corresponds to Europa's rotational position on day 333. Thus the source of the emission is clearly from a region around Europa. Note also that during the early part of day 333 Io is almost directly on the other side of Jupiter from Europa and is not likely to contribute to the observed signals. However, the fact that the signal lasts more than 7 hours indicates that the emissions are coming from a region much wider than Europa's physical disk.

In order to relate the observed count rate to the brightness and spatial extent of the source, the photometer characteristics must be considered. The count rate of the photometer $S(t, \Phi)$ at clock angle Φ and time t, due to a uniform emission source extending from θ_1 to θ_2 in cone angle and ϕ_1 and ϕ_2 in clock angle, can be calculated from

$$S(t, \Phi) \propto \int_{\theta_1(t)}^{\theta_2(t)} d\theta \int_{\phi_1(t)}^{\phi_2(t)} A(\theta, |\Phi - \phi|) d\phi .$$

Here, the limits of integration for θ and ϕ correspond to the spatial extent of the emission source, and vary with time, $A(\theta, |\Phi - \phi|)$ is the angular response of the collimator and attains a maximum value at the center of field of view, for which $\theta_0 = 20°.25$ and the half-width is $\Delta\theta \sim 0°.5$ (Carlson and Judge 1975). To have a signal detected by the photometer, a significant portion of the emission source must lie between $19°.75 < \theta < 20°.75$.

The calculated amplitudes at $\Phi = 20°$ for two source sizes, one equal to that of Europa (~point source) and one of 1.5 R_J (or 70 times Europa's size), are shown in Figure 4 with the *Pioneer* λ_s data superposed. The calculated rates for a point source are normalized to the value at the time $t = 7$ hours when Europa itself is in the center of the field of view. It is clear that the curve for a point source is too narrow to fit the observed data. In particular, no signal could be expected to be detected at 9.5 hours if the emission were from a point source, contrary to the fact that a strong signal of 12 counts s^{-1}, about 0.75 of the maximum value, is observed at this time. It is also noted from the observational data that the trailing side of the cloud has a stronger emission intensity than the leading side. Thus, to fit this observed asymmetry, the calculated rates for a source of 1.5 R_J are normalized and maximized at 7.75 hours, 0.75 hours after Europa's physical disk left the field. At this time the 1.5 R_J emission cloud is centered at ~0.5 R_J from the surface of Europa on the trailing side of the orbit, and the calculated function for the cloud fits the observed data very well. As pointed out by Carlson and Judge (1975) in their analysis of the Io hydrogen cloud, an asymmetry arises in the cloud if the source species are escaping from the satellite surface with relatively high velocity. Unfortunately, it is not yet possible to establish a quantitative value for the velocity of the escaping particles.

b) λ_L Channel Observations

A preliminary report (Judge *et al.* 1976) on the λ_L observations indicated that the data for the morning of day 333 are very noisy and no feature was continuously present or clearly recognized as an optical signal. Only an upper limit of 40 counts s^{-1} for Europa's λ_L signal was given. At present, by selection of the data and by averaging for longer periods of time, these data have been improved and are shown in Figure 5.

From the figures, it may be seen that the emission signals at $\phi \sim 20°$, which corresponds to Europa's rotational position starting at 4.0 hours, are continuously present throughout the observation period. However, the background variations in the λ_L channel cannot be completely removed. In fact, it appears that the background counts at negative clock angles are consistently higher than the average. This may be due to the asymmetry in the interplanetary hydrogen glow or the continuous interference from a unidirectional high energy particle flux. We also note that, according to the viewing geometry, θ' Sgr, a B3 type star at clock angle $\phi = -45°$, is in the field of view on day 333. Thus, the small feature at $\phi = -45°$ in Figure 5 could be caused by emissions from this star.

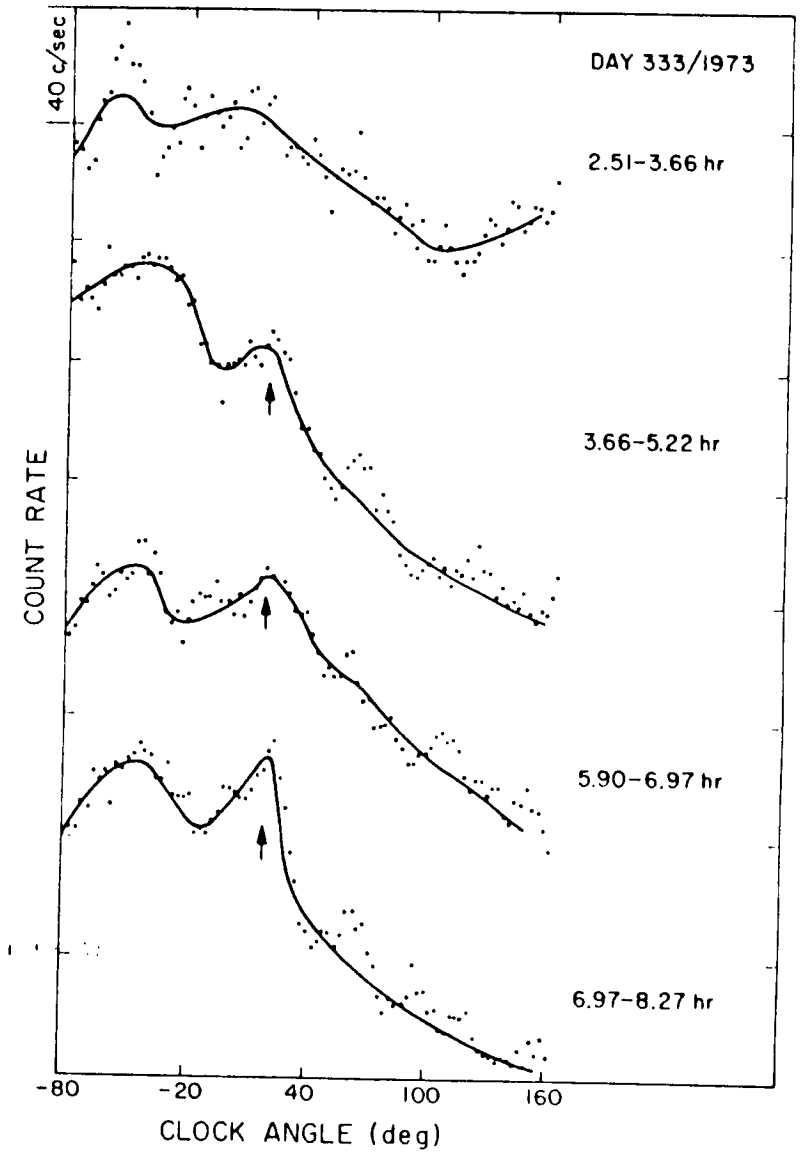

FIG. 5a

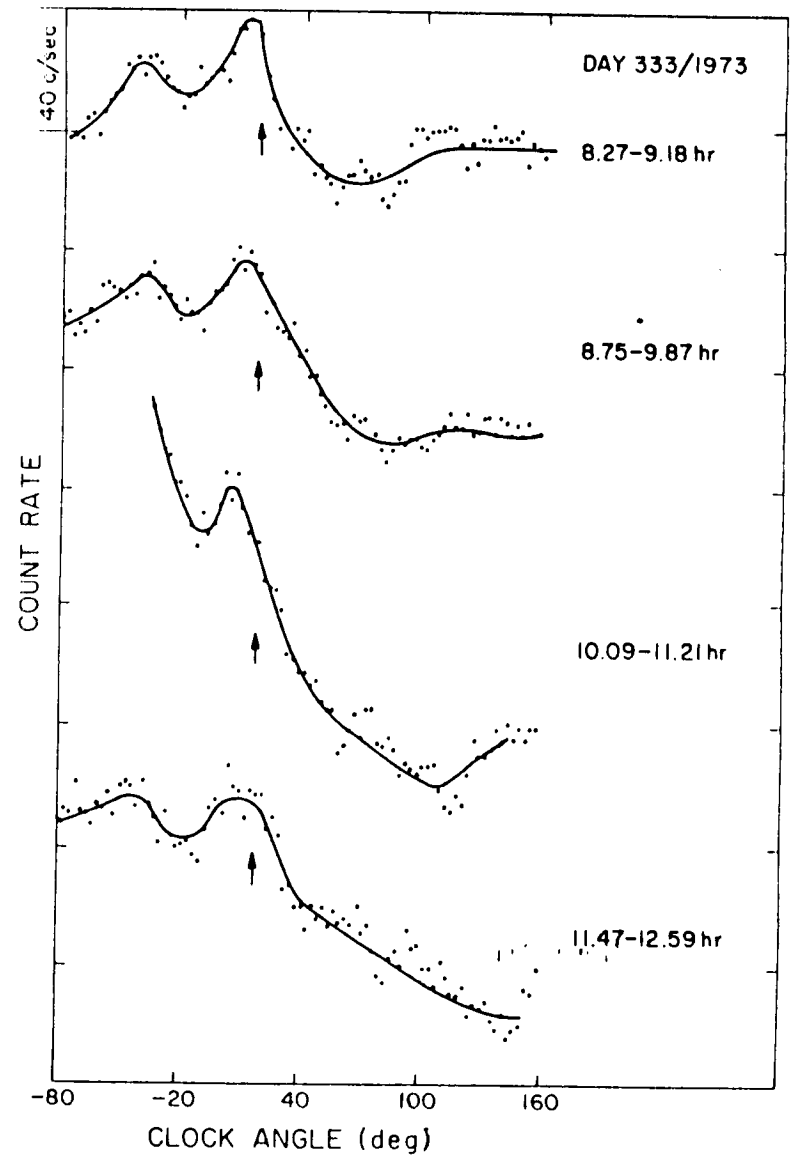

FIG. 5b

FIG. 5.—Emission signals from Europa for $\lambda < 1400$ Å (λ_L channel)

Since the background level is not constant, the amplitudes of the λ_L channel signals cannot be accurately determined. It can be said generally, however, that the amplitude is about 30 ± 15 counts s^{-1} at 5 hours, reaches a maximum of 50 ± 10 counts s^{-1} at ~8 hours, and decreases to 30 ± 10 counts s^{-1} at about 11 hours. Note that the time for the maximum signal for the λ_L channel is the same as for the λ_s channel, that is, immediately after Europa's disk left the field of view. Thus the λ_L signals so discussed are associated with Europa. However, we must note that since Io's H cloud is quite extended (about 60° from Io's center), and is in the field after ~11 hours, the emission features in the latter periods of Figure 5 could include a contribution from Io's cloud.

In short, the λ_L channel count rate on day 333 is about 50 ± 10 counts s^{-1}, but the emission region is at best difficult to estimate, partly due to the large variation in the background counts and partly due to possible contamination from Io's hydrogen cloud.

III. INTERPRETATION OF EUROPA'S UV EMISSION

Processes occurring at Europa's disk, such as production of X-rays and bremsstrahlung yielding UV emissions, have been considered (Judge *et al.* 1976). However, they are not efficient enough to produce the observed brightness of Europa. The present data indicate that the λ_s channel emissions come from an extended cloud around Europa. Among the possible source species for this cloud, oxygen and hydrogen atoms, dissociated and released from the surface of Europa by particle bombardment, are obvious candidates.

The oxygen and hydrogen so released escape from Europa's surface and orbit Jupiter at the orbital distance of Europa to form an extended cloud. Oxygen atoms in the cloud can be ionized through removal of the $2s$ electrons. The O^+ ions so produced are either in the $(2s\,2p^4)\,^2P$ state or the $(2s\,2p^4)\,^4P$ state. The subsequent decay of the ^2P state will produce radiation of $\lambda \sim 537$ Å and 581 Å and are the most likely emissions detected by the λ_s channel. Decay of the ^4P state will radiate at $\lambda \sim 844$ Å, along with the 537 and 581 Å lines, and all will be detected by the λ_L channel. In addition, O I 1034 Å emissions resulting from excitation of atomic oxygen to the $O(2s^22p^33s)^3S$ state, will also be detected by the λ_L channel. Resonance scattering of the solar Lα line at 1216 Å by H atoms in Europa's cloud may also contribute to the observed λ_L signal.

In the following sections we will discuss the mechanisms for the production, ionization, and excitation of the cloud of Europa. The contributions to the observed signals from each of the possible oxygen and hydrogen emissions will then be estimated.

First we estimate the proton and electron flux in Europa's environment.

a) Proton and Electron Flux

Europa is only 9 R_J away from Jupiter and, like Io, is immersed in an intense Jovian radiation belt. The proton plasma density in the vicinity of Europa is 10 cm^{-3} with a typical energy of 400 eV (Frank *et al.* 1976), and the corresponding proton flux is $\sim 3 \times 10^8$ cm^{-2} s^{-1} (about a factor of 3 less than that at Io).

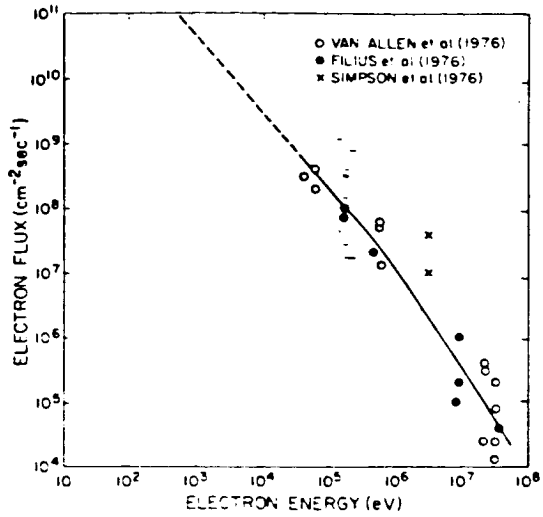

FIG. 6.—Observed electron flux near Europa

The electron plasma density has not been measured but can be estimated in two ways. (1) Assuming charge neutrality for the plasma and equal proton and electron energies, the electron flux is estimated to be 1.2×10^{10} cm^{-2} s^{-1}. If the plasma includes some heavy ions such as S^+ (Kupo, Mekler, and Eviatar 1976) and O^+, the actual electron flux could be a little larger. (2) On the other hand, the integrated flux for high energy electrons has been measured extensively (Fig. 6). For electron energies less than 1 MeV, the integrated flux is well fitted by an E^{-K} power law with $K \sim 1.2$. Extrapolated from this power law, the electron flux at energies < 1 keV is estimated to be of the order of 10^{10} to 10^{11} cm^{-2} s^{-1}.

In the following calculations we will then use the value of 3×10^8 cm^{-2} s^{-1} as the proton flux density and 5×10 cm^{-2} s^{-1} as the electron flux density in the vicinity of Europa, with both having an energy of 400 eV.

As will be argued, the extended atmosphere of Europa is produced through sputtering of H_2O ice at Europa's surface by proton, heavy ion, and possibly electron impact and, the observed UV radiation from Europa is produced through electron excitation of Europa's cloud.

b) Production Mechanism for Europa's Cloud

Most of Europa's surface is known to be covered by H_2O ice. The average surface temperature of Europa is estimated to be 120 to 130 K (Morrison and Cruikshank 1974) while the ice temperature is only 95 ± 10 K (Fink and Larson 1975). The relatively low temperature for the ice has been attributed to the higher albedo for solar radiation of ice relative to the rest of the satellite (Fink and Larson 1975). However, according to Gross (1975), the observed brightness of ~125 K

can be explained only if Europa's surface is heated by energetic particles in addition to solar radiation. Thus the low ice temperature also implies that the H_2O ice is a relatively poor absorber of the energy of impacting particles. Since H_2O molecules can be sputtered from the surface, it is likely that most of the impacting energy is dissipated through sputtering of H_2O molecules from the surface rather than heating of H_2O molecules in the ice mantle.

Europa's resulting atmosphere is likely to be tenuous, consisting primarily of O_2 with a column density of $\leq 10^{17}$ cm^{-2}, assuming a value similar to that suggested for Io (Johnson, Matson, and Carlson 1976). And, since the stopping cross section of an O_2 atmosphere is 10^{-16} cm^2 eV for protons with energy ~ 100 eV (Davidson 1965) and $< 10^{-15}$ cm^2 eV for electrons with energy greater than 10 keV (Green and Peterson 1968), the presence of an O_2 atmosphere cannot stop the protons with energy ~ 400 eV or electrons with an energy greater than 10 keV from bombarding the surface.

The probability of sputtering H_2O by protons is high because of its low value of crystal binding energy (Wickramasinghe 1967). In addition, H_2O molecules can be removed from the ice mantle through chemical reactions with the colliding atomic hydrogen through processes such as

$$H_2O + H^+ \rightarrow H_2O^+ + H$$

and

$$H_2O + H \rightarrow OH + H_2 .$$

The reaction products are in the gas phase and no longer bound in the ice mantle. (Note that the above processes involving H and H^+ have been suggested by Wickramasinghe and Williams 1968 as a mechanism for destroying the ice grains in H II regions.)

The sputtering yield of ice by MeV protons has been measured recently by Brown *et al.* (1977) and found to be about 1 molecule per ion. For keV and lower energy protons, the sputtering yield of ice has not been measured but is expected to be larger, since lower energy particles will penetrate less deeply into the ice mantle. Several measurements on the sputtering of solid targets by ion bombardment (see, e.g., Carter and Colligon 1968), indicate the sputtering yield of keV ions can be an order of magnitude larger than that of MeV ions. With a proton flux of $\sim 3 \times 10^8$ cm^{-2} s^{-1}, the rate of removal of H_2O molecules from Europa's surface could be 10^9 to 10^{10} cm^{-2} s^{-1}.

As was noted, Europa's surface is bombarded not only by protons but by energetic electrons as well. These electrons can also sputter and dissociate H_2O through processes such as

$$e + H_2O \rightarrow e + OH + H$$
$$\rightarrow e + H_2 + O$$
$$\rightarrow e + H + H + O .$$

Since the electron flux on Europa is $\sim 10^9$ cm^{-2} s^{-1} for $E \geq 10$ keV (Fig. 6), the total energy input for electrons is $\geq 10^{13}$ eV cm^{-2} s^{-1} and is quite large in comparison with the proton plasma energy of $\sim 10^{11}$ eV cm^{-2} s^{-1}. Hence the removal of H_2O molecules from Europa's surface by high energy electron impact might also be significant, even though the efficiency of removing H_2O molecules through electron impact is undoubtedly small compared with proton impact. Laboratory data are required to establish whether this postulated physical process is important. In addition, heavy particles such as O and O^+ also participate in the bombardment process, and particles removed from Europa's surface can reimpact the surface. Such processes will increase the sputtering rate. Thus it appears that a rate of 5×10^{10} cm^{-2} s^{-1} for removing H_2O molecules from Europa's surface layer may not be unreasonable. As will be seen, this rate corresponds to the O atom supply rate required to be consistent with the loss rate of O atoms in Europa's cloud, as estimated from the UV observational data.

It is noted, for an ice temperature of ~ 95 K, that the evaporation rate is only about 3×10^3 molecules cm^{-2} s^{-1} (Watson, Murray, and Brown 1963), and is very small in comparison with the removal rate by impacting particles. The loss of ice molecules due to evaporation is thus a negligible process.

The product species resulting from impact collision processes are H, H_2, O, and OH, in addition to H_2O molecules. The H and H_2 species cannot accumulate significantly in the atmosphere of Europa. This follows from the fact that the most probable velocities for H and H_2 at a temperature of $T = 300$ K are 2 and 1.5 km s^{-1}, respectively, and are comparable to the escape velocity at Europa of ~ 2 km s^{-1}. Hence the thermal escape of hydrogen from Europa should be very efficient, since the exobase temperature of an atmosphere of a planet or satellite (for example, Io) is usually several hundred degrees above its surface temperature. With a surface temperature of 125 K, an exobase temperature for Europa of 300 K or higher is quite plausible.

The other dissociation products of H_2O, such as OH and O, will mostly recombine in Europa's lower atmosphere to form stable O_2 molecules through collision processes (e.g., Young and McElroy 1977). The O_2 molecules so produced will accumulate and result in an O_2 atmosphere, since thermal escape for O_2 is not efficient. The O_2 molecules will then be dissociated or ionized by electrons in the following processes:

$$e + O_2 \rightarrow O + O^+ + 2e$$
$$\rightarrow O_2^+ + 2e .$$

The recombination of O_2^+ with ionospheric electrons ($O_2^+ + e \rightarrow O + O$) would also produce O atoms. Most of the O atoms thus produced would have kinetic energy larger than 0.35 eV, the thermal escape energy for O atoms at Europa's surface, and could escape from Europa if their velocities were directed upward. They are, however, along with H and H_2, bound by Jupiter's gravitation field and form oxygen

TABLE 1

PHOTOSENSITIVITY (counts photon^{-1})

Wavelength (Å)	537 or 581	833	1216	1304
λ_s channel.....	0.026	1×10^{-3}	10^{-5}	10^{-5}
λ_L channel.....	0.026	0.044	0.012	0.0058

and hydrogen clouds at Europa's orbit. The rate at which O atoms are supplied to the cloud through this process is assumed equal to the electron flux density times Europa's surface area, that is,

$$\sim(5 \times 10^{10}\ \mathrm{cm}^{-2}\ \mathrm{s}^{-1}) \times (4\pi R_{\mathrm{Europa}}^2) \sim 10^{28}\ \mathrm{s}^{-1}\ .$$

(Note that similar processes, such as electron dissociation of hydrogen-bearing molecules, have been suggested by Johnson *et al.* as a source of H atoms for Io's cloud.)

c) *Excitation Rates for Europa's Cloud*

Once created in the cloud, the oxygen and hydrogen species will be excited by Jovian plasma and solar photons and can emit radiation in the UV range to which the photometer is sensitive (Table 1).

As was noted earlier, the observed λ_s channel emission is mainly due to the O II 537 and 581 Å lines and the λ_L emission is due to the O II 833 Å lines, O I 1304 Å, and hydrogen Lα 1216 Å line, in addition to the O II 537, 581 Å lines. The emission of H Lα from Europa is expected to be resonance scattering of the solar Lα line, as was observed at Io (Carlson and Judge 1975), with a rate of $10^{-4}\ \mathrm{s}^{-1}\ \mathrm{atom}^{-1}$. The oxygen excitation rates due to solar radiation, protons, and electrons are estimated and shown in Table 2. As can be seen, electron excitation is the most important excitation process, with a rate of $6 \times 10^{-7}\ \mathrm{s}^{-1}\ \mathrm{atom}^{-1}$ for the O II 537 and 581 Å lines, $1.3 \times 10^{-6}\ \mathrm{s}^{-1}\ \mathrm{atom}^{-1}$ for the O II 833 Å line, and $5 \times 10^{-7}\ \mathrm{s}^{-1}\ \mathrm{atom}^{-1}$ for the O I 1304 Å line.

Using these estimated rates, along with the *Pioneer* observational data, we can then estimate the abundance of oxygen and hydrogen in the cloud, as indicated in the next subsection.

d) *Abundance of Atomic Oxygen and Atomic and Molecular Hydrogen near Europa*

The λ_s channel emissions, as noted earlier, appear to be from a disk of 1.5 R_J approximately centered at Europa. At a distance of 70 R_J from Europa, the detected count rate was 15 counts s^{-1}, corresponding to a cloud brightness of $4\pi I \approx 10\ R$. This emission was argued to be the O II 537 and 581 Å lines from an oxygen cloud surrounding Europa, with an excitation rate of $g = 6 \times 10^{-7}$ photons s^{-1}. The column density of the atomic oxygen cloud then is $D = 4\pi I/g \approx 10^{13}\ \mathrm{cm}^{-2}$, with a total number in the cloud of $N \approx (1.5\ R_J)^2 D \approx 10^{33}$ atoms.

If the same emissions are being observed in the λ_L and λ_s channels, i.e., the O II 537, 581, 833, and O I 1304 lines, then according to the photon sensitivity (Table 1) and the excitation rates (Table 2) the count rate in the λ_L channel should be $\sim$4.7 times the count rate in the λ_s channel. With the observed λ_s signal of 15 counts s^{-1}, the count rate in the λ_L channel is expected to be 70 counts s^{-1} and is close to the experimental value of 50 counts s^{-1}.

Considering that the cross sections used in the calculation are not very accurate (mainly because the cross sections are dependent upon electron energy, and the exact electron energy is unknown), the near agreement is quite acceptable and consistent with the atomic oxygen source suggested above.

Thus, the observed λ_L emissions may all come from atomic oxygen ions and atoms, while the possible λ_L

TABLE 2

EXCITATION/EMISSION RATES FOR OXYGEN LINES

Particle	Flux (cm^{-2} s^{-1})	Cross Section (cm^2) or *f*-value	Excitation Rate (s^{-1})	Reference for Cross Section
O II 537, 581 Å:				
Photon (100 < λ < 300 Å).....	5×10^{8}*	$< 9 \times 10^{-20}$	$< 5 \times 10^{-11}$	Dalgarno *et al.* 1964
Electron.....	5×10^{10}	1.2×10^{-17}	6×10^{-7}	Peach 1970
Proton.....	3×10^{8}	10^{-17}	3×10^{-9}	Gryzinski 1965
O I 833 Å line:				
Photon (200 < λ < 420 Å).....	8×10^{8}*	$< 7 \times 10^{-22}$	$< 6 \times 10^{-11}$	Dalgarno *et al.* 1964
Electron.....	5×10^{10}	2.6×10^{-17}	13×10^{-7}	Peach 1970
Proton.....	3×10^{8}	10^{-17}	3×10^{-7}	Gryzinski 1965
O I 1304 Å line:				
Photon (λ = 1304 Å).....	4×10^{7}*	0.046	3×10^{-8}†	Lawrence 1969
Electron.....	5×10^{10}	10^{-17}	5×10^{-7}	Julienne 1976
Proton.....	3×10^{8}	$< 10^{-18}$	$< 10^{-8}$	Gryzinski 1965

* All the photon flux data in this table are from Hinteregger 1970 and Hall and Hinteregger 1970.

† The excitation rate is calculated from $g = \pi F_\lambda(\lambda^2/\Delta\lambda)(\pi e^2/m_e c^2)f$, where $\Delta\lambda$ is the emission-line width for the O I 1304 Å line and is 0.26 Å (Bruner and Rense 1969).

contribution due to resonance scattering by a Europa H cloud may be minor. An upper limit to the resonance-scattering contribution by atomic hydrogen may be assumed to be ~ 10 counts s^{-1}. With an excitation rate of $10^{-4}\ s^{-1}$ and an assumed cloud thickness of $\sim 1\ R_J$ (similar to Io), the H atom column density is at most $10^{11}\ cm^{-2}$.

The abundance of molecular hydrogen in Europa's cloud cannot be obtained directly from the present measurements. It can be inferred, however, and is $\sim 10^{12}\ cm^{-2}$, as will be shown in the following subsection.

e) Cloud Geometry and Loss

The lifetime of oxygen and hydrogen atoms in the cloud is determined by their ionization rate. Following ionization, the atoms are swept away from Europa's vicinity by the Jovian magnetic field. The ionization rates of oxygen for different processes are summarized in Table 3.

From Table 3 we see that photoionization is the least important loss process, while electron ionization is the most important process for an oxygen cloud. Proton ionization, because of its high cross section for change transfer, contributes part of the oxygen loss. The loss rate for oxygen in Europa's cloud from all processes considered is then $\sim 10^{-5}\ s^{-1}$. Since the number of atomic oxygen atoms in the cloud is $\sim 10^{33}$ atoms, the number of O atoms lost from the cloud each second is $\sim 10^{28}$ atoms s^{-1} and is equal to the previously estimated rate at which O atoms are supplied to Europa's cloud, as expected.

The cross section for ionizing H atoms through electron impact at $E = 400$ eV is $3 \times 10^{-17}\ cm^2$ (Lotz 1967) and $2 \times 10^{-15}\ cm^2$ for proton impact (Fite *et al.* 1960). With an electron flux of $\sim 5 \times 10^{10}\ cm^{-2}\ s^{-1}$ and a proton flux of $\sim 3 \times 10^8\ cm^{-2}\ s^{-1}$; the ionization rate of H in Europa's cloud is $\sim 2 \times 10^{-6}\ s^{-1}$ and the corresponding lifetime is 5×10^5 s. It is noted that the lifetime of H atoms in Io's cloud is about 2×10^5 s, while the hydrogen torus for Io is about 120° (Carlson and Judge 1974). If the escape processes for hydrogen atoms from Io and Europa are the same, the calculated lifetime of 5×10^5 s would imply that the hydrogen torus in Europa's cloud extends about 300° around Europa's orbit. With the previously derived upper limit to the column density of $\sim 10^{11}\ cm^{-2}$ and a thickness of $\sim 1\ R_J$, the maximum total number of H atoms in the cloud is then $\sim 10^{32}$ atoms. With the ionization rate of $2 \times 10^{-6}\ s^{-1}$, the loss rate of H atoms from the cloud is $\sim 10^{26}$ atoms s^{-1}, or 100 times lower than the supply rate of oxygen from Europa's surface.

In a steady state, the loss rate of hydrogen from the cloud should be equal to the supply rate of oxygen from Europa's surface, since hydrogen and oxygen are both produced through dissociation of water. Thus, the low ionization loss rate for atomic hydrogen, together with the observed weak resonance emission, suggests that a large portion of the hydrogen from Europa's surface is in the form of molecular hydrogen. Similar to atomic hydrogen, H_2 molecules could be formed through the dissociation of H_2O and easily escape from Europa's surface to form a H_2 cloud, with the principal loss mechanism again being electron ionization.

For an electron ionization cross section of $5 \times 10^{-17}\ cm^{-2}$ (Gryzinski 1965) and an electron flux of $5 \times 10^{10}\ s^{-1}$, the ionization rate for molecular H_2 is estimated to be $2.5 \times 10^{-6}\ s^{-1}$ molecule^{-1}. To have the loss rate of $10^{28}\ s^{-1}$, the total abundance of H_2 molecules in the cloud must be 4×10^{33} molecules. With the same procedures as for the H cloud, the total angular extent of a H_2 cloud is estimated to be about 200°. Assuming the cloud thickness is $\sim 1\ R_J$, the H_2 density in the cloud is then $\sim 10^{12}\ cm^{-2}$.

IV. SUMMARY AND CONCLUSIONS

The photometer on the *Pioneer 10* spacecraft detected UV emissions from an extended region of radius $\sim 1.5\ R_J$ centered approximately at Europa. The apparent brightness is ~ 10 rayleighs, for a wavelength of ~ 500 Å. The emission source species have not been unambiguously identified, but have been argued to result from the radiative decay of electron-excited oxygen ions. The contribution of hydrogen Lα lines to the UV emission seems to be insignificant. Neutral oxygen and hydrogen clouds most probably originate from Europa's surface, produced from the dissociation of H_2O molecules by particle bombardment. The resulting abundance in the cloud is $10^{13}\ cm^{-2}$ for atomic O, $\leq 10^{11}\ cm^{-2}$ for atomic H, and $\sim 10^{12}\ cm^{-2}$ for molecular H_2.

Since the analysis here is based on one day of observation, the variation of Europa's UV emission with time or orbital position has not been established. The answer to this may not be available until further spacecraft probes of the Jovian satellites are available.

Besides Europa, Ganymede and Callisto are known to be covered mostly by water frost. However, no

TABLE 3

THE LOSS RATE FOR OXYGEN ATOMS AT EUROPA'S CLOUD

Particle	Flux ($cm^{-2}\ s^{-1}$)	Cross Section (cm^2)	Ionization Rate (s^{-1})	Reference for Cross Sections
Photon* (300 < λ < 800 Å).....	8×10^8	10^{-17}	8×10^{-9}	Cairns and Samson 1965
Electron.....	5×10^{10}	1×10^{-16}	5×10^{-6}	Lotz 1967
Proton.....	3×10^8	2×10^{-15}	6×10^{-7}	Stebbings *et al.* 1964

* The photon flux is from Hinteregger 1970 for solar radiation from 300 < λ < 800 Å. For photons outside this wavelength range, the cross section for photoionization is very small and need not be considered.

extended UV radiation from those satellites has been observed (Judge *et al.* 1976), despite the fact that they are larger than Europa. It is perhaps significant that the energetic particle flux and plasma density near the orbital positions of Ganymede and Callisto are at least a factor of 10 less than that at Europa or Io (Van Allen 1976; Frank *et al.* 1976). These facts support the argument that cloud formation and subsequent UV emissions of the extended clouds result from the interaction of these satellites with the particle flux in their environments, with solar ultraviolet irradiation being important only for Lα resonance scattering by atomic hydrogen.

This work was supported by contract NAS 2-6558 with the NASA Ames Research Center.

REFERENCES

Brown, R. A. 1974, in *Exploration of the Planetary System*, ed. A. Woszczyk and C. Iwaniszewska (Dordrecht: Reidel), p. 527.
Brown, W. L., Lazerotti, L. Z., Poate, J. M., and Augustyniak, W. M. 1977, *EOS*, **58**, 423.
Bruner, E. C., and Rense, W. A. 1969, *Ap. J.*, **157**, 417.
Cairns, R. B., and Samson, J. A. R. 1965, *Phys. Rev.*, **139**, A10403.
Carlson, R. W., and Judge, D. L. 1974, *J. Geophys. Res.*, **79**, 3623.
———. 1975, *Icarus*, **24**, 395.
Carter, G., and Colligon, J. S. 1968, *Ion Bombardment of Solids* (London: Heinemann).
Dalgarno, A., Henry, R. J. W., and Stewart, A. L. 1964, *Space Sci.*, **12**, 235.
Davidson, G. T. 1965, *J. Geophys. Res.*, **70**, 1061.
Fillius, W. 1976, in *Jupiter*, ed. T. Gehrels (Tucson: University of Arizona Press), p. 869.
Fink, U., and Larson, H. P. 1975, *Icarus*, **24**, 411.
Fite, W. L., Stebbings, R. F., Hummer, D. G., and Brackmann, R. T. 1960, *Phys. Rev.*, **119**, 663.
Frank, L. A., Ackerson, K. L., Wolfe, J. H., and Mihalov, J. D. 1976, *J. Geophys. Res.*, **81**, 457.
Green, A. E. S., and Peterson, L. R. 1968, *J. Geophys. Res.*, **73**, 233.
Gross, S. H. 1975, *Science*, **190**, 564.
Gryzinski, M. 1965, *Phys. Rev.*, **138**, A336.
Hall, L. A., and Hinteregger, H. E. 1970, *J. Geophys. Res.*, **75**, 6959.
Hinteregger, H. E. 1970, *Ann. Geophys.*, **26**, 547.
Johnson, T. V., Matson, D. L., and Carlson, R. W. 1976, *Geophys. Res. Letters*, **3**, 293.
Judge, D. L., and Carlson, R. W. 1974, *Science*, **183**, 317.
Judge, D. L., Carlson, R. W., Wu, F.-M., and Hartmann, U. G. 1976, in *Jupiter*, ed. T. Gehrels (Tucson: University of Arizona Press), p. 1068.
Julienne, P. S. 1976, *J. Geophys. Res.*, **81**, 1397.
Kieffer, H. H., and Smythe, W. D. 1974, *Icarus*, **21**, 506.
Kupo, I., Mekler, Y., and Eviatar, A. 1976, *Ap. J.* (*Letters*), **205**, L51.
Lawrence, G. M. 1969, *Canadian J. Chem.*, **47**, 1856.
Lotz, W. 1967, *Ap. J. Suppl.*, **14**, 207.
McDonough, T. R., and Brice, N. M. 1973*a*, *Nature*, **212**, 513.
———. 1973*b*, *Icarus*, **20**, 136.
Morrison, D., and Cruikshank, D. P. 1974, *Space Sci. Rev.*, **15**, 641.
Peach, G. 1970, *J. Phys. B*, **3**, 328.
Pilcher, C. B., Ridgway, S. T., and McCord, T. B. 1972, *Science*, **178**, 1087.
Simpson, J. A., and McKibben, R. B. 1976, in *Jupiter*, ed. T. Gehrels (Tucson: University of Arizona Press), p. 738.
Stebbings, R. F., Smith, A. C., and Ehrhardt, H. 1964, *J. Geophys. Res.*, **69**, 2349.
Trafton, L. 1975, *Nature*, **258**, 690.
Trafton, L., Parkinson, T., and Macy, W. 1974, *Ap. J.* (*Letters*), **190**, L85.
Van Allen, J. A. 1976, in *Jupiter*, ed. T. Gehrels (Tucson: University of Arizona Press), p. 928.
Watson, K., Murray, B. C., and Brown, H. 1963, *Icarus*, **1**, 317.
Wickramasinghe, N. C. 1967, *Interstellar Grains* (London: Chapman & Hall).
Wickramasinghe, N. C., and Williams, D. A. 1968, *Observatory*, **88**, 272.
Young, Y. L., and McElroy, M. G. 1977, *Icarus*, **30**, 97.

R. W. CARLSON: Jet Propulsion Laboratory, 4800 Oak Grove Drive, Pasadena, CA 91103

D. L. JUDGE and F.-M. WU: University of Southern California, Department of Physics, University Park, Los Angeles, CA 90007

THE ASTROPHYSICAL JOURNAL, 225:1045–1049, 1978 November 1
© 1978. The American Astronomical Society. All rights reserved. Printed in U.S.A.

ELECTRON HEATING OF INFLOWING INTERSTELLAR GAS

F.-M. WU AND D. L. JUDGE
Department of Physics, University of Southern California
Received 1977 August 22; accepted 1978 May 4

ABSTRACT

The heating of inflowing interstellar gas by solar electrons is calculated. In the present work it is assumed that the thermal energy of the electrons is constant with distance from the Sun and that the inflowing gas follows Keplerian trajectories, and the contours of constant temperature so obtained are given. At a heliocentric distance of 1 AU the estimated temperature is 500 K upwind and 2000 K downwind for hydrogen atoms, and is 240 K downwind and 100 K upwind for helium.

Subject headings: interplanetary medium — interstellar: matter — Sun: solar wind

I. INTRODUCTION

Recently a temperature measurement by Bertaux *et al.* (1976) has given direct evidence that interplanetary hydrogen in the vicinity of the Sun is in fact hot, with a temperature between 5800 and 13,000 K. However, the temperature so measured cannot be identical to the temperature of interstellar matter unless solar wind heating of the interplanetary medium is negligible.

Both solar protons and solar electrons can transfer kinetic energy to hydrogen and helium atoms in interplanetary space through elastic collision processes. Proton heating of the interplanetary medium has been discussed by Wallis (1973, 1975), Fahr and Lay (1974), Fahr (1974, 1978), and Holzer (1977), and it is estimated that the gas temperature from such heating could increase by several hundred or perhaps several thousand degrees at a distance of 1 AU. However, electron heating of the interplanetary medium has not been considered. In this paper, we will show that, because of the high electron flux and high collision cross section, electron heating can be significant.

First we discuss the data relevant to solar electrons and derive the equations that express the temperature as a function of position. Then we present the temperature distribution of the interplanetary medium due to electron heating. Finally, the significance of temperature in determining the interstellar parameters is discussed.

II. SOLAR ELECTRONS

Electrons in the solar wind at a distance of 1 AU are observed to have a number density of $10\ \mathrm{cm}^{-3}$; 96% of the electrons have a thermal energy of 10 eV and 4% an energy of 60 eV (Feldman *et al.* 1974, 1975). For 10 eV electrons, the average thermal velocity is $2 \times 10^8\ \mathrm{cm\ s}^{-1}$ and for 60 eV electrons the velocity is $4 \times 10^8\ \mathrm{cm\ s}^{-1}$. Thus the thermal electron flux at 1 AU is $2 \times 10^8\ \mathrm{cm}^{-2}\ \mathrm{s}^{-1}$ and $2 \times 10^9\ \mathrm{cm}^{-2}\ \mathrm{s}^{-1}$ for 60 and 10 eV electrons, respectively.

The above-measured electron energy at 1 AU may change with distance. According to *Mars 3* spacecraft measurements (Gringauz and Verigin 1975), the electron temperature between 1 and 1.5 AU varies as $T_e \sim r^{-1/2}$. For distances greater than 1.5 AU no direct experimental measurements are available. However, it may be noted that the theoretical models of Leer and Axford (1972) and Axford (1972) predict an electron temperature at 1 AU of 40 eV with $T_e \propto r^{-4/3}$ far from the Sun. On the other hand, Wallis (1973) has argued that because of cosmic-ray modulation and neutral gas interaction with the solar wind, the electron temperature can rise to 20 eV and above at $r > 10$ AU. Thus, since experimental measurements at distances greater than 1.5 AU are not available and theoretical estimates may be oversimplified, we will assume that the electron energy is independent of distance and adopt the values of Feldman *et al.* (1974).

III. TEMPERATURE INCREASE

A neutral gas moving through the solar system will encounter collisions with solar electrons. The amount of average energy gain by the neutral gas for each elastic collision with an electron is (e.g., McDaniel 1964)

$$\Delta E \approx \frac{2m}{M} E , \tag{1}$$

where m and M are the electronic and atomic masses, respectively, and E is electron mean energy. Hence the amount of energy gain at a distance r per second can be expressed as

$$\beta = \frac{\beta_0 r_0^2}{r^2} ,$$

with

$$\beta_0 = F_1 \sigma_1 \Delta E_1 + F_2 \sigma_2 \Delta E_2 . \tag{2}$$

TABLE 1

RATE OF ENERGY INCREASE, β_0

Energy E (eV)	Electron Flux ($cm^{-2}\,s^{-1}$)	Hydrogen $\sigma(10^{-16}\,cm^{-2})$*	Hydrogen $\beta_0(eV\,s^{-1})$*	Helium $\sigma(10^{-16}\,cm^{-2})$*	Helium $\beta_0(eV\,s^{-1})$
10	2×10^9	4.6	1.0×10^{-8}	4.6	2.5×10^{-9}
60	2×10^9	0.2	3.0×10^{-10}	0.9	3.0×10^{-10}
Sum			1.0×10^{-8}		0.28×10^{-8}

* The cross section for helium atoms at $E = 10$ eV is from Milloy and Crompton (1977), while the cross sections for helium atoms at $E = 60$ eV and hydrogen atoms at $E = 10$ and 60 eV are calculated from the formula

$$\sigma(E) = 2\pi \int_0^\pi (1 - \cos\theta)\sigma(E, \theta) \sin\theta d\theta .$$

Here, $\sigma(E, \theta)$ represents the differential cross sections measured by McConkey and Preston (1975) and Srivastava and Trajmar (1976) for helium atoms and by Williams (1975*a*, *b*) for hydrogen atoms.

Here we assume that the electron flux is proportional to r^{-2}. The quantity β_0 is the energy transfer rate at r_0 (1 AU) due to the two groups of electrons with thermal energies of 10 and 60 eV. F_1 and F_2 are the flux densities and σ_1 and σ_2 are momentum transfer cross sections for 10 and 60 eV electrons, respectively.

The rate of energy increase for H and He atoms is calculated and summarized in Table 1. From the table it is clear that the energy transferred to the atoms is mostly from 10 eV electrons, with less than 10% of the energy from 60 eV electrons. The resulting transfer rate is 1.0×10^{-8} eV s^{-1} for H atoms and 0.28×10^{-8} eV s^{-1} for He atoms at a distance of 1 AU.

Since the elastic cross section decreases as the electron energy increases [at 10 eV, $\sigma(H) \sim E^{-1.4}$ and $\sigma(He) \sim E^{-0.6}$], the energy transfer rate β ($\sim E^{1.5}\sigma$) is not very sensitive to electron energy variation. Thus the assumption that the electron energy is constant with distance is not an important source of error in the present estimate of the interplanetary gas temperature.

Since the energy increase of the inflowing neutral atoms in a time period dt is βdt, the total temperature increase in time t' is

$$T = \frac{2}{3K}\int_0^{t'} \beta dt = \frac{2\beta_0 r_0^2}{3K}\int_0^{t'} \frac{dt}{r^2}, \quad (3)$$

where K is the Boltzmann constant. For a central force, the angular momentum of the neutral atoms is conserved,

$$bV_0 = r^2 d\theta/dt . \quad (4)$$

Here V_0 is the inflow velocity, and b is the value of the impact parameter at position (r, θ) (Axford 1972) and is given by

$$b_{1,2} = \tfrac{1}{2}\{r \sin\theta \pm [r^2 \sin^2\theta + 4r(1 - \cos\theta)/c]^{1/2}\}, \quad (5)$$

where $c = V_0^2/(1 - \mu)GM_S$, μ is the radiation pressure to the gravitational force, M_S is the mass of Sun, and G is the universal gravitational constant.

Substituting equation (4) into equation (3) and completing the integration, we can then write the temperature equation as

$$r = \frac{\{(\alpha/TV_0)[(\pi \pm (\theta - \pi)]\}^2}{(1 - \cos\theta)/c \pm (\alpha/TV_0)[\pi \pm (\theta - \pi)] \sin\theta} . \quad (6)$$

Here $\pi \pm (\theta - \pi)$ is the angular change in radians of the inflowing interplanetary gas, where the plus sign is for $b > 0$ and the minus sign is for $b < 0$, and the parameter $\alpha = 2\beta_0 r_0^2/3K$.

In the above derivation it is assumed that the incoming trajectory of neutral atoms is a hyperbola and will not be disturbed by collisions with solar wind particles. This is justified, since the superposed thermal velocity components of the atoms will cause only a random velocity dispersion, and will not change the average speed and direction of their motion.

IV. TEMPERATURE DISTRIBUTION

By using equation (6), the temperature distribution of interplanetary H and He atoms, resulting from electron heating, can be calculated as long as the values for the parameters V_0 and μ are given. In the following calculations, we will choose $V_0 = 20$ km s^{-1} (Adams and Frisch 1977; Freeman *et al.* 1976; Fahr 1974) as the velocity of the inflowing gas with $\mu = 0.8$ for hydrogen and $\mu = 0.0$ for helium. Since the solar Lα flux and hence the radiation pressure depend on solar activity, a nominal value of μ was chosen corresponding to a Lα flux of 2.6×10^{11} $cm^{-2}\,s^{-1}$ Å^{-1}.

As was noted earlier, for every position (r, θ), there are two possible temperatures (T_1, T_2) corresponding to two possible impact parameters b_1 and b_2. The probability of detecting T_1, T_2 depends on the number density ratio N_2/N_1 at position (r, θ). The ratio N_2/N_1 can be readily determined from the result (eq. [54] by Axford 1972) to be

$$\frac{N_2}{N_1} = \left(\frac{b_2}{b_1}\right)^2 \exp\left[-\frac{\beta_i r_0^2}{V_0}\left(\frac{2\pi - \theta}{|b_2|} - \frac{\theta}{|b_1|}\right)\right] . \quad (7)$$

Here β_i is the ionization rate and has the values 6×10^{-7} and 6×10^{-8} s^{-1} for H and He atoms,

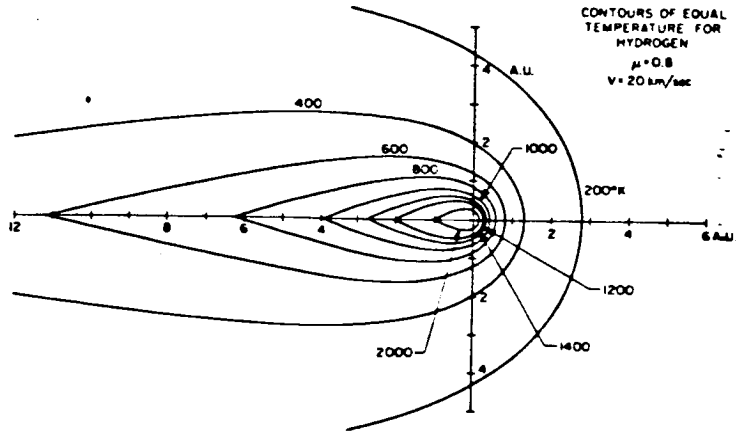

FIG. 1.—Equal temperature contours for neutral interplanetary hydrogen with $\mu = 0.8$, $V_0 = 20$ km s^{-1}. The Sun is located at the center of the diagram. The downwind direction is along the negative X-axis ($\theta = 180°$).

respectively. In the downwind direction ($\theta = 180°$) $b_1 = b_2$, and $N_2/N_1 = 1$. As the angle θ gets small, the ratio decreases. For H atoms, the ratio falls off quickly and is about 0.1 at $\theta = 175°$ and is already negligibly small (<0.02) at $\theta = 170°$. For He atoms however, the ratio decreases slowly. For example, at 1 AU, the ratio N_2/N_1 is 0.3 at $\theta = 140°$ and ~ 0.05 at $\theta = 90°$.

Thus it appears that for H atoms we need discuss only one temperature distribution T. For He atoms, however, two temperatures T_1 and T_2 are required to describe the distributions.

a) Hydrogen

Figure 1 shows the equal temperature contours for H atoms. It is clear that the temperatures increase as the hydrogen gets closer to the Sun, the source of heating. The contours also show long tails in the downwind direction, indicating the hottest region. Downwind the temperature is 600 K at 11 AU and continues to increase as r decreases. In the upwind direction the temperature is less than 500 K for $r \gtrsim 1$ AU. This temperature asymmetry results simply from the different amount of time available for interaction in the upwind and downwind directions.

At the orbit of the Earth the hydrogen temperature due to electron heating is about 500 K in the upwind direction and about 2000 K downwind. It is interesting to compare these temperatures with the temperature resulting from proton scattering. The results are given below.

Proton heating of hydrogen has been discussed by Fahr and Lay (1974). Fahr (1978), Wallis (1973, 1975), and Holzer (1977). Fahr (1978) estimated that the temperature increase at 1 AU from proton heating should be 2600 K upwind and 7000 K downwind. On the other hand, from Wallis's (1975) formula, we estimate that the temperature increase due to proton heating is about 270 K upwind and 1300 K downwind (for $\mu = 0.8$, $V_0 = 20$ km s^{-1}). Recently, Holzer (1977) has determined that the temperature increase is less than 300 K for $r \leq 1$ AU. Obviously, the amount of heating depends on the collision cross section chosen, as has not yet been unambiguously determined.

It may be noted that, because of charge exchange and photoionization processes, the neutral hydrogen densities are depressed in the vicinity of the Sun. However, the interplanetary temperatures reported so far have been inferred directly or indirectly from observations of the interplanetary glow. The importance of the gas element in determining the inferred interplanetary gas temperature depends not only on its density n but also on its volume emissivity Q. For hydrogen, the volume emissivity is proportional to n/r^2. Thus at small heliocentric distances, even though n is small, radiation from the heated gas can still be significant.

Using Blum's density equations and parameters (Blum, Pfleiderer, and Wulf-Mathies 1975), the maximum emissivity in the downwind direction occurs at about 1 to 2 AU at solar minimum and 4 AU at solar maximum. For the upwind direction, the maximum Q is also very close to the Sun, occurring at $r = 2$ AU or less. Therefore the temperature increase of hydrogen near the Sun is a significant effect and should be included in models of the interplanetary medium.

b) Helium

As noted, there are two temperatures T_1, T_2 associated with neutrals in interplanetary space corresponding to two different impact parameters, $b_1 > 0$ and $b_2 < 0$. For hydrogen, the possibility of observing two temperatures is negligible for most regions. But for helium atoms and $\theta > 90°$, the probability of detecting T_2 is not small. In Figures 2*a* and 2*b*, we thus show two sets of temperature contours for He atoms with $V_0 = 20$ km s^{-1}.

Comparing the two figures, we note that in the downwind direction temperatures T_1 and T_2 are equal. But in other directions, T_2 is higher than T_1. The difference between T_1 and T_2 at 1 AU and $\theta = 90°$

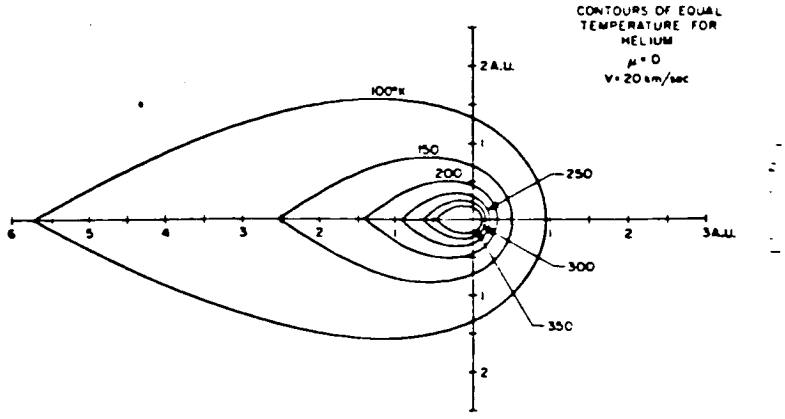

FIG. 2a

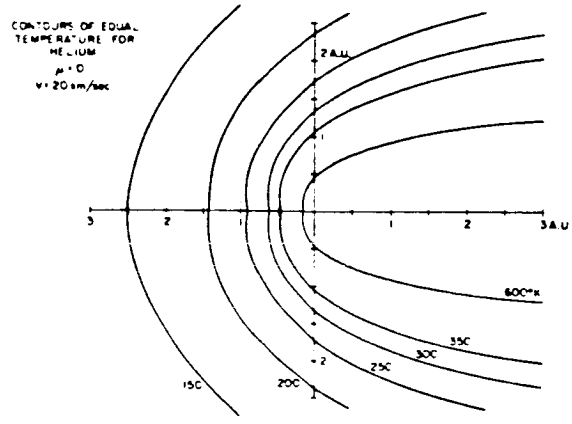

FIG. 2b

FIG. 2.—(*a*) Equal temperature contours for neutral interplanetary helium with $\mu = 0$ and $V_0 = 20$ km s^{-1} for impact parameter $b_1 > 0$. (*b*) Equal temperature contours for neutral interplanetary helium with $\mu = 0$ and $V_0 = 20$ km s^{-1} for impact parameter $b_2 < 0$.

is about 200 K, with the temperature T_2 being higher because of the longer interaction time for the indirect trajectory b_2.

It is clear that the temperature increase for He atoms due to electron heating is not as high as for H atoms. For hydrogen, the temperature can increase to 600 K at a distance as remote as 11 AU. But for helium, the temperature increase is less than 150 K until $r < 2.5$ AU, primarily because of the lower energy transfer rate, β (Table 1).

At Earth orbit, the present results indicate a temperature increase for helium due to electron heating of about 100 K upwind and 240 K downwind. And, according to Wallis (1975), the corresponding temperature increase due to proton heating is about 250 K upwind and 1100 K downwind. Thus electron heating may be a factor of 3 to 5 smaller than proton heating.

V. SUMMARY AND CONCLUSION

The energy transferred from solar electrons can increase the temperature of inflowing H gas at 1 AU by 500 K upwind and by 2000 K downwind, while for helium electron heating is less significant, producing a temperature increase at 1 AU of about 240 K downwind and 100 K upwind. It should be noted, however, that the actual temperature to be realized depends considerably on the rather poorly known low energy electron density at distances > 1 AU.

In the present calculation, we have assumed that the radial flow velocity for solar electrons is constant. Thus the electron density is proportional to $1/r^2$. But it is likely that the bulk flow velocity of the solar wind is decreasing with heliocentric distance because of the presence of ions of interstellar origin which can exert a frictional force on the solar wind flow (Wu and Hartle 1974; Thomas 1978). In such a case, the electron density should decrease more slowly than $1/r^2$. Moreover, electrons of Jovian origin, electrons from ionized interplanetary atoms, and the possible presence of electrons from the nearby interstellar medium would also increase the electron density and thus the heating of interplanetary gas in the solar system. Further, it has been suggested (e.g., Thomas 1978) that there is a region outside the heliosphere

consisting of hot solar wind plasma analogous to the Earth's magnetosheath. Thus the possibility that inflowing interstellar gas is heated as it passes through the heliospheric boundary must also be considered.

It is clear, however, that solar electron heating produces a temperature asymmetry in which the inflowing atoms are coldest in the upwind direction and hottest in the downwind direction. Thus a map of the interplanetary temperature distribution can determine the direction of the inflowing gas. Moreover, since the Sun is the source of heating, the temperatures of both hydrogen and helium increase significantly in its vicinity. A knowledge of the radial dependence of the interplanetary temperature can determine the amount of solar energy transferred to the neutral gas and hence permit the true nearby interstellar temperature to be determined. While Bertaux *et al.* (1976) have reported a direct temperature measurement, they did not comment on possible temperature gradients in interplanetary space due to local heating. A spacecraft mission with direct temperature mapping should prove to be useful and interesting. Such data are intimately related to the physical properties of the interplanetary neutral medium as well as the energy flux of the solar wind.

This work was supported by contract NAS2-6558 with the NASA Ames Research Center. We gratefully acknowledge helpful discussions with R. W. Carlson.

REFERENCES

Adams, T. F., and Frisch, P. C. 1977, *Ap. J.*, **212**, 300.
Axford, W. T. 1972, in *Solar Wind*, ed. C. P. Sonett, P. J. Coleman, and J. M. Wilcox (NASA SP-308), p. 609.
Bertaux, J. L., Blamont, J. E., Tabarie, N., Kurt, V. G., Bourgin, M. C., Smirnov, A. S., and Dementeva, N. N. 1976, *Astr. Ap.*, **46**, 19.
Blum, P. W., Pfleiderer, J., and Wulf-Mathies, C. 1975, *Planet. Space Sci.*, **23**, 93.
Fahr, H. J. 1974, *Space Sci. Rev.*, **15**, 483.
———. 1978, *Astr. Ap.*, in press.
Fahr, H. J., and Lay, G. 1974, *Space Res.*, **14**, 567.
Feldman, W. C., Asbridge, J. R., Bame, S. J., Montgomery, M. D., and Gary, S. P. 1975, *J. Geophys. Res.*, **80**, 4181.
Feldman, W. C., Montgomery, M. D., Asbridge, J. R., Bame, S. J., and Lewis, H. R. 1974, in *Solar Wind Three*, ed. C. T. Russel (Los Angeles: Institute of Geophysics and Planetary Physics, UCLA), p. 334.
Freeman, W. C., Paresce, F., Bowyer, S., and Lampton, M. 1976, *Ap. J.*, **208**, 747.
Gringauz, K. I., and Verigin, M. I. 1975, *Soviet Phys. Doklady*, **20**, 510.
Holzer, T. E. 1977, *Rev. Geophys. Space Phys.*, **15**, 477.
Leer, A., and Axford, W. I. 1972, *Solar Phys.*, **23**, 238.
McConkey, J. W., and Preston, J. A. 1975, *J. Phys. B.*, **8**, 63.
McDaniel, E. W. 1964, *Collision Phenomena in Ionized Gases* (New York: Wiley).
Milloy, H. B., and Crompton, R. W. 1977, *Phys. Rev. A*, **15**, 1847.
Srivastava, S., and Trajmar, S. 1976, *J. Chem. Phys.*, **64**, 3886.
Thomas, G. E. 1972, in *Solar Wind*, ed. C. P. Sonnett, P. J. Coleman, and J. M. Wilcox (NASA SP-308), p. 668.
———. 1974, proceedings of AIAA/AGU Space Science Conf. on Exploration of Outer Solar System.
———. 1978, *Ann. Rev. Earth Planet. Sci.*, **6**, in press.
Wallis, M. 1973, *Ap Space Sci.*, **20**, 3.
———. 1975, *Planet. Space Sci.*, **23**, 419.
Williams, J. F. 1975*a*, *J. Phys. B.*, **8**, 1663.
———. 1975*b*, *J. Phys. B*, **8**, 2191.
Wu, C. S., and Hartle, R. E. 1974, *J. Geophys. Res.*, **79**, 283.

D. L. Judge and F.-M. Wu: University of Southern California, Department of Physics, University Park, Los Angeles, CA 90007

Europa: Ultraviolet Emissions and the Possibility of Atomic Oxygen and Hydrogen Clouds

D. L. Judge, F. M. Wu, R. W. Carlson

Abstract presented at the Fall Meeting of the AGU, San Francisco, 1977

Emission signals of undetermined origin with $\lambda < 800$ Å from Europa were detected by the Pioneer 10 ultraviolet photometer[1]. In the present paper, using improved procedures for data reduction, we determine the region as well as the intensity of the suggested emission sources. The observations indicate a cloud with a radius of 1.5 Rj (Jupiter's radius) and apparent brightness of $\sim$10 Rayleighs, for a wavelength of 500 Å. It is argued that neutral oxygen atoms, along with neutral hydrogen are produced through dissociation of water ice on Europa's surface by particle impact with the observed emission being produced by electron impact ionization excitation of oxygen atoms in the resulting cloud. Using the present source brightness and radius results we estimate an oxygen column density of $\sim 10^{13}$ cm^{-2}, while the density of atomic hydrogen is $< 10^{11}$ cm^{-2} and 10^{12} cm^{-2} for molecular hydrogen.

1. Judge, D. L., Carlson, R. W., Wu. F. M. and Hartmann, U, G., 1976, in Jupiter, ed. T. Gehrels, Tucson, : University of Arizona press, p. 1068.

Electron Heating of Inflowing Interstellar Gas

F. M. Wu, D. L. Judge

Abstract presented at the Fall Meeting of the AGU, San Francisco, 1977.

The local interstellar gas moving through the solar system will encounter collisions with solar electrons and result in temperature increase. Because of the high electron flux and high collision cross section, such electron heating of interstellar gas can be significant. In the present work it is assumed that the thermal energy of the electrons is constant with distance from the sun (with E $\sim$10 eV) and that the inflowing gas follows Keplerian trajectories and the contours of constant temperature so obtained are given. At a heliocentric distance of 1 A. U. the estimated temperature is 1000 ^{o}K upwind and 3000 ^{o}K downwind for hydrogen atoms, and is 200 ^{o}K downwind and 90 ^{o}K upwind for helium.

THE ASTROPHYSICAL JOURNAL, 231:594–605, 1979 July 15
© 1979. The American Astronomical Society. All rights reserved. Printed in U.S.A.

TEMPERATURE AND FLOW VELOCITY OF THE INTERPLANETARY GASES ALONG SOLAR RADII

F. M. WU AND D. L. JUDGE
Department of Physics, University of Southern California
Received 1978 May 24; accepted 1979 January 17

ABSTRACT

The velocity distributions along solar radii for hydrogen and helium in interplanetary space are calculated by using the Danby-Camm formula modified with a loss function. From these distributions the radial temperature and radial flow velocity of the interplanetary gases are determined. The effects of solar gravitation and ionization loss, due to charge exchange and photoionization, on the gas temperature and velocity are described.

Subject headings: interplanetary medium — interstellar: matter

I. INTRODUCTION

Danby and Camm (1957) studied the motion of a cloud of gas particles in the gravitational field of a point mass and found an analytical formula for the distribution function in terms of the phase space volume element. By including a loss function to take into account the destructive effects of charge exchange and photoionization, the Danby-Camm distribution formula can apply to the interplanetary gas moving through the solar system (Wallis 1975; Meier 1977; Fahr 1978).

In this paper a version of the modified Danby-Camm formula was used to calculate the velocity distribution along solar radii for interplanetary hydrogen and helium. From the calculated distribution the radial temperature and flow velocity were determined. The radial velocity distribution is particularly important because such distributions determine the rate of absorption of solar lines by the interplanetary gas. The radial temperature and flow velocity must be considered in order to correctly compute the expected intensity distribution and line profile of the scattered interplanetary radiation along solar radii, as well as the attenuation and line profile of solar lines as the radiation proceeds through interplanetary space.

The radial temperature change of interplanetary helium produced by solar gravitational attraction has been calculated by Blum and Wulf-Mathies (1978), who used an expression requiring a triple numerical integration. In this paper we extend the calculation by including the effect of ionization loss and simplify the calculation by using a formula which involves only one single numerical integration. Moreover, we calculate the temperature of atoms in the indirect orbits as well as the temperature of atoms in the direct orbits. For hydrogen, the radial velocity distribution has not previously been studied.

It is noted that Fahr (1978) calculated the temperatures that characterize the velocity distributions perpendicular and parallel to the local tangent of the zero-order orbit of interplanetary helium at the distance of the Earth's orbit. However, the temperature and velocity that characterize the radial velocity distribution has not been calculated by Fahr. Recently, Wallis and Hassen (1978) calculated the radial temperature of the interplanetary helium by using a solution of Fokker-Planck equation. In this approach the velocity deviations from the mean are assumed small and may not be accurate for high-temperature ($T = 10^4$ K) interplanetary gas.

The velocity distribution functions will also be modified by elastic collisions between the inflowing gas and solar protons and electrons. Such collision processes have been considered previously by Wu and Judge (1978), Holzer (1977), Fahr (1978), and Wallace and Hassan (1978), and are excluded from the present work.

II. RADIAL VELOCITY DISTRIBUTION

For an interstellar gas with a bulk velocity V_b and a Maxwell-Boltzmann (M-B) velocity distribution of temperature T_0, the velocity distribution in interplanetary space can be written as (Danby and Camm 1957; Danby and Bray 1967; Meier 1977; Fahr 1978)

$$F = N_0(\pi^{1/2}V_t)^{-3}\exp(F_1 + F_2 \sin\psi)\,, \tag{1}$$

where

$$F_1 = -V_t^{-2}(V_b^2 + V_0^2 + 2V_0V_b\cos\theta) + 2V_t^{-2}V_0V_b\cos\theta\,\frac{(V_0 - V_r)^2}{V_0(V_0 - V_r) + Q^2} - \frac{\beta r_e^2\theta'}{rV_p}\,,$$

$$F_2 = 2V_t^{-2}V_0V_bV_p\sin\theta\,\frac{(V_0 - V_r)}{V_r(V_0 - V_r) + Q^2}\,,$$

$$Q^2 = (1 - \mu)GM_s/r\,, \qquad V_0 = (V_r^2 + V_p^2 - 2Q^2)^{1/2}\,,$$

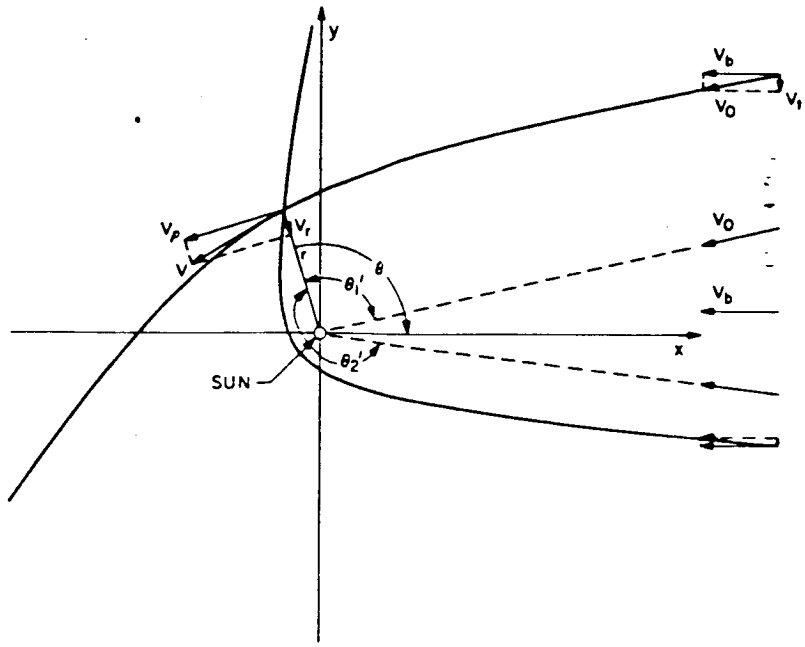

FIG. 1.—Examples of the interplanetary particle's orbits. A particle in the upper orbit (direct orbit) sweeps through an angle $\theta_1 \sim \theta - 17°$ while a particle in the lower orbit (indirect orbit) sweeps through an angle $\theta_2' \sim 353° - \theta$.

and

$$V_t = (2KT_0/m)^{1/2} .$$

Here G is the gravitational constant, M_s is the solar mass, μ is the ratio of radiation to gravitational force, m is the atomic mass, r_e is the distance from the Sun to the Earth's orbit (1 AU), β is the ionization rate at the Earth's orbit, N_0 is the particle density at infinity (density of the interstellar gas), and θ' is the angle swept out by an atom moving along a Keplerian trajectory (Fig. 1). The position of a point in space is specified by $(r\ \theta)$, where r is the distance from the Sun and θ is the angle with respect to the upwind direction $(0 \leq \theta \leq \pi)$. The velocity vector V is specified by cylindrical coordinates (V_r, V_ρ, ψ), with the rotational axis pointing along the r-direction.

In equation (1), the angle θ' varies with position r and velocity V. By solving the Keplerian equation, θ' can be simply expressed as

$$\theta' = \theta_0 \pm \theta_1 , \tag{2}$$

where the plus sign is for $V_r > 0$ and the minus sign is for $V_r < 0$; θ_0 is the perihelion angle of the hyperbolic trajectory,

$$\theta_0 = \tan^{-1}(-V_0 V_\rho / Q^2) , \qquad \pi/2 < \theta_0 < \pi$$

and

$$\theta_1 = \tan^{-1}\left\{\frac{[r_0/r_1 + 2r_0/r - (r_0/r)^2]^{1/2}}{r_0/r - 1}\right\} , \qquad 0 < \theta_1 < \pi$$

with

$$r_0 = rV_\rho^2/Q^2 , \qquad r_1 = Q^2 r/V_0^2 .$$

Using equation (1), the number of particles in the interval dV_r with radial velocity V_r at position r then can be explicitly expressed as

$$dN_r = N(r, V_r) V_t^{-1} dV_r , \tag{3}$$

where

$$N(r, V_r) = \pi^{-3/2} N_0 V_t^{-2} \int_{V_{\rho 0}}^{\infty} \exp(F_1) V_\rho dV_\rho \int_0^{2\pi} \exp(F_2 \sin\psi) d\psi \tag{4}$$

and

$$V_{\rho 0} = (2Q^2 - V_r^2)^{1/2} \quad \text{if } V_r < 2^{1/2} Q$$
$$= 0 \qquad \text{otherwise} .$$

Calculation of the radial velocity distribution thus appears to involve a double integration. However, the integration on ψ can be evaluated analytically by using a power series expansion (Danby and Bray 1967)

$$\int_0^{2\pi} \exp(F_2 \sin\psi)d\psi = 2\pi\left[1 + \frac{(0.5F_2)^2}{(1!)^2} + \frac{(0.5F_2)^4}{(2!)^2} + \frac{(0.5F_2)^6}{(3!)^2} + \dots\right] \quad \text{for } |F_2| \le 10$$

$$= \left(\frac{2\pi}{F_2}\right)^{1/2} \exp(F_2)\left[1 + \frac{1^2}{1!(8F_2)} + \frac{1^2\cdot 3^2}{2!(8F_2)^2} + \frac{1^2\cdot 3^2\cdot 5^2}{3!(8F_2)^3} + \cdots\right] \quad \text{for } |F_2| > 10 . \qquad (5)$$

Only the infinite integral over V_ρ must be integrated numerically and is discussed below.

The infinite integral I was calculated by successively evaluating the subintegral I_n over the interval $V_{\rho_0} + (n-1)d < V_\rho < V_{\rho_0} + nd$, with $n = 1, 2, \dots, M$ and then summing the I_n's. I_n is integrated by using a 16-point Gaussian quadrature formula. The value of M is so chosen that the last subintegral I_M is less than $10^{-2}I$. And the mesh d is chosen so small that the resulting values for the integral I using two different mesh values, d and $2d$, agree to at least $10^{-2}I$. For the case of the interplanetary gases with $T = 10^4$ K, we found that the parameters with $d = 4V_t$ and $M = 4$ satisfy the above criteria reasonably well.

The reasonableness of the calculation of $N(r, V_r)$ may be checked by comparing the present values of the volume density given by

$$N(r) = V_t^{-1}\int N(r, V_r)dV_r \qquad (6)$$

with those given by Thomas (1978) (Table 1). The results agree to two significant figures for most cases even though Thomas's (1978) density calculation is integrated over the velocity at infinity, while our calculation is integrated over the velocity distribution locally. The good agreement suggests the accuracy of our calculation of $N(r, V_r)$.

TABLE 1

COMPARISON OF THE INTERPLANETARY GAS DENSITY CALCULATED IN THE PRESENT WORK AND BY THOMAS (1978)

	Hydrogen Density (cm^{-3})		Helium Density (cm^{-3})	
r(AU)	This Paper	Thomas	This Paper	Thomas
		$\theta = 0°$		
1.....	0.0677	0.0690	0.830	0.861
2.....	0.220	0.221	0.900	0.900
4.....	0.436	0.437	0.927	0.931
7.....	0.606	0.605	0.949	0.952
10.....	0.697	0.696	0.960	0.963
50.....	0.924	0.992	0.989	0.992
		$\theta = 90°$		
1.....	0.0295	0.0300	0.942	0.948
2.....	0.127	0.128	0.958	0.963
4.....	0.310	0.311	0.961	0.965
7.....	0.484	0.483	0.964	0.968
10.....	0.588	0.587	0.967	0.971
50.....	0.886	0.884	0.986	0.989
		$\theta = 180°$		
1.....	0.00218	0.00224	5.05	5.09
2.....	0.0194	0.0197	4.59	4.62
4.....	0.0846	0.0853	3.90	3.92
7.....	0.190	0.191	3.31	3.33
10.....	0.280	0.280	2.96	2.97
50.....	0.704	0.703	1.77	1.77

NOTE.—The parameters used in the hydrogen density calculation are $n_0 = 1\ cm^{-3}$, $v_b = 20\ km\ s^{-1}$, $\beta = 5 \times 10^{-7}\ s^{-1}$, $\mu = 0.75$, and $T = 10^4$ K; while the parameters for helium are $n_0 = 1\ cm^{-3}$, $V_b = 20\ km\ s^{-1}$, $\beta = 7.5 \times 10^{-8}\ s^{-1}$, $\mu = 0$, and $T = 10^4$ K.

It should be noted that in the above distribution function (eq. [1]) we expressed the particle velocity V in cylindrical coordinates (V_r, V_ρ, ψ), in contrast with the usual Danby-Camm spherical coordinates. The use of a cylindrical coordinate system allows the density to be expressed explicitly as a function of V_r and r and can greatly simplify the computation of the radial temperature and velocity for the interplanetary gas. As noted by Wallis and Hassen (1978), the distribution functions developed by Meier (1977) and Fahr (1978), are of limited use because deriving physical observables requires lengthy computations.

As an immediate application of the above distribution function $N(r, V_r)$ the absorption coefficient $\alpha_\nu(r)$ for the solar line at frequency ν can be calculated (Wu and Judge 1979). The result is given by

$$\alpha_\nu(r) = \alpha_0 N(V_r, r)\,, \tag{7}$$

where

$$\alpha_0 = \frac{1}{V_t}\left(\frac{\pi e^2}{mc} f\lambda_0\right), \tag{8}$$

and V_r is related to ν by

$$\nu = \nu_0 + \frac{V_r}{c}\nu_0\,. \tag{9}$$

The emission profile for the interplanetary glow along solar radii at position r_0 then can be simply expressed as

$$I_\lambda(r_0)d\lambda = \pi F_\lambda d\lambda \int_{r_0}^{\infty} \alpha_\nu(r)P(\gamma)dr\,, \tag{10}$$

where πF_λ is the solar flux at wavelength λ, P is the phase function, and γ is the angle between the emission direction and the various solar radii, which is 180° for our cases. And the emission intensity integrated over wavelength is

$$I(r_0) = \int I_\lambda(r_0)d\lambda\,. \tag{11}$$

The detailed results for I_λ and I will not be presented in this paper. However, to further indicate the accuracy of our calculation of $N(r, V_r)$, we show in Figure 2 two of the emission profiles I_λ in comparison with those of Meier (1977). Meier's results are calculated by directly using the Danby-Camm formula without any further simplification. We also use the Danby-Camm formula, but simplified by expressing the distribution function in terms of radial velocity. The comparison of our emission profiles with Meier's shows general agreement. As a practical matter, it is also worth noting that the computer time for obtaining a single line profile and its integrated intensity in a particular direction is between 20 and 60 minutes on a CDC 1604 computer using Meier's (1977) formula, but requires less than 4 minutes on an IBM 370/158 by using the present formula. This provides further evidence that the present calculation is not only accurate but also simple and efficient.

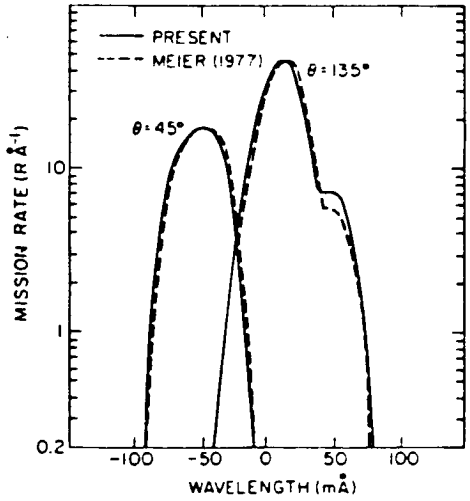

FIG. 2.—Emission line profiles of interplanetary helium at the distance of the Earth's orbit and at angles of 45° and 135° from the upwind direction. The viewing direction is taken to be the antisolar direction. The physical parameters used here are V_0 = 20 km s^{-1}, $T = 10^4$ K, $\beta = 6.8 \times 10^{-8}$ s^{-1} atom^{-1}, and $n_0 = 0.01$ cm^{-3}. The solar flux at He 584 Å line is assumed to be Gaussian with a full line width at half-maximum intensity of 0.12 Å and with a line center intensity of 10^{-9} photons cm^{-2} s^{-1}.

III. RADIAL TEMPERATURE OF HYDROGEN

In Figure 3 we show the calculated velocity distribution $N(r, V_r)$ of hydrogen along with a fitted M-B distribution at a distance of 1 AU for various angles. The parameters used in our calculations are $T_0 = 10^4$ K, $V_0 = 20$ km s^{-1}, $\beta = 5 \times 10^{-7}$ s^{-1}, and $\mu = 0.75$ (Thomas 1978). It is seen that the M-B distribution for specific temperature fits the calculated velocity distribution very well. Thus, the characteristic temperature, T, for the radial velocity distribution can be simply evaluated by using the fact that for a M-B distribution

$$T = \frac{m}{2K}\left(\frac{\Delta V_{1/2}}{1.665}\right)^2, \tag{12}$$

where $\Delta V_{1/2}$ is the full line width at half-maximum (FWHM) of the distribution.

It may be noted that, for every position in space, the neutral particles are composed of two different families, one with swept angle θ' less than 180° (direct orbit) and another with θ' larger than 180° (indirect orbit) (Blum and Wulf-Mathies 1978) (Fig. 1). However, the number of hydrogen atoms decreases rapidly as the swept angle θ' increases because of the high ionization rate. For most regions, the contribution from the family of indirect orbits to the density distribution could be neglected (Wu and Judge 1978). And for the region ($\theta > 170°$) where the number of particles from indirect orbits may be significant, the mean radial velocities of direct and indirect orbits are not much different. Thus, the hydrogen distribution shown in Figure 3 always appears with a single peak.

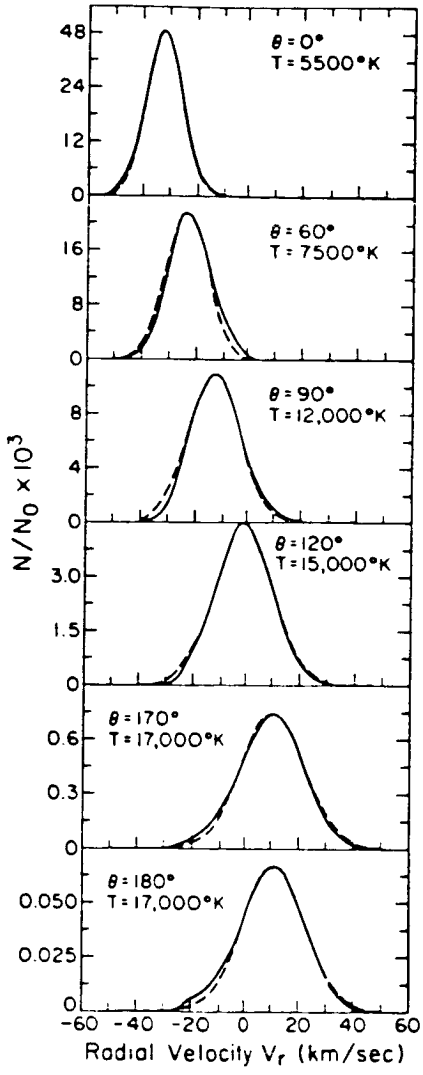

FIG. 3.—The radial velocity distribution of hydrogen at the Earth's orbit. The solid curve is the distribution calculated from eq. (4) with $T_0 = 10^4$ K, $V_0 = 20$ km s^{-1}, $\beta = 5 \times 10^{-7}$ s^{-1}, and $\mu = 0.75$. The dashed curve is the fitted M-B distribution with temperature T. θ is the angle from the upwind direction.

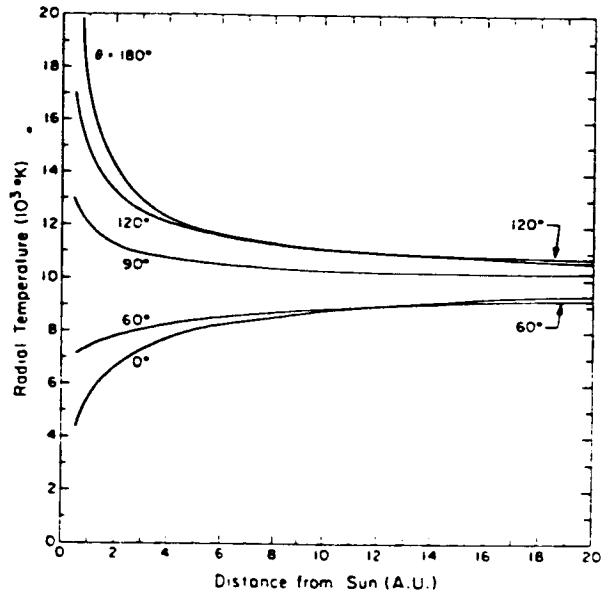

FIG. 4.—The radial temperature of hydrogen as function of the distance from the Sun for various angles θ

Using equation (12) and the value $\Delta V_{1/2}$ determined from the distribution function $N(V_r)$, the radial temperature of hydrogen as a function of position (r, θ) is shown in Figure 4. It is seen that, for θ small (upwind), the temperature of hydrogen decreases as it comes close to the Sun, but for $\theta = 90°$ and larger, the temperature increases as the distance decreases. For all angles, the temperatures at large distance are converging to $T = 10^4$ K, the assumed temperature at infinity.

In general, the interplanetary temperature gradient is caused by two factors: (1) the action of gravity and (2) the effect of ionization loss. In the upwind direction the ionization loss of hydrogen is small and the cause of the temperature gradient is mainly due to the action of solar gravity. But for other directions, the dominant factor that determines the velocity dispersion appears to be ionization loss. This is evident from the fact that the maximum temperature increase is at $\theta = 180°$ where the effect of ionization loss is maximum. We note that if the gravitational force were the main cause of the temperature increase then the maximum temperature should be expected at perihelion ($90° < \theta < 130°$ for $0.5 < r < 20$ AU) where the mean radial velocity is zero (Blum and Wulf-Mathies 1978). However, our calculation indicates that there is no temperature maximum at perihelion. Thus, at large angles from the upwind direction the effect of the gravitational force on temperature is apparently smaller than the effect of ionization loss. The effect of the gravitational force on the temperature of hydrogen is small because the solar gravitational force is nearly balanced by radiation pressure.

The ionization loss does affect the interplanetary temperature, however, since the interplanetary atoms of finite temperature cover a large portion of velocity space. The atoms follow different trajectories and have different loss functions. Hence, the interstellar distribution function will be significantly altered as the atoms approach the Sun. In Figure 5, the radial velocity distributions at $\theta = 180°$ and $r = 1$ AU for three different loss rates are shown for comparison. For a low loss rate, $\beta = 1 \times 10^{-8}$ s^{-1}, the temperature at 1 AU is about 11,000 K and only about 1000 K above the local interstellar temperature. However, as β increases to 5×10^{-7} s^{-1}, the temperature increases to 17,200 K. The hydrogen temperature increase downwind is thus clearly due to ionization loss.

In our calculation of the hydrogen velocity distribution we assumed that the radiation pressure of solar photons on hydrogen atoms, and hence the value of μ (=0.75), does not depend on the hydrogen velocity. This assumption is valid because the depressed central region in the solar Lα line is broad and only weakly reversed. The line profile in the spectral region $\Delta\lambda = 0.12$ Å from the line center can be assumed to be flat with an error of less than 7% (White and Lemaire 1976; Thomas 1978). And the velocities of hydrogen atoms relative to the Sun for $r \geq 1$ AU are less than 30 km s^{-1} in most cases (except for $\theta \approx 0°$ and $r \leq 1.5$ AU). For hydrogen atoms of such low velocities, the Doppler shift from the line center is less than 0.12 Å and the possible variation in μ due to a nonuniform profile is less than $\Delta\mu = 0.05$. It is calculated that, for fixed θ and for hydrogen atoms with $\mu + \Delta\mu = 0.75 \pm 0.05$, the temperature differences are less than 500 K at $r \geq 1$ AU. Thus, it is evident that the velocity distribution is little affected by the weak variation in μ. At $r = 1$ AU and $\theta = 0°$, the hydrogen atoms have a relatively high velocity of ~ 35 km s^{-1} and experience a solar flux which is about 1.2 times larger than the solar flux at the line center, and $\mu = 0.9$. However, even for this case, the calculated temperature is only 900 K or about 16% above the temperature for $\mu = 0.75$. It should be noted that the real effect of a nonuniform profile on the velocity distribution is significantly less than the above estimate since the atoms experience a variable μ, 0.75 to 0.9, along their

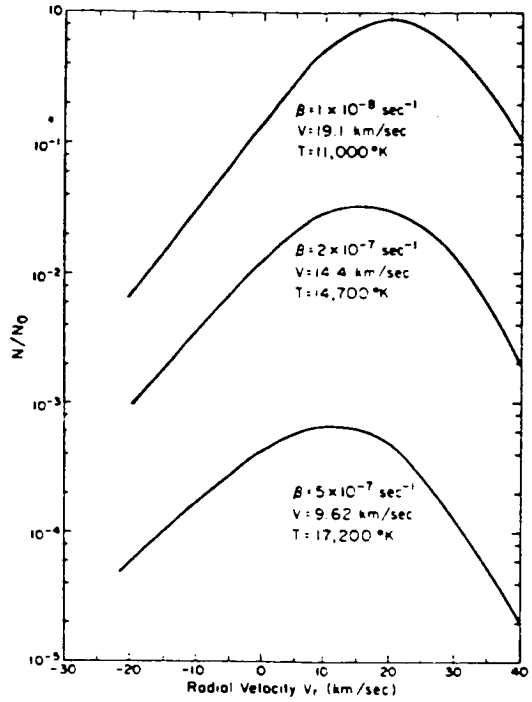

FIG. 5.—The radial velocity distribution of hydrogen for three different loss rates β. T and V are the values for the temperature and mean velocity of the indicated distributions.

trajectory. Thus, the flat profile and hence the absence of a μ dependence with respect to radial velocity, as assumed in our calculation, is quite reasonable.

It may be further noted that the radiation pressure is not constant with time because the solar Lα flux varies with solar activity. From the Vidal-Madjar (1975) measurements, the ratio of radiation pressure to solar gravity varies from 0.6 to 1. However, Thomas (1973) determined that the value of μ most likely exceeds 1. Moreover, the ionization rates of hydrogen and helium atoms are determined by the solar proton flux and solar EUV flux which are also time-dependent. The proton flux is found to vary from 3×10^8 to 2×10^8 cm^{-2} s^{-1} (Diodato, Moreno, and Signorini 1974), and the EUV flux could change by a factor of more than 2 in a single year (see Timothy 1977). The exact variation of flux density with solar sunspot number remains somewhat uncertain. The time-dependent model for interplanetary gases cannot completely be resolved unless our knowledge of solar emitted flux (both photon and particle flux) is greatly improved.

All current models for the motion of the interstellar gas in the solar system assume that μ and β are constant. It must be noted that although it may take more than 10 years for the interstellar gas to move through the solar system, the most significant time is the 2 years of approach to or departure from the Sun. During this time the atoms move through the 10 AU region in which most of the observed glow originates. This is because both solar gravity and flux vary as $1/r^2$ and the atoms at a large distance are little aware of the Sun's presence. The effective variation of μ and β for the hydrogen atoms may be of the order of $\Delta\mu \approx 0.1$ and $\Delta\beta = 0.2 \times 10^{-7}$ s^{-1}.

To see roughly that a constant μ and β cannot make a significant error in our results, we calculate the radial temperatures of atoms with different μ and β. For $r \geq 1$ AU, the results indicate that the temperature difference is less than 10% for atoms with $\Delta\mu = 0.1$ and is less than 5% for $\Delta\beta = 0.2 \times 10^{-7}$ s^{-1}. Hence we may conclude with some confidence that the uncertainty in our calculation of radial temperature due to the possible time variation of μ and β is $\sim$10%.

IV. RADIAL TEMPERATURE OF HELIUM

Using equation (4) and the parameters from Thomas (1978), $T_0 = 10^4$ K, $V_0 = 20$ km s^{-1}, $\beta = 7.5 \times 10^{-8}$ s^{-1}, $\mu = 0$, the radial velocity distribution for helium at a distance of 1 AU is calculated and shown in Figure 6. For $\theta \geq 90°$, atoms with both direct and indirect trajectories contribute to the density and the distribution must be described by two M-B distributions of two different temperatures. But for $\theta < 90°$ the family of indirect orbits correspond to large angular variations ($\theta' \approx 360° - \theta$) and the contribution to the density from such orbits becomes negligible, giving a single peak in the velocity distribution. It is also noted that for θ close to the downwind region ($\theta > 150°$), the distributions for direct and indirect orbits overlap and a single Maxwellian distribution defines the velocity distribution quite well.

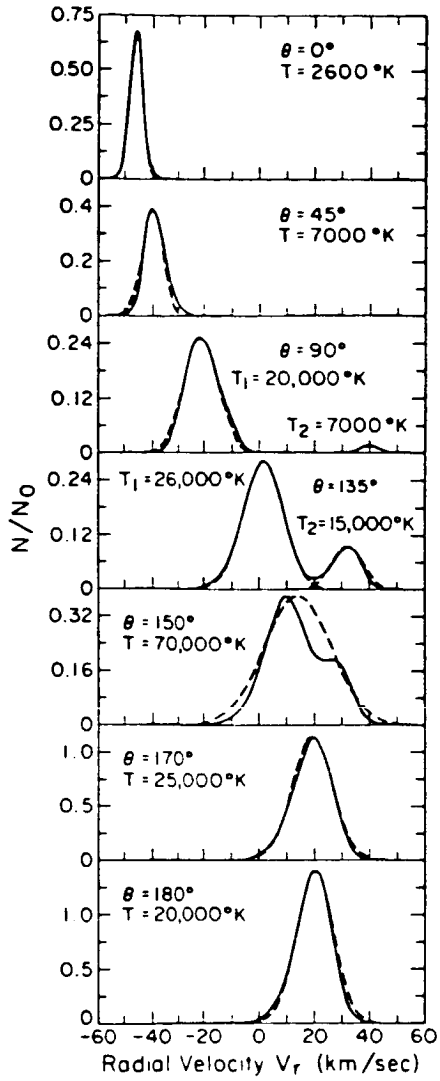

FIG. 6.—The radial velocity distribution of helium at the Earth's orbit. The solid curve is the distribution calculated from eq. (4) with $T_0 = 10^4$ K, $V_0 = 20$ km s^{-1}, $\beta = 7.5 \times 10^{-8}$ s^{-1}, and $\mu = 0$. The dashed curves are the fitted M-B distributions.

The ionization loss process, because of its low rate, is expected to have little effect on the helium temperature except in the downwind region. On the other hand, since the gravitational effect is not balanced by radiation pressure, the helium temperature is significantly altered by it. Moreover, the distribution resulting from indirect trajectories also causes some temperature variation for helium. The temperature distribution for helium is shown in Figure 7 and is discussed below.

As for hydrogen, the helium temperature in the upwind region has its lowest values and approaches 10^4 K at large distances. But, in contrast to hydrogen, the maximum helium temperature is not in the downwind direction, $\theta = 180°$, but at $\theta = 150°$. At $\theta \sim 150°$, it happens that the contributions to the density by the family of indirect orbits is not small and portions of the distribution from indirect orbits overlap those of direct orbits (see Fig. 6) and thus cause a significant velocity spread and an effective temperature increase.

For the region far away from the downwind direction, the velocity distributions of direct and indirect orbits are separated. Thus, the temperature of particles in indirect orbits, in addition to the temperature of the particles in direct orbits, is required to describe the distribution. These are shown in Figure 7, for $\theta = 90°$ and 135° (*dashed lines*). It is seen that the temperature of indirect orbit particles is always less than the temperature of those in direct orbits. In Figure 7, the temperatures associated with indirect orbits are shown for only a limited spatial range, since at large distance the distributions for indirect and direct orbits overlap. A single temperature defined by equation (12) adequately describes the combined distributions of both orbits.

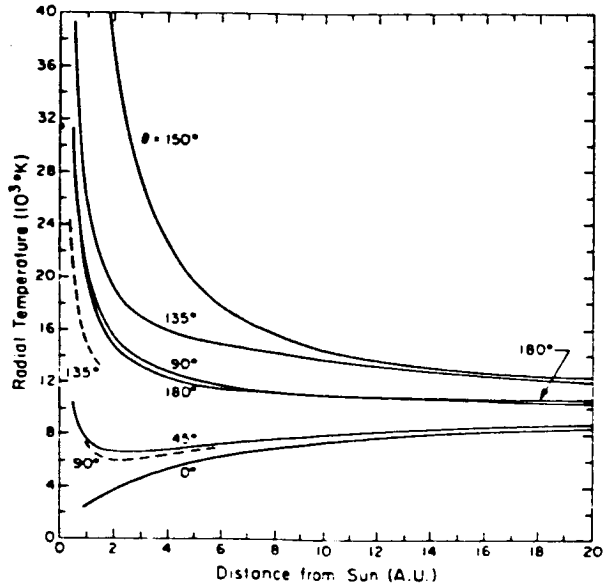

FIG. 7.—The radial temperature of helium as a function of distance from the Sun for various angles θ. *Solid curve*, temperature for the primary distribution (contributed mainly by the atoms with direct orbits). *Dashed curve*, temperature for the secondary distribution (contributed by the atoms with indirect orbits).

Blum and Wulf-Mathies (1977) have determined the radial temperature for helium in the absence of ionization. Their numerical values for small angles agree with ours. For example, at $\theta = 0°$ they find helium temperatures of 2800 K and 6800 K at $r = 1$ AU and 10 AU, respectively, while our values are 2600 K and 7500 K—the agreement is within 10%. However, at large angles the values from Blum and Wulf-Mathies are different from ours. At a distance of 1 AU they find $T = 16{,}000$ K at $\theta = 180°$ and $T = 25{,}000$ K at $\theta = 150°$, while our values are 20,000 K and 70,000 K, respectively. The differences are caused by the fact that Blum and Wulf-Mathies do not include the effects of the ionization loss function and the distribution of the indirect orbits in calculating the helium temperature. This leads to an underestimate of the temperature in the downwind direction.

V. RADIAL TEMPERATURE AT THE EARTH'S ORBIT

The radial temperatures of hydrogen and helium at 1 AU as a function of angle θ are shown in Figure 8 for comparison. It is seen that the hydrogen temperature is 5500 K upwind and increases to 17,000 K downwind. The helium temperature is 2600 K upwind, increases to 70,000 K at $\theta = 150°$, and decreases to 20,000 K downwind. Thus, the helium temperature deviates more significantly from the assumed interstellar temperature of $T = 10^4$ K than does that of hydrogen. The fact that there is negligible radiation pressure on helium ($\mu \sim 0$) while for hydrogen the ratio of radiation pressure to gravitational attraction is $\mu \sim 0.75$ accounts for the difference. Hence, the gravitational effect on the velocity distribution is larger for helium than hydrogen. As noted earlier, the hydrogen temperature is increased significantly by ionization. However, it is apparently smaller than the temperature increase of helium due to gravitational attraction.

In Figure 8 we also show (*dashed line*) the temperature of the secondary distribution from the indirect orbits for $90° < \theta < 140°$. As was noted, the secondary temperature is always less than the temperature of the direct orbit particles. Moreover, the indirect orbits, because of the large angular sweep, are less populated and hence less physically significant than the direct particles.

The most notable feature in Figure 8 is the sharp helium temperature maximum at 150° caused by the distribution overlap; the maximum temperature is about 70,000 K, a factor of 25 larger than the temperature of helium (2600 K) in the upwind direction. Thus, for a viewing direction outward from the Sun, the interplanetary helium width is quite wide (FWHM ≈ 0.05 Å for $T = 70{,}000$ K) for $\theta \approx 150°$, while the line width near the upwind direction is narrow.

VI. RADIAL FLOW VELOCITY OF HYDROGEN

Using the velocity distribution function $N(r, V_r)$, the radial flow velocity of interplanetary gas at any position r can be calculated from

$$\bar{V}_r = \int V_r N(r, V_r) dV_r \Big/ \int N(r, V_r) dV_r \,. \tag{13}$$

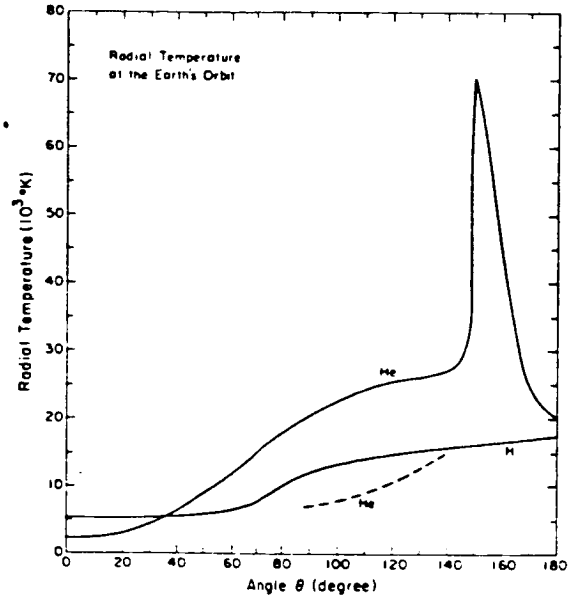

FIG. 8.—The radial temperature of hydrogen and helium at the distance of the Earth's orbit. *Solid curve*, temperature for the primary distribution; *dashed curve*, temperature for the secondary distribution.

For T_0 very low, the flow velocity may be computed from

$$\overline{V}_r = (N_1 V_1 + N_2 V_2)/(N_1 + N_2)\,, \tag{14}$$

where N_1, N_2 and V_1, V_2 are the densities and velocities for the direct and indirect trajectories of a cold gas and can be evaluated simply from the expressions by Axford (1972). As was noted for hydrogen, the density N_2 for the indirect trajectory is very low and the above equation reduces to $\overline{V}_r = V_1$.

The flow velocities for $T = 10^4$ K and $T = 0$ K are shown in Figure 9. The difference in the flow velocities for hydrogen atoms at different temperatures is apparent. At the Earth's orbit, the flow velocity of 10^4 K hydrogen atoms is lower than the velocity of those at 0 K by 3 km s^{-1} upwind and 10 km s^{-1} downwind. At large distance, the velocity difference decreases but still amounts to 1 km s^{-1} upwind and 3 km s^{-1} downwind at $r = 10$ AU. From Figure 9, it is clear that atoms with $T_0 = 10^4$ K always have a lower velocity than atoms with $T_0 = 0$ K.

The fact that the radial velocity of high-temperature hydrogen is significantly lower than that of low-temperature hydrogen is caused by the high ionization rate. This is evident from the velocity distributions shown in Figure 5. When the loss rate β is small ($\beta = 10^{-8}$ s^{-1}), the radial velocity for $T = 10^4$ K is 19 km s^{-1}, close to the velocity of 20 km s^{-1} for $T = 0$ K. But, as the loss rate increases, the radial velocity decreases. The velocity is 14 km s^{-1} for $\beta = 2 \times 10^{-7}$ s^{-1} but is only 9.6 km s^{-1} for $\beta = 5 \times 10^{-7}$ s^{-1}. The dependence of the radial velocity on the ionization loss process is explained as follows.

Hydrogen atoms at $T = 0$ K have only one trajectory for each spatial position, and the mean velocity $\overline{V}$ is the particle velocity. But as the temperature is increased, the deviation of individual particle velocities from the mean velocity $\overline{V}$ increases and becomes omnidirectional. We note that the angle θ' swept out by the particle depends on the direction of the particle velocity. This angle is 0° for a trajectory opposite the r direction but is 360° for a trajectory along the r direction. In general, the angle swept out by the atoms will increase as the angle between the trajectory direction and the radius r decreases. Thus, particles with large radial velocity V_r at position r are preferentially destroyed since the probability of ionization is larger for these particles than for particles with a small radial velocity. The mean radial flow velocity of atoms with finite temperature is thus reduced. The depletion effect is most profound in the downwind direction and at small distances where the ionization effect is maximized.

Recently, Adams and Frisch (1977) have measured the Doppler shift of the interplanetary Lα signal and determined an inflow velocity of $V_b = 22 \pm 3$ km s^{-1}. However, an error may exist in the inflow velocity which they have determined since modification of the bulk velocity through velocity-dependent ionization loss was not considered. As we have calculated, the radial velocity in the upwind direction can be depleted by as much as 3 km s^{-1} due to this effect. We note, however, that the viewing direction in Adams and Frisch's observation was upwind, about 50° from the radial direction, while our radial velocity calculations apply only to observations along the radial direction. Thus, the exact correction to the inflow velocity of Adams and Frisch requires that the present results be generalized to include nonradial components in order to calculate the expected Doppler profile for their field of view.

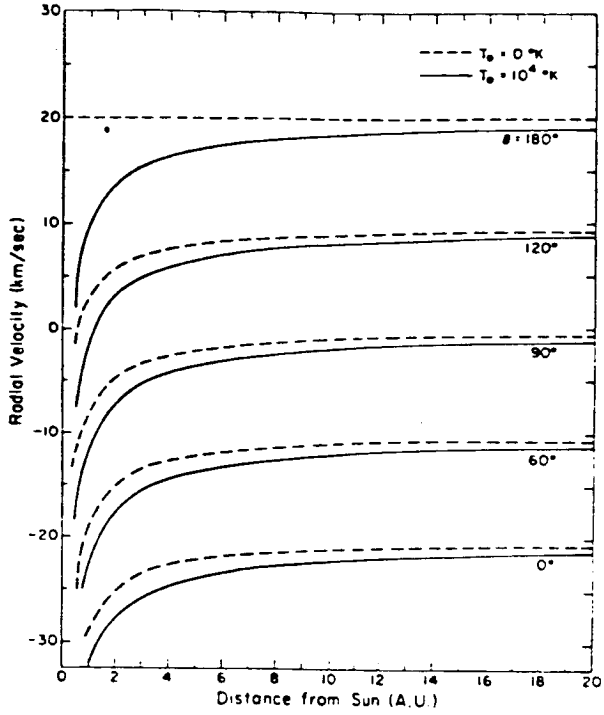

FIG. 9.—The radial velocity of hydrogen. The solid curves are the velocities for $T_0 = 10^4$ K, and the dashed curves are for $T_0 = 0$ K.

VII. RADIAL FLOW VELOCITY OF HELIUM

The radial flow velocity of helium at 10^4 K calculated from equation (13), and the velocity at 0 K calculated from equation (14), are shown in Figure 10. It is clear that the radial velocity for helium does not depend on temperature except near $\theta = 180°$. However, even at $\theta = 180°$ and at a distance 1 AU, the velocity of 10^4 K particles is only about 1 km s^{-1} lower than the velocity of those at 0 K. Thus, although the solar gravitational force can significantly modify the bulk velocity of the inflowing interplanetary helium, the amount of modification is independent of the assumed "interstellar" temperature. And the low ionization loss rate produces little effect on the radial velocity of helium.

VIII. SUMMARY

In this paper we have calculated the temperatures and flow velocities that characterize the radial velocity distributions of the interplanetary gas. At a distance of 1 AU, the hydrogen radial temperature is found to vary from 5500 K to 17,000 K while the helium temperature varies from 2600 K to 70,000 K depending on the angular position from the interstellar wind direction. In general, the temperature gradient for the hydrogen atoms results from velocity-dependent ionization loss and solar gravitation, but for helium the variation is caused primarily by the solar gravitation only. The effect of ionization loss on the helium temperature is small, except in the downwind direction.

The radial temperature determined here assumes that the interstellar temperature is $T_0 = 10^4$ K. The actual interplanetary temperature will be higher or lower, depending on the true value of T_0. However, the results do show that the interplanetary temperature is indeed highly asymmetric. Local heating from solar electrons and protons (Wu and Judge 1978) will in general increase the asymmetry.

The radial flow velocity of helium is found to be independent of the assumed interstellar temperature. On the other hand, the flow velocity of hydrogen varies significantly with interstellar temperature due to its large loss rate. The radial flow velocity of hydrogen at 10^4 K is shown to be lower than the velocity of 0 K hydrogen by as much as 10 km s^{-1} downwind and 3 km s^{-1} upwind, at a distance of 1 AU.

The velocity distribution perpendicular to the radial direction was not calculated in this paper but is expected to be different from the distribution along the radial direction. As we note, the gravitational force is a conservative force and cannot change the internal energy of the interplanetary gas. To conserve the internal energy, interplanetary gas with a high radial temperature must have a low temperature in the orthogonal direction, while a gas of low radial temperature will have a high orthogonal temperature. On the other hand, the ionization loss effect, due to its velocity-dependent ionization rate, can change the internal energy of the interplanetary gas. A complete description for the interplanetary gas temperature requires that the present calculation be extended to include nonradial velocity distributions.

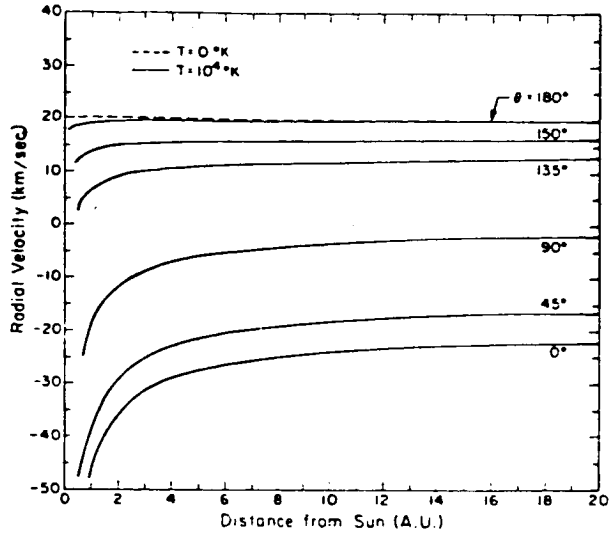

FIG. 10.—The radial velocity of helium. The solid curves are the velocities for $T_0 = 10^4$ K, and the dashed curves are for $T_0 = 0$ K. For all angles except $\theta = 180°$, the solid and dashed curves overlap.

This work was supported by contract NAS2-6558 with the NASA Ames Research Center.

REFERENCES

Adams, T. F., and Frisch, P. C. 1977, *Ap. J.*, **212**, 300.
Axford, W. I. 1972, in *Solar Wind*, ed. C. P. Sonett, P. J. Coleman, Jr., and J. M. Wilcox (NASA SP-308), 609.
Blum, P. W., and Wulf-Mathies, C. 1978, *Space Research*, **18**, 389.
Danby, J. M. A., and Bray, T. A. 1967, *A.J.*, **72**, 219.
Danby, J. M. A., and Camm, G. L. 1957, *M.N.R.A.S.*, **117**, 50.
Diodato, L., Moreno, G., and Signorini, C. 1974, *J. Geophys. Res.*, **79**, 5095.
Fahr, H. J. 1978, *Astr. Ap.*, in press.
Holzer, T. E. 1977, *Rev. Geophys. Space Phys.*, **15**, 467.
Meier, R. R. 1977, *Astr. Ap.*, **55**, 211.
Thomas, G. E. 1973, presented at AIAA/AGU Conf., *Exploration of Outer Solar System*, Denver.
Thomas, G. E. 1978, *Ann. Rev. Earth Planetary Sci.*, Vol. **6**, in press.
Timothy, J. G. 1977, in *The Solar Output and its Variation*, ed. D. R. White (Boulder: Colorado Associated University Press).
Vidal-Madjar, A. 1975, *Solar Phys.*, **40**, 69.
Wallis, M. K. 1975, *Planet. Space Sci.*, **23**, 419.
Wallis, M. K., and Hassen, H. A. 1978, *Planet. Space Sci.*, **26**, 111.
White, O. R., and Lemaire, P. 1976, LASP OSO Report, No. 2, University of Colorado, Boulder.
Wu, F. M., and Judge, D. L. 1978, *Ap. J.*, **225**, 1045.
———. 1979, *J. Geophys. Res.*, in press.

D. L. JUDGE and F. M. WU: University of Southern California, Department of Physics, University Park, Los Angeles, CA 90007

VOL. 84, NO. A3 JOURNAL OF GEOPHYSICAL RESEARCH MARCH 1, 1979

Modification of Solar Lines Propagating Through the Interplanetary Medium

F. M. WU AND D. L. JUDGE

Department of Physics, University of Southern California, Los Angeles, California 90007

The optical depths of the solar H Lyman α and the He 584-Å lines in interplanetary space are calculated. From these the solar line profiles at Saturn and Uranus are determined. It is found that the solar H Lyman α line can be diminished strongly within a spectral region of $|\Delta\lambda| < 0.2$ Å from the line center. On the other hand, there is no significant absorption of the He 584-Å line except in the downwind region where absorption occurs at $\Delta\lambda \sim 0.04$ Å. The effects of solar line modification on planetary and interplanetary glow observations are discussed.

INTRODUCTION

Solar H Lyman α and He 584-Å lines in interplanetary space can be depleted in parts of the line due to the absorption by interplanetary hydrogen and helium atoms. The depletion effect increases with radial distance and could become very significant at the distance of Saturn's orbit and beyond. Although *Thomas* [1972] and *Meier* [1977] have drawn attention to the possibility of solar line depletion, no detailed calculations have been made.

In this paper we calculate the optical depth of the solar lines in interplanetary space. From these results the solar line profiles at the orbits of Saturn and Uranus are determined. Knowledge of those line profiles is necessary to interpet accurately planetary and interplanetary H and He glow measurements.

COMPUTATIONAL METHOD

The local interstellar gas distribution is assumed to be Maxwell-Boltzmann with a temperature $T_0 \sim 10^4$ °K and a bulk velocity $V_b \sim 20$ km/s^{-1} [*Thomas*, 1978]. As the gas particles move from interstellar space into the solar system, the distribution function gradually changes owing to the effects of solar radiation pressure, gravitational attraction, and ionization loss.

The motion of a cloud of gas particles in the gravitational field of a point mass has been studied by *Danby and Camm* [1957], and they have given an analytical formula for the distribution function in terms of the phase space volume element. By including a loss function to take into account the destructive effects of charge exchange and photo-ionization the Danby-Camm distribution formula can be applied to the interplanetary gas moving through the solar system [*Meier*, 1977; *Wallis*, 1975].

With the velocity specified by cylindrical coordinates (V_r, V_ρ, ψ) (Figure 1) the velocity distribution of the gas particles at an interplanetary position (r, θ) is given by

$$F = N_0 [(\pi)^{1/2} V_t]^{-3} \exp (F_1 + F_2 \sin \psi) \tag{1}$$

where F_1 and F_2 are the analytic functions in terms of r, θ, V_r, V_ρ, and the interplanetary physical parameters V_b, T_0, β, μ_0, and N_0 [*Wu and Judge*, 1978; *Danby and Bray*, 1967]. Here r is the distance from the sun, θ is the angular position with respect to the upwind direction, β is the charge exchange and photo-ionization loss rate, μ is the ratio of radiation pressure to gravitational attraction, N_0 is the particle density at infinity (density of the interstellar gas), and V_t is the most probable speed at temperature T_0, given by

$$V_t = (2KT_0/m)^{1/2}$$

Accordingly, the density distribution as a function of the radial velocity and position is described by

$$dN_r = N(\mathbf{r}, V_r) V_t^{-1} \, dV_r \tag{2}$$

with

$$N(\mathbf{r}, V_t) = (\pi^{-3/2}) N_0 V_t^{-3} \cdot \int_{\rho_r}^{\infty} \exp (F_1) V_\rho \, dV_\rho \int_0^{2\pi} \exp (F_2 \sin \psi) \, d\psi \tag{3}$$

In the above formula the integral over ψ can be evaluated analytically by using a power series expansion, while the infinite integral over V_ρ is calculated numerically by using the Gaussian quadrature formula [*Wu and Judge*, 1978]. By using the above density distribution the absorption coefficient α_λ at wavelength λ (frequency ν) can be calculated from

$$\alpha_\lambda = \frac{\pi e^2 f}{mc} \frac{\gamma}{\pi} \int_{-\infty}^{\infty} \frac{N(\mathbf{r}, V_r) V_t^{-1} \, dV_r}{[\nu_0 - (V_r/c)\nu_0 - \nu]^2 + \gamma^2} = \alpha_0 \frac{\Gamma}{\pi} \int_{-\infty}^{\infty} \frac{N(\mathbf{r}, V_r) \, dV_r}{(X - V_r)^2 + \Gamma^2} \tag{4}$$

where ν_0 is the frequency at the line center, f is the oscillator strength, and γ is the natural line width [*Aller*, 1963]. For convenience we have made the substitutions

$$X = c(\nu_0 - \nu)/\nu_0 \qquad \Gamma = c\gamma/\nu_0$$

and

$$\alpha_0 = (\lambda_0/V_t)\left(\frac{\pi e^2}{mc} \cdot f\right)$$

For hydrogen and helium the factor Γ is very small ($\Gamma_H = 6.1 \times 10^{-3}$ km s^{-1}, $\Gamma_{He} = 8.4 \times 10^{-3}$ km s^{-1}), while the half width of $N(\mathbf{r}, V_r)$ is, in general, larger than 10 km/s [see *Wu and Judge*, 1978, Figures 1 and 5]. Thus the function

$$\delta(V_r) = \frac{\Gamma}{\pi} \frac{1}{(X - V_r)^2 + \Gamma^2} \tag{5}$$

is approximately a Dirac delta function, the major contribution to the integral in (4) arising from the region $V_r \sim X$. The absorption coefficient can thus be simply expressed as

$$\alpha_\lambda \sim \alpha_0 N(\mathbf{r}, X) \tag{6}$$

Finally, the transmitted intensity for solar radiation at distance r is

$$\pi F_\lambda(r) = \pi F_\lambda(r_0)(r_0^2/r^2) e^{-\tau_\lambda} \tag{7}$$

This paper is not subject to U.S. copyright. Published in 1979 by the American Geophysical Union.

Paper number 8A0829.

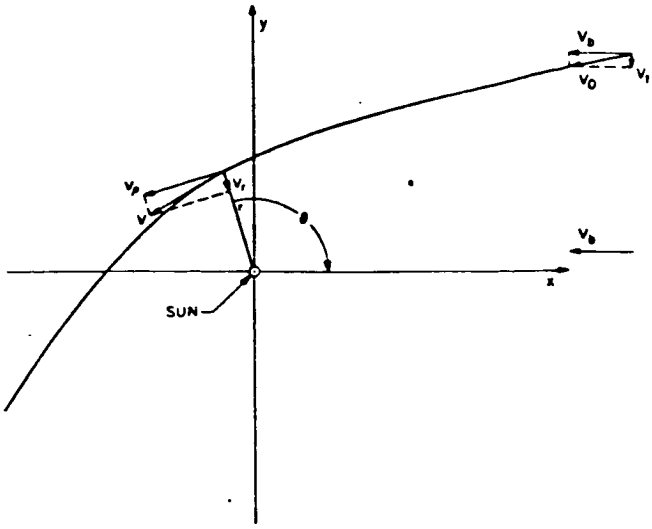

Fig. 1. The coordinate system for describing the distribution function of interplanetary gas.

where τ_λ is the optical depth at wavelength λ defined by

$$\tau_\lambda = \exp\left[-\alpha_0 \int_0^r N(\mathbf{r}, X)\, dr\right] \tag{8}$$

and $\pi F_\lambda(r_0)$ is the solar flux intensity at r_0, the earth's orbit.

SOLAR H LYMAN α LINE ABSORPTION

The radial velocity distribution function $N(\mathbf{r}, V_r)$ for hydrogen is calculated from (3) with $T_0 = 10^4$ °K, $V_b = 20$ km/s, $\beta = 5 \times 10^{-7}$ s^{-1}, $\mu = 0.75$, and $N_0(\mathrm{H}) = 0.1$ cm^{-3} [*Thomas*, 1978]. The variation of $N(\mathbf{r}, V_r)$ with interplanetary position has been studied in detail by *Wu and Judge* [1979], and the derived volume densities $N(\mathbf{r})$ agree well with those of *Thomas* [1978] in his Table 2*a*. By using the calculated $N(\mathbf{r}, V_r)$ the optical depth τ_λ for the H Lyman α line, as a function of wavelength, for various distances and angles is calculated from (8). The results are shown in Figure 2.

Since the radial velocity of the particles is negative upwind ($\theta = 0$) and positive downwind ($\theta = 180°$), the absorption of solar lines will occur in a spectral region of negative $\Delta\lambda$ upwind and of positive $\Delta\lambda$ downwind (Figure 2). For both the upwind and the downwind direction the Doppler shift of the wavelength from the line center $\Delta\lambda = 0$ is significant, and the optical depth at the line center is small. On the other hand, for $\theta = 90°$ the radial speed is not large, and the main absorption is near the line center.

The factor τ_λ will increase with distance because the number of atoms available for absorption is increasing. At $r = 3$ AU and less, the optical depth is small. But as r increases to 5 AU (Jupiter's orbit), the optical depth can approach $\tau \sim 0.1$, and

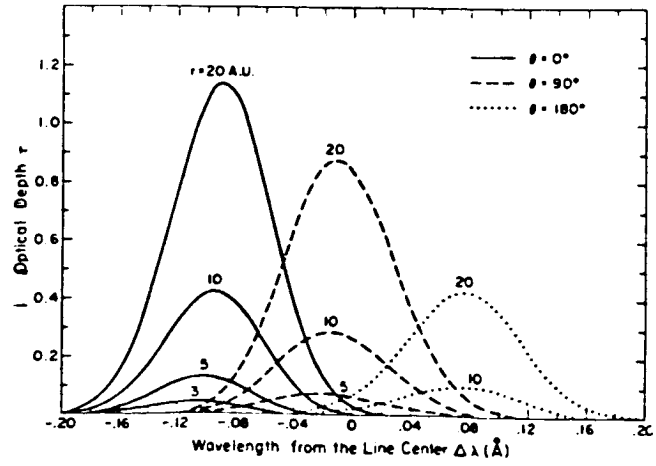

Fig. 2. Optical depth of the solar H Lyman α line in interplanetary space. The parameters used in the calculation are $T_0 = 10^4$ °K, $V_b = 20$ km/s, $\beta = 5 \times 10^{-7}$ s^{-1}, $\mu = 0.75$, and $N_0(\mathrm{H}) = 0.1$ cm^{-3}.

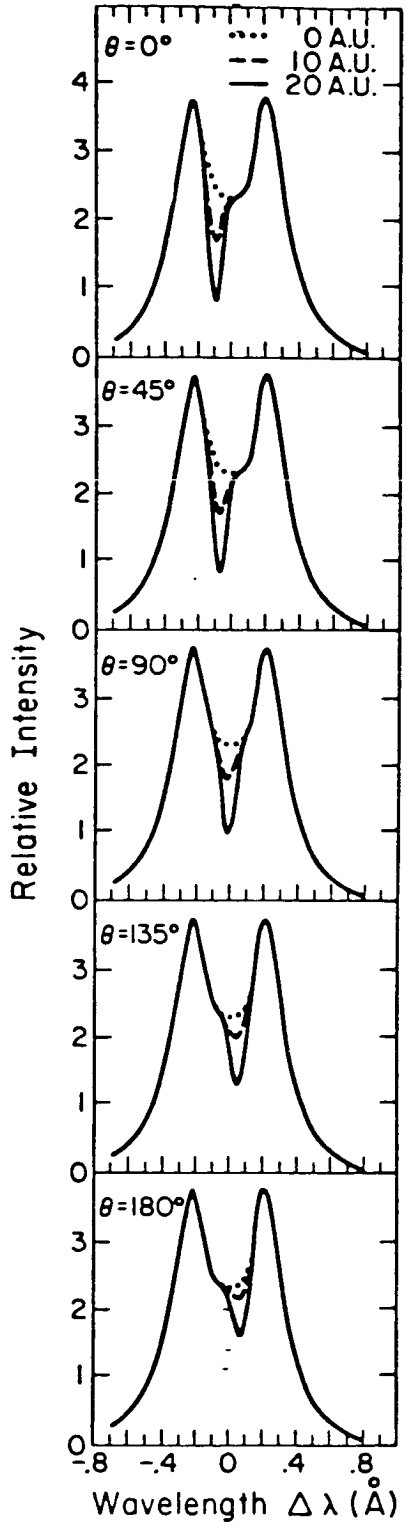

Fig. 3. Line profiles for the solar H Lyman α line at the orbits of Saturn and Uranus.

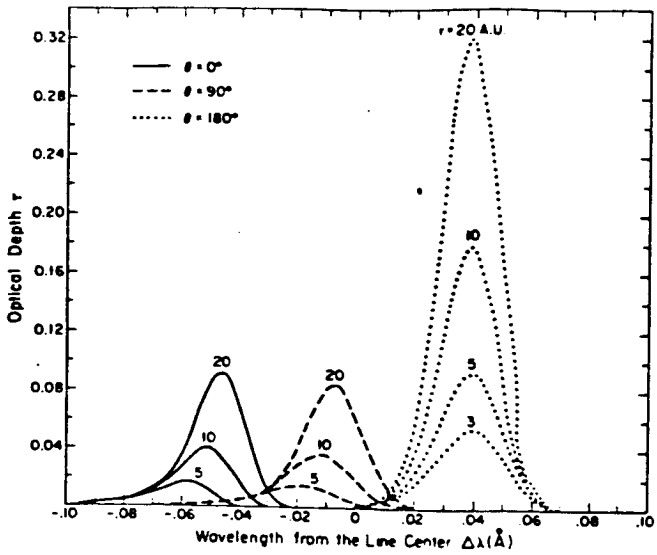

Fig. 4. Optical depth of the solar He 584-Å line in interplanetary space. The parameters used in the calculation are $T_0 = 10^4$ °K, $V_0 = 20$ km/s, $\beta = 7.5 \times 10^{-8}$ s^{-1}, $\mu = 0$, and N_0(He) = 0.01 cm^{-3}.

absorption starts to become important. For r = 10 AU and beyond, the optical depth becomes so large that the solar line profiles are significantly altered. The solar line profiles at a distance of 10 AU (Saturn's orbit) and 20 AU (Uranus' orbit) are shown in Figure 3 and are discussed below.

The solar H Lyman α line profile at the earth's orbit is from *White and Lemaire* [1976]. Since the optical depth at 1 AU is very small, the solar profile measured at the earth's orbit is the same as the unattenuated line profile emitted from the sun's surface. The line center is at 1215.67 Å, and the line width at half maximum is about 0.7 Å. Depression of this line at large distances through interplanetary gas absorption is, in general, over a very narrow region compared with the full solar line width.

As was noted earlier, the spectral region of absorption by the interplanetary gas shifts with the angular position of the particles owing to the change in their radial velocity. However, these narrow absorption features always occur within $|\Delta\lambda| <$ 0.2 Å from the line center and are within the broad minimum region of the solar line. It is further noted that at r = 10 AU the solar flux can be reduced by a factor of 1.1–1.5 owing to interplanetary absorption, depending on the angle from the upwind direction, while at r = 20 AU the reduction factor is from 1.5–3.1. The strong depression in part of the Lyman α line causes the line profile to appear as a composition of two separate spectral lines.

Since the airglow intensity produced by resonance scattering depends on the spectral intensity and profile of the solar line, depletion of the solar H Lyman α line will reduce the hydrogen glow intensity from the outer planets. It may be noted, however, that temperatures of the outer planets are low ($T \sim$ 100°K) and that the Doppler shift for the planetary H atoms is small. Thus the airglow intensity from such planets depends only on the solar intensity near the line center. The planetary glow will, accordingly, not be significantly reduced for planets located either downwind or upwind where the radial speed and the Doppler shift of the interplanetary gas is large.

It is also noted that depression of the solar intensity will reduce the radiation pressure of the interplanetary gas [*Thomas*, 1972]. For example, at θ = 0 a radiation pressure of μ = 0.75 on hydrogen atoms at r = 1 AU will reduce to μ = 0.5 at 10 AU and μ = 0.24 at r = 20 AU. The incoming and outgoing interstellar atoms at large distance are accordingly accelerated at a greater rate than those atoms near the sun. An assumption of constant radiation pressure will thus not accurately describe the motion of interplanetary atoms. In addition, the effect of multiple scattering on the interplanetary glow will become important as the optical depth of the solar line increases [*Thomas*, 1972] and further complicate the problem of interpreting interplanetary glow observations at large distances.

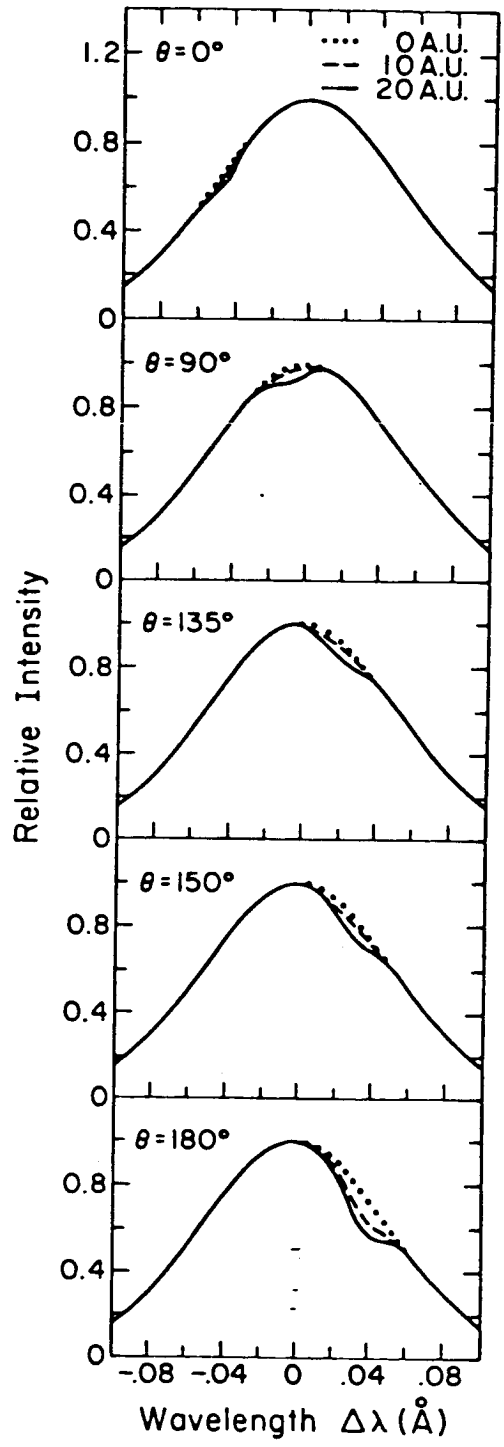

Fig. 5. Line profiles for the solar He 584-Å line at the orbits of Saturn and Uranus.

SOLAR HE 584-Å LINE ABSORPTION

The helium density in interstellar space is 0.01 cm^{-3}, only about 10% of the H atom density. Accordingly, depletion of the solar 584-Å line by interplanetary He absorption should be less profound than that for the H Lyman α line. However, because of the strong gravitational focusing, the helium concentration in the downwind direction is large and can cause a significant absorption effect [*Meir*, 1977].

In Figure 4 we show the optical depth τ of helium, calculated from (3) and (8), with the parameters V_0 = 20 km/s, T_0 = 10^4 °K, $\beta = 7.5 \times 10^{-8}\ s^{-1}$, $\mu = 0$, and N_0 = 0.01 cm^{-3}. It is shown that downwind, τ_λ can reach 0.18 at r = 10 AU and 0.32 at r = 20 AU. However, for other directions the optical depth is less than 0.1 for r < 20 AU. It is also noted that, similar to the case for hydrogen, the absorption spectral region for the solar helium line shifts with the angle θ, with a positive $\Delta\lambda$ downwind and a negative $\Delta\lambda$ upwind.

The line profile of the solar He 584-Å line resulting from interplanetary absorption at r = 10 and 20 AU is shown in Figure 5. Here, the unattenuated solar He profile is assumed to be Gaussian with a line width of 0.122 Å [*Maloy et al.*, 1978] and a line center at 584.33 Å. At r = 10 AU the interplanetary absorption has little effect on the line profile except downwind where the intensity is reduced by a factor of 1.2. At r = 20 AU the absorption effect increases, giving a reduction factor of 1.1 at θ = 90°, rising to 1.4 at θ = 180°.

Since attenuation of the He line at the line center is small, the helium resonances from Uranus and Saturn are affected little by the presence of the interplanetary helium. On the other hand, because of gravitational focusing, the interplanetary He glow downwind could be noticeably affected by interplanetary absorption.

SUMMARY

The optical depth of the 584- and 1216-Å solar lines in the local interplanetary region has been computed. It has been shown that the optical depth depends not only on the distance from the sun but also on the angular position of the gas with respect to the inflow direction. Moreover, the absorption spectral region can vary from a negative $\Delta\lambda$ downwind to a positive $\Delta\lambda$ upwind.

At the distance of Saturn and greater, the solar line profile for the Lyman α line is significantly altered because of interplanetary hydrogen absorption. The absorption region is close to the line center with $|\Delta\lambda|$ < 0.2 Å. For accurate interpretation of the hydrogen airglow observation of the outer planets, as well as the interplanetary glow at large distances, the effect of solar H Lyman α line modification must be included. On the other hand, the effect of the interplanetary helium absorption on the solar He line is small except downwind where absorption occurs at a wavelength shifted from the line center by $\Delta\lambda \sim 0.04$ Å.

Acknowledgments. This work was supported by NASA Ames Research Center contract NAS2-6558.

The Editor thanks G. E. Thomas for his assistance in evaluating this brief report.

REFERENCES

Aller, L. H., *The Atmospheres of the Sun and Stars*, Ronald, New York, 1963.

Danby, J. M. A., and T. A. Bray, Density of interstellar matter near a star, *Astron. J.*, *72*, 219, 1967.

Danby, J. M. A., and G. L. Camm, Statistical dynamics and accretion, *Mon. Notices Roy. Astron. Soc.*, *117*, 50, 1957.

Maloy, J. O., R. W. Carlson, U. Hartmann, and D. L. Judge, Measurement of the profile and intensity of the solar He I λ584-Å resonance line, *J. Geophys. Res.*, *83*, 5685–5690, 1978.

Meir, R. R., Some optical and kinetic properties of the nearby interstellar gas, *Astron. Astrophys.*, *55*, 211, 1977.

Thomas, G. E., Properties of nearby interstellar hydrogen deduced from Ly-α sky background measurements, Solar Wind, *NASA Spec. Publ. SP-308*, 668, 1972.

Thomas, G. E., The interstellar wind and its influence on the interplanetary environment, *Annu. Rev. Earth Planet. Sci.*, *6*, in press, 1978.

Wallis, M. K., Collisional heating of interplanetary gas: Fokker-Planck treatment, *Planet. Space Sci.*, *23*, 419, 1975.

White, O. R., and P. Lemaire, A summary of scientific results from the sail experiments of Oso-8 during the first year of operation, *LASP OSO Rep. 2*, Univ. of Colo., Boulder, Colo., 1976.

Wu, F. M., and D. L. Judge, Temperature and flow velocity of the interstellar gas along solar radii, submitted to *Astrophys. J.*, 1978.

(Received April 25, 1978;
revised August 4, 1978;
accepted August 8, 1978.)

Temperature and Flow Velocity of Interplanetary Gas along Solar Radii and the Resulting Modification of Solar Lines Propagating Through the Interplanetary Medium

F. M. Wu, D. L. Judge

Abstract presented at the Fall Meeting of the AGU, San Francisco, 1978.

The velocity distributions along solar radii for hydrogen and helium in interplanetary space are calculated by using the Danby-Camm formula modified with a loss function. From these distributions the radial temperature and radial flow velocity of the interplanetary gases are determined. Assuming the local interstellar temperature is 10^4 K, the hydrogen radial temperature at distance of 1 A.U. is found to vary from 5500 K to 17,000 K while the helium temperature varies from 2600 K to 70,000 K, depend on the angular position from the interplanetary wind direction. The radial flow velocity of helium is found to be independent of the assumed interstellar temperature. On the other hand, the flow velocity of hydrogen varies significantly with interstellar temperature due to its large loss rate.

Using the radial velocity distribution, we determine the optical depths of the solar H Ly-α and the He 584 lines in interplanetary space. From these, the solar line profiles at Saturn and Uranus are determined. It is found that the solar H Ly-α line can be diminished strongly within a spectral region of $|\Delta \lambda| < 0.2$ Å from the line center. On the other hand, there is no significant absorption of the He 584 line except in the downwind region where absorption occurs at $\Delta \lambda \sim 0.04$ Å. For accurate interpretation of the hydrogen airglow observation of the outer planets, as well as the interplanetary glow at large distances, the effects of solar H Ly-α line modifications must be included.

Pioneer 10 UV Photometer Observations of the Interplanetary Glow at Heliocentric Distances from 2 to 17 AU

F. M. Wu, D. L. Judge

Abstract presented at the Spring Meeting of the AGU, Washington, D.C., 1979

The UV photometer on board the Pioneer 10 spacecraft launch in March, 1972 detects H Ly-α and He 584 Å line emissions. The spacecraft is now more than 17 AU from the sun and is providing the first results on the interplanetary glow at large solar distances. These observed interplanetary data will be presented.

For positions near the sun the interplanetary glow is primarily due to single resonance scattering of sunlight by the interstellar gas flowing into and through the solar system. But, as the heliocentric radius r increase the scattered light intensity drops as n/r and the background radiation, of even a few tens of rayleighs becomes important. In addition, at large solar distances, effects of certain physical parameters of the interstellar gas, such as wind direction and gas temperature, are not important in determining the interplanetary glow intensity. The present Pioneer 10 data provides an excellent opportunity to determine accurately the gas density as well as the background radiation.

In the present analysis of the interplanetary glow observations we have employed the recent model of Wu and Judge (Astrophy. J. 1979, in press). This model properly takes into account the combined effects of ionization loss and solar gravitation in describing the interplanetary gas density and can be used to compute the interplanetary glow for a high temperature interstellar wind. Comparing the observational data with these theoretical calculations we have determined that the constant background intensity for the H Ly-α line is about 40 R, and the nearby interstellar density is 0.04^{-3} for hydrogen and 0.01 cm^{-3} for helium.

PROCEEDINGS

OF

U. S.-JAPAN JOINT SEMINAR

ON PLASMA SPECTROSCOPY

May 7 to May 11, 1979

KYOTO UNIVERSITY

EXTREME ULTRAVIOLET OBSERVATIONS OF ASTROPHYSICAL PLASMA

Darrell L. Judge
Department of Physics, University of Southern California
Los Angeles, California 90007 USA

INTRODUCTION

The primary observations to be presented are of the interaction of solar plasma with the inflowing interstellar hydrogen and helium gas. The extreme ultraviolet glow of these constituents results primarily from solar resonance scattering, and is strongly modified by the interaction of the solar plasma with this neutral gas, leading to both significant heating and ionization. The characteristics of our sun (and other stellar sources), the solar wind, and planetary plasma are all amenable to diagnosis by means of XUV observations. The present discussion will be limited to the dilute plasmas found in the solar wind (≈ 10 cm^{-3}) and in the Jovian magnetosphere (≈ 2000 cm^{-3}). Recent observational and theoretical work relative to such plasmas will be presented. In addition, a brief discussion of the new Voyager 1 XUV observations of Jovian plasma will be given. Ionization equilibrium studies suggest temperatures of 10^5 °K for a plasma consisting primarily of SIII, SIV and OIII at the orbit of Io, six Jovian radii from Jupiter.

INTERPLANETARY PLASMA - SOLAR WIND

The interplanetary plasma consists primarily of protons and electrons of solar origin. The supersonic expansion of the solar corona is usually referred to as the solar wind. The flow velocity of this wind is essentially constant at about 400 km s^{-1}, with a kinetic temperature of about 10 eV for $r > 1$ AU.

As the solar wind proceeds through the interplanetary medium, the dynamic pressure decreases because the ion density decreases as $\approx r^{-2}$. At the heliopause (≈ 100 AU from the sun), the solar wind dynamic pressure is equal to the interstellar magnetic and particle pressure, and a transition from supersonic to subsonic flow will occur abruptly as a shock discontinuity. This transition region is analogous to the earth's magnetosheath and consists of hot solar wind plasma at a temperature of possibly 20 eV or higher. The plasma in the transition region is heated by extracting energy from the bulk flow and partially converting it to thermal energy of the ions and electrons. (Cosmic ray heating may also be important, though such an effect has not yet been established). Thus, the interplanetary plasma referred to consists of two distinct types: one is inside the solar system with $T \sim 10$ eV and one is located beyond the heliopause with $T \sim 20$ eV or higher.

Interplanetary space is filled with, in addition to charged particles, neutral hydrogen and helium which are inflowing from interstellar space at a velocity $V \sim 20$ km s^{-1}. Density of the local interstellar gas is 0.1 cm^{-3} for hydrogen and 0.01 cm^{-3} for helium. The neutral gas is observable primarily by resonance scattering of solar lines. Because of the low interplanetary plasma temperature, and density, particle excitation of the neutral gases is not an important excitation process in interplanetary space. However, plasma particles can cause (1) ionization of the interplanetary gases through charge exchange and electron ionization and (2) a temperat-

ure increase of the interplanetary gases through elastic collisions. Through the interplanetary UV spatial distribution and emission line profiles, one can determine the interplanetary plasma density and its thermal characteristics. The effects of ionization on the UV glow of the interplanetary gas are quite significant. For large loss rate profiles, not only is the absolute emission intensity reduced significantly but the peak intensity is shifted to a lower wavelength. Since the ionization loss of hydrogen particles is mostly due to charge exchange with solar wind protons, analysis of the interplanetary H Ly-α radiation thus provides data on the interplanetary proton flux. Both solar protons and solar electrons can, in addition to ionizing the neutral gas, transfer kinetic energy to the interplanetary atoms through elastic collision processes. It is estimated that such heating could increase the gas temperature by several hundred degrees in the upwind direction (zero angle with respect to the inflowing interstellar wind direction) to several thousand degrees in the downwind direction (ref. 1,2). Thus, the interplanetary line profiles will be broadened most significantly downwind and least significantly upwind.

The hydrogen emission profiles can be measured by a high resolution spectrometer such as one on the Copernicus Satellite (ref. 3) or by a photometer with a hydrogen cell of the type flown on the Prognoz spacecraft (ref. 4). From such measurements, the hydrogen temperatures are estimated to be between 5000 and 15,000 °K. However, due to poor photosensitivity and poor knowledge of the viewing direction, the temperature gradient observation in interplanetary space is not yet available. Thus, a spacecraft mission with direct line-profile mapping should prove to be useful and interesting. Such data are intimately related to the physical properties of the interplanetary neutral medium as well as to the energy flux of the solar wind.

At large radial distances from the sun, the transition region outside the heliopause, the interstellar gas temperature and velocity may further significantly alter the outflowing solar plasma. However, since the nature of the shock front and transition region are still uncertain, the actual effects on both the inflowing interstellar gas and the outflowing plasma are unknown. Their signficance may not be established until both the Pioneer and Voyager spacecraft traverse the outer regions of the heliosphere, and observe the radial dependence of the distant glow.

JOVIAN PLASMA

Since the Jovian encounters of the Pioneer 10 and 11 spacecraft, the innermost part of Jupiter's magnetosphere (< 10 Jovian radii) is known to have a dipole-like magnetic field, the inner portion of this region being responsible for the observed radio emission. In the outer Jovian magnetosphere centrifugal force leads to the concentration of plasma in a sheet near the magnetic equator, and extends to a radius of ~ 100 R_J.

From Pioneer 10 data, the proton densities throughout the range from 2.8 to 7 R_J are estimated to be about 50-100 cm^{-3} with thermal energies of about 100 eV. As the distance from Jupiter increases, the plasma density decreases, and is about 10 to 15 cm^{-3} at $R = 9\ R_J$, and decreases to 1 cm^{-3} for $r > 15\ R_J$.

The two channel broad band XUV photometer on board Pioneer 10 was the

first deep space survey of XUV radiation from the Jovian vicinity (ref. 5). The longwavelength channel detected emission shortward of 1400 Å, while the shortwavelength channel detected emission shortward of 800 Å. Both channels detected emission signals from an extended region centered at Io, the innermost Galilean satellite. At the time of the observations, the longwavelength channel observations were interpreted as resonance scattering of solar Lα by atomic hydrogen in Io's cloud, while the shortwavelength emission was interrupted as arising from the radiative decay of excited atomic ions, produced by electron impact. Subsequently, observations from a high resolution spectrometer on the Voyager spacecraft (ref. 6) have confirmed the presence of strong XUV emissions inside Io's orbit. They detected the H Ly-α line, in addition to the dominant SIII, SIV and OIII lines. However, the Jovian emission intensities at the time of the Voyager encounter are at least a factor of two larger than those observed during the Pioneer 10 encounter. Moreover, the emission signals observed by Voyager 1 are from a complete torus, in contrast to a partial torus (~120°) observed by Pioneer 10. These differences in the XUV emissions may reflect dramatic time variations in the Jovian plasma's condition. In fact, from the observed SIII emission Broadfoot et al. (ref. 6) have derived a plasma temperature of ~ 10 eV and an electron density of 2000 cm^{-3}, consistent with the direct measurement from a plasma analyzer on board Voyager 1. However, these plasma characteristics are quite different from the plasma conditions at the time of the Pioneer 10 encounter, the reported results being $n \sim 50$ cm^{-3} and $T = 100$ eV. Thus, it is evident that the Jovian plasmasphere is quite variable and that XUV observations yield useful data for diagnosing the plasma characteristics.

Clearly astrophysical sources provide opportunities to study plasma in a physical environment difficult or often impossible to provide in research settings of laboratory scale. Plasma studies by sophisticated space flight equipment are really just beginning but it would appear that a detailed study of the various sources of plasma in space can and will provide interesting and useful fundamental data on atomic systems.

ACKNOWLEDGEMENT

This work was supported by contract NAS 2-6558 with the NASA Ames Research Center.

REFERENCES

1. F.M. Wu and D.L. Judge, Astrophys. J. 225, 1045 (1978).
2. J. Fahr, Astron. Astrophys. 66, 103 (1978).
3. T.F. Adams and P.C. Frisch, Astrophys. J. 212, 300 (1977).
4. J.L. Bertzux et al., Astron. Astrophys. 46, 19 (1977).
5. D.L. Judge, R.W. Carlson, F.M. Wu and U.G. Hartmann, in Jupiter, ed. T. Gehrels (Tucson: University of Arizona Press), p 1068 (1976).
6. A.L. Broadfoot, D.E. Shemansky and B.R. Sandel, private communication (1979).

THE ASTROPHYSICAL JOURNAL, 239:389-394, 1980 July 1
© 1980 The American Astronomical Society All rights reserved Printed in U.S.A.

A REANALYSIS OF THE OBSERVED INTERPLANETARY HYDROGEN Lα EMISSION PROFILES AND THE DERIVED LOCAL INTERSTELLAR GAS TEMPERATURE AND VELOCITY

F. M. WU AND D. L. JUDGE
Space Sciences Institute and Department of Physics, University of Southern California
Received 1979 August 20; accepted 1980 January 9

ABSTRACT

An improved model of the interplanetary emission profile is presented. In this model we utilize a new version of the modified Danby-Camm velocity distribution function to calculate emission profiles, and it appears to be very efficient. Using this model, the hydrogen Lα profiles are determined for various viewing directions, and at a solar distance of 1 AU. It is found that the linewidth of the emission profiles and their Doppler shifts depend strongly on the viewing direction, as well as the assumed interstellar temperature. Previous determinations of the interstellar temperature T_0 and the inflow velocity V_b, using approximate theoretical hydrogen profiles, are found to be inadequate. These values are recalculated and are determined to be $T_0 = 7000 \pm 1200$ K and $V_b = 19 \pm 3$ km s^{-1}.

Subject headings: interplanetary medium — interstellar: matter — ultraviolet: spectra

I. INTRODUCTION

Adams and Frisch (1977) were the first to measure the hydrogen emission profile by using a high resolution spectrometer on the *Copernicus* satellite. From these data they have deduced an inflow velocity for the local interstellar hydrogen gas of 22 ± 3 km s^{-1}. But, the inflow velocity they determined is based on an approximate theoretical model in which the interplanetary temperature is assumed to be uniform and the decrease of the bulk velocity due to high temperature (random motion) effects was not considered. However, as Wu and Judge (1979*a*) have calculated, because of the effects of solar gravity, and ionization loss due to charge exchange and photoionization, the hydrogen gas temperature can vary significantly in interplanetary space, and the random motion can decrease the gas bulk velocity considerably. Thus, the inflow velocity deduced by Adams and Frisch is subject to modification. Bertaux *et al.* (1977) used a photometer with a hydrogen cell on *Prognoz 5* to measure the line width of the emission profile to determine a temperature of 8800 ± 1000 K for the emitting interplanetary gas. However, because of the modification of the gas velocity distribution as it passes through the solar system, the temperature Bertaux *et al.* determined cannot be identical to the interstellar temperature at "infinity".

In this work we present an accurate theoretical model for calculating the interplanetary emission profiles. This model uses a new version of the modified Danby-Camm formula (Wu and Judge 1979*a*) to describe the velocity distribution of a high temperature interplanetary gas. Here modification of the velocity distribution due to solar gravity and ionization loss effects has been properly taken into account, ar resulting theoretical hydrogen emission profiles various viewing directions are compared wit observed profiles of Adams and Frisch (1977 Bertaux (1977). The present results provide imp velocity and temperature values for the loc terstellar hydrogen.

II. A THEORETICAL MODEL FOR THE EMISSION PR(

The interplanetary gas with a velocity distrit function $N(\boldsymbol{r}, \boldsymbol{V})$ at position $\boldsymbol{r}$ and with veloc absorbs the solar flux at a rate given by

$$\alpha(\boldsymbol{r}, \boldsymbol{V}) = \alpha_0' N(\boldsymbol{r}, \boldsymbol{V}) \cdot \pi F_\nu\left(\nu_0 + \frac{\nu_0}{c} V_r\right)$$
$$= \alpha_0' \frac{\lambda_0^2}{c} \times N(\boldsymbol{r}, \boldsymbol{V}) \cdot \pi F_\lambda\left(\lambda_0 - \frac{\lambda_0}{c} V_r\right)$$

where $\alpha_0' = \pi e^2 f/mc$, V_r is the particle radial vel πF_ν is the solar flux given in photons cm^{-2} s^{-} frequency, and πF_λ is the solar flux in units of ph cm^{-2} s^{-1}Å^{-1}. From this the interplanetary v emission rate at wavelength λ along the l directic be calculated and is given by

$$\epsilon_\lambda(\boldsymbol{r}, \boldsymbol{l}) = P(\boldsymbol{l}, \boldsymbol{r}) \int \alpha(\boldsymbol{r}, \boldsymbol{V}) \delta\left(\nu - \nu_0 + \frac{\nu_0}{c} V_l\right) d\boldsymbol{V}$$

where P is the phase factor (Meier 1977) and V_l gas velocity along the l direction. The l direct defined by two angles (θ_l, γ_l), with θ_l as the

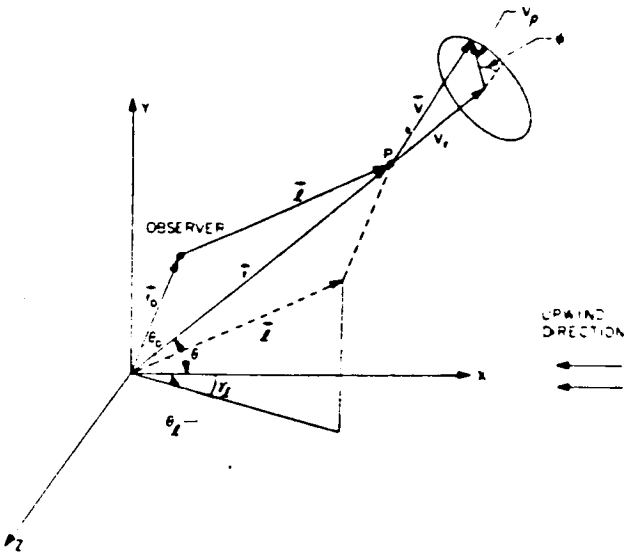

FIG. 1.—The coordinate system for describing the model used to calculate the emission profiles. The observer's position is at $r_0 = (r_0, \theta_0)$ and the viewing is in the direction l. Here l is specified by two angles (γ_l, θ_l) and the wind direction is along the X-axis. The particle velocity is expressed as $V = (V_r, V_\rho, \psi)$ with its position at $r = (r, \theta)$.

between l and the xz plane, and γ_l as the angle between the xy and ly planes (Fig. 1). The velocity V_l can be expressed as

$$V_l = V_r(\cos\theta\cos\theta_l\cos\gamma_l + \sin\theta_l\sin\theta) - V_\rho[\sin\theta(\sin\theta\cos\theta_l\cos\gamma_l - \cos\theta\sin\theta_l) - \cos\psi\cos\theta_l\sin\gamma_l]. \quad (3)$$

The interplanetary intensity at wavelength λ and position r is then found from the integral

$$I_\lambda d\lambda = d\lambda \int \epsilon_\lambda(r, l)dl. \quad (4)$$

The velocity distribution function $N(r, V)$ in equation (1) can be derived by using the Danby-Camm formula (Danby and Camm 1957) modified with a loss function and is expressed by the following formula:

$$N(r, V) = N_0(2\pi KT_0/m)^{-3/2}\exp(F_1 + F_2\sin\psi), \quad (5)$$

where F_1 and F_2 are the analytic functions in terms of the position and velocity coordinates r, θ, V_r, V_ρ, and the interplanetary physical parameters V_b, T_0, β, μ, and N_0 (Wu and Judge 1979*a*). Here N_0, T_0, and V_b are the density, temperature, and inflow velocity of the local interstellar gas, respectively, β is the charge exchange and photoionization loss rate at a distance of 1 AU, and μ is the ratio of radiation pressure to gravitational attraction. The position and velocity parameters $r = (r, \theta)$ and $V = (V_r, V_\rho, \psi)$ for the particles are defined in Figure 1, where r is the distance from the Sun, θ is the angle from the upwind direction, V_r and V_ρ are the velocity components along and perpendicular to the radial direction, respectively, and ψ is the rotational angle about the radial direction.

For the case in which the viewing direction l is along solar radii ($\theta_l = \theta_0$ and $\gamma_l = 0$), we have $V_l = V_r$. By integrating ϵ_λ over V_r, the emission rate at wavelength λ can then be calculated from

$$I_\lambda d\lambda = \alpha_0\pi F_\lambda(\lambda)d\lambda \int_r^\infty P(l, r)\cdot N(r, V_r = V_\lambda)dr,$$

where

$$V_\lambda = c\frac{\lambda - \lambda_0}{\lambda_0}, \quad \alpha_0 = \frac{\pi e^2 f\lambda_0}{mc}(2KT_0/m)^{1/2},$$

and

$$N(r, V_r = V_\lambda) = \pi^{-3/2}N_0(m/KT)\int_{\rho_0}^\infty \exp(F_1)V_\rho dV_\rho \times \int_0^{2\pi}\exp(F_2\sin\psi)d\psi. \quad (6)$$

The integration over ψ in the above formula can be derived analytically by a series expansion, while integration over V_ρ and r must be integrated numerically (Wu and Judge 1979*a*, *b*).

For a viewing direction different from the radial direction, we integrate ϵ_λ over ψ by using the Dirac delta function and obtain the following result:

$$I_\lambda d\lambda = \alpha_0\pi^{-3/2}N_0(m/2KT)d\lambda \times \int_{r_0}^\infty P(l, r)A^{-1}dl \int_{-\infty}^\infty \pi F_\lambda\left(\lambda_0 - \frac{\lambda_0}{c}V_r\right)dV_r \times \int_{V_m}^\infty V_\rho dV_\rho \exp(F_1)(V_\rho^2 - V_m^2)^{-1/2} \times [\exp(F_2\sin\psi_0) + \exp(F_2\sin\psi_1)], \quad (7)$$

where

$$A = [(\sin\theta\cos\theta_l\cos\gamma_l - \cos\theta\sin\theta_l)^2 + (\cos\theta_l\sin\gamma_l)^2]^{1/2},$$

$$V_m = A^{-1}[V_\lambda - V_r(\cos\theta\cos\theta_l\cos\gamma_l + \sin\theta_l\sin\theta)],$$

$$\psi_{0,1} = \sin^{-1}(\cos\theta_l\sin\gamma_l/|A|) \pm \sin^{-1}(-V_m/V_\rho),$$

$$V_{\rho_0} = [2(1-\mu)GM_s r^{-1} - V_r^2]^{1/2}, \text{ if } [2(1-\mu)GM_s r^{-1} - V_r^2]^{1/2} > |V_m|,$$
$$= |V_m|, \text{ otherwise}.$$

Note, the singularity at V_m in the above integration can be avoided by changing the integration variables from V_ρ to $U_\rho = (V_\rho^2 - V_m^2)^{1/2}$.

The calculation of the emission profile thus involves a triple or double numerical integration (depending on the viewing direction) which can be carried out either by Simpson's integration rule or by using the Gaussian quadrature formula. The numerical integration is set up such that the numerical values are accurate to two digits. The reasonableness of our calculations have

been checked by comparing our results on the helium emission profiles with those of Meier (1977) and are found to be in general agreement (Wu and Judge 1979*a*). The accuracy is further checked by using the fact that the volume emission rate ϵ_λ integrated over λ should be the same for all viewing directions.

It may be noted that the procedures we used for calculating the emission profile are very similar to those of Meier (1977). However, our expression for the velocity distribution is from Wu and Judge (1979*a*), and thus the resulting formula for the emission profile is different from Meier's. By using our formula, the computer time for a single line profile is less than 2 minutes on an IBM 370/158 if the viewing direction is along a radial direction, and is less than 15 minutes for other directions. This is compared to the required time of 20–60 minutes on a CDC 1604 computer for a single line profile calculation, using Meier's expression.

III. THE INTERPLANETARY HYDROGEN Lα EMISSION PROFILE

Using equation (6) and the physical parameters $T_0 = 10^4$ K, $V_b = 20$ km s^{-1}, $N_0 = 0.1$ cm^{-3}, $\pi F_\lambda = 2.5 \times 10^{11}$ cm^{-2} s^{-1} Å^{-1} ($\mu = 0.75$), $\beta = 5 \times 10^{-7}$ s^{-1} (Thomas 1978), the interplanetary H Lα emission profiles along solar radii for various angles have been calculated and are shown in Figure 2. In these calculations, the solar H Lα line is assumed to be flat over the spectral region of interest ($\Delta\lambda < 0.2$ Å) (Thomas 1978; Wu and Judge 1979*a*).

Since the interplanetary glow is due to resonance scattering of solar lines by the interplanetary gases, the distribution of the interplanetary glow along various directions reflects the hydrogen density distribution in that direction. As is well known, the hydrogen density decreases as the angle from the upwind direction increases; thus, the interplanetary emission is strongest upwind and weakest downwind. From Figure 2 we see that the line shapes of the emission profiles are, in general, symmetric with respect to the peak intensity and can be described well by Gaussian functions of a characteristic temperature. (The characteristic temperature, T_c, for a Gaussian profile is related to $\Delta\lambda$, the full linewidth at half maximum (FWHM) by $T_c = mc^2/2K[(\Delta\lambda/\lambda)/1.665]^2$. This is in contrast to the interplanetary helium line profiles which are most likely to be asymmetric (Meier 1977; Wallis 1977).

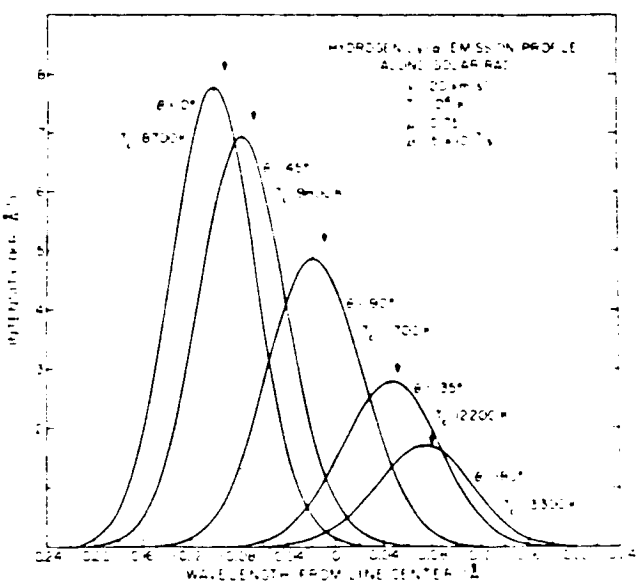

FIG. 2.—The hydrogen Lα emission profiles along solar radii for various angles. Here T_c is the characteristic temperature of the indicated emission profiles. The Doppler shifts due to cold gas emission are indicated by arrows and, as can be seen, are quite different from the mean velocity of the indicated profiles.

Because of the action of solar gravity and velocity-dependent ionization loss, the velocity distribution of interplanetary hydrogen varies with position. Thus, the emission profile can change from a width of $\Delta\lambda = 0.082$Å (corresponding to $T_c = 8{,}700$K) upwind to a width of $\Delta\lambda = 0.096$ Å (corresponding to $T_c = 13{,}000$K) downwind. In addition, the spectral positions of the emission profiles vary with the angle from the upwind direction. Near the upwind direction, because the mean radial velocity of the interplanetary gas is negative, the emission profiles will be on the blue side of the solar line center, $\lambda_0 = 1215.6$ Å. However, in the downwind direction, the mean radial velocities become positive and the emission lines shift to the red. The peak intensity for the emission profile is shifted -0.102 Å in the upwind direction and is shifted 0.072 Å in the downwind direction. It is interesting to compare the above results with the Doppler shifts expected from a gas of zero temperature.

For the cold temperature gas (zero temperature), the Doppler shift for the interplanetary emission can be derived from

$$\langle\lambda\rangle = \frac{\lambda_0}{c} \sum_{j=1,2} \int V_j \epsilon_j dl \Big/ \int \epsilon_j dl$$
$$= \frac{\lambda_0}{c} \sum_{j=1,2} \int V_j N_j r^2 dl \Big/ \int N_j r^2 dl , \qquad (8)$$

where ϵ_j, N_j, and V_j are the emissivities, the densities, and the projected velocities of the cold interplanetary gas, and can be evaluated from the expressions given by Axford (1972). In the above equation, the summation is over $j = 1, 2$ because there are two trajectories which pass through each interplanetary point. The resulting shifts $\langle\lambda\rangle$ for various directions are shown as arrows in Figure 2. It is seen that the wavelengths for $\langle\lambda\rangle$ are in general at the red side of the high temperature emission profile; the wavelength differences between $\langle\lambda\rangle$ and the profile line centers are about $\Delta\lambda \approx 0.01$ Å (corresponding to a difference in Doppler velocity of $\Delta V_D \approx 3$ km s^{-1}).

In Figure 2 the variation of the emission profiles along a solar radius is evident. However, the emission profiles can also vary significantly along a nonradial direction, as illustrated in Figure 3. In this figure, we

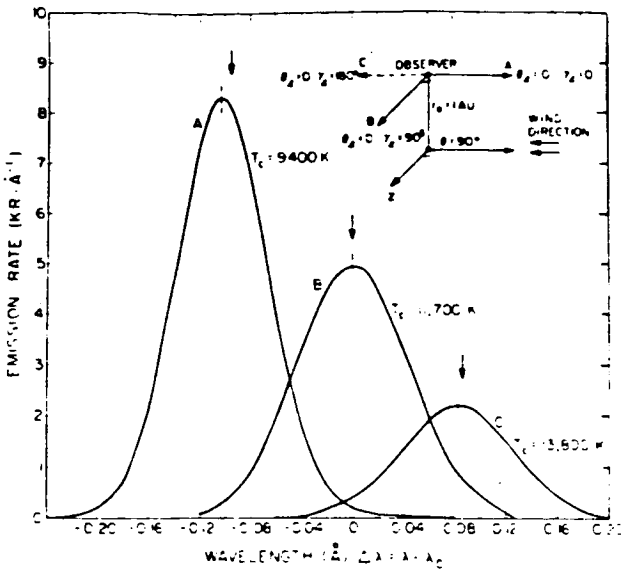

FIG. 3.—The hydrogen profiles in the non-radial directions, with the parameters $V_b = 20$ km s^{-1}, $T_0 = 10^4$ K, $\mu = 0.75$, and $\beta = 5 \times 10^{-7}$ s^{-1}. The observer's position and viewing directions relative to the wind direction are indicated in upper right hand part of this figure.

show the emission profiles for an observer at $r_0 = 1$ AU, $\theta_0 = 90°$, viewing perpendicular to the radial direction and at an angle $\gamma_l = 0$, 90°, and 180° with respect to the upwind direction. We see that not only are the intensities decreasing with the angle relative to the upwind direction (γ_l), but the linewidth varies from 0.084 Å ($T_c = 9400$ K) at $\gamma_l = 0$ to 0.102 Å ($T_c = 13{,}800$ K) at $\gamma_l = 180°$. In addition, the Doppler velocities for these emission profiles could also differ from the cold gas velocities by as much as 2 km s^{-1} ($\Delta\lambda \approx 0.008$ Å).

From the above discussion, we can conclude that the characteristic temperatures for the hydrogen emission profiles are in general quite different from the interstellar temperature (the interplanetary temperature at large distances). Moreover, the Doppler shifts are usually lower than those of the cold gas of high temperature profiles. These differences are mainly caused by the modification of the velocity distribution function in interplanetary space due to the combined effects of solar gravity and ionization loss. To accurately determine the thermal status of interstellar gas from interplanetary glow experiments, the emission profile along the direction of observation must be accurately calculated. The effect of such calculations on the interpretation of flight data is discussed below.

IV. INTERSTELLAR TEMPERATURE

The interplanetary emission profile was measured by Adams and Frisch (1977) using the high resolution spectrometer on the *Copernicus* satellite. The observations did not yield an accurate emission profile because of limited photometric sensitivity. The temperature of the emitting gas was estimated to be between 5 and 20×10^3K.

An alternative way to measure the emission profile is to use an absorption cell in conjunction with a photometer. By comparing the measured intensity with and without an absorbing gas, the emission profile can be determined. From such an absorption cell on board the Soviet probe *Mar 7* (Bertaux *et al.* 1976), the interplanetary temperature was determined to be between 6 and 13×10^3 K. The uncertainty in the above observed temperature is caused by the poor knowledge of the direction of sight. Recently an observation from the Soviet spacecraft *Prognoz 5* (Bertaux *et al.* 1977) also utilized an absorption cell and yielded a much more accurate interplanetary temperature of $T_0 = 8800 \pm 1000$ K.

The *Prognoz 5* data were obtained on 1976 December 1, when the Earth was in the direction $\alpha = 67^h.2$ and $\delta = 21°.8$ relative to the Sun and was nearly opposite the upwind direction ($r_0 = 1$, $\theta_0 = 180°$), while the photometer was viewing in a direction perpendicular to a solar radius ($\theta_l = 90°$). For this viewing geometry, the expected emission profiles for various interstellar temperatures T_0 can be calculated from equation (7) and are shown in Figure 4. As can be seen, the emission profile for $T_0 = 7000$ K is very close

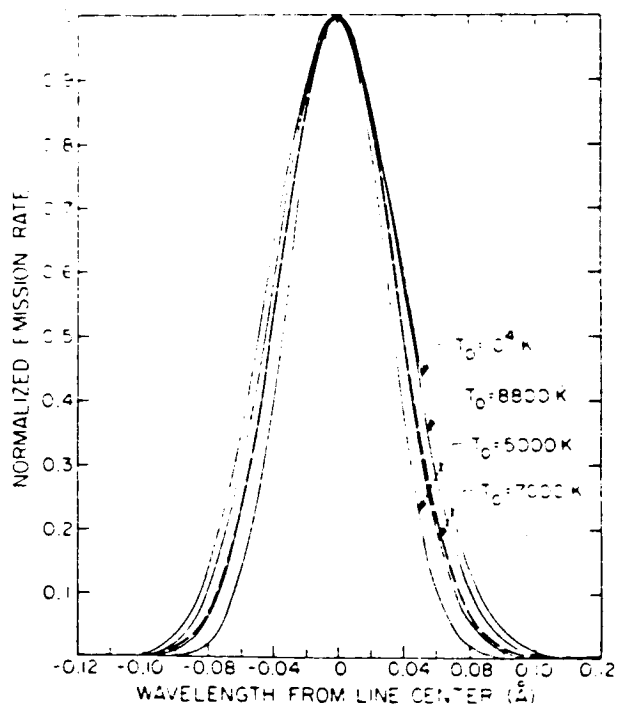

FIG. 4.—The observed and theoretical line profiles observed by the *Prognoz 5* spacecraft. The theoretical profiles are calculated for four different temperatures: $T_0 = 10^4$, 8800, 7000, and 5000 K. The other parameters are $\mu = 0.75$, $\beta = 5 \times 10^{-6}$ s^{-1} and $V_b = 20$ km s^{-1}. The dashed curve is the profile for an observed temperature $T = 8800$ K (assumed to be Gaussian). In this plot, the wavelength is expressed relative to its line center, and the profiles have been normalized to their peak intensity.

TABLE 1

THE CHARACTERISTIC TEMPERATURE FOR THE HYDROGEN EMISSION PROFILE AT $r = 1$ AU, $\theta = 180°$, VIEWED PERPENDICULAR TO THE RADIAL DIRECTION

PARAMETERS				CHARACTERISTIC TEMPERATURE
T_0 (K)	V_b (km s^{-1})	β_0 (s^{-1})	μ	T_c (K)
10^4	20	5×10^{-7}	0.75	12800
8800	20	5×10^{-7}	0.75	10800
5000	20	5×10^{-7}	0.75	6300
7000	20	5×10^{-7}	0.75	8500
7000	20	5×10^{-7}	0.6	9400
7000	20	6×10^{-7}	0.75	8100
7000	17	5×10^{-7}	0.75	8900

to the Gaussian profile for $T_c = 8800$ K. But the profiles for other T_0 values are either too wide or too narrow to fit the Gaussian profile.

In the above calculation of the emission profiles, we assumed the physical parameters $\mu = 0.75$, $\beta = 5 \times 10^{-6}$ s^{-1}, and $V_b = 20$ km s^{-1}. However, it may be noted that at the time of the *Prognoz* observations (1976), solar activity was near a minimum; the solar H Lα flux averaged over the year may be about 1.9×10^{11} photons cm^{-2} s^{-1} (Vidal-Madjor 1975), and thus the effective μ for H atoms may be as low as 0.6. Moreover, possible variations in the ionization loss rate β and the inflow velocity V_b may also cause uncertainty in the determined characteristic temperature. In Table 1 we show the resulting characteristic temperatures T_c for the emission profiles which result for various physical parameters. It is noted that the temperatures T_c are always larger than the interstellar temperature T_0 by at least 1000 K. Thus, the assumptions by Bertaux *et al.* (1977) that the emission profile at each point of the solar system is characterized by a temperature T_0 cannot be correct. From Table 1 we also see that for various possible physical parameters, the characteristic temperatures, corresponding to $T_0 = 7000$ K differ from 8800 K by no more than 700 K. Therefore, including the observational error (1000 K), we may determine from the *Prognoz* observation that the "local" interstellar gas (in the distant region of our solar system) has a temperature of 7000 ± 1200 K.

V. VELOCITY OF THE INFLOWING INTERSTELLAR GAS

The high resolution spectrometer on the *Copernicus* spacecraft (Adams and Frisch 1977) was the first to measure directly the relative velocity of interplanetary gas. During the period of 1975 April 21–26, they observed a Doppler shift of $\Delta\lambda = -0.188$ Å for the emission profile viewed in the direction $\alpha = 263°.75$, $\delta = -8.3$. After correcting for the Earth's orbital motion, the heliocentric velocity of interplanetary gas corresponding to the observed Doppler shift was found to be -24.1 km s^{-1}. From these data, and by employing an approximate function for the velocity distribution of interplanetary gas, they obtained a value of $V_b = -22 \pm 3$ km s^{-1} for the inflow velocity of the interstellar gas. As we have mentioned, however, the approximate velocity distribution which they used assumed that the interplanetary gas had a uniform temperature T_0 and ignored the effect of finite temperature on the bulk velocity of the atoms; thus, the inflow velocity determined by Adams and Frisch (1977) is subject to error.

The expected emission profiles for Copernicus observations calculated from our accurate velocity distribution functions (eq. [7]) are shown in Figure 5. In these calculation, we used the physical parameters $V_b = 20$ km s^{-1}, $\beta_0 = 5.5 \times 10^{-7}$ s^{-1}, and $\mu = 0.6$, and the wind direction $\alpha = 265$ and $\delta = -23$, which are the same as those adopted by Adams and Frisch (1977). From Figure 4 we see that the peak intensity for the profile is at -0.101 Å for $T_0 = 7000$ K and is at -0.104 Å for $T_0 = 10^4$ K. The Doppler shifted velocities at the corresponding wavelengths are $V_D = -24.9$ and -25.7 km s^{-1}, respectively. Thus, the Adams and Frisch theoretical value of $V_D = -23$ km s^{-1} for a gas temperature $T_0 = 10^4$ K differs from the present result by about 2–3 km s^{-1}. The difference is mainly caused by the inaccuracy in the velocity distribution function used by Adams and Frisch, as discussed earlier.

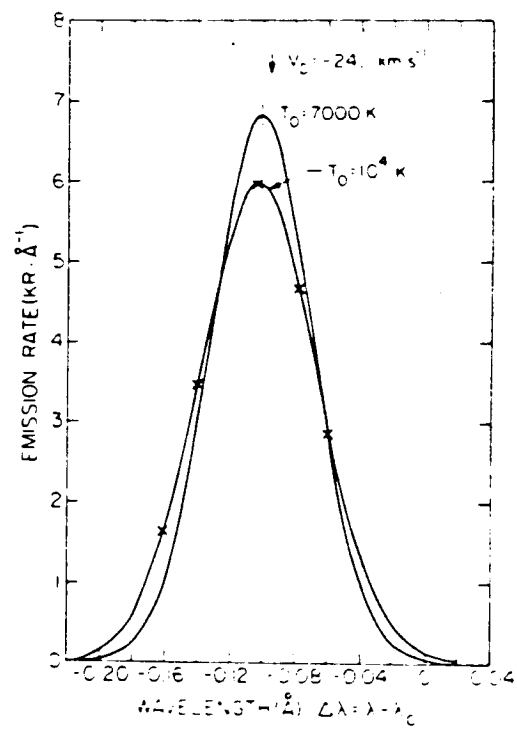

FIG. 5 The theoretical emission profiles for the Copernicus observation. The profiles are calculated for two temperatures, $T_0 = 7000$ K and 10^4 K, and parameters $V_b = 20$ km s^{-1}, $\beta = 5.5 \times 10^{-7}$ s^{-1}, $\mu = 0.6$, and $N_0 = 0.1$ cm^{-3}. The observed Doppler velocity $V_D = -24.1$ km s^{-1} from Adams and Frisch (1977) is also indicated in this figure. The points marked by $\times$ are the result for $T_0 = 10^4$ K from an unpublished report by Meier (1979) and, as can be seen, agree quite well with the present calculations.

TABLE 2

THE EXPECTED DOPPLER VELOCITIES FOR THE EMISSION LINE OBSERVED BY THE COPERNICUS PHOTOMETER*

PHYSICAL PARAMETERS				DOPPLER SHIFT
V_b (km s^{-1})	T_0 (K)	β (10^{-7} s^{-1})	μ	V_D (km s^{-1})
20	0	5.5	0.6	−23.5
20	0	5.5	0.8	−21.4
20	0	5.5	0.6	−23.3
20	10^4	5.5	0.6	−25.7
20	7000	5.5	0.6	−25.2
20	10^4	5.5	0.8	−24.2
20	7000	5.5	0.8	−23.7
20	7000	6.5	0.6	−24.2
20	7000	4.5	0.6	−25.3
19	7000	5.5	0.6	−24.2
18	7000	5.5	0.6	−23.5
18	10^4	5.5	0.6	−23.9
20	5000	5.5	0.6	−24.9

* The interstellar wind direction is assumed to be $\alpha = 265^h$, $\delta = -23°$.

To further improve the accuracy of the inflow velocity, the possible variation of the physical parameters, such as ionization rate, radiation pressure and temperature, which affect the profile's Doppler shift, must also be examined. In Table 2, we show the Doppler velocities for the expected profile for different physical conditions. As can be seen, the Doppler velocities V_D for $T_0 = 0$ K are quite different from those for $T_0 = 7000$ or 10^4 K; the random motion of a high temperature gas shifts the peak intensity to a lower velocity by about 2–3 km s^{-1}. For a high temperature gas with $V_b = 20$ km s^{-1}, the Doppler velocities due to a variation in μ and β lie between −24 and −26 km s^{-1}. Thus, the *Copernicus* observation of $V_D = -24 \pm 2.6$ km s^{-1} suggests an inflow velocity $V_b = 19 \pm 3$ km s^{-1}. Note in the above calculations that the wind direction is assumed to be $\alpha = 265^h$, Dec $= -23°$, which is based on the observed H Lα sky map (Fahr 1974). However, from the He 584 sky maps, we note the wind direction is $\alpha = 252^h$, $\delta = -15°$ (Weller and Meier 1974). The possible error in V_b caused by the uncertainty in the wind direction (i.e., the difference between the above He and H flow directions) is calculated to be ~ -0.2 km s^{-1} and is negligibly small compared to the uncertainty, $\Delta V_D = 3$ km s^{-1}.

VI. SUMMARY

We have developed a new model for the interplanetary emission profiles and, from this, calculated the hydrogen profiles for various viewing directions. Comparing the theoretical profiles with the existing observations, we have determined that the interstellar gas temperature is $T_0 = 7000 \pm 1200$ K and its inflow velocity is $V_b = 19 \pm 3$ km s^{-1}. These values are considerably different from the previous values of $T_0 = 8800 \pm 1000$ K and $V_b = 22 \pm 3$ km s^{-1}, which were determined by an approximate theoretical emission profile.

In our calculation of emission profiles, we have considered the modification of the gas velocity distribution by the action of solar gravity and ionization loss; but, the possible modification by elastic collision with solar protons and electrons has not been included. The effects of electron heating of the interplanetary gas have been discussed by Wu and Judge (1978). However, the importance of proton heating still has not been unambiguously determined (Holzer 1977). In addition, there is an uncertainty in the interplanetary gas density distribution due to (1) the temporal variability of solar radiation pressure and loss rates; and (2) the solar latitude variations of the solar wind plasma and Lα fluxes (Holzer 1977). Further refinement in the present model of interplanetary emission profiles by including the effects of collisional heating and considering the time and latitude dependence of the solar wind and Lα fluxes is desirable. It may also be noted that the present analysis of the interstellar medium is based on only two separate observations, both of which were restricted to a distance of 1 AU. It is thus clearly important that the temperature and velocity so determined be confirmed by further extensive observations. A spacecraft mission with direct line profile mapping to determine the Doppler shifts and the temperature gradient in interplanetary space would be most useful. Such data would provide not only an accurate description of the thermal status of the local interstellar medium, but a determination of the effects of solar wind heating of the interplanetary medium as well.

This work was supported by contract NAS 2-6558 with the NASA Ames Research Center. The authors thank Dr. R. R. Meier for sending us an unpublished report and for his useful comments on the present work.

REFERENCES

Adams, T. F., and Frisch, P. C. 1977, *Ap. J.*, **212**, 300.
Axford, W. I. 1972, in *Solar Wind*, ed. C. P. Sonett, B. J. Coleman, Jr., and J. M. Wilcox (NASA SP-308), 609.
Bertaux, J. L., Blamont, J. E., Tabaric, N., Kurt, V. G., Bourgin, M. C., Smirnov, A. S., and Dementeva, N. N. 1976, *Astr. Ap.*, **46**, 19.
Bertaux, J. L., Blamont, J. E., Mironova, E. N., Kurt, V. G., and Bourgin, M. C. 1977, *Nature*, **270**, 156.
Danby, J. M. A., and Camm, G. L. 1957, *M.N.R.A.S.*, **117**, 50.
Fahr, J. 1974, *Space Sci. Rev.*, **15**, 483.
Holzer, T. E. 1977, *Rev. Geophys. Space Phys.*, **15**, 467.
Meier, R. R. 1977, *Astr. Ap.*, **55**, 211.
——. 1979, unpublished.
Thomas, G. E. 1978, *Ann. Rev. Earth Planet. Sci.*, **6**, 173.
Vidal-Madjor, A. 1975, *Solar Phys.* **40**, 69.
Wallis, M. K. 1977, *Space Res.*, **18**, 401.
Weller, C. S., and Meier, R. R. 1974, *Ap. J.*, **193**, 471; **203**, 769.
Wu, F. M. and Judge, D. L. 1978, *Ap. J.*, **225**, 1045.
——. 1979*a*, *Ap. J.*, **231**, 574.
——. 1979*b*, *J. Geophys. Res.*, **84**, 979.

DARRELL L. JUDGE and F. M. WU: Space Sciences Institute, University of Southern California, University Park, Los Angeles, CA 90007

Pioneer 11 Ultraviolet Photometer Measurements of the Saturnian System

D. L. Judge, F. M. Wu, R. W. Carlson

Abstract presented at the Fall Meeting of the AGU, San Francisco, 1979.

Titan, the rings of Saturn and Saturn itself were observed with the Ultraviolet Photometer aboard the Pioneer Saturn spacecraft during the September 1, 1979 flyby. Emission from all three objects was detected by the long wavelength channel of the two channel photometer. This channel includes the Hydrogen Ly-α wavelength and the major source of the observed glow is attributed to the atomic hydrogen resonance emission. A possible short wavelength emission from the disc of Saturn has also been observed. The spatial distribution of the observed sources, their brightness, and the implications of the observations will be discussed.

Reprint Series
25 January 1980, Volume 207, pp. 431-434

SCIENCE

Ultraviolet Photometer Observations of the Saturnian System

Abstract. *Several interesting cloud and atmospheric features of the Saturn system have been observed by the long-wavelength channel of the two-channel ultraviolet photometer aboard the Pioneer Saturn spacecraft. Reported are observations of the most obvious features, including a Titan-associated cloud, a ring cloud, and the variation of atmospheric emission across Saturn's disk. The long-wavelength data for Titan suggest that a cloud of atomic hydrogen extends at least 5 Saturn radii along its orbit and about 1.5 Saturn radii vertically. A ring cloud, thought to be atomic hydrogen, has also been observed by the long-wavelength channel of the photometer; it shows significant enhancement in the vicinity of the B ring. Finally, spatially resolved observations of Saturn's disk show significant latitudinal variation. Possible explanations of the variation include aurora or limb brightening.*

The ultraviolet photometer on Pioneer Saturn covers two broad spectral regions (*1, 2*). The short-wavelength (λ_S) band is sensitive only to emissions shortward of about 800 Å and includes the 584-Å resonance line of helium. The region of sensitivity of the long-wavelength (λ_L) channel includes the hydrogen resonance line at 1216 Å. The instrument design was based on the assumed dominance of hydrogen and helium gases in the Jupiter and Saturn systems. Accordingly, the emission signal in the λ_L channel is interpreted as resulting mainly from hydrogen emission at 1216 Å, while the signal in the λ_S channel is considered to be due to helium emission at 584 Å and perhaps other species that emit shortward of ~ 800 Å.

The field of view of the photometer is limited by a mechanical collimator whose optical axis is oriented at an angle $\theta_0 = 20°$ with respect to the spacecraft spin axis. The scanning motion that results from spacecraft rotation sweeps the field of view over the surface of a 40° cone whose vertex is on the spacecraft spin axis and whose axis of symmetry is oriented along the spin axis. The spin axis of the spacecraft is parallel to the spacecraft-Earth line. Figure 1 shows the trajectory of the spacecraft and the field of view of the photometer projected on the Saturn equatorial plane near the Sat-

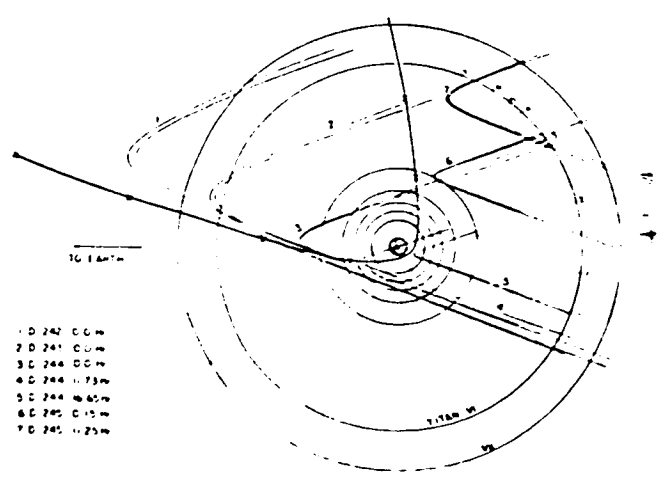

Fig. 1. Viewing hyperbolas in Saturn's equatorial plane as seen from above Saturn's north pole. The width of the hyperbolas represents the 1° cone angle width over which the photometer is sensitive. The view in the plane of the satellite orbits corresponds to seven different spacecraft positions indicated by the seven hyperbolas. Titan is at position 1 when the photometer view is that indicated by hyperbola 1.

0036-8075/80/0125-0431$00.75/0 Copyright © 1980 AAAS

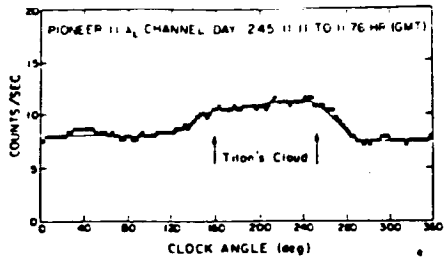

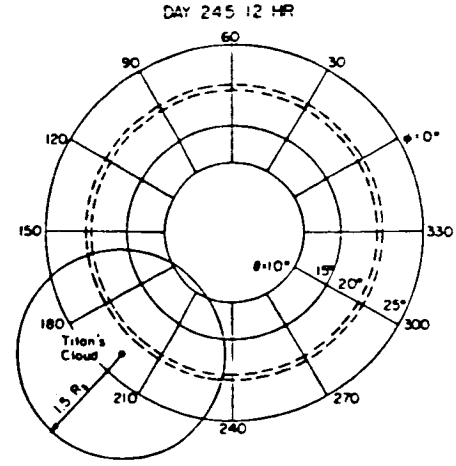

Fig. 2 (left). Emission signals detected by the λ_L channel. The feature centered at clock angle ~ 210° is interpreted as resonance scattering of the solar Ly α line by atomic hydrogen in an extended region of space (~ 1.5 R_S) centered on Titan. Fig. 3 (right). Viewing geometry for the ultraviolet photometer at 1200 on day 245, as seen looking along the spin axis of the spacecraft. The dashed circle represents the field of view. The signal was observed to extend from 160° to 240° and indicates that the extent of Titan's cloud is ~ 1.5 R_S from Titan's center.

urn encounter. As the spacecraft approached Saturn, the photometer field of view swept through Titan's orbit, Saturn's rings, and across the planetary disk. The observed λ_L signals from those objects throughout the encounter period are presented below. The data are presented as the observations were made, moving from the outermost feature, Titan, to the innermost feature, Saturn. In all cases, the observed emissions are assumed to be due to an atomic hydrogen Lyman α (Ly α) glow in a tenuous atmosphere or cloud, consistent with the spectroscopic observation of Saturn and its ring system by Weiser *et al.* (*3*) and Barker's identification of Ly α from the vicinity of Titan (*4*).

Titan observations. Titan and its cloud were in the field of view during most of day 245. Emission signals were detected when Titan was in the center of the field of view (θ = 20°) on day 245 at 1400 and 1530 Spacecraft Universal Time. However, the disk itself was not an obvious feature (Fig. 2). In addition, continuous emission signals were observed from 2300 on day 244 to 1330 on day 245, with the maximum emission occurring at about 1100 on day 245, when Titan's disk was about 2 Saturn radii (R_S) outside the field of view. For the period before 2300 on day 244, the quality of the transmitted data from the spacecraft was poor, and no useful data are available. Moreover, no continuous emission signals were observed from 1330 to 1700 due to background noise. The lack of a clear signature during these periods precludes a single interpretation. Short-term temporal variability of emission from a Titan-associated cloud is one possibility, although aliasing by the time-dependent background noise seems a more likely explanation. After 1700 on day 245, the field of view moved away from Titan's orbit, and no torus-associated features were observed. The Titan-associated emissions are most likely due to the scattering of the solar hydrogen Ly α line by an atomic hydrogen cloud along Titan's orbit. These results are consistent with the tentative identification of a cloud by Barker (*4*), who found a properly Doppler-shifted Ly α signal while viewing just inside Titan's orbit with an Earth-orbiting ultraviolet spectrometer. The apparent width of the emission signal suggests that the vertical extent of the cloud is about 1.5 R_S (Figs. 2 and 3), and the long duration of the emission signals suggests that the emitted cloud extends at least 5 R_S from Titan's disk. The full extent along the orbit could be much greater, but the present observations would suggest a weaker glow at angular distances greater than the above.

The plasma density at Titan's orbit is estimated to be about 5 cm^{-3} or less (*5*). For corotating plasma (velocity V = 200 km sec^{-1}) at the radial distance of Titan, the lifetime of local hydrogen atoms against charge exchange is estimated to be about 10^7 seconds—quite large compared to the Titan's orbital period (4 × 10^5 seconds). The lifetime of hydrogen atoms before photoionization is about 2 × 10^8 seconds, which is longer than the lifetime before charge exchange by a factor of 20. Thus Titan's apparent hydrogen cloud would be expected to form a complete torus, and indeed, emission has been detected ~ 5 R_S from Titan and along its orbit, but the limited amount of data preclude a more definitive statement on the spatial extent of the cloud. Furthermore, the brightness of the observable source has not yet been determined because of a sensitivity change in the λ_L channel during the encounter with the Saturn system.

Ring emission. Several Saturn radii outside the A ring, there is a weak glow that may be associated with the ring atomic hydrogen. The glow is brighter near the rings, suggesting that they are a significant source of atomic hydrogen. The glow does not seem uniform in the

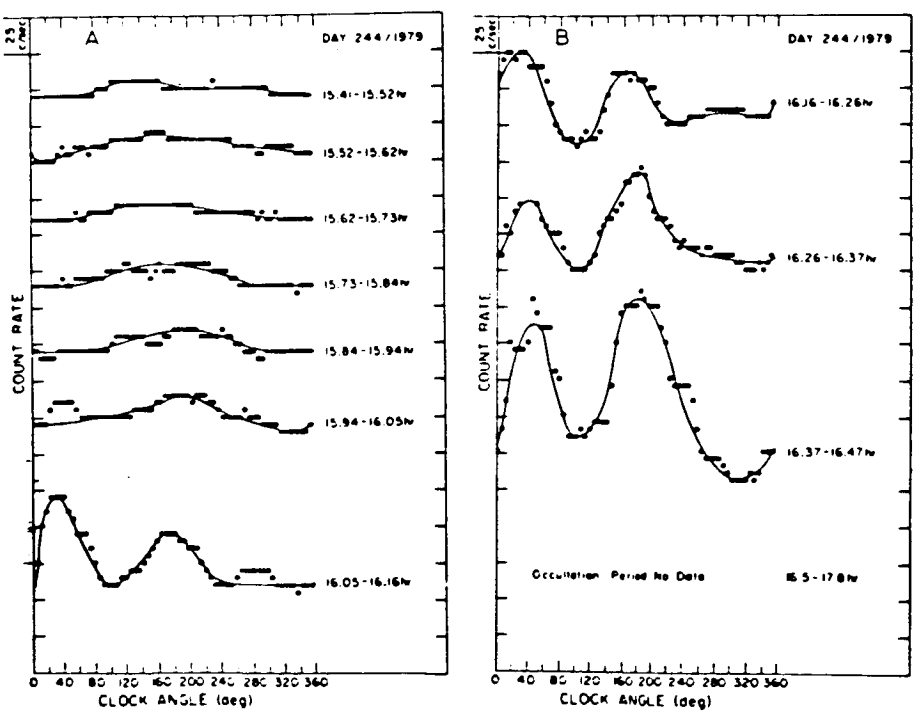

Fig. 4. (A and B) Emission signals from the vicinity of Saturn's rings. The emission features at clock angles ~ 40° and ~ 180° are interpreted as resonance scattering of the solar Ly α line, suggesting a torus of atomic hydrogen.

vicinity of the rings; it is brightest near the B ring. This lack of uniformity suggests that the particles leaving the rings have low kinetic energy, and continue to orbit Saturn at distances not too different from those at which they were formed. Photodissociation of H_2O has a significant cross section for producing ground-state atomic hydrogen and electronically excited OH (*6*). Not all absorption processes will result in low-energy hydrogen, however, and this may account for the relatively weak extended glow. In the present discussion we report only the clearly observed B ring observations.

The most obvious emission signals from the vicinity of the ring plane were observed beginning at 1520, when the spacecraft was about 0.65 AU from the inner edge of the B ring. Prior to this, the signal-to-noise ratio was less than 1, the noise being about 4 count/sec in this period. The signal intensity increased as the spacecraft approached the B ring (Fig. 4).

The signals before 1600 were at clock angles from 120° to 240°, where the field of view crosses the inner portion of the ring plane and its vicinity. The observed signals were centered at 180°, suggesting that the region of maximum intensity is about 0.2 R_S under the B ring plane (Fig. 5). However, only the weak background signals were detected at ~ 300°, where the field of view crosses the outer portion of the A ring plane.

At 1600 and later, the spacecraft flew very close to the B ring and was under its inner edge. Not only did the signal intensity increase significantly, the signals from the B ring were resolved into two sectors, one at a clock angle of ~ 40° and another at ~ 180°. These observations are consistent with arguments that the emissions are from the region close to the B ring and with a vertical extent of ~ 0.4 R_S (Fig. 6).

Strong Ly α radiation from Saturn's vicinity has been observed from a rocket-borne spectrograph (*3*). Our measurements confirmed the presence of such radiation and provided spatial resolution not possible in the sounding rocket observations. Moreover, our results show that the most intense emissions probably result from resonance scattering of the solar Ly α line by atomic hydrogen in the vicinity of the B ring plane. Likely processes for producing atomic hydrogen from the ring material are (i) neutralization of the Saturn photoelectron-ion flux flowing out along magnetic field lines (*7*) and (ii) photodissociation of the water ice molecules on the surface of the ring materials (*8*). The presence of the most intense hydrogen emissions near the B ring may result from an enhanced hydrogen source associated with the relatively high opacity of the B ring.

As mentioned earlier, it has been suggested that the ion flux from Saturn's ionosphere could be neutralized on the ring material and then thermally escape to produce atomic hydrogen in its vicinity (*7*). However, since the crystal-binding energy of water molecules in the ice mantle is low (*9*), and since protons and electrons can react chemically with water molecules (*10, 11*), the ionospheric particles can remove and dissociate these molecules from the ice mantle. Such a process may be much more important than neutralization followed by thermal escape, but no definitive results are available. Cheng and Lanzerotti (*12*) have considered the possible "sputtering" effect of the ring particles at the outer edge of the A ring by the trapped energetic protons in Saturn's magnetosphere.

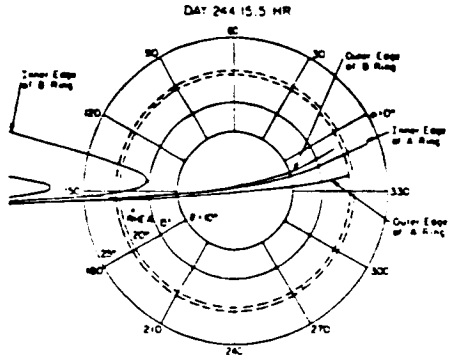

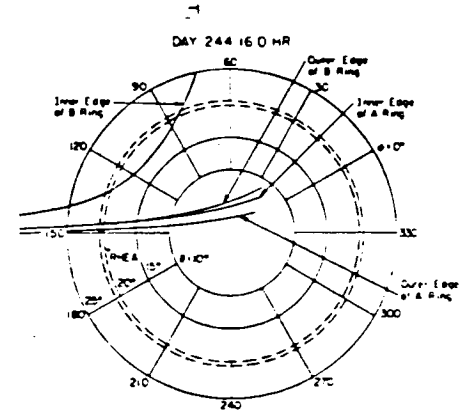

Fig. 5 (left). Viewing geometry for the ultraviolet photometer at 1530 on day 244, as seen along the spin axis of the spacecraft. The field of view (θ = 20°) crosses the ring plane at clock angles ~ 150° and 345°. Fig. 6 (right). Viewing geometry for the photometer at 1600 on day 244, as seen looking along the spin axis of the spacecraft. The field of view now crosses the inner edge of B ring at clock angles ~ 80° and 135°. The observed emission features at clock angles ~ 40° and 180° suggest an extensive hydrogen cloud in the vicinity of the B ring plane.

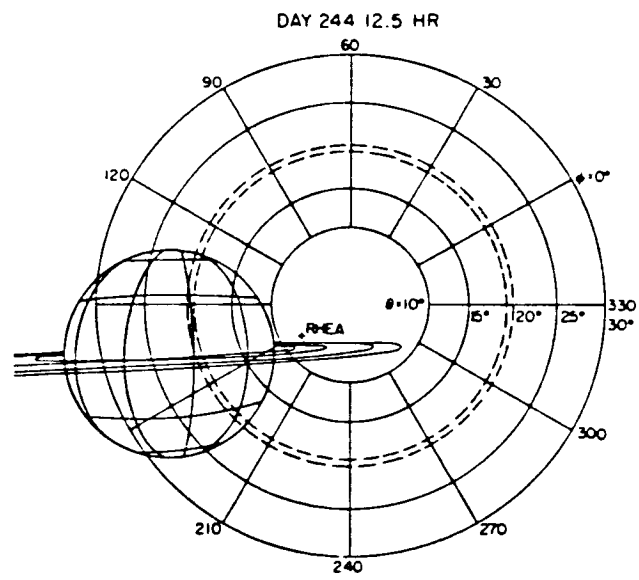

Fig. 7. Portion of Saturn's disk in the field of view at 1230 on day 244.

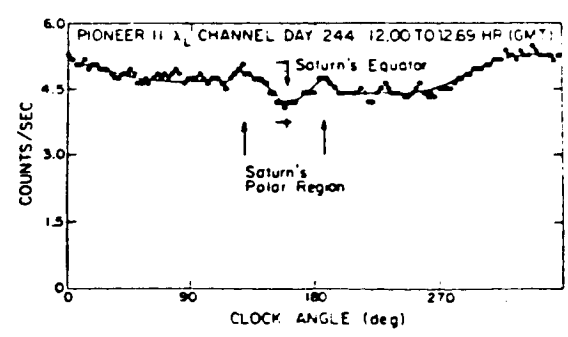

Fig. 8. Emission signals detected in the λ_L channel from Saturn's disk. The enhancement of the emission signal at small and large clock angles corresponds to a slowly changing background signal.

However, such processes should produce a hydrogen cloud with a radius larger than 2.5 R_S and therefore could not account for the observed B ring emission.

Saturn emission. The ultraviolet photometer scanned across Saturn's disk during the period from 1000 to 1400 on day 244, when the spacecraft was about 7.2 to 3.5 R_S from Saturn. During this period, the equatorial region of Saturn's disk was in the field of view at a clock angle of ~ 170°, and the whole disk subtended an angle that varied from 30° to 60° (Fig. 7). The observations show Saturn emissions with a strong latitudinal variation superimposed on a slowly varying background (Fig. 8). The emissions around Saturn's polar regions appear stronger than the emission from the equatorial region. This variation could result from limb brightening of Saturn's disk or auroral emission due to particle precipitation in Saturn's atmosphere.

Possible emissions due to helium and perhaps atomic ions have also been detected. However, due to high background noise in our short-wavelength channel, these emissions cannot be positively identified without further data analysis. In addition, photochemical and radiative transfer calculations for Saturn's atmosphere are required to properly interpret the long- and short-wavelength observations.

D. L. JUDGE
F.-M. WU
Department of Physics, University of Southern California, Los Angeles 90007
R. W. CARLSON
Jet Propulsion Laboratory, Pasadena, California 91103

References and Notes

1. D. L. Judge and R. W. Carlson, *Science* **183**, 317 (1974).
2. R. W. Carlson and D. L. Judge, *J. Geophys. Res.* **79**, 3623 (1974).
3. H. Weiser, R. C. Vitz, H. W. Moos, *Science* **197**, 755 (1977).
4. E. S. Barker, personal communication.
5. L. A. Frank, personal communication.
6. L. C. Lee, in preparation.
7. W.-H. Ip, *Astron. Astrophys.* **70**, 435 (1978).
8. R. W. Carlson, *Bull. Am. Astron. Soc.* **11**, 557 (1979).
9. N. C. Wickramasinghe, *Intersteller Grains* (Chapman & Hall, London, 1967).
10. ——— and D. A. Williams, *Observatory* **88**, 72 (1968).
11. F.-M. Wu, D. L. Judge, R. W. Carlson, *Astrophys. J.* **225**, 325 (1978).
12. A. F. Cheng and L. J. Lanzerotti, *J. Geophys. Res.* **83**, 2597 (1978).
13. We gratefully acknowledge the support that we received throughout this mission from the Pioneer Program Office at NASA headquarters and the Project Office at the NASA/Ames Research Center under the most able direction of C. Hall. We also thank TRW for providing such a reliable spacecraft and Analog Technology Corporation for providing an ultraviolet photometer with the longevity required for a mission to Saturn. Supported by NASA contract NAS 2-6558 with the NASA/Ames Research Center.

3 December 1979

JOURNAL OF GEOPHYSICAL RESEARCH, VOL. 85, NO. A11, PAGES 5853–5856, NOVEMBER 1, 1980

Observations of Extreme Ultraviolet Emissions From the Saturnian Plasmasphere

F. M. WU AND D. L. JUDGE

Earth and Space Sciences Institute, University of Southern California, Los Angeles, California 90007

R. W. CARLSON

Jet Propulsion Laboratory, California Institute of Technology, Pasadena, California 91103

Emission signals from the Saturnian plasmasphere at wavelengths shortward of 800 Å have been detected by the Pioneer ultraviolet photometer. The surface brightness of the emissions is about 0.3 ± 0.2 R. These short-wavelength emissions are interpreted as arising primarily from the radiative decay of electron excited atomic oxygen ions (O^{++}), in the region between 5 and 7 R_s from Saturn. The total power radiated by the Saturnian plasma inferred from these ultraviolet measurements is about $\sim 2 \times 10^{16}$ erg s^{-1}, consistent with in situ plasma measurements. From the observed energy loss rate it is estimated that the ions are introduced into the plasma torus at a rate of 8×10^{25} ions/s, possibly through the sputtering of water ice on the surface of Tethys and Dione by particle impact.

INTRODUCTION

The ultraviolet photometer on Pioneer Saturn has two channels, λ_s and λ_L, which are sensitive to emissions at wavelengths shortward of 800 Å and 1400 Å, respectively. An electronic switch alternately selects one of the two channels every two rolls of the spacecraft. Emission signals from Saturn, Titan, and the ring system were detected by the long wavelength (λ_L) channel and were reported by *Judge et al.* [1979]. From these data hydrogen clouds around Titan and the *B* ring have been identified. Additional emission signals from the Saturnian system have now been detected in the short wavelength (λ_s) channel. The observed λ_s emissions appear to come from three separate regions: the Saturnian magnetosheath, its plasmasphere, and a cloud inside the *B* ring. In the present paper we will discuss only the Saturn plasmasphere observations in the λ_s channel. Observations of the magnetosheath and the ring's emissions will be reported in a later paper.

A description of the ultraviolet photometer instrument has been given by *Carlson and Judge* [1974] and *Judge et al.* [1976]. The field of view of the photometer is determined by a collimator whose optical axis is oriented at a half cone angle of $\theta_0 = 20°$ with respect to the spacecraft spin axis. The spin scanning, which has a period of about 7.7 s, allows one to extract optical emission features in the presence of a substantial background signal. Since the λ_s channel is sensitive to emissions from 800 Å to 200 Å, it can detect the emissions from hot plasmas, as well as from neutral species, including the 584 Å resonance line of helium.

Observations

The size of the Saturn magnetosphere is between that of earth and Jupiter, with the mean distance of the magnetospheric subsolar point to Saturn being about 30 R_s [*Opp*, 1979]. During the Pioneer encounter, Saturn's magnetopause was crossed once at 17.3 R_s on the inbound trajectory (D 243 2209 ERT) and several times at 30–40 R_s on the outbound trajectory (D 245 0916 to D 246 0049 ERT) [*Wolfe et al.*, 1979]. Saturn's magnetosheath between the magnetopause and the shock regions contains shock-heated high temperature flowing plasma, while there is corotating magnetospheric plasma inside the magnetopause [*Wolfe et al.*, 1979]. The magnetospheric plasma is detected mostly in the region between 7 and 4 R_s, with the peaks at the orbital positions of Dione and Tethys where the plasma species have tentatively been identified as O^{++} (or O^{+++}) with a density between 10 to 50 cm^{-3} and a temperature of 2×10^5 to 5×10^6°K [*Frank et al.*, this issue]. Oxygen plasma of high temperature can provide a strong source of radiation in the EUV spectral region ($\lambda <$ 1000 Å) which would be detected by the scanning Pioneer UV photometer. As the Pioneer spacecraft approached Saturn, the field of view of the photometer, because of spacecraft spin motion, periodically swept through the Saturn magnetosphere and thus provided an opportunity to map the plasma distribution in the vicinity of Saturn.

The trajectory of the spacecraft and the field of view of the photometer projected on Saturn's equatorial plane, for the time period near closest approach to Saturn, is shown in Figure 1. The field of view is inside Dione's orbit (a dense plasma region) as early as day 210 (D 210) and remains there throughout most of the pre-encounter period. During this early period and before the spacecraft crossed the bow shock (first bow shock crossing was on D 243 at 1208 ERT) the background count rate in the photometer's λ_s channel was about 30 to 40 c s^{-1}. Thus an emission feature of a few counts per second could be readily recognized. However, no obvious signals were observed until D 240 when the spacecraft was about 70 R_s from Saturn. The possibility that very weak emissions were detected beyond 70 R_s cannot be ruled out, but further analysis will be required to establish such a result.

After crossing the bow shock, magnetospheric energetic particles and hot plasma significantly increased the background noise level in the λ_s channel. This complicates the observation of weak optical signals near the encounter period. A further complication due to sensitivity degradation, coupled with the high noise level, resulted in no detection of λ_L channels optical signals associated with Saturn's plasma. In the present work we report only on the λ_s channel emissions detected between D 240 and D 243 when the background noise level is low.

Typical λ_s emission signals in the time period between D

Copyright © 1980 by the American Geophysical Union.

Paper number 80A0907
0148-0227/80/A-0907$01.00

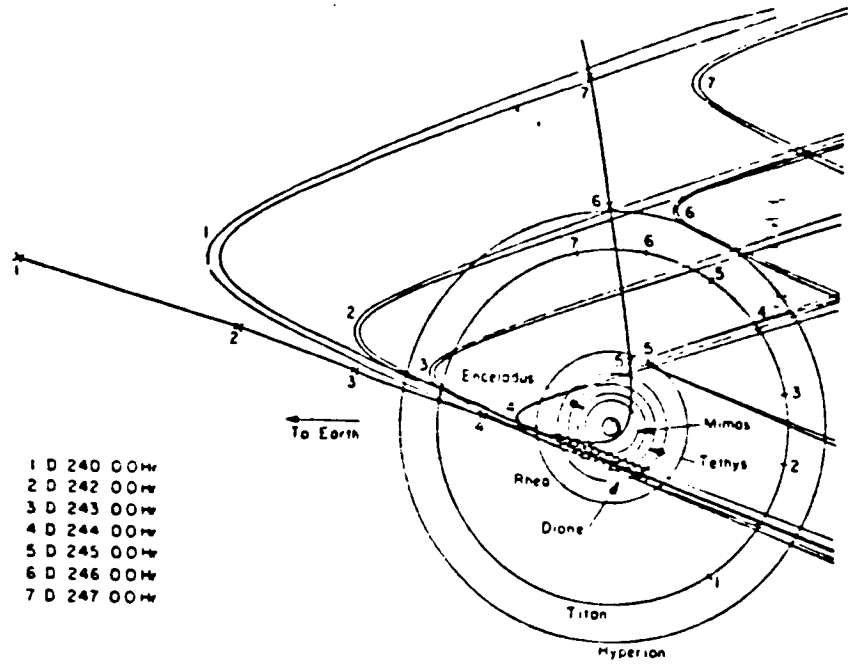

Fig. 1. Viewing hyperbola in Saturn's equatorial plane as seen from above Saturn's north pole. The width of the hyperbolas represents the 1° cone angle width over which the photometer is sensitive. Seven viewing hyperbolas corresponding to different spacecraft positions are shown. The dotted area shown in this figure is the region where the plasmasphere emission is observed.

240 and D 243 are shown in Figure 2. During this period, the region inside Dione's orbit is in the field of view at a clock angle of ~300° (the dotted area in Figure 1). The observations show that the amplitude of the emission feature at this clock angle is about 1.5 c s^{-1} with an uncertainty of ± 1 c s^{-1}, determined by the background noise level. The low spatial resolution at these large distances from Saturn permits only a rough estimate of the extent of the cloud's emission. The data suggest, however, that the primary source is between 5 and 7 R_s from Saturn. From the published plasma analyzer data the vertical extent of Saturn's plasma is observed at to be at least 0.4 R_s above the orbital plane, but an upper limit is not available. We assume here, however, that it extends ±2 R_s from the ring plane, which corresponds roughly to scale heights derived from the ion temperature deduced by *Frank et al.* [this issue]. With the observed count rate of 1.5 c s^{-1} and the above assumed cloud extent, the brightness of the cloud can be evaluated and is found to be about 0.3 ± 0.2 R for photons of 500-Å wavelength. The source of this emission at $\phi \sim 300°$ is primarily due to electron excitation of atomic oxygen ions in Saturn's plasmasphere, as will be discussed in the next section.

INTERPRETATION

Our interpretation of these plasmasphere emissions is guided by the in situ measurements performed by the Pioneer 11 plasma analyzer [*Wolfe et al.*, 1980; *Frank et al.*, this issue]. Analysis of these data by *Frank et al.* [this issue] shows that a high temperature plasma consisting of doubly and triply ionized oxygen ions (OIII, OIV) is present in the inner Saturnian magnetosphere. Maxima in the ion densities occur at the orbital radii of Tethys and Dione (4.9 and 6.3 R_s, respectively). The region from 4–7 R_s, which includes these two maxima, is composed primarily of doubly ionized oxygen (OIII), while triply ionized oxygen (OIV) is the predominant ion in the region from 7–8 R_s. Ion temperatures in these regions range from 2 × 10^5°K to 5 × 10^6°K (17–430 eV).

Emission lines of ionized species such as OIII and OIV generally occur in the extreme ultraviolet: in fact most of the dominant features from OIII and OIV occur within the spectral range of the short wavelength channel of the ultraviolet photometer. A variety of excitation mechanisms are capable of producing these emissions, but the most important process for the observed plasmaspheric emissions is probably electron excitation, with minor contributions from resonance scattering and radiative recombination. The relative importance of these processes is evaluated in the following paragraphs.

The radiative cooling rate, ρ, for electronically excited transitions of OIII and OIV plasmas has been computed by *Shemansky* [1980]. For the plasma temperatures of interest here, a typical value for the total ultraviolet emission rate is $\rho \sim 2 \times 10^{-19}$ erg cm^3 s^{-1}. If the average photon energy is 20 eV (= 3 × 10^{-11} erg) and if the electron density is $[e] \sim 80$ cm^{-3} (appropriate for the Saturn ion torus), then the total ultraviolet photon emission rate per ion is $\nu_e = (\rho/h\omega)\,[e] \sim 5 \times 10^{-7}$ s^{-1}.

Emissions from the Saturn plasma torus can also be produced by resonance scattering of the incident solar ultraviolet flux. In particular, the $^3P_2$–$^3P_2°$ transition of OIII is in near coincidence with the intense solar He II line at 303 Å [c.f. *Carlson*, 1972]. The excitation rate per ion at Saturn is found to be $\nu_{ph} \sim 3 \times 10^{-8}$ s^{-1}, which was derived by using the helium line width and intensity measured by *Cushman et al.* [1975] and atomic parameters presented by *Carlson* [1972]. This is much smaller than the electron excitation rate discussed above. Similarly, resonance scattering of the solar OIII 834-Å lines is expected to be much less than the electron excitation rate. The contribution to the ultraviolet emission rate from radiative recombination can be estimated as follows: if recombination proceeds with a rate coefficient of $\alpha \sim 10^{-13}$ cm^3 s^{-1} [c.f. *Allen*, 1973], and if each recombination leads to emission of an ultraviolet photon, then the emission rate is $\nu_r \sim \alpha\,[e] \sim 10^{-11}$ s^{-1}. This is again much smaller than the electron excitation rate. We therefore conclude that the dominant

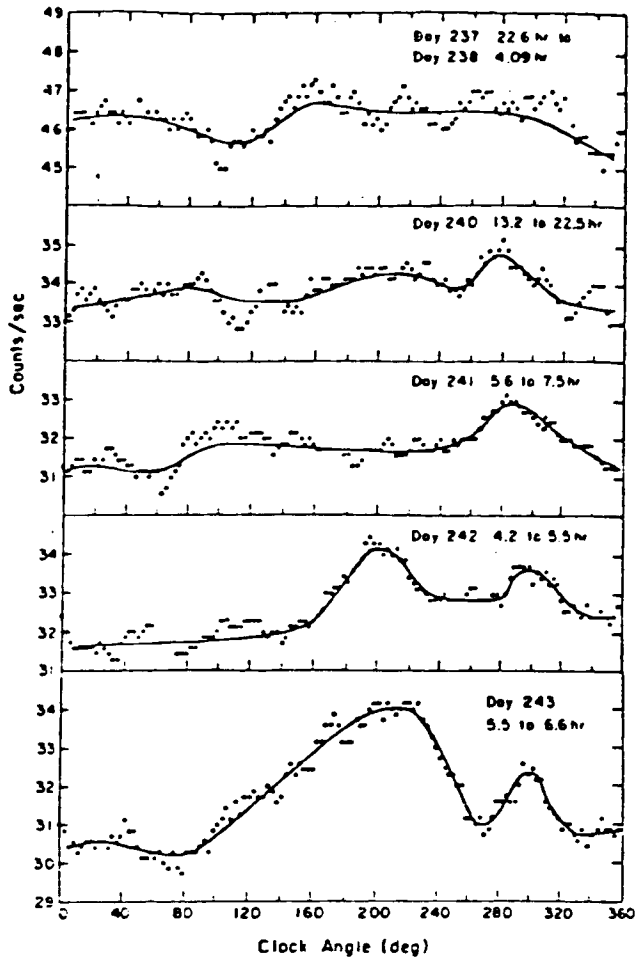

Fig. 2. Emission signals detected in the λ_1 channel from the vicinity of Saturn's magnetosphere. The signal at a clock angle of 300° is interpreted as radiative decay of excited atomic oxygen ions (O^{++}) in an extended region inside Dione's orbit. The feature at a clock angle of 200°, in view of its large angular extent, may be optical emissions or merely background variation, and further investigation is required. The time indicated in this figure is spacecraft universal time, which differs from the earth receipt time by 1.4 hours.

process which produces the observed Saturn plasmasphere emission is electron excitation.

If excitation by electrons is assumed to be the primary excitation mechanism, then the spectral features which contribute to the observed signals can be predicted. Voyager UVS measurements of the Jovian torus show rich and complex spectra, and one can expect similar characteristics from the Saturn torus. Shemansky's calculations of oxygen ion emission rates show that the radiative energy loss rate is primarily through ultraviolet emission, principally in the multiplets listed in Table 1. Radiative loss rates are shown for two different electron temperatures: 10^{5}°K and 10^{6}°K. Electron temperatures in the Jupiter torus appear to be less than the corresponding ion temperatures [*Barbosa and Kurth*, 1979, *Strobel*, 1980; *Sullivan and Siscoe*, 1980], so the lower temperature case is probably to be preferred. Comparisons of these emission rates and the relative instrument response (see Table 1) shows that over one half of the energy radiated by plasma at 10^{6}°K, and about one third at 10^{5}°K, occurs in the spectral region of the λ_1 channel.

It is of interest to estimate the power being radiated by the plasma. Assuming that the torus is four Saturn radii in total vertical extent, then the mean brightness observed is $4\pi I \sim 0.3R$. With a path length of 6 R_s through the torus, and with an average photon energy of 20 eV, then the observed volume emission rate of energy is $\sim 3 \times 10^{-16}$ erg cm^{-3} s^{-1}. For a torus extending radially from 5 R_s to 7 R_s, and taking into account the instrumental response, the total radiated power inferred from these ultraviolet measurements is $\sim 2 \times 10^{16}$ erg s^{-1} (2×10^{9} W). A similar estimate results from the in situ plasma measurements. For an ion density of 40 cm^{-3} [*Frank et al.*, this issue], an electron density of 80 cm^{-3}, radiative cooling rates given in Table 1 and similar to the above torus dimensions, one finds an energy loss rate of 2–4 $\times 10^{16}$ erg s^{-1} depending upon the electron temperatures. This agrees with the ultraviolet-derived estimate to within a factor of two.

These energy loss rates perhaps can be used to infer characteristics of the ion source. It is thought that the energy source for the Jovian torus is the gyration energy of ions created within the magnetosphere. A neutral oxygen atom in Keplerian orbit around Saturn, when ionized, will possess roughly 110–225 eV of energy relative to the frame of reference co-rotating with the magnetic field (assuming a 10^{6}.7 magnetic rotation period [*Kaiser et al.*, 1980] and ionization occurring in the range 4.9–6.3 R_s). If the observed energy loss rate matches the energy input of ions created with an average energy of 150 eV, then approximately 8×10^{25} ions must be introduced into the torus each second. This is much greater than the source flux estimated by *Frank et al.* [this issue], who found fluxes of 1.5×10^{23}–1.5×10^{24} ions s^{-1} based on estimates of inward

TABLE 1. Prominent Spectral Features Predicted for the Saturn Torus

Ion	Transition	Wavelength, Å	Radiative Cooling Rate, ρ, at 10^{5} K, erg cm^3 s^{-1}	Radiative Cooling Rate, ρ, at 10^{6} K erg cm^3 s^{-1}	Relative Instrument Response
OIII	$2p^2\,{}^3P$–$2p^3\,{}^3S^0$	508	2×10^{-20}	8×10^{-20}	1.00
	$2p^2\,{}^3p$–$2p^3\,{}^3D^0$	833	5×10^{-20}	7×10^{-20}	0.02
	$2p^2\,{}^3p$–$2p^3\,{}^3p^0$	703	3×10^{-20}	6×10^{-20}	0.20
	$2p^2\,{}^3p$–$3s^3p^0$	374	0.2×10^{-20}	3×10^{-20}	0.62
	$2p^2\,{}^3p$–$2p^2\,{}^1D$	4950	2×10^{-20}	1×10^{-20}	0.00
	Sum	...	12×10^{-20}	25×10^{-20}	...
OIV	$2p^2p^0$–$2p^2\,{}^2p$	555	4×10^{-20}	12×10^{-20}	0.92
	$2p^2p^0$–$2p^2\,{}^2D$	790	3×10^{-20}	4×10^{-20}	0.08
	$2p^2p^0$–$2p^2\,{}^2S$	609	1×10^{-20}	3×10^{-20}	0.50
	Sum	...	8×10^{-20}	20×10^{-20}	...

These features were based on calculations by *Shemansky* [1980]. The relative instrument response was normalized to the 508-Å multiplet.

diffusion losses. However, outward diffusion in the Jupiter torus is more than an order of magnitude greater than inward diffusion [*Richardson et al.*, 1979]. Therefore the plasma estimates by *Frank et al.* [this issue] may be too low. It may also be noted that the plasmasphere may be a very dynamic phenomenon, and average flux estimates cannot be derived from our limited data.

The source of atoms which produce the torus is subject to speculation. Since ion densities are maximum at the orbits of Tethys and Dione, then it is natural to assume that these satellites are the initial sources. This is plausible since they are thought to possess icy surfaces [*Cruikshank*, 1979], but the mechanism by which material is introduced into the torus is unclear. Sputtering by high-energy particles appears to be insufficient. Using high-energy proton flux values of $\sim 10^5$ cm^{-2} s^{-1} [*Trainor et al.*, 1979] and sputtering yields of $\gamma \sim 0.2$ atoms/proton [*Brown et al.*, 1978], then only $\sim 10^{21}$ atoms s^{-1} will be injected into the magnetosphere. Photo sputtering [*Carlson*, 1980] could be a source of OH, which may be subsequently dissociated and ionized. However, the yield is only $\sim 2 \times 10^{24}$ s^{-1}, a factor of 40 less than required. Sputtering could also occur by impact of the plasmaspheric ions and electrons themselves. Sputtering yields are significant for heavy ions with several hundred electron volts of energy (as is the case for co-rotating oxygen ions). However, the plasmaspheric ions with a sputtering yield of unity would produce only $\sim 3 \times 10^{24}$ s^{-1}. The plasmaspheric electron flux is about 10^{10} cm^{-2} s^{-1} [*Frank et al.*, this issue] and is quite large in comparison with the low-energy proton flux of $\sim 6 \times 10^7$ cm^{-2} s^{-1}. With an assumed sputtering yield of ~ 0.1 atoms per electrons, the plasmaspheric electron flux would produce an ion flux of $\sim 10^{26}$ ions s^{-1} from Tethys and Dione's surface, a number consistent with the observed energy loss rate. However, the efficiency of removing H_2O molecules through electron impact has not been established. Laboratory data are required to conform whether this physical process is important. It may be noted that bombardment of Europa's surface by Jovian plasmaspheric protons and electrons had been suggested by *Wu et al.* [1978] as a possible process for producing an observed oxygen cloud at the orbit of Europa. If sputtering by the plasmaspheric particle is the means of populating the torus, then this regenerative situation could lead to an unstable and highly variable plasmasphere.

Acknowledgments. This work was supported by NASA contract NAS2-6558 with the Ames Research Center. The authors thank L. A. Frank and D. E. Shemansky for helpful discussions and Steve Askew for assistance with the real-time data processing.

The Editor thanks D. F. Strobel for his assistance in evaluating this paper.

REFERENCES

Allen, C. W., *Astrophysical Quantities*, Athlone Press, London, 1973.

Barbosa, D. D., and W. S. Kurth, A model for generation of electrostatic waves in Jupiter's inner magnetosphere (abstract), *Eos Trans. AGU*, *60*, 919, 1979.

Brown, W. L., L. J. Lanzerotti, J. M. Poate, and W. M. Augustyniak, Sputtering of ice by Mev light ions, *Phys. Rev. Lett.*, *40*, 1027, 1978.

Carlson, R. W., Possibility of OIII λ 304-Å emissions in the extreme ultraviolet airglow, *J. Geophys. Res.*, *77*, 6282, 1972.

Carlson, R. W., Photo-sputtering of ice and hydrogen around Saturn's ring, *Nature*, *283*, 461, 1980.

Carlson, R. W., and D. L. Judge, Pioneer 10 ultraviolet photometer observations at Jupiter encounter, *J. Geophys. Res.*, *79*, 3623, 1974.

Cruikshank, D. P., The surface and interiors of Saturn's satellite, *Rev. Geophys. Space Phys.*, *17*, 165, 1979.

Cushman, G. W., L. Farewell, G. Godden, and W. A. Rense, Solar line profile of HeI 584Å and HeII 304Å, *J. Geophys. Res.*, *80*, 482, 1975.

Frank, L. A., B. G. Burek, K. L. Ackerson, J. A. Wolfe, and J. D. Mihalov, Plasmas in Saturn's magnetosphere, *J. Geophys. Res.*, this issue.

Judge, D. L., R. W. Carlson, F. M. Wu, and U. G. Hartmann, Pioneer 10 and 11 ultraviolet photometer observations of the Jovian satellites, in *Jupiter*, edited by T. Gehrel, p. 1068, University of Arizona Press, Tucson, 1976.

Judge, D. L., F. M. Wu, and R. W. Carlson, Ultraviolet photometer observations of the Saturnian system, *Science*, *207*, 431, 1979.

Kaiser, M. L., M. D. Desch, J. W. Warwick, and J. B. Pearce, Voyager detection of nonthermal radio emission from Saturn, *Science*, in press, 1980.

Opp, A. G., Scientific results from the Pioneer Saturn encounter: Summary, *Science*, *207*, 401, 1979.

Richardson, J., G. L. Siscoe, and J. D. Sullivan, Time-dependent radial diffusion in the Io plasma disk (abstract), *Eos Trans. AGU*, *60*, 920, 1979.

Shemansky, D. E., Radiative cooling efficiencies and predicted spectra of species of the Io plasma torus, *Astrophys. J.*, *236*, 1043, 1980.

Strobel, D. F., UV observations of the Io plasma torus, *Coll. 57*, Int. Astron. Union, Kona, Hawaii, 1980.

Sullivan, J. D., and G. L. Siscoe, *In situ* observations of the Io torus, *Coll. 57*, Int. Astron. Union, Kona, Hawaii, 1980.

Trainor, J. H., F. B. McDonald, and A. W. Schardt, Observation of energetic ions and electrons in Saturn's magnetosphere, *Science*, *207*, 423, 1979.

Wolfe, J. H., J. D. Mihalov, H. R. Collard, D. D. McKibbin, L. A. Frank, and D. S. Intriligator, Preliminary results on the plasma environment of Saturn from the Pioneer 11 plasma analyzer experiment, *Science*, *207*, 403, 1979.

Wolfe, J. H., J. D. Mihalov, H. R. Collard, D. D. McKibbin, L. A. Frank, and D. S. Intriligator, Pioneer 11 observations of the solar wind interaction with Saturn, submitted to *J. Geophys. Res.*, 1980.

Wu, F. M., D. L. Judge, and R. W. Carlson, Europa ultraviolet emissions and the possibility of atomic oxygen and hydrogen clouds, *Astrophys. J.*, *225*, 325, 1978.

(Received May 7, 1980;
revised June 23, 1980;
accepted June 25, 1980.)

Planet. Space Sci. Vol. 28, pp. 815–821
© Pergamon Press Ltd., 1980. Printed in Northern Ireland

0032-0633/80/0801-0815$02.00/0

SURVIVAL PROBABILITIES FOR INTERSTELLAR HYDROGEN FLOWING INTO THE INTERPLANETARY SYSTEM FROM FAR REGIONS OF THE HELIOSPHERE

JOSEPH A. KUNC
Space Sciences Institute, University of Southern California, University Park, Los Angeles, CA 90007, U.S.A.

(*Received* 14 *March* 1980)

Abstract—The expressions for "survival" probabilities are presented for an atomic hydrogen particle moving on a trajectory from far regions of the heliosphere to the vicinity of the Sun. Three "destroying" processes have been considered, photoionization, charge transfer and electron ionization. The solar wind has been assumed to be a two-flux steady stream radially expanding with constant flow velocity. Recent profiles of solar-wind electron temperature have been used. The results can be useful for theoretical analyses as well as for analysis of spaceflight observations.

1. INTRODUCTION

Current evidence indicates that the assumption of a very low temperature ($T_\infty \approx 0$ K—so called "cold" particles) of the heliospheric gas very far from the Sun (i.e. at the vicinity of the boundary of heliosphere; called hereafter "infinity") is not valid (see e.g. Thomas, 1972; Feldman *et al.*, 1972; Meier, 1977). Most authors agree with $T_\infty \approx 10{,}000$ K (so called "hot" gas) and usually they assume a Maxwellian distribution function for the gas particles. The state of the interstellar gas beyond the heliosphere as well as the mechanism of transporting particles with such low density (~ 0.1 cm^{-3}) through a heliospheric boundary shock region is not clear enough to define the distribution function of the gas at "infinity". However, in the author's opinion, it may be of interest to take into account the possibility that particles at "infinity" can have reasonably high mean energy (e.g. still about 1 eV) but a non-Maxwellian velocity distribution function. It seems that at least two different situations may be interesting; the first case to be considered is one in which "hot" particles have the same directions, but different absolute velocities (e.g. particles "a" in Fig. 1), and the second in which "hot" particles have different directions but with a Dirac's δ-distribution function for their absolute velocities (e.g. particles "b" in Fig. 1). Because of the very small density of particles [mean free path for H-H collision is about 10^{17} cm rather than 10^{19} cm which was given by Fahr (1978)] and pretty high temperature, the particles should be treated as a gas of independent particles whose motion, on their individual trajectories, is determined by the interaction with other particles from the solar wind and by the field of the Sun (i.e. gravitational and radiation pressure forces). Other forces that might change the individual trajectory of a particle and which can be called "friction" forces (as a result of momentum transfer with solar wind particles) are negligible; the ratio of the gravitational force to the "friction" force given by the interaction of neutrals with the solar wind protons is, in the heliosphere not smaller than 10^9 and, of course, the interaction with solar electrons makes the result a couple of orders of magnitude larger.

Each particle moving along its own trajectory (dependent on its initial velocity vector and initial angular momentum) may take part (i.e. not "survive") in some atomic processes. So far the most important of these processes seems to be the following three:

(A) Process A (photoionization): $h\nu + H(1s) \rightarrow H^+ + e$,

(B) Process B (charge transfer): $H^+ + H(1s) \rightarrow H(1s) + H^+$,

(C) Process C (electron ionization): $e + H(1s) \rightarrow H^+ + 2e$.

In the present paper relationships are given for the three above processes for rate coefficients (β_A, β_B and β_C, respectively) and for the probabilities of atomic hydrogen "avoiding" each of them (P_A, P_B and P_C respectively) along various trajectories from "infinity" to the Sun. The incoming hydrogen atoms interact with the solar wind flux (see paragraph 2) as a radially expanding beams of electrons and protons. Knowing such survival probabilities it is possible to find the density at a given point in the

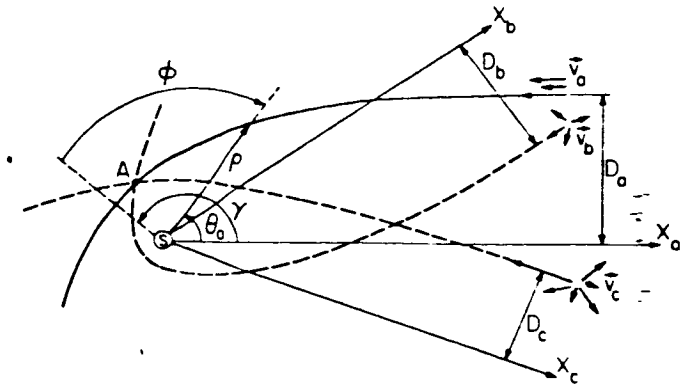

FIG. 1. TRAJECTORIES OF NEUTRALS INCOMING FROM "INFINITY" UNDER GRAVITATIONAL-RADIATIVE INFLUENCE OF THE SUN. AT POINT A OF INTERPLANETARY SPACE PARTICLES FROM DIFFERENT REGIONS OF "INFINITY" AND WITH DIFFERENT INITIAL VECTOR VELOCITY DISTRIBUTIONS CAN TAKE PART IN GIVEN PROCESS.

heliosphere, for particles coming from the distant regions (e.g. as well as particles "a" as "b" or "c" in Fig. 1). Knowledge of the probabilities and the position and velocity distribution functions for particles on their individual trajectories, as influenced by (regardless of the interaction with the solar wind) the gravitational-radiative force of the Sun, (the result of the latter will soon be published), together with a thorough analysis of the processes in the shock region, should be the starting point for a correct description of the density distribution function of neutrals within the heliosphere and other physical quantities, for the "hot" gas model. It should also be noted that using the concept of temperature for the gas at infinity can be a puzzling problem, not only because of a possible non-Maxwellian distribution function there, but also because at such extremely low particle densities ($\sim 0.1\ \mathrm{cm}^3$) using the concept of phase-space can be invalid for small regions (because of fluctuations). Thus, operating with mean particle energy seems to be more proper than with temperature.

2. SOLAR WIND ELECTRONS AND PROTONS

The two-flux radial model of the solar wind has been used in the present work. This often used model assumes that both fluxes (electrons and protons) radially expand with spherical symmetry and also have constant flow velocities ($u_p \approx u_e$) but different thermal velocity distribution functions. The former assumption describes the solar wind plasma as quasineutral since there are no sources of charges in the wind. In the steady-state we can say that solar protons have a Dirac's δ-distribution function (around u_p) and solar electrons have a Maxwellian distribution function with temperature $T_e(r)$. Density $n_e(r)$ and temperature $T_e(r)$ of the solar electrons can be given (e.g. Hollweg, 1976; and Holzer, 1977) in the general forms ($\rho = r/r_e$ where r_e is the distance from the Sun to the Earth):

$$n_e(\rho) = n_e^0 \rho^{-2}, \tag{1}$$

and

$$\begin{aligned} T_e(\rho) &= T_f = \text{const.}, \quad \text{for} \quad \rho \leq 0.08, \\ T_e(\rho) &= T_e^0 \rho^{-\alpha}, \quad \text{for} \quad \rho \geq 0.08, \end{aligned} \tag{2}$$

where the superscript "0" denotes the value of $\rho = 1$.

All above theoretical relations (obtained on the assumption that on the surface of the Sun $T_e^* = T_p^* = 2 \cdot 10^6\ \mathrm{K}$ and $n_e \approx n_p = 1.5 \cdot 10^7\ \mathrm{cm}^{-3}$) give pretty good agreement with the observations of Hundhausen (1972) and Miggenrieder *et al.* (1976). Relation (1) is valid up to distances very close to the surface of the Sun for the solar wind model given by Munro and Jackson (1977) and is identical with the calculations of Hundhausen (1972) (for a spherically symmetric solar wind model) for heliocentric distances $\rho \geq 0.08$. For regions close to the Sun and close to Earth the results of Holzer give $T_f \approx 2 \cdot 10^6\ \mathrm{K}$ and $T_e^0 \approx 1.5 \cdot 10^5\ \mathrm{K}$, respectively. However, there are differences in the estimation of the exponent α; $\alpha = \frac{4}{3}$ (Hollweg) and $\alpha = \frac{7}{8}$ (Holzer). Holzer's exponent α gives values in better agreement with the above mentioned observations. The solar proton density distribution function has in this model a form analogous to relation (1):

$$n_p(\rho) \equiv n_p^0 \rho^{-2}. \tag{3}$$

Even if one assumes some other (non-Dirac's δ) proton velocity distribution function $f(v_p - u_p)$ with an isotropic "effective" temperature $T_p(\rho)$ the component of the thermal energies of the protons arising from such a distribution is much smaller than the flow component. The latter can be shown in a straightforward way from the approximate solution of equations representing a steady, spherically symmetric radial solar wind (Nishida, 1969) of the two-flux model, with the temperature that had been considered for proton–proton Coulomb heating (Leer and Axford, 1972) in the spiral magnetic field (what appears to be justified for $\rho \geq 0.5$). The approximate solution is:

$$T_p(\rho) \approx \tfrac{2}{3} T_{pp} \rho^{-1}, \tag{4}$$

where T_{pp} is the temperature of the solar protons at $\rho = 0.5$ with the value of about $6 \cdot 10^4$ K. In obtaining the last equation it has been assumed that the mean proton temperature is $T_p = \frac{1}{3}(T_p^{\parallel} \times 2T_p^{\perp})$ where $T^{\parallel}$ and $T^{\perp}$ are parallel and perpendicular components of the proton temperature, respectively. The energies of protons which are given by relation (4) are much smaller than the energies (~ 1 keV) obtained from flow velocity (≈ 400 km s^{-1}).

3. RATE COEFFICIENTS

(A) *Photoionization*

Usually it is assumed that the flux density of the solar EUV photons varies inversely as the square of the heliocentric distance (the interplanetary gas should be optically thin in the ionizing frequency range). According to the above

$$\beta_A(\rho) = \beta_A^0 \rho^{-2} \tag{5}$$

where the superscript "0" denotes the values of the EUV photoionization rate coefficient at 1 AU from the Sun. Of course, the rate coefficient β_A^0 depends on the solar EUV photon flux. The latter, however, is not yet so precisely determined (see for instance papers of Hinteregger, 1976 and Timothy, 1977). Nevertheless, it seems to be probable that the value of the rate coefficient β_A^0 given by Banks and Kockarts (1973) is reasonable (their $\beta_A^0 = 0.88 \cdot 10^{-7}$ s^{-1}). It should be noted that for higher solar activities this value can increase by a factor 2 for hydrogen (and even more in the case of interplanetary helium) as has been estimated by Holzer (1977).

(B) *Charge transfer*

If, according to Section 2, the charge transfer process is due to the interaction of fast solar protons with relatively slow interplanetary hydrogen atoms, and the solar proton flux has spherical symmetry and a Dirac's δ velocity distribution function, then the expression for β_B takes the form:

$$\beta_B(\rho) = n_p^0 u_p Q_B \rho^{-2}, \tag{6}$$

where, as previously, n_p^0 is the solar proton density at $\rho = 1$, and Q_B is the charge transfer cross-section. In the above it has been assumed that the solar proton flux varies inversely as the square of the heliocentric distance.

(C) *Electron collisional ionization*

Usually, calculations of the electron ionization rate coefficient (for a Maxwellian distribution function) are done by numerical integration (e.g. Kunc and Zgorzelski, 1975 or Holzer, 1977). The latter calculations, adapted for the interplanetary medium, have shown that the contribution of electron ionization is significant for a heliocentric distance smaller than about 0.5 AU, relative to photoionization, and at distances smaller than about 0.08 AU, relative to charge transfer process. In the present paper the author has used analytical relations for collisional ionization by Maxwellian electrons of ground state hydrogen atoms with rate coefficients based on the results of his recent work (Kunc, 1979).

Taking into account the above, one can write the general relationship:

$$\beta_C(\rho) = 4.765 \cdot 10^{-6} n_e(\rho) U_i^{-3/2} T^{1/2} I_M^R, \text{ s}^{-1}, \tag{7}$$

where $n_e(\rho)$ (in cm^{-3}) is the density of solar wind electrons, U_i (in eV) is the ionization potential of the hydrogen atom, $T(\rho) = T_e(\rho)/U_i$, where T_e is also given in eV. The term $I_M^R(T)$ has the forms given below [see equations (27) and (31) of the paper by Kunc, 1979]:

for $\rho \leq 0.4$:

$$I_M^R(T) = \frac{1.52}{T}\left[\exp(-3.45/T) + \frac{2}{T} - 0.37\right], \tag{8}$$

for $\rho \geq 0.4$:

$$I_M^R(T) = 0.26 \exp(-1/T). \tag{9}$$

If we take into account expressions (1) and (2) we have finally:

for $\rho \leq 0.08$:

$$\beta_C(\rho) = 5.351 \cdot 10^{-7} n_e^0 T_i^{-1/2} \rho^{-2} \times \left[\exp(-3.45 U_i/T_i) + \frac{2U_i}{T_i} - 0.37\right], \text{ s}^{-1}, \tag{10}$$

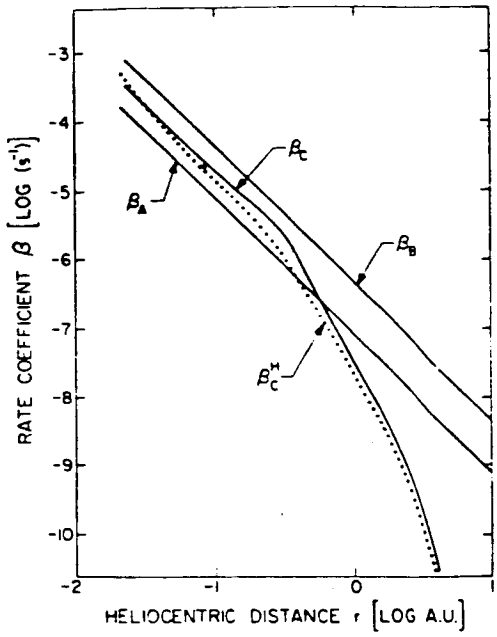

FIG. 2. RATE COEFFICIENTS FOR PHOTOIONIZATION (β_A), CHARGE TRANSFER (β_B) AND ELECTRON IONIZATION (β_C) WITHIN THE SOLAR SYSTEM $\beta_C{}^H$ (DOTTED LINE) IS THE ELECTRON IONIZATION RATE COEFFICIENT OBTAINED BY HOLZER (1977) BY NUMERICAL INTEGRATION OF EXPERIMENTAL DATA GIVEN BY KIEFFER AND DUNN (1966).

for $0.08 \leq \rho \leq 0.4$:

$$\beta_C(\rho) = 5.351 \cdot 10^{-7} n_e{}^0 (T_e{}^0)^{-1/2} \rho^{\alpha/2-2} \times \left[\exp(-3.45 U_i \rho^\alpha / T_e{}^0) + \frac{2U_i}{T_e{}^0}\rho^\alpha - 0.37\right], s^{-1}, \quad (11)$$

for $\rho \geq 0.4$:

$$\beta_C(\rho) = 6.702 \cdot 10^{-9} n_e{}^0 (T_e{}^0)^{1/2} \rho^{-(\alpha/2+2)} \times \exp(-U_i \rho^\alpha / T_e{}^0), s^{-1}. \quad (12)$$

It should be noted that the above relations for β give good agreement with reality (see Fig. 2) throughout the interplanetary system.

4. PROBABILITIES

The analysis is for a particle which has the velocity vector u_∞ at "infinity" anti-parallel to the fixed axis X_a (i.e. for one of the particles of the "a" kind in Fig. 1). This particle moves along its trajectory (full line in Fig. 1) acted upon by the central force of gravitation and radiation pressure of the Sun, and its position can be given by polar coordinates ρ and θ_a. It is obvious that all relations obtained in such a system of coordinates (with θ_a measured from axis X_a, and assuming the spherical symmetry of the solar wind) can be used for every other particle (e.g. particle "b" or "c" in Fig. 1) if the initial velocity vector of the particle is given: then angles θ_b and θ_c measured from axes X_b and X_c can be very easily expressed in terms of θ_a. The angle γ between the axis of symmetry of a particles trajectory and its asymptote can be given by the expression

$$\gamma = \cos^{-1}\left\{-\left[1 + \left(\frac{\delta}{C}\right)^2\right]^{-1/2}\right\}, \quad (13)$$

where δ and C are defined below. Also the trajectory of the particle in polar coordinates ρ and ϕ (ϕ is the angle measured from perihelion of orbit) can be given as follows:

$$\rho = \frac{\delta^2}{C\left\{1 + \left[1 + \left(\frac{\delta}{C}\right)^2\right]^{1/2} \cos\phi\right\}}, \quad (14)$$

where all above coordinates have been shown in Fig. 1. The relation between angles θ and ϕ is:

$$\gamma = \mp(\phi + \theta). \quad (15)$$

According to the above, hereafter we will omit index "a" and use θ and X in place of θ_a and X_a.

Trajectory of independent particle "a" in the ρ^{-2} central field of the Sun can be given in polar coordinates ρ and θ in the convenient undimensional form (which is a little more simple than usually presented):

$$\rho = \frac{\delta^2}{\delta \sin\theta + C(1 - \cos\theta)}, \quad (16)$$

where $\delta = D/r_e$ and $C = (1-\mu)GM_s/(r_e u_\infty{}^2)$. The parameter μ is the value of the ratio of the radiation force to the gravitational force, G is the universal gravitational constant and M_s is the mass of the Sun. In the above, it has been assumed that the radiation force is spherically symmetric and varies as ρ^{-2}, i.e. similar to the gravitational force. It should also be noted that a change of properties of the family of the particle trajectories (with the same $\mathbf{u}_\infty$ but different δ) is characterized by the grad δ, which has a form:

$$\text{grad}\,\delta = \left[\left(\frac{\partial\delta}{\partial\rho}\right)^2 + \frac{1}{\rho^2}\left(\frac{\partial\delta}{\partial\theta}\right)^2\right]^{1/2} = \frac{\delta\left(1 + \frac{2C}{\rho}\right)^{1/2}}{2\delta - \rho\sin\theta}. \quad (17)$$

Moreover, one can find from equation (16) the maximum value of "impact parameter" δ_{max}. Only

particles with $\delta < \delta_{max}$ can reach (regardless of "destroying" atomic processes) a sphere of radius ρ_0. This value is

$$\delta_{max} = [\rho_0(\rho_0 + 2C)]^{1/2}. \quad (18)$$

The probability $P(\rho, n_s, E_s, E)$, for a given atomic process, that a particle coming from infinity into our interplanetary system, has "survived," up to the point defined by coordinates ρ and θ is equal to

$$P[\rho(\theta, \delta, u_\infty), n_s, E_s, E] = \exp[-\omega(\rho, n_s, E_s, E)], \quad (19)$$

where E_s and E are the energies of solar wind particles and incoming particles, respectively. Further, we have

$$\omega = \int_{t_\infty}^{t} \beta(\rho, n_s, E_s, E)\,dt = \int_{-\infty}^{L(\rho)} \beta \frac{dL}{u(\rho)}, \quad (20)$$

where

$$\frac{dL}{u(\rho)} = \begin{cases} \dfrac{-r_e}{u_\infty}\left(1 + \dfrac{2C}{\rho}\right)^{-1/2} d\rho & \text{for} \quad \delta = 0 \\ \dfrac{r_e \rho^2}{u_\infty \delta}\, d\theta & \text{for} \quad \delta \neq 0 \end{cases} \quad (21)$$

$t - t_\infty$ is the interval of time required for a particle to traverse the path L from infinity up to point ρ, θ. According to the above and equations (5)–(12) and (20), after transformations, we have finally:

(A) *Photoionization*

$$\omega_A(u_\infty, \rho) = \frac{r_e \beta_A{}^0}{u_\infty C}\left[\left(1 + \frac{2C}{\rho}\right)^{1/2} - 1\right], \quad \text{for} \quad \delta = 0, \quad (22)$$

and

$$\omega_A(u_\infty, \delta, \theta) = \frac{r_e \beta_A{}^0 \theta}{u_\infty \delta}, \quad \text{for} \quad \delta \neq 0. \quad (23)$$

(B) *Charge transfer*

$$\omega_B(u_\infty, \rho) = \frac{r_e n_p{}^0 u_p Q_B}{u_\infty C}\left[\left(1 + \frac{2C}{\rho}\right)^{1/2} - 1\right], \quad \text{for} \quad \delta = 0, \quad (24)$$

$$\omega_B(u_\infty, \delta, \theta) = \frac{r_e n_p{}^0 u_p Q_B}{u_\infty \delta}, \quad \text{for} \quad \delta \neq 0. \quad (25)$$

(C) *Electron ionization*

For $\delta = 0$ we have finally:

$$\omega_C(u_\infty, \rho) = \frac{r_e}{u_\infty}\int_{-\infty}^{\rho} \beta_C(\rho)\left[1 + \frac{2C}{\rho}\right]^{-1/2} d\rho, \quad (26)$$

where β_C is given in equations (10), (11) or (12). For $\delta \neq 0$ we have; for $\rho \leq 0.08$:

$$\omega_C(u_\infty, \delta, \theta) = 0.81 \cdot 10^7 \frac{n_e{}^0 \theta}{u_\infty T_f^{1/2} \delta} \times \left[\exp(-3.45 U_i/T_f) + \frac{2U_i}{T_f} - 0.37\right], \quad (27)$$

and for $\rho \geq 0.08$:

$$\omega_C(u_\infty, \delta, \theta) = \frac{r_e}{u_\infty \delta}\int_0^{\rho} \beta_C[\rho(\theta)][\rho(\theta)]^2\, d\theta. \quad (28)$$

In the last equations β_C is given by equations (11) or (12) and $\rho(\theta)$ is given in equation (16). Having determined the probability P of "surviving" one can find immediately the probability W, that a particle has taken part in the process considered:

$$W(u_\infty, \delta, \theta) = 1 - P(u_\infty, \delta, \theta). \quad (29)$$

For instance, W_B (which means the probability that a neutral particle incoming from "infinity", with energy about 1 eV, has taken part in charge transfer process) can be used to determine the rate of production and density distribution of the fast neutrals (with energy about 1 keV) within the heliosphere.

5. SUMMARY

Some examples, using the derived relationships, are shown in the Figs 2–6. All calculations have been performed using recent basic astrophysical parameters, which so far seem to be reasonable (see e.g. Adams and Frish, 1977; Holzer, 1977; Emerich and Cazes, 1978; Thomas, 1978; Meier, 1979). The characteristic astrophysical quantities have been assumed as follows:

$$n_e{}^0 \approx n_p{}^0 = 6\ \text{cm}^{-3}$$
$$T_e{}^0 \approx 1.5 \cdot 10^5\ \text{K}, \quad T_f \approx 2 \cdot 10^6\ \text{K} \quad \text{and} \quad \alpha = \tfrac{7}{8}$$
$$u_\infty = 20\ \text{km s}^{-1}, \quad u_p = 400\ \text{km s}^{-1}$$
$$\mu = 0.7, \quad Q_B \approx 2 \cdot 10^{-15}\ \text{cm}^2.$$

In Fig. 2, rate coefficients for all three processes are presented; β_A (photoionization) β_B (charge transfer) and β_C (electron ionization). The latter has been compared with Holzer's (1977) computations ($\beta_C{}^H$—dotted line) which has been obtained by numerical integration of experimental data for ionization cross-sections (Kieffer and Dunn, 1966). As one can see there, the results for β_C given in the present work [by analytical relations (10–12)] are in very good agreement with computations of Holzer for most of the range of interplanetary space. They

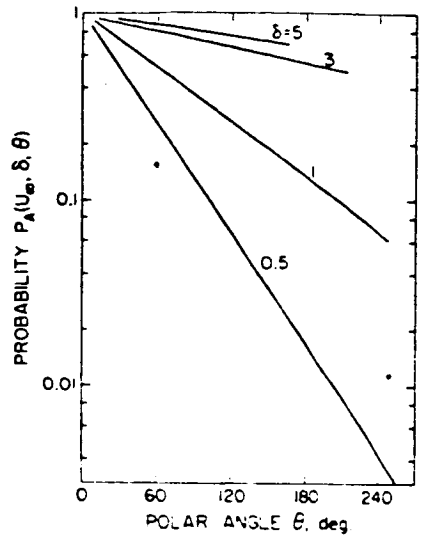

FIG. 3. PROBABILITY P_A VS POLAR ANGLE θ, FOR DIFFERENT IMPACT PARAMETERS δ. P_A IS PROBABILITY THAT A PARTICLE, PASSING THROUGHOUT THE PLANETARY SYSTEM, HAS NOT TAKEN PART IN PHOTOIONIZATION PROCESS.

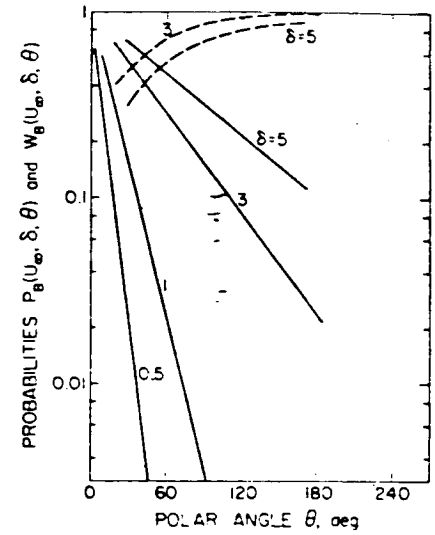

FIG. 4. PROBABILITIES P_B (FULL LINE) AND W_B (DASHED LINE) VS THE POLAR ANGLE θ, FOR DIFFERENT IMPACT PARAMETERS δ. P_B IS PROBABILITY THAT A PARTICLE, PASSING THROUGHOUT THE PLANETARY SYSTEM, HAS NOT TAKEN PART IN CHANGE TRANSFER PROCESS. W_B IS, IN CONTRARY, PROBABILITY THAT THE PARTICLE HAS TAKEN PART IN THE CHANGE TRANSFER PROCESS DURING ITS PASSING THROUGHOUT THE PLANETARY SYSTEM.

give a little worse agreement for $0.1<\rho<0.6$ because the starting formulas [equations (8) and (9)], used by the author here, are less accurate for this range of electron energy.

In Fig. 3, the probability of a particle "avoiding" photoionization, with different δ is presented. This probability decreases very fast as it increases θ (i.e. traversing the solar system) for small values δ, which is due to the fact that in this case the particle comes closer to the Sun, where rate coefficients increase rapidly. For larger values of δ the probability P_A has significant values throughout its path. Of course in the latter case the particle does not come close to high photoionization regions in the vicinity of the Sun.

The above remarks are also valid for the probability of "avoiding" charge transfer process P_B by the particle (see Fig. 4). There is also presented the probability W_B, that a particle has taken part in a charge transfer process. The latter probability is close to unity and changes slowly (within the solar system) for small values of the parameters δ; for higher values of δ (for instance 3 or more) it changes substantially and is about unity as the particle leaves the solar system.

The probability of "avoiding" electron ionization, P_c is presented in Fig. 5. It can be seen that for small impact parameters P_c decreases very rapidly as the particle passes through the solar system, and at the moment of leaving the system the latter probability is getting very small (order 10^{-3}). For δ larger than 3 one can say that a particle can pass through the solar system without taking part in electron collisional ionization.

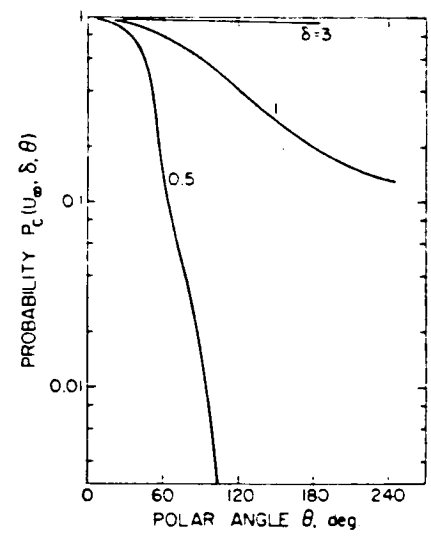

FIG. 5. PROBABILITY P_C VS THE POLAR ANGLE θ, FOR DIFFERENT IMPACT PARAMETERS δ. P_C IS PROBABILITY THAT A PARTICLE, PASSING THROUGHOUT THE PLANETARY SYSTEM, HAS NOT TAKEN PART IN THE IONIZATION (BY ELECTRON) PROCESS

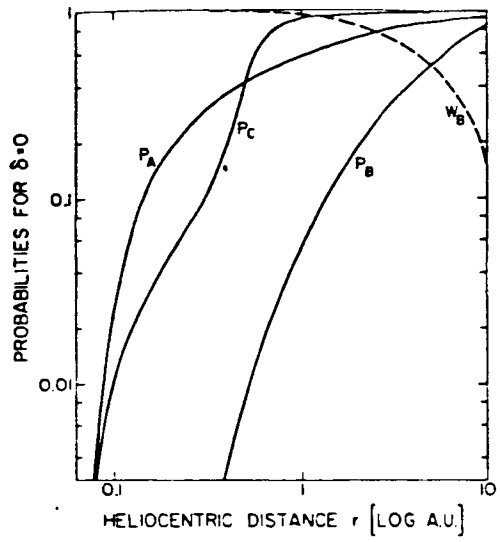

FIG. 6. PROBABILITIES FOR INCOMING PARTICLES WITH $\delta = 0$ VS THE HELIOCENTRIC DISTANCE r. MEANING OF THE SYMBOLS ARE THE SAME AS IN FIGS. 3–5.

In Fig. 6, the probabilities for different processes (with impact parameters equal to zero) are given. One can see that probabilities P_A and P_B change rapidly throughout the solar system. The probability P_C, up to heliocentric distances of about 0.6 A.U. is almost equal to unity and for smaller distances rapidly decreases and becomes comparable with P_A in close to the Sun.

The relations presented in this paper can be used both for general theoretical analyses and for interpretation of data obtained from spaceflight experiments.

Acknowledgements—The author wishes to thank Drs. Darrell L. Judge and F. M. Wu for helpful discussions during this work. This research was supported by the National Aeronautics and Space Administration under contract NASA-6558.

REFERENCES

Adams, T. F. and Frish, P. C. (1977). High-resolution observations of the Lyman Alpha sky background. *Astrophys. J.* **212**, 300.

Banks, P. M. and Kockarts, G. (1973). *Aeronomy*. Academic Press, New York.

Emerich, C. and Cazes, S. (1978). Interplanetary atomic hydrogen parameters inferred from OSO-8 high resolution measurements of the Solar H Lyman Alpha profile. *Astron. Astrophys.* **69**, L13.

Fahr, H. J. (1978). Change of interstellar gas parameters in stellar-wind-dominated astropheres: Solar Case. *Astron. Astrophys.* **66**, 103.

Feldman, W. C., Lang, J. J. and Scherb, F. (1972). Interstellar Helium in interplanetary space. NASA Sp-308, 684.

Hinteregger, H. E. (1976). EUV fluxes in the solar spectrum below 2000 Å. *J. atmos. terr. Phys.* **38**, 791.

Hollweg, J. V. (1976). Collisionless electron heat conduction in the solar wind. *J. geophys. Res.* **81**, 1649.

Holzer, T. E. (1977). Neutral hydrogen in interplanetary space. *Rev. geophys. Space Phys.* **15**, 467.

Hundhausen, A. J. (1972). *Coronal Expansion and Solar Wind*. Springer, New York.

Kieffer, L. J. and Dunn, G. (1966). Electron impact ionization cross-section data for atoms, atomic ions, and diatomic molecules. *Rev. mod. Phys.* **38**, 1.

Kunc, J. A. (1979). Averaged ionization cross sections and rate coefficients in a partially ionized gas for small and high electron energy. *Phys. Lett.* **70A**, 12.

Kunc, J. A. and Zgorzelski, M. (1975). Collisional transition probabilities for atomic hydrogen in thermal plasmas from 1000°K to 8000°K. *Atom. Data nucl. Data Tables* **15**, 543.

Leer, E. and Axford, W. I. (1972). A two-fluid solar wind model with anizotropic proton temperature. *Solar Phys.* **23**, 238.

Meier, R. R. (1977). Some optical and kinetic properties of the nearby interstellar gas. *Astron. Astrophys.* **55**, 211.

Meier, R. R. (1979). Private Communication.

Miggenneider, M., Montgomery, M. D., Philipp, W. G., Rosenbauer, M. and Schwenn, R. (1976). Preliminary results of the electron measurements in the solar wind by the Helios plasma experiment. *EOS Trans. AGU.* **57**, 999.

Munro, R. H. and Jackson, B. V. (1977). Physical properties of a polar coronal hole from 2 to 5 R. *Astrophys. J.* **213**, 874.

Nishida, A. (1969). Thermal state and effective collision frequency in the solar wind plasma. *J. Geophys. Res.* **74**, 5155.

Thomas, G. E. (1972). Properties of nearby interstellar hydrogen deduced from Lyman-α sky background measurements. NASA SP-308, 668.

Thomas, G. E. (1978). The Interstellar wind and its influence on the interplanetary environment. *Ann. Rev. Earth Planet. Sci.* **6**, 173.

Timothy, J. G. (1977). The Solar Output and its Variation. Colorado University Press, Boulder.

Possible H_2^+ Ultraviolet Emissions from Jupiter's Aurora

F. M. Wu, D. L. Judge

Abstract presented at the Spring Meeting of the AGU, Baltimore, 1981

Auroral radiation has been detected near the poles of Jupiter by the UV Spectrometer on the Voyager spacecraft. The emission was identified as the H_2 bands and the H Ly-α line. However, a close comparison between a model calculation and the observed data reveals additional emission structure in the 1100 - 1250 Å spectral region, with an intensity maximum at 1250 Å. We suggest here that this unidentified feature may be part of the electron excited H_2^+ emission spectra, resulting from discrete H_2^+ $2p\ \pi_u$ - $1s\ \sigma_g$ transitions.

Although the H_2^+ UV spectra have not been observed in the laboratory, the transition probability for the H_2^+ system can be accurately determined from theory. With a B-O wave function, the band strength for the $2p\ \pi_u$ - $1s\ \sigma_g$ transition has been calculated. We find indeed that the $2p\ \pi_u\ v' = 1$ - $1s\ \sigma_g\ v'' = 17$ band transiton can result in intense radiation at $\sim$1240 Å, while the other weak H_2^+ transitions will contribute emissions in the 1130 - 1250 Å region. Assuming an integrated spectral intensity of $\sim$5 KR, we find an H_2^+ column density at Jupiter's aurora of $\sim 10^{13}$ cm^{-2}.

The rate of producing H_2^+ by electron ionization of H_2 moleucles is about 100 times higher in the auroral region than elsewhere in the atmosphere. Moreover, due to a relatively high ion temperature in aurora, the radiative association rate between H and H^+ is also very large. On the other hand, we note that the rate of the destrubtion process for H_2^+, namely $H_2^+ + H_2 \quad H_3^+ + H$, decreases significantly for high ion velocities The possibility that the unexplained emissions arise from electron excited H_2^+, and that, in addition, H^+ and H_3^+ are important auroral species, will be discussed.

GEOPHYSICAL RESEARCH LETTERS, VOL. 8, NO. 2, PAGES 177-178, FEBRUARY 1981

ELECTRON-CAPTURE CROSS-SECTIONS FOR SOME ASTROPHYSICAL PROCESSES

Joseph A. Kunc and Darrell L. Judge

Earth and Space Sciences Institute, University of Southern California, Los Angeles, California 90007

Atomic sulphur and oxygen and their ions are expected to be prominent components of the atmosphere of Io [Kumar and Hunten, 1980]. The neutral atoms are formed primarily by photon and electron dissociation of SO_2 while the ions are formed most probably through electron ionization, by both direct dissociative ionization and by electron ionization of the previously formed neutral atoms [McElroy and Yung, 1975; Kumar, 1980]. Atomic ions produced in Io's atmosphere will have the energy of corotating plasma at Io's orbit (i.e. about 400 eV). Subsequent charge exchange of these trapped ions with neutrals in the atmosphere provides a mechanism for loss of these energetic atoms. The cross sections for the charge exchange processes listed below, (1a-d) (where the ions are in ground states), in addition to the atom-molecule process 1e, are accordingly of great interest. In view of the virtual absence of experimental data the present theoretical results will provide reasonably accurate cross sections for detailed modeling of Io's atmosphere. The formalism presented here has broad application and can readily be used to calculate charge exchange cross sections for a variety of atomic systems.

The processes of current interest are as follows:

$$O^+(\cdots 2s^2 2p^3)+O(\cdots 2s^2 2p^4) \rightarrow O(\cdots 2s^2 2p^4)+O^+(\cdots 2s^2 2p^3) \quad (1a)$$

$$O^+(\cdots 2s^2 2p^3)+S(\cdots 3s^2 3p^4) \rightarrow O(\cdots 2s^2 2p^4)+S^+(\cdots 3s^2 3p^3) \quad (1b)$$

$$S^+(\cdots 3s^2 3p^3)+S(\cdots 3s^2 3p^4) \rightarrow S(\cdots 3s^2 3p^4)+S^+(\cdots 3s^2 3p^3) \quad (1c)$$

$$S^+(\cdots 3s^2 3p^3)+O(\cdots 2s^2 2p^4) \rightarrow S(\cdots 3s^2 3p^4)+O^+(\cdots 2s^2 2p^3) \quad (1d)$$

$$Na^+(\cdots 2s^2 2p^6)+SO_2 \rightarrow Na(\cdots 2p^6 3s)+SO_2^+ \quad (1e)$$

To estimate electron capture cross sections for the above processes ($B^+ + A \rightarrow B + A^+$) for moderate and large kinetic ion energies (i.e. larger than about 300 eV), the impulse approximation for the asymmetrical collision model has been employed [Gryzinski, 1965; Vriens, 1967; Gerjuoy, 1966; Garcia, 1966; Garcia et al., 1967; Gryzinski and Kunc, 1981]. This model is traditionally acceptable for electron capture processes (for both resonant and non-resonant processes) at moderate and large relative energies, not only for atomic but also for molecular collisions.

The electron capture cross section Q_c of the $B^+ + A \rightarrow B + A^+$ collision system can be found with the impulse approximation by averaging over the collision parameters. Specifically, the cross section Q_C is obtained from the expression,

$$Q_c(v_{B+}) = \iiiint \frac{\partial \sigma}{\partial \Delta E}(v_A^e, v_{B+}, \Delta E, \theta, \varphi) f(\theta,\varphi) f(v_A^e) d\theta d\varphi d\Delta E dv_A^e, \quad (2)$$

where $\partial\sigma/\partial\Delta E$ is the impulse approximation differential cross section for a binary encounter of particles (e.g. [Gerjuoy, 1966; Gryzinski and Kunc, 1981; Massey et al., 1979]) with velocities $\vec{v}_A^e$ and $\vec{v}_{B+}$, scattering angle θ and their azimuthal angle φ. Since the energy transfer does not depend on azimuthal angle, the distribution function over this angle is uniform. Also, for a multi-electron symmetrical outer shell of the A system, the scattering angle distribution can be approximated by one which is isotropic. The field electron velocity distribution function for an electron of total energy $-E_A^e$ in an attractive Coulomb field can be described by the normalized distribution as given by Bates and Mapleton [Bates and Mapleton, 1965], which is identical to the normalized quantum velocity distribution for electrons in the 1s state in the hydrogen atom [Fock, 1935]. In the case of atomic hydrogen, E_A^e is clearly defined by the ionization potential. In the case of a multi-electron shell the situation is more complicated because the average binding energy of an equivalent shell electron is obviously larger than the first ionization potential. It is experimentally confirmed by higher and higher successive ionization potentials. Therefore, for a multi-electron shell the following procedure (for obtaining of average energy of an equivalent electron) seems to be more realistic [Kunc, 1980]:

$$E_A^e = \frac{1}{N_s}\sum_{j=1}^{N_s} U_j, \quad (3)$$

where the above sum is a sum of successive ionization potentials for N_s electrons in the given shell. It should also be mentioned that using relationship (3) allows one to approximate the field electron velocity distribution function by a δ-function distribution, which is also consistent with the virial theorem for Coulomb forces.

The effective limits of integration over the scattering angle result from energy transfer limitations and, after transformations, (see the detailed discussion in [Kunc, 1979] for our energy range) they can be found as $\cos\theta_{\ell,u} = \pm 1$. The asymmetrical collision model contains some lack of consistency with detailed balancing which, however, is not large over our range of binding and incident energies. The discrepancy results from the asymmetric way of treating the "test" and "field" particles. The analysis of Garcia et al. [Garcia et al., 1967] shows that most of this inconsistency can be avoided by properly choosing the lower and

Copyright 1981 by the American Geophysical Union.

Paper number 80L1780.
0094-8276/81/0002-0177-$00.00

upper energy transfer limits. They are respectively as follows:

$$\Delta E_\ell = \frac{1}{2} m_e v_{B+}^2 + E_A^e,$$
$$\Delta E_u = \frac{1}{2} m_e v_{B+}^2 + E_A^e + E_B^e. \qquad (4)$$

Results and Discussion

Using the impulse approximation to the differential cross section $\partial\sigma/\partial\Delta E$, as discussed above and in paper [Gerjuoy, 1966], the cross sections of Eq. (2) have been calculated and compared with existing experimental data [Stebbings et al., 1964] in Fig. 1. The comparison, however, is unfortunately limited by a lack of experimental data to the processes (1b)-(1f). The good agreement of the present results with experimental data for the oxygen process suggests that the method presented here can be successfully used for multi-electron shell capture processes (1a) - (1d) for intermediate and large incident energies. The departure of the calculated cross sections from the experimental results is evident in Figure 1 for process (1a) at low relative energies. Such behavior is understandable, however, since at low energies the impulse approximation is poorer and the asymmetry of the collision is getting larger. Also at these lower energies the electron capture process is becoming more like a many body interaction rather than a binary process. In the case of process (1e) the situation is more complicated.

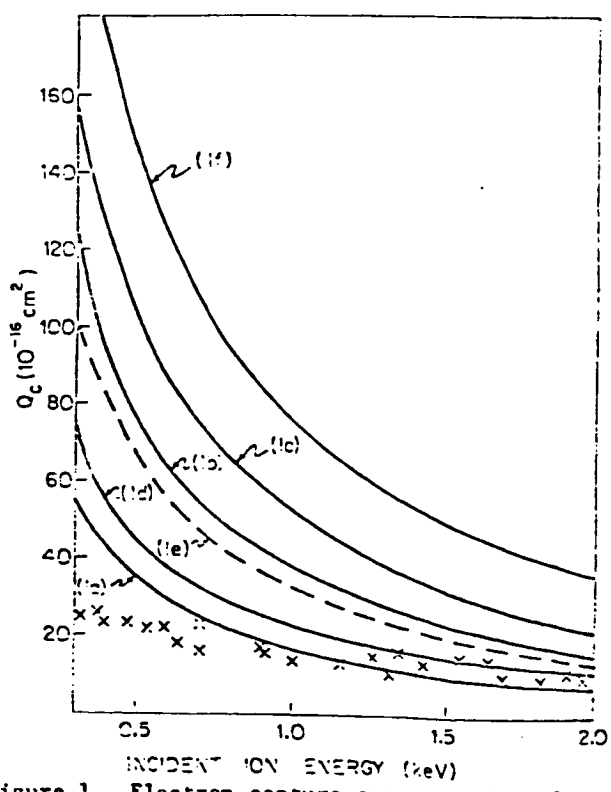

Figure 1. Electron-capture cross sections for processes (1a)-(1f). The full curve is the result of the present work for process (1a)-(1d) and (1f). The "theoretically predicted" curve for the process (1e) is the dashed one. XX- is the experimental data for the process (1a) given by Stebbings et al., 1964.

First of all, neither the distribution of Bates and Mapleton nor the δ-function are adequate for an electron velocity distribution within a polyatomic molecule such as SO_2. The other problem is that the average binding energy of an electron cannot be found from relation (3) for the SO_2 molecule (e.g. higher ionization potentials may not exist at all in general since the molecular structure may be destroyed). The authors have tried to avoid such difficulties by assuming a similarity of the dynamical behavior of the outer electrons in the SO_2 molecule with those of the germanium atom ($\ldots 4s^2\ 4p^2$) i.e., by using the electron capture cross section for the process:

$$Na^+(..2s^2 2p^6) + Ge(..4s^2 4p^2) \rightarrow$$
$$Na(..2p^6 3s) + Ge^+(..4s^2 4p). \qquad (1f)$$

The ratio of the first ionization potential for SO_2 to that of germanium is about 1.3, which is comparable to the ratio of ionization potentials of the "A" atoms (O and S) of processes (1a) and (1b). Assuming the cross sections for processes (1e) and (1f) have an ionization potential dependence similar to that of processes (1a) and (1b) one can obtain "theoretically predicted" electron capture cross section for the process (1e) using the result for (1f). This cross section is shown in Figure 1 as a dashed curve. However, it should be emphasized that the cross-section obtained in such a manner can be treated as a crude estimate only. There are unfortunately no experimental data available to compare with the calculated values and to thereby determine the validity of the above approximation.

This work was supported by NASA Contract NAS2-6558.

References

Bates, D. R. and R. A. Mapleton, Proc. Phys. Soc. 85, 605, 1965.
Fock, V., Z. Phys., 98, 145, 1935.
Garcia, J. D., Phys. Rev., 159, 39, 1966.
Garcia, J. D., E. Gerjuoy and J. E. Welker, Phys. Rev. 165, 72, 1967.
Gerjuoy, E., Phys. Rev. 48, 59, 1966.
Gryzinski, M. Phys. Rev. 138, A336, 1965.
Gryzinski, M., and J. A. Kunc, submitted for publication.
Kumar, S., Geoph. Res. Lett., 7, 9, 1980.
Kumar, S. and D. M. Hunten, IAU Colloquium, Hawaii, May 1980; to be published as a chapter for the book "The Satellites of Jupiter", University of Arizona Press, June 1980.
Kunc, J. A., J. Phys. B., 12, 241, 1979.
Kunc, J. A., J. Phys. B., 13, 587, 1980.
Massey, H. S. W., E. H. S. Burhop and H. B. Gilbody, in "Electronic and Ionic Impact Phenomena", Clarendon Press, Oxford p. 2485, 1979.
McElroy, M. B. and Y. L. Yung, Astrophys. J., 196, 227, 1975.
Stebbings, R. F., A. C. Smith and H. Ehrhardt, in "Atomic Collision Processes" (ed. M. R. C. McDowell), North-Holland, Amsterdam, p. 814, 1964.
Vriens, L., Proc. Phys. Soc. 90, 935, 1967.

(Received October 29, 1980;
accepted December 8, 1980.)

PHOTOCHEMISTRY OF SO_2 IN THE ATMOSPHERE OF IO AND IMPLICATIONS ON ATMOSPHERIC ESCAPE

Shailendra Kumar
Earth and Space Sciences Institute
University of Southern California
Los Angeles, California 90007

J. Geophys. Res., In press, October 1981

ABSTRACT

Photochemical models of Io's atmosphere are presented with the assumption that SO_2 is the major gas and that the SO_2 surface pressure is controlled by vapor-pressure equilibrium at the surface. Photolysis of SO_2 leads to efficient production of SO, O_2, S and O. Of these products, O and S are likely to be the dominant constituents in the upper atmosphere and the atmospheric escape is expected to be in atomic form. Nonthermal escape processes are necessary to populate the plasma torus. SO_2 surface densities greater than 10^{11} cm^{-3} are needed on the dayside to supply the required amounts of S and O to maintain the torus. Surface chemistry presents an interesting possibility, namely the conversion of O to O_2 in which case O_2 will be the dominant constituent throughout the nightside and over the polar caps with a surface O_2 density of 10^{10} cm^{-3}.

INTRODUCTION

The presence of an atmosphere on Io first became evident from the Pioneer 10 radio occultation measurements (Kliore et al. 1974, 1975) of a well developed terrestrial-like ionosphere on Io. Recent Voyager observations have provided some key data that can be used to study the nature of this atmosphere. Basically two types of models have been proposed with respect to the thickness of the atmosphere;

(a) a 'thick' SO_2 atmosphre in vapor pressure equilibrium with the surface leading to a surface density of 10^{11}-10^{13} cm^{-3}, and

(b) a 'thin' SO_2 atmosphere with a surface density of $\sim 10^8$-10^9 cm^{-3}.

The 'thick' atmosphere model is supported by Kumar (1979, 1980), Pearl et al. (1979), Bertaux and Belton (1980) and Kumar and Hunten (1980) and the implied arguements are based on three sets of measurements;

(a) the detection of 0.2 cm-atm of gaseous SO_2 above one of the hot spots (containing the Loki plume) by the Voyager IRIS experiment (Pearl et al. 1979),

(b) the measurements of oxygen and sulfur ions as the major constituents of the associated plasma torus by the Voyager Plasma Science experiment (Bridge et al. 1979) and the UVS experiment (Broadfoot et al. 1979), and

(c) the detection of SO_2 frost on the surface from ground based infra-red measurements (Smythe et al. 1979; Hapke 1979).

However, the absence of UV signatures of SO_2 in the IUE spectra of Io and the absence of any polar caps on Io have led to arguments for the 'thin' SO_2 atmosphere model which is supported by Butterworth et al. 1980; Lane et al. 1979, and Fanale et al. 1980. The large particulate mass evident in the Loki plume (Collins 1980) suggests that if the gas to particulate ratio in the plume is close to 1, and if the gas expands over the first 50 m without condensing, then the Voyager IRIS

observations of gaseous SO_2 would be consistent with the observed gas being transient flow from Loki as well as with an equilibrium atmosphere. But no SO_2 gas was observed by the IRIS experiment above Pele (J. Pearl, private comm.) which is even hotter ($T_s \approx 700°K$) than Loki ($T_s = 290°K$) and would provide a better thermal contrast for observing SO_2 if it was entirely associated with the plume. The Pele observation is consistent with an equilibrium atmosphere because the equilibrium vapor pressure at the local time (16.4 h) of this observation is too low to be detected by the Voyager IRIS experiment. In fact, SO_2 was not detected in association with any of the other hot spots or plumes that were observed by the Voyager IRIS experiment (J. Pearl, private comm.) but all of these observations corresponded to evening or nightside regions where the ambient surface temperature is too small to sustain detectable amounts of SO_2 gas in vapor pressure equilibrium with the surface. Therefore, the likely interpretation of the Voyager IRIS observation is an equilibrium SO_2 atmosphere (Kumar and Hunten 1980).

While the debate continues, we present here a model of photochemistry and composition of Io's SO_2 atmosphere assuming that the surface density is controlled by vapor pressure equilibrium. This study is necessary to understand the transport of gases to the plasma torus and in turn provides further clues to determine whether the SO_2 atmosphere of Io is 'thick' or 'thin'.

II. PHOTOCHEMICAL MODEL AND RESULTS

We assume that SO_2 is the major gas in Io's atmosphere. The thermal structure for such a pure SO_2 atmosphere was calculated in a previous paper (Kumar 1980) in which a SO_2 density profile consistent with the Pioneer 10 ionosphere data was determined. This model corresponds to the atmosphere on the dayside of the evening terminator (solar zenith angle $\sim 81°$) and is adopted here for studying the photochemistry of SO_2. The surface density of SO_2 is 1.2×10^{11} molecules cm^{-3}, surface temperature is 110 K and exospheric temperature is 1030 K.

In Table 1 we list the rate constants for chemical reactions and zero optical depth rates for photodissociation and photoionization processes that we have adopted. The primary reactions in SO_2 photochemistry are illustrated in Figure 1.

Solar UV radiation dissociates and ionizes atmospheric SO_2,

$$h\nu + SO_2 \rightarrow SO + O \qquad \lambda<2210\text{Å}$$

$$\rightarrow S + O_2 \qquad \lambda<2070\text{Å}$$

$$\rightarrow SO_2^+ + e \qquad \lambda<1005\text{Å}$$

Thompson et al. (1963) and Warneck et al. (1964) have reported the SO_2 photodissociation cross-sections at $\lambda>1850$Å. Golomb et al. (1962) have measured the SO_2 absorption coefficient at shorter wavelength down to the ionization threshold. The SO_2 photoionization cross-sections have been recently measured by Wu and Judge (1980). Welge (1974) has reviewed various photoabsorption measurements in 1000-4000Å range. The onset of photodissociation has been measured carefully by Hui and Rice (1972) who show that fluorescence yield drops from unity at 2250Å to 0.1 at 2150Å. Driscoll and Warneck (1968) have photolyzed SO_2 at 1849Å and deduced a quantum yield of $\lesssim 0.5$ for the production of S and O_2. This process is followed by the fast reaction

$$S + O_2 \rightarrow SO + O$$

which is the major loss mechanism for both S and O_2. SO and O_2 are highly reactive and they recycle to form SO_2 with further production of S and O,

$$SO + SO \rightarrow SO_2 + S$$

$$O_2 + SO \rightarrow SO_2 + O$$

We have included the three body reactions in Table 1 for completeness although they do not have any significant influence on the bulk chemistry except right near the surface.

Photoabsorption of SO between 1900 and 2350Å has recently been measured by Phillips (1981) who finds that the cross-sections are about two orders of magnitude larger than those for the analogous Schumann-Runge system of O_2. The photodissociation threshold for SO is near 2400Å (Warneck et al. 1964), hence the SO photodissociation rate is $\sim 6 \times 10^{-6}$ cm^{-3} which is comparable to that for SO_2. However, the SO loss at a density $> 10^8$ cm^{-3} is controlled not by photodissociation by by the self reaction of SO (R17, Table 1) which is therefore predominant near the surface.

We have numerically solved the continuity and diffusion equations for O, S, SO, O_2 and SO_2 by taking molecular diffusion into account. The density of each constituent is calculated from ground level upward to 400 km. Several constituents flow with high vertical velocities approaching 100 m/s at high altitudes and this effect was properly included in the model calculations. The boundary values for fluxes were chosen based on the chemical nature of the surface and the expected escape rates into the plasma torus. The flux values are listed in Table 2 and will be discussed below for each model.

Chemical properties of Io's surface are difficult to ascertain at this time. We examine two possibilities with respect to the reactions of atmospheric S and O with the surface material. Model A assumes a 'chemically passive surface' i.e. atmospheric constituents do not react with the surface, whereas Model B assumes a 'chemically active surface'.

Model A (Chemically Passive Surface)

The density distribution of SO_2, SO, O_2, S and O in this model is shown in Figure 2. The zero fluxes of SO, O_2, S and O at the lower boundary (Table 2) are based on the assumption that these gases after being produced from SO_2 photolysis are either lost by chemical reactions in the atmosphere or escape from the top of the atmosphere. In this sense we are postulating that the escape mechanism is efficient enough to carry large fluxes of these constituents. We will critically examine this postulate in Section III. The assumed SO_2 flux at the surface is driven by the requirement that a net column loss rate of 2.2×10^{11} molecules cm^{-2} s^{-1} results from photolysis of SO_2 in the present model. Hence SO_2 must be supplied either by evaporation from the surface frost or from the volcanoes at a rate of $\gtrsim 2.2 \times 10^{11}$ cm^{-2} s^{-1} in order to maintain an SO_2 surface density of 1.2×10^{11} cm^{-3}. The required flux is well within the estimated gas ejection rate of $\sim 10^{14}$ cm^{-2} s^{-1} from the volcanoes (Johnson et al. 1979; Kumar 1979). In fact bulk of the gas ejected by the volcanoes must be transported laterally until it freezes out on the surface. In the case of vapor pressure equilibrium at the surface there will be large pressure gradient from noon ($\sim 10^{-7}$ bar) to the terminator ($\sim 10^{-9}$ bar) leading to strong horizontal winds which would tend to reduce the horizontal pressure gradient in the atmosphere and enhance terminator densities (Yuk and Summers, 1980). We have not concerned ourselves with these bulk convection patterns which are undoubtedly important but which would not affect the relative densities of SO_2 and its photodissociation products appreciably. We recognize that convection patterns must be included for more sophisticated models describing global variations in atmospheric structure and composition.

Production of all species is high right down to the surface and peaks at altitudes of 5-10 km. The SO and O production near the peak is 10 times the S and O_2 production since the solar radiation at longer wavelengths responsible for SO and O production penetrates deeper into the atmosphere. Most of the SO_2

loss by photolysis takes place within the first 10 km. At higher altitudes the SO_2 production by chemical recycling exceeds the loss by photolysis.

Photochemistry and bulk transport dominate the density distribution within $\sim$ 5 km from the surface where the scale heights of all constituents is about the same as the SO_2 scale height. The mixing ratios relative to SO_2 at the surface are f(O) = 0.17, f(S) = 0.24, f(SO) = 4×10^{-2}, and f(O_2) = 4×10^{-3}. O and S mixing ratios are large because there is little or no chemical loss for either of these constituents. O is lost only by three body reactions which are negligible. S is lost by its reaction with O_2 (R12) but it is rapidly produced from recycling of SO (R17) hence there is very little net chemical loss. Both O_2 and SO are also produced with rates comparable to O and S, but there is substantial chemical loss for them hence they are minor constituents. O_2 is lost primarily by its reaction with S (R12) whereas SO loss is controlled by self-reaction (R17). Since the S density is large this leads to the O_2 density being an order of magnitude smaller than the SO density at the surface.

The chemical lifetimes remain comparable to the diffusion times up to altitudes of $\sim$ 150 km above which diffusive separation is dominant. However the vertical flow of the gas which is close to the limiting values for each constituent is equally important at all altitudes. Due to their large scale heights O and S become the major atmospheric constituents above 125 km. The density distribution of these atomic constituents represents the minimum values needed to sustain the large escape flux which is necessary due to their large production rate. As we noted earlier the net loss rate of SO_2 is 2.2×10^{11} cm^{-2} s^{-1} by photolysis which should mostly appear as net production of S and O. Indeed the needed flux at the upper boundary is $\phi(S) = 2.1 \times 10^{11}$ cm^{-2} s^{-1} and $\phi(O) = 4.1 \times 10^{11}$ cm^{-2} s^{-1}. These flux values are equal to the limiting flux (Hunten 1973) for both S and O and they can be regarded as the maximum escape flux in the terminator region. We note, however, that the production of S and O would be higher at higher SO_2

surface densities which are likely at noon and most of the dayside if the vapor pressure equilibrium prevails (Kumar 1979, 1980; Pearl et al. 1979; Kumar and Hunten 1980; Yung and Summers 1980). For example, the surface density at 1:00 p.m. local time corresponding to the Voyager IRIS measurement is 5×10^{12} cm^{-3} (Pearl et al. 1979). But due to the attenuation of the solar UV flux, the total loss of SO_2 will not exceed

$$L_{max}(SO_2) = J\, e^{-1}/\sigma$$

where J is the total photodissociation rate of SO_2 by solar UV and σ is the absorption cross-section which has an average value of 3×10^{-18} cm^2 over the 1900-2210Å range where most of the photodissociation of SO_2 takes place. Using the solar flux measurement of Donneley and Pope (1973) we have $L_{max}(SO_2) = 1 \times 10^{12}$ cm^{-2} s^{-1}, which will be reached at a surface density of $n_o(SO_2) = 4 \times 10^{11}$ cm^{-3}. Thus, if the gas escape is primarily in the form of atomic S and atomic O atoms which is the case in Model A, the global average escape flux will not exceed $\phi_{esc}(S) \lesssim 5 \times 10^{11}$ cm^{-2} s^{-1} and $\phi_{esc}(O) \lesssim 1 \times 10^{12}$ cm^{-2} s^{-1}. The relative mixing ratios of S and O will be maintained similar to those in our model on the entire dayside above the $\tau = 1$ level for solar UV ($\sim$ 2000Å) absorption.

Model B (Chemically Active Surface)

A chemically active surface is likely if there is rapid turnover of the surface material by volcanic activity or surface sputtering processes, so that fresh material is continually brought to or exposed at the surface. For example, elemental sulfur could provide a sink for C at the surface, and S could simply condense on the sulfur rich surface.

However, an interesting possibility exists if the oxygen atoms hitting the surface recombine to form O_2, analogous to the three body reaction R15, and O_2 molecules are then released to the atmosphere. This could happen if the surface oxidation rate exceeds the material turnover rate. We have investigated this

possibility in Model B with the assumption that all of the O flux into the ground is returned as O_2 to the atmosphere. A similar argument could apply to the conversion of S to S_2 at the surface but in this case higher order sulfur allotropes would be formed and the amount of S_2 released to the atmosphere by this process is likely to be small.

The derived density distribution for Model B is shown in Figure 3. Among the minor constituents, O_2 is the dominant one near the surface in this model with a mixing ratio of $\sim$ 15%. This is significant because a transport of O_2 from day to night could maintain a surface density of $\sim 10^{10}$ cm^{-3} of O_2 throughout the nightside where SO_2 would tend to freeze out ($p(SO_2) \lesssim 2 \times 10^{-14}$ bar, $n(SO_2) \lesssim 2 \times 10^{6}$ cm^{-3} at T = 90K) but such large O_2 densities can be maintained at the characteristic nightside temperatures. With large O_2 surface densities, the recycling of SO_2 is further enhanced by R18 and a surface flux of only 1.6×10^{11} cm^{-2} s^{-1} of SO_2 is required. Also S is removed efficiently by O_2 (R12) so that the S density is the lowest in the model. O is still the dominant constituent above 150 km. Physically acceptable solutions can be obtained for an O atom escape flux in the 10^{10} - 10^{11} cm^{-2} s^{-1} range by properly choosing the O flux into the surface.

III. ATMOSPHERIC ESCAPE

The total escape rate should be at least equal to the ion supply rate needed to populate the plasma torus. Estimates for this supply rate range from 10^{10} cm^{-2} s^{-1} (Shemansky 1980) to 10^{12} cm^{-2} s^{-1} (Sullivan and Siscoe 1980); intermediate values of $\sim 10^{11}$ cm^{-2} s^{-1} are preferred by Broadfoot et al. (1980) and Dessler (1980). Kumar and Hunten (1980) have reviewed the arguments leading to these varying supply rates, the major uncertainty is in the ion diffusion times. The atmospheric model should also be consistent with the available data the neutral escape. Sodium atoms are known to escape Io at a rate of $\sim 10^8$ cm^{-2} s^{-1} forming the observed sodium cloud (Brown and Yung 1976). Recently, neutral atomic oxygen has also been detected by Brown (1981) in the cloud around Io; his estimated supply rate is $\gtrsim 2 \times 10^{10}$ O atoms cm^{-2} s^{-1}.

It is important to note that physically acceptable photochemical models of an SO_2 atmosphere which allow the S and O escape fluxes in the required range can be found as we have demonstrated above. In this section we examine whether these escape fluxes can be realized by various possible escape processes. This in turn will further constrain our models.

First we consider thermal escape. Since Io's gravity is low and the exospheric temperature is expected to be $\sim$ 1000 K (Kumar 1980), the thermal escape could be significant for light consituents. For both models, the atomic oxygen escape rate is $\sim 10^{10}$ cm^{-2} s^{-1} by this process. However for S, the thermal escape rate is $\lesssim 10^7$ cm^{-2} s^{-1}, and thermal escape is negligible for heavier constituents SO and SO_2. Comparable densities of sulfur and oxygen ions have been observed in the plasma torus (Bridge et al. 1979, Bagenal and Sullivan 1980, Broadfoot et al. 1979, 1980) which apparently require comparable supply rates for the two constituents. This cannot be accomplished by thermal escape alone. Some non-thermal escape process must be operating.

One such possibility was proposed by Kumar (1979), namely the ionization of neutrals diffusing above the ionopause or magnetopause by the Jupiter's co-rotating plasma at Io's orbit and the subsequent pickup by the co-rotating magnetic field. To determine the escape rate due to this mechanism, we need the altitude of the ionopause or magnetopause. Taking the Pioneer 10 radio occultation measurements of the ionopause (Kliore et al. 1974, 1975), the ionopause level would vary from $\sim$ 200 km at the subsolar point to $\sim$ 600 km near the terminator (Cloutier et al. 1978, Kumar 1979, Kivelson et al. 1979, Kumar and Hunten 1980). In Model A, since O and S are major constituents above 200 km the supply of gases to the plasma torus by this mechanism will be mainly in the atomic form instead of direct injection of SO_2. The ionization potential of S is 10.36 eV very close to the plasma torus electron energy of 10 eV measured by the Voyager experiments. The measured electron density of $\sim$ 2000 cm^{-3} leads to a 10 eV electron flux of 4×10^{11} cm^{-2} s^{-1}. The electron impact ionization cross-section of S at the threshold is $\sim 2 \times 10^{-18}$ cm^2, and it peaks to a value of 7.8×10^{-16} cm^2 at 70 eV (Peach 1968). The electron flux drops rapidly at energies greater than 10 eV but the actual energy dependence of the flux is unknown. A total electron impact ionization rate of $\gtrsim 10^{-6}$ s^{-1} is conceivable for sulphur atoms. The ionization rate of O will be lower due to its higher ionization potential and lower cross-sections. Cheng (1980) estimates that the O lifetime should be at least four times longer than the S lifetime for electron impact ionization. An ionization rate of $\sim 2 \times 10^{-7}$ s^{-1} would be appropriate for O atoms. The maximum O density at the ionopause level would be $\sim 10^9$ cm^{-3}, in which case the average ion production rate by electron impact would be $\gtrsim 8.5 \times 10^9$ cm^{-2} s^{-1}. The S to O density ratio varies from about 1 to 1/10 in the 200-600 km range for Models A and from 1/10 to 1/100 for Model B. Hence, the sulfur ion production rate would be almost equal to the oxygen ion production rate for Model A, and about one tenth for Model B. Thus, an escape flux of $\sim 10^{10}$ cm^{-2} s^{-1} can be realized for both S

and O by electron impact ionization if the corotating magnetic field can pick up all the ions. For O the escape flux is comparable to that due to thermal escape. But for S, electron impact ionization provides an important escape mechanism. Model B is consistent with this escape but Model A is not since it requires escape fluxes $\gtrsim 10^{11}$ cm^{-2} s^{-1}.

Sputtering by plasma torus ions from the top of the atmosphere has been proposed as a potential escape mechanism by Haff et al. (1980) and Kumar and Hunten (1980). Heavy ions such as S^+ would be about 110 times more effective than H^+. Based on the Voyager plasma torus data, Haff et al. use an incident flux for sputtering of $\sim 10^{10}$ cm^{-2} s^{-1} for S ($\sim$ 520 eV) and O ($\sim$ 260 eV) ions; their estimate of the sputtering yield is $\sim$ 5 at $\sim$ 1 R_{Io} for U = 2.2 eV with an inversely proportional dependence on the gravitational binding energy U. The sputtering process produces escaping atoms near the exobase.

For both models A and B, the exobase is at $\sim$ 1400 km altitude where O would be the major constituent with a density of 1.7×10^7 cm^{-3}. Sulfur density at this level is 2.2×10^5 cm^{-3} for Model A. The escape energy for the two constituents is U_O = 0.31 eV and U_S = 0.62 eV. Scaling the Haff et al. values to these energies, the sputtering yield is y(O) = 34 for a pure O atmosphere and y(S) = 18 for a pure S atmosphere. Allowing for the abundance factors, the net escape flux from sputtering is 3.5×10^{11} cm^{-2} s^{-1} for O and only 2.2×10^9 cm^{-2} s^{-1} for S. The sulfur flux would be much less for Model B. The oxygen flux matches the required upper boundary condition for both Models A and B and the flux value is consistent with the high torus supply rates. But the sulfur flux still falls too short by at least one order of magnitude.

Whether Model A or B is applicable has important implications on sputtering

of sodium from the surface by energetic particle bombardment and subsequent escape which was originally proposed by Matson et al. (1974) as the source of observed sodium cloud around Io. The atmospheric column density must be less than 10^{15} cm^{-2} in order to allow a direct escape of sputtered particles without collisions with the atmospheric constituents which would otherwise thermalize and retain sputtered sodium atoms. In our models, the SO_2 column density on the dayside is $\gtrsim 2 \times 10^{17}$ cm^{-2} which is more than two orders of magnitude too high to permit direct escape of sputtered sodium atoms. This led Kumar and Hunten (1980) and Haff et al. (1981) to their suggestion of secondary sputtering from the 'top' of the atmosphere as an alternative mechanism for the escape of sodium as well as sulfur and oxygen. Note, however, that the O_2 density on the nightside is $\sim 10^8$ cm^{-3} for our Model A and the SO_2 density is even smaller ($\sim 2 \times 10^6$ cm^{-3}), hence the sputtered atoms from the surface on the nightside can escape without colliding with the atmospheric particles. But in Model B, the O_2 density on the nightside is 10^{10} cm^{-3} which is too high to permit direct escape; in this case, sodium atoms ejected from the surface by the sputtering process will be mixed in the atmosphere and spread uniformly along with O_2 thus leading to a globally uniform source of sodium. In Model A, the source of sodium is not symmetric on the day and nightsides which would introduce a marked asymmetry in the geometry of the sodium cloud between eastern and western elongations. But no such asymmetry is observed, the sodium cloud appears to maintain its form to a remarkable degree. Model B with a globally uniform source of sodium therefore appears to be more likely to represent the actual atmospheric conditions on Io.

It is important to point out that the escape fluxes from the atmosphere would be much smaller if the SO_2 surface density was as small as $\sim 10^8 - 10^9$ cm^{-3}, (the 'thin' atmosphere model which has been advocated by Fanale et al. 1980). Thermal escape of O would be $< 10^8$ cm^{-2} s^{-1} and the nonthermal processes described above

would also contribute < 10^8 cm^{-2} s^{-1} for both O and S. Atoms. However, in this case, direct sputtering from the surface would yield S and O fluxes of $\sim 10^{10}$ cm^{-2} s^{-1} (Haff et al., 1981) which is compatible with the lowest of the estimates (Shemansky 1980) on the required supply rate to the plasma torus. However, this source would fall short by a factor of 10 to 100 if the required supply rate is as high as that required by Broadfoot et al. (1980), Dessler (1980) and Sullivan and Siscoe (1980). Cheng (1980) has proposed that a direct escape of volcanic gas to the torus could provide the required supply rate, but Cheng's hypothesis suffers seriously from the fact that the ejection velocity of the volcanic gas is $\lesssim$ 1 km/sec (Smith et al. 1979, Johnson et al. 1979), which is much less than the escape velocity of 2.56 km/sec on Io. Sputtering from a 'thick' atmosphere of SO_2 is more likely than any other mechanism proposed thus far for supplying S and O to the plasma torus if the required supply rate is $\gtrsim 10^{11}$ cm^{-2} s^{-1}.

IV. CONCLUSION

We have shown that for an SO_2 atmosphere dominated by vapor pressure equilibrium at the surface, the major constituent in the upper atmosphere (above 150 km) is atomic oxygen followed by either SO_2 or S depending upon the chemical characteristics of the surface. In order to obtain a physical solution, each model requires escape fluxes that fall within the range of the required S and O supply rates to the plasma torus. The O flux is expected to be close to 10^{11} cm^{-2} s^{-1} but the S flux cannot be much more than 1×10^{10} cm^{-2} s^{-1}. Between the two models presented, Model B is more likely to represent the actual physical atmospheric conditions. O_2 is likely to be the second most abundant constituent on the dayside and the most abundant gas on the nightside with a global surface density of 10^{10} cm^{-3}. Model B is also consistent with the absence of polar caps on Io since O_2 would then be the dominant atmospheric constituent in the polar regions due to the low temperatures.

By considering various atmospheric escape processes we have shown that a thick SO_2 atmosphere with dayside surface density $\gtrsim 10^{11}$ cm^{-3} may be necessary to populate the plasma torus. The thermal escape could be significant in releasing atomic oxygen to the plasma torus, but this process is not sufficient for sulfur. Some non-thermal mechanism is required for populating the torus. Ionization of neutrals diffusing above the ionopause or magnetopause by the corotating plasma and subsequent pick-up by Jupiter's corotating magnetic field leads to escape fluxes of $\sim 10^{10}$ cm^{-2} s^{-1} for both S and O. Sputtering from the top of the atmosphere by energetic ions of sulfur and oxygen in the plasma torus could eject $\sim 4 \times 10^{11}$ cm^{-2} s^{-1} of non-thermal O atoms but only $\sim 2 \times 10^{9}$ cm^{-2} s^{-1} S atoms. Between these two mechanisms a supply rate of $\gtrsim 10^{10}$ cm^{-2} s^{-1} can be realized for both S and O into the plasma torus although much more oxygen is expected to be released into the torus than sulfur.

Significant uncertainties still remain concerning both upper and lower boundary conditions. The photochemical models have been presented here to provide a first order understanding of the connection between Io's atmosphere and the plasma torus and to stimulate further work. Indeed a better understanding of the required supply rate to the plasma torus and of the surface chemistry, will greatly constrain the atmospheric models. Laboratory measurements are needed for electron impact ionization of SO_2, photoionization and photodissociation of SO, and the recombination rate coefficient of SO_2^+. Also reaction rates are needed at low temperatures (110-130k) prevalent on the surface of Io.

ACKNOWLEDGEMENTS

I thank Don Hunten for several stimulating discussions regarding this paper and for suggesting the Model B. Discussions with Don Shemansky on surface interactions and with Bob Brown on plasma torus lifetimes are duly acknowledged. Steven Askew provided the programming assistance. This work was supported by NASA grants NAS2-6558 and NAGW-62.

REFERENCES

Bagenal, F., and Sullivan, J. D., Direct plasma measurements in the Io torus and inner magnetosphere of Jupiter, submitted to J. Geophys. Res., 1980.

Baulch, D. L., and Drysdale, D. D. Evaluated kinetic data for high temperature reactions, The Butterworth Group, University of Leeds, 1976.

Bertaux, J. L., and Belton, M. J. S., Evidence of SO_2 on Io from UV observations, Nature, 282, 813, 1979.

Bridge, H. S., Belcher, J. W., Lazarus, A. J., Sullivan, J. D., McNutt, R. L., Bagenal, F., Scudder, J. D., Sittler, E. C., Siscoe, G. L., Vasyliunas, V. M., Goertz, C. K., Yeates, C. M., Plasma observation near Jupiter: Initial results from Voyager 1, Science, 204, 47, 1979.

Broadfoot, A. L., Belton, M. J. S., Takacs, P. Z., Sandel, B. R., Shemansky, D. E., Holberg, J. B., Ajello, J. M., Atreya, S. K., Donahue, T. M., Moos, H. W., Bertaux, J. L., Blamont, J. E., Strobel, D. F., McConnell, J. C., Dalgarno, A., Goody, R., McElroy, M. B., Extreme ultraviolet observations from Voyager I encounter with Jupiter, Science, 204, 39, 1979.

Broadfoot, A. L., Sandel, B. R., Shemansky, D. E., McConnell, J. C., Smith, G. R., Holberg, J. B., Atreya, S. K., Donahue, T. M., Strobel, D. F., and Bertaux, J. L., Overview of the Voyager ultraviolet spectrometry results through Jupiter encounter, submitted to J. Geophys. Res., 1980.

Brown, R. A., The Jupiter hot plasma torus: observed electron temperature and energy flows, Ap. J., 244, 1072, 1981.

Brown, R. A. and Yung, Y. L., Io: its atmosphere and optical emissions, in 'Jupiter', edited by T. Gehrels, University of Arizona press, pp. 1102-1145, 1976.

Butterworth, P. S., Caldwell, J., Moore, V., Owen, T., Rivola, A. R., Lane, A. L., An upper limit to the global SO_2 abundance on Io, Nature, 285, 308-309, 1980.

Cheng, A. F., Effects of Io's volcanoes on the plasma torus and Jupiter's magnetosphere, Ap. J. 242, 812-827, 1980.

Cheng, A., and Lanzerotti, L., Ice sputtering by radiation belt protons and the rings of Saturn and Uranus, J. Geophys. Res., 83, 2597-2602, 1978.

Collins, S. A., Spatial color variations in the volcanic plume at Loki, on Io, J. Geophys. Res., submitted June 1980.

Dessler, A. J., Mass injection rate from Io into the plasma torus, presented at IAU Colloquium 57, Kailua-Kona, Hawaii, May 1980; submitted to Icarus, June 1980.

Donnelly, R. F. and Pope, J. H., The 1-3000 Å solar flux for a moderate level of solar activity for use in modeling the ionosphere and upper atmosphere, NOAA Tech. Report ERL 276-SEL 25, 1973.

Driscoll, J. N. and Warneck, P., Primary processes in the photolysis of SO_2 at 1849 Å, J. Phys. Chem. 72, 3736, 1968.

Fair, R. W. and Thrush, B. A., Reaction rate for sulfur atoms, Faraday Discussions, 44, 236, 1967.

Fanale, F. P., Brown, R. H., Cruikshank, D. P., and Clarke, R. N., Significance of absorption features in Io's IR reflectance spectrum, Nature, 280, 761, 1979.

Fanale, F. P., Banerdt, W. B., Elson, L. S., Johnson, T. V., Zurek, R. W., Io's surface: Its phase composition and influence on Io's atmosphere and Jupiter's magnetosphere, IAU Colloquium 57, Kailua-Kona, Hawaii, May 1980; to be published in "The Satellites of Jupiter", University of Arizona Press, submitted 1980.

Golomb, D., Watanabe, K., and Marmo, F. F., Absorption coefficients of sulfur dioxide in the vacuum ultraviolet, J. Chem. Phys., 36, 958, 1962.

Haff, P. K., Watson, C. C. and Yung, Y. L., Sputter-ejection of matter from Io, J. Geophys. Res. in press, 1981.

McGuire, E. J., Photoionization cross-sections of the elements Helium to Xenon, Phys. Rev., 175, 20, 1968.

Peach, G., Ionization of neutral atoms with outer 2p and 3p electrons by electron and proton impact, J. Phys. B (Proc. Phys. Soc.), 1, 1088-1108, 1968.

Pearl, J., Hanel, R., Kunde, V., Maguire, W., Fox, K., Gupta, S., Ponnamperuma, C., and Raulin, F., Identification and gaseous SO_2 and new upper limits for other gases on Io, Nature, 280, 755, 1979.

Phillips, L. F., Absolute absorption cross-section for SO between 190 and 235 nm, J. Phys. Chem., submitted, May 1981.

Shemansky, D., Mass loading and diffusive loss rate of the Io plasma torus, Ap. J. 242, 1266, 1980.

Smith, B. A., Soderblom, L. A., Johnson, T. V., Ingersoll, A. P., Collins, S. A., Shoemaker, E. M., Hunt, G. E., Masursky, H., Carr, M. H., Davies, M. E., Cook, A. F. II, Boyce, J., Danielson, G. E., Owen, T., Sagan, C., Beebe, R. F., Veverka, J., Strom, R. G., McCauley, J. F., Morrison, D., Briggs, G. A., Suomi, U. E., The Jupiter system through the eyes of Voyager 1, Science, 204, 951-972, 1979.

Sullivan, J., and Siscoe, G., In Situ observations of the Io Torus IAU Colloquium 57, Kailua-Kona, Hawaii, May 1980, in "The Satellites of Jupiter" edited by D. Morrison, University of Arizona Press, submitted 1980.

Thompson, B. A., Harteck, P., and Reeves, R. R. Jr., Ultraviolet absorption coefficients of CO_2, CO, O_2, H_2O, N_2O, NH_3, NO, SO_2, and CH between 1850 and 4000 A, J. Geophys. Res., 68, 6431, 1963.

Smythe, W. D., Nelson, R. M. and Nash, D. B., Spectral evidence for SO_2 frost or adsorbate on Io's Surface, Nature, 280, 766, 1979.

Warneck, P., Marmo, F. F., and Sullivan, J. O., Ultraviolet absorption of SO_2: Dissociation energies of SO_2 and SO, J. Chem. Phys., 40, 1132, 1964.

Welge, K. H., Photolysis of O_x, HO_x, CO_x, and SO_x compounds, Can. J. Chem., 52, 1424, 1974.

Wu, R., and Judge, D. L., Study of sulfur containing molecules in the EUV region. I. Photoabsorption cross-section of SO_2, J. Chem. Phys., 74, 3804, 1981.

Yung, Y. L., and Summers, M. E., A dynamically controlled atmosphere on Io, presented at the Satellites of Jupiter Colloquium, May 13-15, Kailua-Kona, Hawaii, 1980.

TABLE 1

CHEMICAL RATE CONSTANTS AND ZERO OPTICAL DEPTH RATES FOR PHOTOLYSIS AND PHOTOIONIZATION

	Reactions	Rates	References
R1	$SO_2 + h\nu \rightarrow SO + O$	5.6×10^{-6} sec^{-1}	(1,2,9)
R2	$SO_2 + h\nu \rightarrow S + O_2$	2.9×10^{-6} sec^{-1}	(1,2,9)
R3	$SO + h\nu \rightarrow S + O$	6.0×10^{-6} sec^{-1}	(9,13)
R4	$O_2 + h\nu \rightarrow O + O$	9.5×10^{-8} sec^{-1}	(2,9)
R5	$SO_2 + h\nu \rightarrow SO_2^+ + e$	4.8×10^{-8} sec^{-1}	(9,12)
R6	$S + h\nu \rightarrow S^+ + e$	5.8×10^{-8} sec^{-1}	(4,9)
R7	$O + h\nu \rightarrow O^+ + e$	1.1×10^{-8} sec^{-1}	(3,9)
R8	$SO + h\nu \rightarrow SO^+ + e$	2.3×10^{-8} sec^{-1}	(9,11)
R9	$O_2 + h\nu \rightarrow O_2^+ + e$	2.3×10^{-8} sec^{-1}	(3,9)
R10	$SO_2 + O + M \rightarrow SO_3 + M$	$3.4 \times 10^{-32} \exp(-1120/T)$ $cm^6 sec^{-1}$	(5)
R11	$SO + O + M \rightarrow SO_2 + M$	3.0×10^{-33} $cm^6 sec^{-1}$	(5)
R12	$S + O_2 \rightarrow SO + O$	$2.0 \times 10^{-11} \times \exp(-2820/T)$ $cm^3 sec^{-1}$	(10)
R13	$S + S + M \rightarrow S_2 + M$	2.0×10^{-33} $cm^6 sec^{-1}$	(7)
R14	$O_2 + O + M \rightarrow O_3 + M$	$1.4 \times 10^{-33} (T/300)^{-2.5}$ $cm^6 sec^{-1}$	(6)
R15	$O + O + M \rightarrow O_2 + M$	$3 \times 10^{-33} (T/300)^{-2.9}$ $cm^6 sec^{-1}$	(6)
R16	$SO_2^+ + e \rightarrow SO + O$	1×10^{-7} $cm^3 sec^{-1}$	(8)
R17	$SO + SO \rightarrow S + SO_2$	$5.8 \times 10^{-12} \exp(-1760/T)$ $cm^3 sec^{-1}$	(5)
R18	$O_2 + SO \rightarrow SO_2 + O$	$7.5 \times 10^{-13} \exp(-3250/T)$ $cm^3 sec^{-1}$	(5)

1. Golomb, et al. (1962)
2. Thompson et al. (1963)
3. Henry and McElroy (1968)
4. McGuire (1968)
5. Baulch and Drysdale (1976)
6. Liu and Donahue (1975)
7. Fair and Trusch (1967)
8. Assumed
9. Solar fluxes from Donneley and Pope (1973)
10. Homann et al. (1968)
11. No data available, rates assumed same as that for O_2 from Henry and McElroy (1968
12. Wu and Judge (1981)
13. Phillips (1981)

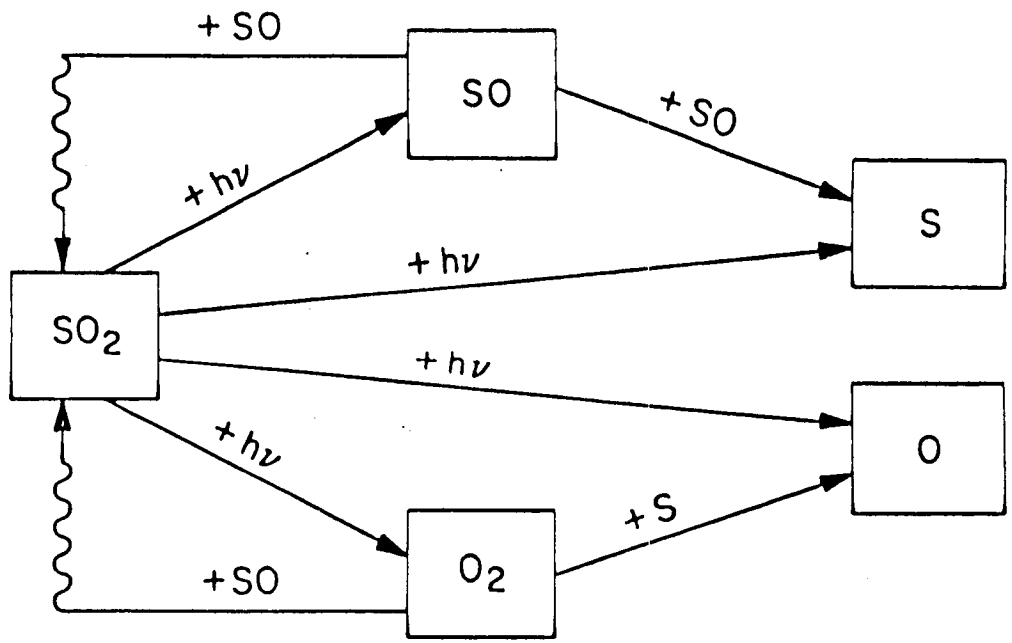

FIGURE 1

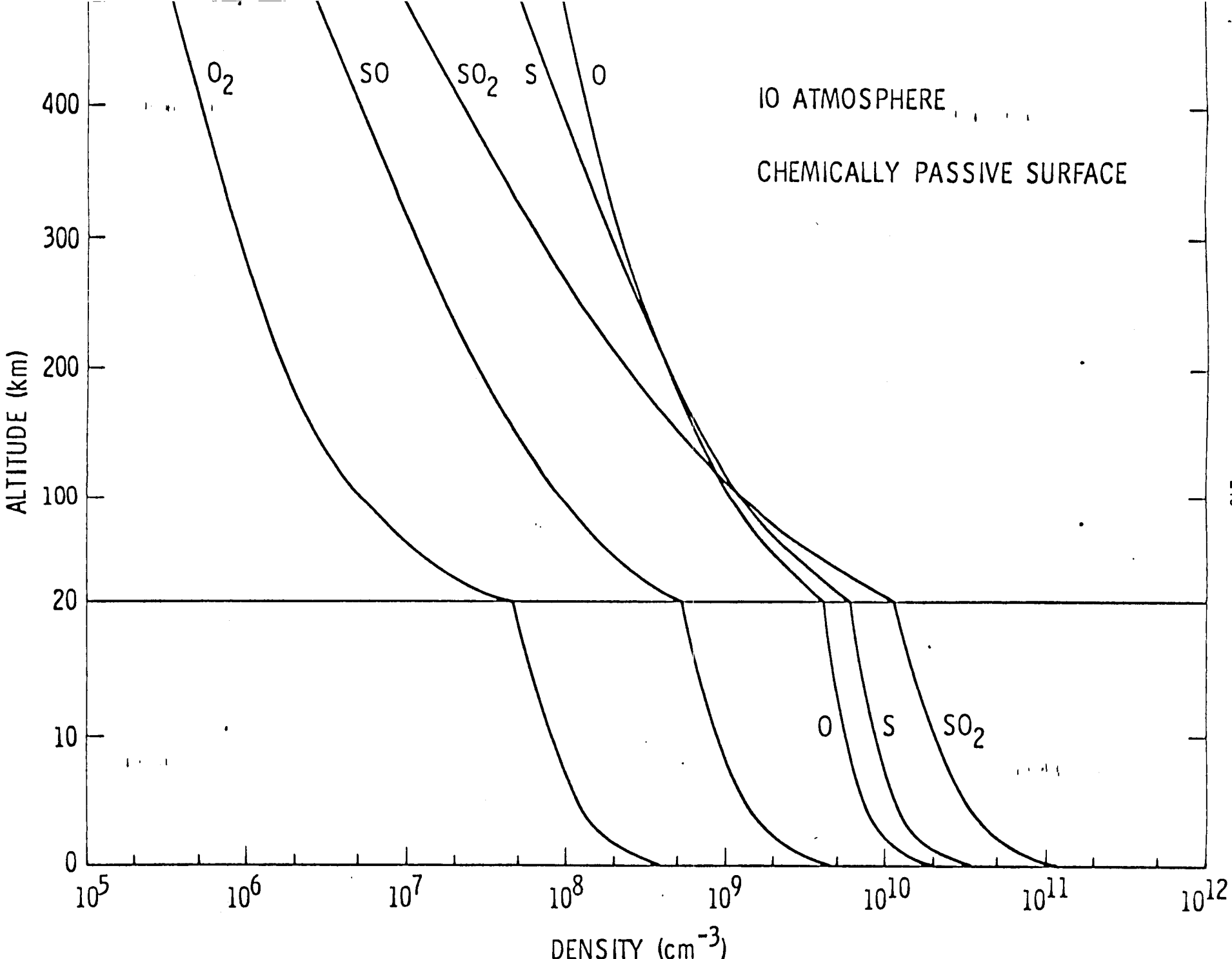
IO ATMOSPHERE
CHEMICALLY PASSIVE SURFACE
O_2
SO
SO_2
S
O
O
S
SO_2
ALTITUDE (km)
400
300
200
100
20
10
0
10^5
10^6
10^7
10^8
10^9
10^{10}
10^{11}
10^{12}
DENSITY (cm^{-3})

FIGURE 2

TABLE 2

BOUNDARY VALUES FOR FLUXES AT THE SURFACE (ϕ_o) AND AT 400 km ALTITUDE (ϕ_{400})

	Model A		Model B	
	ϕ_o	ϕ_{400}	ϕ_o	ϕ_{400}
SO_2	2.3×10^{11}	2.0×10^{10}	1.6×10^{11}	2.3×10^{10}
20	0	2.8×10^{9}	0	1.8×10^{10}
O_2	0	3.4×10^{8}	2.0×10^{11}	2.9×10^{10}
S	0	2.1×10^{11}	-1.0×10^{11}	1.9×10^{10}
O	0	4.2×10^{11}	-4.0×10^{11}	2.0×10^{11}

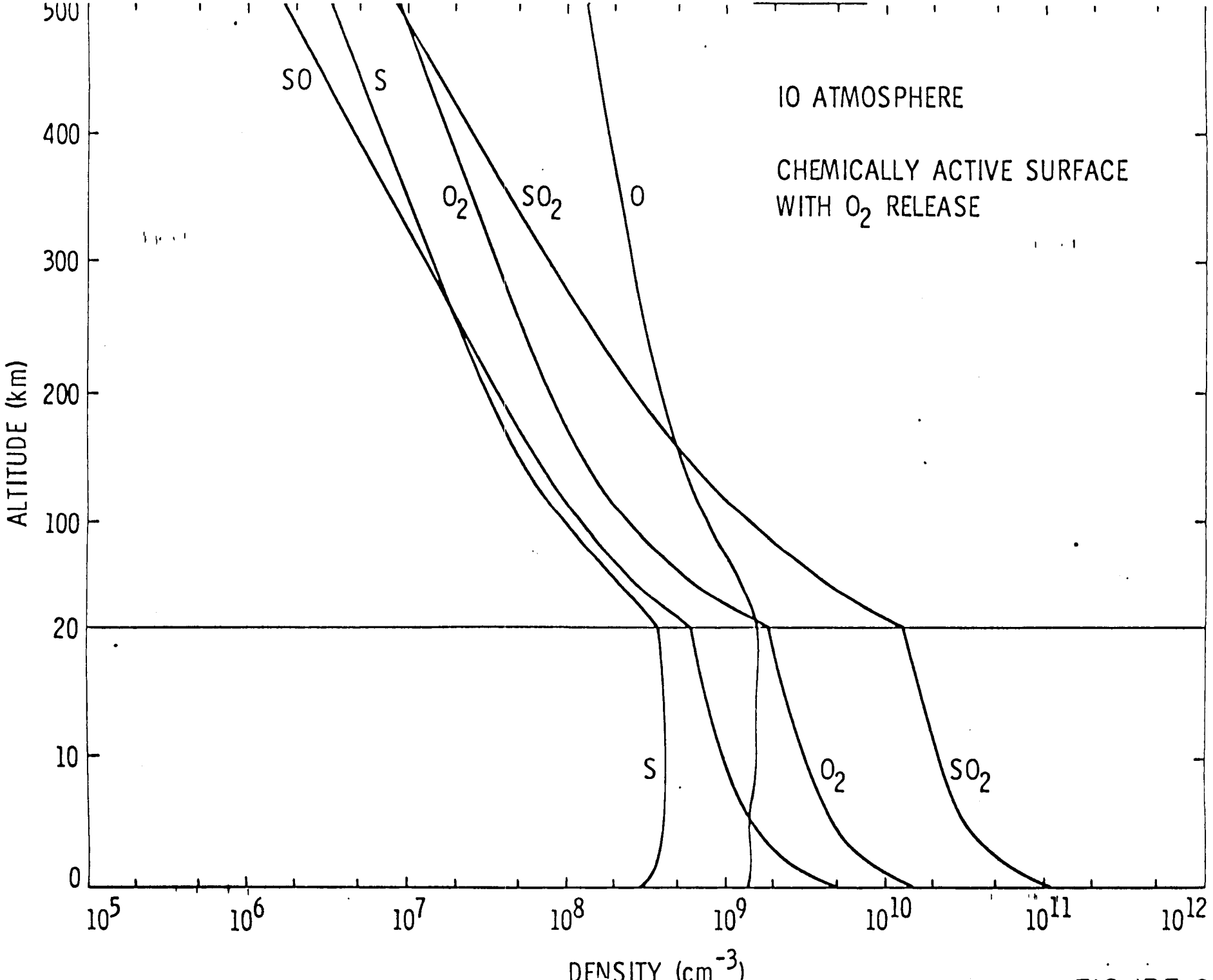
IO ATMOSPHERE
CHEMICALLY ACTIVE SURFACE WITH O_2 RELEASE
SO
S
O_2
SO_2
O
S
O_2
SO_2
ALTITUDE (km)
500
400
300
200
100
20
10
0
10^5
10^6
10^7
10^8
10^9
10^{10}
10^{11}
10^{12}
DENSITY (cm^{-3})

FIGURE 3

THE ASTROPHYSICAL JOURNAL 245:1145-1158, 1981 May 1
© 1981 The American Astronomical Society All rights reserved Printed in U.S.A

PIONEER 10 ULTRAVIOLET PHOTOMETER OBSERVATIONS OF THE INTERPLANETARY GLOW AT HELIOCENTRIC DISTANCES FROM 2 TO 14 AU

F. M. WU
Earth and Space Sciences Institute, University of Southern California
K. SUZUKI
Geophysics Research Laboratory, University of Tokyo
R. W. CARLSON
Jet Propulsion Laboratory, California Institute of Technology
AND
D. L. JUDGE
Earth and Space Sciences Institute and Department of Physics, University of Southern California
Received 1980 February 11, accepted 1980 November 18

ABSTRACT

The interplanetary hydrogen Lyman-α and He 584 Å glow observations obtained by the two-channel extreme-ultraviolet photometer on *Pioneer 10* at distances of 2-14 AU from the Sun are presented. The data are for the time period from 1972 to 1977. For positions near the Sun, the interplanetary glow is primarily due to single scattering of sunlight by the interstellar gas flowing into and through the solar system. But as the heliocentric radius increases, a significant portion of the interplanetary glow detected by the photometer long wavelength channel ($<$ 1400 Å) results from a background glow of galactic radiation. Multiple scattering by the distant interplanetary gas, and scattering by "fast atoms" produced by charge-exchange processes at the heliosphere boundary, can also contribute to the observed background of about 40 rayleighs.

In the present analysis of the interplanetary glow observations, we have employed a theoretical model which takes into account the combined effects of ionization loss and solar gravitation in describing the interplanetary gas density, and which is useful for computing the interplanetary glow for a high temperature interstellar wind. The background glow is assumed here to be isotropic. Comparing the observational data with these theoretical calculations, we have determined that the nearby interstellar density is 0.04 ± 0.01 cm^{-3} for hydrogen and 0.01 ± 0.002 cm^{-3} for helium. Limitations of the present theoretical model and the possibilities for improved analysis of the interplanetary results are discussed.

Subject headings: interplanetary medium — interstellar: matter — ultraviolet: spectra

I. INTRODUCTION

The UV photometer on board the *Pioneer 10* spacecraft, launched in 1972 March, detects the hydrogen Lα and He 584 Å line emissions in planetary and interplanetary space. The spacecraft is now more than 20 AU from the Sun and is leaving the solar system at a rate of approximately 3 AU per year, providing the first results on the interplanetary glow at large solar distances. The interplanetary glow measurements thus far reported are all restricted to a distance of about 1 AU from the Sun (e.g., Thomas and Krassa 1971; Weller and Meier 1974; Broadfoot and Kumar 1978). We describe in this paper an analysis of the observed *Pioneer 10* interplanetary data from 1972 to 1977, and present a radial profile of the interplanetary glow up to a distance of 14 AU. Thus, the theoretical model for the interplanetary glow can be tested in the radial dimension, and the physical parameters of the "local" interstellar gas can be accurately determined.

For positions near the Sun, the interplanetary glow is primarily due to single resonance scattering of sunlight by the interstellar gas flowing into and through the solar system. But as the heliocentric radius increases, the scattered light intensity drops due to the decrease in solar flux, and background radiation of even a few rayleighs (R) becomes important. In addition, at large solar distances, effects of certain physical parameters of the interstellar gas, such as wind direction and gas temperature, are not important in determining the interplanetary glow intensity. The present *Pioneer 10* data provide an excellent opportunity to determine accurately the local interstellar gas density as well as the extreme ultraviolet background radiation. The interplanetary glow background radiation could arise from galactic radiation, from the scattering of solar photons by the "fast" solar protons after they have charge-exchanged with slow hydrogen at the heliospheric boundary (Patterson, Johnson, and Hansen 1963; Blum and Lang 1979), or from multiple scattering of solar protons in the optically thick region of the more distant heliospheric hydrogen (Keller and Thomas 1979; Wallis 1974).

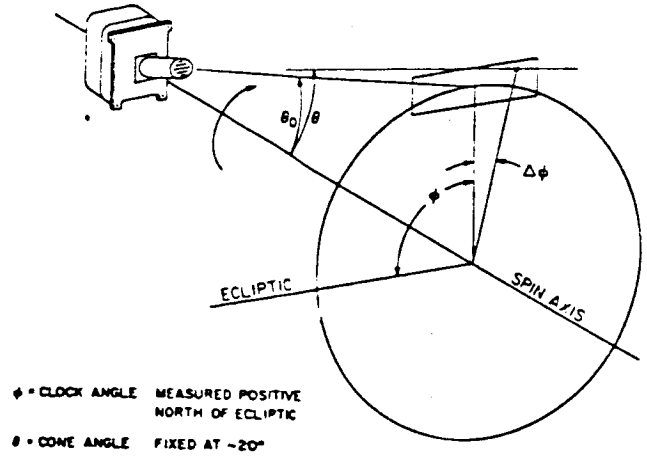

FIG. 1.—Viewing geometry for the *Pioneer 10* UV photometer. The optical axis is at an angle $\theta_0 = 20°$ to the spin axis. The angle ϕ is the clock angle relative to the ecliptic.

II. INSTRUMENTATION AND VIEWING GEOMETRY

The ultraviolet photometer on board *Pioneer 10* covers two broad spectral regions (Judge and Carlson 1974; Carlson and Judge 1974). The short wavelength band (λ_S channel) is sensitive only to emissions shortward of about 800 Å, and includes the 584 Å resonance line of helium. The region of sensitivity of the long-wavelength channel (λ_L channel) is below 1400 Å and includes the hydrogen resonance line at 1216 Å. The instrument design was based on the expected dominance of hydrogen and helium gases in the Jovian atmosphere and the interplanetary medium. In interplanetary space the emission signal in the λ_L channel results mainly from hydrogen emission at $\lambda = 1216$ Å, while the signal in the λ_S channel is due to helium emission at $\lambda = 584$ Å. For a uniform diffuse source that fills the field of view, the sensitivity of the instrument is 7.3 counts s^{-1} R^{-1} at $\lambda = 584$ Å for the λ_S channel and is 4.9 counts s^{-1} R^{-1} at 1216 Å for the λ_L channel.

The photometer field of view is limited by a mechanical collimator whose optical axis is oriented at an angle $\theta_0 = 20°$ with respect to the spacecraft spin axis (Fig. 1). The scanning motion that results from spacecraft rotation sweeps the field of view over the surface of a 40° cone having its vertex at the spacecraft and its cone axis oriented along the spin axis. The spin axis of the spacecraft is parallel to the spacecraft-Earth line.

The trajectory of the *Pioneer 10* spacecraft and the field of view of the photometer projected on the ecliptic plane are shown in Figure 2. In this figure, the positive x-axis is in the ecliptic plane at R.A. = 260°, the approximate direction of the inflowing gas. The spin axis of the spacecraft is as shown by the arrows, and points away from the spacecraft-Earth

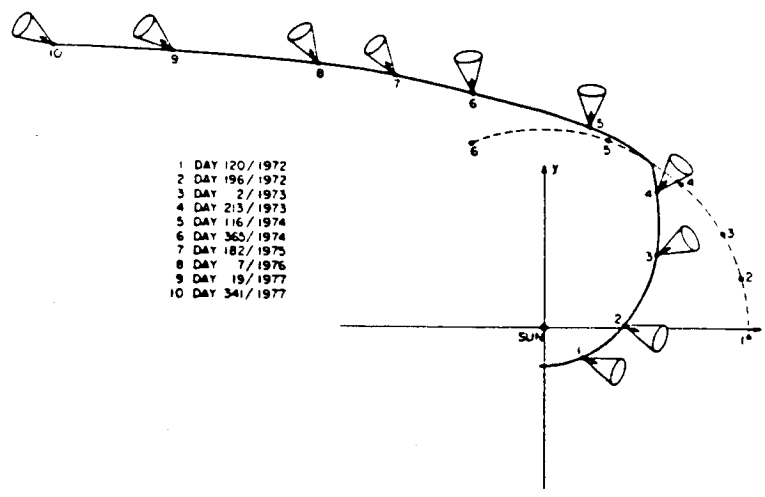

FIG. 2.—The trajectory for the *Pioneer 10* spacecraft and the photometer's viewing field projected on the ecliptic plane. The upwind direction (R.A. = 260°) is along the positive x-axis. The spin axis vector of the spacecraft points away from the spacecraft-Earth direction and is shown by arrows in the figure. Jupiter's position at the time of observation is also indicated.

direction. In Figure 2, we also show Jupiter's position at the time indicated. Because of its large mass and strong radiation field, Jupiter is likely to have a significant effect on the nearby interplanetary gas distribution.

Before the Jovian encounter the photometer viewed a region close to the upwind direction. After encounter, however, the trajectory of the spacecraft was significantly altered, and the photometer's viewing direction was shifted away from the upwind direction. The angle between the viewing direction and upwind, at various times, is shown in Figure 3. In this figure, the solid curve is for a clock angle $\phi = 0°$, while the dashed curve is for $\phi = 180°$. The observation region for other clock angles lies between these two curves.

III. OBSERVATIONAL DATA

Since the UV photometer is windowless, it is somewhat sensitive to particles as well as the intended UV photons. Accordingly, during the early part of the flight (while the spacecraft was near the Sun), bursts of solar particles caused significant increases in the measured count rate. In early 1972 the solar wind particles were very intense, and the background rate in both channels was large with rapid fluctuations. Few useful data were available during this time period. However, as the Sun-spacecraft distance increased (> 2 AU), the duration and the intensity of particle interference decreased significantly, and a consistent and slowly varying count rate is found over long periods.

Typical UV data for the period of time 1972–1977 for both the H and He channels are presented and discussed below. The observed count rate has been converted to rayleighs by correcting for the instrument's response and dark count.

In Figures 4 and 5 we show the observed intensity as a function of the spacecraft's clock angle for both the H and He channels. The curves result from an averaging of the data over a period of 1 day. As can be seen, the variation of intensity with clock angle is significant during 1972, but the amplitude variation decreases with time and becomes flat after 1973. We note that the minimum intensity is not always at $\phi = 180°$, but sometimes shifts to $\phi = 0°$. These amplitude variations during 1973 and earlier are probably not due to variations in the interplanetary glow, but reflect the variable particle flux that entered the photometer. In the H channel there are also several emission signals above the slowly varying background which are due to the UV radiation of early type stars in the field of view. These data, however, will not be further discussed in the present work.

In general, the observed interplanetary glow intensity decreases as the distance of the spacecraft from the Sun increases. In Figures 6 and 7, the intensity averaged over all clock angles is plotted as a function of the Sun-spacecraft distance. The scatter in the experimental intensity possibly reflects the variation of solar flux associated with short-term variations in solar activity. In the H channel the average intensity is ~ 350 R as observed from $r = 2.75$ AU, but decreases to ~ 80 R for $r = 10$ AU. For $r > 10$ AU the H intensity remains at about 80 R and shows little dependence on the radial distance, and thus suggests the presence of a strong ultraviolet background glow. For the He channel, the intensity is 1.5 R at $r = 2.75$ AU and decreases to 0.4 R at $r = 8.5$ AU. There is noticeable structure in the He radial data at $r = 5.5$ AU where the intensity shows a sudden increase. This is due to the fact that the photometer viewing directions after the Jovian

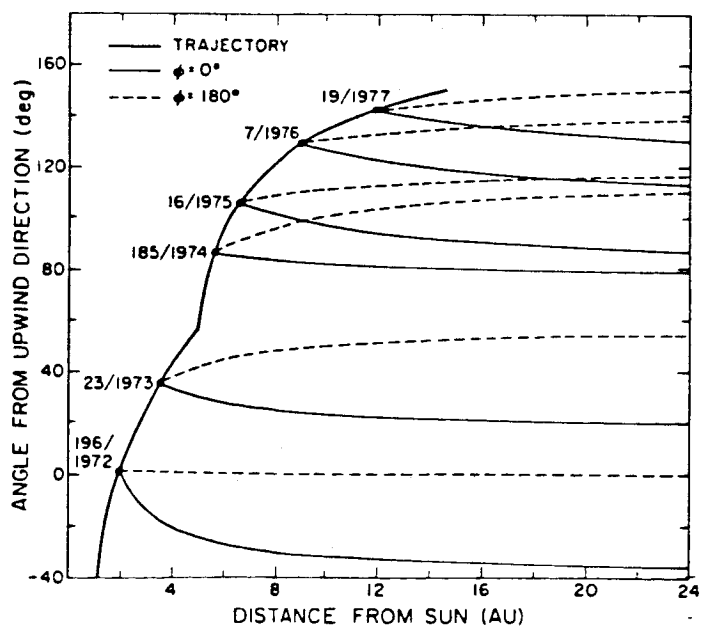

FIG. 3.—Angle between the field of view and the upwind direction (R.A. = 260°). The solid curve is for the field of view with a clock angle of 0°, the dashed curve is for the clock angle of 180°. The trajectory of the spacecraft is indicated by the dark solid curve.

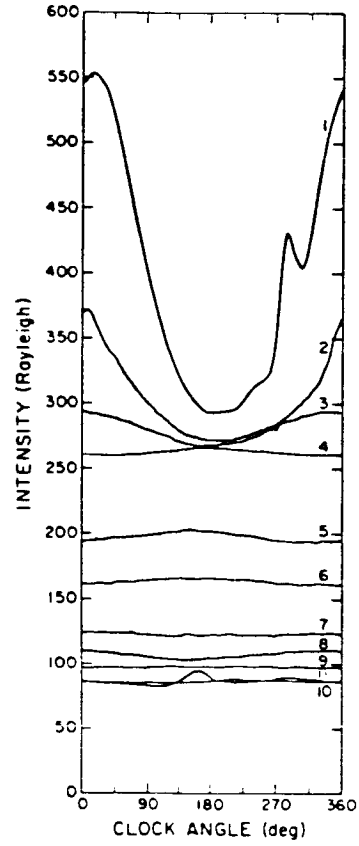

FIG. 4.—Hydrogen channel data averaged over a period of 1 day. (1) Day 227/1972. (2) Day 286/1972. (3) Day 325/1972. (4) Day 24/1973. (5) Day 104/1973. (6) Day 165/1973. (7) Day 253/1974. (8) Day 22/1975. (9) Day 139/1975. (10) Day 125/1976. (11) Day 321/1977.

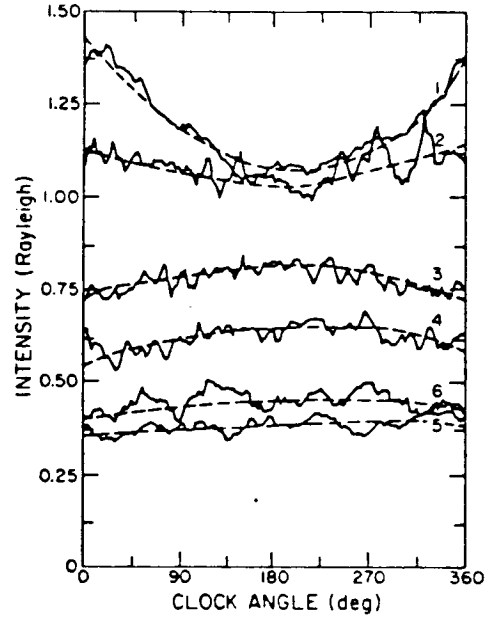

FIG. 5.—Helium channel data averaged over a period of 1 day. (1) Day 286/1972. (2) Day 325/1972. (3) Day 104/1973. (4) Day 163/1974. (5) Day 125/1975. (6) Day 321/1977.

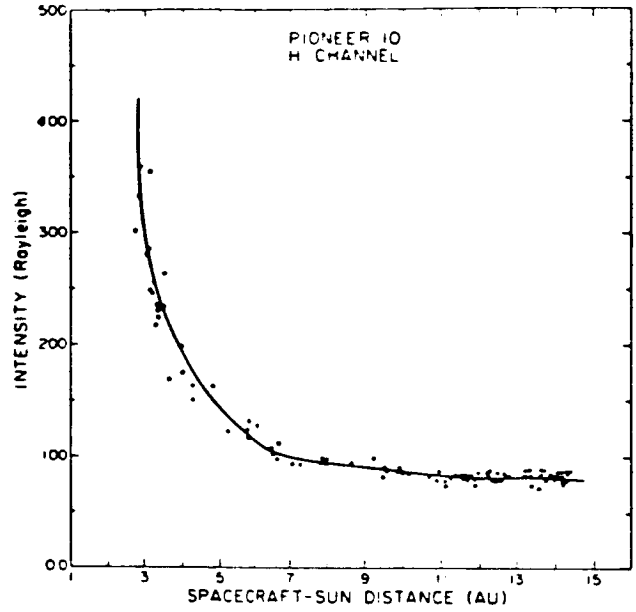

FIG. 6.—H Lα line intensity as a function of the spacecraft-Sun distance

encounter (at $r = 5.2$ AU) were abruptly shifted to near the downwind direction where the helium density, due to solar gravitational focusing, is significantly higher than in the upwind direction.

In the following we will compare these data with our theoretical calculations to deduce the physical parameters of the interplanetary gas. First, we present the theoretical model for the interplanetary glow.

IV. THE INTERPLANETARY GLOW MODEL

The interplanetary glow results primarily from resonance scattering of solar radiation by neutral atoms which enter our solar system from interstellar space (see Thomas 1978, for a review). The inflow velocity of the nearby interstellar gas relative to the solar system is $V_b \sim 20$ km s^{-1} (Adams and Frisch 1977), and the wind direction is near the ecliptic plane at a R.A. = 250° to 260° (Judge *et al.* 1972; Meier 1977; Thomas 1978).

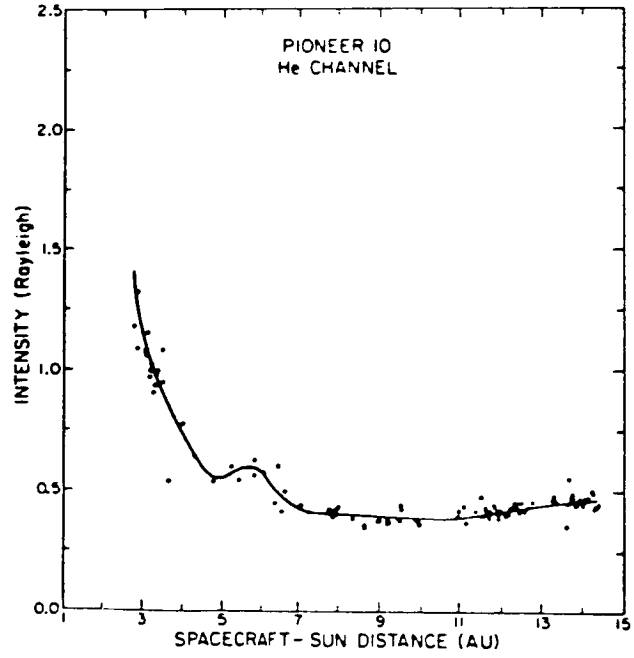

FIG. 7.—He 584 Å line intensity as a function of the spacecraft-Sun distance

As the gas particles move from interstellar space into the solar system, the density distribution function gradually changes due to the effects of solar radiation pressure, gravitational attraction, and ionization loss. For a low temperature gas, the interplanetary particle density n and the radial velocity of the gas V_a can be evaluated analytically as follows (Axford 1972; Blum and Fahr 1970):

$$n(r, \theta) = \sum_{j=1,2} \frac{N_0 p_j^2 \exp(-\beta_0 r_E^2 \theta_j / |p_j|)}{V_b^2 r \sin\theta [r^2 \sin^2\theta + 4r(1-\cos\theta)/C]^{1/2}}, \tag{1}$$

and

$$V_a = \pm \left[V_b^2 + \frac{2(1-\mu)GM}{r} - \frac{p_j^2}{r^2} \right]^{1/2}, \tag{2}$$

where

$$C = \frac{V_b^2}{(1-\mu)GM_s}.$$

Here r is the distance from the Sun, θ is the angular position with respect to the upwind direction, β_0 is the charge exchange and photoionization loss rate at the orbital distance of Earth r_E, μ is the ratio of radiation pressure to gravitational attraction, N_0 is the particle density at infinity (density of the nearby interstellar gas), p_j is the angular momentum at (r, θ), and $\theta_j = \theta$ if $p_j > 0$, $\theta_j = 2\pi - \theta$ if $p_j < 0$. In equation (1), the summation is over $j = 1, 2$ because there are two trajectories which pass through each point. However, for the high temperature gas in which the thermal velocity is comparable to the inflow velocity, the density distribution as a function of radial velocity and position must be integrated over two other velocity coordinates. The density distribution is then given by

$$N(r, \theta, V_r) = \int_{V_{\rho 0}}^{\infty} \int_0^{2\pi} n(r, V) V_\rho \, dV_\rho \, d\psi, \tag{3}$$

where $n(r, V)$ is the interplanetary density distribution function in terms of the phase space volume element (Danby and Camm 1957; Wu and Judge 1979*a*). Here the particle velocity is specified in cylindrical coordinates (V_r, V_ρ, ψ), where V_r is the radial velocity, V_ρ is the velocity component perpendicular to the radial direction, ψ is the rotational angle about the radial direction, and $V_{\rho 0}$ is the lower integration limit for the variable V_ρ (Wu and Judge 1979*a*). The high temperature formula is required according to the recent measurement of the interplanetary hydrogen emission profile (Bertaux *et al.* 1976) who have inferred a gas temperature of 10^4 K with a corresponding thermal velocity of 16 km s^{-1}. Thus equation (3) must be used in order to accurately describe the density distribution. However, as will be seen, the simple formula for the density distribution of a cold gas (eq. [1]) is still a good approximation for a high temperature gas in certain interplanetary regions.

Using the above density distribution, the absorption coefficient, α_ν, for solar photons at frequency ν can now be calculated from Wu and Judge (1979*b*), specifically,

$$\begin{aligned} \alpha_\nu(r, \theta) &= (M/2KT)^{1/2} \alpha_0 N(r, \theta, V_r) && \text{for } T \neq 0 \\ &= \alpha_0 n(r, \theta) \delta(V_r - V_a) && \text{for } T = 0, \end{aligned} \tag{4}$$

where

$$\nu = \nu_0 \left(1 + \frac{V_r}{c}\right), \qquad \alpha_0 = \frac{\pi e^2}{mc} f \lambda_0,$$

and where m and M are the mass of the electron and the atom, c is the speed of light, e is the electronic charge, f is the oscillator strength, and λ_0, ν_0 are the wavelength and frequency at the line center. Accordingly, the volume emissivity ϵ of the interplanetary gas and the interplanetary glow intensity I can be expressed as

$$\epsilon(r, \theta) = \frac{\lambda^2}{c} \int_{-\infty}^{\infty} \pi F_\lambda \alpha_\nu(r, \theta) d\nu \tag{5a}$$

and

$$I = I_G + \int_{r_0}^{\infty} \epsilon(r, \theta) P(\gamma) dl, \tag{5b}$$

where πF_λ is the solar flux at wavelength λ, P is the phase function, l is the viewing direction, γ is the angle between r and l, and I_G is the background intensity, which will be discussed later.

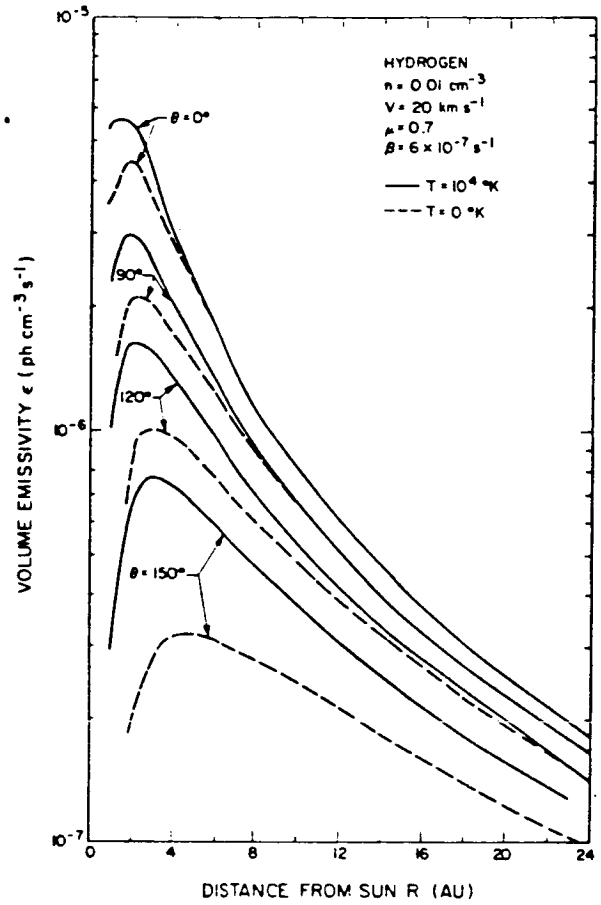

FIG. 8.—The calculated volume emissivity for the interplanetary H Lα line at various look angles. The parameters used in the calculation are $N_0 = 0.1$ cm^{-3}, $V_b = 20$ km s^{-1}, $\pi F_\lambda = 2.2 \times 10^{11}$ photons cm^{-2} s^{-1}, $\mu = 0.7$, and $\beta = 6 \times 10^{-7}$ s^{-1}. The solid curve is for an interstellar gas temperature of 10^4 K, and the dashed curve is for a temperature of 0 K.

In Figures 8 and 9 we show the calculated volume emissivity for interplanetary hydrogen and helium with $T_0 = 0$ and 10^4 K, for an interstellar wind velocity of 20 km s^{-1}, and interstellar densities of $N_0 = 0.1$ cm^{-3} for H and 0.01 cm^{-3} for He. At large distances from the Sun, the solar effect on the density distribution is small, and the interplanetary emissivity due to the decrease in the solar flux will drop approximately as r^{-2}. We note that in the region of small angles and large distances ($\theta < 90°$, $r > 8$ AU for the H glow; $\theta < 120°$, $r > 4$ AU for the He glow), the effect of gas temperature on the resulting emission appears to be negligible, and the density distribution for the cold temperature gas (eq. [1]) appears to be a good approximation for the high temperature distribution (eq. [3]). It may also be noted that interplanetary hydrogen, because of the large ionization rate and the small net effect of solar gravity, has a weak emission in the downwind direction. On the other hand, the helium emission, due to strong solar gravitational focusing and the small ionization rate, has its strongest emission in the downwind direction.

From Figure 8 we see the hydrogen emissitivity at small solar distances is quite different for the hot ($T = 10^4$ K) and cold ($T = 0$ K) models. At $r = 2$ AU, the hot model emissivity at $\theta = 0°$ is a factor of about 1.2 of the cold model, and increases to 3.2 at $\theta = 150°$. However, for the case of helium (Fig. 9) the difference in the hot and cold models is less significant and the ratio of emissivities never exceeds a factor of 1.5 even at small solar distances. The different behavior of hydrogen and helium is related to their loss rates. High-temperature interplanetary atoms cover a large portion of velocity space while the atoms of zero temperature have one trajectory for each spacial position. High temperature atoms from an elemental volume of space will follow different trajectories and will have different loss functions which are proportional to their flight time and loss rate. Hence the interstellar density distribution function of high temperature atoms is likely to be different from the distribution of zero temperature, and the difference is expected to increase with increasing loss rate. Thus, the difference between the hot and cold models will be large for the case of hydrogen due to its large loss rate, and the effect is more profound downwind than upwind because of the large flight time. On the other hand, the difference in helium emissivity is small because the loss rate for helium is a factor of 10 less than that of hydrogen.

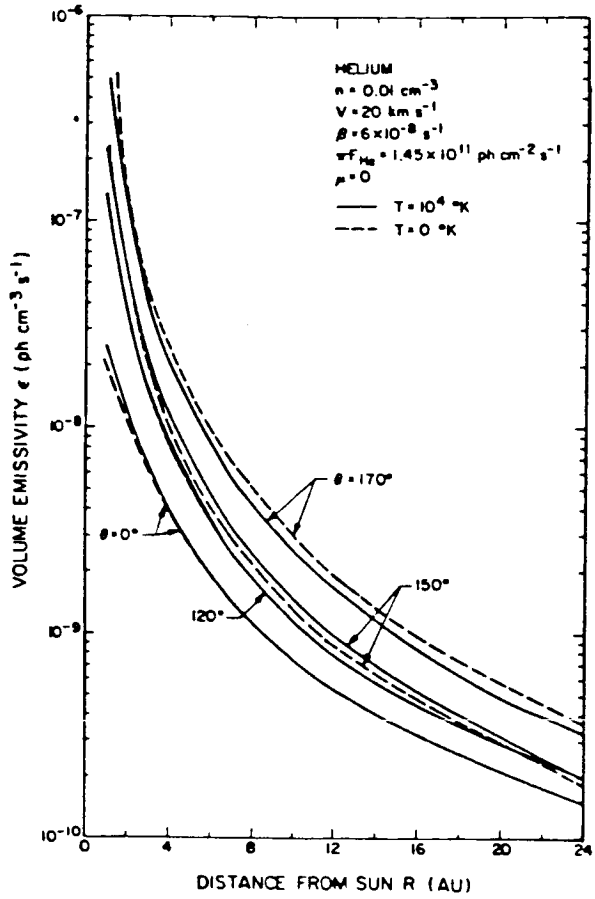

FIG. 9—Calculated volume emissivity for the interplanetary He 584 Å line at various look angles. The parameters used in the calculation are $N_0 = 0.01$ cm^{-3}, $V_b = 20$ km s^{-1}, $\beta = 6 \times 10^{-8}$ s^{-1}, $\pi F_\lambda = 1.45 \times 10^9$ ph cm^{-2} s^{-1}, and $\mu = 0$.

In our calculation of the H Lα intensity, the solar flux πF_λ at 1216 Å is assumed to be constant over the range of Doppler shifts produced by the motion of the hydrogen atoms (Thomas 1978). On the other hand, in the calculation of the He 584 Å intensity, the solar He line profile is assumed to be Gaussian with a line width of 122 mÅ (Maloy *et al.* 1978).

The value of πF_λ depends on solar activity at the time of observation. For the H Lα line the value can be expressed in terms of the solar 10.7 cm radio flux $F_{10.7}$ by (Vidal-Madjar 1975)

$$\pi F_\lambda(\mathrm{L}\alpha) = 0.54 \times 10^{11}(1.17 \times 10^{-2} F_{10.7} + 1.49)^{1.53} \text{ photons cm}^{-2}\text{ s}^{-1}\text{ Å}^{-1}\,, \tag{6}$$

where $F_{10.7}$ is in units of 10^{-2} W m^{-2} Hz^{-1}.

For the He 584 Å line, according to the data of Hall and Hinteregger (1970), the relation is given by

$$\pi F_\lambda(\mathrm{He}) = (0.22 + 0.0034F_{10.7}) \times 10^{10} \text{ photons cm}^{-2}\text{ s}^{-1}\text{ Å}^{-1}\,. \tag{7}$$

However, a more recent measurement by Maloy *et al.* (1978) indicates that the solar He line flux density corresponding to a radio flux of $F_{10.7} = 90$ is 2.0×10^{10} s^{-1} cm^{-2} Å^{-1}, while the corresponding value from Hall and Hinteregger is only $\sim 0.5 \times 10^{10}$ s^{-1} cm^{-2} Å^{-1}. We adopt here the more recent value of Maloy *et al.* and obtain for the solar He flux

$$\pi F_\lambda(\mathrm{He}) = (1.7 + 0.0034F_{10.7}) \times 10^{10} \text{ photons cm}^{2}\text{ s}^{-1}\text{ Å}^{-1}\,. \tag{8}$$

Using equations (6) and (8), the yearly average solar flux from 1972 to 1977 is determined and summarized in Table 1. For the H Lα flux the variation is from 2.9 to 2.0×10^{11} cm^{-2} s^{-1} Å^{-1}, and for the He 584 Å line the variation is from 2.1 to 1.9×10^{10} cm^{-2} s^{-1} Å^{-1}. Thus, the variation of solar flux πF_λ over a period of five years is significant and is included in the following interplanetary glow calculations.

For Lα emission, the scattered light is nearly isotropic and the phase factor can be expressed as (Brandt and Chamberlain 1959)

$$P(\gamma) = 1 + \tfrac{1}{4}(\cos^2\gamma - \tfrac{1}{3})\,, \tag{9}$$

TABLE 1

SOLAR FLUX FOR THE H Lα (1216 Å) AND He 584 Å LINES

Year *	$F_{10.7}$ (10^{22} W m^{-2} Hz^{-1})	πF_λ(Lα) (10^{11} cm^{-2} s^{-1} Å^{-1})	πF_λ(He) (10^{10} cm^{-2} s^{-1} Å^{-1})
1972	122	2.9 (0.9)	2.1
1973	93	2.3 (0.7)	2.0
1974	86.6	2.2 (0.7)	2.0
1975	76	2.0 (0.6)	2.0
1976	73	2.0 (0.6)	1.9
1977	87	2.2 (0.7)	2.0

NOTE—The number in parentheses is the corresponding value of the parameter μ.

and the phase factor for the He 584 Å line is

$$P(\gamma) = \tfrac{3}{4}(1 + \cos^2 \gamma) . \tag{10}$$

The interplanetary hydrogen atoms are ionized primarily through the charge-exchange process with the solar wind proton (Axford 1972). With a possible proton flux varying from 3×10^8 to 2×10^8 cm^{-2} s^{-1} in a single cycle (Diodato, Moreno, and Signorini 1974) and a cross section of 2×10^{-15} cm^{-2} for the charge-exchange process, the loss rate is calculated to be from 4×10^{-7} to 6×10^{-7} s^{-1}. The interplanetary helium loss results from the photoionization by the solar photons at wavelengths less than 500 Å. Using the measured EUV solar flux of Hinteregger (1970) and the photoionization cross section of Cairns and Samson (1965), the loss rate of helium is determined to be 6×10^{-8} s^{-1}. However, the solar EUV flux can vary significantly over a solar cycle (Timothy 1977), but its exact variation remains uncertain (Schimidtke 1978). Here, we adopted a value of $\beta = 6$ to 8×10^{-8} s^{-1} for the interplanetary helium. As we will see later (in Figs. 11 and 13), the uncertainty in our theoretical calculations for the interplanetary glow resulting from the different values in β is less than 10% and is of the order of our data noise level.

The background radiation I_G in equation (5) includes (1) galactic radiation over the band pass of the instrument, (2) multiple scattering of solar photons by the distant interplanetary gas, and (3) the scattering of solar photons by the fast atoms ($V \sim 100$ km s^{-1}) produced by the charge-exchange reaction at and beyond the heliosphere boundary. Based on the measurement of a Lα photometer on the *Mars* 7 spacecraft (Bertaux *et al.*, 1976), the possible galactic radiation over a 200 Å bandwidth which included the Lα line was estimated to be less than 50 R, while the value from the observed Hα background data inferred is less than 10 R (Thomas and Blamont 1976). A recent measurement of galactic radiation by the *Voyager* ultraviolet spectrometer indicate the integrated intensity between 900 and 1200 Å is about 10 R (Sandel, Shemansky, and Broadfoot 1979). The measured intensity is found to fall steeply toward shorter wavelengths, beginning at about 950 Å, but is a slowly increasing function toward longer wavelengths. A linear extrapolation of their observed spectra leads to an intensity of ~ 30 R in the 200 to 1400 Å bandpass of the *Pioneer* λ_L channel photometer. The galactic radiation in the spectral region between 200 and 600 Å where the λ_S channel is most sensitive has never been measured. However, since the wavelength for this radiation is well below the hydrogen ionization limit and can be absorbed strongly by the interstellar medium, the contribution of the galactic radiation to the observed λ_S signal is expected to be very small.

The importance of multiple scattering of solar resonance radiation in the nearby interstellar medium has been investigated by Wallis (1974) and Keller and Thomas (1979). It appears that the problem may be important for the hydrogen Lα line and unimportant for the helium 584 Å line. However, the radiative transfer problem relevant to the interplanetary background intensity has not yet been completely solved. For an accurate quantitative result, more realistic considerations of the interplanetary gas density distribution and the frequency redistribution effects are required (Keller and Thomas 1979).

The possibility of fast hydrogen atoms, produced by charge exchange at and beyond the heliosphere boundary, contributing to the observed interplanetary radiation has been suggested by Patterson *et al.* (1963). It was suggested subsequently, however, that the interplanetary radiation observed from the Earth's orbit results primarily from resonance scattering by penetrating interstellar hydrogen (Blum and Fahr 1970). More recently, Blum and Lang (1979) have proposed that the fast hydrogen may contribute 40–160 R at a distance of 1 AU, with the uncertainty depending on the location of the heliosphere boundary. In the following discussion of our *Pioneer* λ_L data, the possible contribution from these sources to the observed radiation will be included in one term, I_G, and, because of a lack of accurate information, this radiation will be assumed to be isotropic and independent of radial position with respect to the Sun.

As mentioned above, the contributions of galactic radiation and multiple scattering by interplanetary helium appear to provide an insignificant part to the observed λ_S signals. Moreover, scattering of the solar 584 Å line by fast helium is also likely to be small because of the narrow line width (~ 0.1 Å) of this solar line, and the expected low concentration of hot helium plasma at the heliosphere boundary, required to produce the fast helium atoms through charge exchange processes. Thus, in the discussion of the *Pioneer* λ_S data, the constant term I_G in our expression for the interplanetary glow (eq. [5]) will be assumed to be zero.

V. HYDROGEN GLOW

In Figure 10, we show the theoretical results for the hydrogen glow as a function of spacecraft clock angle. Here, the physical parameters for interplanetary hydrogen adopted are $I_G = 0$, $V = 20$ km s^{-1}, $\alpha = 250°$, $\beta = 6 \times 10^{-7}$ s^{-1}, and $N_0 = 0.088$ cm^{-3}. The interstellar density N_0 is chosen so that the theoretical values for $r > 10$ AU are consistent with our observational data.

Comparison of Figure 10 with Figure 4 indicates that the experimental data during 1972–1973 deviate significantly from the theoretical calculations. Specifically, depending on clock angle, the intensity variation can be as great as 100 R. On the other hand, the theoretical calculation indicates that the variation should always be less than 50 R. Moreover, the observational data show that the intensity during 1973 reached a minimum at the clock angle $\phi = 0°$, while the theoretical calculation predicts a minimum at $\Phi = 180°$. The source of these discrepancies is a solar particle background as discussed below.

Close to the Sun it has not been possible to fit the experimental data, even for an extended range of parameters: $\alpha = 250°$–$260°$, $\beta = 4$–6×10^{-7} s^{-1}, $I_G = 0$ to 40 R. This is primarily due to the direct detection of solar wind particles, superposed on the true interplanetary glow. The strong variations in the experimental curves (Fig. 4) are most certainly due to the variable particle flux that enters the photometer. Since the energetic particles are flowing from the Sun, the particle interference should be minimum when the photometer is viewing in the direction with a phase angle (the angle between the viewing direction and the direction to the Sun) closest to 180°. For the data of day 227/1972, the intensity at a clock angle $\phi = 180°$ is lower than the intensity at $\phi = 0°$. That is because the phase angle for the viewing direction along $\phi = 180°$ is 175°, while for $\phi = 0°$ the phase angle is 135°; thus, the probability of energetic particles entering the photometer at $\phi = 180°$ is smaller than the probability at $\phi = 0°$. Similar correlations between the phase angle and the intensity variation are also found in the observed data from launch through 1973. However, the interference effect decreases rapidly with distance from the Sun, since the solar flux varies as $1/r^2$. During 1973, the observed intensity variation is less than 20 R for $I \sim 200$ R, or less than 10%. During 1974 and later ($r > 5$ AU), variations in either the experimental or theoretical curves are insignificant and the particle effect appears to be negligible for the viewing directions accessible to the *Pioneer 10* instrument.

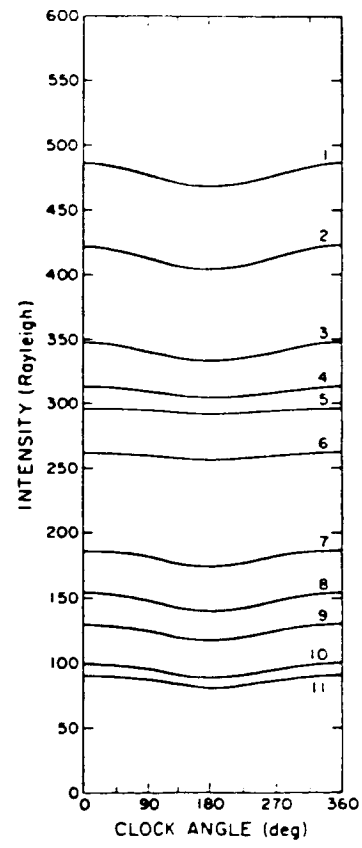

FIG. 10.—Theoretical data for the H Lα line intensity. The time sequence is the same as in Fig. 4. The parameters used in the calculation are $V_0 = 20$ km s^{-2}, $\alpha = 250°$, $\beta = 6 \times 10^{-7}$ s^{-1}, $\mu = 0.7$, $N_0 = 0.88$ cm^{-3}, and $I_G = 0$.

It may be noted that the model used in Figure 10 (with the parameters $n = 0.88$ cm^{-3}, $I_G = 0$) does not fit the observational data very well even at large distances from the Sun (Fig. 4). For example, the theoretical results for day 253/1974 (curve 7) give an average brightness of about 180 R while the observational value is only about 125 R. However, if we change the parameters n and I_G in the theoretical calculation from the values of 0.88 cm^{-3} and 0 R to 0.44 cm^{-3} and 40 R, then the theoretical data after 1973 correspond quite closely to the experimental results.

In Figure 11, the theoretical data averaged over all clock angles are plotted as a function of the Sun-spacecraft and are compared with the experimental data. In this figure, the theoretical data are calculated from equation (5) with various combinations of possible parameter values. In the model calculation we assume that the wind direction is in the ecliptic plane with right ascension, α, between 250° and 270°, with a wind velocity $V = 10$–20 km s^{-1} and an ionization rate $\beta = 4$ to 6×10^{-7} s^{-1}, an interstellar temperature $T_0 = 0$–10^4 K, and a background radiation $I_G = 0$–40 R. The densities N_0 are chosen so that the theoretical curves would fit the experimental data at large distances. It is clear that the theoretical data set with $I_G = 0$ does not fit the experimental data well. The theoretical values at distances from 4 to 10 AU are always higher than the experimental values. However, as the parameter I_G increases to 40 R $\pm$ 10 R, the theoretical data are consistent with the experimental data for $r > 4$ AU. The uncertainty of 10 R in the background radiation is determined primarily by the background noise level and the uncertainties in the parameter values for α and β_0. For $r < 4$ AU, the experimental data give higher intensities than the theoretical data for $I_G = 40$ R, possibly due to particle interference as discussed earlier.

To fit the observed data with $I_G = 40 \pm 10$ R, the hydrogen density at infinity is required to be $N_0 = 0.04 \pm 0.01$ cm^{-3}. This density is consistent with the result from *Mariner 10* measurements (Ajello 1978), but is lower than the *Copernicus* value of 0.08 cm^{-3} (McClintock *et al.* 1978) and the value of ~ 0.1 cm^{-3} from Thomas and Krassa (1974) and Bertaux, Ammar, and Blamont (1973).

It may be noted that our value of $I_G = 40 \pm 10$ R includes the 30 R value of the galactic radiation between 200 and 1400 Å, inferred earlier from the measurement of Sandel, Shemansky, and Broadfoot (1979). Accordingly, the constant background glow due to multiple scattering of solar Lα by the interplanetary gas at large distances, or scattering from fast atoms which originate at the heliosphere boundary, is probably about 10 R.

VI. HELIUM GLOW

In Figure 12, the theoretical helium glow intensity with $I_G = 0$, $V_b = 20$ km s^{-1}, $\alpha = 260°$, $\beta = 6 \times 10^{-8}$ s^{-1}, $\mu = 0$, and $N_0 = 0.01$ cm^{-3}, is calculated as a function of spacecraft clock angle. Comparing Figure 5 with Figure 12, it may be seen that the experimental curves for 1972 through 1973 deviate significantly from the theoretical curves. As in the hydrogen data, this deviation is also caused primarily by the interference of charged particles. Such data are not used in the following analysis.

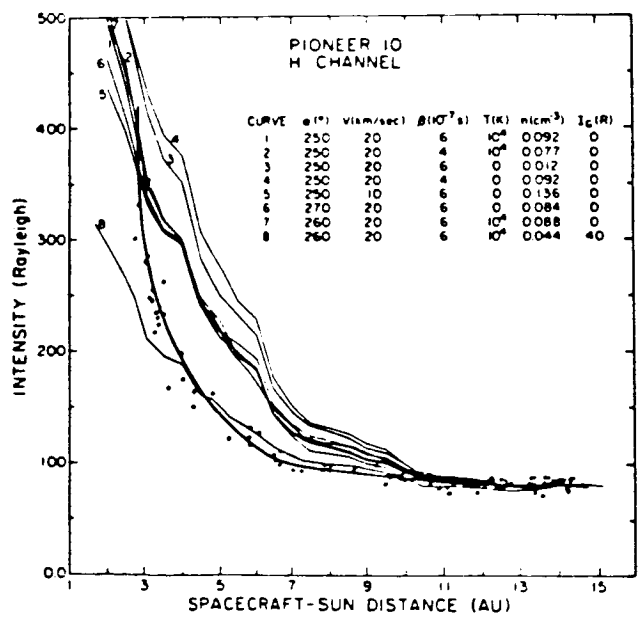

FIG. 11.—Comparison of theoretical and experimental radial profiles for the H Lα glow. The small structure in the theoretical curves results primarily from the rather irregular variation in the solar flux and the usage of a finite number of points in the theoretical calculations (at an interval of 0.5 AU).

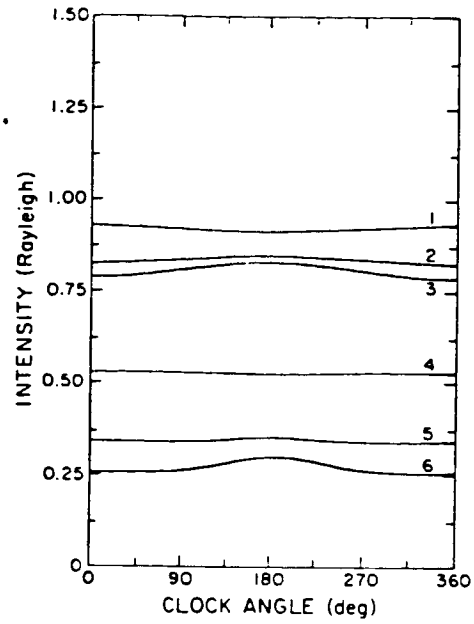

FIG. 12.—Theoretical data for the He 584 Å line intensity. The time sequence is the same as in Fig. 5. The parameters used in the calculation are $V_b = 20$ km s^{-1}, $\alpha = 260°$, $\beta = 6 \times 10^{-8}$ s^{-1}, $\mu = 0$, and $N_0 = 0.01$ cm^{-3}.

It is noted that the theoretical curves would predict an intensity peak with an amplitude of ~ 0.05 R at $\phi = 180°$, for the data of 1977, since the viewing field is close to the downwind direction. However, no apparent maximum was detected in the experimental data, perhaps because the expected signals are small and near the background noise level.

In Figure 13, the theoretical intensity averaged over clock angle is plotted as a function of distance and is compared with the experimental data. In general, the theoretical curves with $N_0 = 0.01 \pm 0.002$ cm^{-3} and $V = 20$ km s^{-1} fit the observational data quite well between 4 and 10 AU. The uncertainty in the helium density is determined by the data's noise level. It is noted that the observational values for $r < 3$ AU are larger than the theoretical values and this is again due to charged particle interference. However, for $r > 10$ AU, the observational data are also above the theoretical

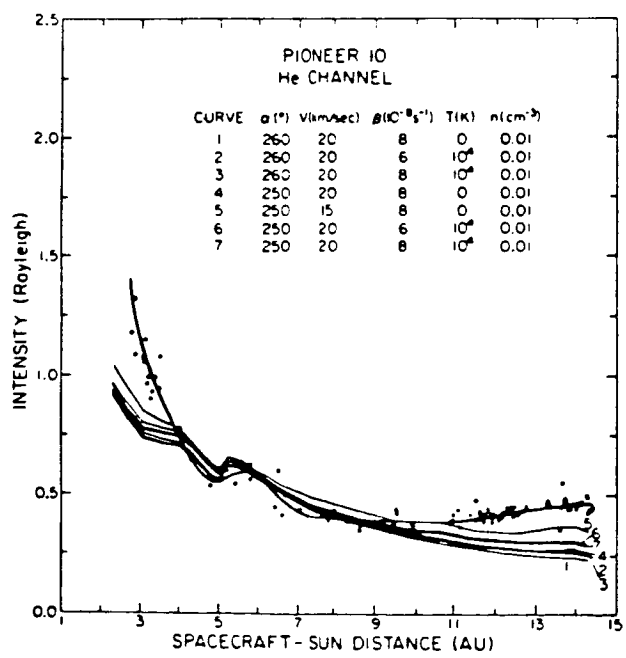

FIG. 13.—Comparison of the theoretical and experimental radial profiles for the He 584 Å glow. The theoretical profiles are calculated at intervals of ~ 0.5 AU.

curves, although the charged particle flux is small. One possible explanation for the large background is that the dark count rate has increased with spacecraft age due to the increasing gamma radiation from the radioisotope thermoelectric generators on the spacecraft. Unfortunately, the exact time variation of this dark count rate is not yet known, and even a small variation of about 1 count s^{-1} could significantly affect the accuracy of the experimental data, which is less than 7 counts s^{-1} for $r > 10$ AU. It should be noted, however, that our values of $N_0 = 0.01 \pm 0.002$ cm^{-3} are determined from the data between 4 and 10 AU where charged particle interference and the variation in dark count are minimal. Our value of $N_0 \sim 0.01$ cm^{-3} is consistent with the upper bound value of 0.0089 ± 0.005 cm^{-3} determined by the extreme-ultraviolet telescope observations made during the 1975 *Apollo-Soyuz* Test Project (Freeman, Paresce, and Bowyer 1979), and compared well with the value 0.008 ± 0.002 cm^{-3} of the *Mariner 10* measurement (Ajello, Witt, and Blum 1979).

VII. DEVIATIONS OF THE OBSERVATIONS FROM THE MODEL CALCULATIONS

Even with the best possible fit, the theoretical calculation for the H and He glow deviates significantly from the experimental data for $r < 3$ AU, and for $r > 10$ AU in the case of helium. The discrepancy has been attributed to (1) interference from energetic particles and (2) possible gamma-ray contamination of the He channel at large distances. However, the deviation may also be caused by the inadequacy of the theoretical model which neglects the following factors:

1. *Jovian perturbation of the interplanetary density distribution in its vicinity, which arises because of its large mass and its intense radiation belts (Fahr 1976).*—Not only was the UV photometer on the *Pioneer* spacecraft close to Jupiter for a significant period of time during the Jovian approach, but it also viewed a region less than 0.5 AU away from Jupiter before the Jovian encounter for a period longer than 1 year. Thus, the theoretical calculation near $r \sim 5$ AU, which does not include the Jovian perturbation, should be modified to include this effect.
2. *The uncertainty in the solar hydrogen Lyman-α and helium* 584 Å *flux and their dependence on the* 10.7 cm *radio flux.*—For example, for the same solar conditions with a 10.7 cm solar radio flux $F_{10.7}$ equal to ~ 100, the intensity of the solar He 584 Å line is found to be 0.5, 1.2, and 2×10^{10} cm^{-2} s^{-1} $Å^{-1}$ in three different experimental measurements (Hall and Hinteregger 1970; Schmidtke 1976; Maloy *et al.* 1978). Perhaps the solar He line flux is not adequately given by equation (8) above, thereby contributing to errors in the model calculation of the helium glow, especially for $r > 10$ AU.
3. *The absorption of solar light by interplanetary gas.*—In the theoretical calculations, we assumed that the solar line profiles are unchanged with distance and that the solar flux density varies as $1/r^2$. These assumptions are not correct at large distances because of interplanetary absorption (Wu and Judge 1979*a*).
4. *The radial dependence of the background glow and its variation with the viewing direction.*—As mentioned earlier, the background glow can arise from galactic radiation, multiple scattering, and scattering from fast atoms which originate at the heliosphere boundary. The magnitude of this radiation may vary significantly over the heliosphere (Keller and Thomas 1979; Blum and Lang 1979). The assumption of constant background radiation in our calculation may thus also require modification.

VIII. SUMMARY AND CONCLUSIONS

The interplanetary glow intensity observed by the *Pioneer 10* UV photometer at Sun-spacecraft distances of 2–14 AU has been presented. From these data we have determined that the background intensity for the 200–1400 Å band pass of the λ_L photometer channel is about 40 ± 10 R, and that the nearby interstellar density is 0.04 ± 0.91 cm^{-3} for hydrogen and $\sim 0.01 \pm 0.002$ cm^{-3} for helium. Accordingly, the He/H number density ratio is ~ 0.25 at large distances from the Sun.

The *Pioneer 10* spacecraft is leaving the solar system in the downwind direction, while both *Pioneer 11* and *Voyager* will leave in the upwind direction. The combined UV observations of the interplanetary glow will provide accurate results on the physical status of the inflowing interstellar gas and the variability of background radiation as well. As we have noted, one possible source of the background radiation is the "fast" atoms which arrive from the region beyond the heliosphere boundary. Continued *Pioneer 10* and other spacecraft UV observations at great distances may allow us to determine the radial and angular dependence of these "fast" atoms, and hence to determine the location and shape of the heliosphere boundary. Finally, since *Pioneer* and *Voyager* spacecraft occasionally view the same UV stars, a cross calibration of sensitivity is available to assure the reliability of the data and the usefulness of continued deep space observations.

This work was supported by contract NAS2-6558 with the NASA Ames Research Center.

REFERENCES

Adams, T. F., and Frisch, P. C. 1977, *Ap. J.*, 212, 300.
Ajello, J. M. 1978, *Ap. J.*, 222, 1068.
Ajello, J. M., Witt, N., and Blum, P. W. 1979, *Astr. Ap.*, 73, 260.
Axford, W. I. 1972, in *Solar Wind*, ed. C. P. Sonnet, P. J. Coleman, Jr., and J. M. Wilcox (NASA SP-308), p. 608.
Bertaux, J. L., Ammar, A., and Blamont, J. E. 1973, *Space Res.*, 12, 1559.
Bertaux, J. L., Blamont, J. E., Tabarie, N., Kurt, V. G., Bourgin, M. C., Smirov, A. S., and Dementeva, N. N. 1976, *Astr. Ap.*, 46, 19.
Blum, P. W., and Fahr, H. J. 1970, *Astr. Ap.*, 4, 280.
Blum, P. W., and Lang, R. 1979, preprint.
Brandt, J. C., and Chamberlain, J. W. 1959, *Ap. J.*, 130, 670.
Broadfoot, A. L., and Kumar, S. 1978, *Ap. J.*, 222, 1054.

Cairns, R. B., and Samson, J. A. 1965, *J. Geophys. Res.*, **70**, 99.
Carlson, R. W., and Judge, D. L. 1974, *J. Geophys. Res.*, **79**, 3623.
Danby, J. M. A., and Camm, G. L. 1957, *M.N.R.A.S.*, **117**, 50.
Diodato, L., Moreno, G., and Signorini, C. 1974, *J. Geophys. Res.*, **79**, 5095.
Fahr, H. J., Lay, G., and Blum, P. W. 1976, *Astr. Ap.*, **52**, 363.
Freeman, J., Paresce, F., and Bowyer, S. 1979, *Ap. J. (Letters)*, **231**, L37.
Hall, L. A., and Hinteregger, H. E. 1970, *J. Geophys. Res.*, **75**, 6959.
Hinteregger, H. E. 1970, *Ann. Geophys.*, **26**, 547.
Judge, D. L., and Carlson, R. W. 1974, *Science*, **183**, 317.
Judge, D. L., Carlson, R. W., Suzuki, K., and Mose, A. L. 1972, *EOS*, **54**, 1194.
Keller, H. U., and Thomas, G. E. 1979, *Astr. Ap.*, **80**, 227.
Maloy, J. O., Carlson, R. W., Hartmann, U. G., and Judge, D. L. 1978, *J. Geophys. Res.*, **83**, 5685.
McClintock, W., Henry, R. C., Linsky, J. L., and Moos, H. W. 1978, *Ap. J.*, **225**, 465.
Meier, R. R. 1977, *Astr. Ap.*, **55**, 211.
Patterson, T. N. L., Johnson, F. S., and Hanson, W. B. 1963, *Planet. Space Sci.*, **11**, 767.
Sandel, B. R., Shemansky, D. E., and Broadfoot, A. Lyle 1979, *Ap. J.*, **227**, 808.
Schmidtke, G. 1976, *Geophys. Res. Letters*, **3**, 573.
———. 1978, *Planet. Space Sci.*, **26**, 347.
Thomas, G. E. 1972, in *Solar Wind*, ed. C. P. Sonnett, P. J. Coleman, Jr., and J. M. Wilcox (NASA SP-308), p. 668.
———. 1978, *Ann. Rev. Earth Planet. Sci.*, **6**, 173.
Thomas, G. E., and Blamont, J. E. 1976, *Astr. Ap.*, **51**, 283.
Thomas, G. E., and Krassa, R. F. 1971, *Astr. Ap.*, **11**, 218.
Timothy, J. G. 1977, in *The Solar Output and Its Variation*, ed. O. R. White (Boulder: Colorado Associated University Press), p. 237.
Vidal-Madjar, A. 1975, *Solar Phys.*, **40**, 69.
Wallis, M. K. 1974, *M.N.R.A.S.*, **167**, 103.
Weller, C. S. and Meier, R. R. 1974, *Ap. J.*, **193**, 417.
Wu, F. M., and Judge, D. L. 1978, *Ap. J.*, **225**, 465.
———. 1979*a*, *Ap. J.*, **231**, 594.
———. 1979*b*, *J. Geophys. Res.*, **84**, 979.

R. W. CARLSON: Jet Propulsion Laboratory, Pasadena, CA 91103

DARRELL L. JUDGE and FUN-MIN WU: Space Sciences Institute, University of Southern California, University Park, Los Angeles, CA 90007

K. SUZUKI: Geophysics Research Laboratory, University of Tokyo, Tokyo, Japan

"HEATING OF THE INTERSTELLAR MEDIUM BY THE SOLAR WIND"

J. A. Kunc, F. M. Wu and D. L. Judge
Space Science Center, SHSci-274
University of Southern California
University Park
Los Angeles, CA 90007

Subject Headings: Interplanetary Medium - Interstellar: matter - Sun: Solar Wind

Shorted Title: Heating of The Interstellar Medium.

ABSTRACT

The heating of inflowing interstellar gas by the solar wind is calculated. The experimental differential cross sections have been used for calculating electron - H (He) and proton - H (He) elastic scattering rate coefficients. The solar wind is assumed to be a two-component (protons and electrons), steady, spherically symmetric stream moving radially outward, with the inflowing gas following Keplerian trajectories. The spatial distributions of effective temperature increase within interplanetary space have been obtained.

I. INTRODUCTION

Solar wind protons and electrons can transfer their kinetic energy to interplanetary gas (H and He) through elastic collisions. The possible temperature increase of the interplanetary gas from proton heating (at 1 A.U.) has previously been calculated to range from several thousand degrees (Fahr, 1978) to a few hundred degrees only (Wallis, 1975 and Holzer, 1977). Obviously, the amount of the estimated heating depends on the collision cross sections for elastic scattering which have not been chosen consistently in the above work (see discussion in Section II). However, the elastic collision cross sections for scattering of protons by H and He have been measured (Houver et al., 1974 and Löster, 1971), as well as those for appropriate electron scattering (the heating of interstellar gas by solar electrons based on these cross sections have been estimated by Wu and Judge, 1978). These experimental cross sections appear to be more reliable than the theoretically estimated cross sections that have been used in the previous papers on proton heating. We propose to employ the measured laboratory elastic collision cross sections to derive the temperature distribution of hydrogen and helium in the interplanetary medium as a function of radial distance from the Sun, r, and the angle, θ, between the antiparallel direction of the interstellar wind and the radial position vector $\vec{r}$. The trajectories of the interstellar particles can be assumed to be Keplerian (in the gravitational field of the Sun), and the exchange of collision energy with the radially outward flowing solar wind will occur in all three directions.

Models of the interaction between the solar wind and the interstellar wind flowing into the interplanetary system are often based on a simple picture of both winds. The common model (Axford, 1972; Fahr, 1974, 1978; Fahr and Lay, 1974; Wallis, 1973, 1975; Holzer, 1977; Thomas, 1978; Wu and Judge, 1978, Kunc, 1980) is based on the assumption that the solar wind is

a two-component (protons and electrons) steady stream having spherical symmetry and moving radially outward (the stream speed is about 400 km/s). The physical properties of the wind are determined for the average activity of the Sun and the interstellar particle trajectories are regarded as Keplerian and independent of each other. The interstellar wind is considered as a mixture of mostly atomic hydrogen (90%) and atomic helium (10%) inflowing from far regions of the heliosphere where its temperature seems to be equal to about 10,000°K. The velocity of the interstellar wind at this far region is equal to about 20 km/s. Moreover, both winds have very low density; $n \cong 5\ cm^{-3}$ for the solar wind at 1 A.U. and $n \cong 0.1\ cm^{-3}$ for the interstellar wind at "infinity". The temperature measurements of Bertaux et al. (1976) seem to give direct evidence that the interplanetary hydrogen is hot in the vicinity of the Sun with the further conclusion that its "infinite" distance temperature is equal to about 10,000°K. The models based on the above assumptions have been successful in investigating the processes of energy exchange between the solar wind and the interstellar wind. The above assumptions allow one to use binary encounter theory (e.g. Gryzinski, 1965) for analysis of single scattering events and to then average the results over the dynamical properties of both winds. Such an approach is very convenient for devising and interpretating spacecraft based experiments measuring energetic properties of the interplanetary medium, because it gives detailed "directional" changes in dynamical properties of the particles. As mentioned previously, Section II discusses the differential elastic cross sections. Section III presents the general approach used in this work. Section IV summarizes the results of the present work for heating the interstellar wind by solar protons and, by analogy, data for heating by solar electrons. The last Section discusses the results for both solar proton and electron heating.

II. DIFFERENTIAL CROSS SECTIONS

As has been mentioned above, there is common agreement that the velocity of the solar wind is about 400 km/s for average solar activity. This velocity corresponds to proton energies of about 800 eV. The differential elastic scattering cross sections used by other investigators mentioned above (Wallis, 1973, 1975; Holzer, 1977 and Fahr, 1978) were based on theoretical estimates and were inconsistent with each other resulting in large discrepancies in the final results. The elastic cross section used by Wallis was independent of scattering angle χ and was equal to about $120a_o^2$. It was calculated from interaction potentials using the electronic potential data of Bates and Reid (1968). Using Wallis' formulas obtained from the Fokker-Planck approach, we have estimated that the atomic hydrogen temperature increase due to proton heating is equal to about 270°K (upwind) and 1300°K (downwind) at r = 1 A.U. Similar calculations for helium heating yield a temperature increase of about 250°K (upwind) and 1100°K (downwind).

The calculations of Holzer (1977) were based on elastic collision cross sections evaluated from the theoretical models of Dalgarno et al. (1958) and Wallis (1976). This cross section was evaluated as a function of scattered particle velocity greater than a certain "threshold" velocity w_o. The corresponding temperature increase was based on the mean velocity change $< w >$. For example, the value of the cross section for a velocity change greater than 1 km/s was equal to about $20a_o^2$, whereas the corresponding cross section for a velocity change greater than 4 km/s was equal to about $5a_o^2$ and exponentially decreasing with w_o. These numerical calculations performed for heating interstellar hydrogen gave a temperature increase of less than 300°K for r = 1 A.U.

The method of Dalgarno et al. (1958) was used in Fahr's (1978) calculations to determine the elastic cross section for collisions with impact parameters larger than the Bohr radius a_o. For smaller impact parameters the well-known Rutherford formula had been used. The cross sections, obtained in this

way, gave values four times larger than those of Holzer (1977). Using these cross sections and the kinetic approach he had estimated that the temperature increase of the inflowing gas, resulting from proton heating, should be 2600°K (upwind) and 7000°K (downwind) at r = 1 A.U.

As one can see from the above discussion all elastic cross sections of the previous works were estimated theoretically and they differ markedly from each other. Because the importance of the correct cross sections in such calculations is essential, the experimental differential elastic cross sections have been used in the present work. These experimental cross sections are based on the measurements of Houver et al. (1974) for the H^+ + H interaction at E_o = 700 eV and the measurements of Löster (1971) for the H^+ + He interaction at E_o = 800 eV. In the range of the scattering angle χ where the experimental data are not available ($\chi > 2°$ for H^+ + H scattering) the "common trajectory" method of Gaussorgues et al. (1975a, b) was used in the present calculations for determination of the differential cross section. This method gives cross sections that are in good agreement with existing measurements (for $\chi < 2°$) and it seems to be reliable for relatively larger angles as was discussed by Gaussorgues et al. (1975a, b). It should be emphasized that the values of the cross section for relatively larger values of the scattering angle χ are much smaller than those for $\chi < 2°$ where measured values are available.

It should also be mentioned that the angular distribution of azimuthal scattering angle ϕ has been assumed to be isotropic thoughout our calculations, which is well-justified for our physical model.

III. THE METHOD

The geometry of a three-dimensional elastic collision between a solar proton and an interstellar atom is shown in Figure 1. The energy increase of the neutral

atom during the collision can be obtained from general binary collision consideration. After obvious transformations the components of the energy increase are as follows:

$$\Delta E_x = E\,(\cos\alpha\,\cos\theta - \sin\alpha\,\cos\phi\,\sin\theta)^2 \tag{1}$$

$$\Delta E_y = E\,(\cos\alpha\,\sin\theta + \sin\alpha\,\cos\phi\,\cos\theta)^2 \tag{2}$$

$$\Delta E_x = E\,\sin^2\alpha\,\sin^2\phi \tag{3}$$

with

$$E = 2\left(\frac{m^2 M}{m+M}\right)^2 v_o^2$$

Further geometrical considerations yield the following relationship between the angle α and the angle χ:

$$\alpha = \frac{\pi}{2} - 1/2\,[\,\chi + \sin^{-1}(\frac{m}{M}\sin\chi)\,] \tag{4}$$

The energy increase of an inflowing neutral in the ith direction (x, y, or z) during a time period dt is $\beta_i dt$. The energy transfer rate β_i can be obtained from the following general expression:

$$\beta_i = \frac{\partial E_i}{\partial t} = \int \frac{d\sigma}{d\Omega}\,F_p\,\Delta E_i\,d\Omega\,, \tag{5}$$

where $\frac{d\sigma}{d\Omega}$ is the differential cross section for elastic scattering of an interstellar neutral by a solar proton. F_p is the solar proton flux and $d\Omega$ is the element of solid angle oriented in the spherical coordinate system; $d\Omega = \sin\chi\,d\chi\,d\phi$. Introducing the expressions (1) - (3) into equation (5) one gets:

$$\beta_i(r,\theta) = \lambda \int_0^{2\pi}\int_0^{\pi} F_p(r,\theta)\,E_o(r,\theta)\,\frac{\partial(\chi,\phi)}{\partial(\theta,\phi)}\,g_i(\theta,\chi,\phi)\,d\chi\,d\phi, \tag{6}$$

where

$$\lambda = \frac{4m}{M\,(1+\frac{m}{M})^2},$$

and $E_o = mv_o^2/2$ is the solar proton energy. The functions $g_i\,(\theta, \chi, \phi)$ appearing in relations (6) have the following forms:

$$g_x(\theta, \chi, \phi) = \cos^2\theta \sin\chi \cos^4[\alpha(\chi)] + $$

$$+ 1/4 \sin^2\theta \sin\chi \cos^2\phi \sin^2[2\alpha(\chi)], \qquad (7)$$

$$g_y(\theta, \chi, \phi) = \sin^2\theta \sin\chi \cos^2[\alpha(\chi)] + $$

$$+ 1/4 \cos^2\theta \sin\chi \cos^2\phi \sin^2[2\alpha(\chi)] \qquad (8)$$

$$g_z(\theta, \chi, \phi) = 1/4 \sin\chi \sin^2\phi \sin^2[2\alpha(\chi)], \qquad (9)$$

where the relation $\alpha(\chi)$ is given in Equation (4).

The energy increase of an interstellar atom moving in the ith direction in time $\tau = t - t_\infty$ is (Kunc 1980):

$$\Delta E_i = \int_{t_\infty}^{t} \beta_i dt = \int_0^{\ell(r)} \beta_i \frac{d\ell}{V_o(\ell)}, \qquad (10)$$

with

$$\frac{d\ell}{V_o(\ell)} = \begin{cases} -\frac{1}{V_o^\infty}\left(1 + \frac{2}{C \cdot r}\right)^{-1/2} dr & \text{for } \delta = 0 \\ \frac{r^2}{V_o^\infty \delta} d\theta', & \text{for } \delta \neq 0 \end{cases} \qquad (11)$$

where

$$C = \frac{(V_o^\infty)^2}{(1-\mu)GM_s}. \qquad (12)$$

In the above $t-t_\infty$ is the interval of time required for a neutral to traverse the path ℓ from infinity up to a point (r, θ). V_o^∞ is the interstellar wind velocity at "infinity", let us say at the boundary of the heliosphere, and δ is the atom trajectory impact parameter. The quantities G, M_s and μ are the universal gravitational constant, the mass of the Sun, and the ratio of the radiation force to the gravitational force of the Sun, respectively.

It should be emphasized that two different trajectories with two different impact parameters can meet at a local spatial point defined by r and θ (Axford, 1972). The appropriate impact parameters can be found from the following relations:

$$\delta_{1,2} = 1/2 \left\{ r\sin\theta \pm [r^2\sin^2\theta + 4r(1-\cos\theta)/C]^{1/2} \right\} \qquad (13)$$

The particles of these two trajectories contribute to the neutral density at point (r, θ) by different amounts. The ratio of the density of neutrals can be found from the following expression:

$$\frac{N_2}{N_1} = \left(\frac{\delta_2}{\delta_1}\right)^2 \exp\left[-\frac{\beta_{ion} \cdot r_e^2}{V_o^\infty} \left(\frac{2\pi-\theta}{|\delta_2|} - \frac{\theta}{|\delta_1|}\right)\right], \qquad (14)$$

where β_{ion} is the ionization rate.

Having the ratio (14) one can get the total energy increase of the interstellar atoms in ith direction

$$\Delta E_i = \left(1 + \frac{N_2}{N_1}\right)^{-1} \left[\int_0^{\ell_1} \beta_i \frac{d\ell}{V_o(\ell)} + \frac{N_2}{N_1} \int_0^{\ell_2} \beta_i \frac{d\ell}{V_o(\ell)} \right]. \qquad (15)$$

Equation (15) can be expressed in terms of θ using equations (11) and (13). The appropriate upper limits of the integrals in equation (15) are then θ and $2\pi-\theta$, respectively. It should be noted that during integration in Equation (15), $\delta = \delta_1$ when $\phi \leq \pi$ and $\delta = \delta_2$ when $\theta > \pi$.

Let us now discuss the notion of "temperature" that is used in the present work. Because of the lack of equilibrium between translational degrees of freedom of a heated atom (in the case of heating by protons this anisotropy is a strong one which was suggested by Holzer (1977) and has been confirmed by the present calculations) the concept of temperature should be used with caution and the terms "effective temperature" will be used instead. First of all we will define the dependence between the effective temperature increase of the heated atom and the appropriate translational energy increase. This is necessary for any theoretical or experimental data analysis and interpretation. For the case of heating by electrons the total effective temperature increase is here defined as

$$\Delta T = \frac{2}{3k} \Delta E_{tot} = \frac{2}{3k} \Delta E_o, \qquad (16)$$

and the "directional" effective temperature increase in the ith direction can be given as

$$\Delta T_i = \frac{2}{k} \Delta E_o \tag{17}$$

For the case of heating by solar protons the total effective temperature increase is defined as:

$$\Delta T = \frac{2}{3k} \sum_{i=1}^{3} \Delta E_i , \tag{18}$$

and if one defines the appropriate "directional" effective temperature as

$$\Delta T_i = \frac{2}{3k} \Delta E_i \tag{19}$$

then

$$\Delta T = \sum_{i=1}^{3} \Delta T_i \tag{20}$$

IV. EFFECTIVE TEMPERATURE DISTRIBUTIONS

The spatial distributions of the effective temperature increase of interstellar gas within the interplanetary system due to proton heating are shown in Figures 2-9. The following assumptions of characteristic astrophysical quantities have been used in the calculations:

- as mentioned in the first section the spherically symmetric steady stream of protons and electrons has been taken as a model of the solar wind. In such a model the solar proton flux $Fp(r) = F_o r^{-2}$, where F_o is the flux at $r = 1$ A.U. In our calculations a value of F_o (average over a solar cycle) equal to $2.5 \cdot 10^8$ $cm^{-2}sec^{-1}$ has been assumed (Thomas 1978).
- the ratio of the radiation force to the gravitational force μ has been taken as equal to 0.7 for hydrogen and zero for helium (Emerich and Cazes 1978). It should be mentioned that these values were obtained on the basis of an assumption that the radiation force is spherically symmetric and varies as r^{-2}, similar to the gravitional force;
- the interstellar wind velocity at "infinity" is equal to 20 km/s.

- the ionization rate β_{ion} has been taken as equal to $6 \cdot 10^{-7}$ and $6 \cdot 10^{-8}$ for the interaction of solar protons with hydrogen and helium, respectively. These values result from the recently investigated models (see review of Thomas 1978).

The results for the total effective temperature increase of interstellar gas due to electron heating have also been updated using the method of Wu and Judge (1978), but with a value of $\mu = 0.7$. The numerical results for electron heating of hydrogen and helium are shown in Figures 10 and 11, respectively.

V. CONCLUSIONS

The results presented here show clearly that the heating of the interstellar wind flowing toward the Sun, due to the solar wind, is significant within the interplanetary system. As can be seem from Figure 5 and 9, the total effective temperature increase in the vicinity of the Earth is equal to about 400°K (upwind) and 1600°K (downwind) for hydrogen heating by solar protons and about 500°K (upwind) and 1400°K (downwind) for helium heating by solar protons. For comparison, the appropriate values of effective temperature increase of interstellar gas as a result of heating by solar wind protons are summarized below as given by other authors:

- the calculations of Wallis (1973, 1975) gave 270°K (upwind) and 1300°K (downwind) for hydrogen heating and 250° (upwind) and 1100° (downwind) for helium heating.
- the values obtained by Fahr (1978) gave 2600°K (upwind) and 7000°K (downwind) for hydrogen heating.
- the values obtained by Holzer (1977) for heating of the interstellar hydrogen are close to those of Wallis.

It should be emphasized that the present results agree in order of magnitude with the results of Wallis and Holzer and strongly disagree with those of Fahr. As mentioned earlier, only the present calculations have used the experimental differential cross sections for elastic collisions while others used theoretical

estimates which differ significantly from each other. Also, different general approaches were used by the other authors to estimate the temperature increase. Therefore, it is difficult to point to the main source of discrepancy between particular authors without a special, separate analysis devoted to this problem. However, it seems that one of the major sources of the discrepancy (except perhaps doubtful reliability of the theoretical estimates of the cross sections) results from the fact that Fahr has used the general Boltzmann Kinetic Equation in a casual way. Such an approach requires a well-defined "phase fluid" in the physical description of the problem. This requirement may not be fulfilled under conditions existing during the interaction of the solar wind with the interstellar wind. In other words, the local fluctuations of the density of phase points may be larger than their average local values. In such a case the casual kinetic approach should be markedly modified, and such modification can give a significant difference in the final results.

Another important conclusion that can be obtained from the results presented here is that the heating of the interstellar atoms by solar protons takes place primarily in the directions perpendicular to the atoms trajectories and this is true for both the heating of hydrogen and helium.

In addition, it should be noted that the temperature increase for atomic hydrogen heating by solar protons is comparable to the helium heating throughout most of the interplanetary space. Thus, heating of the interstellar wind by solar protons does not cause significant differences in energy equilibration between both major components of the interstellar wind. For a full description of the problem, the results of heating of interstellar hydrogen and helium by solar electrons are shown in Figures 10 and 11, respectively. These results have been obtained with the characteristic astrophysical quantities specified above. The temperature increase of hydrogen and helium heated by solar electrons is equal to 450°K (upwind) and 1700°K (downwind) for hydrogen and 80°K (upwind) and 200°K (downwind) for helium, at the orbit of Earth. These values lead to the interesting

result that the temperature increase of interstellar hydrogen resulting from heating by solar protons is comparable to the temperature increase resulting from heating by solar electrons. This results from dynamical properties of the interparticle collisions, differential cross sections and energetic properties of electron and proton components of the solar wind. It should also be added that there is, however, remarkable difference in the spatial distributions of the scattered particles; in the case of electron heating the spatial distribution of the interstellar atoms is close to isotropic, whereas in the case of proton heating the spatial distribution of the scattered atoms is strongly anisotropic. In the latter case, as was discussed previously, the atoms are scattered mostly in directions perpendicular to their original trajectories. This fact must be taken into account in further development of the problem discussed in the present work. Also, the heating of the interstellar hydrogen should have a significant effect on dissipative energy processes within the solar wind during its radial propagation outward. Both the heating by electrons and by protons has been calculated on the basis of a model of the solar wind moving with a constant speed. Because of the effects of growing entropy, the energy associated with the wind velocity is transformed into its thermal energy, changing the the velocity of the wind. However, these effects become significant only for large radial distances where the heating is much smaller than at distances close to the Sun.

It should also be remembered that some temperature distributions shown in Figures 2-11 have been obtained for radial distances as small as 0.5A.U. However, in reality, some of the atoms will not reach the interplanetary regions close to the Sun because of the increasing probability (with decreasing radial distance from the Sun) of their being destroyed (Kunc 1980) and also because of the deflection of the interstellar atoms from their original trajectories due to radiation pressure (Thomas 1978).

It should be mentioned that the approach used in the present work is very convenient for interpreting spacecraft-based experiments measuring the effective temperature of the interplanetary medium. Such measurements should be taken in a plane containing the Sun and the axis-direction of the interstellar wind, but at various rotational positions. Because of the very low density of the interplanetary neutrals such a "directional" approach, like that presented here, seems to be convenient from the experimental point of view and the subsequent interpretation of the measurements.

VI. ACKNOWLEDGEMENTS

This work was supported by NASA contract NSG2-146.

REFERENCES

Axford, W. I., 1972, in Solar Wind, ed. C. P. Sonett, P. J. Coleman, and J. M. Wilcox (NASA SP-308), p. 609.

Bates, D. R. and Reid, R. H. G., 1968, Advan. At. Mol. Phys., 4, 13.

Bertaux, J. L., Blamont, J. E., Tabarie, N., Kurt, V. G., Bourgin, M. C., Smirnov, A. S., and Dementeva, N. N., 1976, Astr. Ap., 46, 19.

Dalgarno, A., McDowell, M. R. C. and Williams, A., 1958, Phil. Trans. Roy. Soc. London, 250, 411.

Emerich, C. and Cazes, S., 1978, Astron. Astrophys. 69, 13.

Fahr, J., 1974, Space Sci. Rev., 15, 483.

Fahr, J., 1978, Astr. Ap., 66, 103.

Fahr, J. and Lay, G., 1974, Space Res., 14, 567.

Gaussorgues, C., Le Sech, C., Masnou-Seeuws, F., McCarroll, R. and Riera, A., 1975a, J. Phys. B: Atom. Molec. Phys. 8, 239.

Gaussorgues, C., Le Sech, C., Masnou-Seeuws, F., McCarroll, R. and Riera, A., 1975b, J. Phys. B: Atom. Molec. Phys. 8, 253.

Gryzinski, M., 1965, Phys. Rev., 138A, 305.

Holzer, T. E., 1977, Rev. Geophys. Space Phys., 15, 467.

Houver, J. C., Fayeton, J. and Barat, M., 1974, J. Phys. B: Atom. Molec. Phys., 7, 1358.

Kunc, J. A., 1980, Planet. Space Sci., 28, 815.

Löster, W., 1971, Proc. of 7th ICPEAC, 274.

Thomas, G. E., 1978, Ann. Rev. Earth Planet. Sci., 6, 173.

Wallis, M. K., 1973, Ap. Space Sci., 20, 3.

Wallis, M. K., 1975, Planet. Space Sci., 23, 419.

Wallis, M. K., 1976, Celestial Mech., 13, 65.

Wu, F. M. and Judge, D. L., 1978, Astroph. J., 225, 1045.

FIGURE CAPTIONS

Figure 1. Dynamics of the elastic collision between a solar proton and an interstellar wind atom.

$\vec{v}_o$ and $\vec{v}$ - proton velocities before and after elastic collision, respectively.

m - the proton mass

$\vec{V}$ - atom velocity after collision

M - the atomic mass

r - radial direction

θ - the angle between r and the upwind direction

α - the angle between r and velocity of the atom after collision

χ - the angle between r and velocity of the proton after collision

ϕ - azimuthal scattering angle

Figure 2. Effective temperature increase contours (x-direction component) for heating the neutral interstellar hydrogen by solar wind protons with μ=0.7 and V_o^∞=20 km/s.
r is the radial distance from the Sun in A.U., θ is the angle between r and the upwind direction. The upwind direction is along the positive x-axis (θ=0°).

Figure 3. Effective temperature increase contours (y-direction component) for heating neutral interstellar hydrogen by solar wind protons with μ=0.7 and V_o^∞=20 km/s. Meaning of the symbols is the same as in Figure 2.

Figure 4. Total effective temperature increase contours (z-direction component) for heating neutral interstellar hydrogen by solar wind protons with μ=0.7 and V_o^∞=20 km/s. Meaning of the symbols is the same as in Figure 2.

Figure 5. Total effective temperature increase contours for heating neutral interstellar hydrogen by solar wind protons with μ=0.7 and V_o^∞=20 km/s. Meaning of the symbols is the same as in Figure 2.

Figure 6. Effective temperature increase contours (x-direction component) for heating neutral interstellar helium by solar wind protons with μ=o and V_o^∞=20 km/s. Meaning of the symbols is the same as in Figure 2.

Figure 7. Effective temperature increase contours (y-direction component) for heating neutral interstellar helium by solar wind protons with μ=o and V_o^∞=20 km/s. Meaning of the symbols is the same as in Figure 2.

Figure 8. Effective temperature increase contours (z-direction component) for heating neutral interstellar helium by solar wind protons with μ=o and V_o^∞=20 km/s. Meaning of the symbols is the same as in Figure 2.

Figure 9. Total effective temperature increase contours for heating neutral interstellar helium by solar wind protons with μ=o and V_o^∞=20 km/s. Meaning of the symbols is the same as in Figure 2.

Figure 10. Total effective temperature increase contours for heating neutral interstellar hydrogen by solar electrons with μ=0.7 and V_o^{∞}=20 km/s.

Figure 11. Total effective temperature increase contours for heating neutral interstellar helium by solar electrons with μ=o and V_o^{∞}=20 km/s.

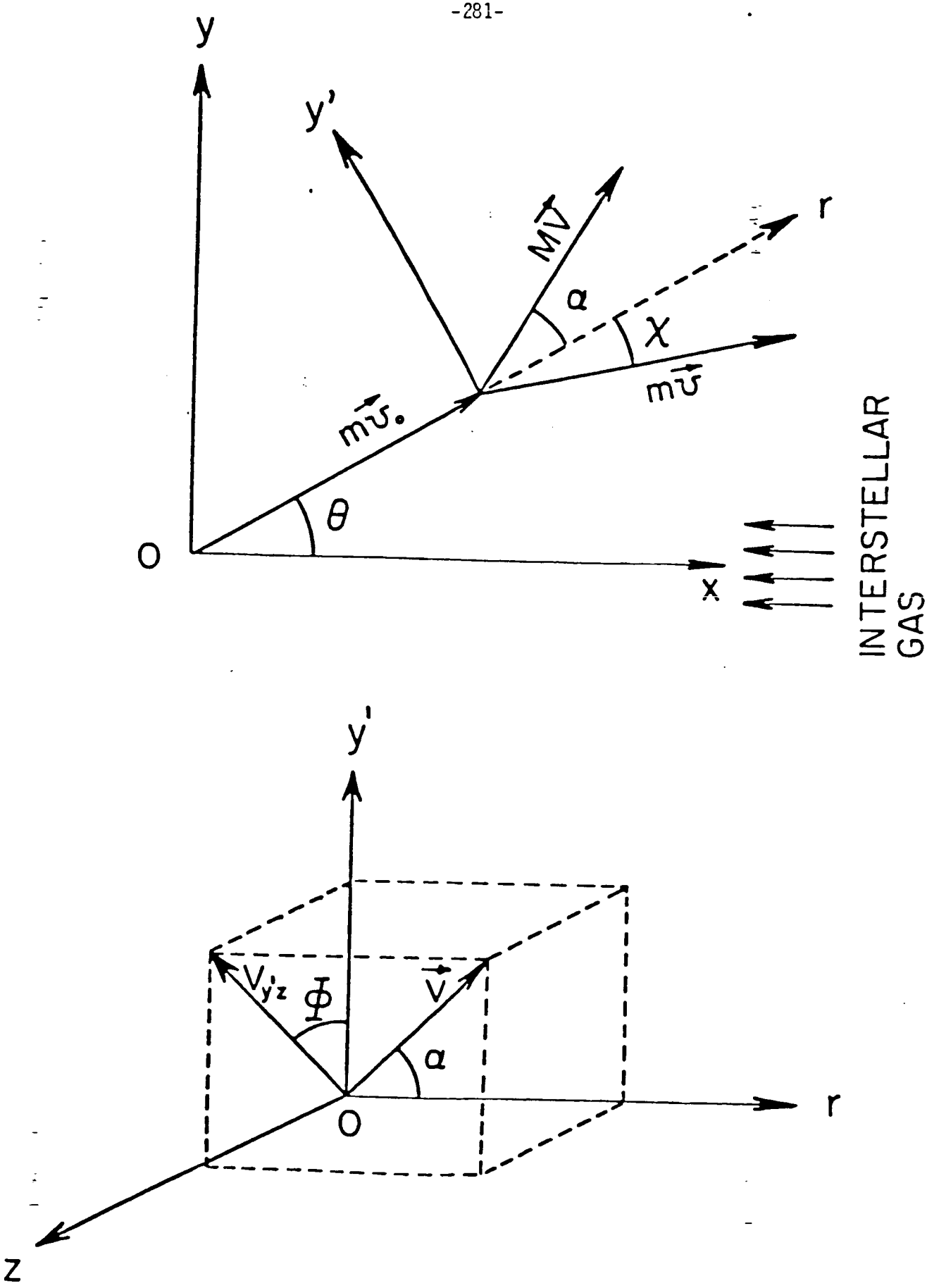
y
y'
$M\vec{V}$
r
α
χ
$m\vec{v}$
$m\vec{v}_0$
θ
O
x
INTERSTELLAR GAS
y'
$V_{y'z}$
Φ
$\vec{V}$
α
O
r
z

FIG. 1

~~FIG 1~~

FIG. 2

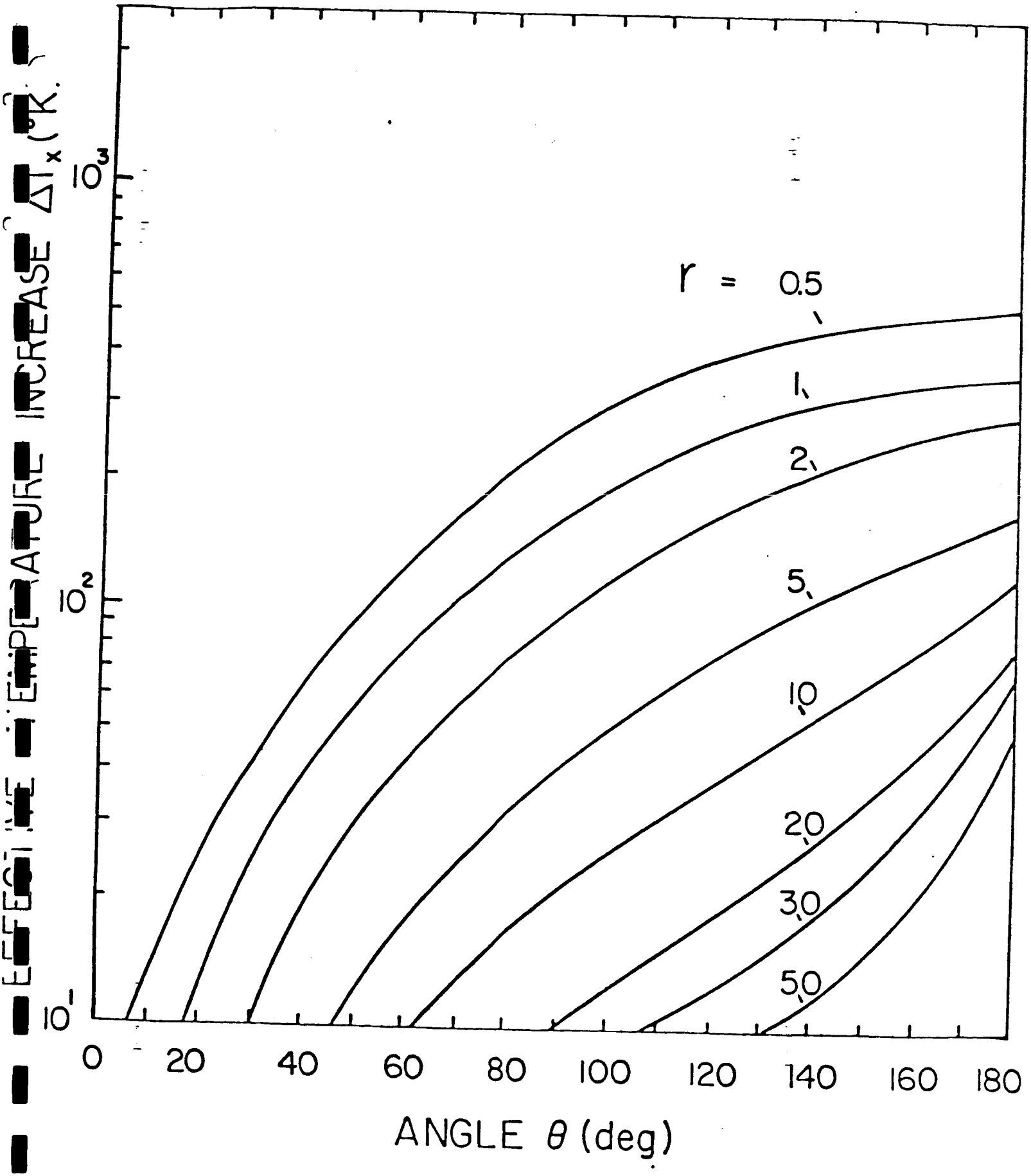
EFFECTIVE TEMPERATURE INCREASE ΔT_x (°K)
10^3
10^2
10^1
r = 0.5
1
2
5
10
20
30
50
0
20
40
60
80
100
120
140
160
180
ANGLE θ (deg)

FIG. 3

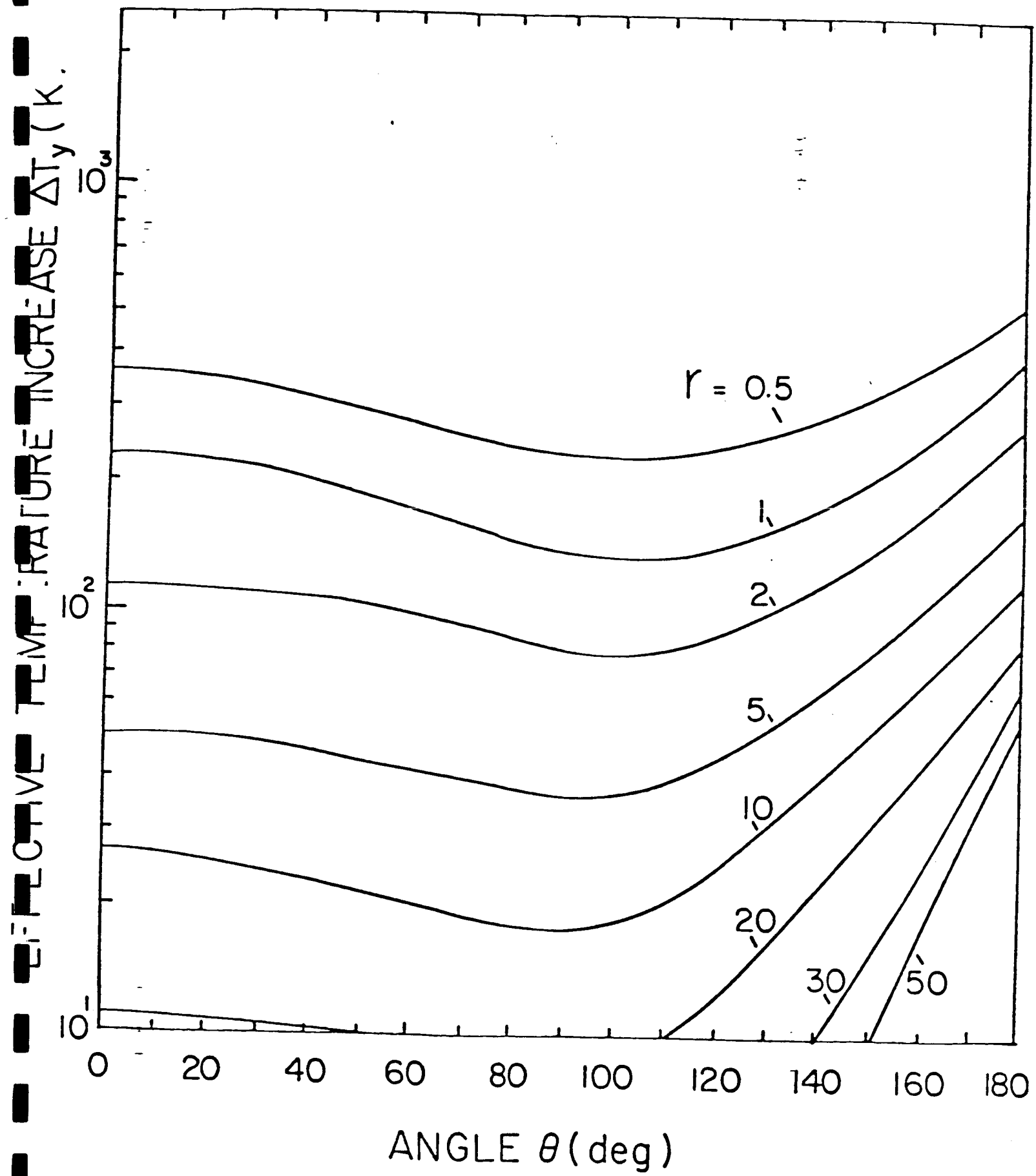
EFFECTIVE TEMPERATURE INCREASE ΔT_y (K.)
10^3
10^2
10^1
r = 0.5
1
2
5
10
20
30
50
0
20
40
60
80
100
120
140
160
180
ANGLE θ (deg)

FIG. 4

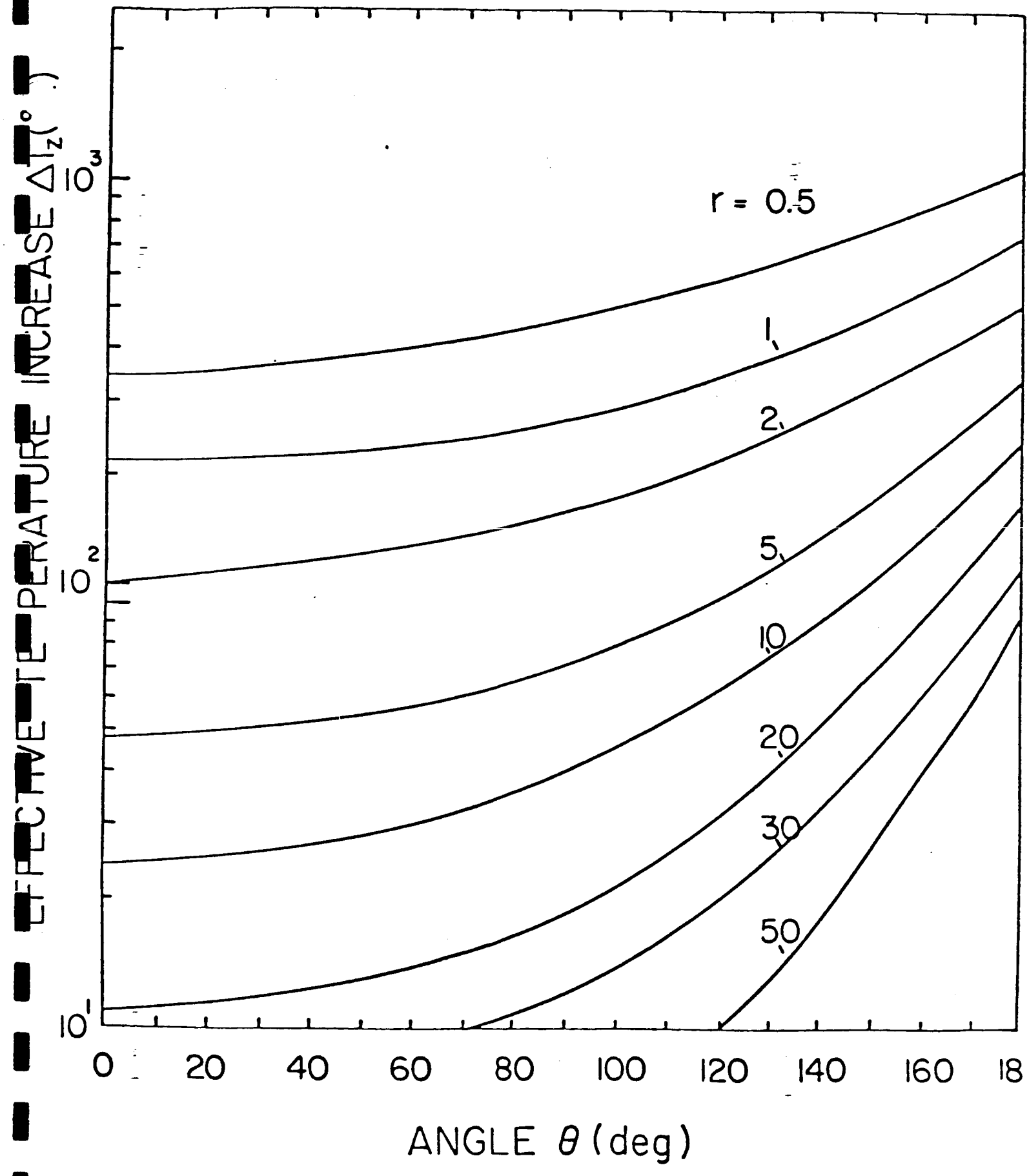
EFFECTIVE TEMPERATURE INCREASE ΔT_z (°)
10^3
10^2
10^1
r = 0.5
1
2
5
10
20
30
50
0
20
40
60
80
100
120
140
160
18
ANGLE θ (deg)

FIG. 5

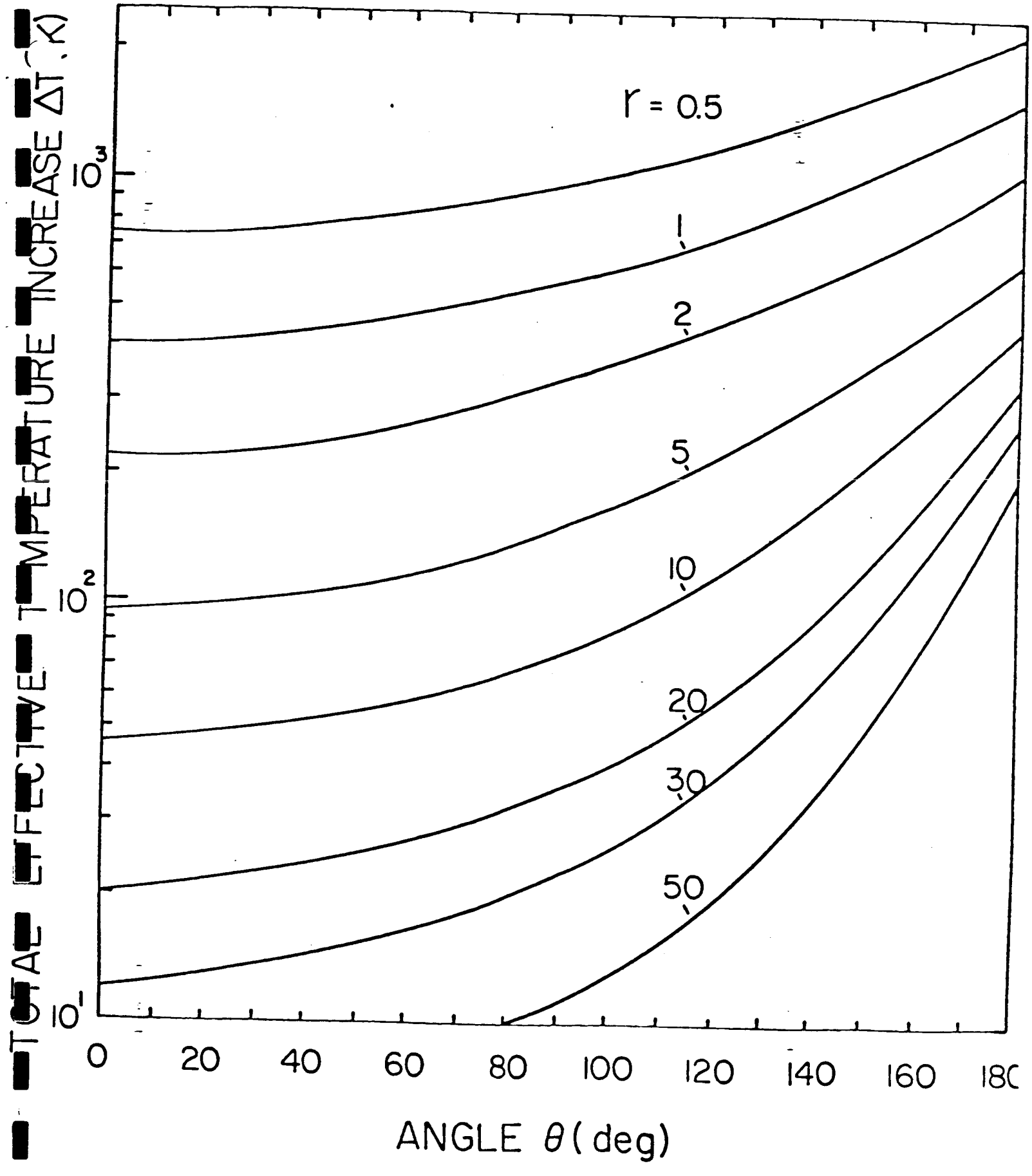
TOTAL EFFECTIVE TEMPERATURE INCREASE ΔT (K)
r = 0.5
1
2
5
10
20
30
50
10^3
10^2
10^1
0
20
40
60
80
100
120
140
160
180
ANGLE θ (deg)

FIG.6

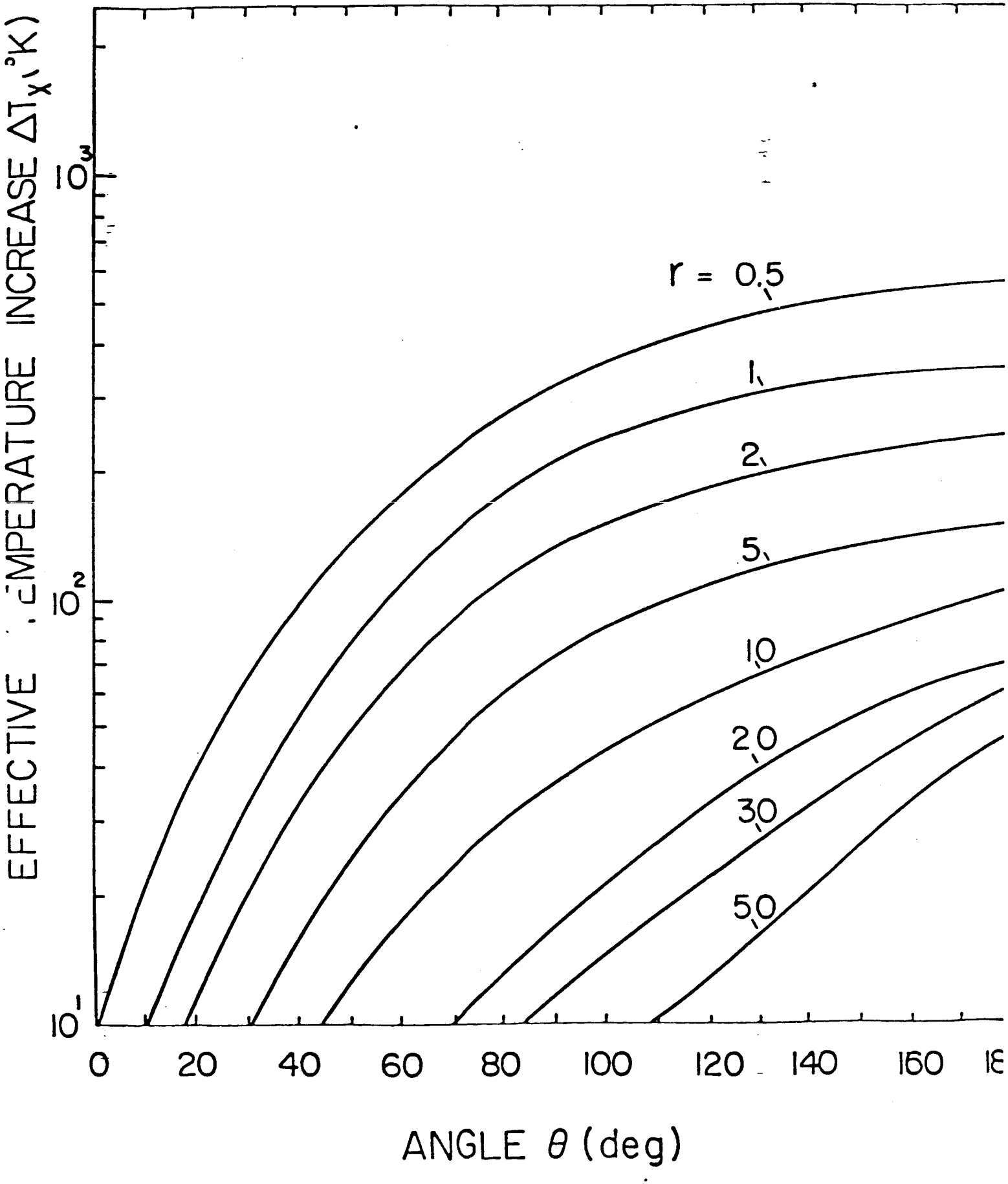
EFFECTIVE TEMPERATURE INCREASE ΔT_χ (°K)
10^3
10^2
10^1
r = 0.5
1
2
5
10
20
30
50
0
20
40
60
80
100
120
140
160
ANGLE θ (deg)

FIG. 7

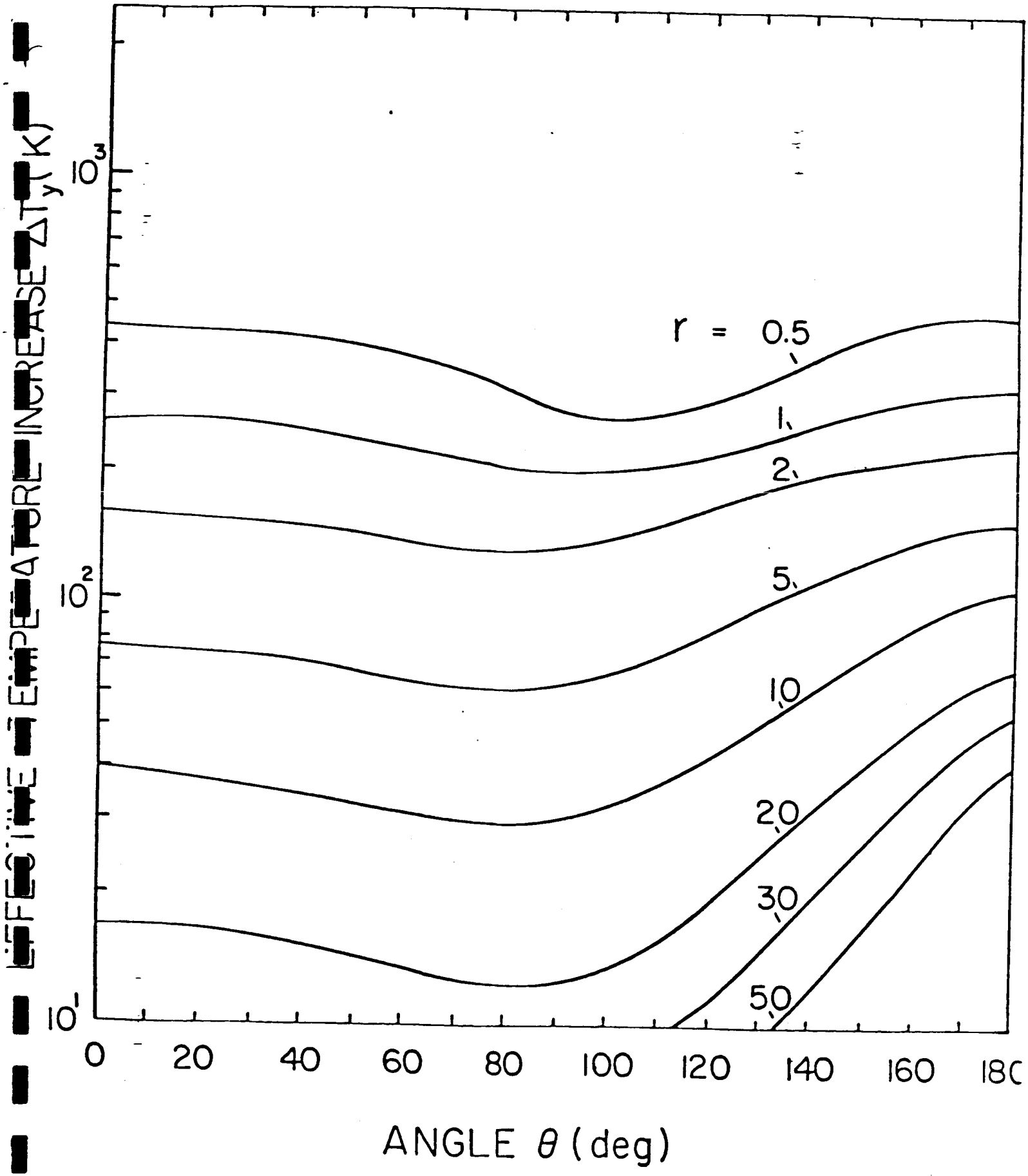
EFFECTIVE TEMPERATURE INCREASE ΔT_y (K)
10^3
10^2
10^1
r = 0.5
1
2
5
10
20
30
50
0
20
40
60
80
100
120
140
160
180
ANGLE θ (deg)

FIG. 8

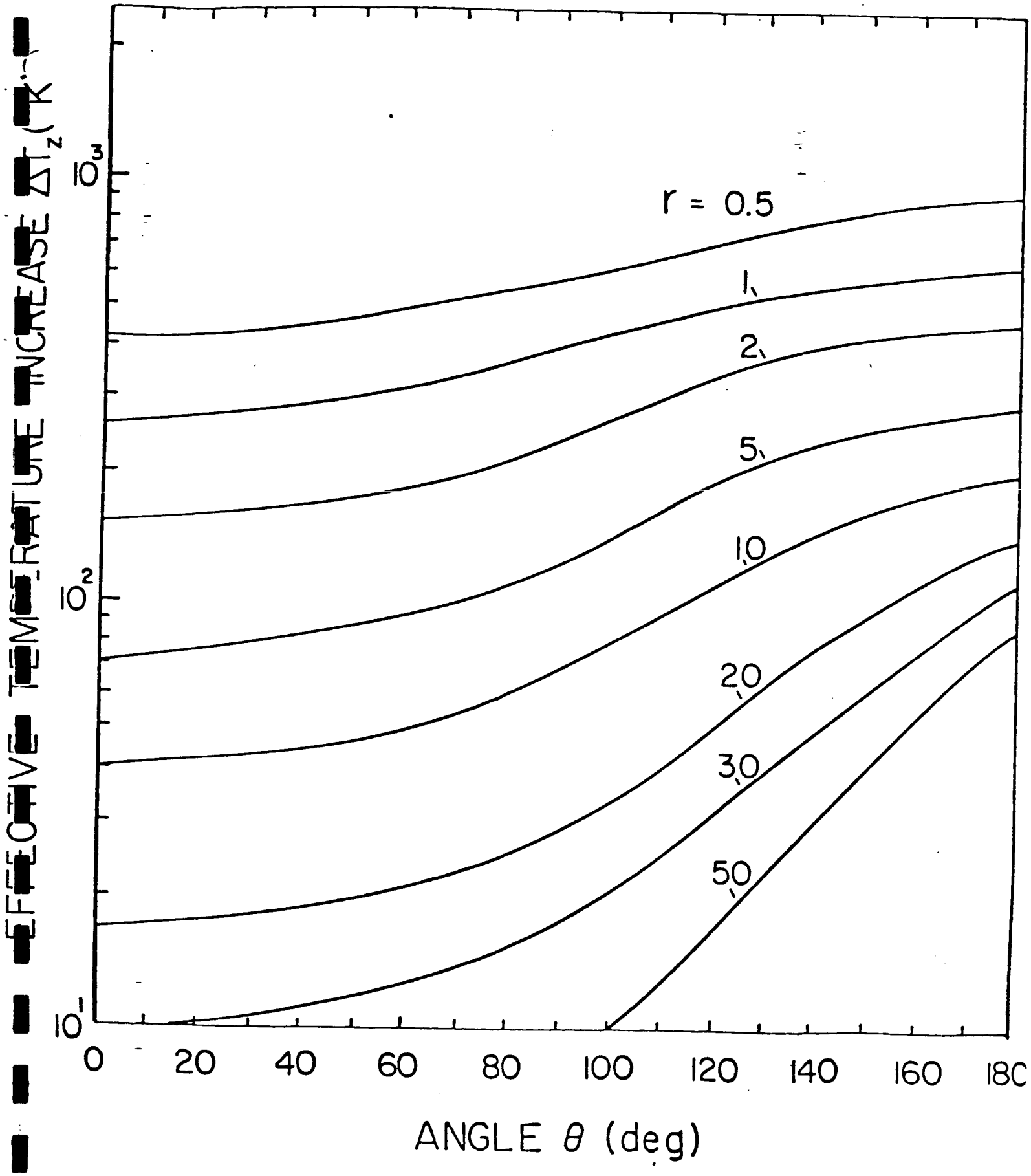
EFFECTIVE TEMPERATURE INCREASE ΔT_z (K)
10^3
10^2
10^1
r = 0.5
1
2
5
10
20
30
50
0
20
40
60
80
100
120
140
160
180
ANGLE θ (deg)

FIG. 9

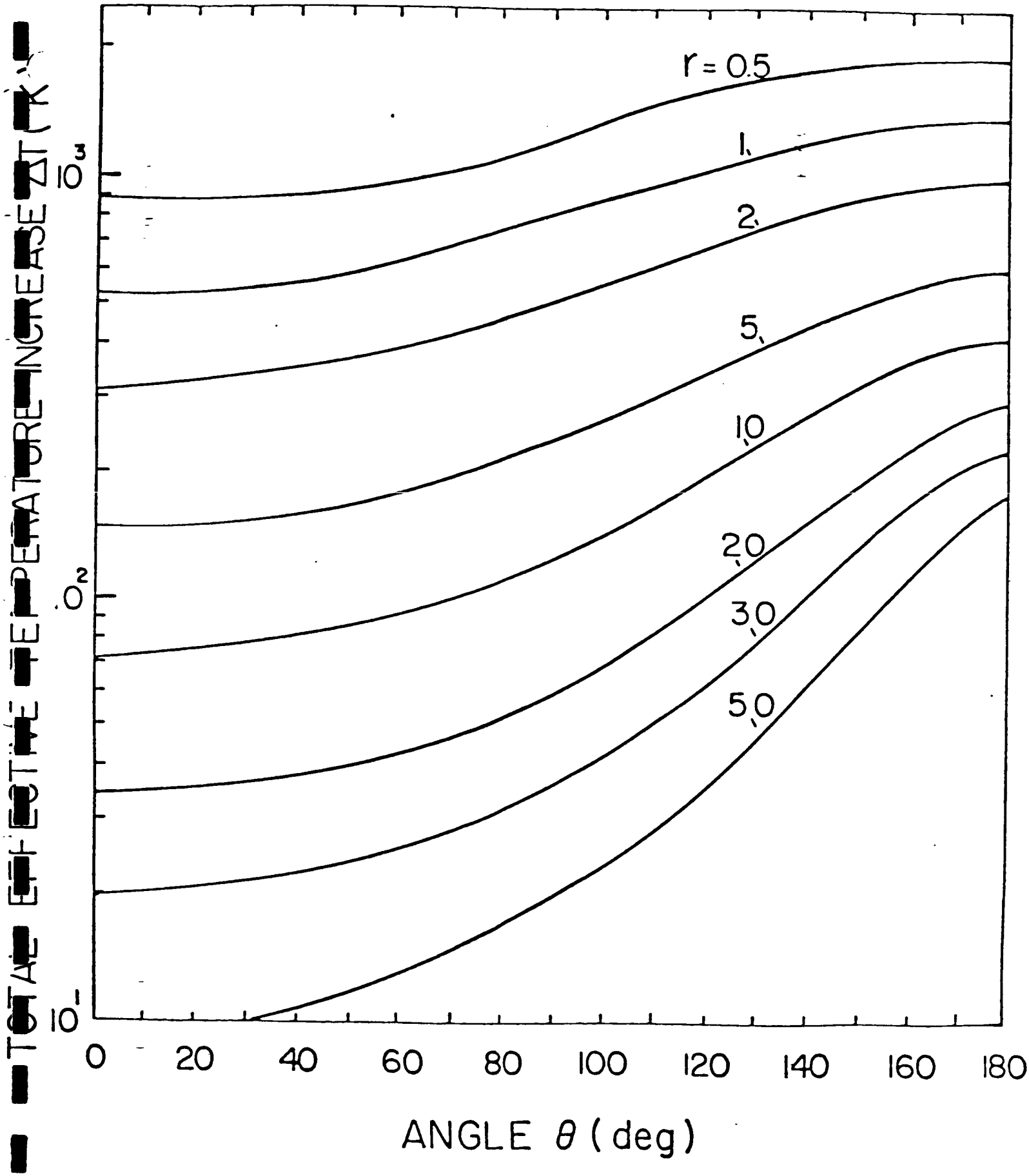
r = 0.5
1.
2.
5.
10
20
30
50
10^3
10^2
10^1
0
20
40
60
80
100
120
140
160
180
ANGLE θ (deg)
TOTAL EFFECTIVE TEMPERATURE INCREASE ΔT (K)

FIG. 10

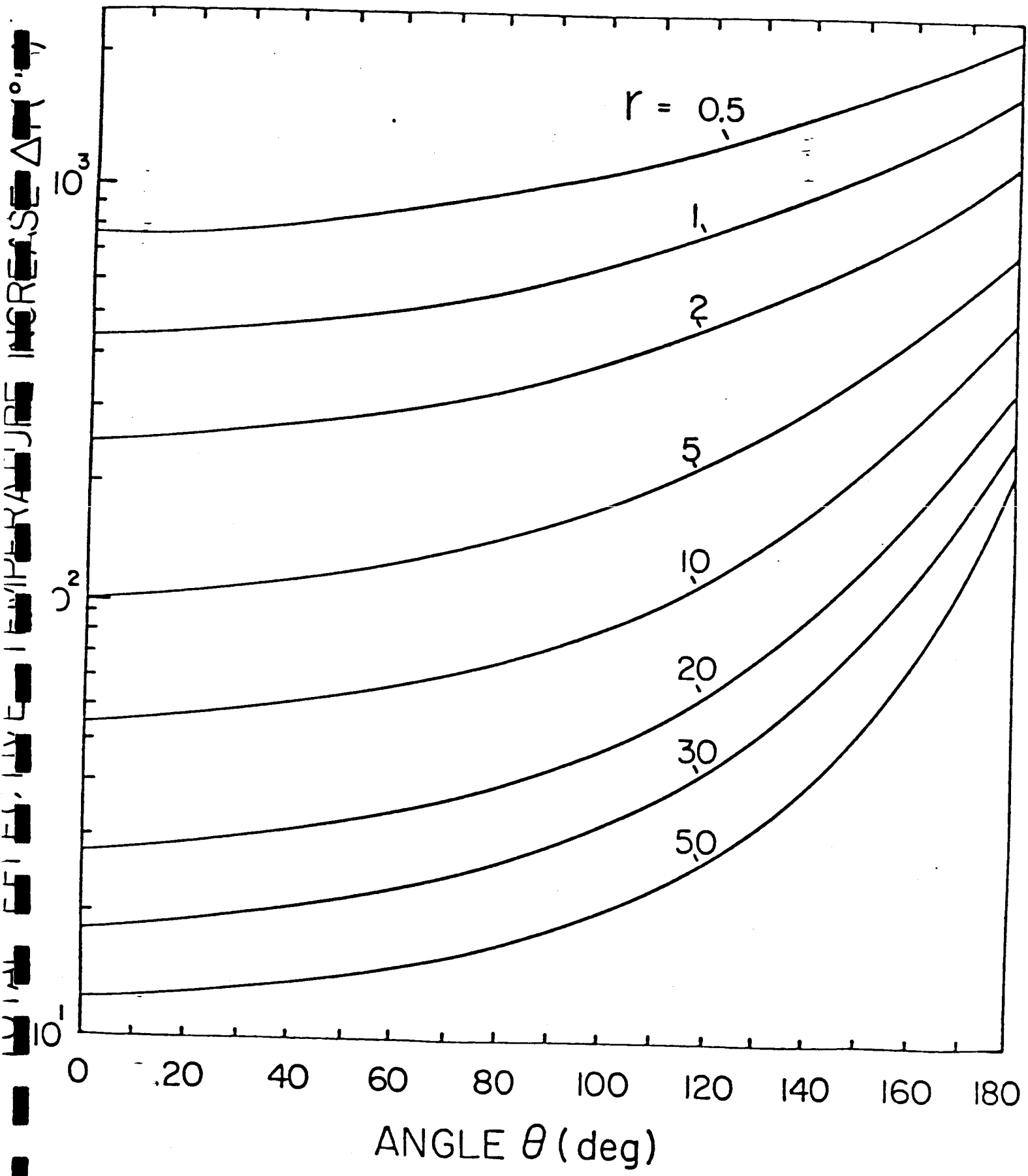
r = 0.5
1
2
5
10
20
30
50
10^3
10^2
10^1
0
20
40
60
80
100
120
140
160
180
ANGLE θ (deg)

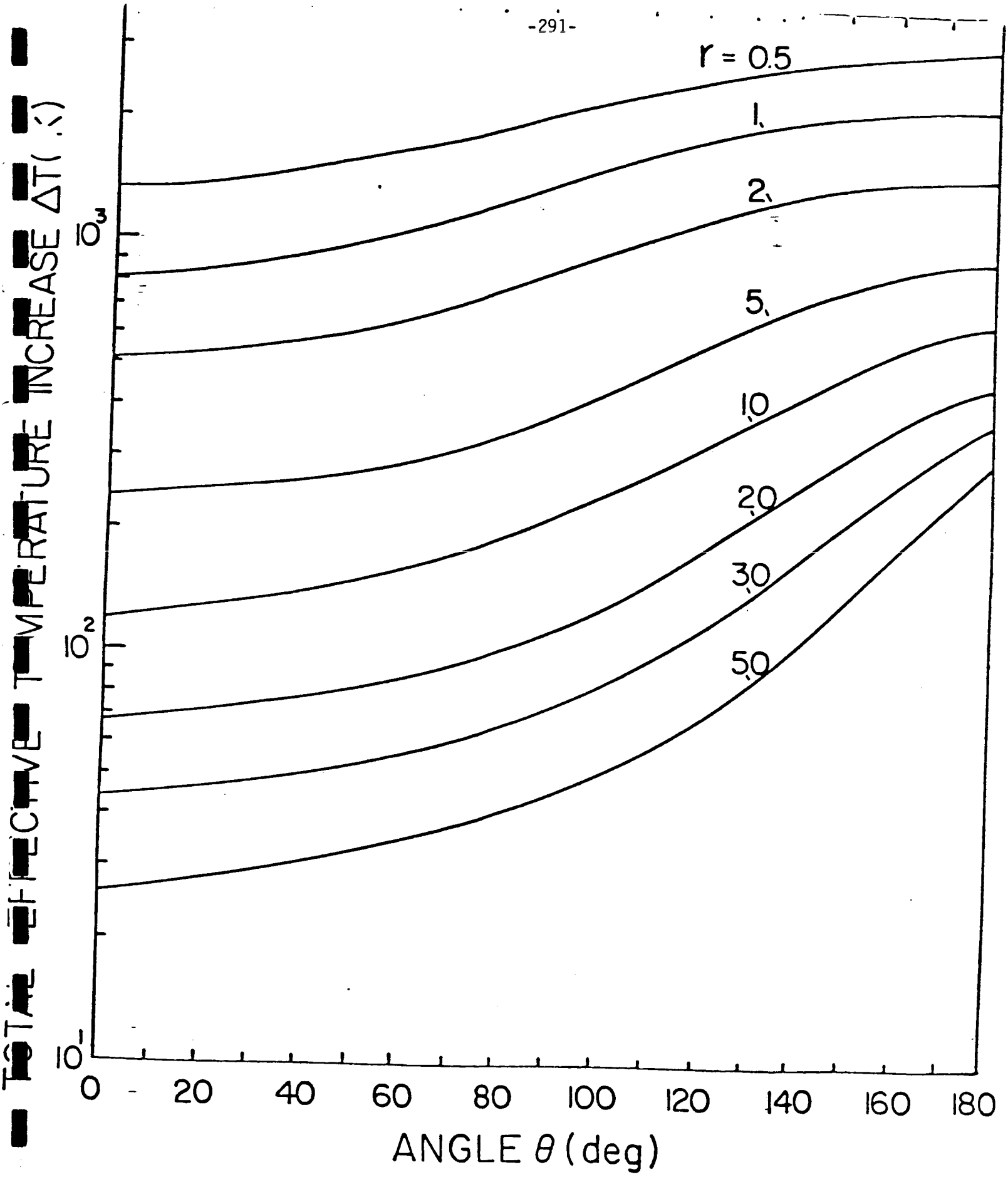
r = 0.5
1.
2.
5.
10
20
30
50
10^3
10^2
10^1
0
20
40
60
80
100
120
140
160
180
ANGLE θ (deg)
TOTAL EFFECTIVE TEMPERATURE INCREASE ΔT(°)

FIG. 11

"RADIAL ENERGY DISTRIBUTION OF THE LOW ENERGY PROTONS IN IO'S ATMOSPHERE"

I. INTRODUCTION

The presence of protons in the vicinity of Io's oribt was detected by the Pioneer 10 and 11 (Frank et al. 1975) and the Voyager 1 and 2 spacecraft (Krigimis et al. 1981). The measured energy spectra ranged from a few kilo-electron volts to few million electron volts with indications that the majority of the protons have energies below 500 keV. These protons can penetrate the direct environment of Io (hereafter called "atmosphere") that ranges from the satellite surface up to about 600 - 700 km in altitude. This "atmosphere" seems to contain a cloud of neutrals such as SO_2, SO, O_2, S, O and perhaps some others and also electrons and different ions (see discussion in the next paragraph). Most of high energy protons can penetrate the atmosphere deeply and get to the satellite surface. The low energy protons (< 100 keV) can be slowed down remarkably by the atmosphere constituents and some of them may not reach the surface whereas the energy of others can decrease significantly. The knowledge of the radial distribution of the protons energy in Io's atmosphere is essential for two processes that may be relatively efficient in producing neutral hydrogen within the atmosphere; 1) interaction of the protons with the surface containing eventually hydrogen related substances (Trainor et al. 1973 and Matson et al. 1975), and 2) production of atomic hydrogen thanks to recombination of the protons and the electrons of the atmosphere (Carlson and Judge, 1974b and Frank et al. 1975). The latter possibility was also suggested by the existence of some strong analogies between an Io torus and a Titan torus (McDonough and Brice, 1973; McDonough, 1975). In both cases mentioned above the radial energy distributions (and therefore density) of the

protons in the atmosphere are essential. Therefore, in further development of the problem we will analyze efficiency of production of neutrals through both the above processes and the results will be published elsewhere. In the present work we will concentrate on the slowing down of the low energy protons in Io's atmosphere. Then, we will determine (assuming the densities of the constituents of the atmosphere) the radial energy distributions and ranges of the low energy protons of initial energie's (at the top of the atmosphere) being within the interval 5 - 100 keV. This range of the initial energie's seems to be especially important for the possible production of the atomic hydrogen through recombination with electrons. The protons with such initial energies decrease their energy even more during their way toward the surface. Only the existence of protons of such energy within the atmosphere together with a relatively large proton and electron populations can make the recombination efficiency relatively significant and larger than appropriate loss processes. The solving of the last problem can give at least a partial answer to the question of whether the atomic hydrogen can be produced in Io's vicinity in a noticeable amount as was suggested by the interpretation of Pioneer data but was not confirmed by Voyager measurements. It should be added that if the noticeable recombination takes place in the vicinity of Io's orbit, it should rather happen in Io's atmosphere than in the plasma torus. This seems to be suggested by the remarkable difference in the measured electron densities in the atmosphere ($n_e = 10^5$ cm^{-3}; dayside peak; Kliore et al. 1975) and in the torus ($n_e = 2 \cdot 10^3$ cm^{-3}; Shemansky, 1980; Begenal and Sullivan, 1981). Also the atmospheric neutral cloud slows the protons down much better than the torus plasma, and therefore the number of low energy protons in Io's atmosphere should be much larger (especially at low altitudes) than in Io's torus.

II. GENERAL APPROACH

Let us consider a charged particle of Jovian origin (of a charge $Z_p e$, mass m_p and velocity v_p) slowed down along a direction h by a group of particles of Io's atmosphere (e.g. electrons). We will denote such a group by index i and the charge, mass and velocity of a particle of the ith group by Z_a^i, m_a^i and v_a^i, respectively. Also, we denote the densities of these particles by $N_a^i(h)$, their scattering angle distribution $p_a^i(\theta_a^i, h)$ and their velocity distribution function by $f_a^i(v_a^i, h)$. The above quantities are, in general functions of position within the atmosphere h because of the possibility of e.g. local fields. The total number of groups i_{tot} is larger than the number of the atmosphere gas components because it concerns all particles taking part in slowing down, i.e. free electrons, nuclei of ions, atoms and molecules and the electrons of their outer and inner shells.

The total average stopping power of the slowing down medium can be given as

$$\frac{d\,E_p(h)}{d\,h} = - \sum_i N_a{}^i(h) \int_0^\infty \int_0^\pi \int_{\Delta E^-}^{\Delta E^+} \sigma(\Delta E_a{}^i, \theta_a{}^i, v_a{}^i)\ \Delta E_a{}^i\ p_a{}^i(\theta_a{}^i, v_a{}^i, h).$$

$$f_a{}^i(v_a{}^i, h)\ d(\Delta E_a{}^i)\ d\theta_a{}^i\ dv_a{}^i, \quad (1)$$

where $\Delta E_a{}^i$ is the amount of energy exchanged between particles in a single collision and is the cross section for the collision in which proton experiences a change in energy $\Delta E_a{}^i$. The quantities ΔE^- and ΔE^+ denote minimum and maximum energy exchanged during the collision, respectively. A convenient analytical form of the cross section can be taken from binary encounter theory (Gryzinski, 1965). This cross section gives better agreement with experiment especially in the low energy region,

than the well-known Born approximation cross section used in Bethe's (1930) formulation of the stopping power cross section. Use of this cross section is also more convenient in calculations of the contribution of "ionizing" slowing down collisions (with the transferred energies larger than appropriate ionization potentials) that may play a certain role in the slowing down of protons with energies below 100 keV. This cross section does not depend on the azimuthal scattering angle for central forces and has the following form:

$$\sigma(\Delta E_a{}^i, \theta_a{}^i, v_a{}^i) = \frac{\pi(Z_p\, Z_a{}^i\, e^2)^2}{v_p\, |\Delta E_a{}^i|} \; \frac{|\vec{V}_a{}^i|}{(\mu_a{}^i\, \vec{V}_a{}^i)^2}$$

$$\times\, [2\, (\theta_a{}^i)^2 + b_a{}^i\, \Delta E_a{}^i] \cdot H\, [\xi\, (\Delta E_a{}^i)], \qquad (2)$$

where

$$H\, [\xi\, (\Delta E_a{}^i)] = \begin{cases} 1 & \text{if } \xi \geq 0 \\ 0 & \text{if } \xi < 0 \end{cases} \qquad (3)$$

with

$$\xi\, (\Delta E_a{}^i) = (a_a{}^i)^2 - b_a{}^i\, \Delta E_a{}^i - (\Delta E_a{}^i)^2\, . \qquad (4)$$

In Eq. (2), $\vec{V}_a{}^i$ is the relative velocity vector and $\mu_a{}^i$ is the reduced mass of the colliding system. Also

$$\Delta E^{\pm} = -\, \kappa\, [\, \vec{V}_a{}^i \cdot \vec{p}_{cm} \pm \vec{V}_a{}^i\, \vec{p}_{cm}\,] \qquad (5)$$

where

$$a_a{}^i = \kappa\, |\, \vec{p}_{cm} \times \vec{V}_a{}^i| \qquad (6)$$

$$b_a{}^i = 2\, \kappa\, |\vec{p}_{cm} \cdot \vec{V}_a{}^i\, | \qquad (7)$$

and

$$\kappa = \frac{m_p \, m_a^{\,i}}{(m_p + m_a^{\,i})^2} \quad . \tag{8}$$

In the above $\vec{p}_{cm}$ is the vector of the toal momentum of the colliding system.

Because there are no strong fields in the Io atmosphere, the spatial polarization of the particles taking part in slowing down is not significant and their angular distributions are close to isotropic). Thus, the angular distributions $p_a^{\,i}$ are independent of position h, and one can approximate them by

$$p_a^{\,i} \, (\theta_a^{\,i}, v_a^{\,i}, h) \, d\theta_a^{\,i} = 1/2 \sin \theta_a^{\,i} \, d\theta_a^{\,i}. \tag{9}$$

The triple integral (1) can now be reduced to a single integral with using relationships (2) - (9). However, to do this it is necessary to introduce the value of the minimum amount of energy $\delta E_a^{\,i}$ that is transferred in a binary collision or the appropriate value of the maximum impact parameter $D_a^{\,i}$ (otherwise the integral (1) diverges in the vicinity $\Delta E_a^{\,i} = 0$). Asssuming for the time being that the values of $D_a^{\,i}$ are known (we will discuss it later) the integration of the integral (1) with respect to $\Delta E_a^{\,i}$ and $\theta_a^{\,i}$ can be done now. After long but obvious transformations one gets:

$$\frac{d \, E_p(h)}{d \, h} = - \sum_{i=1}^{i_{tot}} N_a^{\,i}(h) \, A_a^{\,i} \int_0^{\infty} g \, (\lambda_a^{\,i}) \, f_a^{\,i} \, (\lambda_a^{\,i}, h) \, d\lambda_a^{\,i} \tag{10}$$

where

$$g \, (\lambda_a^{\,i}) = (\lambda_a^{\,i})^{-1} \, \{ \, F(s) - F(r) \, \} \tag{11}$$

with

$$F(x) = \frac{t - p}{\sqrt{2}} \begin{bmatrix} tg^{-1}\left(\frac{\sqrt{2x}}{1 - x}\right) & \text{if } x \leq 1 \\ \pi - tg^{-1}\left(\frac{\sqrt{2x}}{1 - x}\right) & \text{if } x > 1 \end{bmatrix} +$$

$$+ \frac{t + p}{\sqrt{2}} \ln \frac{x + \sqrt{2x} + 1}{\sqrt{1 + x^2}} + 1/2 \left(\frac{p}{\sqrt{x}} + t\sqrt{x}\right) \ln (1 + x^2)$$

$$- 2t\sqrt{x} \quad , \tag{12}$$

where

$$p = B(\lambda^2 - 1)$$

$$s = B(\lambda + 1)^2$$

$$r = B(\lambda - 1)^2$$

$$t = \frac{m_p - m_a{}^i}{m_p + m_a{}^i} \tag{13}$$

$$B = \frac{\mu_a{}^i D_a{}^i v_p{}^2}{Z_p Z_a{}^i e^2}$$

$$A_a{}^i = \frac{\pi (Z_p Z_a{}^i e^2)^{5/2}}{(\mu_a{}^i)^{3/2} v_p{}^3 \sqrt{D_a{}^i}} \left(1 + \frac{m_a{}^i}{m_p}\right)$$

and a new variable $\lambda_a{}^i$ defined as

$$\lambda_a{}^i = \frac{v_a{}^i}{v_p}$$

The relationship (10) can be rewritten in a form, sometimes more convenient, as

$$\frac{d\, E_p(h)}{d\, h} = - \sum_{i=1}^{i_{tot}} N_a{}^i(h) \cdot S_a{}^i(h) \tag{14}$$

where the $S_a^i(h)$ is well-known stopping power cross section for the ith kind of slowing down particles and its form results in an obvious way from the relationship (10).

III. ATMOSPHERIC PARTICLES

The direct environment of Io (hereafter called "atmosphere"), that is of our interest, ranges from the satellite surface up to altitude equals to about 600 - 700 km. The first direct evidence of an atmosphere on Io came from radio occultation experiment on Pioneer-10 (Kliore et al. 1974). The ultraviolet photometric measurements by Judge and Carlson (1974) and Carlson and Judge (1974a) detected an extended hydrogen cloud around Io and observations by Brown (1974) and Brown and Chaffee (1974) suggested that Io's atmosphere contains also metallic atoms such as sodium. It may be added that there were some theoretical models constructed for Io's atmosphere that considered such gases as CH_4 (Webster et al. 1972), NH_3, N_2 and N_a(McElroy et al. 1974), Na and NH_3 (McElroy and Yung, 1975; Gross and Ramnathan, 1976 and Johnson et al. 1976), Ne (Whitten et al. 1975) and N_2 (Gross and Ramnathan, 1976). However, most of these theoretical models appear to be unrealistic in light of the Voyager data on Io's atmosphere. After Voyagers encounters with Jupiter, basically two kinds of models have been proposed with respect to the Io atmosphere; so called "thick" model and "thin" model. The first model was investigated by Kumar (1979), Pearl et al. (1979) , Kumar (1980), Bertaux and Belton (1980) and Kumar and Hunten (1980) and it is supported by the data from Voyager UV (Broadfoot et al. 1979) and Plasma Science (Bridge et al. 1979) experiments (detection of sulfur and oxygen ions in Io plasma torus), the infrared measurements by Smythe et al. (1979) and Hapke (1979) (detection of sulfur dioxide by Voyager IRIS experiment (Pearl et al. 1979). The "thin" model was investigated by Lane et al. (1979) Butterworth et al. (1980), and Fanale et al. (1980)

and is supported by the absence of UV signatures of SO_2 in IUE spectra and the absence of polar caps on Io. In his recently published paper, Kumar (1981a) has made anlaysis of composition and photochemistry of Io's atmosphere based on the assumption that the surface density is controlled by vapor pressure equilibrium. His study (based primarily on Voyager data) was the next step to better understanding whether the atmosphere is "thick" or "thin".

The results are shown in Figures 1 and 2. The final conclusions of the analysis seem to favor the "thick" atmosphere with a chemically active surface. However, some remarkable uncertainties still remain and further development of the problem is necessary. These results, presented in Figures 1 and 2, have been assumed in the present calculations as the composition of Io's neutral atmosphere. It should also be added that argon atoms and sulfur molecules (Kumar and Hunten, 1980) as well as sodium and potassium atoms (Krimigis et al. 1981) may still be present in noticeable amount in Io's atmosphere.

The debate on ion composition of the Io's environment still continues (Shemansky, 1980; Bagenal and Sullivan, 1981; Shemansky and Smith, 1981; and Brown and Shemansky, 1981) nevertheless the major components seem to be SIII, SIV and OII ions (with ion densities of order 200 cm^{-3} each).

Another component of Io's atmosphere that should be taken into account in our considerations are free electrons. The spatial distributions of the electrons in Io's atmosphere for the day side, assumed for the present calculations, and night side as measured by Pioneer 10 (Kliore et al. 1975) are shown in Figure 3.

As it was mentioned before, the protons getting to the atmosphere

are slowed down by a large number of different kinds of particles; nuclei and electrons of various shells of the neutrals and ions and free electrons. The introductory esimations show, as expected, that the slowing down of protons by nuclei of the neutrals and ions is much less efficient than slowing down by bounded electrons of the atomic and molecular shells and free electrons.

Moreover, the electrons of ionic shells and the electrons of the inner shells of the neutrals play less significant role in slowing down than outer shell electrons because their remarkably larger binding energy i.e. larger average kinetic energy. Therefore, we have chosen, for final analysis, the free electrons and the outer electrons of the neutrals as the particles having major contribution in slowing down the protons penetrating the atmosphere. These species are specified in column (1) of Table 1. Having the density distributions $n_a{}^i(h)$ and the number of the most important outer shell electrons of the given kind of particles, $\beta_a{}^i$ one can determine the value of $N_a{}^i(h)$ as equal to their product $\beta_a{}^i\ n_a{}^i(h)$.

IV. ENERGY RANGE OF THE INTERACTING PARTICLES

There are three possible major sources of protons that can penetrate Io's atmosphere; the protons of Jovian origin, the protons from Io's plasma torus and the solar wind protons that were able to get into Jupiter's magnetosphere through the magnetosheath boundary. The measurements taken by the LECP instrument of Voyager 1 and 2 during the recent Jovian encounters (March and July, 1979) showed a large number of protons of Jovian origin (Zwickl et al. 1981, 8125). In the outer magnetosphere protons of energy from 30 keV up to 1780 keV (Voyager 1) and from 28 keV to 1450 keV (Voyager 2) were observed. However, most of the protons seemd to have energies below 500 keV. The analysis of these measurements in the middle and outer Jovian magnetosphere ($\gtrsim$ 10 Rj) (Krimigis et al. 1981) has showed that protons within the energy range below 200 keV can be described well by a convected Maxwellian distribution characterized by a temperature kT in the range from $\sim$ 20 to $\sim$ 45 keV. Also the existence of low energy protons was suggested by the measurements by the Pioneer 10 and 11 plasma instrument (Frank et al. 1975). They measured the energy spectra from 4.8 to 100 keV and the proton densities from 10 to 100 cm^{-3} within the inner magnetosphere ($\lesssim$ 10 Rj). There have been also some modeling of middle magnetosphere low energy plasma (Kennel and Coroniti, 1977; Goldstein, 1977; Walker et al. 1978; and Goertz, 1979) that produced estimates of temperatures ranging from 1 keV up to some tens of keV. It should be mentioned that several authors (Neugebauer and Eviatar, 1976; Goertz and Thompsen, 1979) suggested that these ions might not have been protons, but heavier ions, however, there is no hard experimental evidence for this suggestion. The electrons that get to the atmosphere directly from the torus can

also have low energy. The optical radiation observations of the region near Io, by Kupo et al. (1976) were interpreted by Brown (1976) as concerning a plasma of electorn density about $10^{3 \cdot 5}$ cm^{-3} and temperature about 20 eV, whereas the interpretation of Mekler et al. (1977) suggested plasma of density about 500 cm^{-3} with a temperature of about 10 eV.

The radial distributions of the electron temperature in the vicinity of Io's orbit were also measured by Voyager 1 and 2; Plasma Science and EUV experiments (Bridge et al. 1979; Broadfoot et al. 1979; Bagenal et al. 1980; Bagenal and Sullivan, 1981 and Gurnett et al. 1981). The observations indicated the existence of two regions in Io's plasma torus; an inner cooler part and the warm outer part and that the outer torus is centered at about the location of Io's orbit (about 6 Rj). The radial temperature distributions of so called "high-temperature" and "low-temperature" electrons are shown in Figure 4. As can be seen from there, the ratio of densities of high temperature electrons to low temperature electrons in the environment of Io is equal to about $2 \cdot 10^{-4}$. Thus, the vast majority of the free electrons are of low temperature with the effective temperature equal to about 10 eV. The very small amount of high-temperature electrons at the orbit of Io have an effective temperature equal to about 1 keV as can be seen from Figure 4. Because the temperature of the low-temperature electrons varie's rapidly in the vicinity of Io's orbit (within the distance equal to about a half R_j) therefore, the temperature of most of the electrons in the vicinity of Io's orbit should be considered as being within the 1 - 10 eV range (Figure 4). However, the fact that the orbit of Io is located about the center of outer region would suggest that the temperature of electrons in the immediate environment of the satellite Io should rather be taken as being close to the upper limit of the range.

It should be added that the ion temperature in the inner part of the torus appears to be about the same order as the electron temperature, whereas most of the ions in the outer part seem to have a temperature of a factor of 3 to 5 higher than the electron temperature in this region (Scudder et al. 1981).

The solar wind proton flux at distances from the Sun equal to about a few A.U. has representative speed equal to about 400 km/s which corresponds to an energy of an order of 1 keV (the thermal component is much smaller at these distances). With dynamic magnetosphere such as that of Jupiter, a certain amount of solar protons can reach the vicinity of Io. However, it should be remembered that the proton density at these heliocentric distances is $< 1\ cm^{-3}$.

Summarizing the above discussion, one can say that the amount of low energy protons (< 100 keV) getting into Io's atmospehre may be relatively large' so may be the number of protons slowed down to even smaller energies. Also, the energy of most of the atmosphere electrons seems to be about 1 - 10 eV. Because the protons of low energy will be slowed down significantly, especially at the lower limit of the range, the spatial distributions of protons energy and density in Io's atmosphere will be far from uniform.

V. IMPACT PARAMETER D_a^i

The minimum kinetic energy transfer during a collision can be determined pretty easily in the case of slowing down by outer electrons of molecules and atoms given in column 1 of Table 1. As it was said earlier, it is well-known since Bethe (1930) that the major role in slowing down of protons by neutrals is played by the Coulomb interaction of the protons with electrons of the outer shells. The models for slowing down of low energy protons based on such assumption gives the results that are in good agreement with reality for molecular media (e.g. Bethe, 1930; French and Seidl, 1951; Segre, 1953). This clearly suggests, at least for low energy protons, that the abosrption of potentially large amounts of energy by vibrational degrees of freedom of molecules does not play a significant role in comparison with the energy transfer to electronic degrees of freedom in the slwoing down process.

It has also been found experimentally that the low energy proton stopping power cross section in H_2) is almost independent of the physical state of H_2) (Reynolds et al. 1953; Phillips, 1953 and Wentzel and Whaling, 1952). These authors measured the energy losses of low energy protons in ice and in water vapros and their results are in very good agreement with each other for the proton energies below 100 keV. The lack of distinguished differences in the stopping power cross sections in those two media, having quite different contribution of the vibration degrees of freedom in their physical structure, seems to be a hard evidence that the excitation of electronic states, not vibrational, is dominant in global behavior of the molecular medium slowing down low energy protons.

The minimum energy δE_a^i transferred to the electrons must be related to the properties of these electrons in their electronic quantum states.

The smallest amount of the total electronic energy absorbed by a molecule or atom in the ground electronic state can be found from the energy needed for electronic excitation from the ground state to the first excited state. These lowest transitions for species of our interest are shown in column 4 of Table 1. The average kinetic energy of an outer electron in the ground state depends on its total energy and its velocity distribution function. Once can assume, as a first order approximation, that the outer electron distribution is δ-function, of course, independent of position of the molecule or the atom in Io's atmosphere, having the following form

$$f_a^{\,i}\,(\lambda_a^{\,i},\, h)\, d\lambda_a^{\,i} = \delta\,(\lambda_a^{\,i} - \langle \lambda_a^{\,i} \rangle)\, d\lambda_a^{\,i}, \qquad (15)$$

where $\langle\lambda_a^{\,i}\rangle = \langle v_a^{\,i}\rangle / v_p$.

The low energy proton losses in molecular medium do not obey Bragg's additivity rule (Reynolds et al. 1953; French and Seidl, 1951) which says that the stopping power of a molecule is equal to the sum of the stopping powers of its constituent atoms. Because of this, using of δ-function seems to be necessary but reasonable first order approximation. Also, the approximation presented above seems to be supported by the fact that Io atmospheric components have a temperature equal to some hundreds of degrees Kelvin (Kumar, 1980). It means that the percent of the molecules in higher vibrational excited states is small. These states could cause a significant distortion of average energies and distributions of the electronic states considered above.

The bounded electron, moving in an r^{-1} potential field with a distribution has its kinetic energy half its total energy. Thus, the minimum kinetic energy transfer in our calculations can be taken as

$\delta E_a^{\,i} = \Delta U_a^{\,i}\ (0 \rightarrow 1)/2$, where $\Delta U_a^{\,i}\ (0 \rightarrow 1)$ is the excitation energy for the first electronic level. Also, the average velocity of the electron in the ground state can be written in this case as

$$\langle v_a^{\,i} \rangle = \frac{\sqrt{I_a^{\,i}}}{m_a^{\,i}} \qquad (16)$$

where $I_a^{\,i}$ is ionization potential of a neutral of the ith kind. It is obvious that the energies $\Delta U_a^{\,i}$ should be chosen for the lowest electronic transitions with relatively large transition probabilities. Determination of these transitions can be done in the following way. The two lowest optical transitions in SO_2 are of distinctly different kinds; the transition $\tilde{a}^3 B_1 - \tilde{X}^1 A_1$ (25766.9 cm^{-1}) is spin-forbidden and the transition $\tilde{A}^1 B_1 - \tilde{X}^1 A_1$ (29622 cm^{-1}) is allowed. In case of SO molecules the lowest optical transition $B^3 \Sigma^- - X^3 \Sigma^{-c}$ (39356.3 cm^{-1}) is a dipole-allowed transition. In case of the O_2 molecule, the two lowest transitions $a^1 \Delta g - X^3 \Sigma g^-$ (7918.1 cm^{-1}) and $b^1 \Sigma g^+ - X^3 \Sigma g^-$ (13195.22 cm^{-1}) are forbidden whereas the third one $A^3 \Sigma_u^{\,+} - X^3 \Sigma g^-$ (36096 cm^{-1}) is allowed. The lowest strong transition in sulfur atom $3p^4 - 3p^3\,4s$ (55331 cm^{-1}) is optically allowed so is the lowest transition in oxygen atom $2p^4 - 2p^3\,3s$ (76795 cm^{-1}). Because the collisional cross section for excitation of a particle in the kth electronic level to the ℓth electronic level is proportional to allowed optical transition probability from the level ℓ to the level k, the above mentioned energy gaps seem to be appropriate as the smallest amount of energy to be transferred for the lowest allowed transitions. These transitions can be highly probable for both processes, i.e., for optical absorption and collisional excitation. However, the excitation cross sections for optically forbidden transitions can be the same order (maximum values) as those for optically allowed transitions, but they

decrease more rapidly with increasing electron energy. The appropriate energy gaps for the allowed and forbidden transitions discussed above are comparable to each other, except the oxygen molecule where the gap of the lowest forbidden transition (7918.1 cm^{-1}) differs significantly from that of the lowest allowed transition (36096 cm^{-1}). As it was said previously, the electron mean energy in the atmosphere is equal to about 1 - 10 eV and therefore it is the same order as the energy of expected maximum of the appropriate excitation cross section (about 3 - 4 times greater than the threshold energy). Because of that it is difficult to say which transition is more probable for collisional excitation and which ΔU_a^i should be taken into account. Therefore, the calculations of the stopping power of the Io's atmosphere will be done for both transition values of ΔU_a^i in case of oxygen molecule. The appropriate values of δE_a^i and I_a^i for our species are given in columns 5 and 6 of Table 1, respectively.

The minimum energy transfer δE_a^i can be related to the maximum impact parameter D_a^i through the following dependence

$$D_a^i = \frac{Z_p Z_a^i e^2}{E_a^i} , \qquad (17)$$

because in our formulation of the problem, the most important slowing down forces in our medium are coulomb type.

In case of free electrons (i = 6) the local thermal model can be assumed (Scudder et al. 1981) with the maxwellian distribution function having the following form in our notation:

$$f_a^{\,i}(\lambda_a^{\,i}, h)\, d\lambda_a^{\,i} = \sqrt{\frac{2}{\pi}}\; v_p^{\,3} \left\{ \frac{m_a^{\,i}}{kT_a^{\,i}(h)} \right\}^{3/2} (\lambda_a^{\,i})^2$$

$$\exp\left\{ -\frac{m_a^{\,i}\, v_p^{\,2}}{2\, kT_a^{\,i}(h)} (\lambda_a^{\,i})^2 \right\} d\lambda_a^{\,i} \qquad (18)$$

The value of $D_a^{\,i}$ in case of slowing down by free electrons can be obtained from the mean interelectron distance, i.e.

$$D_a^{\,6}(h) = [n_a^{\,6}(h)]^{-1/3} \qquad (19)$$

The above results from the fact that we have used the binary collision cross section (2) to describe the multiparticle system. Such an approach is well justified for conditions existing in Io's atmosphere however, it should be emphasized that the binary encounter approach makes sense only for collisions with impact parameters smaller than the means interparticle distance. Therefore, the equality (19) seems to be a good approximation for the maximum collision impact parameter in the discussed case. This is also supported by the fact, that the electron density is low, therefore $D_a^{\,i}$ is large and the slowing down interaction is getting weaker rapidly for even larger distances.

VI. "IONIZING" AND "CAPTURING" COLLISIONS

There are two kinds of collisions among those causing slowing down of the low-energy protons, that should be analyzed here; so called "ionizing" and "capturing" collisions. The former represent the processes with the amount of energy transferred to an outer shell electron equal to or larger than its ionization potential. They cause the deviation of the densities of the slowing down particles from the values assumed to calculations. This is done not only by direct ionization by the protons but also by the ionization caused by the electrons from the direct process. This also changes the factors β_a^i because of two effects: 1) the fact that it decreases the number of the outer electrons that are of great importance for the slowing down, 2) the contribution of the outer electrons left after ionization act also changes because they have larger binding energies than in preionization state.

The "capturing" collisions are those in which the outer electrons can be captured by the low-energy protons, and the reverse process can occur after a while. The estimation of the slowing down in such case is very difficult. Also, the capture process decreases the cross section for proton excitation because some of the electrons gaining enough energy to be excited to a certain energy level are removed from the neutrals by the positive potential well of the proton.

In this paragraph, we will calculate first, as an illustration, contribution of the stopping power of sulfur dioxide constituent caused by the purely "ionizing" collisions at the altitude equal to 100 km. The appropriate results are presented in Figure 8. Comparison of these results with those in Figures 5 and 6 leads to the conclusion that the

"ionizing" collisions do not cause any remarkable changes in total stopping power of the medium. Moreover, the contribution of the "ionizing" collisions with transferred energies larger than sometens of electron volts can be neglected. The results shown in Figure 8 were obtained assuming the conditions existing at 100 km. of altitude. The stopping power for higher altitude will be smaller because relatively lower densities of the atmospheric medium.

We will also make some rough estimations of proton ionization rates and proton excitation rates for sulfur dioxide constituents. It will be done by using the binary encounter approximation (Gryzinski, 1965) and taking into account some further development of it (Kunc, 1979; Kunc, 1980 and Gryzinski and Kunc, 1982). These estimations are also necessary for determination of "ionizing", "exciting" and "capturing" collisions for slowing down process.

As it was said previously the "ionizing" collisions changes the free electron densities and the factors $\beta_a{}^i$ as well. The proton ionization rate for sulfur dioxide is difficult to determine because of lack of appropriate cross sections in the literature of the subject. Using the b. e. approximation and assuming that an outer shell electron of a sulfur dioxide molecule has delta distribution with the average velocity given by equation (16). The proton ionization cross section Q_{ion} and the appropriate ionization rates K_{ion} for various energies of the protons passing through sulfur dioxide atmosphere (of physical properties as before) are shown in Table 2. The last row of the Table 2 displays the number of ionization acts (L_{ion}) caused by a proton of constant energy E_p along its path from the top of the atmosphere down to the satellite surface. As can be seen there, the number of those acts is low when

compared with the population of free electrons in the atmosphere. This fact together with the fact that the densities of the low-energy protons are not large leads to the conclusion that the variation of free electron density and factors β_a^i caused by "ionizing" collisions in Io atmosphere is small.

The effective (taking into account the capture process) proton excitation (from ground state to the first excited) cross section can be given by the following approximate relationship:

$$Q_{exc}(E_p) \approx Q'_{exc}(E_p) - \gamma \cdot Q_c(E_p) \qquad (20)$$

where $Q'_{exc}(E_p)$ is the excitation cross section without correction for the capture process, $Q_c(E_p)$ is the capture cross section and the correction factor γ can be roughly estimated as

$$\gamma \sim \frac{\Delta v_a^i (0 \rightarrow 1)}{1/2\, m\, v_p^2 + I_a^i} \qquad (21)$$

Taking the above into account the effective cross section Q_{exc} for proton excitation (of the first energy level of the dioxide molecule) and the appropriate rates have been estimated and are presented in Table 3.

Comparison of the results presented in Tables 2 and 3 and in Figure 8 shows that the presence of the "ionizing" and "capturing" collisions seem not to introduce a significant error in estimation of the efficiency of slowing down low-energy protons by Io's atmosphere. Therefore the "reliability interval" of one order of magnitude (that was assumed for calculation of stopping power of the medium) appears to be reasonable assurance for quite accurate reflection of reality. The results of calculations done for lower (solid curves) and upper (broken curves) limits of this interval are shown in figures 5 and 6.

TABLE 1

Component	i	β_a^i	Electronic Transition	δE_a^i(eV)	I_a^i(eV)
(1)	(2)	(3)	(4)	(5)	(6)
SO_2	1	2	$\tilde{a}^3 B_1 - \tilde{X}^1 A_1$	1.837	12.340
SO	2	2	$B^3 \Sigma^- - X^3 \Sigma^-$	2.439	12.102
O_2	3	2	a) $A^3 \Sigma_u^+ - X^3 \Sigma_g^-$	2.238	12.063
			b) $a^1 \Delta g - X^3 \Sigma_g^-$	0.491	
S	4	4	$3p^3\ 4s - 3_p^4$	3.431	10.360
O	5	4	$2_p^3\ 3s - 2_p^4$	4.760	13.618
e	6	1	-	-	-

TABLE 2

E_p(keV)	5	10	50	100
$Q_{ion}(cm^2) \times 10^{-16}$	1.76	2.72	2.02	1.28
$K_{ion}(sec^{-1})$	34	75	124	112
L_{ion}	21	33	24	16

TABLE 3

E_p(keV)	5	10	50	100
$Q_{exc}(cm^2) \times 10^{-16}$	4.1	5.15	2.22	1.64
$K_{exc}(sec^{-1})$	79	142	138	143
L_{exc}	50	63	27	20

TABLE CAPTIONS

TABLE 1. The electronic transitions of Io's atmosphere neturals taken into consideration in the present calculations.

i - the superscript denoting the kind of particle.

a^i - the number of the outer electrons in the ith particle.

E_a^i - the minimum energy transfer during collision between a proton and a particle of ith kind.

I_a^i - the ionization potential of the particle of ith kind.

TABLE 2. The estimation of the ionizational properties of the low energy protons in pure sulfur dioxide atmosphere with characteristic parameters as those at the altitude equal to 100 km.

E_p - the energy of a proton.

Q_{ion} - the proton ionization cross section.

K_{ion} - the average ionization rate.

L_{ion} - the average number of ionizing collisions caused by the proton on its path from the top of the atmosphere down to the satellite surface.

TABLE 3. The estimation of the proton excitation (from ground to the first excited level) properties of the low-energy protons in pure sulfur dioxide atmosphere with characteristic parameters as those at the altitude equal to 100 km.

TABLE CAPTIONS
Page 2

E_p - the energy of the proton.

Q_{exc} - the proton excitation cross section taking into account the electron capture.

K_{exc} - the average proton excitation rate.

L_{exc} - the average number of the excitations by the proton on its path from the top of the atmosphere down to the satellite surface.

FIGURE CAPTIONS

Figure 1. The densities of atmospheric constituents of Io (for the model with chemically passive surface) as assumed to the calculations.

Figure 2. The densities of atmospheric constituents of Io (for the model with chemically active surface) as assumed to the calculation.

Figure 3. The electron density profiles in Io atmosphere for day side or night side of the satellite, as measured by Pioneer 10 spacecraft.

Figure 4. Radial profiles of the electron temperatures in vicinity of Io orbit as found from Voyager 1 and Voyager 2 measurements. The superscripts "low" and "high" denote low-temperature and high-temperature electrons, respectively. The parameter $\eta = n_e^{high}/n_e^{low}$.

Figure 5. Stopping power of Io's atmosphere with chemically active surface as a function of altitude for various proton energies E_p. The broken curve represents average stopping power for low energy protons.

Figure 6. Stopping power of Io's atmosphere with chemically passive surface as a function of altitude for various proton energies E_p. The broken curve represents average stopping power for low energy protons.

Figure 7. Slowing down of low-energy protons with different initial energies by Io's atmosphere. Solid curves represent the slowing down for actual conditions used in the present calculations. The broken curves represent the slowing down with stopping power being one order of magnitude larger.

Figure 8. Stopping power of sulfur dioxide of Io's atmosphere at the altitude 100 km for different proton energies E_p and for different proton energies E_p as a function of energy transferred during collisions. The "ionizing" collisions are those with the amount of transfer energy equal or greater than ionization potential of the sulfur dioxide molecule (12.34 eV).

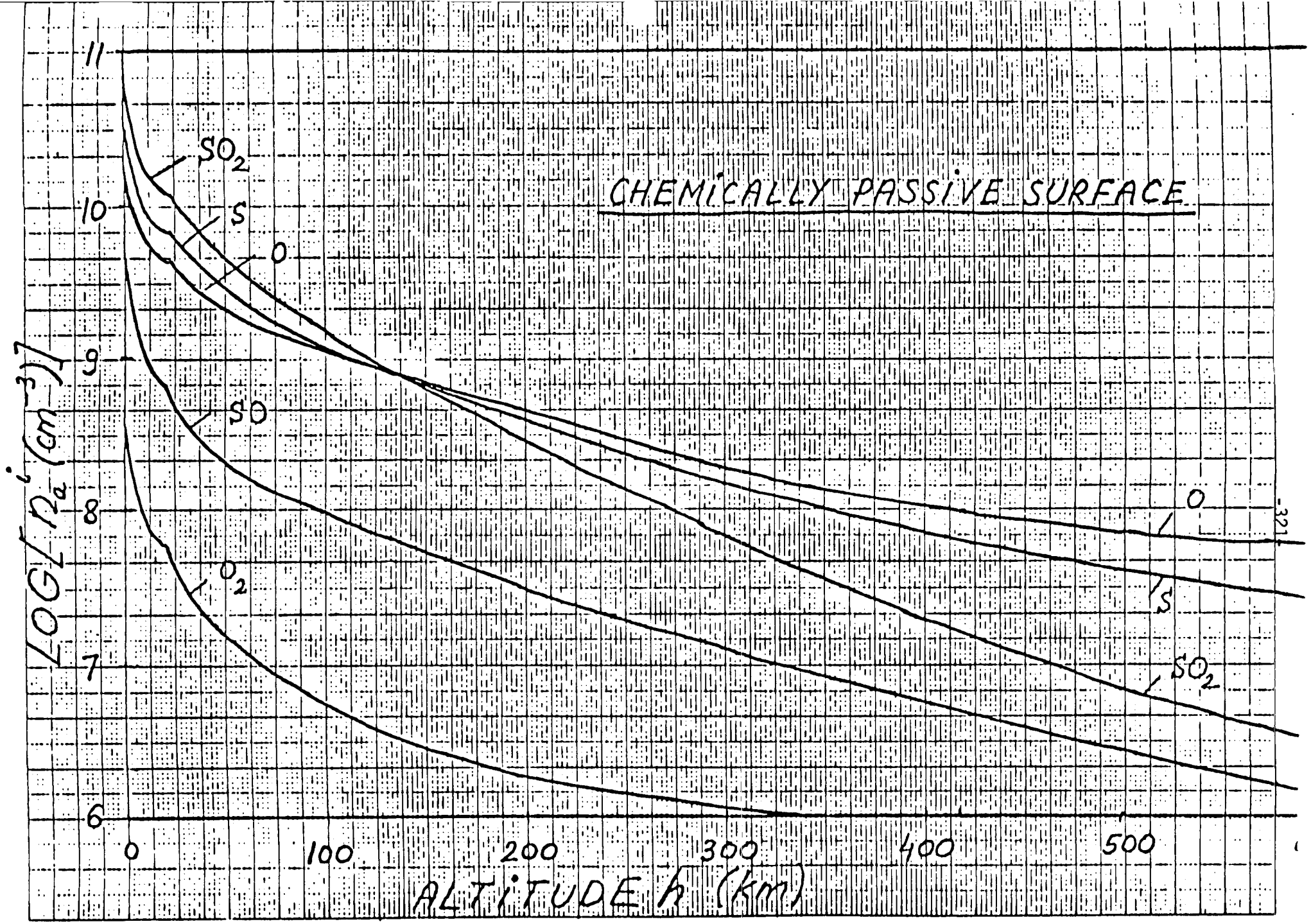

K+E 10 X 10 TO THE CENTIMETER 18 X 25 CM
KEUFFEL & ESSER CO. MADE IN U.S.A.
46 1510

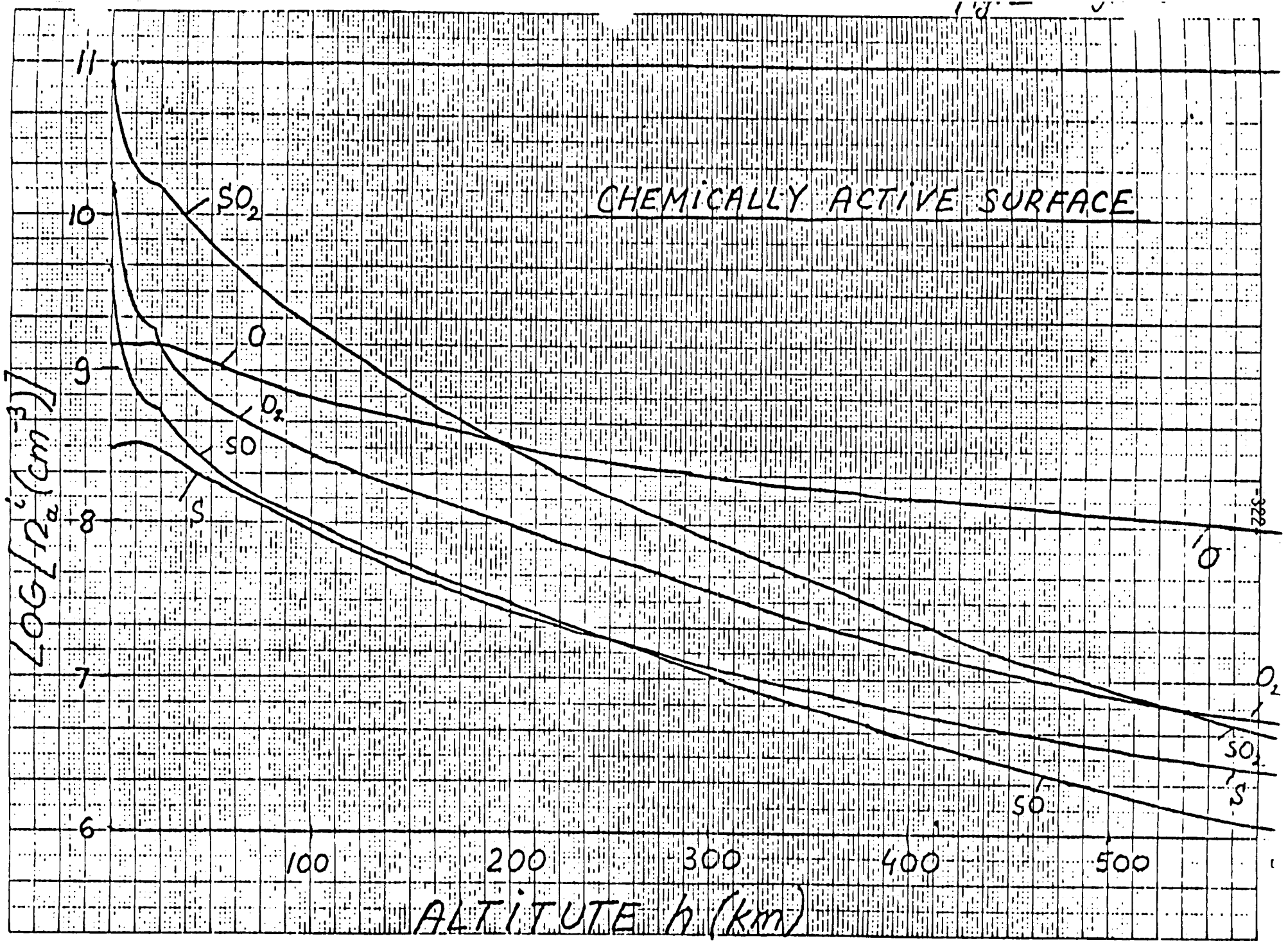
CHEMICALLY ACTIVE SURFACE
LOG[n_a^i (cm^-3)]
11
10
9
8
7
6
SO2
O
O2
SO
S
100
200
300
400
500
ALTITUTE h (km)

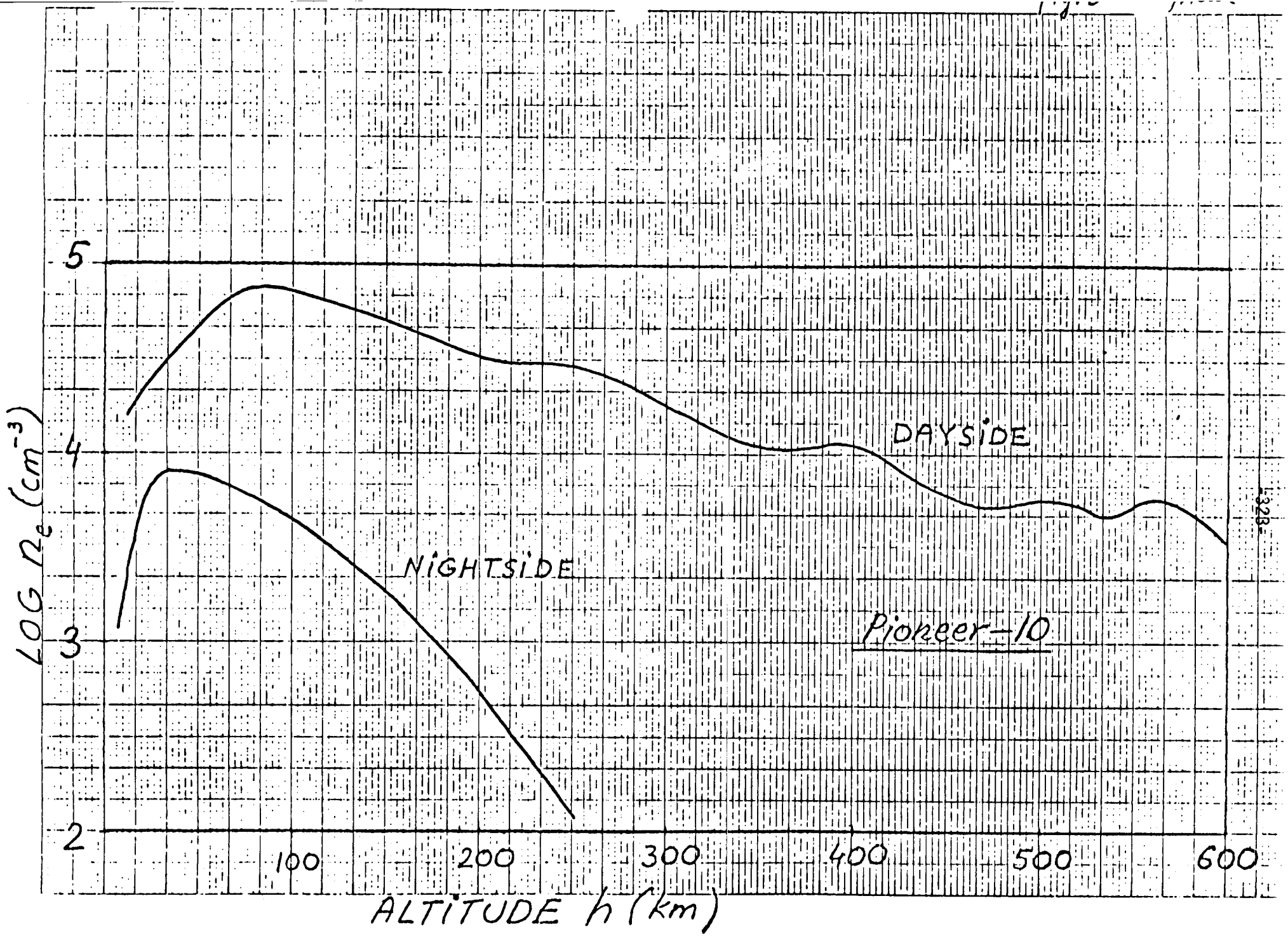

K+E 10 X 10 TO ½ INCH 7 X 10 INCHES KEUFFEL & ESSER CO. MADE IN U.S.A.
46 1320

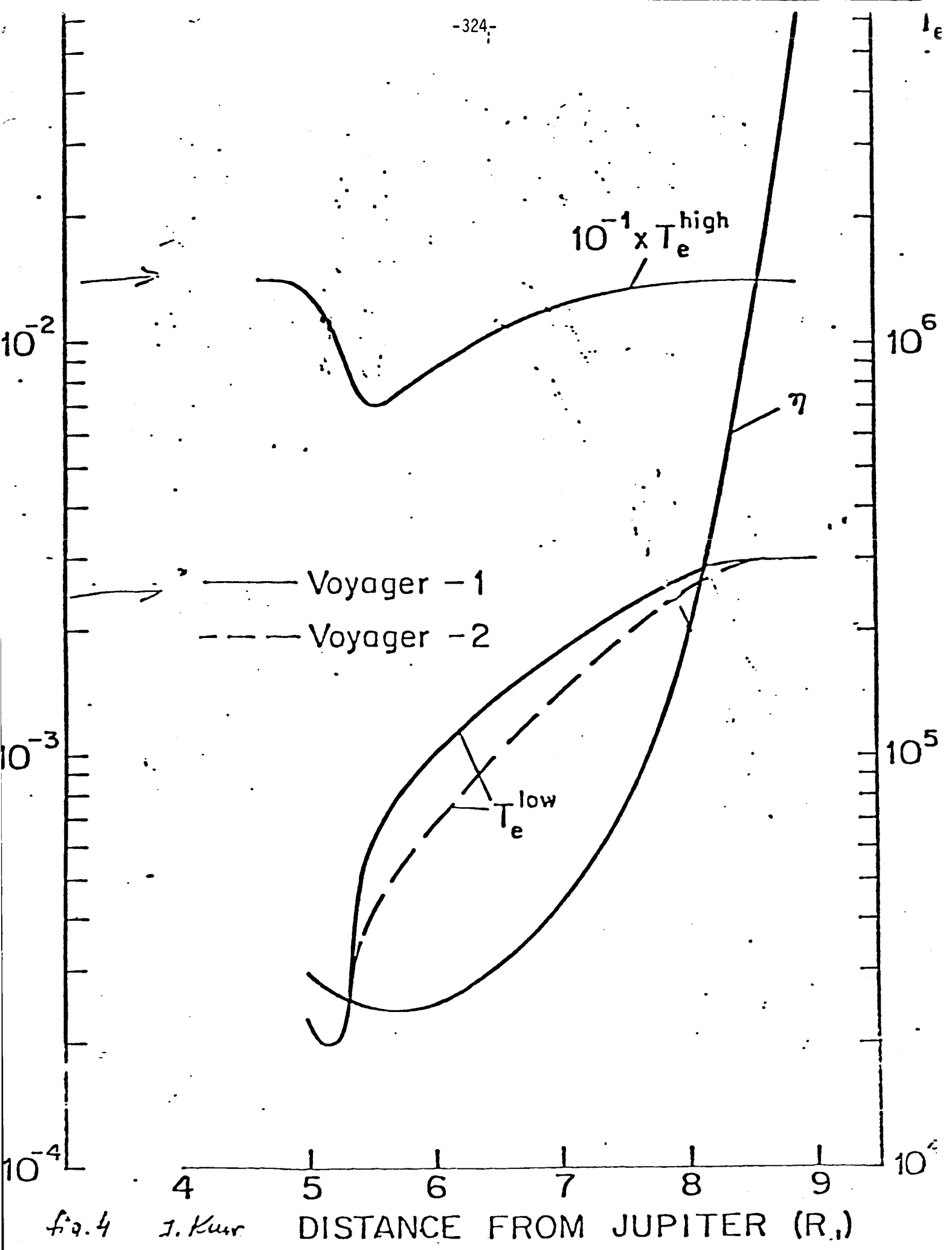
$10^{-1} \times T_e^{high}$
η
Voyager -1
Voyager -2
T_e^{low}
10^{-2}
10^{-3}
10^{-4}
10^{6}
10^{5}
4
5
6
7
8
9
DISTANCE FROM JUPITER (R_J)

fig. 4 J. Kurr

J. Kunc Fig 5

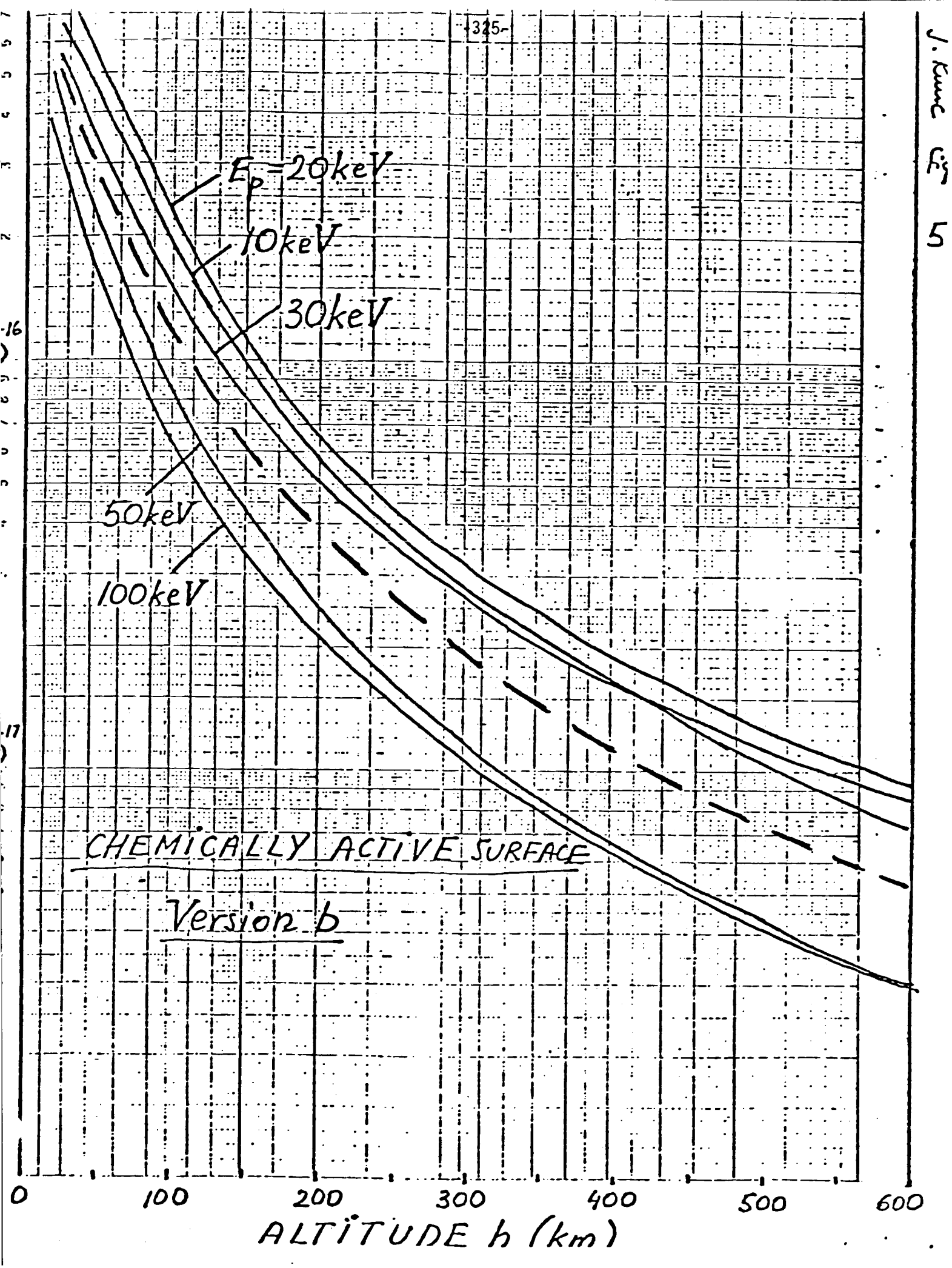
E_p=20keV
10keV
30keV
50keV
100keV
CHEMICALLY ACTIVE SURFACE
Version b
-16
-17
0
100
200
300
400
500
600
ALTITUDE h (km)

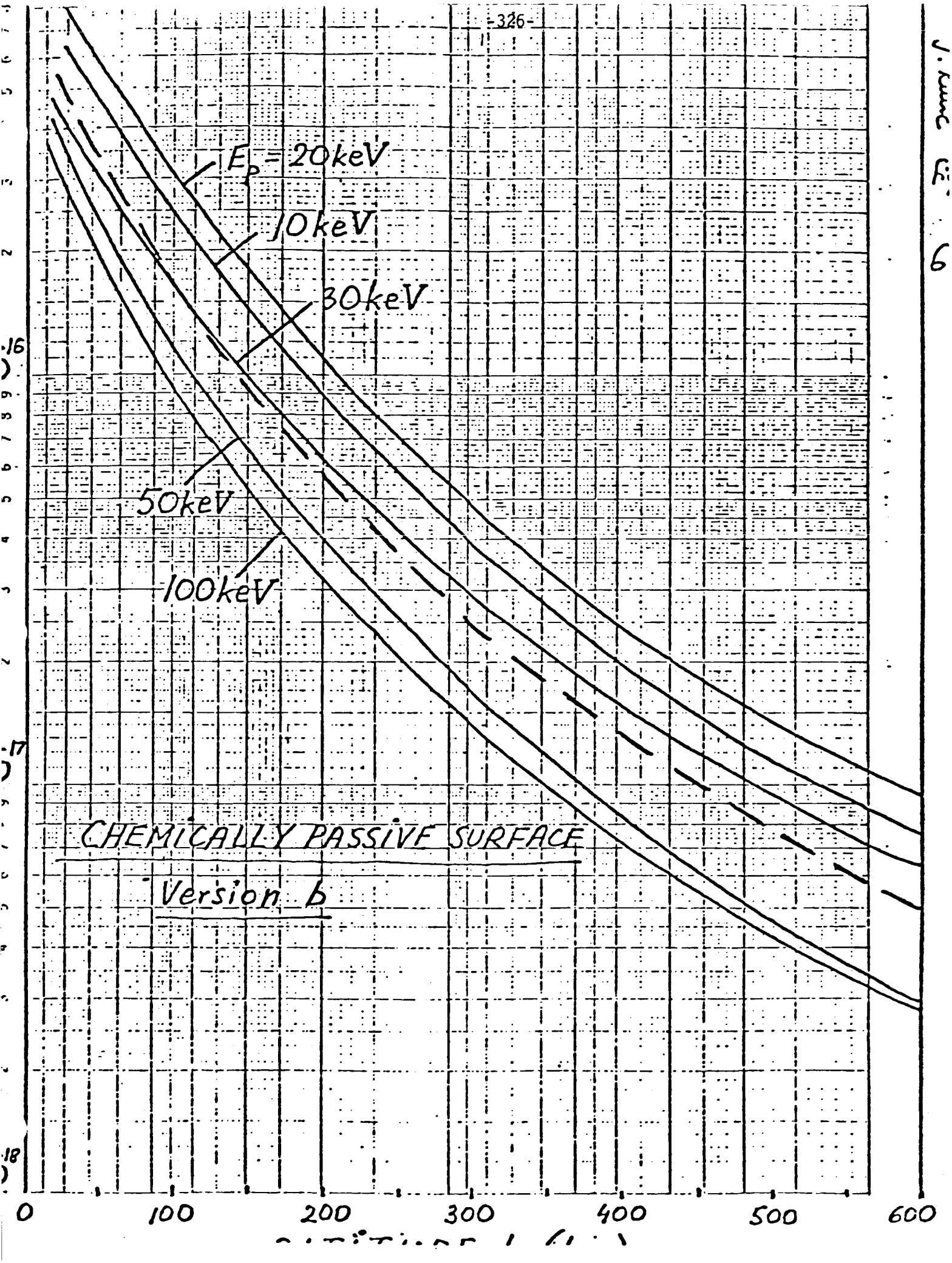
E_p = 20keV
10keV
30keV
50keV
100keV
CHEMICALLY PASSIVE SURFACE
Version b
-16
-17
-18
0
100
200
300
400
500
600

J. Func Fig. 6

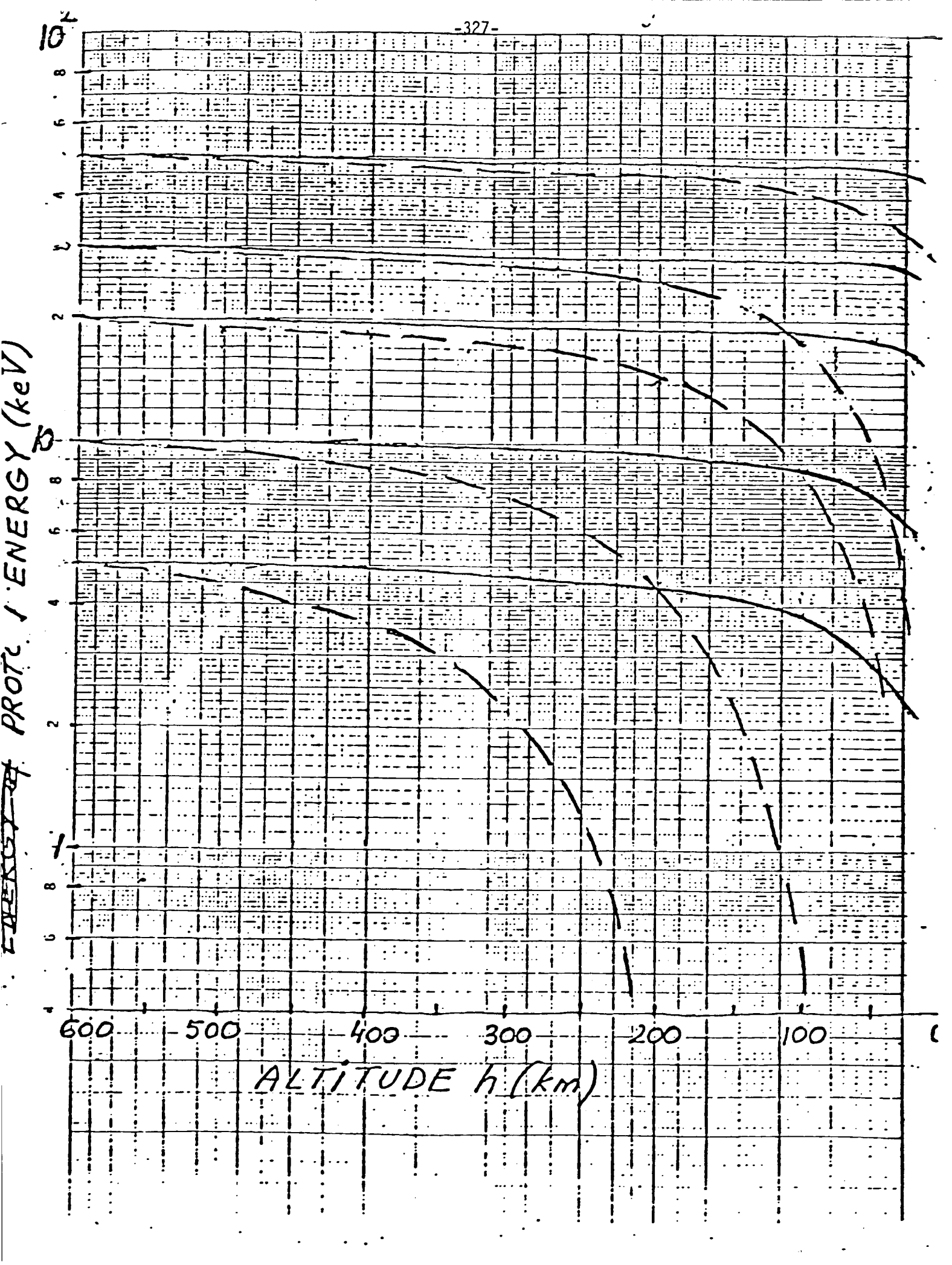
10²
8
6
4
2
10
8
6
4
2
1
8
6
4
PROT. ENERGY (keV)
600
500
400
300
200
100
ALTITUDE h (km)

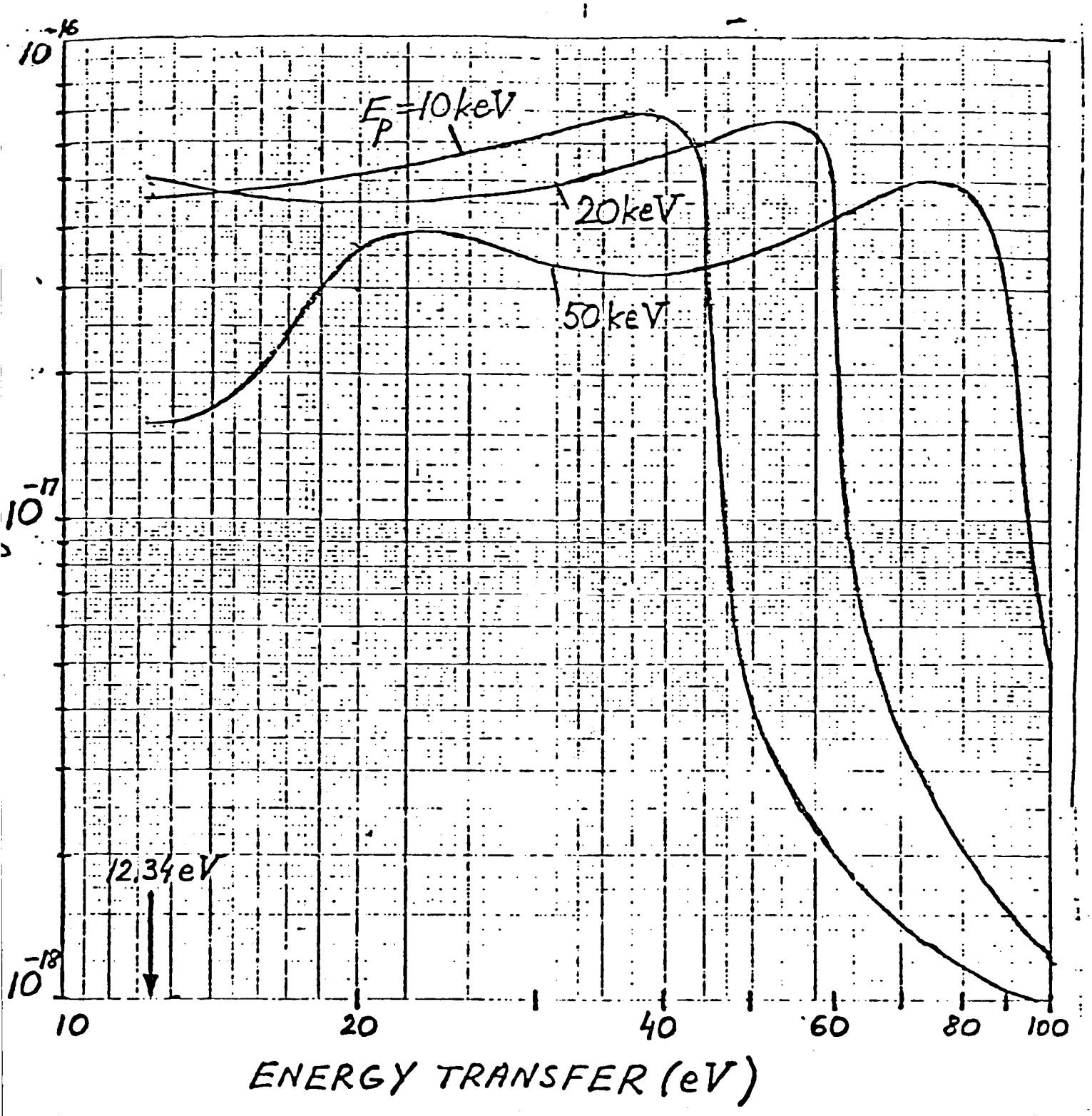
10^{-16}
10^{-17}
10^{-18}
E_p=10keV
20keV
50keV
12.34eV
10
20
40
60
80
100
ENERGY TRANSFER (eV)

FIG. 8

REFERENCES

Bagenal, F., Sullivan, J. D. and Siscoe, G. L., 1980, Geophys. Res. Lett., 7, 41.

Bagenal, F. and Sullivan, J. D., 1981, J. Geophys. Res., 86, 8447.

Bertaux, J. L. and Belton, M. J., 1980, Nature, 282, 813.

Bethe, H. A., 1930, Ann. Phys. 5, 325.

Bridge, H. S., et al., 1979, Science, 204, 987.

Broadfoot, A. L., et al., 1979, Science, 204, 979.

Brown, R. A., 1974, IAU Circular #2682.

Brown, R. A., 1976, Astrophys. J., 206, L17g.

Brown, R. A. and Chaffee, F. H., 1974, Ap. J. Lett. 187, L125.

Brown, R. A. and Shemansky, D. E., 1981, private communication.

Butterworth, P. S., Calwell, J., Moore, V., Owen, T., Rivola, A. R. and Lane, A. L., 1980, Nature, 285, 308.

Carlson, R. W. and Judge, D. L., 1974a, J. Geophys. Res. 79, 3623.

Carlson, R. W. and Judge, D. L., 1974b, EOS Trans. AGU, 55, 339.

Fanale, F. P., Banerdt, W. B., Elson, L. S., Johnson, T. V. and Zurek, R. W., in "The Satellites of Jupiter" ed. by D. Morrison, University of Arizona Press, in press.

Frank, L. A., Ackerson, K. L., Wolfe, J. H., and Mihalov, J. D., 1975, J. Geophys. Res. 81, 457.

French. A. P. and Seidl, A. G. P., 1951, Phil. Mag. 42, 537.

Goertz, C. K., 1979, Space Sci. Rev., 23, 319.

Goertz, C. K. and Thompsen, M. F., 1979, J. Geophys. Res. 84, 1499.

Goldstein, H., 1977, Planet. Space Sci., 25, 673.

Gross, S. H. and Ramnathan, G. V., 1976, Icarus, 29, 493.

Gryzinski, M., 1965, Phys. Rev., 138A, 322.

Gryzinski, M. and Kunc, J. A., 1982, submtted for publication.

Gurnett, D. A., Scarf, F. L., Kurth, W. S., Shaw, R. R. and Poynter, R. L., 1981, J. Geophys. Res., 8199.

Hapke, B., 1979, Geophys. Res. Lett., 6, 799.

Judge, D. L. and Carlson, R. W., 1974, Science, 183, 317.

Kennel, C. F. and Coroniti, F. V., 1977, Rev. Astron. Astrophys., 15, 389.

Kliore, A. J., Cain, D. L., Fjeldbo, G., 1974, Science, 183, 323.

Kumar, S., 1979, Nature, 280, 758.

Kumar, S., 1980, Geophys. Res. Lett., 7, 35.

Kumar, S., 1981a, J. Geophys. Res., in press.

Kumar, S. and Hunter, D. M., in "The Satellites of Jupiter" ed. by D. Morrison, University of Arizona Press, in press.

Kunc, J. A., 1979, J. Phys. B, 12, 241.

Kunc, J. A., 1980, J. Phys. B, 13, 587.

Kupo, I., Mekler, Yu. and Eviatar, A., 1976, Astrophys. Space Sci., 40, 63.

Lane, A. L., Owen, T., Nelson, R. M. and Motteler, F. C., 1979, BAAS, 11, 597.

Matson, D. L., Johnson, T. V. and Fanale, F. P., 1974, Ap. J., 192, L43.

McDonough, T. R., 1975, Icarus, 24, 400.

McDonough, T. R. and Brice, N. M., 1973, Incarus, 20, 1973.

McElroy, M. B. and Yung, Y. L., 1975, Ap. J., 196, 227.

Mekler, Yu., Eviatar, A. and Kupo I., 1977, J. Geophys. Res., 82, 2809.

Neugebauer, M. and Eviatar, A., 1976, Geophys. Res. Lett., 3, 708.

Pearl, J., Hanel, R., Kunde, V., Maguire, W., Fox, K., Gupta, S., Ponnamperuma, C. and Raulin, F., 1979, Nature, 280, 755.

Phillips, I. A., 1953, Phys. Rev. 90, 532.

Reynolds, H. K., Dunbar, D. N. F., Wentzel, W. A. and Whaling, W., 1953, Phys. Rev. 92, 742.

Scudder, J. D., Sittler, E. C. and Bridge, M. S., 1981, J. Geophys. Res., 86, 8157.

Segre, E., 1953, Experimental Nuclear Physics, New York.

Shemansky, D. E., 1980, Ap. J., 236, 1043.

Shemansky, D. E. and Smith, G. R., 1981, J. Geophys. Res., 86, 9179.

Smythe, W. D., Nelson, R. M. and Nash, D. B., 1979, Nature, 280, 766.

Trainor, J. M., Teegarden, B. J., Stilvell, D. E., McDonald, F. B., Roelof, E. C. and Webber, W. R., 1974, Science, 183, 311.

Walker, R. J., Kivelson, M. G. and Schardt, A. W., 1978, Geophys. Res. Lett., 5, 799.

Webster, D. L., Alksne, A. Y. and Whitten, R. C., 1972, Ap. J., 174, 685.

Wentzel, W. A. and Whaling, W., 1952, Phys. Rev., 87, 499.

Whitten, R. C., Reynolds, R. T. and Michelson, P. F., 1975, Geophys. Res. Lett., 2, 49.

Zwickl, R. D., Krimigis, S. M., Carbary, J. F., Keath, E. P., Armstrong, T. P., Hamilton, D. C. and Gloeckler, G., 1981, J. Geophys. Res., 86, 8125.

SOME REMARKS ON THE USE OF SPACECRAFT-BASED MEASUREMENT TO DESCRIBE THE DYNAMICS OF PLANETARY MAGNETOSPHERES

by

J. A. KUNC and D. L. JUDGE
Space Sciences Center, SHS-274
University Park - MC1341
University of Southern California
Los Angeles, California 90089-1341

ABSTRACT

A statistical method for investigation of the dynamic properties of a planetary magnetosphere is presented. The idea is based on the comparison of probability functions for various magnetospheric properties that can be obtained from spacecraft-based observations with appropriate theoretically fitted probabilities obtained from distribution functions of the dynamical properties of the magnetosphere and the spacecraft.

The approach proposed in the present work is based on the distribution fucntions of some dynamic quantities (position, energy, or momentum) of the spacecraft instrument and the investigated phenomenon e.g. a magnetospheric bow shock or a magnetopause. There are several functions that can be used to describe the behaviour of the spacecraft and the property of the phenomenon. Two of these functions that are the most convenient are; position of the spacecraft $g_s(\vec{r})$ (where position can be taken as the distance from the planet associated with the phenomenon) and the position of the "property" (e.g. bow shock) $g_p(\vec{r})$. These distributions are defined in a classical way i.e., as the probability density that the spacecraft ("property") is between $\vec{r}$ and $\vec{r} + d\vec{r}$. Another pair of suitable functions may be the spacecraft velocity distribution $f_s(\vec{v})$ and the "property" velocity distribution $f_p(\vec{v})$ which determine the densities of probability that the spacecraft ("property") has its velocity within the interval $\vec{v} - \vec{v} + d\vec{v}$. Having the above functions, one can easily introduce the probability that both "objects" have their positions within the finite interval $\Delta\vec{r} = \vec{r}_2 - \vec{r}_1$;

$$P_r(\vec{r}_1, \vec{r}_2) = \int_{\vec{r}_1}^{\vec{r}_1 + \Delta\vec{r}} g_s(\vec{r})\, g_p(\vec{r})\, d\,\vec{r} \qquad (1)$$

because the dynamical behaviours of the "objects" are uncorrelated processes. Similarly, the probability that both "objects" have their velocities within the finite interval $\Delta\vec{v} = \vec{v}_2 - \vec{v}_1$

$$P_v(\vec{v}_1, \vec{v}_2) = \int_{\vec{v}_1}^{\vec{v}_1 + \Delta\vec{v}} f_s(\vec{v})\, f_p(\vec{v})\, d\,\vec{v} \qquad (2)$$

The above approach contains a certain complexity from analytical of view associated with the definition of position $\vec{r}$ and velocity $\vec{v}$ of

the "object" that represents a magnetospheric phenomenon such as, for example, bow shock. This is because such magnetospheric bow shock can not be treated as a point, but rather as a surface moving in the space. However, the measurements of the position and velocity of such a surface are made along the path of the spacecraft passing the bow shock region. Such region is usually located far enough from the planet and therefore the appropriate fragment of trajectory of the spacecraft in this region (in general Keplerian hyperbola in gravitational field of the planet) can be regarded in a first approximation as a straight line. Thus, one can reduce the problem to more convenient form with scalar variables r and v measured along the spacecraft path. The distribution functions of the spacecraft $g_s(r)$ and $f_s(v)$ can be given in close analytical forms as it will be shown below. The distributions of a "property" (bow shock etc.) $g_p(r)$ and $f_p(r)$ are unknown and the subject for an investigation since they can supply a lot of information about the behaviour of the magnetosphere. The probabilities $P_r(\Delta r)$ and $P_v(\Delta v)$ can be found from measurements of a properly oriented spacecraft based experiment. When one is interested in behaviour of the magnetospheric bow shock, the "experimental" probability $P_r(\Delta r)$ can be found as a ratio of the number of "meetings" of the spacecraft instrument with the bow shock within an interval Δr to the total number of such "meetings" in certain fragment of the spacecraft trajectory. The number of "meetings" is simply the number of crossings of the bow shock by the instrument. The probability $P_v(\Delta v)$ can be determined in similar manner from, for instance, measurements of the relative velocities of the instrument and the bow shock. It is obvious that for better accuracy of the approach the number of the crossings should be large enough in whole observed interval and in subintervals. Having these measurement, one can construct at least two

probability functions:

1) The function of position r':

$$P_r(r', \Delta r) = \int_{r'}^{r' + \Delta r} g_s(r)\, g_p(r)\, d\, r \qquad (3)$$

2) The function of velocity v':

$$P_v(v', \Delta v) = \int_{v'}^{v' + \Delta v} f_s(v)\, f_p(v)\, d\, v \qquad (4)$$

Other functions can be built (e.g. momentum etc.) depending on the spacecraft instrument measuring capability and accuracy.

In the last two relationships, one has two functions $g_s(r)$ and $f_s(r)$ given in analytical form (however they can also be taken from the spacecraft trajectory measurements) and two functions $P_r(r', \Delta r)$ and $P_v(v', \Delta v)$ obtained from measurements taken by the spacecraft instrument. The two unknown functions $g_p(r)$ and $f_p(v)$ characterizing behaviour of the bow shock can be assumed (e.g. Fourier's series of polynomial forms) and then fitted (with various coefficients) to the equalities (3) and (4). The best fitted functions $g_p(r)$ and $f_p(v)$ can be used in further analysis of the bow shock properties.

The distributions $g_s(r)$ and $f_s(v)$ can be obtained from theoretical considerations because, as it was said previously, the trajectory of the spacecraft in the region of our interest can be approximated (with high accuracy) by Keplerian hyperbola with focus in the center of the planet. The equations of the hyperbola can be written in a parametric form (with parameter $-\infty < \xi < \infty$) as

$$\begin{aligned} r_s &= a\,(e \cosh \xi - 1) \\ t &= T_o\,(e \sinh \xi - \xi) \end{aligned} \qquad (5)$$

where

$$T_0 = \left(\frac{\mu a^3}{\alpha}\right)^{1/2}$$

and

$$\alpha = a\, m_s (\dot{v}_{s\,\infty})^2$$

In the above, m_2 is mass of the spacecraft and $v_{s\,\infty}$ is its velocity at "infinity" i.e. somewhere in the space far enough from the planet to neglect the gravitational energy of the spacecraft in comparison with its kinetic energy. However, the "infinity" distance should be chosen as the one after the last spacecraft trajectory correction before close encounter with the planet, because of the requirements of the conservation laws in evaluation of the trajectory properties. The symbol μ denotes the reduced mass of the spacecraft-planet system (and it equals almost exactly to m_s) e is eccentricity (> 1) and a is "semi-major axis" of the spacecraft orbit. The last two quantities can be found from the analysis of the general properties of conic curve and conservation laws of energy and angular momentum. After transformation one gets

$$a = \frac{G \cdot M}{(v_{s\,\infty})^2} = \frac{G\,M}{v_0^{\,2}} \; \frac{e+1}{e-1} \quad , \qquad (6)$$

$$e = \left(\frac{r_0}{a} + 1\right) \quad ,$$

where G is the universal gravitational constant and M is mass of the planet. r_0 is the distance of the closest approach and v_0 is speed of the spacecraft at the moment of the closest approach. A convenient approximate solution of the system of parametric equations (5) can be obtained in the following way; the parameter ξ can be evaluated as follows :

$$\xi = d \sinh u \qquad \text{for } \xi \leq 2.5 \; (t \leq 5\, T_0\, (e - 1/2))$$

or

$$\xi = n\left(\frac{2t}{T_o\, e}\right) \qquad \text{for } \xi > 2.5 \; (t > 5\, T_o\, (e - 1/2)) \tag{7}$$

with

$$d = \left[\frac{8\,(e-1)}{e}\right]^{1/2}$$

and

$$u = 1/3 \sinh^{-1} \left[\frac{3t}{T_o\, d\,(e-1)}\right]$$

Using properties of the hyperbolic functions and Cardan's rule, the hyperbolic sinus in equations (7) can be transformed to the following form:

$$\sin u = 1/2 \sum_{i=1}^{2} \left\{ B\left[1 + (-1)^i \left(1 + \frac{1}{27\, B^2}\right)^{1/2}\right] \right\}^{1/3} \tag{8}$$

with

$$B = \frac{3t}{d\,(e-1)\, T_o}$$

Further, the velocity of the spacecraft at the planetcentric distance r_s is

$$v_s(r_s) = \left[GM \left(\frac{2}{r_s} + \frac{1}{a}\right) \right]^{1/2} \tag{9}$$

The relationships (5) - (9) are convenient tools for investigation of the spacecraft dynamics.

The probability of finding the spacecraft in the interval r - r + dr is equal to the probability of finding the spacecraft inthe appropriate interval of time. Introducing the density of probability with respect to time p (t) one has

$$g_s(r)\, d\, r = p(t)\, d\, t \tag{10}$$

The distribution p(t) is uniform and it should rather be normalized in certain (long enough) interval of time than in the period of the conic curve because the spacecraft trajectory is not periodic. Taking the

normalization time equals to 2τ (symmetric with respect to the moment of the closest approach to the planet) one gets

$$\tau = T_0 \, (e \sinh \xi_\tau - \xi_\tau) \tag{11}$$

where

$$\xi_\tau = \cosh^{-1} \left[\frac{1}{e} \left(\frac{r_\tau}{a} + 1 \right) \right]$$

and r_τ is the planetcentric distance at which $t = \pm \tau$.
Taking the above into account one gets

$$g_s(\rho) \, d\rho = (c\,\tau)^{-1} \, [\rho^2 + 2\,c\,\rho + c^2 \, (e^2 - 1)]^{-1/2} \, d\rho \tag{12}$$

with

$$\rho = r/a \text{ and } c = G \cdot M/A \, (v_{s\,\infty})^2$$

where 2A is a chosen distance of observation.

Similar procedure (with a new dimensionless variable $w = (v/v_{s\,\infty})^2$ leads to the appropriate velocity distribution function

$$f_s(w) \, dw = (2\,\tau)^{-1} \left\{ (1 - w)^4 \, \left[1 - \frac{(1 - w)^2}{4w} \, (e^2 - 1) \right] \right\}^{-1/2} dw \tag{13}$$

The approach presented above is quite general and can be used to study any planetary megnetosphere investigated by spacecraft-based instruments.

To illustrate the method presented here we will use it for estimation of behaviour of Jupiter's magnetospheric bow shock and magnetopause during Pioneer 10 and Voyager 2 outbound passings, respectively. (Smith et al., 1974, 1976; Wolfe et al. 1974; Ness et al., 1979; Lepping et al., 1980a, 1980b). The number of BS outbound crossings of the bow shock by the Pioneer 10 instrument was equal to at least seventeen whereas the appropriate number of Voyager 2 crossing the magnetopause was equal to fifteen. As it was said earlier, these numbers are too small for correct representation of the probability functions, but, the best available so far and

making the partial illustration of the method possible. The probability functions P_r (r_1, r_2) built on these experimental data are shown in Figures 1 and 2.

It should be remembered that these data have some uncertainties associated with measurements because of a few, occasionally appearing, partial gaps in data during encounters, as for example the 8 hour gap indicated in Figure 2 with arrow. There are also some differences between appropriate magnetic field and plasma measurements. All regions of this sort of uncertainty are marked in Figures 1 and 2 by using broken lines. Also, these experiments (based on measurements of the magnetic field and plasma streams during crossing the bow shock and magnetopause) did not supply enough information (at least in form published so far) for taking of full advantage of the method proposed here. The numbers of crossings were not large in either of the missions mentioned above and the measurements were not oriented toward to detail registration of the relative velocities of the spacecrafts and the bow shock or magnetopause. Therefore, the construction of high reliability functions P_r (r_1, r_2) based on these data is difficult and the construction of the function P_v $(v_1, \Delta v)$ is in fact impossible for time being. Perhaps an additional combine analysis of the appropriate magnetic field and plasma stream measurements already existing for the region of our interest would yield some results reliable enough to build the functions P_v $(v_1, \Delta v)$ for Jupiter magnetospheric bow shock or magnetopause or both. Another way of obtaining such cmplete data would be an eventual spacecraft-based experiment capable to select the dynamic properties useful for getting full advantage of our method. Before such data are available, the only way to illustrate the application of our approach with using already

existing data is to apply our method to partial analysis of the problem i.e. to use it to limited analysis by construction only the position related functions P_r $(r_1, \Delta r)$, $g_s(r)$ and $g_p(r)$. It may be added that a reasonable using the four sets of measurements of all Pioneer and Voyager missions (as one data set describing behaviour of the Jupiter magnetosphere) would be incorrect because of the remarkable differences in geometry and dynamics of each close encounter. These differences are so distinguish that it is impossible to create a sensible method of statistical averaging of the data, that still form relatively small statistical ensemble.

The oscillations of the bow shock and the magnetopause along the spacecraft path has been assumed, for numerical illustration, as harmonic ones. Using the procedure presented above, the appropriate distribution functions can be given in analytical form:

$$g_p(\hat{\rho})\, d\,\hat{\rho} = (2\,\pi)^{-1}\,(1 - \hat{\rho}^2)^{-1/2}\, d\,\hat{\rho} \qquad (14)$$

where $\hat{\rho} = |\rho_{min} - \rho + 1|$; with a convenient choice for A as the amplitude of the oscillations (i.e. $2A = r_{max} - r_{min}$). Similarly;

$$f_p(\hat{w})\, d\,\hat{w} = (2\,\pi)^{-1}\,(1 - \hat{w}^2)^{-1/2}\, d\,\hat{w} \qquad (15)$$

where $\hat{w} = v/w\,A$ and w is oscillation angular frequency.
It may be worth adding that despite the sinularities, the distributions (14) and (15) have finite integrals (equal to $\sin^{-1}\hat{x}$) i.e. can be normalized not only on particular fragments of trajectory but also in entire oscillation interval.

The comparison of the theoretical probability P_r^{theor} (based on the predicted functions $g_s(r)$ and $g_p(r)$ given in equations (12) and (14), respectively) with the appropriate experimental probability P_r^{exp} (based

on measurements of Pioneer 10 and Voyager 2) is done in Figures 1 and 2 and as it can be seen from these they show similarity in shape.. However, it should be emphasized that the practical example shown above should be treated as an illustration only, of the approach presented here. As it was said before neither the number and accuracy of existing measurements is high enough for reliable statistical ensemble of data nor the oscillations of Jupiter's magnetosphere are harmonic ones. Also, a more sophisticated experiment would be desirable for full efficiency of the method. The data obtained from such measurements should allow one to build the experimental probability function of higher orders (e.g. momentum) in vectorial representation. The situation is much simpler in case of theoretical probabilities P_r^{theor} obtained from functions g_s, g_p, f_s, f_p etc. The latter functions can be represented by, for example, general Fourier series, and the class of these functions can be predicted or estimated pretty easily. Finally one can add that the analytical forms of the distributions g_s, f_s etc. give highly accurate approximations for the dynamic behaviour of spacecraft encountering with planet.

ACKNOWLEDGEMENT

The authors thank Dr. L. W. Klein from Goddard Space Center for supplying the detailed printouts of the spacecraft-planet encounters. This work was performed under National Aeronautics and Space Administration Contract N.

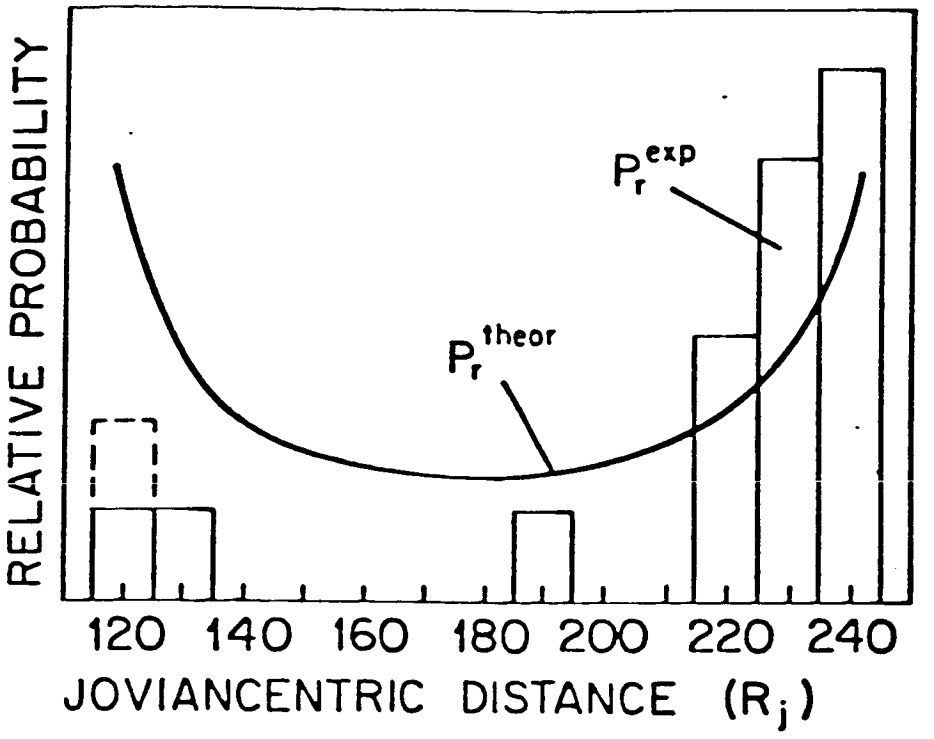
RELATIVE PROBABILITY
P_r^{exp}
P_r^{theor}
120 140 160 180 200 220 240
JOVIANCENTRIC DISTANCE (R_j)

J. Kunc

FIG. 1

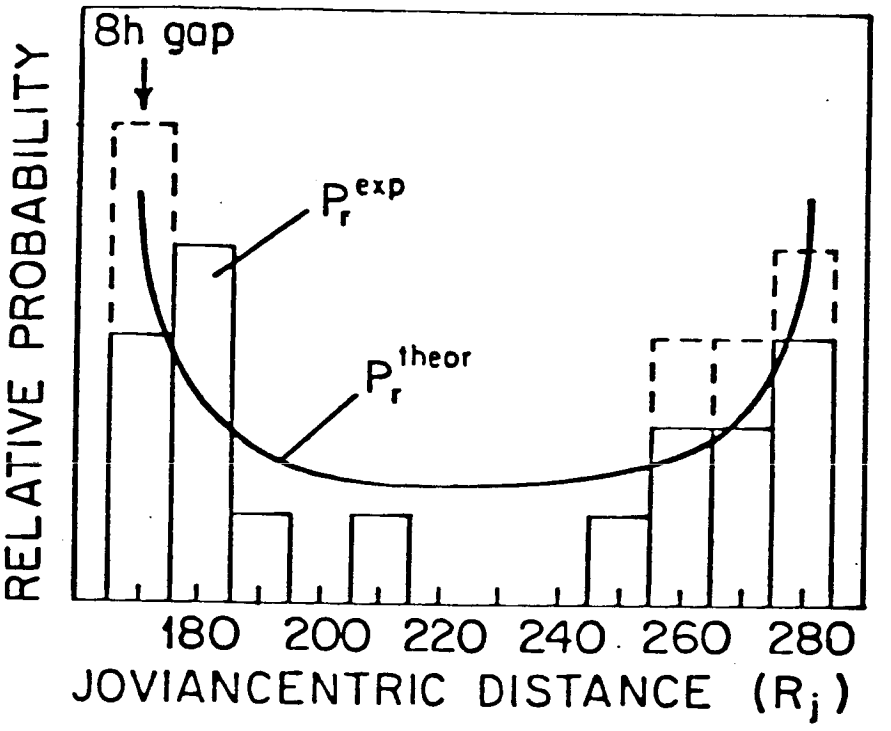
8h gap
RELATIVE PROBABILITY
P_r^{exp}
P_r^{theor}
180 200 220 240 260 280
JOVIANCENTRIC DISTANCE (R_j)

J. Kunc

FIG. 2.

REFERENCES

Lepping, R. P., Burlaga, L. F. and Klein, L. W., Jupiter's Magnetopause, Bow Shock and 10-hour Modulated Magnetosheath: Voyagers 1 and 2, NASA Tech. Memorandum 82033, 1980.

Lepping, R. P., Burlaga, L. F., Klein, L. W., Jessen, J. M. and Goodrich, C. C., Observations of the Magnetic Field and Plasma Flow in Jupiter's Magnetosheath, NASA Tech. Memorandum 82035, 1980.

Ness, N. F., Acuna, M. H., Lepping, R. P., Burlaga, L. F., Behannon, K. W. and Neubauer, F. M., Magnetic Field Studies at Jupiter by Voyager 2, Science, 206, 966, 1979.

Smith, E. J., Davis, L., and Jones, D. E., Jupiter's Magnetic Field and Magnetosphere, "Jupiter", ed. Gehrels, T., 788, 1976.

Smith, E. J., Davis, L., Jones, D. E., Coleman, P. J., Colburn, D. S., Dyal, P., Sonett, C. P. and Frandsen A. M. A., The Planetary Magnetic Field and Magnetosphere of Jupiter: Pioneer 10, J. Geophys. Res., 79, 3501, 1974.

Wolfe, J. H., Mihalow, J. D., Collard, H. R., McKibbin, D. D., Frank, L. A., and Intilligator, D. S., Pioneer 10 Observations of the Solar Wind Interaction with Jupiter, J. Geophys. Res., 79, 3489, 1974.